DESIGN AND DEVELOPMENT OF ADVANCED CASTABLE REFRACTORY MATERIALS

Robert Bruce Davis

B. S., Washington State University, Pullman Washington, 1976

M. S., Oregon Graduate Institute, Beaverton Oregon, 1998

A dissertation submitted to the faculty of the

OGI School of Science & Engineering at OHSU

in partial fulfillment of the requirements of the degree of

Doctor of Philosophy

in

Materials Science and Engineering

August 2001

The dissertation "Design and Development of Advanced Castable Refractory Materials" by Robert Bruce Davis has been examined and approved by the following Examination Committee:

Milt Scholl, Thesis Advisor
Associate Professor

David G. Atteridge
Professor

Jack McCarthy
Assistant Professor

Carl Palmer
Assistant Professor
Portland State University

Daniel Danks
Consultant

ACKNOWLEDGEMENTS

I would like to thank Dr. Milt Scholl, my thesis advisor, for the time, patience and attention he devoted to my research and the arrangements for financial support. I am grateful to Dr. Dave Atteridge, Dr. Jack Devletian, Dr. Jack McCarthy, Dr. Margaret Ziomek-Moroz, Dr. Lemmy Meekisho, and Dr. William Wood for their valuable instruction during my thesis work. Thanks are extended to other the members my dissertation committee Dr. Carl Palmer and Dr. Daniel Danks for their time and effort in reviewing the manuscript. I wish to thank the department's technical staff, namely Bob Turpin, Doug Davis, and Andy Huffstutter and the department secretary, Roxanne Workman, for the help and constant positive support they have provided to myself and the students throughout the years spent at the Oregon Graduate Institute. Acknowledgements would not be complete without recognizing my fellow students, namely, Graham Tewksbury, Heidi Davis, Dr. Hamid Faridi, Dr. Fabian Radulescu, Dr. Jim VanWinkle, Dr. Jinhong Yang, and Dr. Kevin Searles. Finally, I would like to express my deep gratitude to my wonderful family for their patience, support and encouragement over the last five years.

Dedicated to my daughter Charlotte,

my Mother and Father, Gloria and Bruce Davis, and my Wife Sharon.

TABLE OF CONTENTS

List of Tables

List of Figures

Textbooks and heaven only are Ideal;
Solidity is an imperfect state.
Within the cracked and dislocated Real
Nonstoichiometric crystals dominate.
Stray Atoms sully and precipitate;
Strange holes, *excitions*, wander loose; because
Of dangling Bonds, a chemical Substrate
Corrodes and catalyzes—surface Flaws
Help Epitaxial Growth to fix adsorptive claws.

From The Dance of the Solids
by John Updike
Midpoint and other poems
Random House, 1969

ABSTRACT

DESIGN AND DEVELOPMENT OF ADVANCED CASTABLE REFRACTORY MATERIALS

Robert Bruce Davis

Ph.D., Oregon Graduate Institute of Science and Technology
August 2001

Thesis Advisor: Dr. Milton R. Scholl

New formulations of castable refractory composite materials were studied. This technology is used to produce low cost composite concrete structures designed for high temperature stability, superior wear resistance and improved strength.

An *in situ* fired, castable cement installation is a heterogeneous structure divided into three zones according to the temperature history and microstructure. The properties of each zone depend on the predominant bonding mode between constituents. Each zone has a characteristic microstructure that influences the integrity of the monolith. The hot side may have a highly dense and developed network of ceramic bonds between constituent particles while the cold side may never reach temperatures sufficient to drive off free water. The thermal, structural and tribological properties depend on the microstructure and the type of bonding that holds the monolith together.

The phase distributions are defined by sets of metastable phase conditions driven by the local hydrated chemistry, nearest neighbor oxide compounds, impurities and sintering temperature. Equilibrium phase diagrams were used to select optimum compositions based on higher melting point phases. The phase diagrams were also used to target high temperature phase fields that are stable over wide temperature and stoichiometric ranges.

Materials selection of candidate hydraulic clinkers, high temperature oxides, and reinforcement phases were based on requirements for high temperature stability. The calcium aluminate ($CaO\text{-}Al_2O_3$) and calcium dialuminate ($CaO\text{-}(Al_2O_3)_2$) are common refractory clinkers used in castable refractory cements. The thermodynamics and kinetics of cement hydrate formation are well studied and suited to become the building block of a design for a superior refractory castable cement. The inert oxides mixed with the calcium aluminate clinkers are magnesia (MgO), alumina (Al_2O_3), spinel ($MgAl_2O_4$) and chromia (Cr_2O_3). The bulk of the experiments concentrated in the Al_2O_3 – MgO – CaO ternary system.

Materials selection criteria for reinforcement materials was based on improved high temperature stability, increased strength, reduced thermal expansion mismatch, low thermal conductivity and increasing wear resistance. The reinforcement phases selected for this investigation are zircon ($ZrSiO_4$), zirconia (ZrO_2), spinel ($MgAl_2O_4$) and dead burnt magnesia (MgO).

Batches of the formulations were tested for thermal conductivity, wear resistance and mechanical strength. Relative rankings of the formulations against commercial products indicate improved or similar performance with increased maximum temperature limits and improved thermal insulating power. The new cement formulations proved to exhibit superior high temperature stability with an increasing volume fraction of high temperature oxides. The addition of reinforcement aggregates and powder sizing to offset the loss of strength. The room temperature compression strength and wear resistance of the optimized formulations exceeded the properties of conventional refractory brick and castable cement tested concurrently.

DESIGN AND DEVELOPMENT OF ADVANCED CASTABLE REFRACTORY MATERIALS

1.0 PREFACE

This study investigates new formulations of castable refractory composite materials. These formulations combine three significant materials science advancements in ceramic technology: ceramic forming, ceramic firing and composite structures. The castable, shapeless, self-flowing, monolithic refractories are formed into useable shapes using techniques like gunning, spraying and ramming. These new low cost techniques provide for the formation of complex shapes and blending new raw materials to yield refractories with properties superior to any now in use. *In situ* firing of castable refractory linings has fundamentally changed the economics of production, operation and maintenance of refractory installations. Additionally, the study examines the benefits of composite technology used to increase strength and improve tribological properties through use of tailored reinforcement phases.

Industry demands for higher temperature processing of materials and products have increased the technical requirements of containment structures beyond common refractory materials. The next generation of high-performance refractory materials are expected to be resistant to conditions and environments that few materials could withstand. Refractories were considered as consumable products up until the last decade. Recognition of the economic benefits that favor use of longer lasting refractories is relatively recent. Demand for lower product contamination, higher yields and reduced maintenance costs has changed the economics of refractory technology.

Castable refractory technology coupled with ceramic-ceramic composite design and improved materials selection provide customized solutions to application problems.

The castable refractory cement is an engineered formulation of high-temperature ceramic oxides cast to final shape. It is comprised of two components: cement refractory clinkers and refractory ceramic oxides. Cement clinkers are materials that are calcined to produce chemical reactions between the constituents when exposed to water. Cement refractory materials are cast to their final shape and achieve strength by three bonding mechanisms: hydraulic bonding, mechanical interlocking and ceramic bonds. Castable refractory cements offer considerable economic advantages such as ease of installation, lower cost and quick-setting hydraulic reactions which provide superior unfired strength that shorten scheduled outages. Monolithic structures are gunned or sprayed to the final shape up to 20 cm thick. By contrast, conventional refractory bricks are made elsewhere and shipped to the job site and skilled masons are required to build structures.
By reducing manpower requirements and construction time, castable refractory products offer large potential savings to industry. Nevertheless, the castable refractory products have been unable to compete with premium quality bricks in the following three areas: extreme high temperature, high thermal cyclic loading and high erosion applications.

Castable refractory cement installations are heterogeneous and metastable structures. The cast structures are fired from one side and develop three important microstructure zones. The properties of each zone depend on the predominant bonding mode between particles. Figure 1.1 illustrates the cross section of an installed and initial fired castable cement.

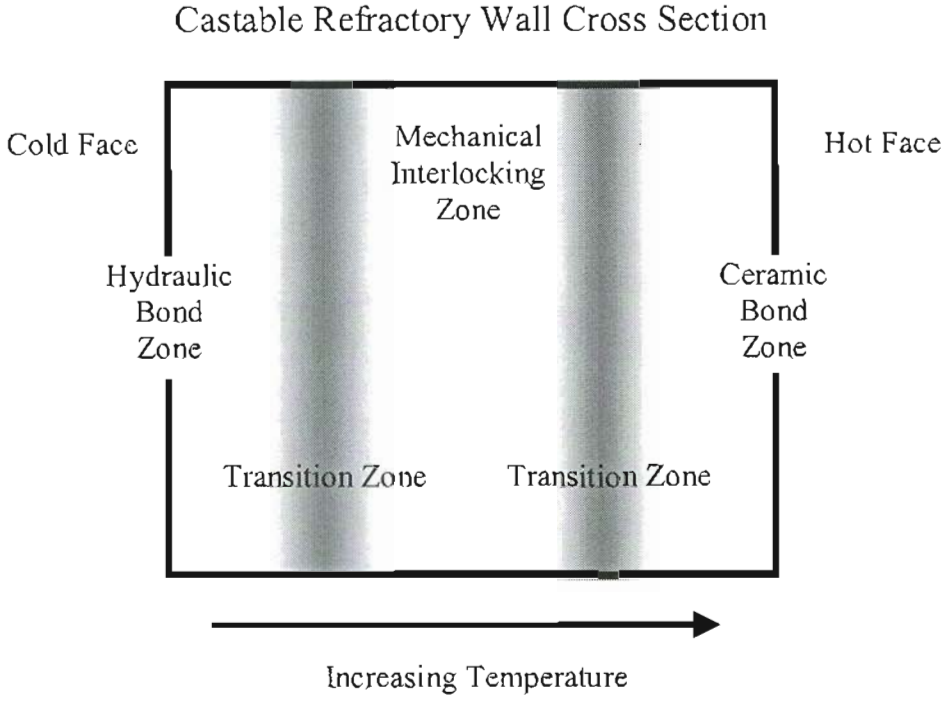

Figure 1.1 Illustration of castable refractory wall and the three principal bonding zones.

The *in situ* firing process complicates understanding the microstructure. The three zones have characteristic microstructures that influence the integrity of the monolith. The hot side may have a highly dense and developed network of ceramic bonds between constituent particles. The cold side may never reach temperatures sufficient to drive off water. The thermal, structural and tribological properties depend on the microstructure and the type of bonding that holds the monolith together.

Castable refractory cements initially rely on the hydraulic properties from hydrate structures for cohesive strength. Products of the hydration process contain physically and chemically bound water that is driven off at elevated temperatures. Physically adsorbed waters are driven from pores at temperatures around the boiling point of water. Evolution of chemically bound water occurs at higher temperatures. With all the water removed, the remaining cement structure is held together by the chemical bonds and mechanical interlocking of the dry hydrate skeletons. Sintering mechanisms contribute to molecular and atomic movements at temperatures greater than 900°C. As molecules reach their respective softening points ($0.8T_m$), atomic rearrangement takes place. The surface free-energy of the former hydrate structures causes the cement to experience a

deduction in volume and free energy of formation causes compounds to form that quickly bond particles at contact points. The characteristics and properties of the bonding phase depend on the cement's hydrate chemistry and microstructure.

Conventional low-cement premium quality castable refractory cements are limited to operating temperatures less than 1400°C. The strength and wear resistance drops dramatically by creep processes and the thermal conductivity increases through densification. Higher temperatures produce significant molecular movements and formation of an increasingly larger liquid-phase volume fraction. The disruption of the microstructure is exacerbated by phase transformations that occur in the bonding phase. The lower shear modulus of the glassy phases accelerates grain displacements and microstructure degradation.

Common refractory cement clinkers contain silica, calcia, iron and other impurity oxides that soften and form liquid compounds at lower temperatures. The limited solubility of corundum and calcia promote intermediate phase formation. Some of these impurities tend to form either glass or low melting point ternary compounds. Glassy phases are detrimental to a compound's resistance to thermal shock and high temperature creep and are susceptible to corrosion at elevated temperatures. Some examples of problems created by impurities are:

- silicate-rich glassy phases undergo polymorphic transformations,
- thermal cycling across the transformation temperatures drastically lowers the structural integrity of the monolith, and
- dimensional mismatches from thermal expansion differences lead to interface degradation.

Dozens of dependent and independent binary, ternary, quaternary and quinary component systems are present in the castable refractory. Thermally activated reaction processes compete for dominance leading to molecular chaos at elevated temperatures. Table 1.1 lists the energetic thermally activated processes in ionic ceramic cements. Loss of integrity in castable installations is directly related to the disruption of the microstructure. A new look at the materials science of a castable refractory concludes improvements are possible. Materials science is guided by the fundamental understanding that the microstructure defines the material properties. Materials selection

and reinforcement are used to produce a superior microstructure and high temperature properties of the castable cement. This research undertakes the materials selection and development of castable refractory formulations to increase high temperature stability, and strength, reduce thermal conductivity and improve wear resistance.

In summary, the structural integrity is defined by the microstructure which, in turn, defines properties of the castable refractory cement. The microstructure of the composite castable cement is a result of materials selection, temperature and thermal history. The materials selection defines the temperature limits based on thermally activated processes. The final microstructure of an *in situ* fired castable refractory is a combination of hydration reaction products and elevated temperature reactions of these reaction products interacting with the inert oxides or non-reacted cement clinkers.

Table 1.1 Energy Processes in Ionic Solids

Processes	**Driving Force**	**Joules/mole @1000°K**	**Comments**
Fracture	$V_m\sigma^2/(2Y)$	0.5	Y is Young's Modulus, σ is stress at failure and V_m is the molar volume
Grain growth	$2\gamma_{gb}/r$	20	γ_{gb} is grain boundary energy and r is particle radius
Sintering	$2\gamma/r$	100	γ is surface energy term
Creep	σV_m	1000	σ is applied stress on a molar volume, V_m
Crystallization	$\Delta H\Delta T/T_m$	3000	ΔH is the enthalpy of transformation, ΔT is undercooling and T_m is melting t
Inter diffusion	$RT(x_a \ln x_a + x_b \ln x_b)$	5000	
Oxidation	ΔG°_{form}	50,000 to 500,000	ΔG°_{form} is free energy normalized to a mole of oxygen

The purpose of the research program was to develop a castable composite cement material with wear resistance, strength, high temperature stability and thermal conductivity properties superior to other castable and conventional ceramic brick refractory products. The research consists of five phases.

- A survey of the literature to benchmark industry status, study refractory cement research and elucidate the microstructure interactions that are important to the properties. These microstructure interactions are the target for improvement.
- Materials selection of candidate hydraulic clinkers, high temperature oxides, reinforcement phases and reaction products.
- Microstructural study of the candidate formulations before and after exposure to elevated temperatures. The different microstructures are used to compare to the properties.
- Thermal property characterization of selected matrix and reinforcement formulations.
- Characterization of the tribological and mechanical properties of selected formulations.

The thesis consists of in six sections and four appendices. The literature review presents the state of the refractory industry and the technology behind the castable refractory cement. The literature review also provides the basis for the development of high temperature ceramic materials. The experimental plan follows the literature review and provides a listing of the experiments used to validate the new formulations. The experimental data was extensive and is presented in the result section. Additional details and procedures used are further presented in the appendices.

2.0 INTRODUCTION

2.1 Literature Review

2.1.1 Introduction

The use of ceramic refractory materials dates back to the dawn of civilization. Refractories have been used to line fire chambers, ovens and pottery kilns. Early refractories were made of natural clays and sands. Over time, man discovered that certain natural mud formations were better for pottery and refractory bricks. The first refractories were simple formulations, composed of several parts clay and one part lime. Mineral-rich ores were added to improve the fired density and impart color. Local ores and clays produced a regional uniqueness to the refractory products. Particle sizing and benefaction of minerals achieved improved performance in the early refractories. Tree pitch and alkaline soaps were added to formulations for increased strength. Greater strength allowed for more complex shapes that further expanded refractory applications. Archaeologists trace the spread of cultures using assays for indigenous impurities. Advancements in refractory technology claim an important cornerstone in the development of modern materials science.

The refractory materials are usually blends of several oxides. Typically, refractory blends have two main components and a number of minor constituents that vary according to the origin of the raw materials. Refractory ceramic material are complex, multi-phase microstructures with limited phase-to-phase solubility. Compositional equilibrium is difficult to achieve in refractory ceramics.

Roy[1] describes the ceramic refractory microstructure as a series of heterogeneous equilibrium processes between ceramic grains. High grain boundary energies, porosity and slow diffusion kinetics retard equilibrium processes. Sintering processes in ceramic powders are characterized as closest-neighbor metastable equilibrium reactions.

2.1.2 Refractory Classifications

The United States Department of Commerce categorized refractory materials as either clay or non-clay. The principal differences between the two are the types of raw materials used. The clay type ceramics are made from ores and clays with little or no chemical benefaction. Non-clay refractory products are considered premium products in part due to the extra cost using processed raw materials. The Commerce Department has further classified refractories based on the composition used for each of the principal product forms: bricks and shapes, unshaped mortars, castables and gunning mixes. These classifications are held throughout the industry as Standard Industrial Classification (SIC) 3255 and 3297 for clay and non-clay, respectively. [2]

A more common nomenclature, accepted worldwide, differentiates between the silicate, acidic and basic types of refractories. The refractory types are based on the mineral chemistry and performance [3]. For example, a distinguishing feature of basic refractories is that they are resistant to attack by basic slags and oxides in steel making. The common refractory oxides are alumina (Al_2O_3), silica (SiO_2), calcia or lime (CaO), magnesia (MgO), chromia (Cr_2O_3), and zirconia (ZrO_2). Table 2.1 lists the shorthand notation and melting temperature for the common refractory oxides. Refractories that contain SiO_2 or ZrO_2 are labeled acidic and those with MgO, CaO, Al_2O_3, and Cr_2O_3 are considered basic refractories. Acid refractories will react unfavorably when exposed to high-temperature acid environments and vice versa for basic refractories. The refractory industry commonly uses designations of acid, basic and neutral refractories when describing the properties needed for an application. [4,5,6,7]

Table 2.1 Common Refractory Oxides and Nomenclature

Phase	Chemical Formula	Mineral Notation	Melting or Decomposition Temperature, °C
Silica	SiO_2	S	1723
Alumina	Al_2O_3	A	2050
Magnesia	MgO	M	2800
Monticellite	$CaO{\cdot}MgO{\cdot}SiO_2$	CMS	1495
Merwinite	$3CaO{\cdot}MgO{\cdot}2SiO_2$	C_3MS_2	1575
Calcia	CaO	C	2572
Doloma	$MgO{\cdot}CaO$	MC	
Forsterite	$2MgO{\cdot}SiO_2$	M_2S	1890
Spinel	$MgO{\cdot}Al_2O_3$	MA	2135
Magnesia ferrite	$MgO{\cdot}Fe_2O_3$	MF	1750
Magnesia chromite	$MgO{\cdot}Cr_2O_3$	MK	2400
Mullite	$3Al_2O_3{\cdot}SiO_2$	A_3S_2	1810
Enstatite	$MgO{\cdot}SiO_2$	MS	1557
Dicalcium silicate	$2CaO{\cdot}SiO_2$	C_2S	2130
Dicalcium ferrite	$2CaO{\cdot}Fe_2O_3$	C_2F	1435
Chromia	Cr_2O_3	K	2275
Zirconia	ZrO_2	Z	2690

2.1.3 Refractory Industry Status

The refractory industry is a worldwide sector of commerce. Research and technological advancements are documented in accepted journals that span ceramic engineering, iron producing, material processing, atomic energy and metallurgical industries. The economic health of the industry has been reviewed by a number of experts and consultants [8-13]. Most conclude that the industry has not fully recovered from a downturn in steel production through the 1980's and 1990's. The depressed

market and high inventories of raw materials combined to financially limit the long-standing refractory industry giants. The Pacific Rim economic problems and the decline in U.S. steel production resulting from the North American Free Trade Agreement produced a negative effect on United States refractory industry. The steel industry's recovery in mid 1990's brought growth in the non-clay type refractory product sectors. But, overall the refractory industry has not met expectations for growth and continues to be soft [9,10]. Strategic alliances, licensing agreements and mergers have kept the industry competitive. The United States is a leader in research and development, but major acquisitions have transferred the new technologies to foreign holdings. The more noted acquisitions since 1994 are Saint-Gobain acquiring Norton, Osram/Siemens acquiring GTE Products, Sulzer took over Perkin-Elmer's Metco Division and TDK acquiring Allen-Bradley. The foreign interests have captured the U.S. technology base as an edge against raw material oversupply and increased environmental regulation costs.

The refractory industry's economic periods are tied to the world's production of steel. Heine [9] and Semler [14] stated that > 50% of the refractory industry is dedicated to iron and steel making. Advancements and changes to iron and steel production affects refractory material demand. Clean steel technology shifted demand away from the low cost clay refractories because of product contamination. The demand for high-duty technical refractories increased the need for new low-cost benefaction processes and refined raw materials. The drift away from the large blast furnace to the smaller basic oxygen furnace and electric arc furnace is an example of the trend. Between 1975 and 1997 the number of operating blast furnaces dropped from 197 to 43 (79% reduction) while pig iron steel production stayed the same, Semler [14]. The same period saw a reduction of coke batteries and ovens from 5,447 to 4,321 installations. Iron and steel made using advanced melting processes are cleaner partially because of the use of premium non-clay type refractories.

The application of technical refractories has reformed the industry from providing consumable product to a product that may last the design life of the structure. The refractory linings are in direct contact with molten metals, slags and glasses. Refractory loss rates are measured in kg/ton of product produced. With the technical refractories the overall refractory consumption rate has dropped from 25 kg/ton of steel to less than 10

kg/ton of steel produced over the last 15 years [15]. Re-lining a furnace had been a frequent occurrence, but now maintenance outages are less common. Improved refractories have changed the furnace design. Fedoruk et al. [16] discusses how the furnace design and heat balance are now specific to the technical specifications of the refractory materials. Similarly, the economics now make it common to design a furnace lining as a composite using different types of refractories in different zones to enhance thermal, structural and corrosion performance. New practices include using layered thermal walls to optimize the structurally weak thermal ceramic and the structurally strong basic refractory.

High purity nickel alloys, chromium-rich duplex steels, zirconium, and titanium alloys produce aggressive slags. The non-clay, corrosion resistant refractories are the only products that can meet the technical specifications for product purity. The furnaces are smaller and use magnesia-chrome refractories with designed thermal control to limit overheating. Thermal stress distribution is an increasingly important consideration with the improved thermal efficiencies and high temperature gradients. Steel arc melting furnaces represent large capital investments, and higher performance (higher value) refractories are now used for longer life. High alumina refractories continue to demonstrate good performance in arc melting applications. In 1996, steel mill use of extra high alumina refractories has increased three-fold [16]. The premium alumina refractories are made from higher purity forms of alumina such as tabular alumina, fused cast alumina, or fused mullite [25].

Furnace maintenance and poor ladle performance continue to plague steel manufacturers. New monolithic and expansive refractories have been developed to limit penetration and slag corrosion. Initially the Portland cements were blended with alumina for temporary patch [16] materials in the steel making refractories. The success of these patches led to the development of high-density alumina cement. High alumina castable refractories saw increased use in severe duty blast furnace troughs. The castable refractory directly increased steel production; enabling higher tapping rates and longer tapping times [16,17,18]. Castables have a significant installation cost advantage. Research brought about the development of low cement castables [20] and self-flow castable [19]

formulations. Castable monolithic refractory applications have increased with the improved quality and higher levels of thermal performance availability [21,22].

Fundamental changes have occurred in refractory installation techniques with the use of monolithic castables. Cold pressed, rammed, cast and gunned castable cements are relatively new techniques. Conventional pressing and sintering bricks is a manpower and energy-intensive process. The requirement for large inventories of many shapes and the need for skilled craftsmen to install archways and roof sections are not necessary with castable products. Subrata Banerjee[23] indicated that the monolithic and castable products have overtaken 60% of the refractory market.

The economics of waste disposal is the driving force behind the need to recycle spent refractory materials. The increasing profitability of recycle programs is also credited with the re-use of ceramic refractory powders. Oxnard [24] credits Professor Gilbert Robinson at Clemson University in the 1960's with developing blends with recycled "inert" filler (grog).

Use of fired refractory grog faces the challenges of high contaminant levels and government restrictions for landfill disposal. The regulations that affect the refractory recycle and disposal options are established by the Conservation and Recovery Act of 1967 (RCRA). The regulations take into consideration how the refractory was generated and the composition of the refractory at the time of removal. The Conservation and Recovery Act was amended in 1984 by the Hazardous and Solid Waste Amendments which give the responsibility of refractory disposal regulations to the Environmental Protection Agency (EPA). EPA rules 40CFR 262.11 provide for the generator of the waste to be responsible for designation of the waste per 40CFR 262.30. According to Alexander [25] the EPA does not differentiate between trivalent or hexavalent chromium compounds and considers all forms of chromia-containing refractories as hazardous.

2.1.4. Refractory Materials

Refractory science is old and many refractory terms predate the modern understanding of materials. The terms are rooted in Geology, Mineralogy and Metallurgy. Common refractory names are fireclay, silica, heavy duty and high duty

alumina, insulating firebrick, mullite and acid brick. Refractory standardization has long been a problem because the compositions do not necessarily reflect the performance, the microstructure, powder processing, porosity, manufacturing and application impact performance. The America Society for Testing and Materials publishes refractory composition ranges as they become standardized through the consensus process [26]. The minerals and ores used in refractory manufacture are alumina, andalusite, bauxite, dolomite, kyanite, magnesite, magnesia, chromia, mullite, silica and more recently zirconia.

2.1.4.1. Aluminosilicate Refractories

Raw materials used for the first refractories were part of the alumina silica system. Aluminosilicate refractories are the mainstay product for lower temperature applications (800 - 1000°C) because of their low cost, availability and good performance. Table 2.2 lists the composition range of the common refractories in the aluminosilicate system.

Table 2.2 Common Aluminosilicate Refractory Types [26, 3]

Refractory	**Specific Class**	**Al_2O_3 wt %**
Fireclay low-duty	Siliceous	7-22
Fireclay medium-duty	Firebrick	22-38
High duty & Super duty	Aluminosilicate	38-50
Sillimanite	Aluminosilicate	50-65
Mullite	Mullite	65-75
High Alumina	Corundum (bauxite)	75-98

Fireclay is one of the more common clay refractories. Fireclay is a mineral blend of hydrous alumina, alumina silicates, iron oxides and titania. The alumina content ranges from 7% to 38%. In the lower alumina fireclay refractories the iron oxides and impurities define the thermal properties. The stability at elevated temperature increases with increasing amounts of alumina and decreases with increases in silica compounds and

other impurities. Synthetic fireclay is a blend of the mineral kaolinite ($Al_2O_3.2SiO_2.H_2O$) with iron oxide and titania. The iron oxide increases the grain boundary-bonding phase, and the titania increases the viscosity of the high temperature glass phases during the brick making process. Fireclay compositions vary with the kaolinite mined from region to region. The fireclay refractories are typically graded according to the resistance to temperature [3]. Classifications of low-duty, medium-duty, high-duty, super-duty or super-duty-high alumina are used to differentiate the refractories. High-alumina refractory products out-perform fireclay refractories for structural properties and resistance to alkali vapors. These refractories are generally composed of mineral ores with higher alumina, like bauxite, kyanite, silliminite and andalusite. Extensive benefaction or preprocessing can be avoided by selecting the optimum blend of ores.

A special form of the alumina-silicate refractory is the naturally occurring mineral Mullite. Mullite is a high temperature compound in the alumina silica binary system, $Al_6Si_2O_{13}$. Mullite is the mineralogical name given to a naturally occurring mineral found on the Isle of Mull located off the West Coast of Scotland [15]. The natural mineral abundance is not sufficient to supply industry needs but its natural composition possessed excellent refractory properties. Mullite is a unique natural refractory material with good thermal shock resistance and strength. Most alumina refractories with silica will form mullite at elevated temperatures because of the wide stoichiometric range.

The alumina-silica ratio (60/40) of andalusite makes it a natural refractory. The natural mineral is relatively inert and does not need benefaction or calcination prior to use. It converts to mullite when heated above 1200°C. Andalusite is mined principally for refractory use. The favorable characteristics of a mulletized andalusite include low thermal conductivity, good slag and creep resistance, high hot strength and low porosity. Kyanite, bauxite kaolin and bauxite mixed with other alumina and silica clays produce mullite at temperatures greater than 1150°C. Andalusite and sillimanite ores do not require blending before conversion to mullite.

Pure synthetic mullite, alumina and quartz are produced in electric arc furnaces; the product is called fused mullite [27]. The amount of mullite formed varies on the chemical composition and thermal cycle. Mullite has a useful thermal limit of 1650°C,

and then the properties degrade until it finally dissociates into corundum and silica at 1840°C. Table 2.3 lists the common aluminosilicate refractories and the Mullite conversion temperatures.

Table 2.3 Temperature Conversion to Mullite

Common Mineral Clay	Conversion Temperature (°C)	Volume Change
Kyanite	1350-1380	18% expansion
Andalusite	1380-1400	2-4%
Sillimanite	1550	Little
Bauxite (domestic70%)	1650	20% reduction
Kaolin (pure)	1750	Little
Alumina and Silica (pure)	1750	Little
Mullite to Fused Mullite	1840	2-4% reduction

Extra high alumina refractories are high-density forms of bauxite and alumina. Fused cast and high-sintered products are used for mechanical stability and durability. The higher density materials are processed at higher temperatures and calcined then crushed, sized, pressed and sintered into bricks and shapes. Extra high alumina refractory contains greater than 87% alumina that produces an equilibrium structure of alumina and mullite.

2.1.4.2. Expansive Type Refractories

The "ladle type" classification of clay refractories is another term for expansive cements. They are high-density products known for expansion with heat. Kyanite and andalusite are used, and the conversion to mullite and corundum produces a volume expansion. The expansion during the transformation acts to seal the seams between cracks and joints, therefore preventing liquid metal from attacking the ladle. Ladles are relatively small and can be sintered as a single unit providing a seamless barrier between

molten metals and the steel ladle. The ladle types of refractories were the first monolithic refractories available. The good performance of ladle monolithic products strongly influenced the development of plastic ramming mixes and castables refractories.

2.1.4.3. Premium Refractories

Basic refractories are refractory products made with calcined magnesia, blended dolomite, chrome ore and carbon. Magnesia refractories are known for their high thermal stability. Basic refractories are based on the mineral periclase, which is the solid solution form of magnesia. Calcia, silica, alumina and alumina spinel are soluble in periclase. The magnesia can be hydraulic and absorb CO_2 and H_2O to form hydrates. The reactivity is reduced when made denser by heating between 1500° to 1700°C. The dense non-reactive form of magnesia is called "dead burnt magnesia." Seawater derived magnesia contains excess calcium. A common magnesia-based refractory product is produced using dead burnt magnesia and wood pitch as a binder. Magnesia refractory thermal performance is related to the impurities and grain-boundary phases. Higher purity magnesia is produced from the seawater precipitation processes. Low cost basic refractories are made from the calcination of natural mineral dolomite, $CaCO_3.MgCO_3$. Further benefaction of the magnesia-dolomite refractories is not cost effective as compared to the seawater-produced magnesia. Table 2.4 lists the composition ranges for the three grades of magnesia-based refractories.

Table 2.4 Composition Range of Magnesia Basic Refractories, wt %

Brand Name	Description	MgO	Fe_2O_3	Al_2O_3	CaO
Sintered Magnesia	Clinker	96-99	0.2	0.2	0.6-2.4
Sintered Doloma	Clinker	39-40	0.6-1.0	0.3-0.8	57-58
Fused Magnesia	Non reactive	97-98	0.1-0.5	0.1-0.2	0.9-2.5
Harklase Magnesia	Non reactive	98.2	0.2	0.2	1.4
SSH Magnesia	Spinel	85.0	0.2	13.8	

Magnesia refractory fabrication requires the addition of silica, alumina and iron oxide to form a low melting point phase to bond periclase grains. The silicate-bonding phase is a critical microstructure feature, which is influenced by the CaO/SiO_2 ratio in magnesia refractories. High ratios produce more C_2S and C_3S calcia compounds and low ratios produce more glassy-bond phase C_3MS_2, CS, CMS, and M_2S compounds. Alumina and iron oxides can be added to toughen the bonding matrix.

A class of basic refractories also contains chromite ores. The chromite refractories are highly corrosion resistant and exhibit superior refractoriness or refractory qualities. The first chrome refractory products were made from naturally occurring chrome ores. Chromite refractories found application in the open-hearth steel reduction furnaces in France in 1879. Ten years later the chromite refractories were used in U.S. steel production furnaces. The natural ores were complex solid solutions with spinel type crystal structures. The two principal spinel compounds were picrochromite ($MgO{\cdot}Cr_2O_3$) and ferrous chromite ($FeO{\cdot}Cr_2O_3$). Both compounds possessed high temperature stability and wide stoichiometric range. The natural mineralogy of the ores served as a map for a number of synthetic refractory materials. Chromite or synthetic magnesia chromia spinel is preferred in atmospheric, high alkaline chemical reactor vessels and glass furnace applications. Chromite bricks find use in high-temperature applications. Synthetic chromite blended with magnesia has been used where high corrosion resistance is needed.

Chromite refractories are being phased out as open-hearth furnaces are retired and clean steel technologies come into dominance. Electric arc, oxygen degassing and vacuum furnace technologies do not need the high alkaline slag resistance. Environmental concerns for disposal of spent brick has also contributed to the decline of chromite refractories. The hexavalent chromium is a listed carcinogen, and the concern for the volatilization of the chromite during use has been referenced [24].

The toxic properties of the chromium-containing refractory oxides were reviewed by Bray [28]. The carcinogenic nature of chromium is based on the valance state and the solubility. Chromium compounds used in refractories have oxidation states +2, +3 and +6, that correspond to the oxides CrO, Cr_2O_3, CrO_3, respectively. Divalent chromium is unstable, and rapidly oxidizes to the trivalent form. The more common forms are the

trivalent and hexavalent states. Trivalent chromium oxides have low solubility in water, acids, alkalis and alcohol. It does not enter the tissue, and therefore the toxicity is low. Chrome ores with trivalent chromium do not appear to be carcinogenic. Hexavalent compounds are thought to be toxic because they are strong oxidizers. The hexavalent chromium reacts with tissues and affects the skin, lungs and nasal passages. Because of the unknowns with chromium-containing materials, the Occupational Safety and Health Act, Resource Conservation and Recovery Act and the U. S. Environmental Protection Agency regulate their installation, use and disposal [25,28,29,30].

Hexavalent chrome is formed at elevated temperatures and alkali environments. These conditions are present in some refractory applications. The common hexavalent compounds are found in the chromia-calcia system: $CaCrO_4$, $3CaO.2CrO_3$, $2Cr_2O_3$ and $9CaO.4CrO_3.Cr_2O_3$. The chromite-magnesia system has only one intermediate compound that is the trivalent spinel, $MgCr_2O_4$. Several of the commercially available magnesia-chrome refractories are listed in Table 2.5.

Non-clay refractories are known for high cost due in part to benefaction of the raw material. Lower impurities produce better performance. Non-clay refractories exhibit high density and durability and are fired at higher temperatures. Economics drive the trade off between refractories made from natural ores and clays or synthetic materials. The high relative cost of synthetic products continues to limit their application. Over the last 10 years, a greater emphasis has been placed on synthesis of refractory oxides for purity and improved performance. Synthetic refractories remain only special-use items.

Table 2.5 Composition of Commercial Magnesia-Chrome Refractories, wt % [26,32]

Brand Name	Description	MgO	Cr_2O_3	Fe_2O_3	Al_2O_3	Other
CRL Guidon	Magnesia-chrome, fused grain	61.3	17.3	11.10	8.10	2.20
CRL Nucon 60	Magnesia-chrome, direct-bonded	60.6	17.0	9.0	10.7	2.7
Novus	Magnesia-chrome, direct-bonded	31.9	44.6	12.4	8.6	2.5
CRB-20	Chrome-magnesia	31.6	26.8	12.1	22.5	7.0
CRL Nucon 70	Magnesia-chrome, direct-bonded	70.2	12.3	6.4	8.5	2.6
C104 Electrocast	Magnesia-chrome, fused cast	56.5	20.0	10.5	8.0	5.0
REXAL 4NA	Magnesia-chrome, direct-bonded	62.3	15.5	7.5	11.7	3.0
NAARMAG FG	Magnesia-chrome, rebonded fused	62.0	18.0	12.0	6.3	1.7
RUBINAL RNA	Chrome-magnesia	36.2	26.1	12.5	20.9	4.3
DH45U	Magnesia-chromite	70.9	19.2	4.4	3.6	
DH45UC	Magnesia-chromite	66.9	22.7	5.5	3.2	

2.1.4.4 Castable Refractories

Castable refractories originated from common hydraulic cements and evolved into a highly specialized class of high temperature materials made from calcium aluminate cements (CAC). Castable or shapeless refractories are an engineered product that use hydraulic setting clinkers to gain high green strength and the high thermal stability of calcium aluminate compounds (1400° to 1600°C). The castable refractory can be poured,

pumped or sprayed in place. Following a relatively short cure cycle, the castable is dried and fired to produce a structural ceramic. Castables are finding increasing application because of the possible complex shapes, low cost installation and *in situ* sintering.

The cured castable product is a heterogeneous distribution of hydration reaction products, unreacted clinkers and porosity. The castable cement particles are bound together by hydration reaction products of calcium aluminate. The structural hydrates use silica, calcia, alumina and ferrous oxides as the building blocks. These oxides form bonding phases that are useful for higher temperature applications. Improvement in purity and the quality of calcium aluminate enable still higher temperature use. Improved particle sizing and deflocculants produce better flow characteristics and allow the cement powder to be pumped. Products applied by a gunning or spray application process have greater economic advantage. Higher temperature applications of castable cement increased with the development of low, ultra low and no-cement castables. The reduction of calcia and silica in these formulations lowered the volume fraction of material available to form lower melting point eutectic compounds.

The no-cement, self-flow, low-water "shotcrete" castable technology now represents the state of the art. But even with these improvements, they lack the properties of some of the conventional refractory brick type products. Workmanship, cure times and drying are critical to the final performance of the castable. Uneven application thickness, water variation, uneven temperature distribution and water vaporization in pores are common problems. *In situ* sintering is also critical to the castable service life. Excessive thermal gradients increase stress across the wall and cause cracking that propagates upon cyclic operation.

2.1.5 Cement Materials

Cements are synthetic materials that use hydrates to bind powders and reinforcements into agglomerates for dimensional shape control. Cements are optimized to develop high strength through chemical and mechanical processes. Cements were common construction materials prior to the Roman era. Joseph Aspdin of England patented a standard composition range for hydraulic cement in 1824. Aspdin produced

cement by calcining lime and clay. The blend was mixed with water and set into a stone-like surface. The color and texture of the hardened cement was similar to stone quarried near Portland in Dorset [33,34] and therefore called Portland cement. The discovery produced an important structural material that can be made from easy to obtain low cost materials.

Portland cement is a term that describes a specific composition of mineral compounds that contain calcia, silica and alumina as the principal constituents. The raw materials consist of limestone ($CaCO_3$), silica (SiO_2), alumina (Al_2O_3) and iron oxide (Fe_2O_3). These mineral constituents are pulverized and calcined to produce a cement clinker. Several of the common cement clinkers are shown in Table 2.6. Minor concentrations of other mineral compounds are also found in cements. Common cement impurities are MgO, TiO, MnO and the alkali oxides KO and NaO. In sufficient quantities, these impurities can influence the properties of the cement. The alkali reactions with calcium hydrates are detrimental for most refractory applications. The Portland cement is limited to temperatures between 400° and 600°C. The alumina-rich clinkers exhibit higher refractoriness and are more resistant to alkali oxides than the others.

"Ciment Fondu" is the icon for the commercial manufactured calcium aluminate cement, patented by J. Bied in 1908. The initial preparation of alumina-rich cements was in response to the demand for sulfate resistance in the Portland cements. A series of calcium aluminate products are produced based on the eutectic reactions between calcia and alumina, (as illustrated in the phase diagrams listed in Appendix A). Fondu cement is a collection of several calcium aluminate clinkers. Fondu is dark brown due in part to the high iron, silica and calcia content. The clinker for this cement is prepared by calcining raw materials calcia and alumina ores (limestone and bauxite). The fused, very dense clinker is moisture stable. Fondu cement composition is approximated to have a total alumina content of 40% and at least 50% of that is in the form of calcium aluminate (CA) and 16% iron oxide content. The remainder of the alumina is either bound into an alumino-ferrite or free alumina.

Table 2.6 Cement Clinkers [33,34]

Name Chemical	Composition	Mineral Notation	Melting Point, °C
Tricalcium Silicate	$3CaO.SiO_2$	C_3S	
Dicalcium Silicate	$2CaO.SiO_2$	C_2S	
Tricalcium Aluminate	$3CaO.Al_2O_3$	C_3A	1542
Tetracalcium Aluminoferrite	$4CaO.Al_2O_3.FeO_2$	C_4AF	
	$12CaO.7Al_2O_3$	$C_{12}A_7$	1415
Calcium aluminate	$CaO.Al_2O_3$	CA	1605
Calcium hexa aluminate	$CaO.6Al_2O_3$	CA_6	1860
Calcium dialuminate	$CaO.2Al_2O_3$	CA_2	1789

2.1.5.1 Calcium Aluminate Cements

Calcium aluminate cements are produced from lime and a high alumina or aluminous material mixed at temperatures between 1450° and 1600°C. The molten clinker is poured from the furnace, solidified and crushed to a high surface area. The essential hydraulic component is a CA or monocalcium aluminate phase. The commercial calcium aluminate cements contain the aluminate phases $C_{12}A_7$, CA, CA_2 and CA_6. Other calcium aluminate variations are commonly differentiated by the iron, silica and calcia concentrations. The higher temperature clinkers are produced with higher alumina and may include α-Al_2O_3 phase.

The phase identification and composition of the commercial calcium aluminate cements are reviewed by Taylor [34]. The phase equilibria relating the formation of the calcium aluminate cement clinkers are dependent on raw materials, sintering processes and the reaction conditions. The commercial mixtures can vary from the simple CA and CA_2 to the full range of phases in the CaO-Al_2O_3-Fe_2O_3-SiO_2 system. Under oxidizing conditions the possible equilibrium assemblages are four phase groups of CA-C_2S-C_2AS-Fe_2O_3 and CA-C_2S-$C_{12}A_7$-Fe_2O_3. The phases CA, C_2AS and Fe_2O_3 are solid solution single phases in each phase groups.

Determination of the quantitative phase composition is difficult due to the complexity and the variety of the possible phases combined with wide ranges of solid solutions and the departure from equilibrium during the manufacturing process. The most impure form of commercial calcium aluminate cement is the Fondu composition. Taylor reports that the Fondu cement composition is typically 40% to 50wt.% CA and that 20% to 40wt.% is the iron rich ferrite phase, Fe_2O_3. Other constituent phases include $C_{12}A_7$ and C_2S, present fewer than 10wt.%. The equilibrium CA solid solution contains up to 5wt.% Fe_2O_3. The iron phase contains alumina and silica in significant concentrations; Al/Fe ratios vary from 0.9 to 1.6. Higher purity or white commercial calcium aluminate cement is made from raw materials with lower silica and iron. Quick lime instead of limestone reduces the silica concentration in the final clinker. The high solubility of the CA phase easily accommodates impurity concentrations of several percent simplifying the phase distribution in the high purity commercial calcium aluminate cement.

2.1.5.2 Hydration

Nearly all materials hydrate to some extent given sufficient time and temperatures. However, in the case of refractory cements, there are relatively few clinkers that form structural hydrates. The practicable time constraints for CAC cement are short. The installed product should cure and be able to thermally cycle in 48 hours. The physical properties of the hydration reaction products in the 48 hours define the usefulness as castable refractory cement. Hydration reactions and the development of strength are found in a number of textbooks [4,5,6,7,23,33,34] and technical papers [35-53].

The hydration reaction products range from thin monolayers that are structurally insignificant to extensive networks of crystalline phases. Composition variability is produced by the heterogeneous collection of dissolved ions in the pore water that nucleate and grow into stable crystalline structures. Solubility curves [34] of the calcia and silica or calcia and alumina are used to explain the composition of the reaction products. Reaction products can be crystalline or amorphous or start out amorphous and

transform to a short-range crystal structure upon dehydration. Hydrates are produced from calcia, alumina, silica, magnesia and iron oxide reacting with water. The hydrate bonds are polar and relatively weak. The compounds vary in structure and stiochiometry with pore water ion concentrations and time. The bulk structure at any given time is the sum of a number of competing molecular processes: solidification, precipitation, growth and the formation of ionic reaction products. The generalized mechanics of the paste formation, nucleation-limited incubation period, and formation of crystal networks are common to most calcia and alumina clinkers.

The only phases that hydrate over relatively short intervals are CA and $C_{12}A_7$. The reaction of CA_2 is slow due to the thick gel-like layer formed around the grain. However, when CA_2 and CA are blended, the CA_2 hydrates at reasonable rates. The compound C_2S hydrates slowly and does not contribute to the strength of the refractory cement. C_2AS and the ferrite phase similarly hydrate at a slow rate and do not contribute to the strength. The reactivity of the clinker decreases with decreasing C/A ratio, thus $C_{12}A_7$ is the most active and the CA_6 is the least active. The calcium aluminate hydrate chemistry is complex, more than thirty different hydrates and polymorphs have been identified by X-ray diffraction (XRD), IR spectroscopy, thermal analysis, electron diffraction, extended X-ray absorption fine structure spectroscopy (EXAFS), electron spectroscopy for chemical analysis (ESCA) and nuclear magnetic resonance spectroscopy (NMR) based on ^{27}Al. The phases, crystal lattice, coordination, thickness and transformations are variable depending on ionic ratios, relative humidity, temperature and impurity ions. The important crystalline hydration reaction products formed from the calcium aluminates are CAH_{10} at low temperatures, $C_2AH_8 + AH_3$ at intermediate temperatures, and C_3AH_6 and AH_3 at higher temperatures. A composition vs. temperature diagram is used to illustrate the relative concentrations of the three types of calcium aluminate hydrates present. Figure 2.1 illustrates that at room temperatures the two hydrates formed are CAH_{10} and $C_2AH_8 + AH_3$. Longer hydration periods and elevated temperatures will convert metastable hydrates to C_3AH_6 and AH_3. Table 2.7 lists the thermal-physical properties of some of the more common cement materials along with their chemical notations. The heat of formation energy indicates stable compounds.

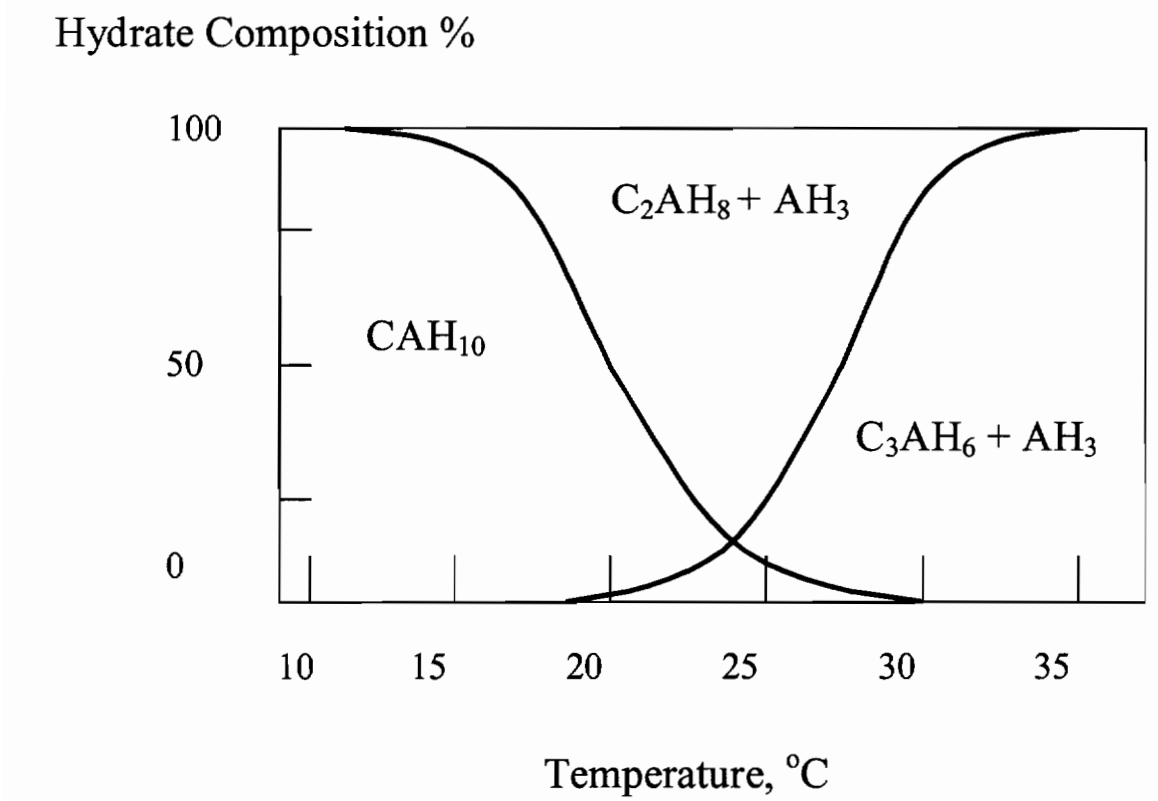

Figure 2.1 Illustration of the relative fraction of the three principal hydration products of calcium aluminate that form at different cure temperatures.

Table 2.7 Thermal-physical Properties of Common Cement Materials

Compound	Mineral Notation	Density gm/cc	Molar Volume cc/mole	Heat of Formation kJ/mole
Tricalcium silicate	C_3S	3.21	71.0	-2927.8
Dicalcium silicate	C_2S	3.28	52.0	-2311.6
Tricalcium aluminate	C_3A	3.03	89.1	-3587.8
Tetracalcium aluminoferrite	C_3AF	3.73	128.0	-5090.3
Gypsum	$C\underline{S}H_2$	2.32	74.2	-2022.6
Calcium silicate hydrate	$C_{1.7}SH_4$	2.12	108.0	-3283.0
Calcium hydroxide	CH	2.24	33.1	-986.1
Ettringite	$C_6A\underline{S}_3H_{32}$	1.7	735.0	-17539.0
Monosulfate	$C_4A\underline{S}H_{12}$	1.99	313.0	-8778.0
Hydrogarnet	C_3AH_6	2.52	150.0	-5548.0

2.1.5.3 Hydrate Growth and Microstructure

Williamson [51], Taylor [34] and Lea and Desch [103] and others attribute the precipitation and growth model to Henry Le Chatelier published in 1887. The model is still used to describe the microstructure development of hydrates.

The hydrate growth is a discontinuous process. The hydration process begins with the wetting and dissolution of the clinker. Surface tension holds the water on the surface that forms a colloidal gel surrounding the cement particle. The chemistry of the colloidal gel or paste -- a heterogeneous mixture of solid, liquid and gaseous phases -- is characterized in many studies [50-54]. The solid phases are inert particles and unreacted

clinker. In the simplest terms, the colloidal paste is an aqueous suspension of mineral ions and submicron-sized particles that permeates the matrix of reactive clinkers and inert particles. The paste dissolves, saturates and precipitates as it works through the various surface edges and holes in the clinkers. The structural network of precipitates is a heterogeneous collection of crisscrossed long and slender hydrate crystals. The gaps between crystallites are pores filled with water. Diamon et al. [47] studied the morphology of the pore water and defined four types of pores based on the location in the structure of the hydrate: macro, meso, micro and ultra-micro. Diamon defined macro and meso scale pores as having micrometer-size dimensions and initially containing a large percentage of the water. As the reaction time increases, the water molecules diffuse through the growing hydrate structures to the unreacted clinker surface. The micro pore water is found in the inter-crystallite and intra-crystallite spaces between hydrates or sheets of hydrate structures. Hydrates expand and shrink with the water migration. The pore water is pushed into the smaller volumes. Once the water has been consumed or dehydrated, the pore surface is left with an adsorbed monolayer of water on the surface. The water is transported by surface diffusion between the growing hydrate structure. The hydrate structure has a high surface area, variable composition and variable structure. The sheets will have aspect ratios of 10 to 15 with their long axis approximated as long as 10 micrometers.

The aluminum, calcium and iron ions are dissolved and transported with the pore water. The ion concentrations effect the pore water chemistry and therefore influence the hydration process. The ionic properties of the pore water define hydrate chemistry. Thomas [54] and Lankard and Hackman [55] reviewed the work of several researchers looking at ion concentrations and species in the pore water. A number of ions were ranked by their effectiveness and flocculation power. The effectiveness was found to have a strong correlation to ionic solubility in water. The atomic size of the ions and their charge are important towards defining the mobility, solubility and effectiveness to alter hydration. Ions with high charge and small size are highly mobile and make the best hydration accelerators. Ions with large size, lower charge and poor solubility exhibit a decreased influence on the hydration reactions and physically retard ion mobility.

Anions of soluble salts give rise to porous hydrate structures because of the high flocculating power. Salts that form insoluble species or precipitates retard the hydration. Thomas ranked a number of anions according to their influence on the hydration reaction:

Accelerators: strongest to weakest:

$$Cl^- > S_2O_3^{2-} > Br^- > NO^{2-} > CrO_4^{2-} > NO^{3-} = SCN^- > I^- > ClO^{4-} > SO_4^{2-}$$

Retarding agent: strongest to weakest:

$$BO_3^{3-} = P_2O_7^{4-} = VO_4^{3-} > B_4O_7^{2-} = PO_4^{3-} = BO^{2-} > AsO_4^{3-} > SiF_6^{2-} > F^-$$

The ions that accelerate hydration can be placed into two groups based on function: those that are highly soluble and those that aid in the dissolution of the clinker. The highly soluble ions are small and easily penetrate the colloidal paste. Small anions reduce the surface tension causing better wetting and thinner colloidal paste layers. The ions that aid dissolution change pH, therefore aiding solubility, and these ions are able to bond with the forming hydrate. Thomas also argues that these ions can physically nucleate hydrate crystallites. Alkali ions keep the pore solution alkaline and aid the dissolution of the clinker.

The osmotic model of hydration considers the ions with respect to how they influence the surface gel membrane. The membrane acts as a barrier to further clinker dissolution as long as it remains an amorphous gel. As the membrane thickens by dissolving more of the clinker surface, the advancing dissolution front becomes hypotonic. The water needs to permeate through the thick gel to the advancing dissolution front. Insoluble particles and precipitates can block the water path. Insoluble ions make thicker and higher density membranes. The osmotic pressure builds and the onset of the hydration is delayed. Large ions retard hydration. A less common mechanism is discussed whereby organic complexing materials, like citric acid or sucrose, bind ions in the pore water and physically close the interconnected porosity [67]. The organic molecule retards the hydration by preventing the dissolution. These molecules chelate the cations removing their contribution to the supersaturation and subsequent nucleation of hydrates.

Omotoso, Ivey and Mikula [65,66] studied ion hydrate interaction in context to stabilization of hazardous wastes. A hexavalent chromium cation was added to the hydration process of a C_3S clinker. They found chromium associated with both the gel and the hydrate (C-S-H) columnar structure as Ca_2CrO_5 and $CaCrO_4$ hydrates. The C-H membrane was found to be porous and lacked continuity with chromium ion addition. The hydration rates were slowed because of the large cations. The aspect ratio in the chromium containing hydrate was found shorter with the addition of chromium. Teramoto and Koie [67] mixed both $CaSO_4$ and $CaCrO_4$ with a Portland clinker and found the stunted growth of C-S-H crystals with $CaCrO_4$ and increased hydrate growth with $CaSO_4$.

Gypsum ($CaO.SO_3.H$) is a common additive to the calcium aluminate clinker. Skalny and Tadros [68] and Collepardi et al. [42] investigated calcium sulfate reactions for hydration rate control. They report that gypsum retards the hydration of the C_2A by the formation of a thin film of ettringite ($C_3A.3CS.H_{32}$) on the surface. The ettringite has a large molar volume with low density capable of trapping water and therefore removing it from formation of hydrates. Sujata and Jennings [46] also report water migration to the un-reacted clinker is slowed by the porous network of ettringite crystals forming on the surface of the C_2A clinker.

Magnesia hydrates have poor properties and are not structurally useable as cements. The hydrates decompose easily with temperature and exposure to CO_2. Magnesium chloride added to water and active magnesia forms several stable hydrates, $Mg_3(OH)_5Cl.4H_2O$ and $Mg_2(OH)_3Cl.4H_2O$. Matkovic et al. [69] and Sorrell and Armstrong [70] have studied the magnesia oxychloride hydration. They documented a colloidal paste on the magnesia clinker formed by a similar precipitation and growth mechanism. Needle-like crystals grew from the paste and interlocked to form a network structure. The magnesia hydrates are useable as construction materials if the magnesia has been completely reacted. Incomplete hydration lead to slaking and loss of integrity in atmospheric conditions. Phosphate admixtures can also react with magnesia and form a mix of hydraulic and acid-base magnesia phosphate cements. Sugama and Kukacka [57,58] investigated phosphate additives to the magnesia.

Diammonium phosphate added to magnesia will produce three hydrate products: orthophosphate tetrahydrate ($Mg_3 (PO_4)_{2.4H2O}$), magnesium ammonium phosphate hexahydrate ($MgNH_4PO_4.6H_2O$), and brucite ($Mg (OH)_2$). The samples were heated, and the three phases decomposed into a single phase, anhydrous magnesium orthophosphate ($Mg_3 (PO_4)_2$) that was thermally stable at elevated temperatures. Other experiments by Suguma and Kukacka used ammonium polyphosphate to produce similar compounds. The essential difference was the latter admixture produced hydrates that formed plate-like structures estimated to be 7 μm long with an interlocking morphology instead of rods. These products were stronger that the diammonium phosphate products.

The amorphous or colloidal precursor phase discontinuously coats the surface of the inert particles blended with the cement clinkers. The inert particles act as a substrate for hydrate growth. Surface tension, weak electrostatic and van der Waals forces work to hold the colloidal groups of mineral oxides on the substrate. Hydrate structures nucleate from the substrate surface and a layer forms on or around the inert particle. The process of dehydration causes volume contraction and localized areas of high strain.

A number of studies have attempted to understand the initial stages or incubation period of the hydration process [41,44,45,46,50]. As a result, the hydration process is now understood to be a complex transformation of a colloidal paste to a solid over several hours. Williamson [51] has observed the transformation during the first few hours to up to several years after mixing. The length of the incubation period has been found sensitive to several parameters: water to solid ratio, particle size, temperature, and chemical makeup of the clinker. Tong, Young and Berger [52] and Tong and Young [53] studied the composition of the pore water with respect to the hydration reactions concluding that nucleation process is rate controlling. The induction period has been correlated to the concentration of the Ca^{2+} and OH^- ions in solution. The induction period was reasoned to be complete when the Ca^{2+} ions supersaturated the local pore water, and sufficient material was available to form stable nuclei. The growth of the hydrate crystals from the liquid lowers the concentration. Laboratory experiments by Young and Tong indicated agreement between the pore water Ca^{2+} ion concentration change and the incubation period based on analysis of the hydrate surface area and ion selective electrodes. Experiments were repeated on other clinkers finding similar supersaturation peaks in pore

water concentration profiles. The pore water supersaturation occurred at different relative concentrations for the different clinkers. The Tong and Young experimental work used the silica concentration in the pore fluid to indicate the end of the incubation period. Silica has low solubility in high pH solutions, and therefore the highest alkali content indicated the point of nucleation. Lei and Struble [44] studied the structure using the environmental scanning electron microscope (ESEM) and micro x-ray dispersive energy analysis on the paste. The growth rate was reported to be relatively constant over the first few hours, followed by a sharp increase and a gradual tail. The ESEM was used to observe the clinker in the early stages. The clinker was observed covered with a semi-continuous gelatinous layer in the initial stage. The layer was found to fill in and thicken with time. The colloidal layer C/S ratio changed from 3 to 2 after 10 minutes and to 1.5 after 30 minutes on a C_3S clinker. The ratio was found to remain constant at 1.5 after the incubation period. C-S-H crystals became microscopically visible after three hours.

Williams [51] discusses the hydration process based on two parameters: the microstructure divided into zones and the time since hydration started. Each cement grain has an un-reacted core, inner zone, outer zone and the interstitial zone. The inner zone boundary starts at the original clinker surface and grows into the unreacted material. The outer zone starts at the original clinker surface and grows out in columnar structures perpendicular to the surface. On mixing, the gel-like paste forms immediately on the clinker surface. The columnar zone hydroxide crystals nucleate and grow from centers on the gel. The inner hydration zone dissolves more and more of the cement clinker. The columnar crystals increase coverage and size with time. The inner zone thickens, distorts and loses uniformity due to the increasing stress caused by crystal mismatches. The interstices of the cement are initially filled with water. The water concentration of calcia and alumina increase as the water is used in the hydration of the columnar structure formation. The Ca^{2+} supersaturation in the pore water results in the formation of Portlandite nuclei that grow in long sheets in the open space of the pore. Several classifications are used to describe growth and different hydrates (see Table 2.9). Early C-S-H contains dimeric silicate structure in long oriented sheets and form over the first 6 hours; late C-S-H contains polymeric or crosslinked silicate structure with higher density.

The hydration of a clinker is hardly ever complete in application. Unless admixtures are used to aid the hydration, the gel-like paste phase thickens and seals the non-reacted clinker core.

2.1.5.4 Porosity and Particle Size

Conventional pressed and sintered ceramic materials set out to achieve high density. Depending on the ceramic material design function, the porosity influences the dimensional stability, strength, electrical and tribological properties. The pores are considered flaws and contribute to the loss of properties depending on their location, either on the grain boundary or inter-granular. Product density that approaches the theoretical density (0% porosity) is desirable. Independent of sintering, high density is achieved with high packing factors and high packing pressures.

Porosity in castable refractories is considered desirable depending on the location and size. Porosity resists heat flow and acts to arrest crack growth and aids in thermal shock resistance. Porosity in the castable ceramic is divided into four size ranges: molecular, submicron, micron and millimeter. The castable ceramic has three microstructure zones defined by the type of bonding, porosity size and porosity distribution. The chemical hydrate bond zone contains porosity in the spaces between the molecules, between the sheets of molecules, between the hydrate plates and the space between the unreacted clinkers. The finest porosity lies between the molecules in the hydrate structures. The submicrometer porosity lies in the interstices of the crisscrossing hydrate rods and plates. The micrometer- and millimeter-size porosity is distributed throughout the cement matrix resulting from interfacial shrinkage and pore water.

Typical cold isostatic pressing of powder compacts achieve green porosity range between 30 to 35%. Empirical models account for the pressure applied to the compact and the resulting density [5,6]. The density change is related by a power function to the applied pressure, $D_g - D_o = k (P_a^2)$, where the green density is D_g, and the applied pressure is P_a. The constant, k, is related to the material hardness, particle geometry, and packing factor. The density of consolidated ceramic powder is dependent on the particle shape,

size, and distribution. For example, the optimum packing factor for a uniform size distribution of spherical particles is 30% porosity. The optimum density for a bimodal particle distribution with $r_2 \cong 0.2r_1$ is 26% porosity, and for three particle sizes, the minimum porosity is 23% if all small particles fit into the gaps between the larger particles. Therefore a wide distribution of particle size produces greater densities.

Cements strengthen by hydration reactions, and therefore any actions to increase the degree of hydration are important to the development of strength. As previously discussed, the hydration process is a surface-area dependent process. Smaller particle sizing increases the total surface area and the degree of hydration, independent of the water and time. Manufacturing efforts to produce fine powder sizes have proved to be a critical development in the production of high strength cements.

2.1.5.5 Castable Cement Blends

Additives and admixtures have been blended into ceramic formulations long before our current understanding of cement chemistry. Additives enhance properties by changing the composition and microstructure and are selected to increase strength, toughen grain boundaries, improve sintering, change porosity, improve thermal shock resistance, improve high temperature stability and increase resistance to aggressive slags and gasses. References to additives that influence the cured properties of the cement are similar. Additives that increase the cured strength are those that influence the hydration chemistry. The materials selection for strength optimization uses additives that influence the hydrate characteristics creating longer and thicker hydrate structures. The additives can be the oxides or phosphates blended dry with cement prior to mixing with water. Dry additives are fine powders that must dissolve into the pore water before being incorporated into the growing hydrate. Admixtures are those materials that are mixed with the water prior to the mixing with the clinker. Additives and admixtures are widely used in the concrete industry and are designed to function as accelerators and agents to

entrain air, control set period, increase expansion and reduce water. Using additives or admixtures, the optimum chemical composition and microstructure for a specific set of properties can be designed.

2.1.5.6 High Temperature Additives and Reinforcements

Structural ceramic materials are typically formulated with additives to enhance properties and forming processes. Additives can impart strength and creep resistance in some ceramic products. Glass-formers like potassium, lithium and sodium produce low temperature liquid phases that wet higher temperature phases and promote grain-to-grain bonding. The glass formers also lower the sintering temperature and time, which then reduce cost. Lower sintering temperatures are desirable in some structural ceramic materials but not advantageous for refractory applications.

Two types of additives, reactive and inert, can be used in the development of calcium aluminate cements structures. Reactive additives generally influence the hydration reaction by changing the reaction rate or chemistry of the hydrate. Other hydraulic clinkers are often used as reactive additives to increase the strength and improve interface bonding or to shorten the cure. Calcium aluminate (CA) and calcium dialuminate (CA_2) are blended to increase the kinetics of CA_2 hydration and promote more rapid cure. Alkaline salts are blended to retard the CA hydration and improve workability of the cement. High temperature additives are hydraulically inert additives. These additives have higher softening points than the calcium aluminate cement and their addition promotes thermal stability.

Inert ceramic additives are oxide fillers dry-blended with the cement formulations. Additives range from synthetic pure powders to impure frit and processed grog. Frit and grog are generally scraps and wastage from other ceramic processes and are usually sintered. Inert additives are intended to control cost in the traditional cement and concrete formulations. The purity of the low cost scrap is not as important in low temperature applications. Additives for high temperature calcium aluminate cement

formulations are selected for their purity, high temperature stability and thermal compatibility with the cement. Purity is important for thermal stability in the calcium aluminate cements and when synthetic materials are used.

Ceramic materials with low elastic properties are sensitive to internal thermal stress caused by the differential thermal expansion. Differential thermal expansion stress is induced in heterogeneous cements (multiphase materials) that are operated at temperatures different than their cure. The resultant stress and direction depends on the relative values of the thermal expansion coefficient for the additive and the matrix as well as the temperature. If the coefficient of the additive is greater than the matrix, the additive will try to expand to a size greater than the matrix upon heating. The matrix restrains the additive, and both the ceramic additive and matrix are placed in compression. Using Eshellby's method, the strain on each can be approximated by, $\varepsilon_{additive} = \alpha_{additive} \Delta T$ and $\varepsilon_{matrix} = \alpha_{matrix} \Delta T$. The strain is approximated by $\sigma_{additive} = -E_{additive} \alpha_{additive} \Delta T$ and $\sigma_{matrix} = -E_{matrix} \alpha_{matrix} \Delta T$. Young's modulus is given as E and the stress and strain are σ and ε, respectively. During heating ΔT is positive and during cooling it is negative. Difficulty lies in determining the highest acceptable temperature because residual stress relief is possible. At high enough temperature, the stress relaxation by diffusive or viscous flow will participate in the residual stress reduction. The method is simplistic and only considers radial strain. Axial and tangential strains also need consideration to determine the total strain, and more importantly to determine the stress distribution. The calcium aluminate cement elastic modulus varies depending on the type of bonding. For materials selection purposes, a meaningful generalization is to keep the $\Delta\alpha$ near zero and no stress develops.

The thermal expansion of a ceramic phase is changed with the purity. The degree of change is dependent upon the solubility limits of the phase for the specific impurity. Calcium aluminate cements and high temperature additives are less likely to have differential thermal-expansion mismatch stress difficulties if the additive is selected to have high solubility for calcium, alumina, silica and iron.

Thermal stresses generated in rapid heating or cooling can exceed critical stresses for rapid brittle-crack propagation. Thermal expansion dimensional differences, $\alpha\Delta T$, cause thermal shock fracture if the stresses exceed critical fracture strength, σ_c, of the

material. Kingery [6] solved for the maximum thermal stress based on linear elastic fracture mechanics and defined a thermal shock severity coefficient β where β =hb/k. The value h is the heat transfer coefficient, b is the distance of the thermal gradient and k is the thermal conductivity. The severity coefficient can range between 0 and ∞ depending on the heat transfer and the material's ability to transport heat and reduce the thermal gradient. The thermal stresses can be approximated for rapid cooling conditions with thick samples and low thermal conductivity β>>1 as follows,

$$\sigma_{thermal} = \frac{E\alpha\Delta T}{1-\nu}$$

For β<<1,

$$\sigma_{thermal} \propto \frac{E\alpha\Delta T}{1-\nu}\beta$$

Where E is Young's modulus and ν is the Poison's ratio (a ceramic material's ν is between 0.2 and 0.28). The thermal stress, $\sigma_{thermal}$, can be solved for the critical stress and the critical temperature difference determined for thermal shock. For β>>1,

$$\Delta T_c = \frac{\sigma_c(1-\nu)}{E\alpha}$$

For β<<1, but not equal to zero, the critical temperature difference is approximated by,

$$\Delta T_c \propto \frac{\sigma_c(1-\nu)}{\beta E\alpha}$$

A simplified illustration of the stress distribution caused by the differential thermal expansion of the reinforcement and matrix phases is shown in Figure 2.2. The coefficients of thermal expansion for the principal constituent are listed in Table 2.8.

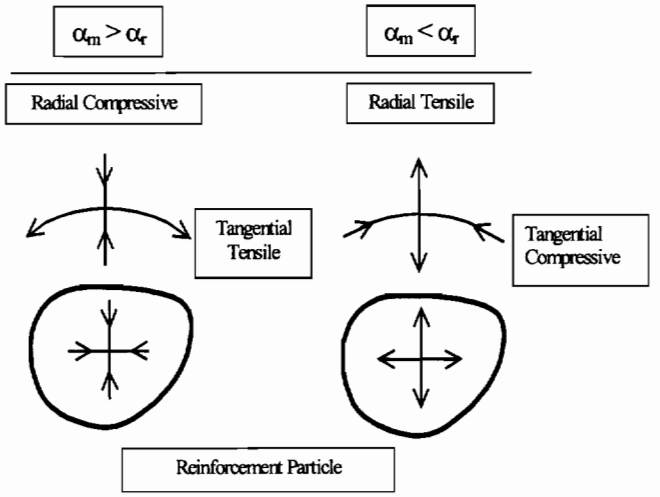

Figure 2.2. Illustration of the thermal stress distribution in the reinforcement places on the matrix.

Table 2.8 Coefficient of Thermal Expansion

Compound	**Theoretical Density g/cm^3**	**α 10^{-6}/°C**
$\alpha - Al_2O_3$	3.98	7.2-8.8
$\perp$ c axis		8.3
= c axis		9.0
MgO	3.60	13.5
$Al_2O_3 \cdot MgO$ (spinel)	3.58	7.6
$2CaO \cdot SiO_2$		14.4
$MgO \cdot SiO_2$		10.8
$2SiO_2 \cdot 3Al_2O_3$ (mullite)	3.20	5.1
$\perp$ c axis		4.5
= c axis		5.7
ZrO_2 (tetragonal)	6.10	12.0
$MgO \cdot ZrO_2$		12.0
$SiO_2 \cdot ZrO_2$ (zircon)	4.20	4.5
$\perp$ c axis		3.7
= c axis		6.2

2.1.6 Composite Materials

Composite materials are designed to optimize properties for specific requirements. The castable cement composite is designed for four functions: thermal shock resistance, low thermal conductivity, high strength and high wear resistance. The castable refractory cement is a composite with three phases:

1. Matrix phase for structural continuity, thermal stability and corrosion resistance,
2. Reinforcement phase for wear resistance and resistance to crack propagation,
3. Porosity improves the thermal shock resistance and low thermal conductivity.

The properties of the composite depend on the relative distribution, shapes and amounts of the constituents. The final composite properties are generally determined by the properties of the constituent phases and the way these are joined. The rule of mixing is used to understand the contributions and physical arrangements of each phase as applied to different properties.

The second phase influence on thermal conductivity depends on the relative differences of the conductivity and the volume fraction of each component. Kingery [6] provides an approximation for the thermal conductivity of an idealized distribution of continuous cement matrix phase and a discontinuous spherical secondary phase. The thermal conductivity of the bulk is k_b, matrix phase is k_m, and the second phase is k_s. The relationship is as follows:

$$k_b = k_m \left(\frac{1 + 2V_s \dfrac{1 - \dfrac{k_m}{k_s}}{\dfrac{2k_m}{k_s} + 1}}{1 - V_s \dfrac{1 - \dfrac{k_m}{k_s}}{\dfrac{k_m}{k_s} + 1}} \right)$$

When the conductivity of the matrix material is greater than the secondary phase, $k_m > k_s$, then the bulk conductivity is approximated by,

$$k_b \cong k_m \frac{1 - V_s}{1 + \frac{V_s}{2}}$$

Additionally, when the thermal conductivity of the matrix phase is less than the secondary phase, km<< ks then the bulk conductivity is approximated by,

$$k_b \cong k_m \frac{1 + 2V_s}{1 - V_s}$$

The two cases are illustrated in Figure 2.3.

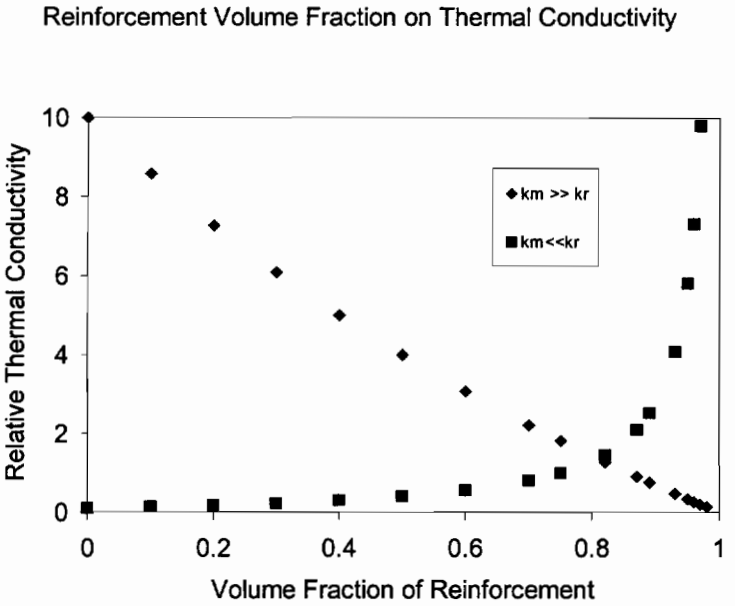

Figure 2.3. Illustration of the relative thermal conductivity change with volume fraction of reinforcement phase.

The effect of the porosity on the thermal conductivity of the bulk material depends on the pore concentration and distribution. The porosity can range from fine and dispersed to large and segregated. The porosity can be either closed or interconnected. The bulk conductivity with closed and dispersed pores is approximated from the previous equation by,

$$k_b \cong k_m(1 - Vp)$$

However, if the pores are connected, a different approach using a series of slabs is modeled. The bulk conductivity depends on the relative conductivity of the two materials, and the conductivity contribution by a pore is small compared to the solid. If the phases (pores) are aligned parallel, the heat flow the approximation is

$$k_b = k_m V_m + k_p V_p$$

And if the phases are aligned normal to the heat flow, the conductivity of the bulk composite is,

$$k_b = \frac{k_m k_p}{V_m k_p + V_p k_m}$$

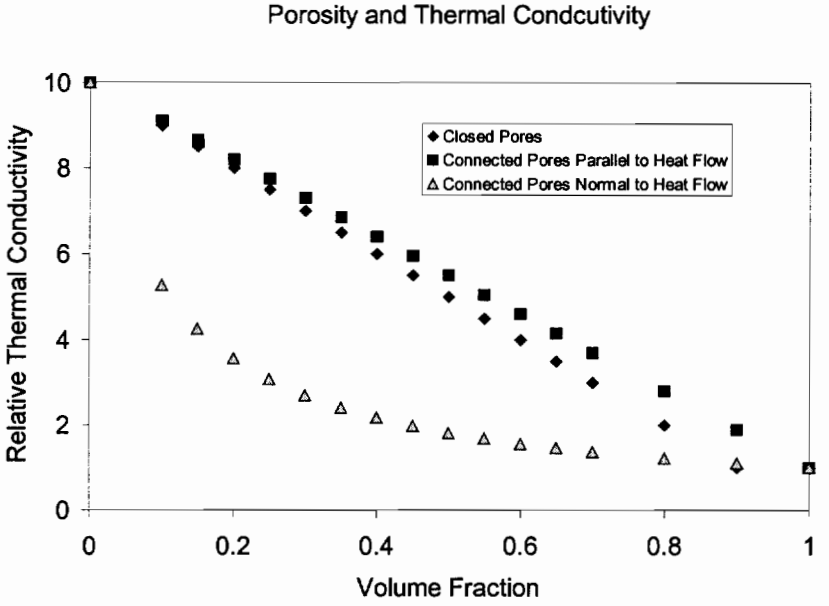

Figure 2.4. Illustration of the Porosity influence on the Thermal Conductivity.

The conductivity of the pore complicates this analysis because convection and radiation heat transfer modes contribute to the total heat transfer. Kingery makes the assumption that convection is present in the larger pores, several millimeters in size, and radiative heat flow is a high temperature process. Radiation heat transfer is directly proportional to the pore size and the third power of temperature. Consequently, large

pores contribute to increases in thermal conductivity, and small pores contribute to the lowering the thermal conductivity. Optimum thermal resistance is obtained with small pores and interconnected porosity.

The interface is the volume between cement hydrates and the following: clinkers, inert additives and reinforcement oxides. A network of crystalline and amorphous solids, insoluble precipitates, water and voids develops in the interface zone through the hydration process. The substrates are wetted with the colloidal gel from which the hydrates grow.

Experiments by Fu and Chung [59] demonstrated a microstructure relationship to the bulk strength of the cement and the interface structure. They used a resistance measurement between a metallic reinforcement and the cement matrix to indicate a coherent interface. The resistance of the contact between the reinforcement and the matrix was correlated to the pull-out strength. Higher interface bond surface area produces an increased the pull out strength. The contact resistance is a function of current path, as the interface bond area decreases the resistance that correlates to an increase in pull out strength. Jennings' [60] review on the mechanism of strength development in hydrated cement indicated an aggregate to matrix interface relationship to the bulk cement strength. Jennings states that the hydrates nucleate on the substrate and are held by van der Waals force. Later, as the hydrate matures and thickens the hydrate structure interlocks at the surface roughness and porosity of the aggregates.

The interface microstructure is a critical factor in composite mechanical properties. Bentur and Cohen [61] and Barnes et. al, [62] used glass slides and SEM to understand the morphology of the interface. Spiky outcrops that grow from the colloidal gel on the reinforcement surface were observed. The wetting of the gel into the surface irregularities of the reinforcement was also observed. Bentur and Cohen[61] studied the Portland cement clinker interface zone. Based on their work, the interfacial zone structure can be altered by changing the composition of the clinker and pore water chemistry. The reinforcement composition, surface irregularities and size also influence the strength of the bond. The interface material composition and structure can be modified by the use of admixtures. Admixtures can be used to accelerate early stages of hydration and therefore increase the number of substrate-nucleated hydrates. This, in effect, increases the

strength of the interface bond. Lankard and Hackman [55] reviewed admixtures for changing the structure and chemical makeup of the interface zone. Modification of the cement interface is possible by using phosphoric acid and various water mixtures. The use of acids improves the interface bond strength by involving acid-base bond reactions. Admixtures can also be used to change the porosity of the interface zone, thereby increasing the volume of solid material in contact with the reinforcement to increase strength.

2.1.7 Sintering

Modern sintering technology has grown from ceramic and powder metallurgy engineering. New trends appear in trade journals and, to lower overall costs, deal mostly with optimization of the heating and cooling cycles, furnace design, atmospheric controls and thermostatic controls. The traditional sintering process uses large batch furnaces or a continuous heated tunnel oven to heat the product uniformly for several days for efficient and economical operations. Sintering schedules are developed for each product composition and form. The *in situ* firing of the castable is a major advantage for the producer and puts the burden for attainment of final ceramic properties on the user. Special heating blankets and insulation are required to heat the castable cements uniformly and avoid explosive spalling or overheating of the containment structure. Control of the castable cement final microstructure is difficult. The sintered microstructure depends on the time-at-temperature and temperature [63, 71-77]. Figure 2.5 illustrates the microstructure and property changes with temperature for an *in situ* fired refractory. The figure divides the refractory into the dominant microstructures from the cold face to the hot face.

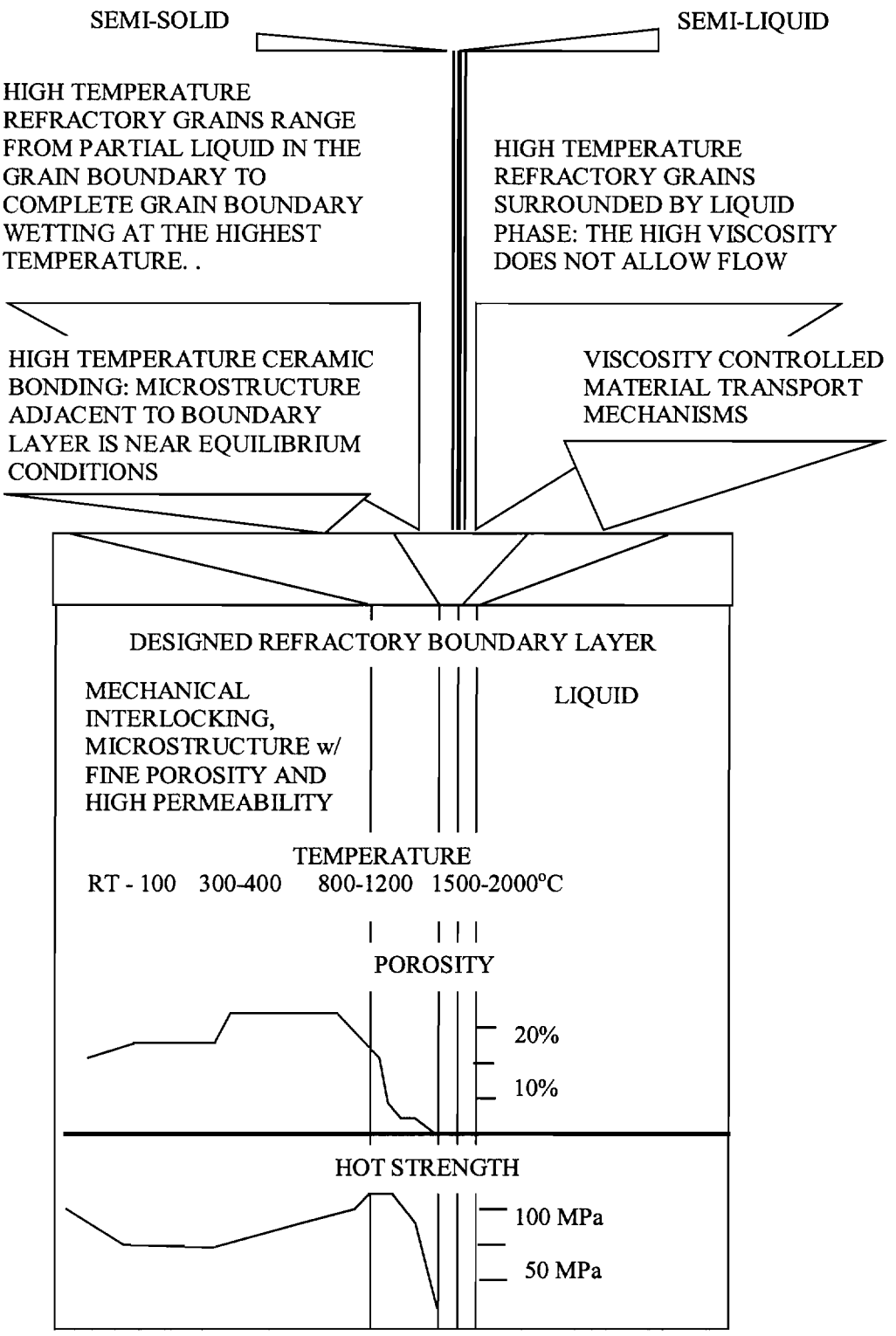

Figure 2.5. Illustration of the refractory cement *in situ* fired showing the bonding type over the temperature range and the corresponding property trend.

Sintering is an elevated temperature process where discrete particles agglomerate and form a polycrystalline solid. Ceramic powders require thermal energy to develop ceramic bonds and obtain the properties to be structurally useful. The originally porous compact is transformed into a denser and stronger solid. The changes that occur during sintering are related to the particle size, solid state bonding and the pore characteristics. The pore size, shape, and distribution change during sintering. Higher density products are also more wear- and corrosion-resistant. The thermal conductivity is increased with reduced porosity and increased density. The thermal shock resistance is reduced as the material approaches the theoretical density.

Several authors have reviewed sintering and the various mechanisms [4,5,6,7]. Traditional ceramic sintering involves three microstructure stages: rearrangement, solution precipitation and final pore removal [4,6,73,74,76]. Liquid phase bonding, direct bonding, reaction bonding and vapor-phase sintering mechanisms can sinter ceramic materials. Surface energy, volume diffusion, surface diffusion, and solubility control sintering processes in ceramic materials.

Sintering refractory castable cement differs from conventional ceramics from two perspectives. First, complete densification is not the desired outcome. Second, the diffusion rates are much slower for the refractory oxides, and therefore higher temperatures (>1200°C) are required to achieve the ceramic bonding between particles. The temperatures are highly specific to the raw material composition, particle size and green density. Sintering aids are often added to form lower temperature transient liquid phases to reduce time at elevated temperatures. Sintering is a dynamic process, and there are many dependent parameters. Several of the parameters can be normalized through experimental procedure and standardization of the thermal cycle.

The typical castable refractory cement applications are reactors, batch vessels, furnace firebox or ladle. The refractory is structurally supported with pins and spikes attached to a steel framework. The curing of the castable cement is critical to the development of the hydrated microstructure [78,79]. The hydrated microstructure is decomposed during the dry-out. The capillary porosity and permeability of the cement are important to the dry-out phase prior to sintering [79,80]. Improper dry-out can cause explosive spalling if insufficient permeability retards the dehydration [81].

Several researchers have developed drying schedules using finite element models [81,82,83]. In these models, the permeability of the cured cement is the critical factor that is used to determine the heating rate, hold temperature, and hold time. Thermal gradients also influence the surface stresses in the castable refractory. Designs call for an insulation layer between the castable cement and the containment structure.

Sintering is a thermodynamically spontaneous process where the total free energy of the system is decreased from the initial to the final state. The free energy is that which is associated with the surface free energy change where the driving force for the sintering process is the surface tension of the particles. The cement particle surface molecules, in this case hydrates, are subjected to a resultant attraction to grain contact areas or boundaries because of the unsaturated chemical bonds at the surface of the pore.

In the first stage of sintering, the surface roughness is decreased, and particles start to move around with the thermal expansion. Interparticle spacing is reduced, and they begin to adhere and grow together. Only a modest percentage of shrinkage takes place during the initial stage. In this stage, the nearest neighbors will form compounds. The first sintering stage spans a relatively short time-at-temperature.

The second stage has been assigned to the point in the sintering process that grain growth process begins and grain boundaries are established. The pore volume becomes defined and bulk shrinkage closes the space between particles. Throughout the second stage, grain growth continues, and the pore volume decreases until the body achieves 90% to 95% density. The 90% theoretical density range marks the change from open to closed porosity. The mass transfer is by the solution-precipitation mechanism. The solid at the grain-to-grain contacts dissolves into a mushy liquid phase. The liquid dissolves the solid that it contacts. The solubility is proportional to the normal forces at the contacts caused in part by the Laplacian force that develops at the grain contact due to the concave liquid lens. The dissolved solute transfers to the uncompressed part of the grain structures by diffusion throughout the liquid phase and is precipitated on the uncompressed part of the grain. This mass transfer results in contact point flattening and linear shrinkage. The process is dynamic and as mass transport continues the contact angle increases and the driving force reduces slowing the rearrangement of atoms. Full closure of the porosity becomes increasingly more difficult because of competing

mechanisms. Grain growth begins to dominate and porosity can be absorbed into the grain volume. During the latter part of stage two and solution precipitation process the interconnected pores are all pinched off and the porosity is closed.

The third stage of sintering and is marked by the point in the microstructural rearrangement process where the open porosity drastically drops to less than 1% and the remainder is closed porosity, an estimated at 5% to 7%. The final stage can be taken to the point of complete removal of the remaining closed pores leading to a theoretically dense material. Discontinuous growth may occur in the third stage where large grains grow at the expense of the small grains. Consequently, the closed porosity can be swallowed by the larger grain growth. Once a pore has been separated from a grain boundary, it cannot be removed by further sintering.

The formation of a liquid phase during sintering has a large influence on the final density of the product, the mass transport, location of phases and the chemical composition of the microstructure. The liquid contributes to the densification permitting flow and shear accommodation between particles placed in compressive stress by the compact. The dissolved solute material is from small high-surface-area particles or sharp corners of larger particles and will condense on the coarser particles and low surface-energy surfaces. Coarse particles grow, and the fine particles are adsorbed or eliminated. Considering the hydrated clinker, the hydrates have high surface energy and will dissolve first. The composition of the former hydrates becomes the liquid bonding phase between particles and reinforcement.

Thicker hydrates will grow at the expense of the fine hydrates. High contact angles between the interlocking networks of hydrate plates assure high Lapacian force and liquids forming at temperatures lower than the compositional melting point. Transport to lower energy surfaces and precipitation on the substrate causes growth. The rate of growth is either controlled by diffusion or interface reaction, depending on the materials and sintering conditions. Table 2.9 is a collection of diffusion constants for various refractory oxides [85]. Local binary couples form between the mushy liquid and the substrate. The high temperature substrates with greater solubility will grow out into the liquid phase. The substrates with low solubility will thicken the liquid layer. The magnesia and spinel will likely grow while the CA particles will reduce in size. The

amount of the liquid phase can be a dominant variable for the grain growth. A small concentration of additives in the liquid phase can strongly influence the kinetic of the grain growth. Sintering aids work to increase the wetting of the substrate and lower the viscosity of the liquid. Examples are calcium phosphate lowers the viscosity of the liquid in SiO_2 alumina, and calcia results in faster grain growth in magnesia ceramics.

Table 2.9 Stable Phases in a Hydrated Calcium Aluminate with Excess an Al_2O_3

Temperature Range, °C	**Phases Stable**
0 – 20	AH_3 gel, CAH_{10}, CA and Al_2O_3 Not Reacted
20 – 40	AH_3, C_2AH_8, $CAH_{x\ (x=8\text{-}12)}$, C_3AH_6
40 – 60	AH_3, C_2AH_8, $C_3AH_{x\ (x=8\text{-}12)}$, C_3AH_6
60 – 100	AH_3, $C_3AH_{x\ (x=8\text{-}12)}$, C_3AH_6
100 – 350	AH_3, $C_3AH_{x\ (x=8\text{-}12)}$, C_3AH_6
600 – 1300	A, CA, CA_2
1400 – 1650	CA_6

Castable refractory cements can be made with a range of particles differing in shape, size and phase distribution. The particle size and size distribution are important parameters which set up conditions that determine the competing mechanisms at any given temperature. Finer particles will tend toward faster firing and produce high density faster but can also lead to runaway grain growth before all voids are removed [4, 63]. Larger particles lead to slower sintering and greater porosity in the final product. The proper particle sizing for high density and uniform grain growth are based on development of a high packing factor [71]. A size distribution of dry particles improves the packing factor. High packing factors allow for higher green densities, lower shrinkage and rapid (optimized) sintering. The sintering atmosphere and pressure may influence the final densification [4]. In the initial stage, when the porosity starts to close, the trapped gases diffuse along the grain boundaries filling the larger voids and permeate to the surface. When gaseous species are trapped in the closed pores, the pressure will build with shrinking pore size. The internal gas pressures can slow pore removal rate and therefore slow final densification.

Research has explored the atmospheric influence of the various sintering mechanisms. The furnace gas and pressures are changed and the sintering thermodynamics and kinetics were studied. Adjustments of the atmosphere during the final stages of sintering can be used to reduce porosity and change the final microstructure [4,5,86,87]. Reduction of the vapor pressure has an almost immediate response to the solubility of oxygen and pore removal. The sintering of cement materials can be highly specific to the impurities in the raw materials. Lower melting point impurities in small quantities increase the rate of atomic rearrangement. Rate-controlled sintering using iron and silicate compounds is common and used to save energy and avoid grain growth while increasing density. The temperature is adjusted to maintain a constant rate of densification. This method requires specific control on particle size and initial green density of the cast part and may be more applicable to systems where the final microstructure does not need to be homogeneous.

A two-step sintering technique developed by Lin and DeJonghe [76], involves an initial pre-coarsening step before final sintering. The pre-coarsening step is a medium temperature hold for a long period followed by a short high temperature period for final densification. The two-step process improves the microstructural homogeneity during the subsequent sintering. In addition, the materials that are produced by the two-step technique generally have a slightly higher density, a smaller average grain size, and a narrower grain size distribution when compared with conventional sintering. Grain refinement is modeled as follows: pores exert a drag on the grain boundaries and can inhibit grain growth. Large continuous pores during the initial and intermediate stages of sintering provide a greater drag and inhibit grain growth more effectively in comparison to smaller pores or their presence during the final stage of sintering. This can result in a transition in the grain-growth behavior. A delay in the pinching off of the continuous pores has been suggested as a mechanism to explain the grain size refinement during the subsequent sintering of the pre-coarsened compacts.

Direct bonding [4,88] is a form of lower temperature sintering that does not proceed to final pore removal. Porosity is not removed. The process is similar to precoarsening in the two-step process; however it is selective to the intermediate compound formed. Exchange or displacement reactions between the two or more condensed phases take

place to form a third thermodynamically stable phase. The three-phase assemblage bonds the particles. These reactions occur at moderate to high sintering temperatures. The principal advantage envisioned for these processes is the ability to form *in situ* multiphase composites with fine and uniform microstructures. The diffusion is an important process in the sintering mechanics.

Reinforcement particles resist the unrestrained flow of material during sintering. The degree of influence is a function of the size, concentration, aspect ratio, surface roughness and coefficient of expansion. Larger particles with high surface roughness and high aspect ratios restrain matrix particles. Also, matrix and reinforcement thermal expansion mismatches can result in the development of cracks and reduce the thermal shock resistance. Sizing and classification of raw feed stock are designed to provide uniform size distributions for optimum surface area and reduce void formation during sintering. The voids from powder reinforcements are often the strength-limiting flaw in the ceramics. The sintering rates decrease with increasing reinforcement content. The sintered density as been found to increase after a series of isothermal holds when reinforcements are used in the ceramic compact. The microstructure of the reinforcement can influence the sintering process. The reinforcement materials can range from single phase and fully dense to a multi-phase heterogeneous solid with porosity. In the later, the sintering temperature will cause similar sintering process and shrinkage in the reinforcement. Consideration for reinforcement shrinkage is important in these cases. Reinforcement and matrix coherent bonding can have beneficial effects on the final composite properties. The porosity inside the reinforcement can be eliminated and lead to a localized high-density grain. Examples of the common dense reinforcement phases are zircon, zirconium mullite, fused zirconia or fused alumina. Examples of common porous reinforcement materials are tabular alumina, zirconia grog and calcined spinel clinker.

Table 2.10 Diffusion Constants for Refractory Oxides [85] $D = D_o \exp^{(-Q/RT)}$

Diffusion Process	D_o cm^2/sec	Q kcal/mole	Remarks
Al in Al_2O_3	28	114	Single Crystal
O in Al_2O_3	2.0	110	Polycrystal
O in Al_2O_3	1.9×10^{3}	152	Single xl > 1600°C
O in Al_2O_3	6.3×10^{-8}	57.6	Single xl < 1600°C
M in MgO	.249	79	
Cr in MgO	9.8×10^{-4}	68	
Fe in MgO	8.83×10^{-5}	41.6	
Fe in MgO	3.2×10^{-4}	41.8	
Ca in MgO	2.95×10^{-5}	49.0	
Ca in MgO	8.9×10^{-4}	63.0	
Ca in CaO	0.4	81	900-1600°C air
Ca in CaO	1×10^{-8}	28.2	1000-1400°C
Ca in CaO	3.08×10^{-8}	28.2	1000-1400°C
Ca in CaO	1.125×10^{-4}	64.3	1465-1760°C
O in ZrO_2	9.7×10^{-3}	56	800-1000°C monoclinic
O in $Zr_{.85}Ca_{.15}O_{1.85}$	1.8×10^{-2}	31.2	
O in $Zr_{.858}Ca_{.142}O_{1.858}$	1×10^{-2}	28.1	
Ca in $Zr_{.85}Ca_{.15}O_2$	4.44×10^{-1}	100.2	
Zr in $Zr_{.85}Ca_{.15}O_2$	3.5×10^{-1}	92.5	
Cr in Cr_2O_3	4×10^{3}	100	1150-1500°C
O in Cr_2O_3	15.9	100.8	1200-1500°C
Fe in $Fe_{.907}O$	0.118	29.7	Wustite
Fe in Fe_3O_4	5.2	55	750-1000°C Magnetite
Fe in Fe_2O_3	4×10^{5}	112	900-1250°C
O in Fe_2O_3	1×10^{11}	146	1170-1250°C
O in SiO_2 quartz	3.7×10^{-9}	55	1010- 1220°C
O in SiO_2 fused	4.3×10^{-6}	56.1	900-1200°C

Data from Kofstad, "Nonstoichiometry, Diffusion and Electrical Conductivity in Binary Metal Oxides," Wiley, 1972.

2.1.8 Ceramic Tribology

Engineered ceramic materials are known for their high hardness, resistance to plastic deformation, high compressive strength, retention of properties at elevated temperatures, and good chemical stability. These properties are typically associated with good wear resistance. Ceramic materials have proven to be an excellent selection for tribological applications. Optimization of the material properties to the engineering system is important to durability. Ceramic tribology has been studied and reviewed by many researchers [89,90,91,95].

The high melting point of ceramic material imparts high thermal stability for high-temperature wear applications. The low thermal conductivity of ceramic materials increases the local temperature rise caused by friction and influences the contact boundary layer. The local high temperatures can produce high thermal gradients, which in turn produce high thermal-stress fields. The thermal stresses added to the contact pressure can be the difference between mild and severe tribological process. Low thermal shock resistance can influence wear by the cyclic thermal loads.

The contact surface of a ceramic material is fundamentally different than that of an alloy. Ceramic materials owe their thermal, chemical, and strength properties to the ionic nature of the bonding. Ionic bonds are highly specific and energetic. High relative forces are required to change the chemical structure. Ionic bonding is also responsible for the relatively low fracture toughness and high hardness. The ceramic contact boundary layer does not have an oxide-to-substrate interface. Therefore, the boundary layer is considered to have the same chemistry as the bulk and thus does not change during mild or moderate wear. Severe wear and friction loads can influence the thermal or chemical stability resulting in second phases and possible liquid boundary layers.

Ceramic materials are characterized by low fracture toughness. The higher loads produce fracture and a severe wear process. Factors like grain size, second phases, porosity, strain rate, cyclic loads, dislocations, vacancies, and crystal structure influences the friction and wear of ceramics.

Ceramic materials exhibit defined wear regimes that match well with certain transitions in the ceramic mechanical properties. Wear regimes ranging from mild to severe, correlate to a load and critical flaw size relationship [90, 91] or the change in strength based on grain size [91].

Wear data on ceramic materials is noted for a large degree of scatter. Mumarouglu, et. al. [92] and more recently Terheci [93] point out the unreliable and often notoriously variable wear measurements reported. Even experiments with the same type of material and test machine can give significantly different test results and very few round robin inter-laboratory projects are funded. The large differences are mostly due to poor control of the test conditions and measurement techniques. Cherif et al. [94] indicate a relative humidity of 40% is sufficient to form moisture-adsorbed hydroxides on alumina that in turn influences the coefficient of friction. Specification and control of the tribological test parameters are most important in the more complex ceramic tribo systems.

Ceramic tribology has grouped ceramic materials into three categories based on the chemical makeup: oxide ceramics, non-oxide ceramics, and cermet (ceramic + metal) materials. These materials exhibit different wear properties that can be related to their basic chemistry. Each of these material groups has unique conditions that influence the wear to a greater degree; for example, oxide ceramics tend to be chemically heterogeneous and have porosity. The non-oxide ceramics are known for their high density and narrow grain-size distribution, but have a lowered chemical stability and are sensitive to the oxygen activity at higher temperature applications. Cermets are two-phase, and the ductile phase limits the temperature range; and the two-phase materials have interface problems because they react differently to loads.

The castable ceramic cement is a composite material. Ceramic composites are known for their high hardness, resistance to plastic flow, high compressive strength, and good chemical stability. These properties are typically associated with good wear resistance. Generally, castable ceramic composite materials have proven to be an excellent selection for tribological applications ranging from large ladles and pour spouts to gas lances.

Moore and King [90] observe that the wear properties of ceramic materials have been found to vary over a large range of parameters. No simple relationship exists between ceramic mechanical properties, three body wear contact dynamics, or fretting wear process. In the broadest terms, materials with high hardness and high fracture toughness will generally have lower wear rates.

As in metals, understanding the mechanical loading is the basis for understanding the wear mechanics of ceramic materials. Hertizan mechanics can be used to determine contact pressures and area over which the load is applied. If the elastic modulus is known, the stress distribution at the wear surface can be compared against the fracture toughness. The comparison analysis will look for the onset of crack formation at the high stress locations. Hertz's equations, published in 1895, (Uber die Beruhrung fester elastischer Korper, Gesammelte Werke) were used by Buckley and Miyoshi [97] and Moore and King [90] to correlate ceramic wear processes in fully dense poly-crystal and single crystal ceramics. Looking for the tribological similarities to metallic materials, these researchers demonstrated a hydrostatic force influence was also present in ceramic single crystals when tangential forces are applied to impart elastic and plastic strains to the contact area. Measurements were made at very low loads using sensitive instruments. The significance is that a tribological continuum between metallic materials and ceramic materials was found.

Analysis of the contact mechanics begins with two surfaces, brought together with different hardness ratios H/H_a. The relative hardness ratio is a common tool used in metallic material tribology, but because ceramics have high relative hardness and limited plastic flow, a large hardness ratio range is difficult to study for most ceramics. The hard particle or abrasive is brought into contact with the surface as a spherical cone according to Hertizan mechanics. The surface is loaded normal to the cone axis. The wear surface responds to the load distribution based on its mechanical properties. With increasing loads, a ductile metallic surface first moves into an elastic-plastic response. As the load continues to increase, the elastic- and plastic- zone sizes increase until the energy is dissipated through Hertizan fracture. Hard ceramic materials exhibit shallow plastic zones and reach the linear elastic range at lower loads. Because of the high hardness or high strength a much greater load is required to initiate fracture. Circumferential cracks

develop around the spherical cone when loading exceeds the local fracture toughness. Two orientations of fracture are generally observed. Fracture ring cracks form initially and at low loads, whereas at higher loads, radial cracks initiate at discontinuities in the ring cracks or subsurface microstructural discontinuities. The discontinuities can be either lattice level effects, pores, or grain boundaries in a highly strained condition. Increased loads to the surface cause deep fractures and chipping. The size of the damage area and depth of the indentation are influenced by the compressive strength and notch sensitivity of the bulk material. Upon application of a tangential force to the spherical cone, the stress field is not symmetrical, changing the load distribution at the point of contact. The zone of material ahead of the direction of the applied stress will compress, whereas the zone behind the applied load will have a tensile component to be added to the Hertizan stress field. The greatest tensile stresses are placed on the trailing edge.

Hutchings, and others [98,99,100,101] conducted pin-on-disk experiments on single crystal alumina and silicon carbide to determine the critical load as a function of tangential force. Detachment of the wear debris and fragments trapped in the groove path appeared as tangential force increased. At higher tangential force loading, the radial cracks extended further into the material, perpendicular to the direction of the load. The shape of the pin indenter was also found to be a major influence on crack formation. Changes in the indenter geometry were found to change the appearance of the scratches and the volume of the average wear debris. The smaller radius produced fewer ring cracks and radial type cracks but the radial cracks were deeper whereas the larger radius pin produced cracks that were shorter but increased in number. In addition, the onset of abrasive wear was found to occur at a much lower load using a smaller radius pin. This suggests a relationship between the fracture toughness and the critical load for abrasive wear. The equivalent contact pressures were not given in these experiments. The transitions between wear regimes were accompanied with a stick-slip process, identified by both fracture-debris changes and sudden changes in the tangential force. There may be several reasons for such changes. The detachment of debris may cause the tangential force to drop as support of the indenter tip is lost. Small fragments within the groove bottom may cause a transient change due to the increased friction force. Subsurface non-homogenous microstructural discontinuities like grain boundaries, porosity, or second

phase materials would change the required energy for crack propagation. These would be expected to increase or decrease the friction force as it has been shown for the porosity in polycrystalline alumina ceramics.

Conventional tribological test methods like pin-on-disk, or reciprocating wear test techniques, do not work well on composite materials. These methods were developed for homogenous materials. The anisotropy caused by the second phase require a larger sample size for study. The large number of dependent parameters relating to the fabrication, drying, *in situ* sintering and inherent porosity further complicates the testing of castable refractory composites. With the heterogeneous nature of the castable reinforcement, sample standardization will be difficult, and replicates should be used. The castable refractory tribo-system is also difficult to understand for any given installation. A three-body wear test removes the counter-sliding surface from the tribo-system. The three-body abrasive wear process assures singular microstructure features will not influence the results.

Tribology, abrasive wear, of composite materials was initially expressed in terms of total wear resistance and the volume fraction of the different phases. Khruschov [102] arrived at the understanding that the total wear resistance was numerically the sum of the wear resistance of each component adjusted by the volume fraction of that phase with respect to the total wear surface area. This is known as Khruschov's Rule, formulated in 1974 as referenced through Garrison [102].

$$\Omega_T = \sum V_i \Omega_I$$

$$\Omega_T = V_i\Omega_i + V_{i+1}\Omega_{i+1} + V_{i+2}\Omega_{i+2} + V_{i+3}\Omega_{i+3} \ldots\ldots$$

Where V is the volume fraction of one component and Ω is the load-specific wear resistance, as defined in Archard's equation. The wear resistance also is related to the ratio of the hardness (H) and the wear coefficient (K), H/K. Khruschov's Rule was found to apply in some of the two phase ceramic materials tested but over-estimated the abrasive wear in metal-ceramic composites.

Garrison reviewed the subject in 1982[102] and reasoned that because ceramic materials have a relationship with load $(L^n, n \neq 1)$, the wear resistance Ω of each component could be corrected, and Khruschov's rule could be made to work. Two types of wear behaviors were observed: a linear type, where $\Omega_i \propto L_i$; and non-linear, where Ω_i

$\propto L_i / A_i$. The model allowed use of the relationship which best fit observed wear on each phase. However, even with the corrections, Khruschov's rule overestimated the wear of cermet composites by 2.5 times.

Since Garrison's work, other researchers have documented wear conditions that fit a corrected rule of mixtures. Composite materials follow this relationship at higher abrasive velocities and larger abrasive particle sizes. With sufficient wear energy, the material could be forced into a linear relationship with load: the greater the force, the faster the cutting rate. However, the typical applications of ceramic materials are at far lower loads. The abrasion mechanism at lower loads is influenced by material properties that are not linear with load. Axen and Jacobson [98] addressed the composite-ceramic abrasive wear problem in 1994. Their model considers the composite structure as two (or more) volume fractions with a different wear resistance, $\Omega_{reinforcement}$ and Ω_{matrix}. The wear resistance of the composite is functional on the Ω_r, Ω_m and area fraction of each phase. The relationship depends on one of two wear processes related to the distribution of the load across the phases. The equal wear process defines a condition that both phases wear at the same linear rate, and the equal pressure mode defines a condition where each phase is loaded the same. The equal wear mode follows the Khruschov's rule giving a linear relationship to wear resistance and volume fraction of second phase. The equal pressure mode follows an inverse rule of mixture for the wear resistance influenced by the second phase. The Axen-Jacobson model starts with Archards's equation and rewrites it in terms of a load specific wear resistance,

$$dV/dS = K\,(L/H) = L/\Omega.$$

Where Ω is equal to H/K; hardness and wear coefficient. Using this definition for the wear resistance, Khruschov's rule for composite materials is applied to the total wear rate in terms of the reinforcement phase and matrix phase.

$$dV/dS = L/\Omega = L_r/\Omega_r + L_m/\Omega_m.$$

By definition, the equal wear produces a flat wear scar; each phase has worn the same depth. The equal pressure produces a rough surface where the harder phase stands out. The equal wear mode is the most optimum for wear resistance because the

reinforcing phase takes a greater portion of the load, that amount specified by equal wear with the matrix phase. In the equal wear mode, the wear resistance is linear with the volume fraction of the reinforcement phase and the total wear resistance is given by,

$$\Omega=(A_r/A)\,\Omega_r + (A_m/A)\,\Omega_m.$$

The equal pressure mode produces the greatest wear because the pressure on each phase is equal, $P_c=P_r=P_m$.

$$\Omega=[A_r/(A\Omega_r) + A_m/(A\Omega_m)]^{-1}$$

It is interesting that this derivation also provides for the understanding of the load distribution and therefore the contact pressure.

Axen and Lundberg [99], Axen and Hutchings [100] and Axen, Hutchings and Jacobson [101] further contributed to the equal wear and equal pressure models by adapting a relative pressure coefficient each phase supports. An intermediate mode of wear was also reasoned to explain experimental results. The intermediate mode corrected the equal pressure mode wear resistance for the fraction of material that behaved in equal wear mode. The latter work uses the same principals to calculate the load distribution on each phase. Based on the load model, the relative friction coefficients and total wear rate of a composite material is correlated to the volume fraction of the reinforcement phase.

Experimental investigations for the mechanisms and parameters that control ceramic abrasive tribology in single crystals and poly-crystal materials have concentrated on loads, abrasive travel velocities and abrasive particle sizes. Tribological studies of composite materials have concentrated on the relative volume fractions of the second or third phases. These studies use simplified abrasive geometry and carefully controlled indenter materials and the same abrasive hardness. In all cases, the material degradation mechanism, at room temperatures, are dominated by a fracture process. Understanding the parameters that influence wear in general engineered ceramics and porous cement materials is complicated because of their sensitivity to flaws. Future research towards understanding the wear behavior in porous ceramics and materials with high flaw densities is needed. The influence of thermal transients at the wear scar, micro-thermal shock, relative hardness of the abrasive and elevated temperature tribological mechanisms remains to be studied.

2.1.9 Mechanical Properties

Refractory ceramics are brittle materials, and experience has demonstrated that the strength of heterogeneous ceramic materials is more influenced by the microstructure and flaws instead of the intrinsic material properties. The prediction of the mechanical properties of a ceramic structure depends on strain, strain rate, stress fields, material properties, temperature, temperature history and microstructure. The external loading conditions, material geometry and elastic modulus are needed for analysis. Typically, ceramic refractory materials are loaded in compression and have simple geometry. The elastic modulus is temperature dependent and ceramic materials undergo a gradual brittle to ductile transition. Heterogeneous ceramics change over a wider temperature range and therefore temperature limits are conservatively specified several hundred degrees lower than the softening point or PCE (pyrometric cone equivalent temperature). At higher temperatures, creep deformation is possible, depending on the loading characteristics. Non-linear mechanics are applicable at elevated temperatures.

Mechanical property analysis is restricted to linear-elastic methods because of the brittle nature of ceramics. Depending on the stresses and microstructure, a ceramic may fail by a number of alternative damage processes. The important damage mechanisms in ceramic materials are brittle failure, subcritical crack growth, and cyclic fatigue. Through most of the operating temperature range the most important failure mechanism is brittle failure. No plastic deformation is associated with brittle failure. Components fail by fast propagation of one or more cracks; the strain energy released during the fast-crack propagation is equal to the energy of the newly created fracture surface. The crack starts from the critical flaw within the material. The stress intensity reaches some critical value K_{Ic}, and failure occurs. A critical flaw depends on the loading conditions, defect size and orientation. Brittle failures are probabilistic, depending on the chance of finding a critical defect within the component.

Sub-critical crack growth is a process of crack growth at loads and flaw sizes less than the critical values. The flaw size grows as the component is loaded in brittle glass materials and crystalline materials with glass-bonding phases. The strength of the component is lower after loading than before loading. Kingrey [6] and Barsoum [7] use an

activation-energy approach to understand sub-critical crack growth. The cracking activation energy is lowered by the elastic strain energy at the crack tip. The crack tip stress field also lowers the energy for healing broken bonds. The crack growth rate depends on the number of broken bonds reduced by the number of bonds healed. The rates of bond breaking and healing are Arrhenius relationships based on a stress-intensity type factor and the activation energy. The sum of the two processes or the sub-critical crack-growth rate can be approximated by $v \approx K^n$, where n is a material parameter. The sub-critical crack growth changes with microstructure, volume of glass bonding phase, temperature, environment and composition.

Fatigue damage is generally not considered possible in ceramic materials because of the linear elastic behavior. However, crack initiation and growth due to cyclic applied loads can cause fatigue damage in ceramics. Initiation from crack-like defects in crystalline ceramic materials is attributed to small non-elastic events like microcracking, thermal stress, and friction at crack surfaces, twinning and phase transformations. The number of cycles to failure is dependent on the environment and load amplitude. The useful life of the component is dependent on the load and cyclic load frequency. Thermal fatigue is an active mechanism in refractories that operate at elevated temperatures.

Creep deformation is a degradation process that is specific to the microstructure. The deformation mechanisms are different for single-phase ceramics than for heterogeneous ceramics with a boundary phase, porosity or duplex structures. Creep in pure, single-phase ceramics is dominated by either volume or grain boundary diffusion mechanisms. Deformation rates depend on the applied stress, temperature and grain size, increasing linearly with stress and decreasing with increasing grain size. Dislocation creep is active at high temperatures and stresses but not usually significant aside from the study of displacements during hot isostatic pressing. Multi-phase ceramic materials and ceramics with grain-boundary phases that have lower melting points than the larger grains are dominated by diffusion creep processes. Diffusion creep rates increase with stress and temperature and are found to dramatically increase above the brittle-to-ductile transition temperature which is approximately $0.8T_m$. These temperatures are above the softening point, beyond the normal operating conditions for the specific refractory material. Heating refractories above the softening temperature activates the common

sintering mechanisms: diffusion creep, dislocation creep and grain-boundary sliding. These result in grain nucleation and growth of the grains and void movement. Under applied stress the more voids will form and coalesce at the grain boundaries and triple points. Cracks initiate at the voids and contribute the defect population that limits the useful life of the material.

Castable cement microstructure is a heterogeneous multi-phase material with a complex microstructure and a number of flaws, Jennings [60]. The most common flaws are porosity and shrinkage microcracks resulting from drying and sintering. The type of flaws spans the scale from molecular-sized pores to macro-sized cracks. The effect of the porosity and reinforcement phases counters the propagation of cracks, preventing cracks from reaching the critical-flaw size. The final strength of the castable cement refractory depends on the microstructure, specifically the distribution of the flaws and their orientation to the direction of the applied load. The castable installations are exposed to compressive and expansive stresses. The common castable refractory is restrained from free thermal expansion by the external support from the wall.

The strength and elastic modulus are used to characterize the mechanical properties of refractory materials. The strength is quantified using compression and bend test methods. Compression test crushes square or rectangular specimens recording the maximum stress or load achieved before failure. Modulus of rupture (MOR) is determined from three-point bend tests. Generally all ceramic materials are sensitive to the temperature. A brittle-to-ductile transition occurs at elevated temperatures after the bonding phases start to soften. Ceramic materials exhibit slower crack growth rates with increasing amorphous phase content in the bond material. Below the softening temperature the strength behavior increases with temperature due to the relaxation of internal stresses. The viscosity of the bonding phase is important to the loss of strength above the softening temperature. The modulus of rupture decreases as the volume fraction of viscous bond phase increases. High strength may not be as important to refractory materials as other ceramic material applications and likely depend on the intended use of the product.

2.2 Experimental Plan Synopsis

The core purpose of this thesis was to optimize the refractory cement properties via manipulation of the high temperature microstructure by changing the ceramic constituents. The *in situ* fired castable cement installation is a heterogeneous structure and can be divided into three zones according to the temperature and bonding structure. The function of each zone and the microstructural changes with temperature are important to the improvement of the tribological and strength properties. The low temperature (hydraulic bond) zone functions to structurally support the other zones. The low temperature zone is anchored to the furnace or oven framework. The low temperature zone requires strength, which is drastically reduced with decomposition of the hydrates. The intermediate (mechanical interlocking) zone has the greatest porosity and is weaker than the hydraulic bond zone. As a consequence, the intermediate zone offers the greatest resistance to heat flow. The hot (ceramic bond) zone is expected to maintain good strength characteristics, high chemical stability, good wear resistance and resistance to thermal shock.

Optimization of the hydration process and selection of reinforcement phases with high aspect ratios can improve the hydraulic bond microstructure. Modifying the composite microstructure, reducing the volume fraction of decomposed hydrate structures and promoting high packing factors can optimize the mechanical interlocking microstructure. The latter two items are accomplished by the addition of an inert material sized to optimize the packing factor. Ceramic bonding zone improvement can be achieved by increasing the volume fraction of high temperature phases with wide stoichiometric range that form stable ceramic bond phases. An additional measure will be taken to optimize the microstructure using reinforcement phases matched for thermal expansion with the matrix phase.

One technique for the study and improvement of an engineering property is to modify an existing product and study the change in a comparative and sequential process. The experimental process used refractory cement clinkers and added different high

temperature stable oxides and reinforcement phases to formulate batches. The batches were cured, dried, sintered and tested. Reformulation and testing are continued until optimization is complete.

Materials selection criteria were based primarily on improved high temperature stability, increased strength, low thermal conductivity and increasing wear resistance. Additional materials selection criteria included consideration for green strength and corrosion resistance.

Modifying the hydration microstructure can be accomplished by several methods: changing the hydraulic clinkers, diluting clinker concentrations with inert oxides, altering cement to water ratios, altering hydration temperatures, altering hydration times and using admixtures to chemically favor or retard growth of one hydrate over another. Three hydraulic matrix clinkers and three inert oxides were selected as the basis for altering the hydration products. The cement to water ratio was standardized although experimentation included changing the ratio to determine the sensitivity of properties to changes in the cement to water ratio. The hydration time and temperature of the cure are important considerations towards the development of strength. Because of the sensitivity, the experimental procedure standardized these two parameters.

An equilibrium microstructure over the refractory wall cross section is not likely. The phase distributions are defined by sets of metastable phase conditions given by the local hydrated chemistry, nearest neighbor oxide compounds, impurities and sintering temperature. Equilibrium phase diagrams are used to select optimum compositions based on higher melting point phases. The diagrams are also used to target high temperature phase fields that are stable over wide temperature and stoichiometric ranges.

Calcium aluminate was selected as the base material to build the composite castable refractory. The calcium aluminates CA (T_{Mp}=1605°C) and CA_2 (T_{Mp}=1750°C) are common refractory clinkers used in castable refractory cements. Depending on the aluminate, commercial supplies are found with 2% to 20% iron oxide, 0% to 5% silica and free lime and alumina. Impurities depend on the origin of the alumina- and calcia-containing ore's use for the raw materials. Impurity ions of sulfur, chlorine, sodium and potassium are typically less than 1%. Suppliers may intentionally add iron oxides

to promote the formation of tetracalcium aluminoferrite (C_4AF_3). Tetracalcium aluminoferrite is a hydraulic active clinker common in cement production. Calcium aluminates are readily available at low cost.

The inert oxides selected to mix with the calcium aluminate clinkers are magnesia MgO (T_{Mp}=2852°C), alumina Al_2O_3 (T_{Mp}=1605°C) and spinel $MgAl_2O_4$ (T_{Mp}=1605°C). Some experiments using chromia Cr_2O_3 (T_{Mp}=2330°C) and titania (T_{Mp}=1875°C) are preformed, but the bulk of the experiments concentrated in the Al_2O_3 – MgO – CaO ternary system. The experimental formulations followed the three principal binary joins in the C-A-M system. Figure 2.6 illustrates the three isopleths: CA - MgO, CA – $MgAl_2O_4$, (MA) and CA_2 – MgO. A commercial blend of CA_2 and Al_2O_3 was also used for experimental formulations using chromia, magnesia and spinel. The molar compositions are selected to lie in the equilibrium periclase and spinel phase fields. The periclase and spinel phases are high temperature structures that have wide stoichiometric ranges for each of the selected additives.

The reinforcement materials selection is important to the performance of the composite. Aside from the geometric considerations, matching the reinforcement material thermal expansion to that of the matrix is important to the refractory undergoing thermal cycling. The reinforcement phases selected for this investigation are zircon $ZrSiO_4$ (T_{Mp}=2200°C), zirconia ZrO_2 (T_{Mp}=2677°C), spinel $MgAl_2O_4$ (T_{Mp}=2135°C) and dead burnt magnesia MgO (T_{Mp}=2800°C) all exhibit thermal expansion close to that of the selected matrix materials. Different concentrations of the reinforcement phases are blended to cement clinker and additive blends to increase strength and improve wear resistance.

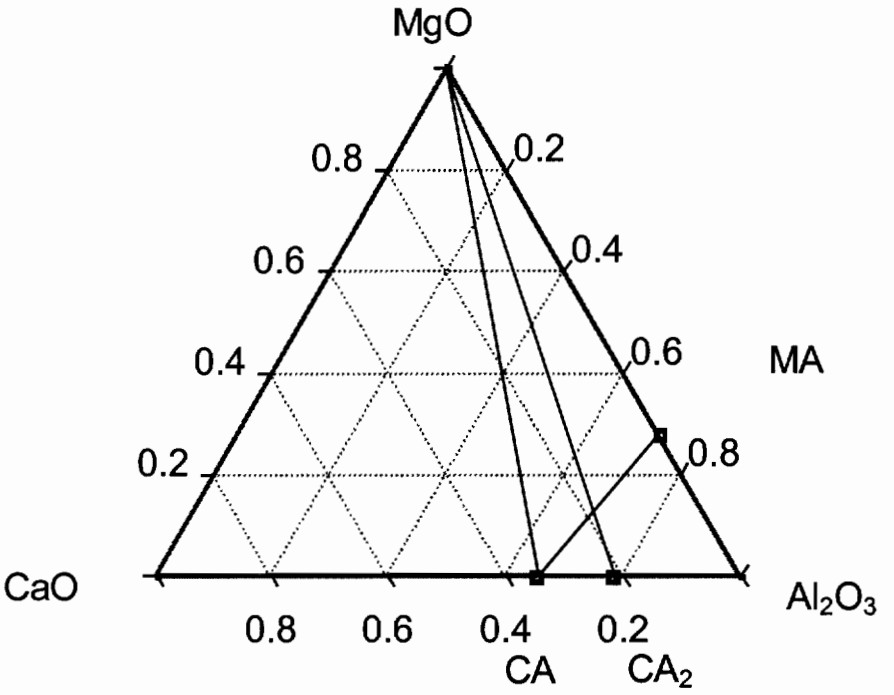

Figure 2.6. Ternary diagram of the C-A-M system illustrating the experimental formulation psuedo-binary isopleths.

2.3 Sample Formulation

2.3.1 Introduction

The experimental objective was to optimize high temperature stability, strength, wear resistance and thermal conductivity using experimentation. The material parameters were adjusted by changing matrix composition and reinforcement volume fraction. Degradation resistant microstructures can be designed by knowing the degradation mechanism and selecting the materials and the processing to resist degradation. The microstructure in this case can be improved using composite technology and using high temperature oxides and wear resistant reinforcement phases to strengthen and thermally stabilize high temperature cement.

Materials experimentation on complex heterogeneous, non-equilibrium multi-variable systems are time consuming, tedious and resource intensive. Property modeling by developing empirical relationships between key parameters and composition reduces the complexity of testing. Therefore, reducing the complex system to the important parameters is essential. The functionality of the material provides direction for simplification. Refractory castable cements are used at elevated temperatures and are expected to function in conditions of two-phase flow, gas and particulate, and under severe thermal gradients. Low thermal conductivity, high wear resistance and strength are properties that would indicate a material would perform well in service. Empirical results are meaningful when the boundaries of the relationships are known. Comparative testing, duplicate samples and reference standards are used to define the boundaries and the validity of the testing.

2.3.2. Concrete Design

Composite material designs are intended to extract the best properties of two or more materials coupled through an interface. The refractory composite cement design uses the binding properties of cement, high temperature resistance of ceramic oxides and the strength and wears resistance of ceramic aggregates. The requirements for the cement matrix phase are high cohesion, elevated melting point, and resistance to heat flow and good thermal shock properties. The requirements of the additives are high thermal stability, wide stoichiometric range and high melting point. The reinforcement phase material requirements are to provide strength, high wear resistance, a matched thermal expansion with the matrix, a high melting point and high surface roughness. The additives can be optimized for purity and size distribution. The reinforcement phase can be optimized for thermal expansion, porosity, size, distribution, aspect ratio, and purity.

Raw materials, particle size, aspect ratio, packing density, thermal processes and time influence the microstructure. Molecular rearrangement in the castable cement is by two processes: hydration and thermal diffusion. The castable ceramic cement is mixed with water and cured to form hydrates. The hydrates bond with the parent cement clinker and interlock with the hydrates from adjacent clinkers. A complex network of

interlocked hydrate structures binds the additive and reinforcement particles. Diffusion processes are activated during firing and high temperature operation. The metastable hydrate structures rearrange at elevated temperatures to form lower energy structures. The temperature history and thermal profile across the installed refractory cement produces three characteristic microstructure zones based on the predominant bonding mechanism. The microstructure changes across the wall thickness, normal to the heat flow. Ceramic diffusion bonding predominates at high temperatures, mechanical interlocking bonds the structure at intermediate temperatures and chemical hydrate bonding is present at low temperatures. The material properties depend on the type of bonding.

The composite cement design must account for microstructure (and chemical) and thermal gradients across the structure. Heterogeneous composite materials are complex structures and often competing or synergistic mechanisms change bulk properties through a wide range of operating temperatures and environments. An example is the differential thermal expansion. The thermal expansion is an important design consideration across a steep thermal gradient. The mismatch stress is made more severe by the high range of temperatures in refractory applications. Operating thermal gradient can produce thermal stresses that exceed the critical fracture strength for crack initiation. The ideal selection of additive oxides and reinforcement aggregates are materials with matrix matched thermal expansion to reduce the stress to zero. Highly porous and polycrystalline phases are more tolerant of micro cracking through arresting the propagation. Additive oxides and reinforcement phases with high solubility for the matrix atoms promotes diffusion and therefore reduces the thermal expansion differences.

The design of the composite cement also needs to consider the strength, thermal conductivity and wear properties. Mechanical strength in a brittle material is a statistical process defined by the weakest component and the stopping of a propagating crack before it reaches critical flaw size. Under loading conditions, the matrix flaw will propagate until catastrophic failure or the crack will arrest at a pore or reinforcement particle. The cracks can also grow to critical size when many pores are connected or aligned in the direction of the propagating crack. The composite interface can be either coherent or incoherent. Interface incoherence is a flaw and it will grow when the ceramic

body is loaded in the right direction for propagation. The interface volume increases with volume fraction of reinforcement, and depending on whether the interface is coherent or incoherent, an increase of the reinforcement volume fraction will change probabilities of critical flaw size and failure.

In conventional ceramic materials, intergranular and transgranular cleavage cracks initiate at free surfaces like grain boundaries. The energy to propagate a crack in the grain boundary is much less than the energy to propagation in the grain. All grain boundaries represent intrinsic flaws in ceramic materials. Intrinsic flaws propagate up and down a grain to grain interface until arrested at the triple point or the abutting grain boundary. The intrinsic flaw size becomes the length of the grain boundary or is about one grain diameter. Larger size particles used for ceramic compacts have larger intrinsic crack lengths. Using the Griffith fracture criterion, the strength of the polycrystalline ceramic is proportional to $d^{-1/2}$. For example, the intrinsic flaw size for a high strength ceramic, single phase, spinel material ranges from 25 microns to 100 microns depending on the handling and forming process [7]. The particle diameters in the ceramic cement clinkers range between 10 microns and 50 microns. Hydrates range from 5 microns to 20 microns and additives range from 20 to 50 microns in size. The strength limiting degradation mechanisms in ceramic cements take place on the dimensional scale of microns to millimeters. The composite cement formulations are designed to block crack propagation and beneficially influence the microstructure on this scale. The optimum reinforcement material should be sized between 1 mm and 8 mm.

Increasing the volume fraction of reinforcement material can optimize the composite wear resistance. However, sufficient matrix material to bind the additives and reinforcement is also important. The distribution of the reinforcement material is determined by the nearest neighbor distance. The distance should not be greater than the critical flaw size for catastrophic failure. The reinforcement to reinforcement particle spacing also should be designed to be farther apart than the strain field resulting from the thermal expansion. The interface bond should be coherent for optimum shear stress distribution to the reinforcement and the transfer of compressive loads from the matrix

to the reinforcement. Reinforcement particles with high aspect ratio and surface roughness improve the interface properties. The microstructure arrangement of reinforcement with a high aspect ratio is important to the development of directional properties and high packing factors.

The initial ceramic particle size can influence the final strength of the fired ceramic product. Conventional ceramic materials are sintered to achieve high density. Grain growth and large grains produce long grain boundaries that may approach the critical flaw size. Conventional, highly dense ceramics exhibit an inverse strength correlation to the grain size. Selection of smaller initial particle size can be used to produce fine grains and a higher strength product. Smaller grains also provide for high surface area to volume ratio that produces more rapid sintering.

The thermal history, thermal stresses and environmental exposure are design conditions that need consideration. The castable product must be designed for extreme thermal gradients and therefore must have a dynamic microstructure, one that can function at each end of the temperature range. This can be accomplished by material selection and limiting the size of the reinforcement. The reinforcement strengthening and thermal expansion are competing processes. Large reinforcement particles improve compressive strength and wear resistance but also increase the strain energy that the matrix must accommodate. Matching the reinforcement material to the porous matrix material is not simple. Thermal gradients and cycling in the castable product during service produce severe strains concentrated at the matrix to reinforcement interface. A highly porous reinforcement can minimize strain, however, the decreasing density offsets the wear resistance and strength.

Materials selection also necessitates the need to factor impurities and the economic off set commercial products provide. Impurities are found in the matrix cement, additive oxides and reinforcement aggregates. Matrix cement impurity control centers on silica and calcia, both important ingredients in the cementation process but detract from the high temperature stability. Both form liquid and glass-like phases at elevated temperatures, which on one hand aid in the formation of ceramic bonding but also decrease the strength when present in concentrations greater than 10 percent. The higher the temperature the more sensitive the matrix cement is to the impurities.

However, in a high thermal gradient the loss of strength is confined to the high temperature skin of the refractory installation. The composite design allows for the reinforcement aggregates to offset the loss of strength. The high temperature additive oxides also offset the lack of strength on the hot face of the castable cement installation. Economic penalties are paid for high purity matrix phases. The objective is to promote high thermal stability by minimizing or avoiding the formation of glassy and low melting point phases. Also, additive oxides and reinforcement aggregates selected for high solubility ranges can compensate for impurities found in more economical commercial matrix cement products.

The reinforcement phase aspect ratio and surface roughness can be optimized to improve interface microstructure and shear stress distribution. Higher aspect ratio reinforcements distribute shear stresses over a greater area normal to the long axis and geometrically greater toughness by presenting a larger cross section to crack propagation perpendicular to the long axis. Conversely, an oriented microstructure produces anisotropy and exaggerates the differential thermal expansion stress at the ends of the reinforcement phase. The high surface roughness increases the foot print surface area for micron size cement hydrates to set and bond to the reinforcement. Increasing the number of interface bonding hydrates, mechanical interlocking and ceramic bond surface area reduces the effective unit shear stress.

Ceramic materials are poor conductors of heat. Thermal conductivity in ionic solids is by phonon conduction. Thermal conductivity increases with density as porosity reduces the volume of material for phonon flow and therefore directly influences the thermal conductivity. The porosity in the fired castable refractory cements is distributed in as many as five morphological scales: molecular, nano, meso, micro and macro scales. Fine porosity also has an additional benefit as a crack arrest feature. Porosity is an important microstructure feature that imparts high thermal shock resistance and increases the toughness. Small micro cracks are arrested when the crack tip reaches the edge of a pore. The porosity size and distribution are unique to the three different bonding zones.

The composite design, abrasive properties, test parameters and the substrate material properties define the ceramic abrasive wear mechanism. The important material properties are hardness, density and the material response to internal and external loads as

well as thermal strains. The thermal strains are intensified at the wear surface because of the low dissipation of heat caused by both the intrinsic ceramic properties and the porosity. The installed refractory operational wear occurs at elevated temperatures. The thermal strains in the refractory are the greatest at the hot face because of the thermal gradient. Reinforcement phase materials with higher density, hardness and strength are added to increase the wear resistance. The reinforcement dissipates the contact pressure over a larger area. The microstructure of the interface zone is important to the abrasive wear resistance and transfer of the contact pressure away from the surface to the bulk ceramic.

2.3.3 Formulation Matrix

The batch formulations were based on changing the additives and reinforcement to determine the relationships listed above. Composition weight fractions and reinforcement volume fractions were standardized where possible. The test matrix used random duplicate tests for validity checks.

The compositional matrix was designed to canvas a composition range in the calcia-aluminate-magnesia (CaO-Al_2O_3-MgO) ternary system. The periclase and spinel phase fields offer the greatest promise for high temperature stability. The formulations aim to minimize the calcium aluminate phase and maximize the magnesia and spinel phases. Sufficient calcium aluminate is needed to bind particles at low and intermediate temperatures. Excess calcium aluminate contributes to the fraction of material available to form low temperature liquid eutectics which is counter productive. Impurities like silica and iron similarly produce low melting point compounds.

The experimental approach called for initial investigation of the microstructure and the influence of additives and temperature. Based on the results from the initial investigation, formulations for mechanical property and thermal conductivity tests were prepared. Early formulations used premixed high alumina-calcium aluminate blends and smaller batch sizes for rapid results. Formulations for mechanical property testing (strength and wear resistance) were made from all three calcium aluminate cement types.

Efforts were taken to standardize preparations to enable cement to cement and batch to batch comparisons. Duplicate and control batch formulations were made to develop secondary relationships between formulations.

The premix (high alumina calcium aluminate blend) formulations are limited to compositions along the two main binary joins between CA-M-MA in the calcium aluminate cement-magnesia-spinel ternary component subsystem. Also, a series of formulations with chromia are designed compare the new formulations with the historical benchmark for high strength and corrosion resistant compositions. The premix high alumina calcium aluminate compositions provide a wide range of microstructures for comparisons of the bonding and strength the addition of magnesia, spinel and chromia.

The Fondu cement formulation matrix was limited to compositions along the two main binary joins in the cement-magnesia-spinel ternary subsystem. The batches are formulated to include both high-density zirconia grog and crushed spinel brick as the reinforcement phases.

Calcium aluminate blend formulations to include a wide variety number of compositional binary and ternary joins for study. Crushed and milled commercial dead burnt magnesia is the primary additive in these formulations. But, other formulations include fuse cast magnesia and chromia blended powders, alumina, alumina and titania blends, and cerium oxide. The formulations also varied the cement to water ratio and compared two compaction methods to improve the density of the cast test specimens. These formulations also used three types of reinforcements. The reinforcement volume fraction and the size distribution were changed to study and compare the microstructure and properties.

2.3.3.1 Batches

Batch formulations were used for experimentation and testing. Mineral composition and/or reinforcement volume fraction was adjusted in each batch. The wear and strength properties can be influenced independent of the composition by variations to the batching process, for example: sample size, molds, mixing, curing and sintering. The

more important of these parameters are powder sizing, mixing sequence, water temperature, pressing force or green density, hydraulic set times, sintering time/temperature and heat rates. Even third order variables like shelf life or relative humidity could influence the final ceramic properties. These second and third order effects can bias test results or totally obfuscate trends. Independent testing to develop correction factors was not practicable in all cases. Careful laboratory practices, standard conditions and using recommended test practice are effective strategies to minimize these influences. Examples of these steps are common batch sizes, standard mixing tools, same molds and standard compaction techniques, common water source, autoclave powders and standard cure cycles and temperature. A unique batch number is assigned to each formulation and records are maintained in a batch log.

2.3.3.2 Sample Types

Sample types and dimensions were selected to help standardize all ceramic forming, curing and sintering processes. The number of samples required depended on the tests to be performed and their specifications. The tests include microstructure analysis, measurement of the density, wear resistance, strength and thermal conductivity experiments.

Sample size for microstructure analysis was limited by the sample preparation process and analysis equipment constraints. Care is taken to avoid introduction of artifacts or stresses that would distort, change or alter the microstructure. Ceramic materials are brittle and contain a fair amount of porosity. Cutting to size ceramic material for microstructure analysis can induce a defect zone and propagate cracks perpendicular to the cut surfaces. The cracks are difficult to remove.

The test method and validity of the results define sample sizes for wear and strength testing. Strength and wear tests are destructive and therefore duplicate samples or coupons made from the same batch are required. The coupons or remains are intended for post-test microstructure analysis and therefore have similar sample preparation constraints.

The coupons are sized to be interchangeable with each test procedure. The coupons are intended to represent material conditions inside the typical gunned, rammed or cast installation thickness.

Heat transfer is less a function of the material property and more a function of the microstructure. Samples for thermal conductivity testing are constrained by the test objective and test method. The test objective is to determine the conductivity under application-simulated conditions. Typical industrial castable applications range from the thin 5 cm first wall liner to a full 24 cm structural installation. The castable materials are efficient insulators and therefore the temperature gradients are steep. The microstructure is heterogeneous across the installation with three defined zones. The zone width is dynamic and changes with temperature exposure. The resultant thermal conductivity is a function of all three microstructures. The sample size and test apparatus needs to be sufficiently sized to develop all three microstructures. The thermal gradient at steady state one-dimensional heat flow conditions is used to determine the thermal conductivity. Heat flow in a direction that is not one dimension greatly affects the results. Edge effects and hot face area influence heat flow direction. A large sample compared to the hot face area and a small sampling volume with respect to the hot face area negates errors due to edge effects. One directional heat flow can also be forced by selecting geometry such that the distance in the heat flows in one direction is less than the other two.

2.3.3.3 Mixing

The objective of mixing ceramic powders was to produce a uniform distribution of particles. Uniform distributions of the different particles favor the greatest packing factors, higher densities and stronger products. Some powders are fragile and excessive mixing produces unwanted fines.

2.3.3.4 Cure and Drying

The growth and development of hydrates takes place during the cure period. The optimum period for hydrate growth depends on temperature, hydrate chemistry and water availability. The calcium aluminate cements typically reach 70% of the final strength in 24 hours and 90% by 48 hours at ambient temperatures. Microstructural rearrangement is important for interface property development, and standardization of the hydrate growth through the cure period allows batch to batch comparisons. Hydration is stopped when the material is dried and free water removed. Physically adsorbed water is removed at temperatures greater than 100°C and the permeability of the cement. Rapid vaporization may damage the samples by thermal expansion. Slow drying at temperatures near 100°C does not damage the samples and therefore the hydrate structures.

2.3.3.5 Sintering

Most ceramic materials are processed from the solid state where as metals, polymers and glasses are usually processed from a molten state. A common thread to solid state processing is compacted fine particles held at elevated temperatures. Fine particles with high packing factors enhance sintering. Temperatures above the softening point are necessary to provide thermal energy for solid state reactions. The ceramic strength development is the result of particles moving together to form ceramic bonds by diffusion processes. Conventional ceramics strive for highly dense final products.

Commercial castable ceramic cements are cast or gunned in 5cm to 24cm thick layers and fired from one side. The industrial application defines the thickness and operation temperature. Maximum hot face temperatures of 1600° to 1800°C can be expected while cold face temperatures may be less than 100°C. Sintering and densification is rapid at the hot face while the cold face remains unchanged from the as-cast microstructure. Microstructure zones are established by the sintering temperature, temperature gradient, thermal history and the thickness of the installation. The low thermal conductivity of a porous cement produces a high thermal gradient within the

highest temperature zone that is located along a relatively thin layer on the hot surface. The low temperature ceramic molecules may melt on the surface and be drawn into the pore spaces by surface tension. Any liquid material (low melting point eutectic compositons) may wet the solid grains and serve as an adhesive between the higher melting point ceramic grains. The liquid bonding zone is a thin dense surface layer. The solid state ceramic-bonding layer is thicker and consists of several types of porosity depending on temperature. The porosity can be several types; found as either intragranular microscopic closed porosity, closed porosity along the grain boundaries and interconnected open porosity. The mechanical interlocking zone is thicker and most of the porosity is open. The mechanical interlocking structure allows the particles to move and shift with thermal stresses and tends to have the highest resistance to thermal conductivity. The cold face material is held together by hydrate bonds.

Cement drying and sintering can be a complex model of simultaneous and sometimes competing processes. Two hold periods are used during the thermal ramp to minimize spalling. The hold temperatures are based on the physical and chemically bound water in the matrix structure. The physically bound water is pore water located in the open and closed porosity. The water is driven from the sample as steam through the open porosity. The chemically bound water is found in the hydrate structures. Chemical decomposition of the hydrates leaves molecular scale porosity in the hydrate crystallites.

The castable composite material is not likely to reach equilibrium. The particle interface bond mechanism is dynamic and the corresponding microstructure changes with service time and temperature. The high temperature (>1200°C) microstructural model has the inert high temperature additive particles bound together with a low melting point liquid phase or solid state diffusion bond. The sintering temperature is selected to provide both solid state (direct bonding) and liquid phase sintering.

2.4 Material Property Evaluation

The ceramic-ceramic composite cement formulations were optimized for thermal stability, compressive strength, wear resistance and thermal conductivity. Material property testing was used to quantify the effectiveness of the changes to the matrix

composition and the reinforcement material and concentration. Four test methods were used to characterize formulated ceramic cement test coupon properties: density, thermal conductivity, wear rate, and cold compression strength. Test data are used to develop empirical relationships between the various test parameters. The tests and procedures are standardized and testing performed in large batches minimize error. Checks on the data quality is provided by using duplicate sampling, blind controls and relative standards.

2.4.1 Microstructural Characterization

Specimens of the sintered samples are prepared for microstructure analysis using metallographic techniques. Microstructure analysis and phase identification used optical and scanning electron microscopy. Open and closed porosity, liquid sintering, reaction zones and micro-cracks are some of the features examined.

2.4.2 Density

The ceramic reinforced cement is not a fully dense material and density measurement requires an understanding of the porosity. The porosity is a key microstructure feature in three bonding zones of the castable cement. The porosity changes characteristics from the green state to the fully sintered state. The porosity in the cement can be found in five different size ranges: molecular, nano, meso, micro and macro scales as discussed earlier.

Theoretical density of a material assumes zero porosity. Shapes and product forms less than the theoretical density contain porosity. The porosity can be either open or closed with respect to the outside atmosphere in the sintered product. Three common expressions are used to describe density of porous materials in ceramic technology. The total porosity is the sum of the open and closed porosity. The apparent density describes the density of the shape that includes closed porosity. The third expression is the volume fraction of the open porosity based on experimental determination of the weight saturated

with a fluid. In the three expressions the terms are defined by, D is the theoretical density of the material, W is the weight, V is the volume, r is the density other than theoretical density and P is the Porosity

$$P_{total} = P_{open} + P_{closed}$$

$$r_{apparent} = \frac{W_{air}}{DV} r_{fluid}$$

$$P_{open} = \frac{(W_{dry} - W_{wet})}{V_{displaced} * r_{fluid}}$$

2.4.3 Thermal Conductivity

The melting point, thermal insulation properties and durability in high thermal gradients all define thermal stability. Thermal conductivity changes intrinsically with temperature and experimentally with microstructure. Refractory composite cement microstructures are dynamic, changing with temperature and time at temperature. The heat must flow through a combination of solid cement clinkers, hydrate skeletons and sintered particles.

The objective is to determine the heat flow through a block of castable cement with a porous reinforcement phase, contrast the matrix composition and reinforcement volume fractions and compare the results against a reference material. The reference material is a magnesia spinel refractory brick.

The thermal conductivity is determined by measuring the thermal gradient at steady state one dimensional heat flow conditions. The data quality is directly influenced by heat flow not parallel to the direction of the set of thermocouples measuring the gradient. Heat flow considerations favor a cement block geometry that has a smaller width to the height or length, thus the geometry forces the heat flow parallel to the direction of the aligned thermocouple set.

The thickness of the sample should be sufficient to have all three porosity zones: hydraulic/chemical bonding, mechanical interlocking and ceramic bonding. These microstructure requirements for meaningful results favor much thicker sample sizes.

2.4.4 Wear Properties

Abrasive wear resistance is an important property for a refractory material. Refractories used in combustion applications require resistance to hot gasses entrained with ash and slag. Gas velocities can reach several hundred feet per second. The wear resistance in brittle composites is strongly influenced by the contact pressure and the distribution over the interface surface. The abrasive wear testing serves two goals; compare formulations to a reference conventional refractory brick and use the results to select optimum formulations based on wear results.

The three-body abrasive test method was selected because it minimizes the influence of the second material, applies a uniform contact pressure over a large sample test area and minimizes the influence of abrasive particle. The test coupon surface is separated from the second material surface by abrasive particles which distribute the load over numerous of contact points. The contact load and abrasive particles are easily standardized from test to test. One standard abrasive wear test is the Dry Sand Rubber Wheel test as described in the ASTM G 65 standard. The test involves loading the coupon in compression against a rotating rubber wheel. A controlled flow of abrasive sand is directed into the contact zone. The test is a standard test used by a number of laboratories for materials selection ranking for abrasive wear service. The wear rates are expressed in terms of mass loss and wear scar characterization. The test apparatus and illustration of the three body wear process are shown in Figures 3.5 and 3.6.

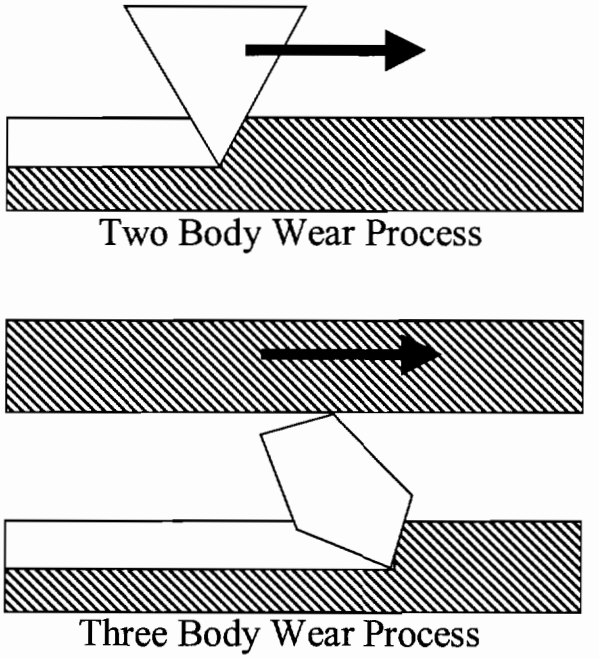

Figure 2.7. Sketch illustrating the difference between two body and three body wear.

2.4.5 Strength Properties

The strength of a ceramic material is limited by brittle fracture. The tensile strength of ceramic materials is more indicative of the flaws than the strength of the bonds. Ceramic materials are usually tested in compression to minimize the influence of the flaw and provide information on the intrinsic strength of the ceramic bond. The compressive strength of dense ceramic materials is directly related to the bond strength. The porous microstructure of the castable ceramic microstructure is inherently flawed and crack initiation is not a problem. The fine porosity is an efficient crack arrest phase. The strength of the composite ceramic is improved with crack bridging and crack deflection using composite design. The compressive strength depends on the shear strength of the interface zone. The mechanical property test results are used to rank the experimental formulations and are used to indicate the coherency between the two phases. The compression test minimizes the influence of parameters other than matrix and reinforcement interface zone. The test is a destructive test and therefore screening of

the weakest interface zone is straightforward. The cold compression strength test is a standard test for refractory ceramics. Results are published in the literature and are used for qualitative comparisons.

As the composite ceramic cement coupons are prepared by pressing, the high aspect ratio reinforcements develop an orientation that may influence the results. The coupons are prepared using standardized methods, the same mold and pressing parameters to normalize the influences caused by processing. During testing the orientation of the applied load is important in anisotropic materials. Coupons are loaded in a direction normal to the press load and along the short direction. This orientation increases the interface zone area that is loaded in compressive shear and allows for a comparison of the different reinforcement materials tested to challenge the compressive shear strength.

2.4.6 Fractography

Observations of the fracture sequence and the fracture surface are important toward understanding the failure process. The composite cement is based on optimizing those features that reduce the effects of the limiting degradation mechanism. The microstructure features that indicate resistance to shear loading are fracture points initiating in the matrix and not at the interface. Observations of reinforcement particles arresting cracks or breaking apart are also important. Observations of the crack path are important in determining the limiting microstructure feature.

3.0 EXPERIMENTAL PROCEDURES

3.1 Materials Selection

Composite design technology allows exploiting the properties of dense and porous ceramic microstructures to produce a structure that is stable at high temperatures, with high strength, good wear resistance and a superior thermal insulator. The melting point of an oxide material provides a benchmark for thermal stability. A second indicator of thermal stability is wide stoichiometric range. Ceramic oxides with the highest melting points are magnesia (2800°C), zirconia (2690°C), calcia (2552°C), magnesia chromite (2400°C), chromite (2275°C) and spinel (2135°C). Magnesia and spinel have the greatest solubility ranges of these six oxides. Calcium aluminate cement alloyed with one or more of these structure-modifying oxides might improve thermal stability.

The properties, economics and impurity concentrations are also considerations used in the selection of additives. Chemical compatibility in this context means to remain inert up to the melting point and/or form stable high melting point phases that span the expected thermal range of the product. As a general rule, the higher purity ceramic oxides are more inert. The impurities in the commercial products are not controlled and make interpretation of the experimental results difficult as well as degrade cement performance. However, performance gains using high purity minerals compete against the economics. Careful experimental practice, using raw materials from the same production batch and controls to homogenize the raw materials before use are employed

to promote uniform impurity effects between batches. Use of the commercially available materials favor the economics as well as make the empirical testing more useful and application driven.

The castable cement composite is fired or sintered in place to impart properties. Conventional ceramic materials are processed to produce homogenous microstructures with specific properties. High performance microstructures in conventional ceramics are characterized by several factors. High strength and flaw free structures are a function of small grain size, uniform microstructure, and high density. Toughness is imparted by composite structures where the second phase behaves like a crack deflector. Composite microstructures with high aspect ratio reinforcement phases provide superior shear strength in at least one direction. A large grain size and absence of amorphous glassy phases provide high creep resistance. Wear resistant microstructures are dense single-phase materials or are composite structures with crack free interface zones. High chemical resistance is obtained from dense microstructures with no open porosity or cracks. Highly porous microstructures with a fine pore size distribution exhibit the greatest resistance to heat flow.

The raw materials used to develop the castable ceramic reinforced composite fall into one of three types: matrix, additive and reinforcement. All materials are oxides in the form of processed cement clinkers or refined/processed oxide powders and aggregates. The materials are listed in Table 3.1.

Table 3.1. Materials Selection

Cement Matrix	**Additive**	**Reinforcement**
Commercial Castable Blend Fondu Calcium Dialuminate Blend	Magnesia Spinel Chromia Dead Burnt Magnesia Alumina Alumina Titania Blend Cerium Oxide	Zircon Zirconia Grog Spinel Crushed Brick Dead Burnt Magnesia

Commercial purity powders and reinforcements are used where possible. Detailed information and product specifications are presented in Appendix A. The powders and reinforcement materials are characterized by product form, purity and bulk density.

3.2 Experimental Sample Preparation

3.2.1 Molds and Shapes

Mold geometry was simple and designed for ease of sample removal. Mold release agents were used to aid sample removal and minimize rough handling. Silicone and oil-base, low molecular weight release coatings were used. Contamination of the samples by the release coatings was minimal and volatilized at low temperatures.

Molds for microstructure analysis samples were made from seamless thin wall aluminum tubing. The mold diameters were sized to minimize cutting necessary for metallographic sample preparation. Two diameters were used; 15.8 mm (0.625 in) and 25.4 mm (1 in) cut into 9 cm lengths. The molds were prepared by covering one end with laboratory Parawax Film. The inside surfaces were coated with a mold release agent. The samples were prepared in groups of two or three to produce multiple samples of the same formulation. The aluminum molds were filled vertically to no greater than 7 cm and limited to three times the diameter to normalize the sidewall resistance and promote samples with nearly the same green density (L/D > 3 produces about a 30% green density difference between the centerline and the wall). The samples were cast in a series of three filling steps, pouring and compacting. An ID ram was used to compact the samples from one end. After curing, the samples were removed by hydraulically driving a ram through the cylinder. Most samples came out of the mold as tight compact cylindrical slugs with little damage. Occasionally a sample jammed in the mold and the samples were removed by cutting the mold, damaged samples were discarded.

Samples for wear and strength testing required duplicate coupons from the same batch. The coupons were sized to be compatible with the two test procedures ~ 13 mm (0.5 in) x 25mm (1 in) x 76 mm (3 in). A four-piece carbon steel mold was used to cast

five standardized coupons. See Figure 3.1 for an illustration of the mold. Figure 3.2 illustrates the samples made from the mold, the sample identification and designated test for standardization. The mold was designed to produce representative samples of the interior of a typical cast refractory wall. The mold and casting process provides for hydrostatic restraint during curing and the formation of hydrates. The cement formulations are initially poured in the mold uniformly to about ¾ height and tamped with a one centimeter diameter flat rod. Extra effort was placed into packing the corners and edges to minimize the packing factor edge effect in the final coupons. The mold was final filled and tamped to a level flush with the sides. The mold top was designed with a protruding section to press the material to a uniform thickness. A Wabash hydraulic press was used to compact the coupons and press the samples to a uniform density. The press was set to deliver a maximum 4000 psi. Bolts were used to secure the top of the mold in place through the setting period.

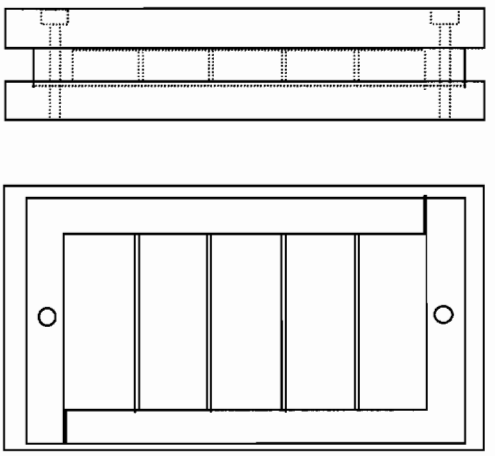

Figure 3.1. Illustration of mold used to produce coupons for testing.

A large rectangular block sample was cast for the thermal conductivity tests. The thermal conductivity test block is illustrated in Figure 3.3. A casting table was made to standardize the sample sizes and provide support for the thermocouple positioning. The casting table consisted of a single plywood platform 40 cm (16 in) x 60 cm (24 in)

and a simple box mold. Vertical walls were made of plywood and secured in place by permanent supports. The test blocks for the thermal conductivity measurements measure 25 cm (10 in) x 26 cm (10.5 in) and range from 6 cm (2.5 in) thick to 12 cm (4.5 in) thick.

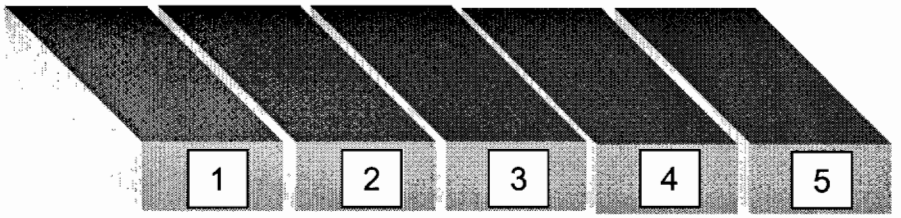

Coupon	
1	1200 °C Firing- Microstructure Analysis, Full Size CCS
2	1200 °C Firing- DSRW Wear Test, Microstructure Analysis
3	1200 °C Firing- Half Size CCS
4	1000 °C Firing- DSRW Wear Test,
5	Archive

Figure 3.2. Illustration of coupons and designation of their function.

Four 16 gage wire type K thermocouples with alumina sheath were selected for durability and stiffness to insert into wet cast refractory with reinforcement. The thermocouples were positioned within the unidirectional heat flow zone spaced ~ 2.5 cm (1 in) apart to avoid interference. The thermocouples were pre measured to reference points on the alumina sheath. The thermocouples were inserted at different depths across the thickness. The array of four thermocouples was positioned in the center of the pre-determined zone where heat flow was one directional. After curing, the reference points were used to determine the distance from the hot face. The distance from the thermocouple tip to the mark was measured to the nearest 0.0025 cm (.001 inch), however the surface roughness was greater than 0.254 cm (0.1 inch).

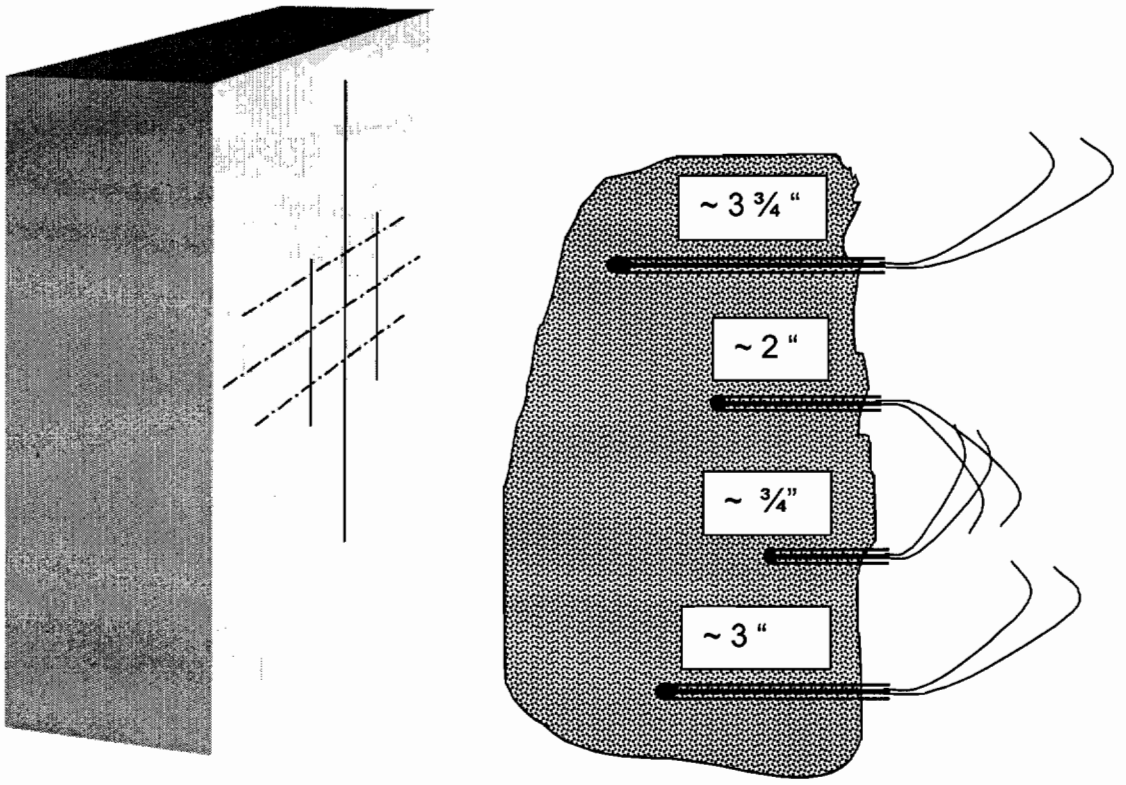

Figure 3.3. Illustration of the test block used for the thermal conductivity measurements. The relative position of the thermocouples are illustrated, distance is from the test block test face.

3.2.2 Mixing

The commercial premix high alumina calcium aluminate blend material provides a high level of consistency. The premix cement and reinforcement phase concentrations were changed with the additives. Separated cement and reinforcement were added to the batches to modify concentrations. Powder sized less than Tyler Standard No. 270 mesh was classified as cement and greater than Tyler Standard No. 170 mesh was considered reinforcement. A greater flexibility for wide compositional and reinforcement ranges was accomplished with the calcium aluminate cement powders. Additives and reinforcement were blended independently.

The grog, spinel and dead burnt magnesia reinforcement particles were pre-soaked >24 hr in room temperature tap water to lower surface tension and promoting good interface bonding. Pre-soaking the zircon reinforcement in the premixed cement was not practicable.

The commercial premix cement was drawn from a freshly mixed supply container into a smaller ½ liter glass container. A watch glass was use to cover the container for cleanliness in the low temperature furnace. The Fondu and calcium dialuminate blends were drawn from a freshly mixed storage container. The powders were heated between 50° and 75 °C, for a minimum of 6 hours prior to use. The physically adsorbed atmospheric water was removed to prevent the formation of agglomerates from daily and seasonal relative humidity changes.

The additives were stored in sealed containers and completely blended before removing material. Raw powders were baked similar to the cements. Premixed blends of the magnesia, chromia and spinel were produced for the entire experimental matrix to assure inter-batch consistency.

Samples made for microstructure analysis and material property testing used the same mixing tools and the same procedures were followed. Batch constituents were weighed on a laboratory gram balance to the nearest 0.5 gram. All portioning was by weight percent. Batches ranged between 80 to 500 grams total weight. The powers removed from the furnace were allowed to cool prior to batch mixing. The temperature of the cement powder and reinforcement, mixing water and room were held within a range between 19° and 27°C. The weighed powders were kept in separate containers until the mixing sequence was started.

A 1-liter screw cap plastic bottle was filled with the dry powders to no greater than 50% and shaken between three to five minutes. The dry constituents were placed in a clean dry 1-liter PET mixing bowl, tap water, used for mixing, was added in two steps. A steel mixing rod was used between three to five minutes to mix the cement to a uniform consistency. The cement was then poured and tamped into the molds. Final vigorous tamping was performed to fill the mold to a uniform level.

Low water cements cure to highly porous structures but are necessary if the castable cement was to be gunned, rammed or shot-created. Unless otherwise noted the water was mixed at an approximate 7.5 wt. % of the total batch weight which constitutes a low water cement formulation. Vigorous mixing was necessary to produce a dry paste-like material. Mix times were controlled in the range between three and five minutes based on producing a paste with uniform consistency. Mixing, workability and uniform filling of the mold increase in difficulty with increasing reinforcement. High cement formulations tend to flash set during the mixing.

Samples for thermal conductivity testing were oversized and a makeshift mixing tray was used. Batch sizes ranged from 12kg to 20kg. The dry blends were autoclaved prior to mixing. The reinforcement was pre-soaked to improve interface bond. The water was added in several steps.

3.2.3 Cure and Drying

The objective of the initial microstructure analysis samples was to observe a fully developed hydrate microstructure and follow the changes as the structure was heated. The microstructure analysis samples were cured above the dew point for 7 days at ambient room temperature (21°C). Samples were kept in the mold for 48 hours to gain strength and to facilitate easy removal.

The coupons designated for material property tests need to replicate actual microstructures and were allowed to cure for 48 hours before stopping the hydration. Coupons were hydrostatically held for 24 hours in the mold and at 48 hours the coupons were autoclaved to remove free water.

The samples for thermal conductivity testing were cured for 48 hours before testing. Block samples were removed from the mold at 24 hours. The blocks were dried from the hot side, for 48 hours, holding the furnace at 75°C before thermocouple measurements were taken and the heating tests started. Thermal conductivity samples were tested immediately after curing to better simulate actual conditions.

3.2.4 Sintering

An electric box furnace was used for sintering coupons. Care was taken to control heating and cooling schedules between the batches. The coupons were soaked at 125°C from 6 to 24 hours to start and at 315°C for 24 hours to remove all physical and chemical bound water. Coupons were sintered at 1200° and 1000°C. A sintering period of 96 hours was used to standardize the microstructure developed. The furnace instrumentation was capable of holding temperatures to ± 10°C. The heat rate was controlled between 50 and 150°C/hr up to sintering temperature. The coupons were furnace cooled over 12 to 24 hours.

The samples were stored dry at constant temperature until batch sintering. Coupons were fired in batches of 20 to 36 samples. A firing plate was used to hold the samples for easy loading. The labeled coupons were placed on the plate and documented on a firing map. The coupons on the bottom layer were placed on their sides with a centimeter between each coupon for airflow. The second layer coupons were placed on end oriented opposite to the first layer for stability. The third layer and fourth were alternated similar to the first two layers.

A box furnace was used for the sintering and thermal conductivity measurements. The furnace was modified with additional thermocouples and alumina furniture was used to support the samples and maintained a uniform heat around the samples. Figure 3.4 illustrates the furnace and chamber.

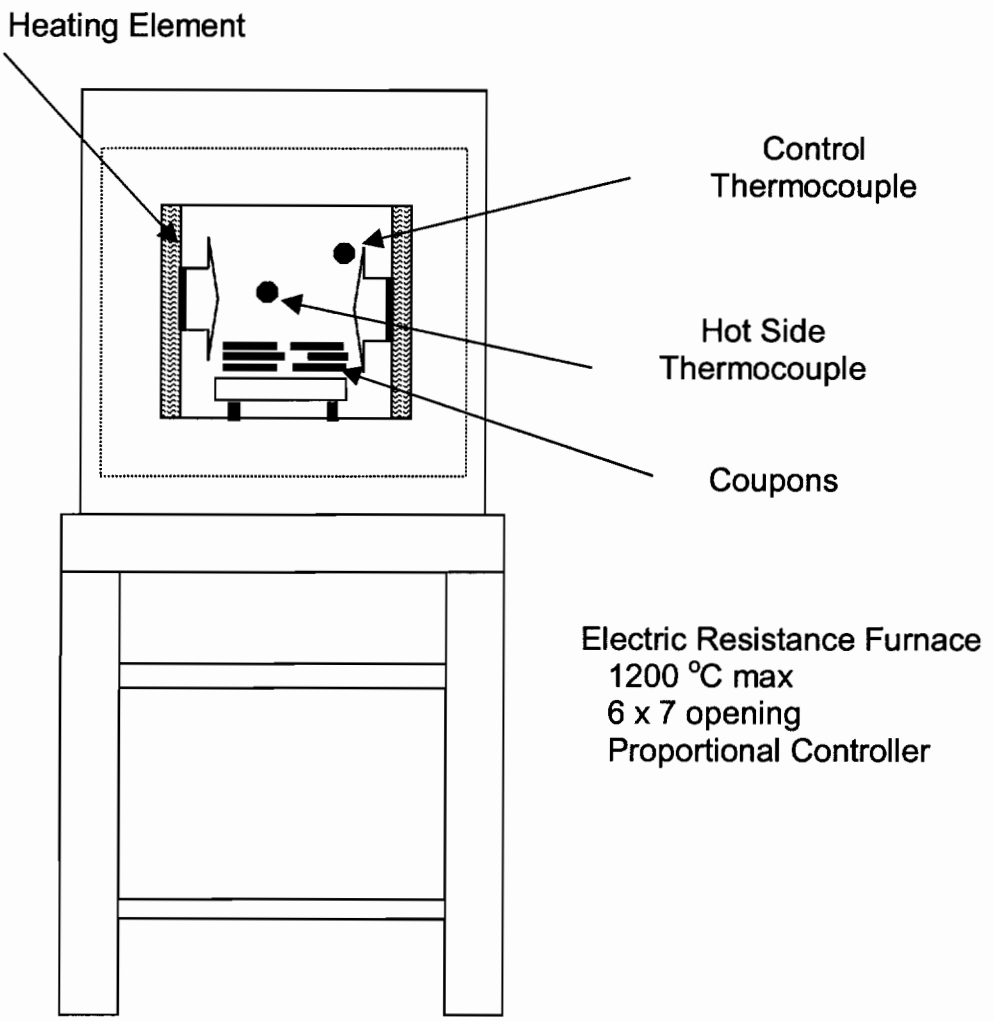

Figure 3.4. Sketch of furnace used for thermal conductivity experiments and sintering of castable cement coupons.

3.3 Experimental Test Matrix

Previous sections discussed the importance of the ceramic properties matched to the designed application of the ceramic refractory composite cement. The properties of the cement are dependent on both the operation temperature and the previous thermal history. Comparisons of the material properties must keep in mind these influences and try to devise test methods and techniques that, at a minimum, normalize these parameters. The thermal stability is a critical property; poor thermal stability renders the composite useless. Equipment was not available for testing for extreme thermal stability, or for determining the pyrometric cone equivalent softening temperature. The quenching

thermal shock test is not standardized and equipment was not available. Moderate temperature cyclic ultra sound thermal shock crack propagation testing has not been standardized for composite cements. Extreme tests exceed the design operation temperatures as well and are difficult to consider representative because the thermal shock of small laboratory samples and that of huge installations are driven by drastically different dead weight loads and thermal stresses.

The experimental approach then used research tests to assess the relative difference between the various formulations of composite cement. Industry standards were produced for both room temperature conditions and elevated temperatures. Room temperature tests were selected for both logistic and equipment hardware reasons. Several elevated temperature mechanisms contribute to the experimental measured properties. The thermal processes can be influenced by the formulation chemistry, the microstructure and reinforcement properties. Examples of these processes are bulk brittle to ductile transition, microstructure creep and thermal gradients. These mechanisms are normalized or made non-existent with room temperature testing. Room temperature testing for relative material property testing has been used by past researches with the understanding that the thermal histories, densities and testing parameters are understood to be similar.

The test matrix design is based on using relatively simple ambient temperature testing to optimization the composition and reinforcement of the castable cement. Cold compression strength (CCS) testing and dry sand rubber wheel (DSRW) abrasive wear test methods used because they challenge the interface properties. The tests were representative of the conditions that limit the functional life of the refractory cement. Testing details are found in sections 3.4.3 and 3.4.4. The test methods are standardized by the American Society for Testing Materials (ASTM).

The experimental approach was to alloy the matrix cement with higher melting point additives and thereby increase the refractoriness. The volume fraction of the cement (the strength producing component) is reduced with additives. The strength loss is compensated for lower temperatures by the reinforcement. The reinforcement phase can be optimized for differential expansions, interface strength, wear properties, chemical inertness and thermal conductivity.

The experimental design provided for an understanding of the calcium aluminate castable cement formulated for high temperature resistance and reinforced for strength with high temperature wear resistant aggregates. Three different matrix base compositions were selected to develop a number of formulations that span the calcium aluminate cement mineral system. Cement formulations had two variables: matrix compositional changes and reinforcement changes. The experimental test matrix was based on changing the volume fraction of the two variable components.

The overall experimental matrix included a number of studies: microstructure examination, DSRW testing and CCS testing, and thermal conductivity measurement. Comparative and empirical relationships were used to establish trends and quantify properties. Comparative relationships were made between commercial samples and control samples free of additives and reinforcement phases. Empirical relationships were developed by carefully holding constant all but one or two variables and testing a series of samples made with different concentrations. Relationships became more complex when two or three variables are changed. Multi-variable trends were possible with sufficient forethought and large sampling populations. The range for which a trend was valid was determined by the use of relative control samples tested at the extreme ends of the composition scale. The test matrix was designed to duplicate some formulations to flag inconsistent trends. The data from some formulations was used in more than one empirical data set thus providing added confirmation of trends. The following material empirical relationships are determined by experimentation.

- Influence of changing reagent grade magnesia on the microstructure and properties in all matrix cements.
- Influence of changing dead burnt magnesia on the microstructure and properties in all matrix cements.
- Influence of changing spinel on the microstructure and properties in all matrix cements.
- Influence of changing chromia on the microstructure and properties in the matrix cements.
- Influence of changing a blend of chromia and magnesia on the microstructure and properties of the matrix cement.

- Influence of changing alumina on the microstructure and properties.
- Influence of changing a blend of alumina-titania on the microstructure and properties.
- Influence of cerium oxide on the microstructure and properties.
- Influence of the changing volume fraction of zircon reinforcement phase on the microstructure and properties of the cement matrix.
- Influence of the changing volume fraction of high-density zirconia grog reinforcement phase on the microstructure and properties of the cement matrix.
- Influence of the changing volume fraction of spinel and a graded spinel reinforcement phase on the microstructure and properties of the cement matrix.
- Influence of the changing volume fraction of dead burnt magnesia reinforcement phase on the microstructure and properties of the cement matrix.
- Trends between the cements, additives and reinforcements.

The test matrix relies on all of the secondary parameters that influence the properties to remain constant. However, heterogeneous ceramic composites systems are complex and there may be influences not anticipated. The microstructure and properties sensitive to the secondary parameters were examined to define the validity of the empirical relationships and give assurance to the final conclusions. The following secondary influences were characterized in the test matrix.

- Influence of cement to water ratio.
- Influence of the sintering cement density with additives and reinforcements.
- Influence of the porosity size and distribution between the formulations.
- Influence of green density with final sintered density.
- Influence of sintering temperature.
- Influence of pressing and vibratory compaction on final sintered properties.
- Influence of changing cement on density.

3.4 Experimental Test Methods

The experimental test data reported in the results section and Appendicies were obtained using the following described experimental test methods.

3.4.1 Microstructural Characterization

The samples were diamond saw cut or fractured into small pieces to place in the standard 1¼-inch metallographic mount. The ceramic pieces were cast in an epoxy resin and catalyst (Struers EPOFIX™). Pressure and vacuum impregnation techniques were used to assist the flow of the resin into the open porosity. Samples were allowed to cure for 24 hours at room temperature prior to sample surface preparation.

The initial rough grinding step used silicon carbide to provide a flat surface. All further grinding used diamond abrasive disks and pastes because of the hardness of the ceramic. Automated grinding and polishing were used to promote consistency. Diamond impregnated grinding disks were used for rough grinding through 45-micron. The grinding steps were standardized at a wheel speed or 200 rpm and 30 lbs. pressure. The grinding times were standardized to 60 seconds.

A three step automated polishing procedure was developed to produce consistent results. The first step was a 6-micron diamond paste, followed by a 1-micron diamond paste polish. A 0.25 micron size alumina slurry polish followed the diamond steps. Each of the polishing steps were made on nylon cloth, 175 rpm and 25 lbs. pressure. Polish times were set at 70 seconds for optimum results. The specimens were cleaned between each step using soap and filtered tap water followed by an alcohol rinse and blow dry. Specimens that exhibited greater porosity were found to retain the 1-micron diamond paste in the open pores.

Visual observations of the polished samples were made using a Nikon Epiphot inverted microscope. The samples were viewed at magnifications from 50 to 400, using both differential contrast and polarizing filters.

Mounted and polished samples were examined at low and high magnifications using either the Nikon SMZ-U Stereoscopic Microscope; Nikon Epiphot inverted

metallograph with halogen illumination or the Zeiss 960 Analytical Scanning Electron Microscope. The stereoscope provided for the examination and observation of the reinforcement and large-scale porosity. The stereoscope was capable of magnifications up to 125 times using the 7.5 zoom lens.

Samples examined using the inverted metallograph were examined at four magnifications, 50, 100, 200 and 400 times. The translucent nature of the alumina and spinel compounds caused the light path to diffuse and at high magnifications edge contrast and microstructure were obscured. Use of polarized light filters and differential contrast improved the observations. A light coating of a carbon film on the sample surface prevented the absorption of light by the sample and improved the ability to detect the edges.

The nonconductive nature of the ceramic samples required a conductive coating for examination in the scanning electron microscope. Samples were coated for conductivity using an Au-Pd sputter film of approximately 300 to 500 angstroms. The samples were examined in both secondary and backscatter imaging. The secondary electron observations were used to identify cracking and porosity changes. The backscatter electron mode images were based on the atomic number of the elements. Differentiation between constituents with widely different atomic numbers was relatively straightforward, for example zirconia reinforcement and the calcium aluminate matrix. However, differentiation between the magnesia and the free alumina phases were more difficult requiring use of x-ray analytical techniques. The scanning electron microscope was equipped with an energy dispersive analysis system using a solid state detector and the Link analytical software program. A semi-quantitative elemental analysis, no standard, was used to identify constituents in the samples.

3.4.2 Density

The green and sintered densities were determined using the Archimedes' principle. Coupons were autoclaved in dry air for 24 hours and cooled to room temperature prior to initial weight measurement. A 100-ml glass graduated cylinder filled with room temperature tap water was used to determine the volume change. The

water miscues was approximately .5 ml and cylinder tick marks at 1 ml. The coupons were allowed to soak in the water 3 to 4 minutes. Air bubbles rise from the surface for the first 60 seconds and the rate decays over several minutes. The sintered coupons reach static conditions more rapidly than the green coupons. The displacement was recorded after bubbles were not seen rising to the surface.

The accuracy of the coupon density determination was dependent on the precision of the volume measurement. The coupon weights were determined to 0.0001 gram. The accuracy of the volume determination was the limitation on the coupon density precision. The measurements were recorded accurate to 1 ml. The ± 1.0 ml accuracy on the volume was an 8% total span or ± 4% due to the volume measurement error. Density measurements were generally taken immediately upon cool down from the furnace to lessen the effects of storage. Rough handling of the coupons can cause chipping, slaking and spalling.

Measurement sensitivity to the length of time allowed to soak was determined with a series of sintered coupons that were allowed to equilibrate as long as 24 hours. A separate test of six coupons were placed in a 100 ml graduated cylinder and displaced volume recorded at 5 minutes and periodically there after. Over a displaced volume range from 21 mm to 29 mm the volume change after a 24-hr period was 1 ml or between three to four percent. The coupon density can be reported to an accuracy of about 10% using the methods described.

3.4.3 Thermal Conductivity

The test matrix is listed in Table 3.2. All three refractory cement matrix materials were tested and two different reinforcement phase volume fractions. An electric box furnace was used as the heat source. The door was modified with a removable section and the instrumented test blocks fit into the door, flush to the face of the furnace. Temperature measurements were taken over a series of hot face temperatures between 300° and 1200 °C.

The furnace was proportional controlled with a maximum 12°C swing at 1200°C. A thermocouple placed in the hot zone center was used as a reference throughout the testing of all blocks. The temperature of the furnace was held constant until the test block reached equilibrium and steady state conditions prevailed. Using a hand held meter the temperature was then determined to be within 1 degree.

Table 3.2 Thermal Conductivity Experimental Test Matrix

Experimental Condition	**Test Run**						
	1	**2**	**3**	**4**	**5**	**6**	**7**
Reinforcement Volume %							
0% Reinforcement			X	X			
60% Reinforcement		X			X	X	
75% Reinforcement							X
Reinforcement Type							
Zircon		X					
Zirconia					X	X	X
Matrix Composition							
Fondu			X		X		
Calcium Dialuminate Blend				X		X	X
Premix		X					
Spinel Reference Brick	X						

The experimental method used determined the steady state temperature gradient across the sample block using the embedded thermocouples. The thermocouples were positioned in the zone of one directional heat flow.

3.4.4 Wear Properties

The abrasive wear rate is determined for each coupon using a dry sand rubber wheel test method. The sample is held in a modified fixture against a rotating wheel with a constant force. The test equipment is sketched and illustrated in Figure 3.5. The sand abrasive is metered onto the wear surface at a constant rate from a hopper. A modified sample holder was made for the thicker castable cement coupon size. The modified holder maintained the orientation of the load normal to a tangent with the pivot point. Constant dead weight load of 88N was used on all test coupons. Coupons were exposed to the wear conditions in sets of revolutions (usually 50) and weighed. A series of seven to ten weight loss measurements comprised a wear test. At least 100 meters of sliding wear were required for a valid test. Coupons were weighed using an electronic micro balance and all measurements recorded to 0.0001 gm. Wear rates were determined following a period of burn-in identified by a uniform wear scar size and the weight loss was relatively constant between equal increments of wear. A linear regression analysis was used to determine the best fit over the greatest number of data points.

The coupon edges and sharp corners were friable and require careful handling. Coupons were individually prepared for wear testing by fixing the friable corners with a thin watered down coating of white glue. Permeation into the coupon was minimal and a 50/50 water to glue ratio does not affect the wear rate and Elmer's® glue mixture. Samples were pre-dried in the autoclave before coating and allowed to dry for 24 hours. All coupons were autoclaved at 75°C for 24 hours before testing.

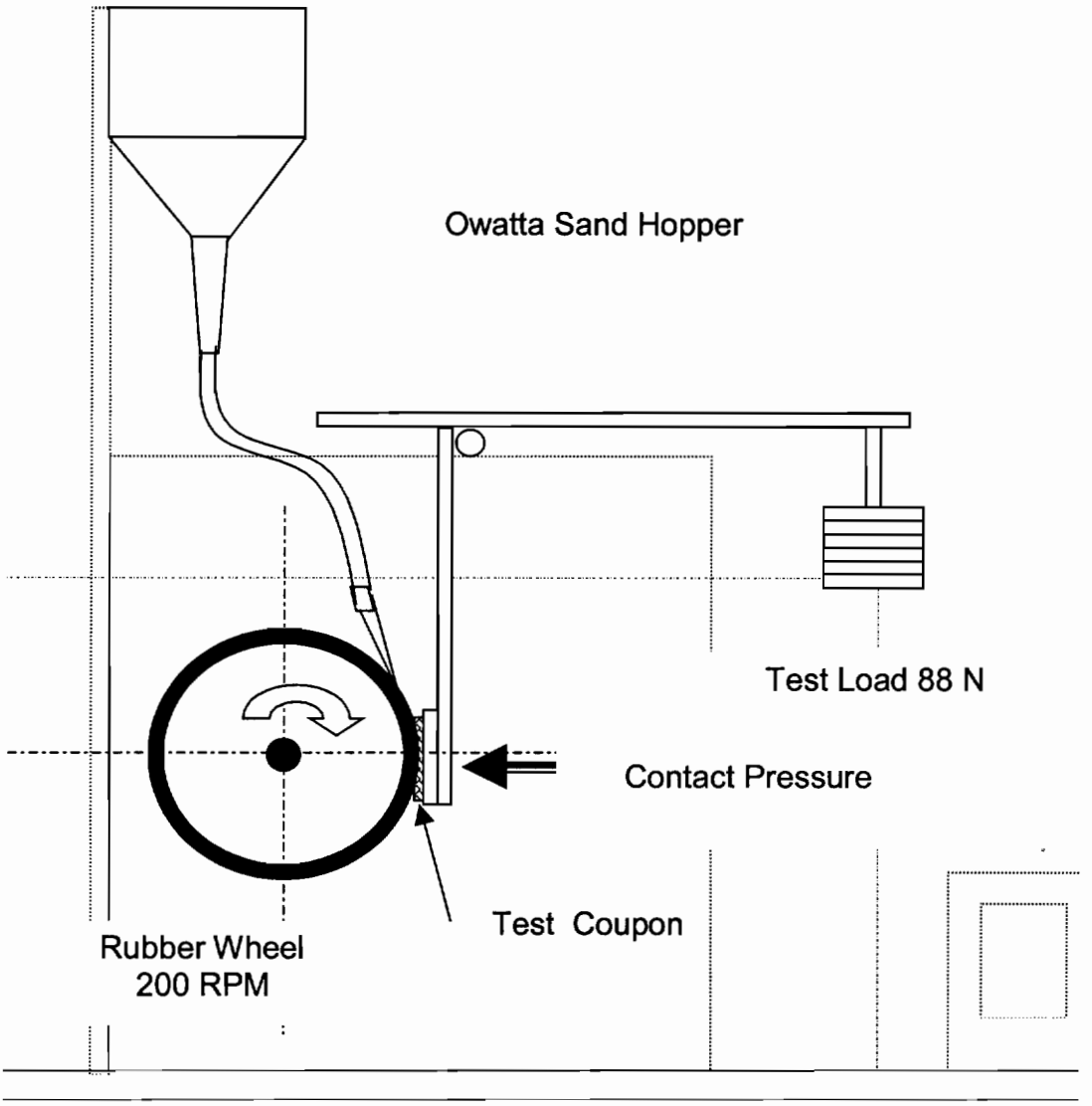

Figure 3.5. Sketch of the dry sand rubber wheel abrasive wear test apparatus.

3.4.5 Strength Properties

The standard ASTM C 133 test method was used as a reference for compression testing. Figure 3.6 illustrates the compression test apparatus.

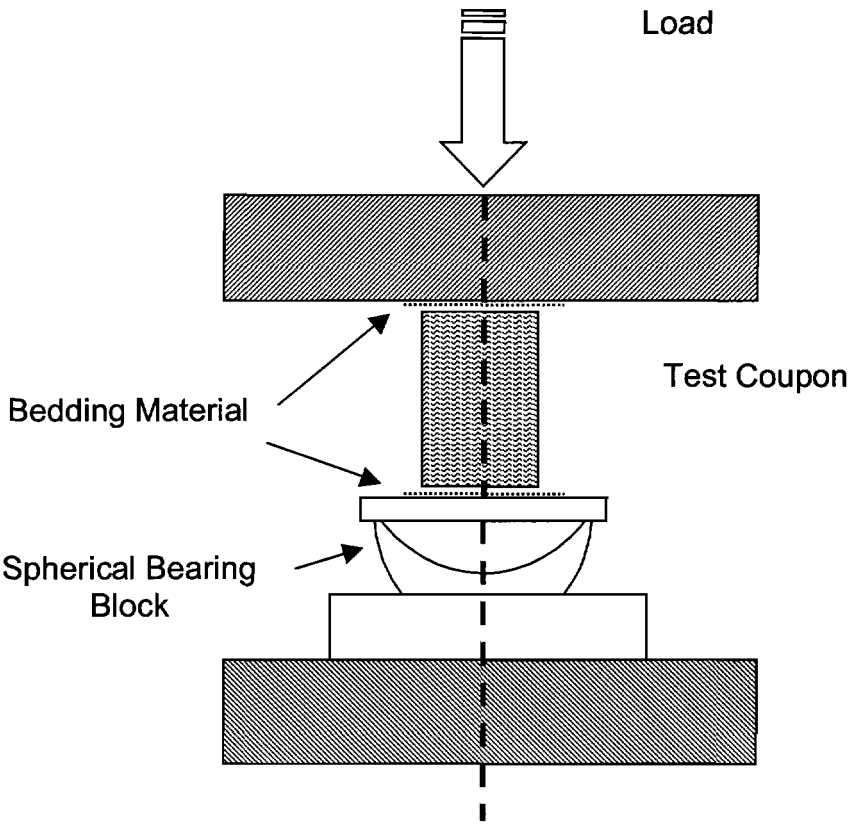

Figure 3.6. Illustration of the compression test apparatus.

Experimental formulations were tested using two sizes. The larger size was the full length coupon dried at over 100°C for 24 hours before testing. Small samples were cut from the larger coupons allowing for two 2.5 cm x 2.5 cm x 1 cm samples. Samples were cut fully restrained using a diamond high speed saw with forced lubrication. Identity and orientation were maintained and samples rinsed and dried at over 100°C for 24 hours before testing. Care was taken during sample preparation to avoid damage to the edges and introduction of flaws.

The coupons were inspected and measured just prior to testing. Three dimension measurements on each side were taken to the nearest .001 inch using a dial caliper. The three measurements were averaged and used to determine the cross section area. Defects, cracks and uneven surfaces were qualitatively ranked to the area of the feature. Features with an area greater than 5% of one end were discarded.

A SATEC hydraulic test machine with a spherical bearing block was used for compression testing. The spherical bearing block allows for loads to be collinear with the axis of the coupon, allowing for non-parallel surfaces. The coupon was placed on top of the bearing block on a cellulose fiberboard greater than the size of the coupon. The coupon was aligned in the center of the sphere. The loading rate was maintained using a hydraulic needle valve. The valve was set to apply a constant loading rate over an approximate 2 minute test. The maximum test load was recorded and cold crushing strength calculated.

3.4.6 Fractography

The fracture surface of selected compression test and impact broken coupons were preserved for observation. Three observation techniques were used to identify fracture characteristics: stereoscope, microscope and scanning electron microscope (SEM).

A stereo zoom microscope was used for detailed examination at magnifications ranging from 3 to 70 times. Remains from compression test coupons were observed for reinforcement particle coverage with the cement matrix material. The evidence of micro-cracking in the interface material which remained attached to the reinforcement was noted. The SEM (scanning electron microscope) was used for magnifications of 50 to 2000 times. The broken pieces were carefully placed on stubs for examination. The ceramic was coated with Au-Pd for conductivity. The area of material adjacent to the reinforcement was observed at the interface for continuity, penetration into the reinforcement surface roughness and crack surface appearance was assessed.

Several samples were examined post test, using the reflecting light microscope. Characterization of the main cracking mechanism, the crack path and orientation were determined using optical microscopy at 100 to 200 times magnification. The controlled rate of loading allows the test to be stopped just following maximum load and before catastrophic failure of the shape.

The failed coupon and all the debris were fixed using a low viscosity epoxy compound. The samples were cured under pressure to completely fill all open porosity. After the polymer has cured, the samples were prepared for optical microscopy.

3.5 Melting Experiments

The upper limits of thermal stability was qualitatively determined by heating the samples and coupons while observing the temperature at which the first liquid formed. The coupons were placed in a thermal insulating brick and an acetylene-oxygen torch with a number 5 tip used to heat the surface. An optical pyrometer using a comparative hot wire was used to estimate the temperature of the sample. The gas regulators were set at the same pressure for each experiment, acetylene at 4-6 psig and oxygen at 18-20 psig. The stand off distance as set at 2 inches. Melting was achieved in 3 to 4 minutes. The surface under went several changes in color from red to white hot. Pyrometer measurements required several minutes to tune the filament to a matching intensity. The samples were allowed to cool and solidify before re-heating and repeating the measurement. Samples that did not disintegrate upon cooling were set aside for visual and metallographic examination.

4.0 RESULTS

4.1 Introduction

The results present the information base of the formulation process, microstructure examinations, density, thermal conductivity, wear and compressive strength. A large number of experimental formulations were made using high temperature additives blended with the three cements and five reinforcement phases. A summary of the experimental formulations can be found in Appendix II. Coupons were tested at room temperature. Results are compared to the other formulations and special coupons made from conventional refractory bricks. The test results and comparisons are presented in the following section and in Appendix IV. The new castable cement formulations were tested in the course of optimization of high temperature stability, strength, thermal conductivity and wear resistance. High temperature stability is an intrinsic function of the melting point of the material and volume fraction in the bulk composite. Thermal conductivity measurement is a function of the material properties but also dependent on the arrangement of the constituents and void space. The thermal conductivity of the castable cement is also dependent on thermal history. Strength and wear properties were directly measured using standardized coupons.

4.2 Melting and Sintering

Overall, more than two hundred formulations have been produced. Selected samples were heated to surface melting or sintered in an electric furnace at either 1000°C or 1200°C. The samples selected for melting and the results are listed in Table 4.1. The temperatures listed for each sample represent the temperature when the first liquid formed on the surface. It was typical for the surface to froth and bubble as the sample was heated. Two temperature measurements were taken and are listed in the table. The samples containing magnesia were found to form a dark discoloration where as the samples with alumina remained white. A number of samples cracked upon cool down from the melting experiments.

Table 4.1. Melt Test Results.

BATCH NUMBER	B10-08-1	B10-08-2	B10-08-3	B10-08-4	B10-08-5	B10-28-1	B10-28-2	B10-28-3
DESCRIPTION	Control Premix	5% Cr_2O_3 Premix	10% Cr_2O_3 Premix	15% Cr_2O_3 Premix	25% Cr_2O_3 Premix	15% MgO Premix	20% MgO Premix	Control Premix
Cement %, of Batch	40.0	38.0	36.0	34.0	30.0	34.0	32.1	40.0
Reinforcement, % Batch	60.0	57.0	54.0	51.1	45.1	51.0	48.1	60.0
Additive % of Batch		5.0	9.9	14.9	24.9	15.0	19.8	
Wt. % H_2O, Batch Total	7.5	11.0	7.4	7.5	7.3	7.3	7.4	7.8
W/C Ratio	0.19	0.29	0.21	0.22	0.24	0.21	0.23	0.20
MATRIX COMPOSITION								
Additive % of Matrix		11.6	21.6	30.5	45.3	30.6	38.2	
Cement % of Matrix	100	88.4	78.4	69.5	54.7	69.4	61.8	100
Alumina, Al_2O_3 as CA	80.0%	70.8%	62.7%	55.6%	43.7%	55.5%	49.5%	80.0%
Calcia, CaO as CA	10.0%	8.8%	7.8%	7.0%	5.5%	6.9%	6.2%	10.0%
Iron Oxide, Fe_3O_4 as C_4AF	<1%	<1%	<1%	<1%	<1%	<1%	<1%	<1%
Silica, SiO_2 as C_2S or C_3S	10.0%	8.8%	7.8%	7.0%	5.5%	6.9%	6.2%	10.0%
Chromia, Cr_2O_3		11.6%	21.6%	30.5%	45.3%			
Titania-Alumina $TiO{\cdot}Al_2O_3$								
Magnesia, MgO						30.6%	38.2%	
Spinel, $MgAl_2O_4$								
Dead Burnt Magnesia, MgO								
Alumina, Al_2O_4								
Cerium Oxide, CeO								
Liquid Temperature, °C								
First reading	1875	1925	1905	1900	1940	2015	2000	1795
Second reading	1800	1900	1965	1870	1890			1835
Surface Condition								
Frothy	partial	minor	minor	minor	minor	major	major	partial
Black	major	major	partial	partial	partial	major	major	major

Table 4.1 Melt Test Results (continued).

BATCH NUMBER	B10-28-4	B10-28-5	B10-28-6	B10-28-7	B10-28-8	B11-24-1	B11-24-2
DESCRIPTION	30% 2:1 Blend Premix	15% 2:1 Blend Premix	25% 2:1 Blend Premix	30% 1:1 Blend Premix	30% 1:2 Blend Premix	20% 2:1 Blend Premix	25% 2:1 Blend Premix
Cement %, of Batch	28.1	34.0	30.0	27.9	27.9	32.0	30.0
Reinforcement, % Batch	42.1	51.0	45.0	41.9	41.9	48.0	45.1
Additive % of Batch	29.8	15.0	25.0	30.1	30.2	20.0	24.9
Wt. % H_2O, Batch Total	7.7	7.2	7.3	7.5	7.3	7.6	7.5
W/C Ratio	0.27	0.21	0.24	0.27	0.26	0.24	0.25
MATRIX COMPOSITION							
Additive % of Matrix	51.5	30.6	45.5	51.9	52.0	38.5	45.3
Cement % of Matrix	48.5	69.4	54.5	48.1	48.0	61.5	54.7
	38.8%	55.6%	43.6%	38.5%	38.4%	49.2%	43.8%
Calcia, CaO as CA	4.9%	6.9%	5.5%	4.8%	4.8%	6.2%	5.5%
Iron Oxide, Fe_3O_4 as C_4AF	<1%	<1%	<1%	<1%	<1%	<1%	<1%
Silica, SiO_2 as C_2S or C_3S	4.9%	6.9%	5.5%	4.8%	4.8%	6.2%	5.5%
Chromia, Cr_2O_3	34.0%	20.2%	30.0%	25.9%	17.2%	25.4%	29.9%
Titania-Alumina $TiO{\cdot}Al_2O_3$							
Magnesia, MgO	17.0%	10.1%	15.0%	25.9%	34.3%	12.7%	14.9%
Spinel, $MgAl_2O_4$							
Dead Burnt Magnesia, MgO							
Alumina, Al_2O_4							
Cerium Oxide, CeO							
Liquid Temperature, °C							
First reading	1985	1975	1950	2010	2075	1985	2015
Second reading	1940	2085		2000	2080		
Surface Condition							
Frothy	partial	partial	major	major	major	major	major
Black	partial	partial	partial	partial	partial	partial	partial

Table 4.1. Melt Test Results (continued).

BATCH NUMBER	B11-24-3	B11-24-4	B12-29-5	B12-29-6	B12-29-7	B1-20-2	B1-20-3
DESCRIPTION	30% 2:1 Blend Premix	35% 2:1 Blend Premix	20% Spinel Premix	25% Spinel Premix	30% Spinel Premix	35% 2:1 Blend Premix	45% 2:1 Blend Premix
Cement %, of Batch	30.1	26.1	32.0	30.0	28.1	26.1	22.1
Reinforcement, % Batch	45.1	39.1	48.0	45.0	42.1	39.1	33.1
Additive % of Batch	24.8	34.9	20.0	25.0	29.8	34.8	44.8
Wt. % H_2O, Batch Total	7.5	7.4	7.0	6.4	6.5	6.8	7.2
W/C Ratio	0.25	0.28	0.22	0.21	0.23	0.26	0.33
MATRIX COMPOSITION							
Additive % of Matrix	45.2	57.2	38.5	45.5	51.5	57.2	67.0
Cement % of Matrix	54.8	42.8	61.5	54.5	48.5	42.8	33.0
Alumina, Al_2O_3 as CA	43.8%	34.2%	49.2%	43.6%	38.8%	34.2%	26.4%
Calcia, CaO as CA	5.5%	4.3%	6.2%	5.5%	4.9%	4.3%	3.3%
Iron Oxide, Fe_3O_4 as C_4AF	<1%	<1%	<1%	<1%	<1%	<1%	<1%
Silica, SiO_2 as C_2S or C_3S	5.5%	4.3%	6.2%	5.5%	4.9%	4.3%	3.3%
Chromia, Cr_2O_3	29.8%	37.8%				37.8%	44.2%
Titania-Alumina $TiO{\cdot}Al_2O_3$							
Magnesia, MgO	14.9%	18.9%				18.9%	22.1%
Spinel, $MgAl_2O_4$			38.5%	45.5%	51.5%		
Dead Burnt Magnesia, MgO							
Alumina, Al_2O_4							
Cerium Oxide, CeO							
Liquid Temperature, °C							
First reading	2120	2080	2015	2010	2035	2030	2125
Second reading	2100	2115	1980	2000	1950	1990	2060
Surface Condition							
Frothy	major	major	minor	minor	minor	major	major
Black	partial	partial	minor	minor	minor	partial	major

Table 4.1. Melt Test Results (continued).

BATCH NUMBER	B1-20-4	B1-20-5	B1-20-6	B1-20-7	B1-20-8	B1-20-9	B1-20-10
DESCRIPTION	55% 2:1 Blend Premix	35% 1:1 Blend Premix	45% 1:1 Blend Premix	55% 1:1 Blend Premix	35% 1:2 Blend Premix	45% 1:2 Blend Premix	55% 1:2 Blend Premix
Cement %, of Batch	18.0	26.1	22.0	18.0	25.9	22.0	18.0
Reinforcement, % Batch	27.0	39.1	33.1	26.9	38.9	33.1	27.1
Additive % of Batch	55.1	34.8	44.9	55.1	35.2	44.9	54.9
Wt. % H_2O, Batch Total	7.2	7.4	6.3	5.9	6.3	7.1	5.9
W/C Ratio	0.40	0.28	0.29	0.33	0.24	0.32	0.33
MATRIX COMPOSITION							
Additive % of Matrix	75.4	57.2	67.1	75.4	57.5	67.1	75.3
Cement % of Matrix	24.6	42.8	32.9	24.6	42.5	32.9	24.7
Alumina, Al_2O_3 as CA	19.7%	34.3%	26.4%	19.7%	34.0%	26.3%	19.8%
Calcia, CaO as CA	2.5%	4.3%	3.3%	2.5%	4.2%	3.3%	2.5%
Iron Oxide, Fe_3O_4 as C_4AF	<1%	<1%	<1%	<1%	<1%	<1%	<1%
Silica, SiO_2 as C_2S or C_3S	2.5%	4.3%	3.3%	2.5%	4.2%	3.3%	2.5%
Chromia, Cr_2O_3	49.8%	28.6%	33.5%	37.7%	17.3%	20.1%	22.6%
Titania-Alumina $TiO{\cdot}Al_2O_3$							
Magnesia, MgO	24.9%	28.6%	33.5%	37.7%	38.0%	44.3%	49.7%
Spinel, $MgAl_2O_4$							
Dead Burnt Magnesia, MgO							
Alumina, Al_2O_4							
Cerium Oxide, CeO							
Liquid Temperature, °C							
First reading	2100	2110	2050	2080	2010	2040	2050
Second reading		2005	1975	1930	1980	1950	2130
Surface Condition							
Frothy	major	major	major	major	major	major	major
Black	major	partial	partial	partial	partial	partial	partial

Table 4.1. Melt Test Results (continued).

BATCH NUMBER	B8-24-1	B8-28-1	B9-1-1	B9-3-1	B9-10-1	B9-26-1	B2-8-1	B2-8-2
DESCRIPTION	LD	Zircon	None	None 1:1	HD 1:1	Spinel	HD Grog	HD Grog
	CA	CA	CA	CA-M	CA-Sp	CA	CA	CA
Cement %, of Batch	50	50	100	50	25	50	40	20
Reinforcement, % Batch	50	50			50	50	60	60
Additive % of Batch				50	25			20
Wt. % H_2O, Batch Total	7.5%	7.5%	7.1%	7.1%	7.3%	7.4%	6.7%	6.7%
W/C Ratio	0.15	0.15	0.07	0.14	0.29	0.15	0.17	0.33
MATRIX COMPOSITION								
Additive % of Matrix				50	50			50
Cement % of Matrix	100	100	100	50	50	100	100	50
Alumina, Al_2O_3 as CA or CA_2	40.0%	40.0%	40.0%	20.0%	20.0%	40.0%	62.0%	31.0%
Calcia, CaO as CA or CA_2	45.0%	45.0%	45.0%	22.5%	22.5%	45.0%	30.0%	15.0%
Iron Oxide, Fe_3O_4 as C_4AF	13.0%	13.0%	13.0%	6.5%	6.5%	13.0%	5.0%	2.5%
Silica, SiO_2 as C_2S or C_3S	2.0%	2.0%	2.0%	1.0%	1.0%	2.0%	3.0%	1.5%
Chromia, Cr_2O_3								
Titania-Alumina $TiO{\cdot}Al_2O_3$								
Magnesia, MgO				50.0%				
Spinel, $MgAl_2O_4$					50.0%			
Dead Burnt Magnesia, MgO								
Alumina, Al_2O_4								
Cerium Oxide, CeO								
Liquid Temperature, °C								
First reading	1875	1900	1875	1750	2015	1900	1850	1895
Second reading	1950	1950	1950	1800	2045	2000	1875	1850
Surface Condition								
Frothy	minor	minor	minor	minor	minor	minor	minor	Minor
Black	major	major	major	major	major	major	major	Major

Table 4.1. Melt Test Results (continued).

BATCH NUMBER	B2-8-3	B2-8-4	B2-8-5	B2-8-6	B2-8-7	B2-8-8	B2-9-1	B2-9-2
DESCRIPTION	HD Grog	HD Grog	HD Grog	HD Grog	HD Grog	HD Grog	HD Grog	HD Grog
	CA	CA	CA_2	CA_2	CA_2	CA_2	CA_2-M	CA-M
Cement %, of Batch	20	20	40	20	20	20	20	20
Reinforcement, % Batch	60	60	60	60	60	60	60	60
Additive % of Batch	20	20		20	20	20	20	20
Wt. % H_2O, Batch Total	6.7%	6.7%	6.7%	6.7%	6.7%	6.7%	6.7%	6.7%
W/C Ratio	0.33	0.33	0.17	0.33	0.33	0.33	0.33	0.33
MATRIX COMPOSITION								
Additive % of Matrix	50	50		50	50	50	50	50
Cement % of Matrix	50	50	100	50	50	50	50	50
Alumina, Al_2O_3 as CA or CA_2	31.0%	31.0%	62.0%	31.0%	31.0%	31.0%	31.0%	31.0%
Calcia, CaO as CA or CA_2	15.0%	15.0%	30.0%	15.0%	15.0%	15.0%	15.0%	15.0%
Iron Oxide, Fe_3O_4 as C_4AF	2.5%	2.5%	5.0%	2.5%	2.5%	2.5%	2.5%	2.5%
Silica, SiO_2 as C_2S or C_3S	1.5%	1.5%	3.0%	1.5%	1.5%	1.5%	1.5%	1.5%
Chromia, Cr_2O_3								
Titania-Alumina $TiO{\cdot}Al_2O_3$	50.0%							
Magnesia, MgO		50.0%				50.0%		
Spinel, $MgAl_2O_4$								
Dead Burnt Magnesia, MgO							50.0%	50.0%
Alumina, Al_2O_4								
Cerium Oxide, CeO								
Liquid Temperature, °C								
First reading	1900	2000	2050	2075	2040	2075	2100	2025
Second reading	1865	1980	2060	2015	1980	2050		
Surface Condition								
Frothy	Minor	minor	partial	partial	partial	major	major	partial
Black	Major	major	minor	minor	minor	partial	major	major

Table 4.1. Melt Test Results (continued).

BATCH NUMBER	B2-9-3	B2-9-4	B3-9-2	B3-9-3	B3-9-4	B3-9-5	B3-9-6	B3-9-7
DESCRIPTION	HD Grog Fe layer CA_2	HD Grog Fe Layer CA	none 1:1 CA_2-MgO	none 1:2 CA_2-MgO	none 2:1 CA_2-MgO	none 1:1 A-MgO	none 1:2 A-MgO	none 2:1 A-MgO
Cement %, of Batch	50	50	50	33	67	50	33	67
Reinforcement, % Batch	50	50						
Additive % of Batch			50	67	33	50	67	33
Wt. % H_2O, Batch Total	5.6%	5.6%	15.0%	15.2%	15.2%	15.0%	15.2%	15.2%
W/C Ratio	0.11	0.11	0.30	0.45	0.23	0.30	0.45	0.23
MATRIX COMPOSITION								
Additive % of Matrix			50	67	33	50	67	33
Cement % of Matrix	100	100	50	33	67	50	33	67
Alumina, Al_2O_3 as CA or CA_2	62.0%	62.0%	31.0%	20.7%	41.3%	31.0%	20.7%	41.3%
Calcia, CaO as CA or CA_2	30.0%	30.0%	15.0%	10.0%	20.0%	15.0%	10.0%	20.0%
Iron Oxide, Fe_3O_4 as C_4AF	5.0%	5.0%	2.5%	1.7%	3.3%	2.5%	1.7%	3.3%
Silica, SiO_2 as C_2S or C_3S	3.0%	3.0%	1.5%	1.0%	2.0%	1.5%	1.0%	2.0%
Chromia, Cr_2O_3								
Titania-Alumina $TiO{\cdot}Al_2O_3$								
Magnesia, MgO								
Spinel, $MgAl_2O_4$								
Dead Burnt Magnesia, MgO			50.0%	66.7%	33.3%			
Alumina, Al_2O_4						50.0%	66.7%	33.3%
Cerium Oxide, CeO								
Liquid Temperature, °C								
First reading	2005	2045	2095	2110	2050	1995	1975	2015
Second reading	2070	1975	2000	2135	2075	2080	2030	2100
Surface Condition								
Frothy	minor	minor	Major	major	major	partial	partial	partial
Black	minor	minor	Minor	minor	minor	partial	partial	partial

Table 4.. Melt Test Results (continued).

BATCH NUMBER	B3-9-8	B3-9-9	B3-26-1	B3-29-1	B3-30-1	B3-31-1	B4-1-1
DESCRIPTION	none 1:1 CA_2-A	none 1:1:1 CA_2-A-M	HD Grog 1:1(1:2) CA_2-K-M	HD Grog 1:1(1:1) CA_2-K-M	HD Grog 1:1(2:1) CA_2-K-M	HD Grog 1:1(1:4) CA_2-K-M	HD Grog 1:1(2:1) CA_2-K-M
Cement %, of Batch	50	33	20	20	20	20	10
Reinforcement, % Batch			60	60	60	60	60
Additive % of Batch	50	67	20	20	20	20	30
Wt. % H_2O, Batch Total	15.0%	15.2%	4.8%	4.8%	4.8%	4.8%	4.8%
W/C Ratio	0.30	0.45	0.24	0.24	0.24	0.24	0.48
MATRIX COMPOSITION							
Additive % of Matrix	50	67	50	50	50	50	75
Cement % of Matrix	50	33	50	50	50	50	25
Alumina, Al_2O_3 as CA or CA_2	31.0%	20.7%	31.0%	31.0%	31.0%	31.0%	15.5%
Calcia, CaO as CA or CA_2	15.0%	10.0%	15.0%	15.0%	15.0%	15.0%	7.5%
Iron Oxide, Fe_3O_4 as C_4AF	2.5%	1.7%	2.5%	2.5%	2.5%	2.5%	1.3%
Silica, SiO_2 as C_2S or C_3S	1.5%	1.0%	1.5%	1.5%	1.5%	1.5%	0.8%
Chromia, Cr_2O_3			16.8%	25.0%	33.2%	9.8%	16.8%
Titania-Alumina $TiO{\cdot}Al_2O_3$							
Magnesia, MgO			33.2%	25.0%	16.8%	40.2%	8.2%
Spinel, $MgAl_2O_4$							
Dead Burnt Magnesia, MgO		33.3%					
Alumina, Al_2O_4	50.0%	33.3%					
Cerium Oxide, CeO							
Liquid Temperature, °C							
First reading	2035	2060	2115	2100	2090	2090	2050
Second reading	2060	2000	2025	2075	2030	1990	1935
Surface Condition							
Frothy	partial	major	minor	minor	minor	minor	minor
Black	partial	partial	minor	minor	minor	minor	minor

Samples from nearly all the formulations were sintered. The surface shrinkage and cracking following sintering is a qualitative assessment of the thermal compatibility of the reinforcement and matrix phases in the composite cement. A set of five figures illustrates the coupon surface from selected batches. Figure 4.1 illustrates the difference of four different types of reinforcement while maintaining the matrix phase constant, namely Low Density Zirconia Grog, Zircon Mullite, High Density Zirconia Grog and Crushed Spinel Brick. Observe that the cracking is finer on the coupon made with the Zircon Mullite that is more closely matched to the thermal expansion of the Fondu cement. The second Figure illustrates the effect of increasing the reinforcement concentration while maintaining a constant matrix material. Figure 4.2 shows the surface cracking at 40, 60 and 75 wt. % reinforcement. Figure 4.3 shows the Fondu cement matrix with changing magnesia and spinel additive concentrations. Figure 4.4 illustrates a calcium dialuminate cement matrix with changing dead burnt magnesia concentration. A high volume fraction of reinforcement is maintained to reduce the total cement. The zirconia grog reinforcement at 75% concentration was used. Figure 4.5 illustrates the effect of changing the concentration of dead burnt magnesia on the surface cracking in the calcium dialuminate cement matrix. The reinforcement is the same for all three batches shown.

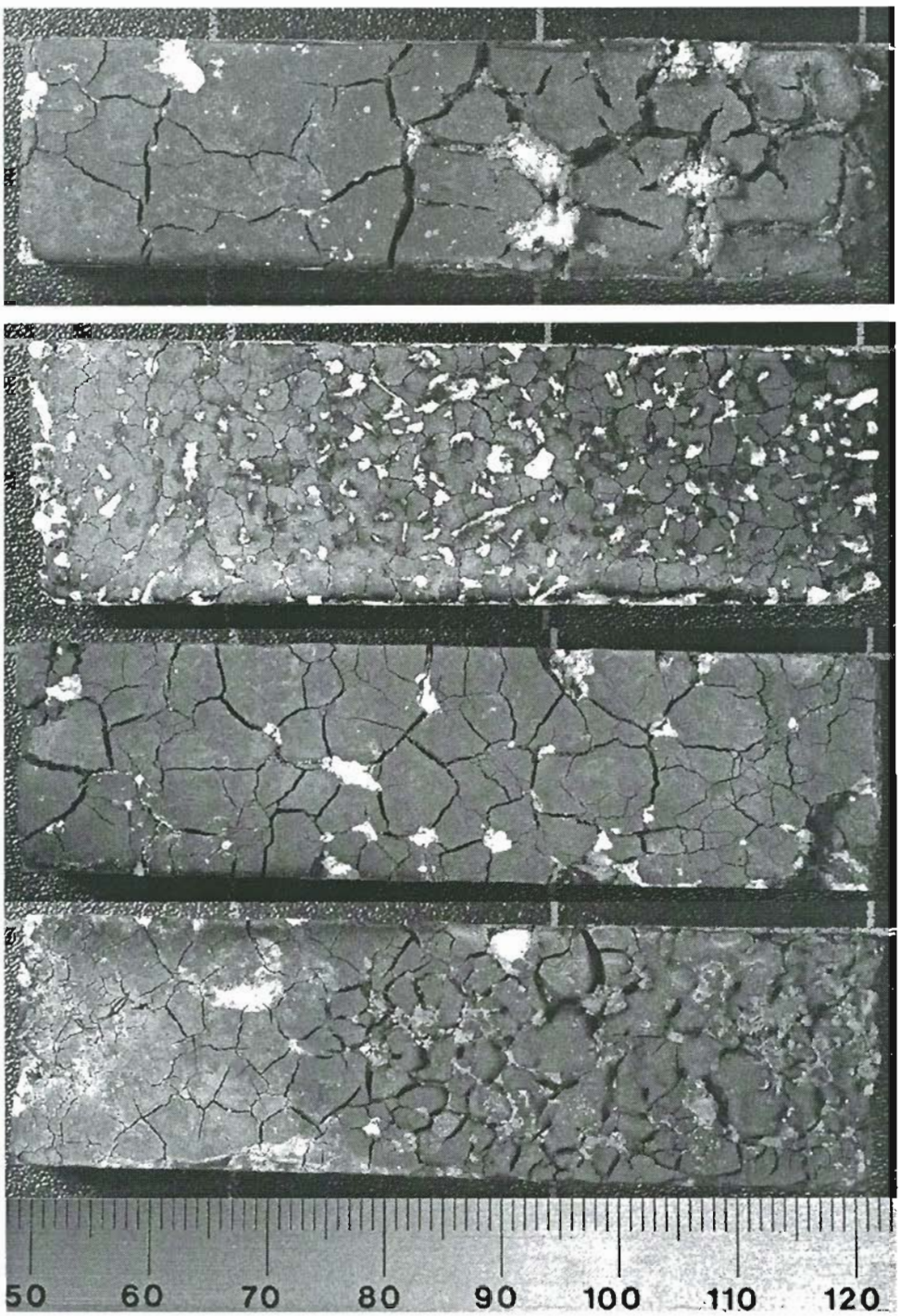

Figure 4.1. Fondu Cement, no additives and four different types of reinforcement phase. Coupon #3 from four batches B8-24, B8-28, B11-23 and B9-26. Photographs illustrate the degree of surface cracking following sintering. Four types of reinforcement phase are shown from top to bottom, low density zirconia grog, zircon mullite, high density zirconia grog and crushed spinel brick. The cracks are clustered around the reinforcement phases.

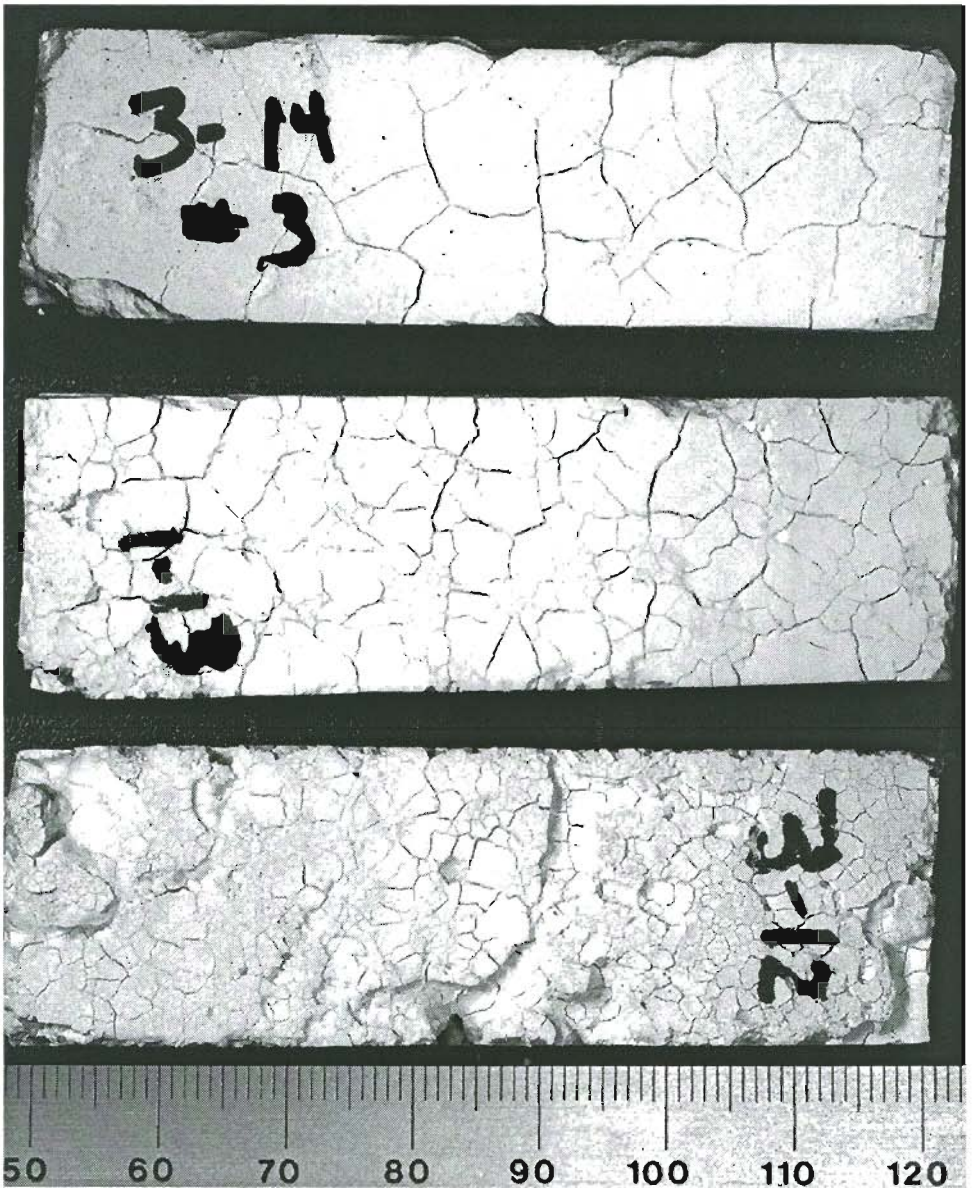

Figure 4.2. Calcium Dialuminate Cement, no additives and high density zirconia grog reinforcement at three different concentrations from top to bottom, 40, 60 and 75 wt. %. Coupon #3 from three batches B3-14, B1-15 and B3-12. Photographs illustrate the degree of surface cracking following sintering.

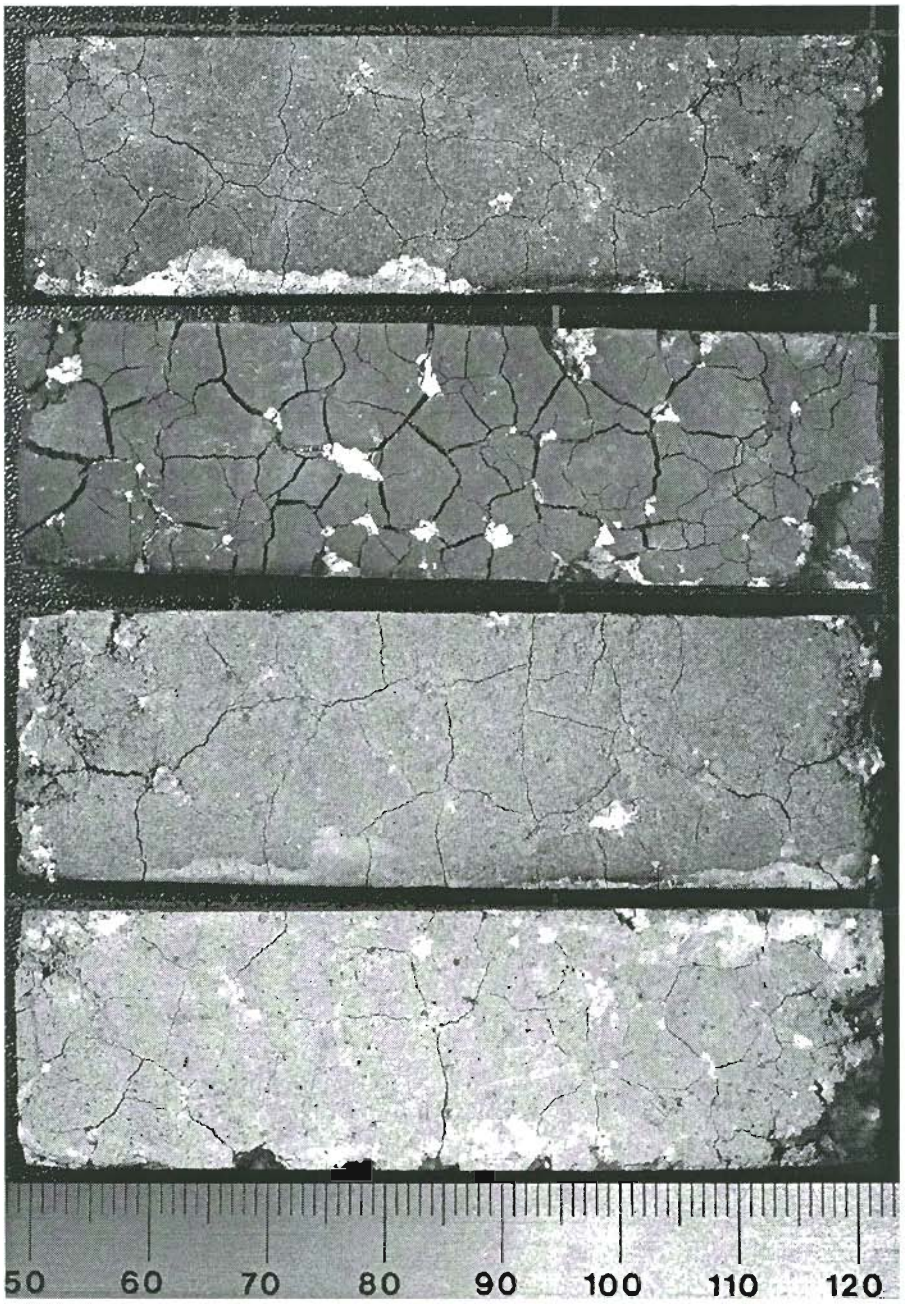

Figure 4.3. Fondu cement, changing magnesia and spinel additive concentrations. zirconia grog reinforcement concentration held constant. Coupon #3 from four batches B12-3, B9-10, B11-23 and B9-26. Photographs illustrate the degree of surface cracking as the concentration of additive is increased. The top batch was made with 50% spinel additive, the second coupon was made without additive, the third coupon was made with 50% DB magnesia additive and the bottom batch was made with 66% DB magnesia additive. The series of four coupons illustrate the change due to increasing additive concentration.

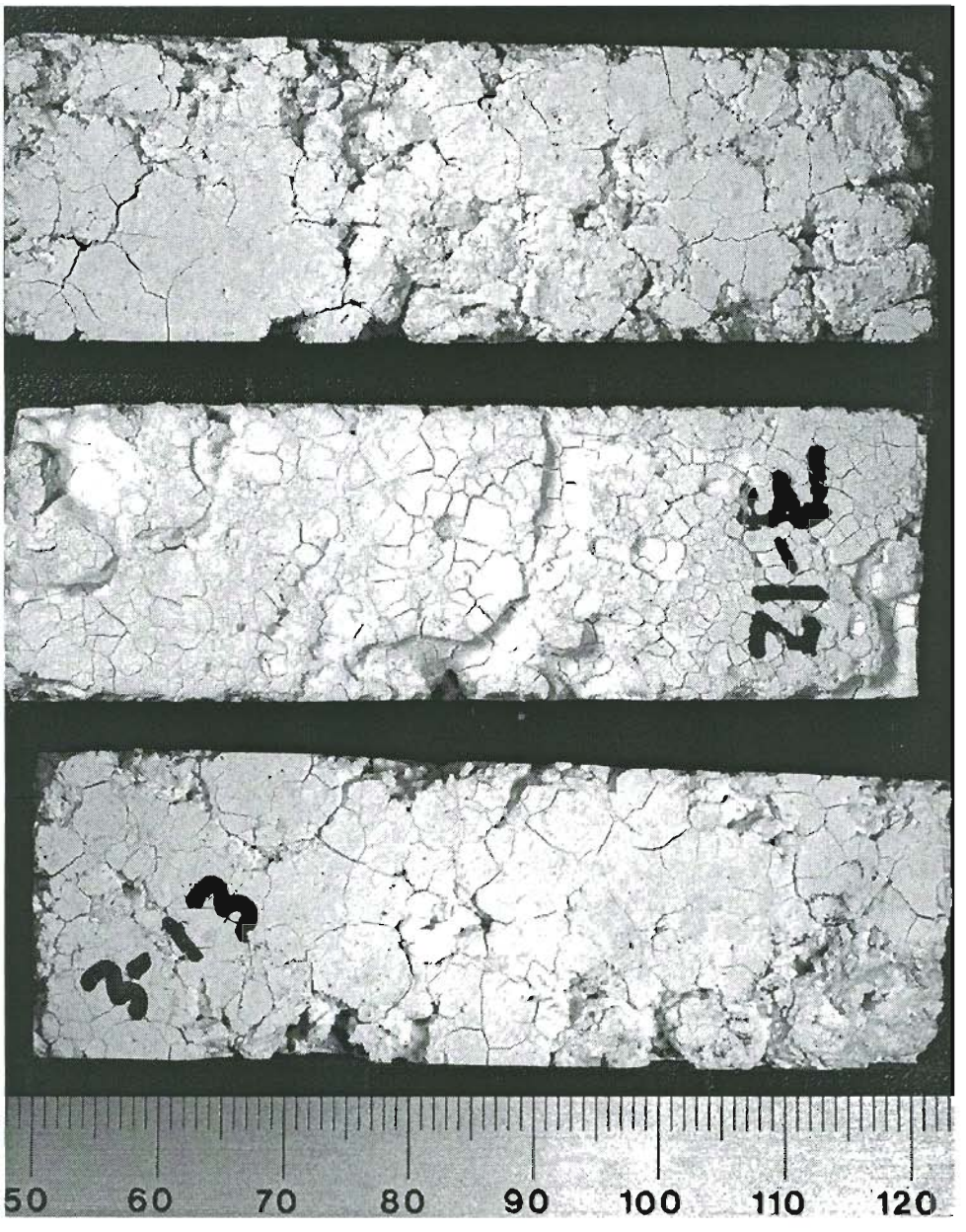

Figure 4.4. Calcium dialuminate cement, changing magnesia additive concentration and high density zirconia grog reinforcement at 75% same concentration. Coupon #3 from three batches B3-11, B3-12 and B3-13 are shown. Photographs illustrate the degree of surface cracking with high concentrations of reinforcement phase.

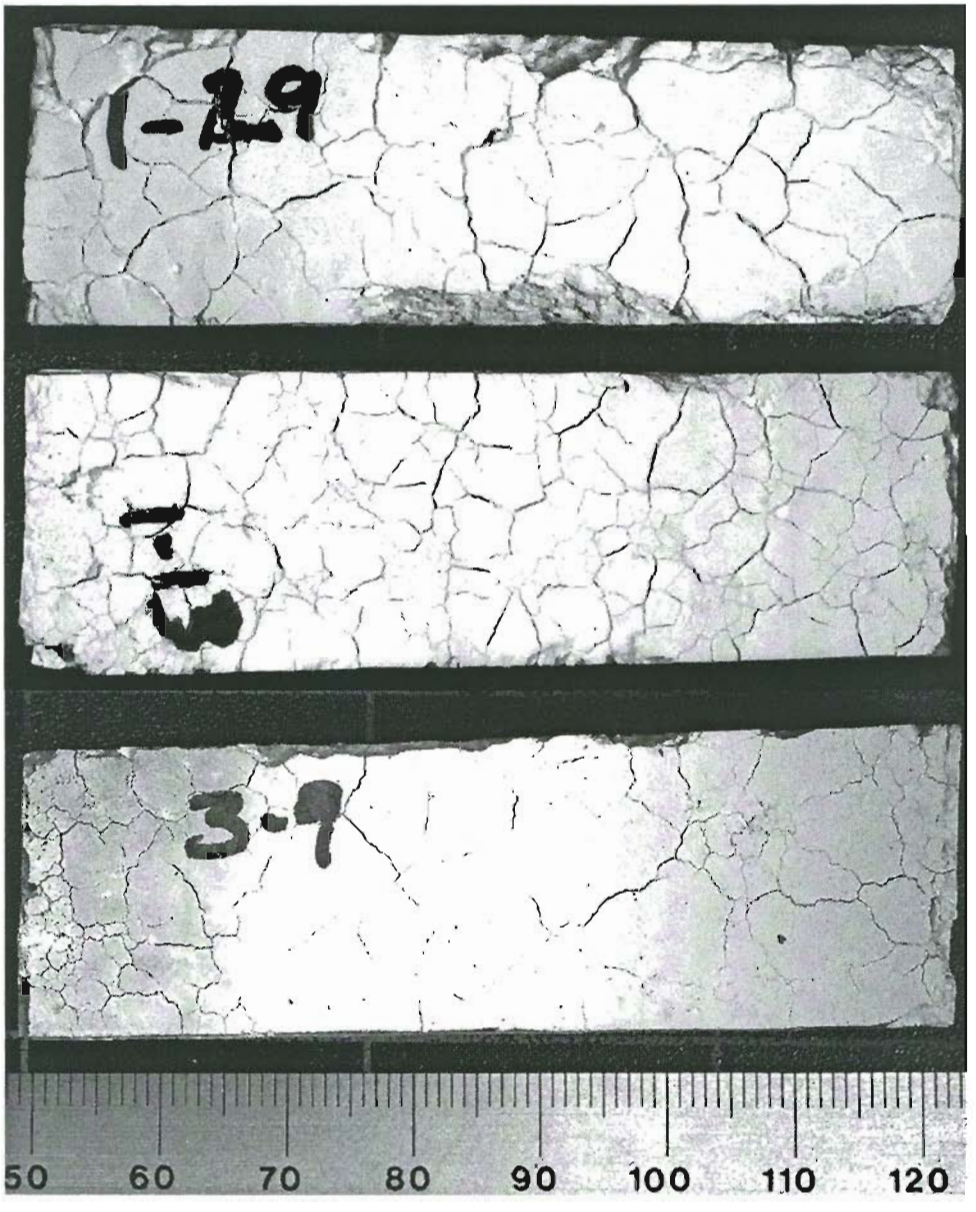

Figure 4.5. Calcium dialuminate cement and changing magnesia additive concentration and high density zirconia grog reinforcement. Coupon #3 from three batches B3-11, B3-12 and B3-13 are shown. Photographs illustrate the degree of surface cracking following sintering.

4.3 Microstructural Results

Observations of cement and additive particles, particle boundaries, diffusion zones, voids and porosity, gaps between the reinforcement and matrix and cracking provide a solid basis to select different cement additive and reinforcement materials. The important microstructural features are based on the functionality of the microstructure to the properties. The properties of the composite cement are dependent on the thermal history and temperature, which is reflected, in the bonding microstructure.

Microstructure samples were prepared from coupons and specimens in three conditions; cured, fired to the onset of ceramic bonding and the fully dense. The samples were prepared from sections of coupons used for wear testing or special plugs cast for metallographic specimen preparation. Procedures for the sample preparation were provided in the experimental section of this thesis. The samples prepared to observe the fully dense conditions were surface heated up to the melting point using an oxygen acetylene gas torch. The process was found to produce a graded microstructure that ranged from the central area with high open porosity to a fused cast ceramic structure on the surface.

The samples were observed either as freshly fractured surfaces using fractrographic techniques or in the mounted and polished surface condition using metallographic techniques. Characteristically, the porosity is either open or closed. The closed porosity appears dark black in the photomicrographs. The generally the open porosity fills with the mounting epoxy and reflect light producing a dark gray appearance. Numerous samples were prepared and selected images were recorded.

Examples of the reinforcement phase microstructures are shown in the following set or Figures 4.6A through 4.9B. The photomicrographs illustrate the condition of the reinforcement phases prior to sintering. The open and closed porosity is shown as the dark areas in the micrograph. Figures 4.6A and 4.6B illustrate the zircon reinforcement separated form the premix cement. The lath like phases are zirconium and aluminum rich phases. The light gray matrix phase is rich in zirconium and silicon (zirconium silicate) and the white phases are rich in both aluminum and silicon (mullite). Figure 4.7A and 4.7B are examples of the zirconia grog reinforcement. Figures 4.8A and 4.8B show the

microstructure of the dead burnt magnesia reinforcement. Figures 4.9A and 4.9B shows the crushed spinel brick used as reinforcement. The Fondu cement microstructure is illustrated in the set of Figures 4.10A through 4.15. The microstructure of samples formulated with no additives are shown in Figures 4.10A and 4.10B The micrograph shows unreacted calcium aluminate clinkers, sintered hydrates and porosity. The unreacted clinkers have a two-phase structure, light areas and dark areas. The calcium aluminate phase is light gray. The white phases are iron rich ferrite phases. The sintered hydrates are shown as the gray phase between the particles. Figures 4.11A and 4.11B show the sintered cement microstructure with the reagent grade magnesia additive. The magnesia grains are the particles with uniform size and shade of gray, these particles are free of porosity. Figures 4.12A and 4.124B show the sintered cement microstructure with a spinel additive. No reaction rim was observed around the reagent grade magnesia or the spinel additive. Figures 4.13A and 4.13B show the Fondu cement with the zircon reinforcement. The interface between the cement and reinforcement is fuzzy and not well defined. This is an indication of the formation of a low temperature liquid silicate rich phase during sintering. Figures 4.14A and 4.14B show the Fondu cement and zirconia reinforcement. The interface between the cement and a zirconia grog reinforcement is incoherent and the matrix exhibits cracking. Figure 4.15 shows the sintered cement microstructure with the crushed spinel reinforcement. The interface is incoherent and the matrix exhibits cracking in this sample.

The calcium dialuminate blend cement microstructure with and without additives is shown in the set of Figures 4.16A through 4.24D. Figures 4.16A, 4.16B and 4.16C show the sintered microstructure of the calcium dialuminate blend cement with no additives. Figures 4.17A and 4.17B show the microstructure of the cement with spinel additive. Figure 4.18 show the microstructure of the cement with dead burnt magnesia additive. All three of these different type of samples exhibit regions of open and closed porosity. Regions of higher density and closed porosity were found specific to the calcium dialuminate cement samples. The dense regions varied in size and were found as large as a millimeter. The regions were found to contained additive particles. Figures 4.19A and 4.19B illustrate the calcium dialuminate microstructure with different concentrations of dead burnt magnesia additive. The batch formulated and shown in

Figure 4.19A was blended with 33% dead burnt magnesia where the batch shown in Figure 4.19B was formulated with 75% additive. Figure 4.20 shows the interface between the matrix cement and a large particle of dead burnt magnesia reinforcement. The interface zone was wetted with silica rich compound with calcia. Figure 4.21 illustrates the sintered microstructure of the calcium dialuminate blend cement formulated with magnesia and chromia 2:1 blend. Figure 4.22 illustrates the sintered microstructure of a calcium dialuminate with zirconia grog reinforcement. The batch was formulated with 75% reinforcement. The photomicrograph illustrates a high degree of cracking due to reinforcement binding and the CTE mismatch. Figures 4.23A, 4.23B, 4.23C and 4.23D show several examples of a diffusion rim surrounding the zirconia reinforcement. The cement interfaces with the dead burnt magnesia reinforcement are illustrated in the set of Figures 4.24A, 4.24B, 4.24C and 4.24D. The interface does not exhibit the diffusion or reaction rim. The interface is gap free.

Examples of the high alumina calcium aluminate premix cement are shown in the set of Figures 4.25A through 4.29. The microstructure of the sintered cement formulated with chromia is shown in Figure 4.25A and 4.25B. The photomicrographs show the chromia particles surrounded by a cement reaction rim. The porosity is shown open and has filled with mounting epoxy. Figures 4.26, 4.27 and 4.28 show the high alumina calcium aluminate premix cement interface with the zircon reinforcement. The premix cement was found with iron oxide impurities as shown in Figure 4.29. The matrix is shown with crack radiating from a large iron oxide particle. Iron oxides are added to improve the cement hydraulic strength through the formation of calcium aluminoferrite. Sometimes the larger iron oxides are not consumed during calcining.

Figures 4.30 and 4.31 are scanning electron microscope photomicrographs of a fracture surface prepared from a batch formulated from calcium dialuminate blend cement and dead burnt magnesia additive. The images show cement and additive particles connected by a viscous phase that is rich in calcia and alumina.

Figure 4.6A. Microstructure of the as received zircon reinforcement.

Figure 4.6B. Microstructure features of the as received zircon reinforcement are shown in frames A and B. Lath like phases are zirconium and aluminum rich phases. The light gray matrix phase is zirconium, silicon rich and the white areas are a silica and alumina mullite.

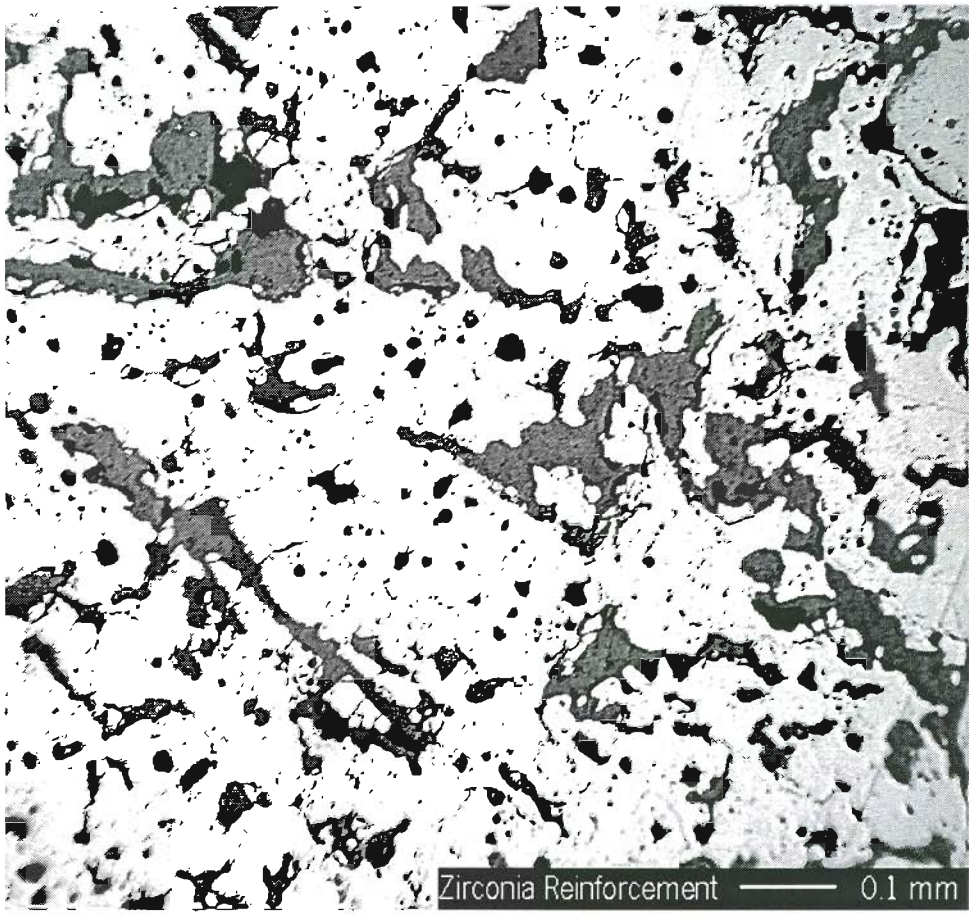

Figure 4.7A. Microstructure of the as received zirconia grog reinforcement.

Figure 4.7B. Microstructure features of the as received zirconia grog reinforcement are shown in frames A and B. The grains are partially sintered with open and closed porosity at the triple points and along the grain boundaries. The white material is zirconia and the dark areas are the porosity. The closed porosity is shown as the dark black areas. Closed porosity is shown inside the volume of the grain.

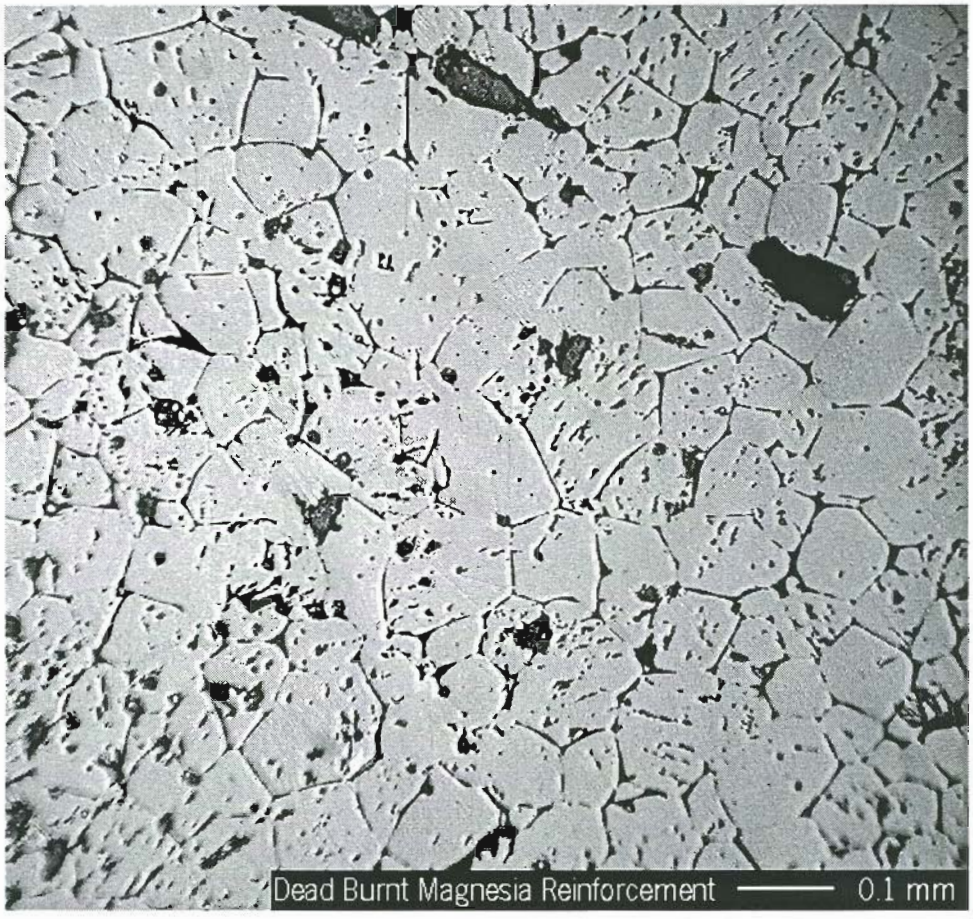

Figure 4.8A. Microstructure of the as received dead burnt magnesia reinforcement material.

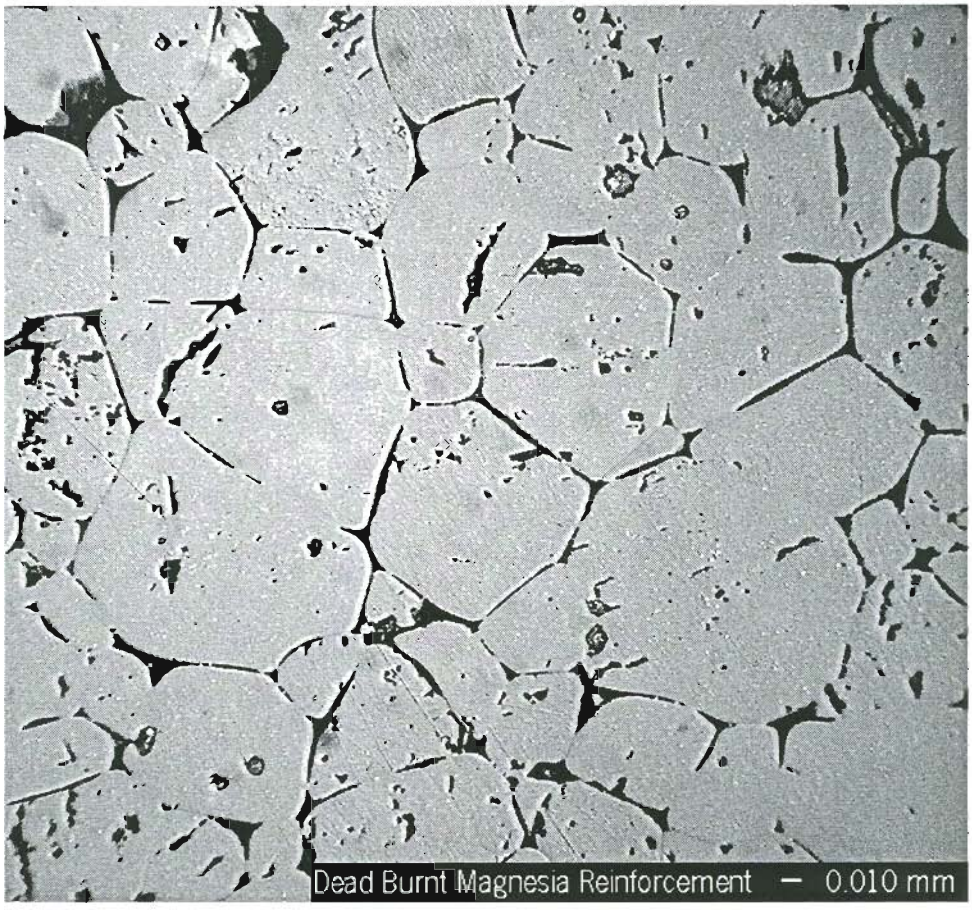

Figure 4.8B. Microstructure features of the as received dead burnt magnesia reinforcement material are shown in frames A and B. The open and closed porosity are illustrated as light and dark areas.

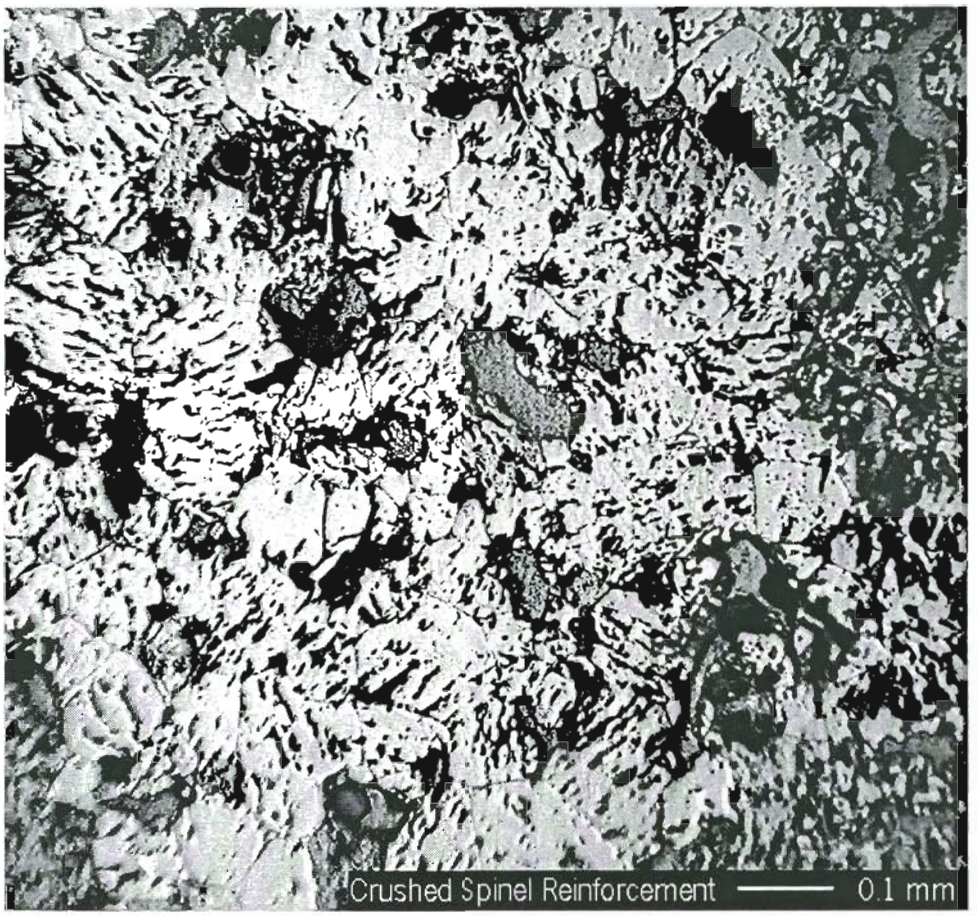

Figure 4.9A. Microstructure of the crushed spinel brick reinforcement.

Figure 4.9B. Microstructure features of the crushed spinel brick reinforcement are shown in frames A and B. Initial condition microstructure of the crushed spinel brick reinforcement material. The open and closed porosity are illustrated as light and dark areas. The gray phase is the mounting epoxy used for sample preparation. The open and closed porosity are illustrated as light and dark areas.

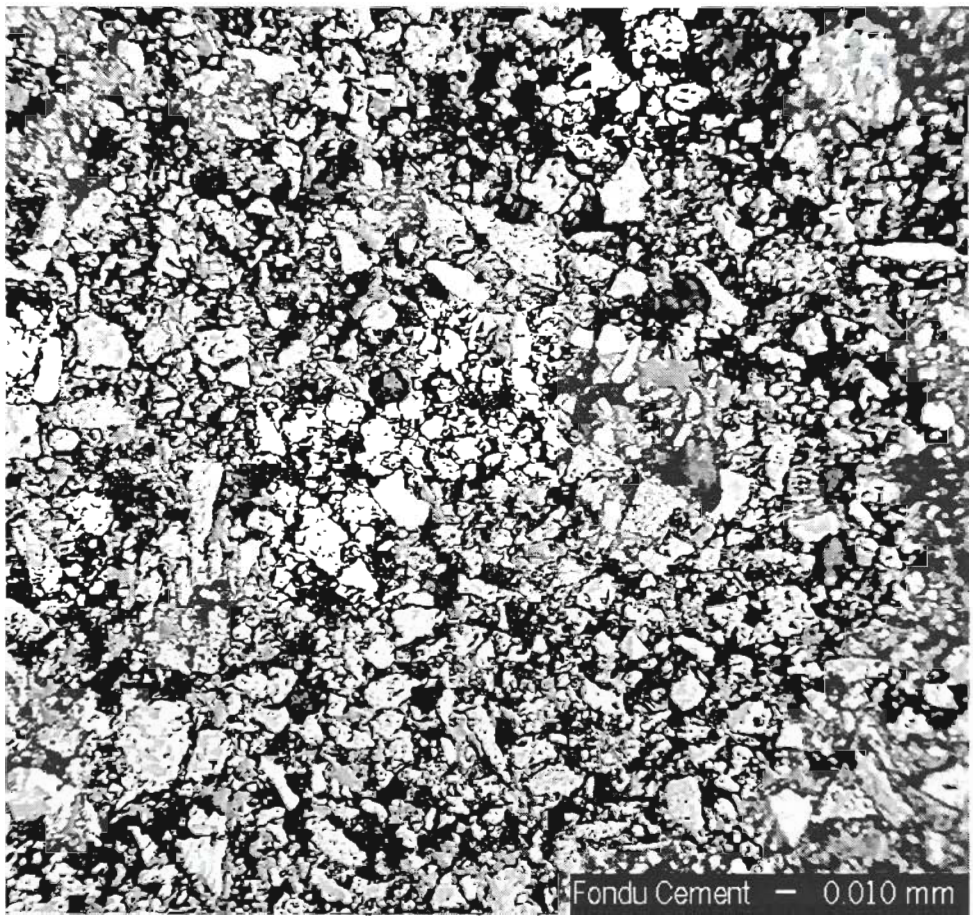

Figure 4.10A. Fondu cement microstructure without additives or reinforcement, Batch B9-1.

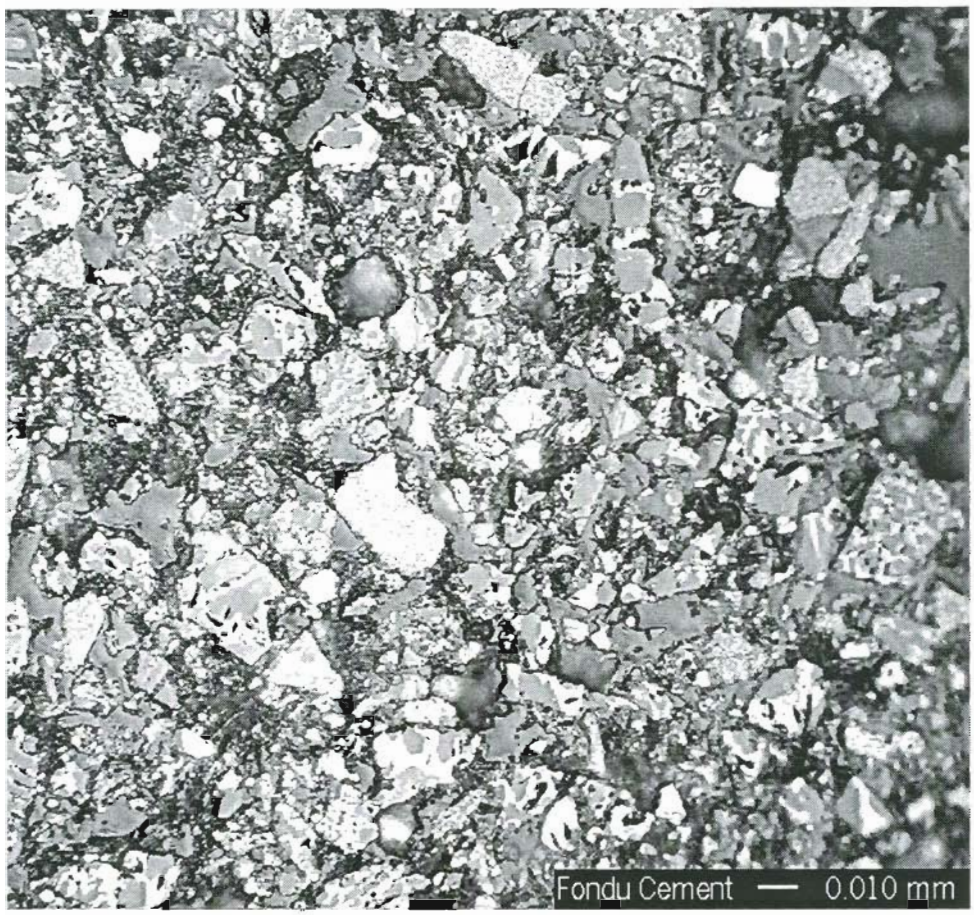

Figure 4.10B. Fondu cement microstructure features with no additives or reinforcement in frames A and B. The lighter gray phases are calcium aluminate, the white phases are calcium aluminoferrite and the dark regions are voids and porosity. Batch B9-1

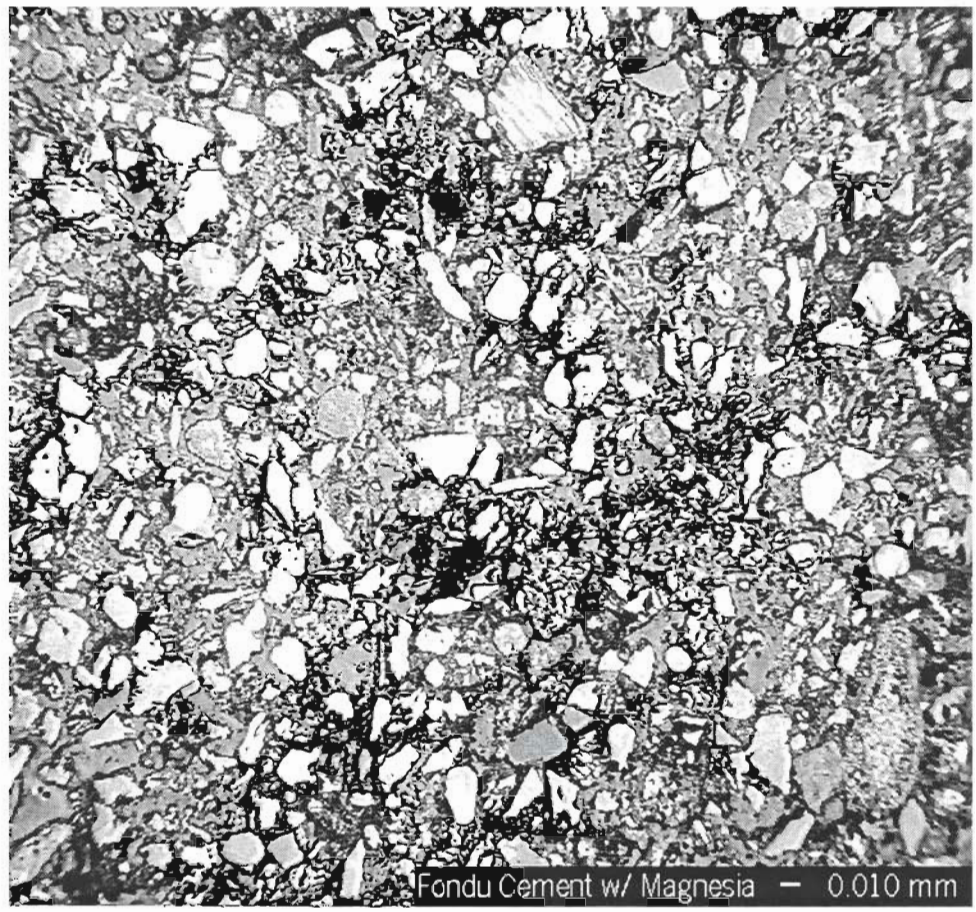

Figure 4.11A. Fondu cement microstructure with reagent grade MgO added. Batch B9-3

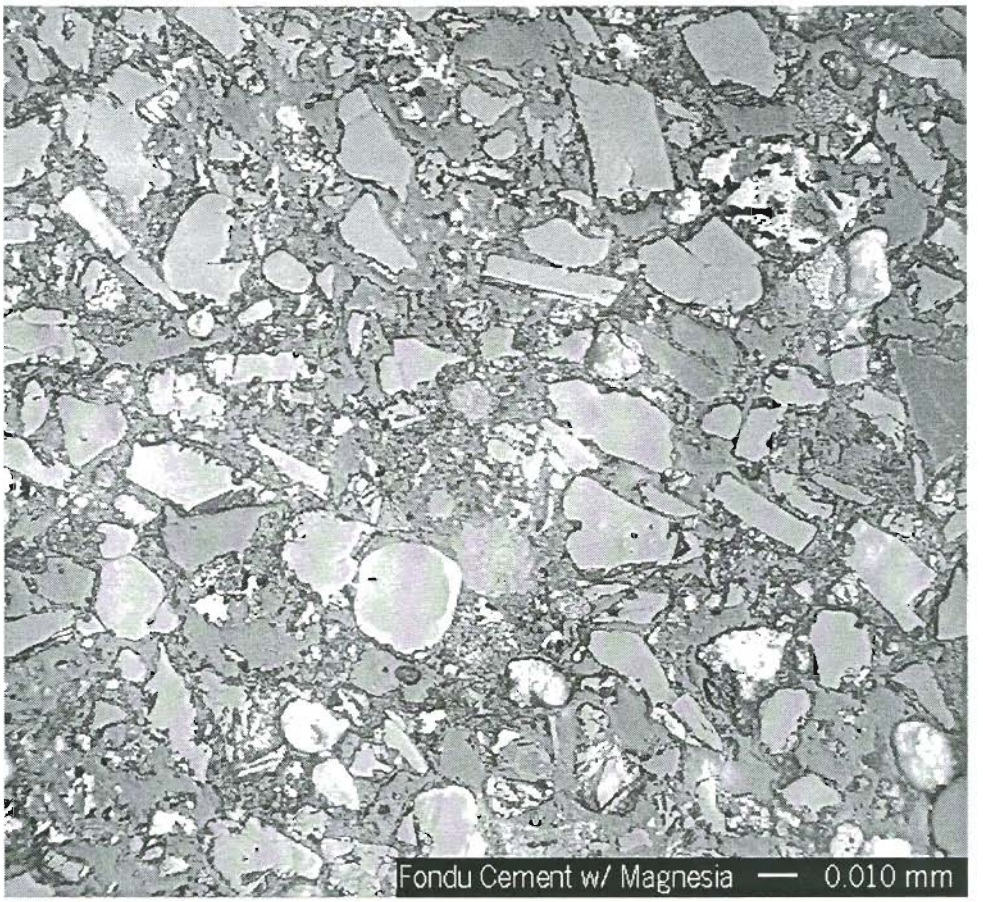

Figure 4.11B. Fondu cement microstructure features with reagent grade MgO added are shown in frames A and B. The magnesia particles are shown as white phases with relatively uniform particle size. Batch B9-3

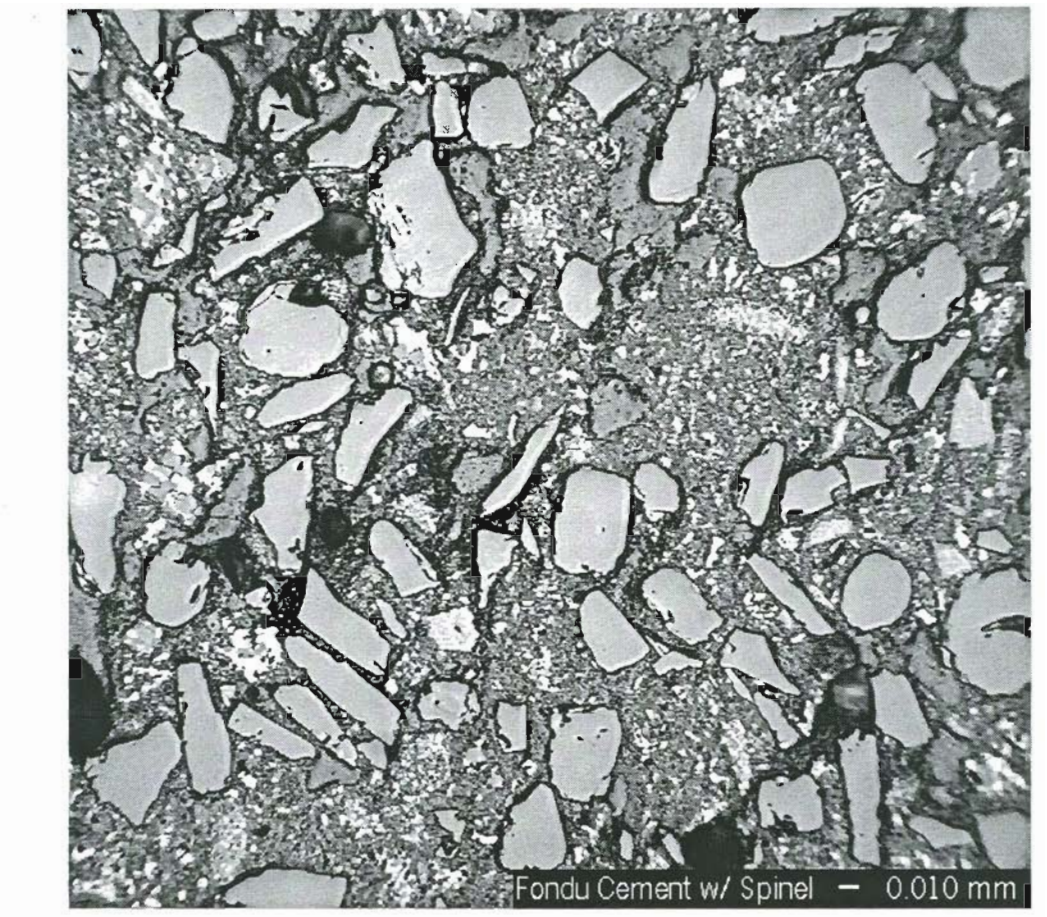

Figure 4.12A. Fondu cement microstructure with reagent grade spinel added. Batch B9-10

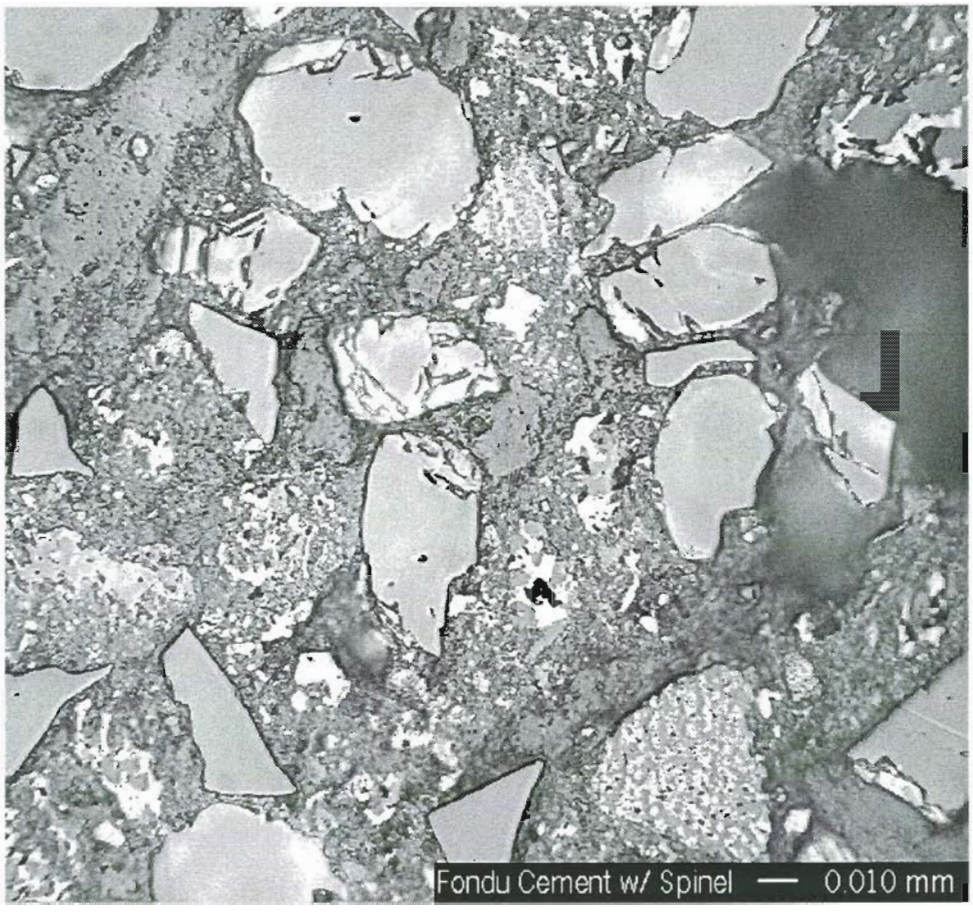

Figure 4.12B. Fondu cement microstructure features with reagent grade spinel added are shown in frames A and B. The spinel particles are gray with relatively uniform particle size. Batch B9-10

Figure 4.13A. Fondu cement microstructure with Zircon reinforcement. The matrix to reinforcement interface is shown. Batch B8-28

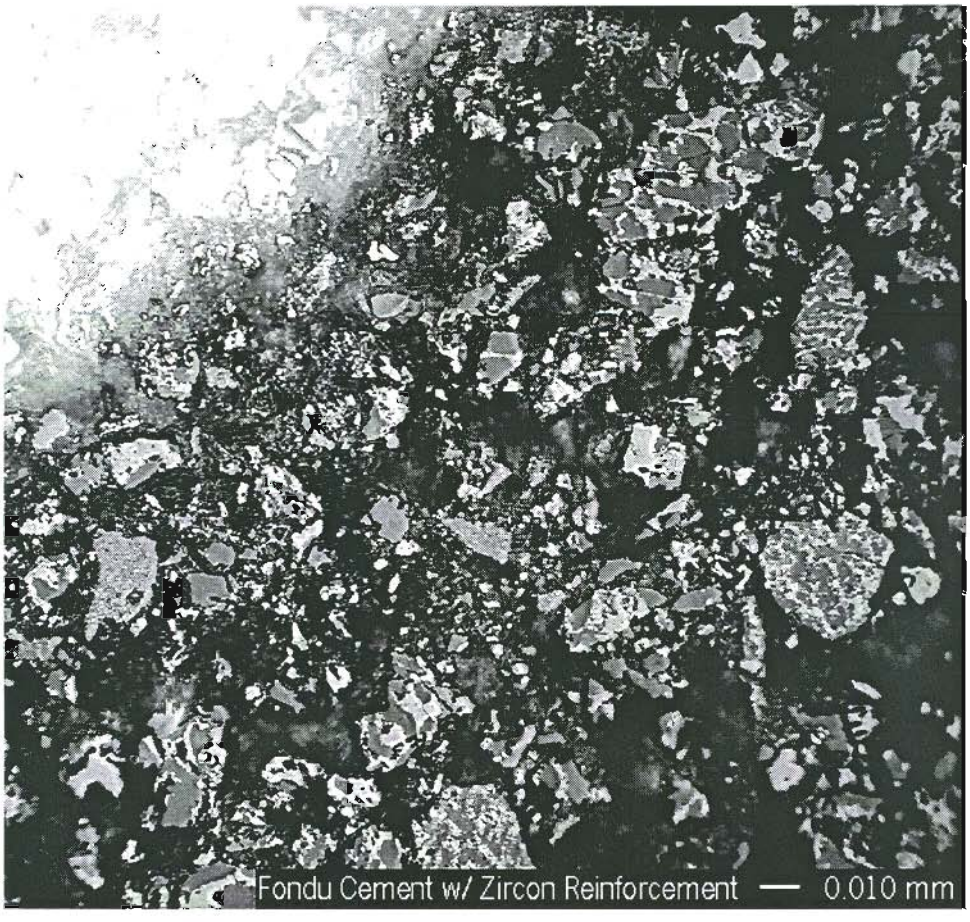

Figure 4.13B. Fondu cement microstructure features with zircon reinforcement are shown in frames A and B. The matrix and reinforcement interface is shown. Batch B8-28

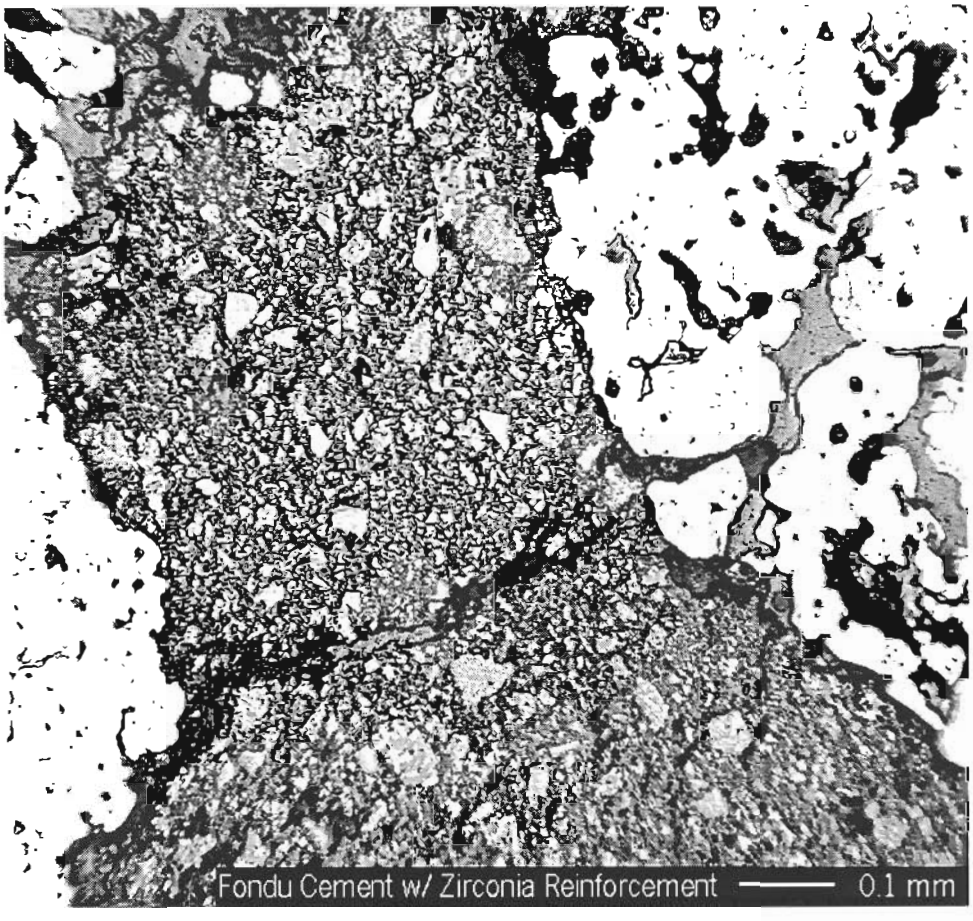

Figure 4.14A. Fondu cement microstructure with zirconia grog reinforcement, no additives. The matrix cement and reinforcement interface is shown. Batch B11-23

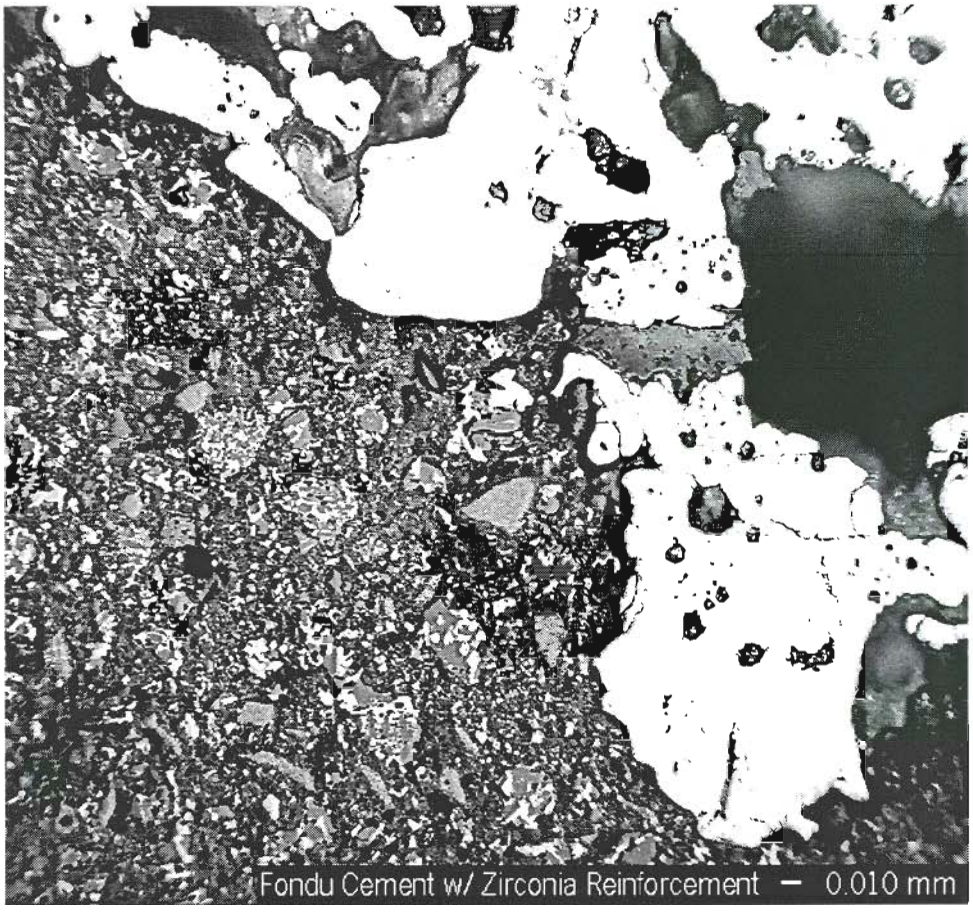

Figure 4.14B. Fondu cement microstructure features with zirconia grog reinforcement, no additives are shown in frames A and B. The matrix cement and reinforcement interface is shown. Batch B11-23

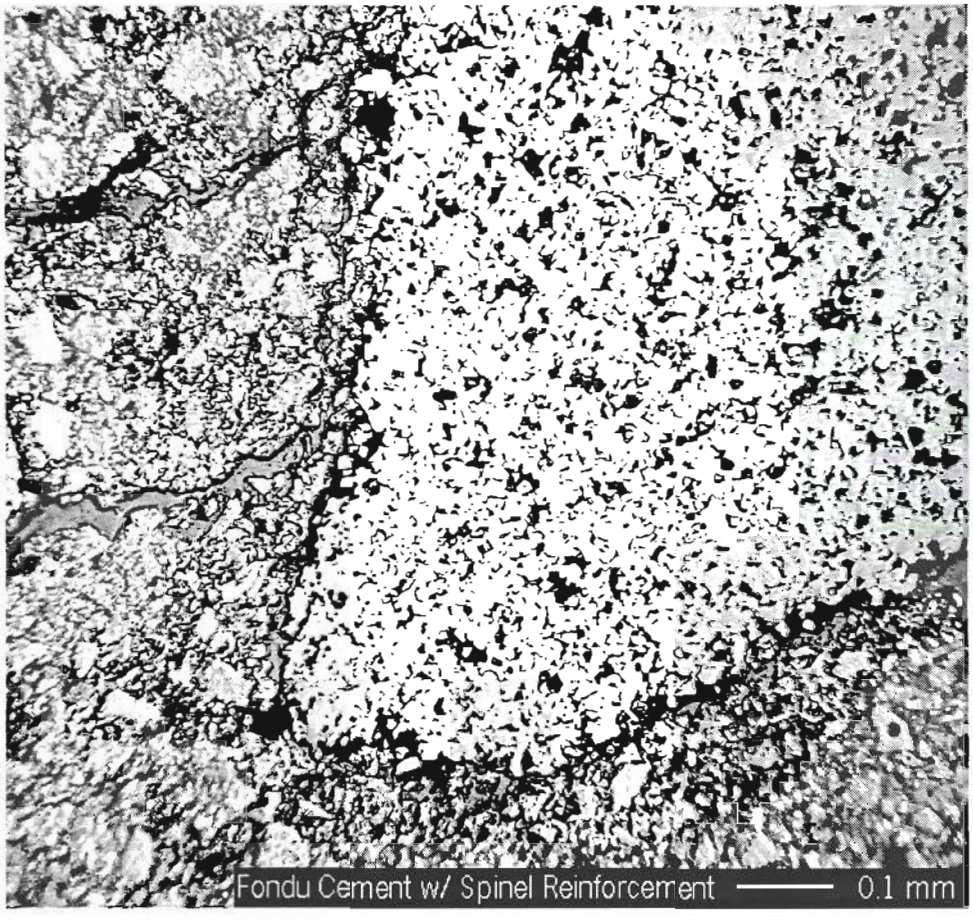

Figure 4.15. Fondu cement microstructure with crushed spinel reinforcement, no additives. The matrix cement and reinforcement interface is shown. Batch B9-28

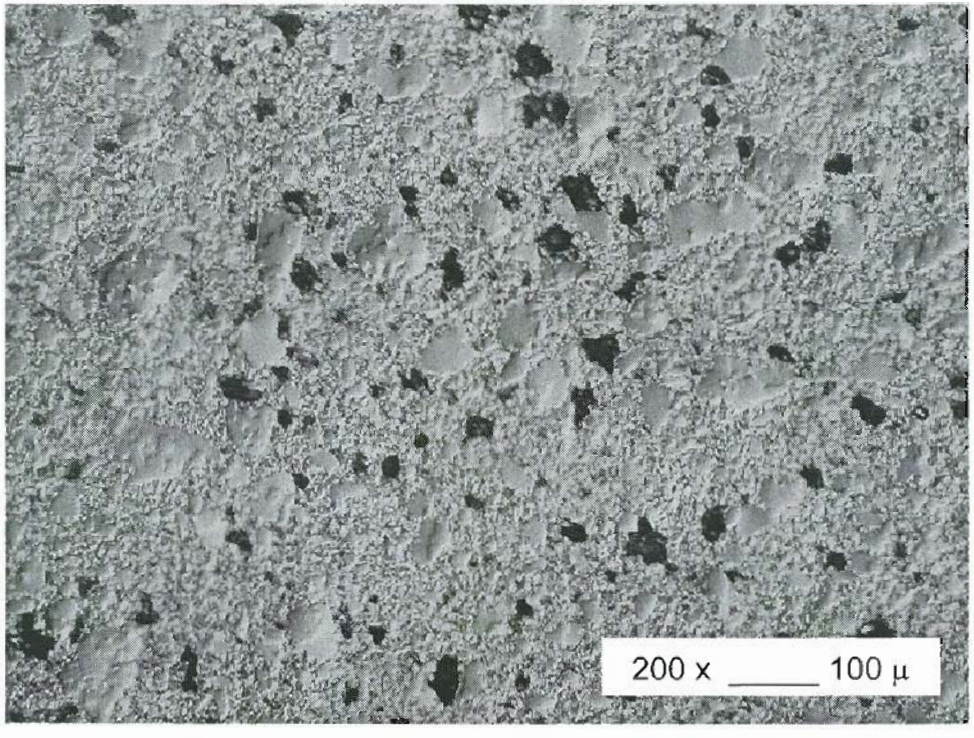

Figure 4.16A. Calcium dialuminate blend microstructure. Batch B1-20

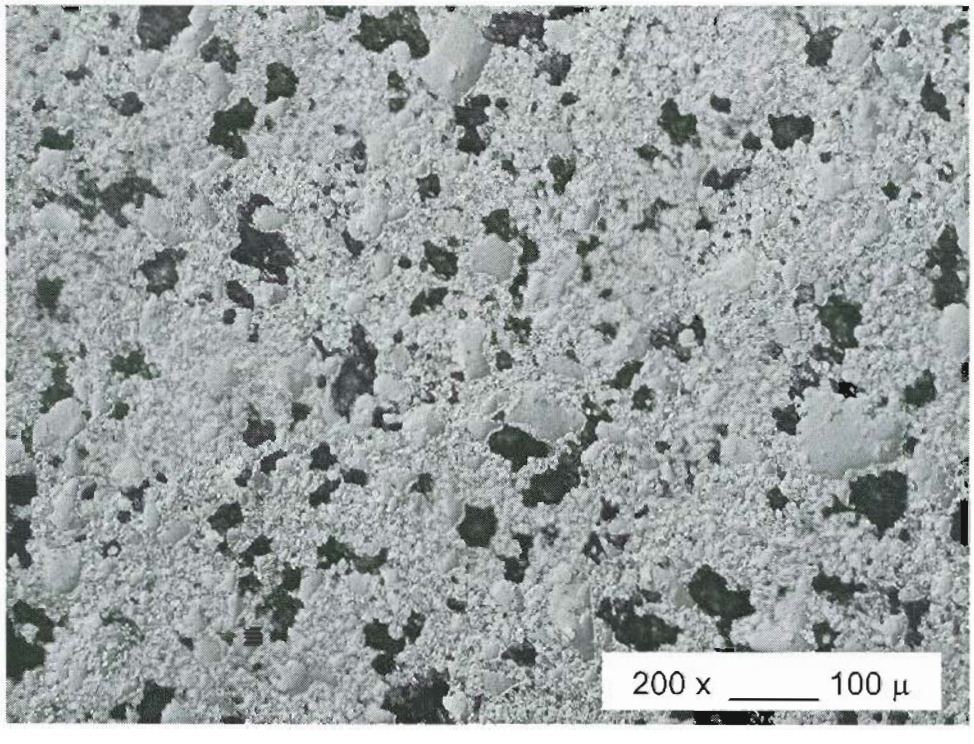

Figure 4.16B. Calcium dialuminate blend microstructure. Batch B1-20

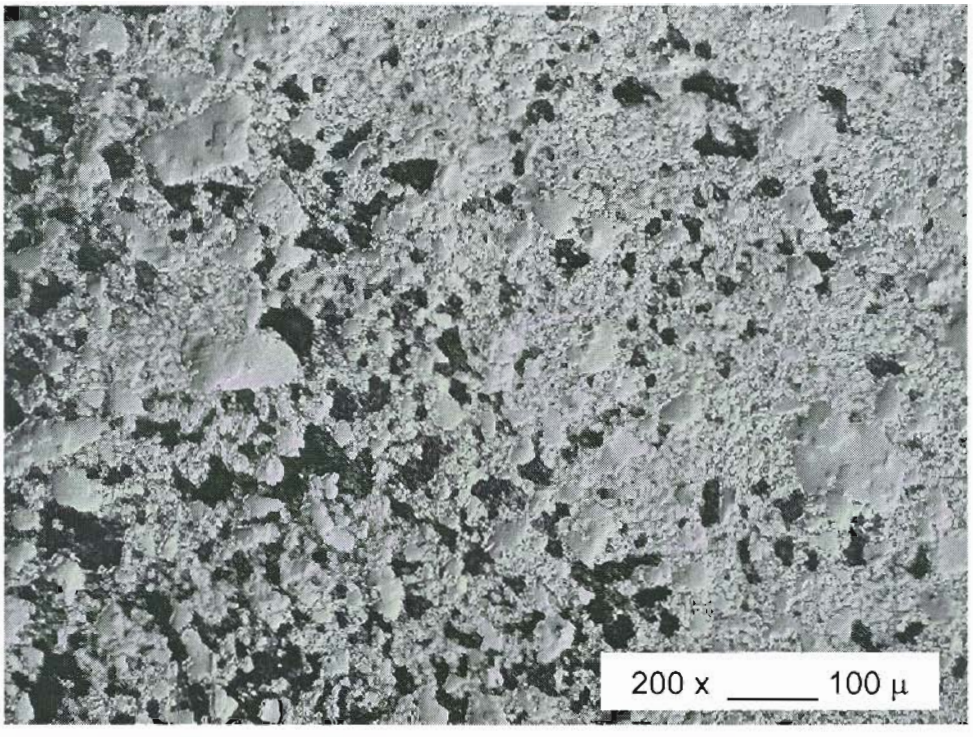

Figure 4.16C. Calcium dialuminate blend microstructure features without additive is shown in frames A, B and C. Regions of closed and open porosity are shown. Figure A illustrates an area within the coupon that has a predominance of closed porosity, B illustrates an area with mostly open porosity and C shows the transition zone. Batch B1-20 sample coated.

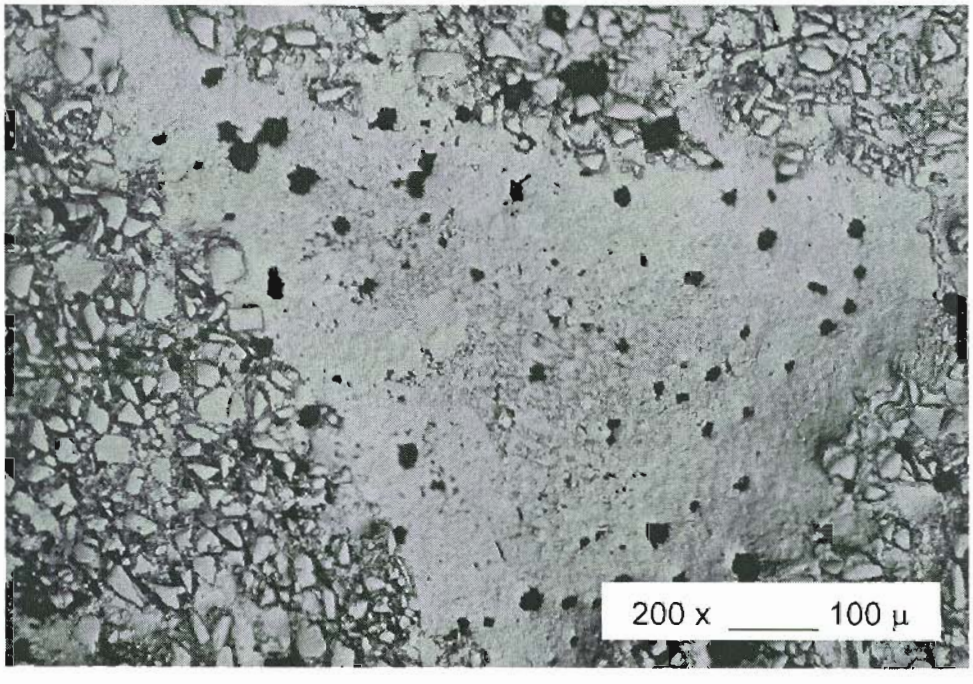

Figure 4.17A. Calcium dialuminate blend microstructure. Batch B1-22 sample coated.

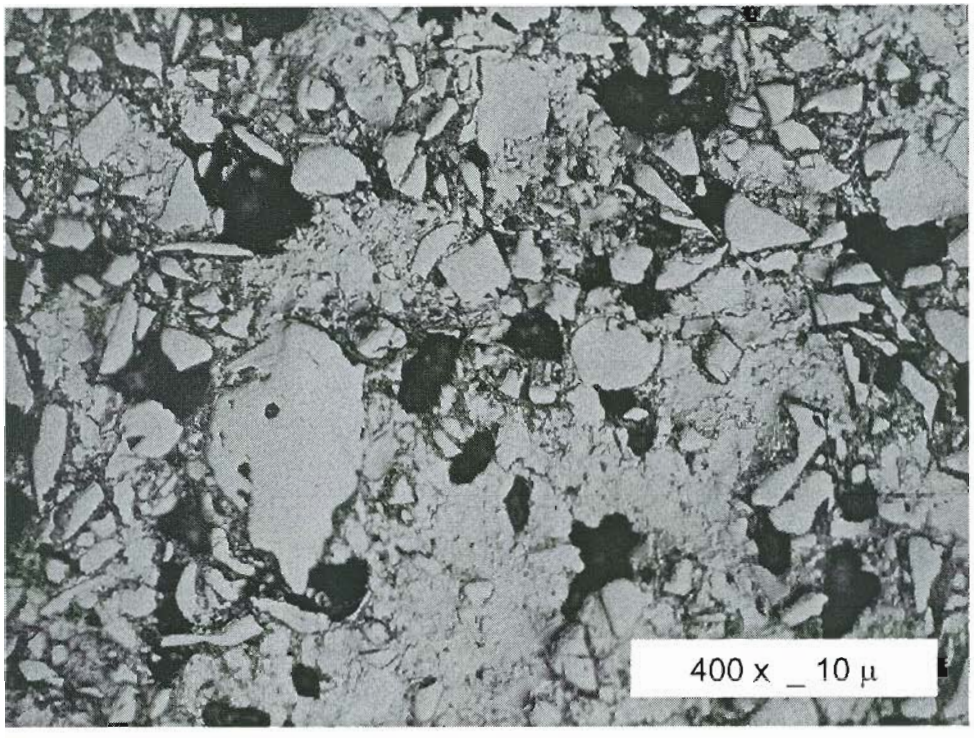

Figure 4.17B. Calcium dialuminate blend microstructure features with spinel additive. Regions of closed and open porosity are shown. Figure A illustrates a local region of densification and Figure B illustrates the microstructure at the edge of the dense area. Batch B1-22 sample coated.

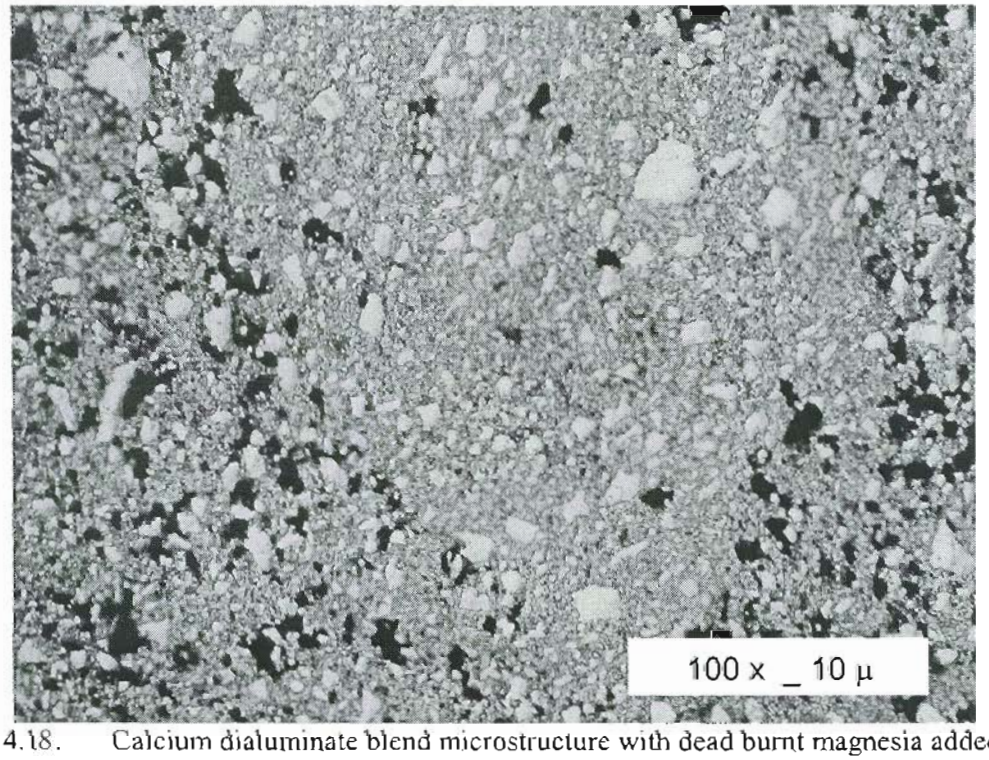

Figure 4.18. Calcium dialuminate blend microstructure with dead burnt magnesia added. Regions of closed and open porosity are shown. Batch B3-13

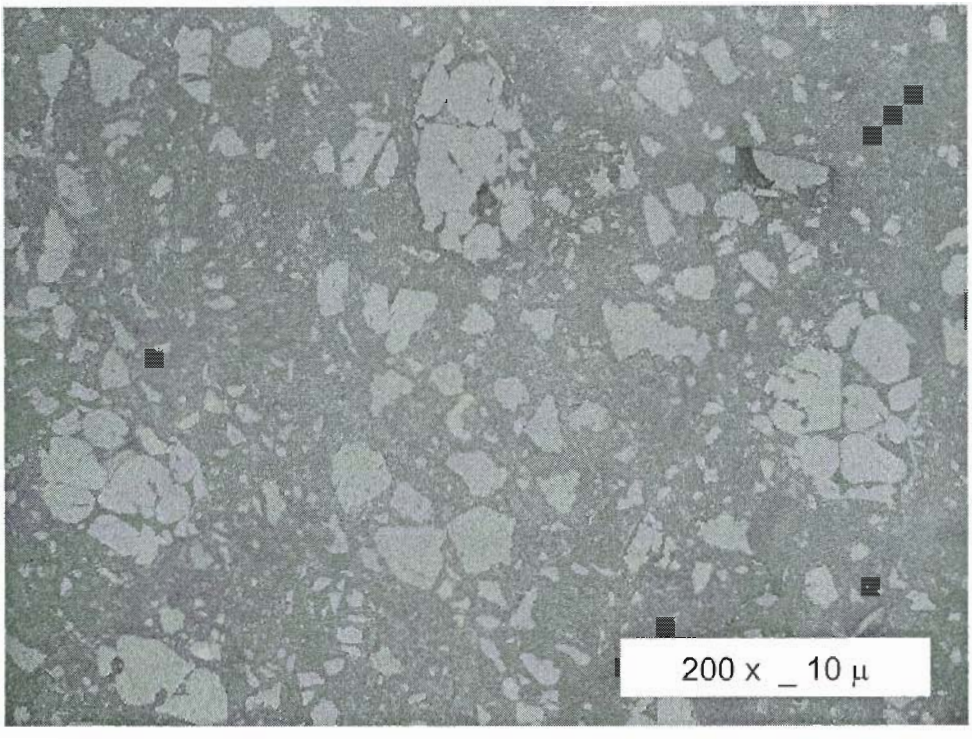

Figure 4.19A. Calcium dialuminate blend microstructure. Batch B3-23

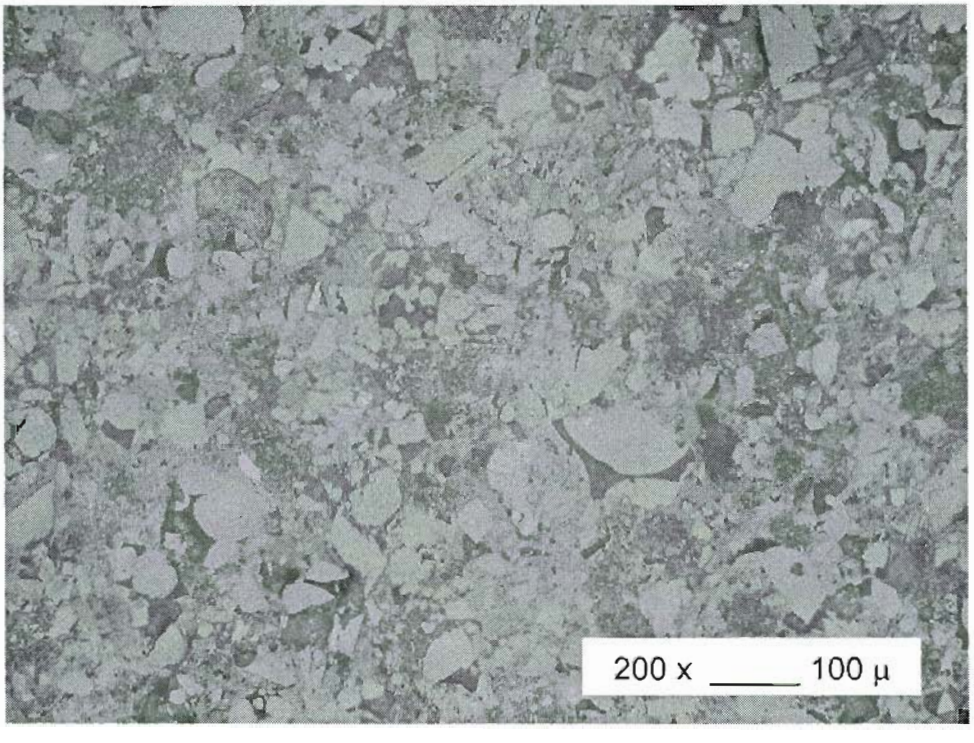

Figure 4.19B. Calcium dialuminate blend microstructure features with dead burnt magnesia added are shown in frames A and B, 33% (A) and 75% (B). The Figures illustrate agglomeration of the magnesia additive grains. Batch B 3-25

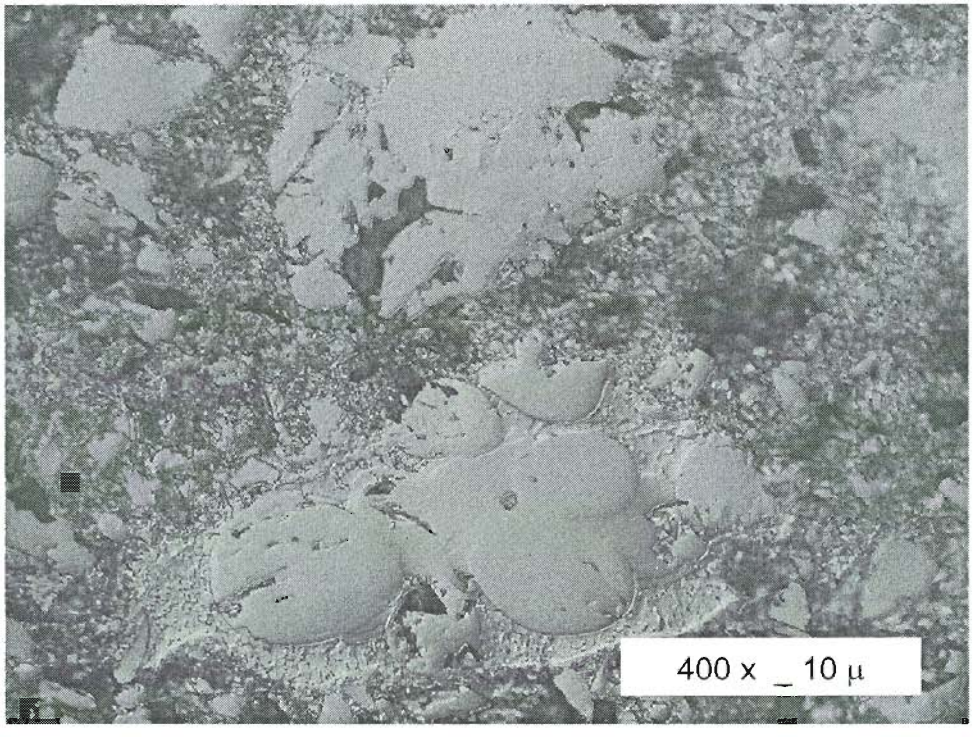

Figure 4.20. Calcium dialuminate blend microstructure with dead burnt magnesia additive. A diffusion zone between reinforcement and matrix is shown. Batch B3-10

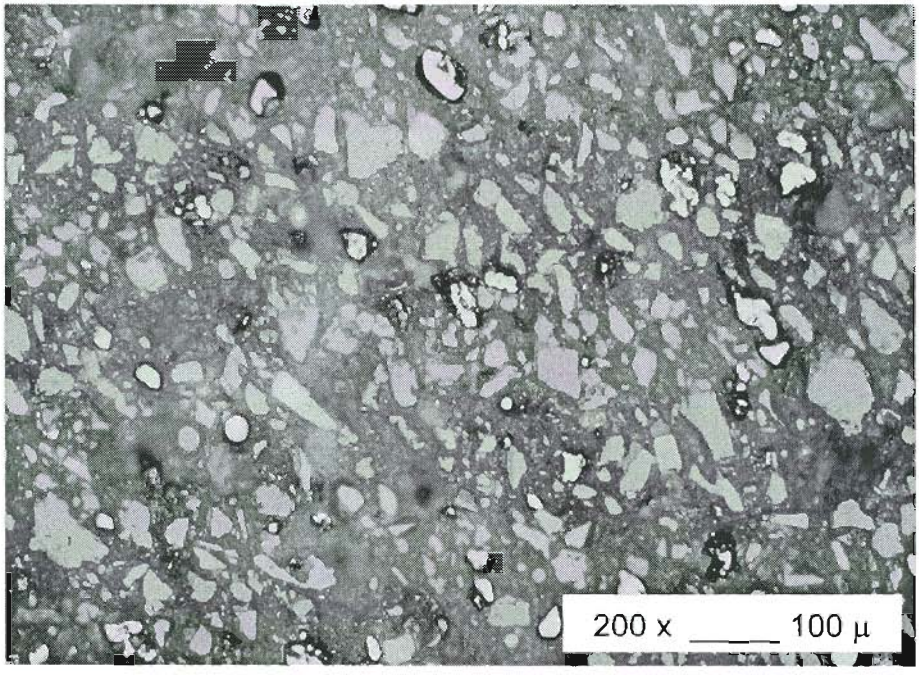

Figure 4.21. Calcium dialuminate blend microstructure with a 2:1 blend of reagent grade magnesia and chromia added. Chromia particles are reflective and shown in white and magnesia particles are lighter gray. Batch B3-26

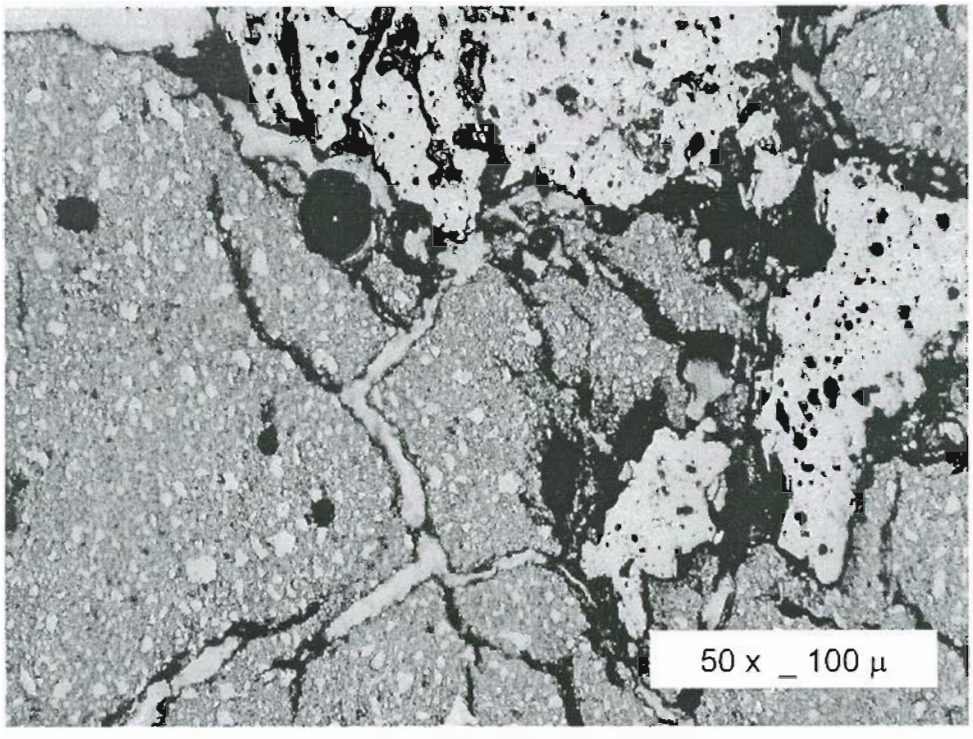

Figure 4.22. Calcium dialuminate blend microstructure with no additive and zirconia grog reinforcement. Matrix cracking due to CTE mismatch is shown. Batch B3-12

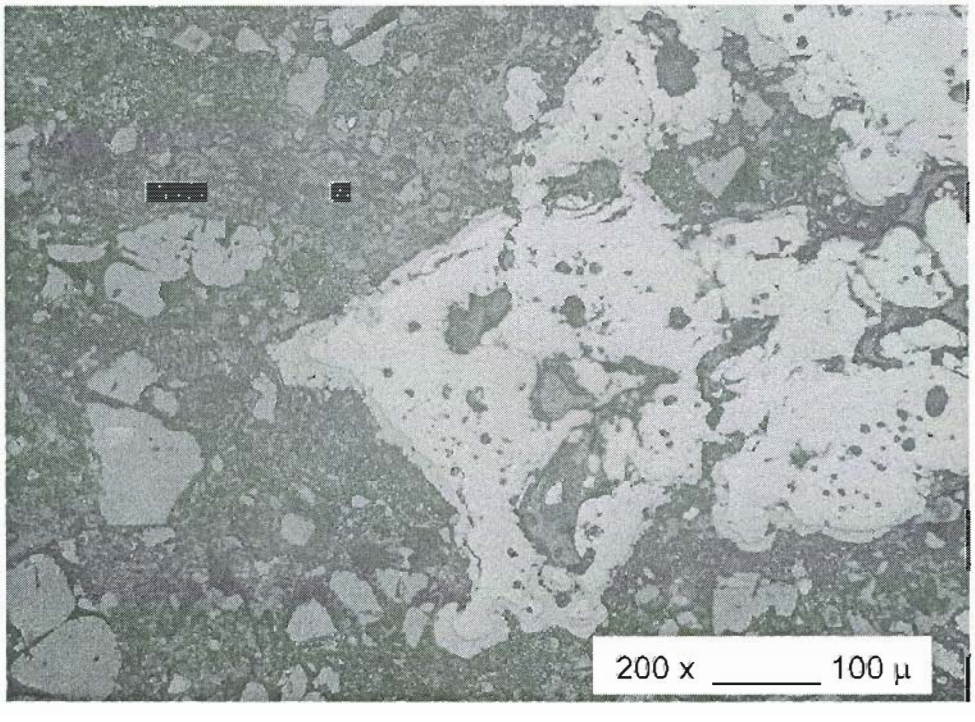

Figure 4.23A. Calcium dialuminate blend microstructure. Batch B 3-15

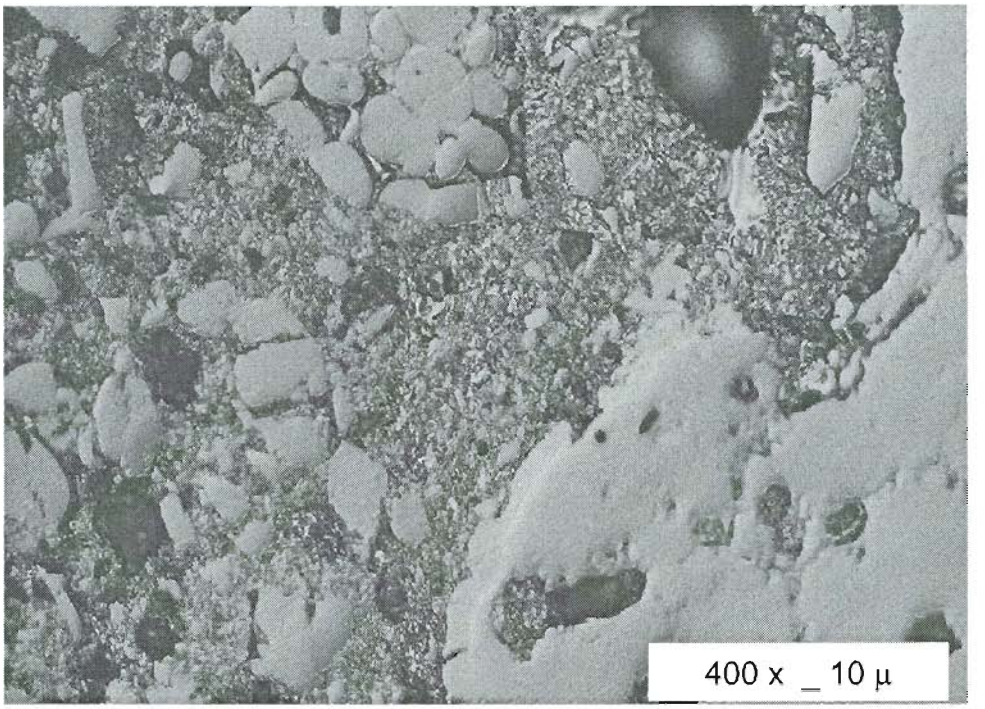

Figure 4.23B. Calcium dialuminate blend microstructure. Batch B3-10

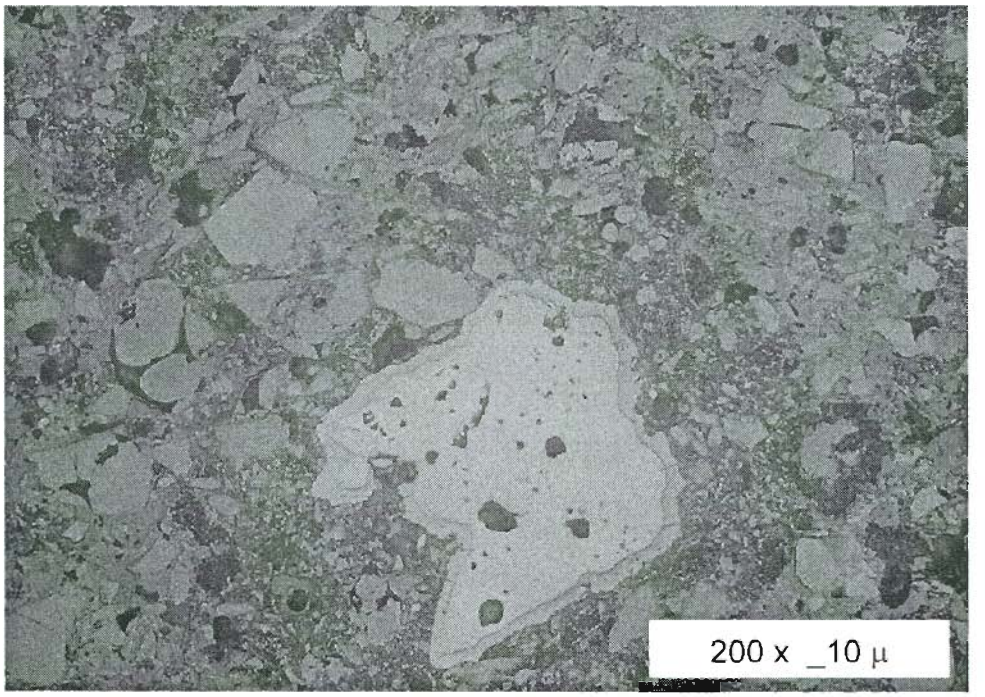

Figure 4.23C. Calcium dialuminate blend microstructure. Batch B3-24

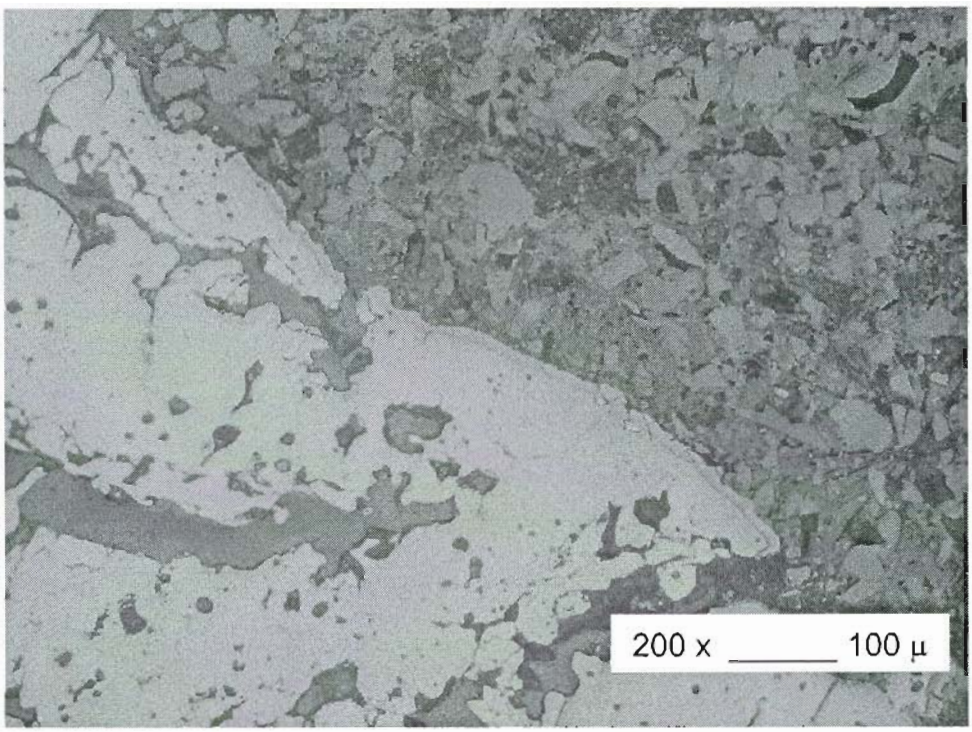

Figure 4.23D. Calcium dialuminate blend microstructure features with dead burnt magnesia additive and zirconia grog reinforcement are shown in frames A, B, C and D. The diffusion zone between reinforcement and matrix on four different formulations is shown. Batch B 3-25

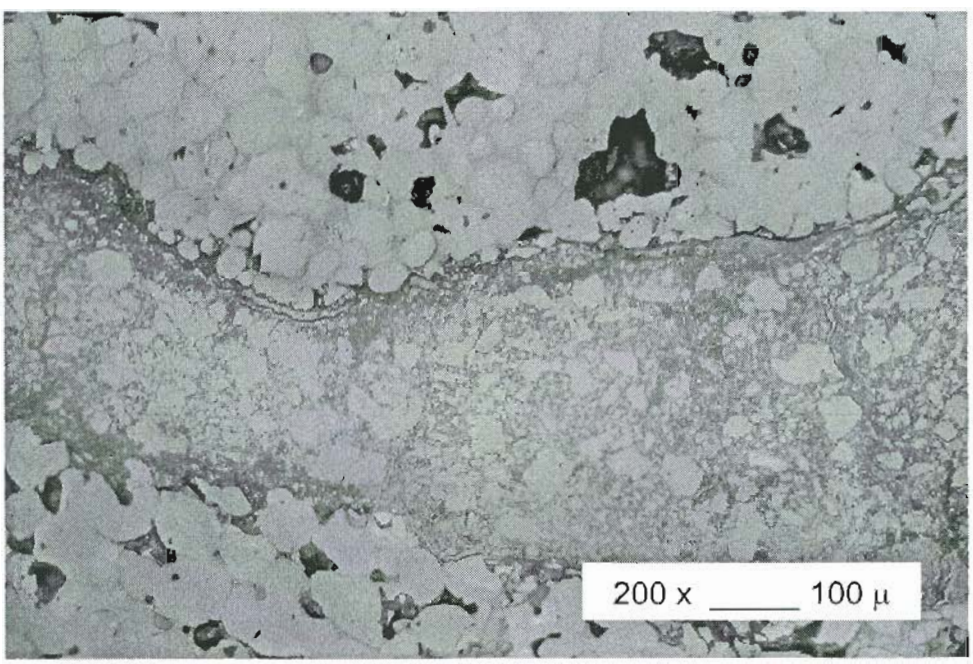

Figure 4.24A. Calcium dialuminate microstructure. Batch B5-12

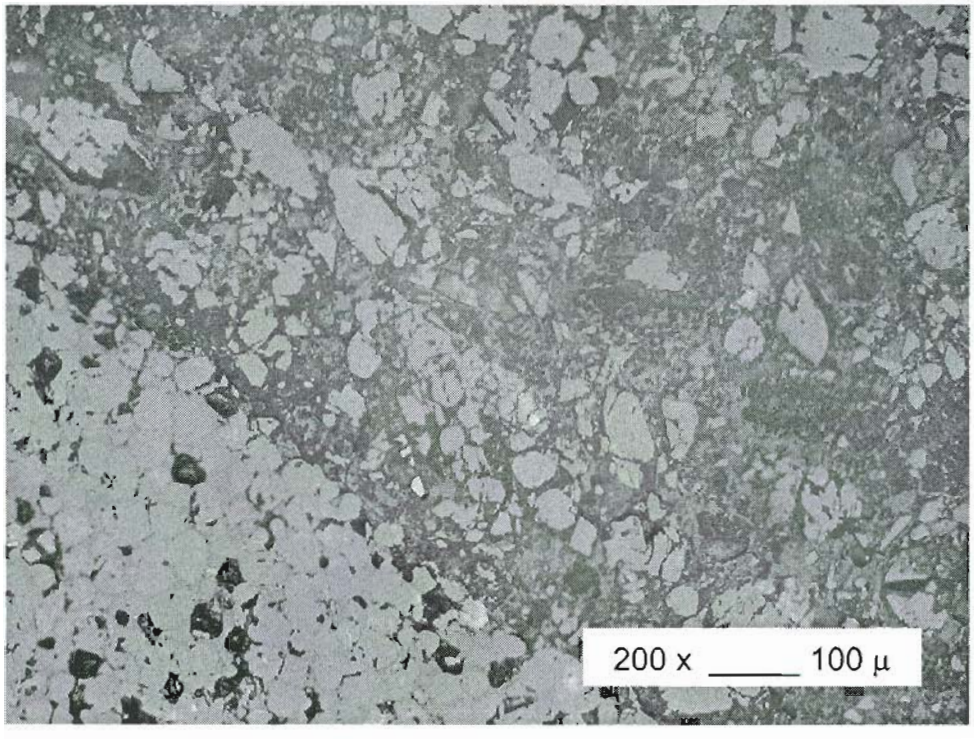

Figure 4.24B. Calcium dialuminate microstructure. Batch B 5-10

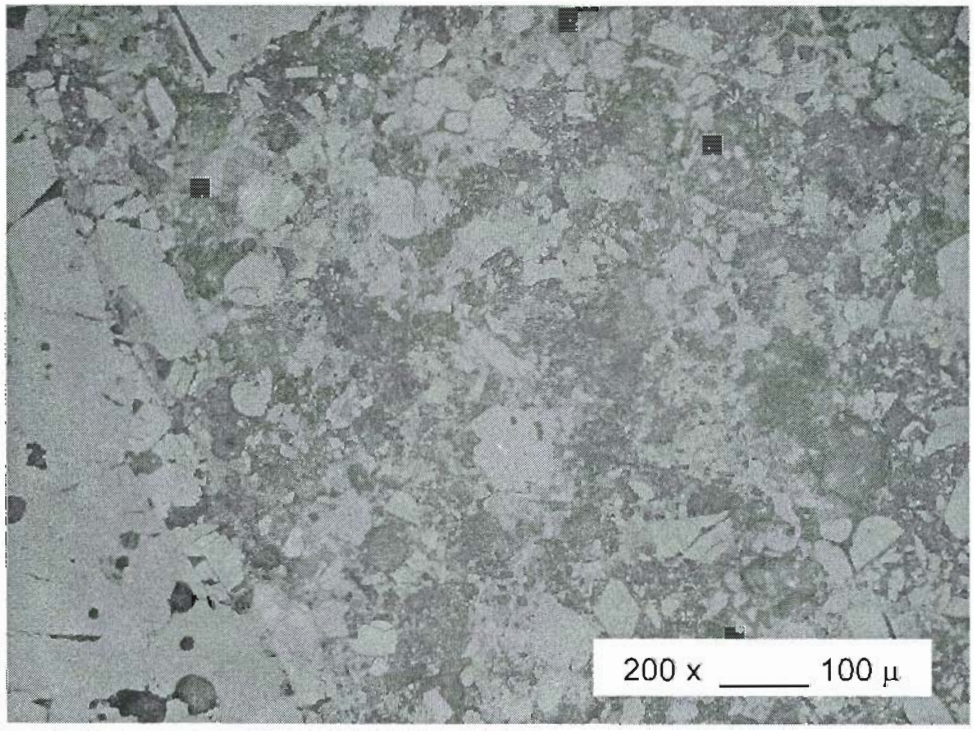

Figure 4.24C. Calcium dialuminate microstructure. Batch B4-16

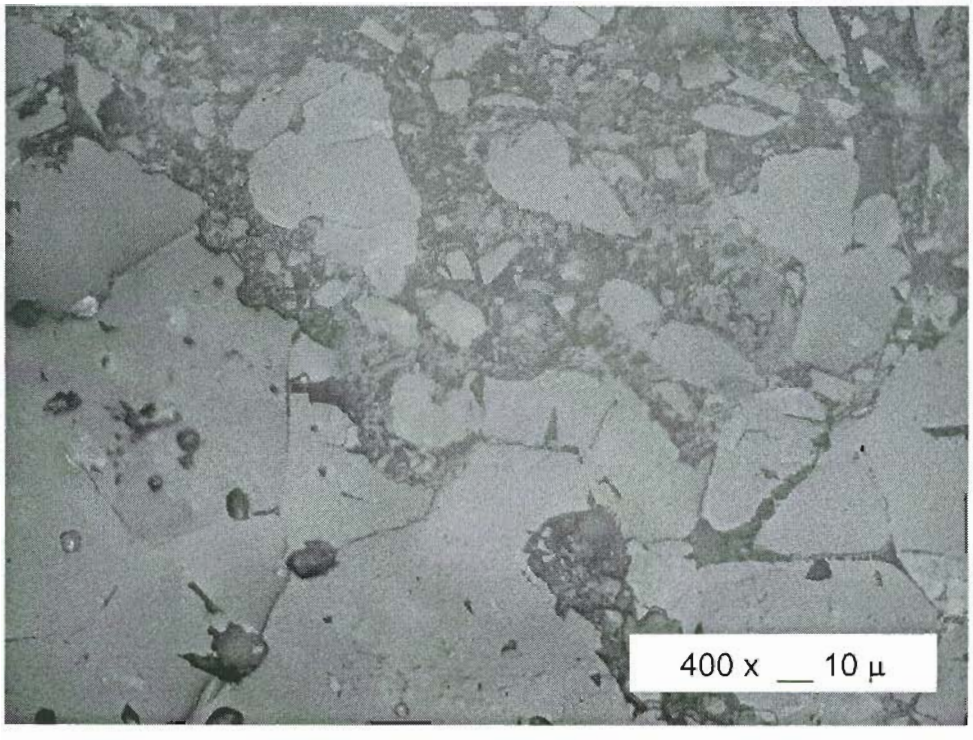

Figure 4.24D. Calcium dialuminate microstructure features with dead burnt magnesia additive and reinforcement. Frames A, B, C and D show examples of the interface between the reinforcement and matrix interface. Batch B4-15

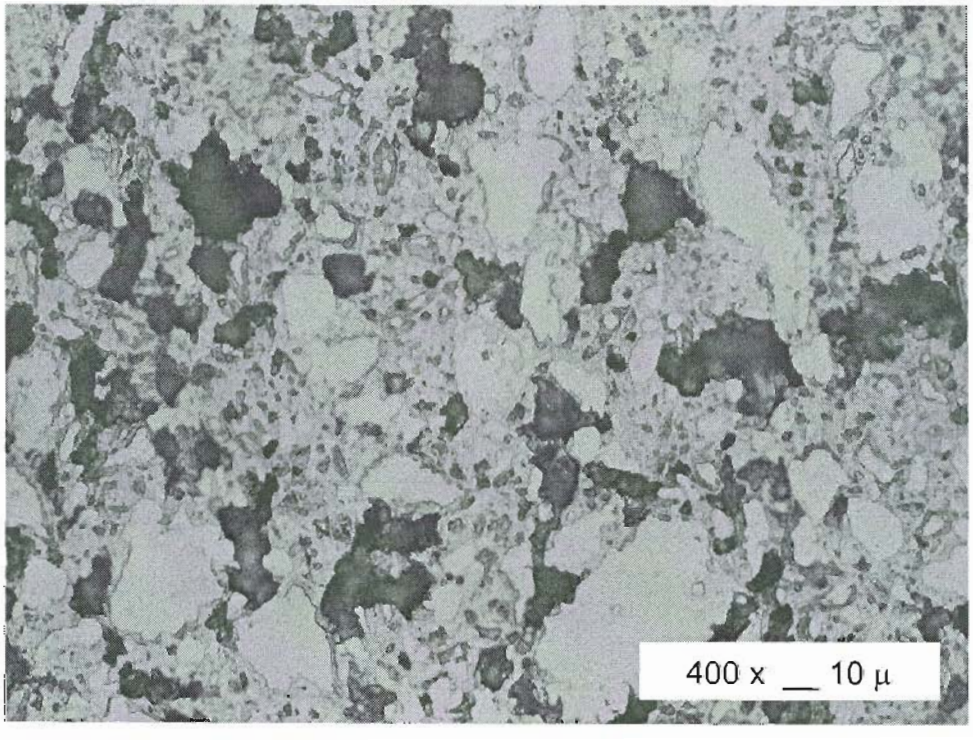

Figure 4.25A. High alumina calcium aluminate premix microstructure. Batch B1-9

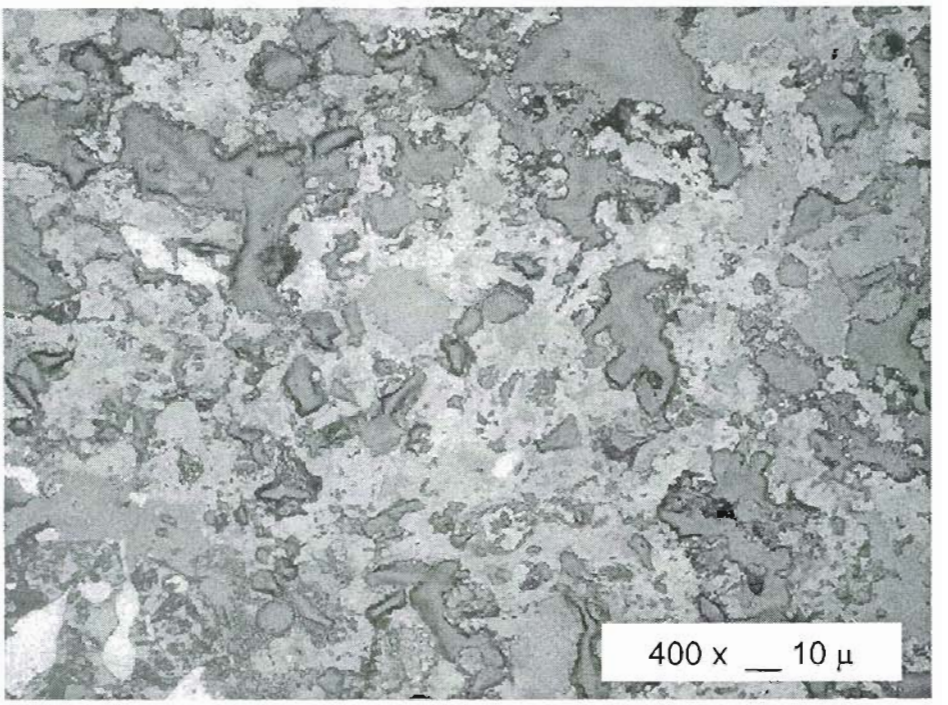

Figure 4.25B. High alumina calcium aluminate premix microstructure with chromia added. Chromia particles are shown surrounded by cement. Frames A and B illustrate areas of closed and open porosity in the same sample. Batch B1-9

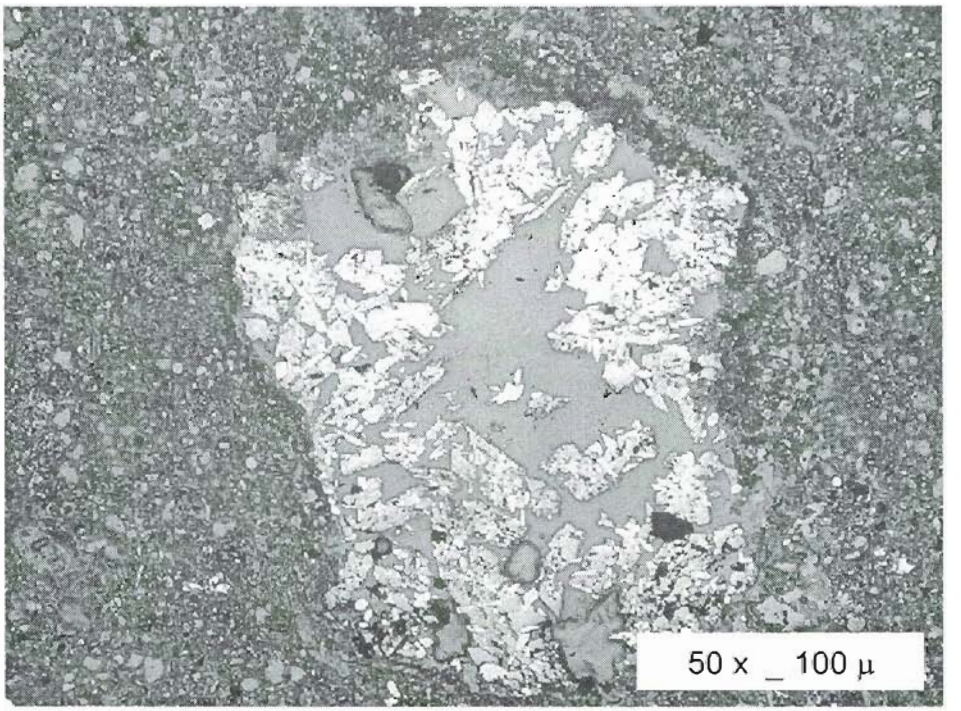

Figure 4.26. High alumina calcium aluminate premix microstructure with chromia added. Interface between reinforcement and matrix is shown. Batch B10-28

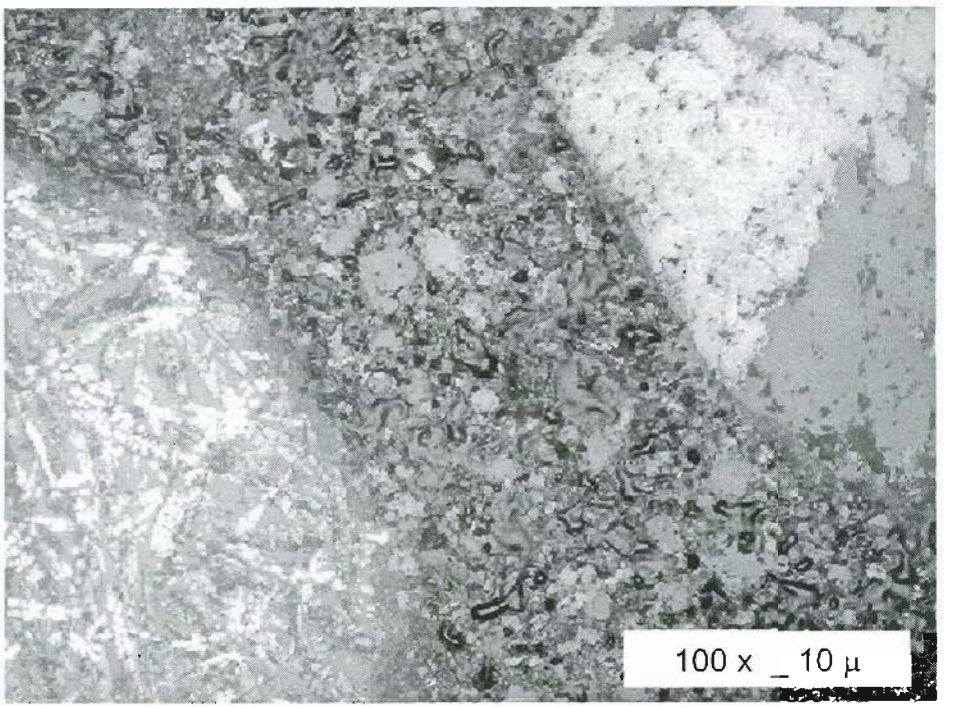

Figure 4.27. High alumina calcium aluminate premix microstructure with chromia added. Region of zircon reinforcement and interface is shown. Batch B1-9

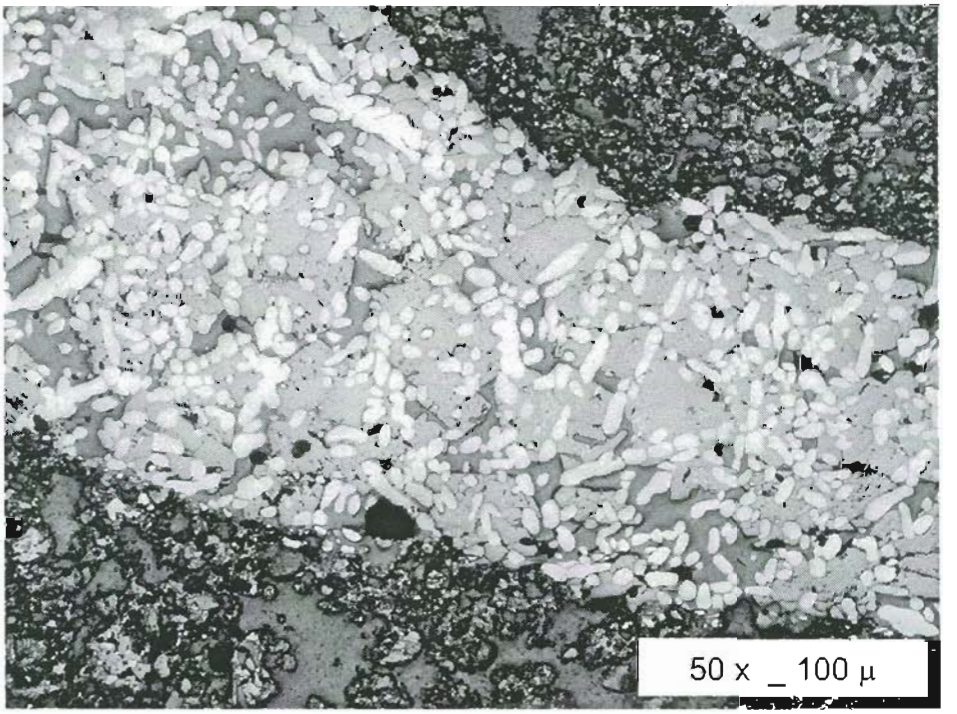

Figure 4.28. High alumina calcium aluminate premix microstructure with chromia added. Interface between reinforcement and matrix is shown. Batch B10-28

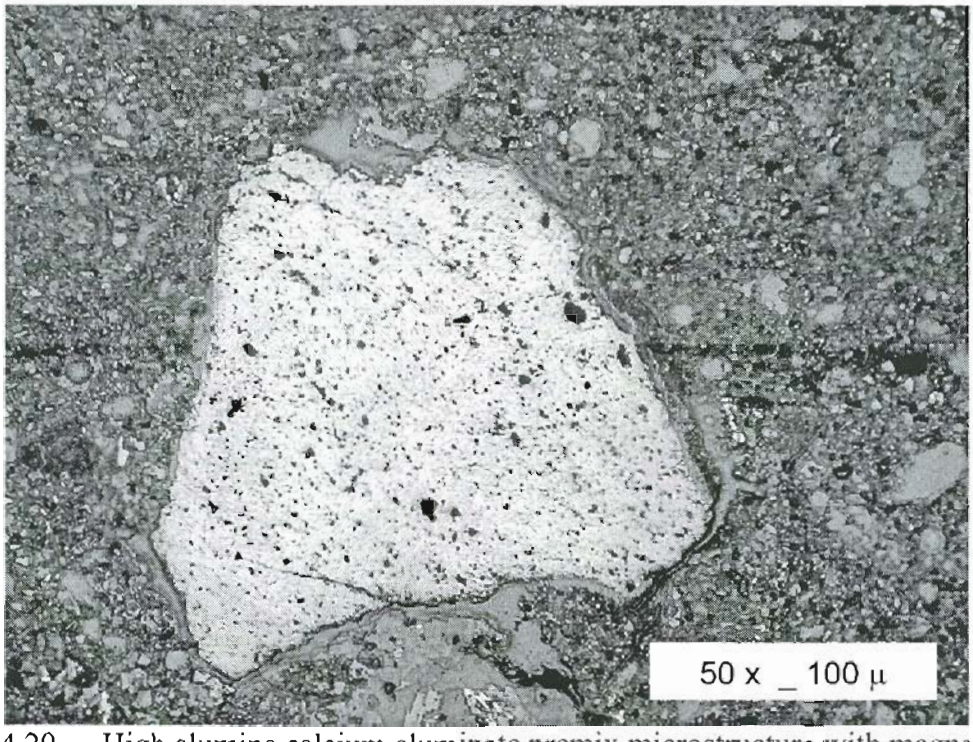

Figure 4.29. High alumina calcium aluminate premix microstructure with magnesia added. The Figure shows an iron oxide impurity and matrix cracking due to CTE mismatch. Batch B 10-8

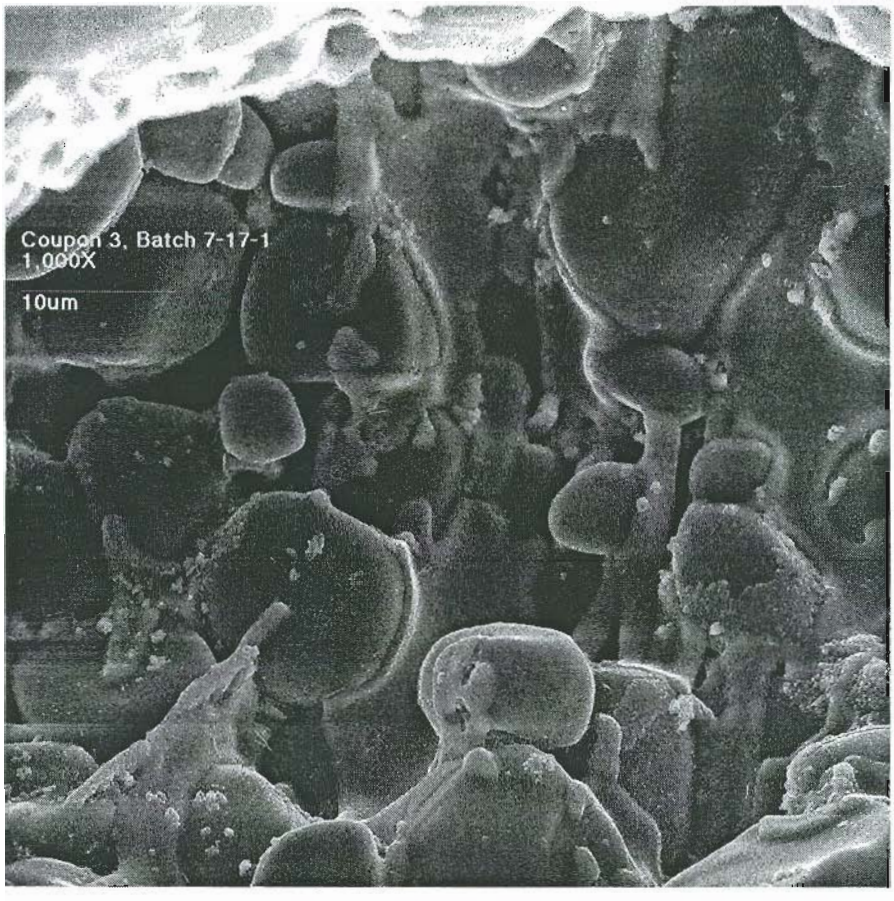

Figure 4.30. SEM photomicrograph shows the sintered microstructure adjacent to a pore. The particles are dead burnt magnesia and calcium dialuminate blend cement connected by a viscous phase, rich in calcia and alumina. Particle wetting is incomplete in some areas. Batch B7-17

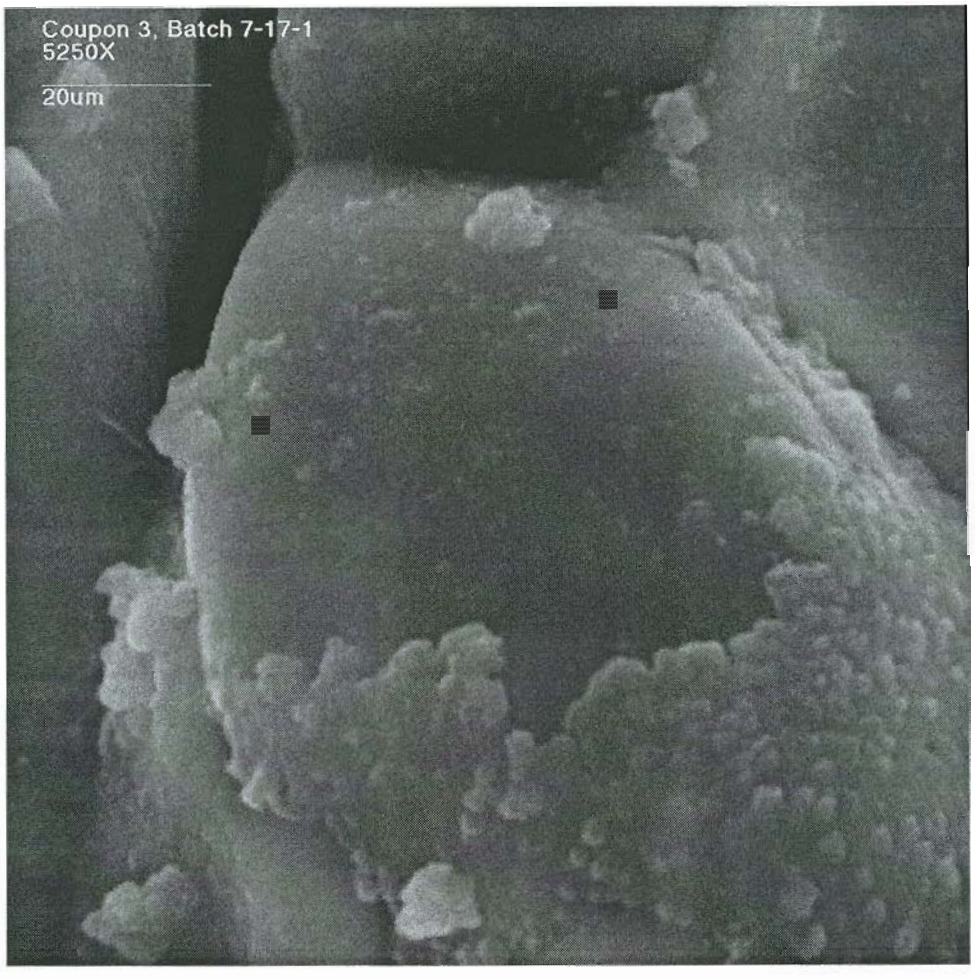

Figure 4.31. SEM photomicrograph illustrating remains of hydrate structures collapsed onto the grains of dead burnt magnesia and non hydrated calcium aluminate blend cement. A triple point is shown between three grains resulting from surface diffusion. Batch B 7-17

4.4 Density

4.4.1 Water Loss and Dry Weight Change

The coupon water loss following the curing and drying steps was used to determine the relative amount of water used in the hydration of the cement. A number of coupons were weighed following the curing, heating to 121°C and 315°C. The weight change due to water loss was measured on coupons from each of the three cement types.

The weight loss after a 121°C soak ranged between 1 and 3 % of the weight of the coupon from the as cured state. The weight loss at 315°C ranged between 3 and 7% of the coupon weight. The data results were relatively consistent. The trend was established indicting that 60 to 80% of the total water added was used in the hydration of the cement or the formation of chemically bound water phases. The evaporation losses over the 48-hour cure period may lower the estimation.

4.4.2 Sintering Density

The density measurement and open porosity results are listed in Table 4.2. The table presents the batch, composition, sintering temperature and density for multiple coupons from 141 formulated batches. The density is presented for the sintered coupons and the average of the coupons from the batch. The relationship of the batch variables to the density are illustrated in the set of Figures 4.32 thorough 4.39. Figure 4.32 shows the average density of 106 batches sintered at 1200°C. The density measurements from multiple coupons were averaged and the standard deviation is shown. In most cases the density range of the set is greater than the standard deviation between the density of the coupons in the same batch. The final sintered density change with the concentration of cement is shown in Figure 4.33. Cement type is separated to show the density change for each of the calcium aluminate cements. The final sintered density relationship to the water/cement ratio is shown in Figure 4.34. In this Figure the density data are separated into the type of cement matrix cement used. The sintered coupon densities are compared to the concentration of total additive and are separated into groups according to the type of matrix cement shown Figure 4.35. The density data and influence of the additive is examined in finer detail as shown in Figures 4.36 and 4.37. The final sintered density change is compared to the specific additive concentration for the premix high alumina calcium dialuminate blend in Figure 4.36. The final sintered density compared to the additive concentration separated into the four major additives (Cr_2O_3, MgO, dead burnt-MgO and Spinel) for the Fondu and the calcium dialuminate cement blend is shown in Figure 4.37. Influence of the reinforcement concentration on the coupon density

is separated into the three types of cement are shown in Figure 4.38. Figure 4.39 shows the coupon density relationship with the reinforcement concentration separated into the different reinforcement material groups for the Fondu cement and the calcium dialuminate blend.

Conventional ceramic materials lose strength with increasing porosity or lower density. Because of the large porosity in ceramic cements the influence of density may conceal changes produced by the various reinforcement and additive changes. It is important that the bulk data does not exhibit a trend of increasing strength with increasing density or the conclusions drawn using these experimental methods can be questioned. Figures 4.40, 4.41 and 4.42 present several relationships that all indicate a relatively wide spread in the compression strength over a similar density range. The trend suggests the strength is independent of the density over the range of sintering conditions tested. The Figures present the experimental conditions of full size and half size coupons in both the dry and saturated conditions to illustrate the sensitivity of the compression strength test measurements. Figure 4.40 presents the full size, half-size, dry and saturated cold compressive strength data for coupon #1. The saturated coupons exhibit a strength enhancement, but overall the dry coupons are independent of a trend of increased strength with density. Figure 4.41 presents similar results for coupon #3. Figure 4.42 combines all the cold compressive strength data.

Table 4.2. Density and Open Porosity Results.

BATCH NUMBER	B1-28-1	B2-2-1	B2-4-1	B2-7-1	B2-12-1	B2-16-1	B2-18-1	B2-23-1
DESCRIPTION	Premix	Premix	Premix	Premix	Premix	Premix	Premix	Premix
Cement, % of Batch	26.0	40.0	40.0	26.0	30.0	30.0	32.0	32.0
Reinforcement, % Batch	39.0	60.0	60.0	39.0	45.1	45.0	48.0	48.1
Additive % of Batch	35.0			35.0	24.9	25.0	20.0	19.9
MATRIX COMPOSITION								
Chromia, Cr O	28.7%				9.1%	22.7%	19.2%	12.6%
Magnesia, MgO	28.7%			57.4%	36.3%	22.7%	19.2%	25.3%
Spinel, $MgAl_2O_4$	0.0%							
Alumina, Al_2O_3	34.1%	80.0%	80.0%	34.1%	43.7%	43.6%	49.2%	49.3%
Calcia, CaO	4.3%	10.0%	10.0%	4.3%	5.5%	5.5%	6.2%	6.2%
Silica, SiO_2	4.3%	10.0%	10.0%	4.3%	5.5%	5.5%	6.2%	6.2%
FINISHED COUPONS								
Coupon 1								
Sinter Temperature, °C	1200	1200	1200		1200	1200	1200	1200
Density, gm/cc	3.15	3.17	2.99		3.04	2.95	2.89	3.22
Coupon 2								
Sinter Temperature, °C		1200		1200				
Density, gm/cc		3.39		3.35				
Coupon 3								
Sinter Temperature, °C	1200		1200		1200	1200	1200	1200
Density, gm/cc	3.30		3.46		3.15	3.33	3.15	3.30
Open Porosity (minimum)	10.2%		6.6%		10.1%	6.8%	8.2%	6.7%
Coupon 4								
Sinter Temperature, °C	1000	1000	1000	1000	1000	1000	1000	1000
Density, gm/cc	2.99	3.12	3.38	3.31	3.57	2.90	3.02	2.88
DENSITY SUMMARY								
Std. Dev.	0.15	0.15	0.25	0.03	0.28	0.24	0.13	0.23
Average Density, gm/cc	3.14	3.23	3.28	3.33	3.25	3.06	3.02	3.13

Table 4.2. Density and Open Porosity Results (continued).

BATCH NUMBER	B2-25-1	B3-2-1	B3-4-1	B3-6-1	B3-10-1	B3-12-1	B3-16-1	B3-18-1
DESCRIPTION	Premix	Premix	Premix	Premix	Premix	Premix	Premix	Premix
Cement, % of Batch	36.0	30.0	34.0	29.6	31.5	24.7	24.7	24.7
Reinforcement, % Batch	54.0	45.1	51.0	62.8	59.8	59.9	59.9	59.9
Additive % of Batch	10.0	24.9	15.0	7.6	8.6	15.4	15.4	15.4
MATRIX COMPOSITION								
Chromia, Cr O	7.2%	29.9%	20.2%	13.5%	7.1%	12.6%	7.7%	19.2%
Magnesia, MgO	14.3%	15.0%	10.1%	6.8%	14.2%	25.3%	30.7%	19.2%
Spinel, $MgAl_2O_4$								
Alumina, Al_2O_3	62.6%	43.8%	55.5%	63.6%	62.8%	49.3%	49.3%	49.3%
Calcia, CaO	7.8%	5.5%	6.9%	8.0%	7.9%	6.2%	6.2%	6.2%
Silica, SiO_2	7.8%	5.5%	6.9%	8.0%	7.9%	6.2%	6.2%	6.2%
FINISHED COUPONS								
Coupon 1								
Sinter Temperature, °C	1200	1200	1200	1200	1200	1200	1200	1200
Density, gm/cc	2.94	2.94	3.28	3.17	3.29	3.30	3.32	3.22
Coupon 2								
Sinter Temperature, °C				1200	1200	1200	1200	1200
Density, gm/cc				3.47	3.38	3.37	3.26	3.18
Coupon 3								
Sinter Temperature, °C	1200	1200	1200	1200	1200	1200	1200	1200
Density, gm/cc	3.16	3.24	3.25	3.33	3.29	3.19	3.38	3.30
Open Porosity (minimum)	5.5%	6.5%	4.8%	5.0%	5.7%	5.2%	6.4%	5.4%
Coupon 4								
Sinter Temperature, °C	1000	1000	1000	1000	1000	1000	1000	1000
Density, gm/cc	2.90	2.92	3.16	3.39	3.03	3.02	2.97	3.02
DENSITY SUMMARY								
Std. Dev.	0.14	0.18	0.06	0.13	0.15	0.15	0.18	0.12
Average Density, gm/cc	3.00	3.03	3.23	3.34	3.25	3.22	3.23	3.18

Table 4.2. Density and Open Porosity Results (continued).

BATCH NUMBER	B3-30-1	B4-1-1	B4-3-1	B4-6-1	B4-8-1	B4-13-1	B4-16-1	B4-20-1
DESCRIPTION	Premix	Premix	Premix	Premix	Premix	Premix	Premix	Premix
Cement, % of Batch	24.7	19.4	19.4	42.6	44.0	44.8	36.0	36.0
Reinforcement, % Batch	59.9	60.0	60.0	44.4	36.1	31.5	54.1	54.1
Additive % of Batch	15.4	20.6	20.6	13.0	19.9	23.8	9.9	9.9
MATRIX COMPOSITION								
Chromia, Cr O	25.3%	10.3%	17.0%				21.6%	10.8%
Magnesia, MgO	12.6%	41.3%	34.1%					10.8%
Spinel, $MgAl_2O_4$								
Alumina, Al_2O_3	49.3%	38.7%	38.7%	80.0%	80.0%	80.0%	62.7%	62.7%
Calcia, CaO	6.2%	4.8%	4.8%	10.0%	10.0%	10.0%	7.8%	7.8%
Silica, SiO_2	6.2%	4.8%	4.8%	10.0%	10.0%	10.0%	7.8%	7.8%
FINISHED COUPONS								
Coupon 1								
Sinter Temperature, °C	1200	1200	1200	1200	1200	1200	1200	
Density, gm/cc	3.37	3.18	2.75	3.09	3.10	3.31	3.23	
Coupon 2								
Sinter Temperature, °C	1200	1200	1200	1200	1200	1200	1200	1200
Density, gm/cc	3.26	3.23	3.11	3.06	3.18	3.10	3.28	3.07
Coupon 3								
Sinter Temperature, °C	1200	1200	1200	1200	1200	1200	1200	1200
Density, gm/cc	3.25	3.37	3.32	3.15	3.31	3.08	3.54	3.50
Open Porosity (minimum)	4.5%	6.1%	5.8%	8.5%	11.4%	8.9%	5.8%	7.2%
Coupon 4								
Sinter Temperature, °C	1000	1000	1000	1000	1000	1000	1000	1000
Density, gm/cc	3.22	3.03	2.96	3.12	3.27	3.27	3.28	3.25
DENSITY SUMMARY								
Std. Dev.	0.07	0.14	0.24	0.04	0.10	0.11	0.14	0.21
Average Density, gm/cc	3.27	3.20	3.03	3.10	3.21	3.19	3.33	3.28

Table 4.2. Density and Open Porosity Results (continued).

BATCH NUMBER	B4-22-1	B4-24-1	B4-27-1	B4-29-1	B5-1-1	B5-4-1	B5-6-1	B5-8-1
DESCRIPTION	Premix	Premix	Premix	Premix	Premix	Premix	Premix	Premix
Cement, % of Batch	36.0	36.0	41.8	36.0	30.0	36.0	32.0	32.1
Reinforcement, % Batch	54.1	54.1	49.2	54.1	45.1	54.1	48.0	48.1
Additive % of Batch	9.9	9.9	9.0	9.9	24.9	9.9	20.0	19.9
MATRIX COMPOSITION								
Chromia, Cr O	4.3%	10.8%						
Magnesia, MgO	17.3%	10.8%				21.6%	38.5%	
Spinel, $MgAl_2O_4$				21.6%	45.3%			38.3%
Alumina, Al_2O_3	62.7%	62.7%	80.0%	62.7%	43.8%	62.7%	49.2%	49.4%
Calcia, CaO	7.8%	7.8%	10.0%	7.8%	5.5%	7.8%	6.1%	6.2%
Silica, SiO_2	7.8%	7.8%	10.0%	7.8%	5.5%	7.8%	6.1%	6.2%
FINISHED COUPONS								
Coupon 1								
Sinter Temperature, °C								
Density, gm/cc								
Coupon 2								
Sinter Temperature, °C	1200	1200	1200	1200	1200	1200	1200	1200
Density, gm/cc	2.93	2.86	3.13	2.84	2.93	2.84	3.06	3.08
Coupon 3								
Sinter Temperature, °C	1200	1200	1200	1200	1200	1200	1200	1200
Density, gm/cc	3.31	3.64	3.20	3.24	3.31	3.19	3.12	3.24
Open Porosity (minimum)	9.4%	7.3%	7.0%	6.3%	6.1%	6.8%	7.8%	5.8%
Coupon 4								
Sinter Temperature, °C	1000	1000	1000	1000	1000	1000	1000	1000
Density, gm/cc	2.98	3.01	3.04	2.92	3.04	3.00	2.96	3.13
DENSITY SUMMARY								
Std. Dev.	0.21	0.41	0.08	0.21	0.19	0.17	0.08	0.08
Average Density, gm/cc	3.07	3.17	3.12	3.00	3.09	3.01	3.05	3.15

Table 4.2. Density and Open Porosity Results (continued).

BATCH NUMBER	B5-11-1	B5-13-1	B5-15-1	B5-18-1	B5-20-1	B5-22-1	B5-26-1	B5-28-1
DESCRIPTION	Premix	Premix	Premix	Premix	Premix	Premix	Premix	Premix
Cement, % of Batch	32.0	20.0	20.0	30.6	30.6	30.6	30.6	30.6
Reinforcement, % Batch	68.0	80.0	63.3	61.1	61.1	61.1	61.1	61.1
Additive % of Batch			16.6	8.3	8.3	8.3	8.3	8.3
MATRIX COMPOSITION								
Chromia, Cr O					4.3%	10.7%	7.5%	
Magnesia, MgO					17.1%	10.7%	13.5%	21.3%
Spinel, $MgAl_2O_4$			45.4%	21.3%				
Alumina, Al_2O_3	80.0%	80.0%	43.7%	62.9%	62.9%	62.9%	62.9%	62.9%
Calcia, CaO	10.0%	10.0%	5.5%	7.9%	7.9%	7.9%	7.9%	7.9%
Silica, SiO_2	10.0%	10.0%	5.5%	7.9%	7.9%	7.9%	7.9%	7.9%
FINISHED COUPONS								
Coupon 1								
Sinter Temperature, °C								
Density, gm/cc								
Coupon 2								
Sinter Temperature, °C	1200	1200	1200	1200	1200			
Density, gm/cc	2.75	3.15	3.11	2.88	2.98			
Coupon 3								
Sinter Temperature, °C	1200	1200	1200	1200	1200	1200	1200	1200
Density, gm/cc	3.24	3.27	3.53	3.47	3.65	2.65	3.40	3.14
Open Porosity (minimum)	10.3%	7.5%	5.9%	5.6%	6.2%	5.9%	5.8%	7.0%
Coupon 4								
Sinter Temperature, °C	1000	1000	1000	1000	1000	1000	1000	1000
Density, gm/cc	3.13	2.97	3.07	3.06	3.18	2.63	3.20	3.29
DENSITY SUMMARY								
Std. Dev.	0.26	0.15	0.25	0.30	0.34	0.02	0.14	0.10
Average Density, gm/cc	3.04	3.13	3.24	3.14	3.27	2.64	3.30	3.22

Table 4.2. Density and Open Porosity Results (continued).

BATCH NUMBER	B8-24-1	B8-28-1	B9-1-1	B9-3-1	B9-8-1	B9-10-1	B9-26-1	B9-28-1
DESCRIPTION	CA	CA	CA	CA	CA	CA	CA	CA
Cement %, of Batch	50	50	100	50	26	25	50	50
Reinforcement, % Batch	50	50			51	50	50	50
Additive % of Batch				50	23	25		
MATRIX COMPOSITION								
Alumina, Al O as CA or	40.0%	40.0%	40.0%	20.0%	21.1%	20.0%	40.0%	40.0%
Calcia, CaO as CA or CA_2	45.0%	45.0%	45.0%	22.5%	23.7%	22.5%	45.0%	45.0%
Iron Oxide, Fe_3O_4 as C_4AF	13.0%	13.0%	13.0%	6.5%	6.8%	6.5%	13.0%	13.0%
Silica, SiO_2 as C_2S or C_3S	2.0%	2.0%	2.0%	1.0%	1.1%	1.0%	2.0%	2.0%
Magnesia, MgO				50.0%	47.4%			
Spinel, $MgAl_2O_4$						50.0%		
Dead Burnt Magnesia, MgO								
FINISHED COUPONS								
Coupon 1								
Sinter Temperature, °C	1000	1000	1000	1000	1000	1000	1000	1150
Density, gm/cc	3.64	3.38	2.71	3.10	4.01	3.89	3.89	3.24
Coupon 2								
Sinter Temperature, °C	1200	1200	1200	1200	1200	1200	1200	1150
Density, gm/cc	3.40	3.27	2.96	3.13	4.16	3.73	3.73	3.10
Coupon 3								
Sinter Temperature, °C	1200	1200	1200	1200	1200	1200	1200	1200
Density, gm/cc	3.59	3.24	2.92	3.04	4.09	3.81	3.90	3.26
Open Porosity (min)	5.4%	4.5%	12.2%	15.3%	10.7%	7.5%	3.8%	4.8%
Coupon 5								
Sinter Temperature	1000	1000	1000	1000	1000	1000	1000	
Density, gm/cc	3.65	3.20	2.83	3.06	3.80	3.79	3.79	
DENSITY SUMMARY								
Std Dev	0.11	0.08	0.11	0.04	0.16	0.07	0.08	0.09
Average	3.57	3.27	2.86	3.08	4.02	3.81	3.83	3.20

Table 4.2. Density and Open Porosity Results (continued).

BATCH NUMBER	B9-30-1	B10-2-1	B10-5-1	B10-7-1	B10-12-1	B10-14-1	B10-16-1	B10-19-1
DESCRIPTION	CA	CA	CA	CA	CA	CA	CA	CA
Cement %, of Batch	25	25	50	13	10	25	17	13
Reinforcement, % Batch	50	50	50	50	50	50	50	50
Additive % of Batch	25	25		38	40	25	33	38
MATRIX COMPOSITION								
Alumina, Al O as CA or	20.0%	20.0%	40.0%	10.0%	8.0%	20.0%	13.3%	10.0%
Calcia, CaO as CA or CA_2	22.5%	22.5%	45.0%	11.3%	9.0%	22.5%	15.0%	11.3%
Iron Oxide, Fe_3O_4 as C_4AF	6.5%	6.5%	13.0%	3.3%	2.6%	6.5%	4.3%	3.3%
Silica, SiO_2 as C_2S or C_3S	1.0%	1.0%	2.0%	0.5%	0.4%	1.0%	0.7%	0.5%
Chromia, Cr_2O_4								
Titania-Alumina $TiO{\cdot}Al_2O_3$								
Magnesia, MgO				75.0%	80.0%			
Spinel, $MgAl_2O_4$	50.0%	50.0%				50.0%	66.7%	75.0%
Dead Burnt Magnesia, MgO								
Alumina, Al_2O_4								
FINISHED COUPONS								
Coupon 1								
Sinter Temperature, °C	1150	1150	1150	1150	1150	1150	1150	1150
Density, gm/cc	3.31	3.24	3.21	3.13	3.15	3.08	3.18	3.22
Coupon 2								
Sinter Temperature, °C	1150	1150	1150	1150	1150	1150	1150	1150
Density, gm/cc	3.16	3.20	3.22	3.04	3.23	3.22	3.22	3.28
Coupon 3								
Sinter Temperature, °C	1200	1200	1200	1200	1200	1200	1200	1200
Density, gm/cc	3.26	3.26	3.15	3.29	3.08	3.21	3.21	3.18
Open Porosity (min)	7.1%	5.3%	8.1%	8.1%	8.1%	6.1%	5.8%	6.3%
DENSITY SUMMARY								
Std Dev	0.08	0.03	0.04	0.13	0.08	0.07	0.02	0.05
Average	3.24	3.23	3.19	3.15	3.15	3.17	3.20	3.22

Table 4.2. Density and Open Porosity Results (continued).

BATCH NUMBER	B10-21-1	B10-23-1	B10-26-1	B11-23-1	B11-30-1	B12-1-1	B12-2-1	B12-3-1
DESCRIPTION	CA	CA	CA	CA	CA	CA	CA	CA
Cement %, of Batch	10	33	50	50	20	13	10	08
Reinforcement, % Batch	50	67	50	50	60	60	60	60
Additive % of Batch	40				20	27	30	32
MATRIX COMPOSITION								
Alumina, Al O as CA or	8.0%	40.0%	40.0%	40.0%	20.0%	13.3%	10.0%	8.0%
Calcia, CaO as CA or CA_2	9.0%	45.0%	45.0%	45.0%	22.5%	15.0%	11.2%	9.0%
Iron Oxide, Fe_3O_4 as C_4AF	2.6%	13.0%	13.0%	13.0%	6.5%	4.3%	3.2%	2.6%
Silica, SiO_2 as C_2S or C_3S	0.4%	2.0%	2.0%	2.0%	1.0%	0.7%	0.5%	0.4%
Magnesia, MgO					50.0%	66.7%	75.0%	80.0%
Spinel, $MgAl_2O_4$	80.0%	0.0%						
Dead Burnt Magnesia, MgO								
FINISHED COUPONS								
Coupon 1								
Sinter Temperature, °C	1150	1150	1150	1000	1000	1000	1000	1000
Density, gm/cc	3.28	3.19	3.23	3.74	4.09	3.76	3.92	4.18
Coupon 2								
Sinter Temperature, °C	1150	1150	1150	1000	1000	1000	1000	1000
Density, gm/cc	3.13	3.20	3.11	3.78	3.93	3.94	4.04	3.80
Coupon 3								
Sinter Temperature, °C	1200		1200	1200	1200	1200	1200	1200
Density, gm/cc	3.17		3.14	3.59	3.84	4.13	3.91	3.96
Open Porosity (min)	6.7%		7.8%	7.7%	8.3%	8.0%	8.6%	9.2%
Coupon 4								
Sinter Temperature, °C				1000	1000	1000	1000	1000
Density, gm/cc				3.78	3.83	4.02	3.76	3.82
DENSITY SUMMARY								
Std Dev	0.08	0.01	0.06	0.09	0.12	0.16	0.11	0.18
Average	3.20	3.20	3.16	3.72	3.92	3.97	3.91	3.94

Table 4.2. Density and Open Porosity Results (continued).

BATCH NUMBER	B12-7-1	B12-8-1	B12-9-1	B12-18-2	B1-12-1	B1-15-1	B1-19-1	B1-20-1
DESCRIPTION	CA	CA	CA	CA	CA	CA	CA	CA
Cement %, of Batch	20	14	10	43	40	40	100	100
Reinforcement, % Batch	59	59	59	57	60	60		
Additive % of Batch	20	27	31					
MATRIX COMPOSITION								
Alumina, Al O as CA or	20.0%	13.3%	10.0%	40.0%	62.0%	62.0%	62.0%	62.0%
Calcia, CaO as CA or CA_2	22.5%	15.0%	11.3%	45.0%	30.0%	30.0%	30.0%	30.0%
Iron Oxide, Fe_3O_4 as C_4AF	6.5%	4.3%	3.3%	13.0%	5.0%	5.0%	5.0%	5.0%
Silica, SiO_2 as C_2S or C_3S	1.0%	0.7%	0.5%	2.0%	3.0%	3.0%	3.0%	3.0%
Chromia, Cr_2O_4								
Titania-Alumina $TiO{\cdot}Al_2O_3$								
Magnesia, MgO	50.0%	66.7%	75.0%					
Spinel, $MgAl_2O_4$								
Dead Burnt Magnesia, MgO								
FINISHED COUPONS								
Coupon 1								
Sinter Temperature, °C								
Density, gm/cc								
Coupon 2								
Sinter Temperature, °C	1200	1200	1200	1200	1200	1200	1200	1200
Density, gm/cc	4.15	4.07	4.04	3.79	3.68	3.71	2.77	2.83
Coupon 3								
Sinter Temperature, °C	1200	1200	1200	1200	1200	1200	1200	1200
Density, gm/cc	3.86	3.90	4.06	3.89	3.90	3.95	2.76	2.76
Open Porosity (min)	7.9%	8.6%	8.3%	6.2%	7.2%	7.2%	16.1%	12.4%
DENSITY SUMMARY								
Std Dev	0.20	0.12	0.01	0.07	0.16	0.17	0.01	0.05
Average	4.00	3.98	4.05	3.84	3.79	3.83	2.77	2.79

Table 4.2. Density and Open Porosity Results (continued).

BATCH NUMBER	B1-22-1	B1-28-1	B1-29-2	B2-10-1	B2-14-2	B2-22-1	B2-24-1	B2-25-1
DESCRIPTION	CA	CA	CA	CA	CA	CA	CA	CA
Cement %, of Batch	23	40	100	20	100	40	20	20
Reinforcement, % Batch	55	60		60		60	60	60
Additive % of Batch	23			20			20	20
MATRIX COMPOSITION								
Alumina, Al O as CA or	31.0%	62.0%	62.0%	31.0%	40.0%	62.0%	31.0%	31.0%
Calcia, CaO as CA or CA_2	15.0%	30.0%	30.0%	15.0%	45.0%	30.0%	15.0%	15.0%
Iron Oxide, Fe_3O_4 as C_4AF	2.5%	5.0%	5.0%	2.5%	13.0%	5.0%	2.5%	2.5%
Silica, SiO_2 as C_2S or C_3S	1.5%	3.0%	3.0%	1.5%	2.0%	3.0%	1.5%	1.5%
Chromia, Cr_2O_4								
Titania-Alumina $TiO{\cdot}Al_2O_3$								
Magnesia, MgO								
Spinel, $MgAl_2O_4$	50.0%							
Dead Burnt Magnesia, MgO				50.0%			50.0%	50.0%
Alumina, Al_2O_4								
Cerium Oxide, CeO								
FINISHED COUPONS								
Coupon 1								
Sinter Temperature, °C				1200		1200	1200	1200
Density, gm/cc				3.87		3.09	3.32	3.21
Coupon 2								
Sinter Temperature, °C	1200	1200	1200	1200		1200	1200	1200
Density, gm/cc	3.93	3.99	3.25	4.15		3.12	3.12	3.92
Coupon 3								
Sinter Temperature, °C	1200		1200	1200	1200	1200	1200	1200
Density, gm/cc	3.93		3.61	3.83	4.09	3.10	2.97	3.25
Open Porosity (min)	7.0%		7.6%	7.2%	7.4%	7.0%	9.2%	6.7%
DENSITY SUMMARY								
Std Dev	0.00		0.26	0.18		0.01	0.17	0.40
Average	3.93	3.99	3.43	3.95	4.09	3.10	3.13	3.46

Table 4.2. Density and Open Porosity Results (continued).

BATCH NUMBER	B3-9-1	B3-10-1	B3-11-1	B3-12-1	B3-13-1	B3-14-1	B3-16-1	B3-23-1
DESCRIPTION	CA	CA	CA	CA	CA	CA	CA	CA
Cement %, of Batch	27	13	13	25	17	60	30	40
Reinforcement, % Batch	60	60	75	75	74	40	40	40
Additive % of Batch	13	27	13		9		30	20
MATRIX COMPOSITION								
Alumina, Al O as CA or	41.3%	20.7%	31.0%	62.0%	41.3%	62.0%	31.0%	41.3%
Calcia, CaO as CA or CA_2	20.0%	10.0%	15.0%	30.0%	20.0%	30.0%	15.0%	20.0%
Iron Oxide, Fe_3O_4 as C_4AF	3.3%	1.7%	2.5%	5.0%	3.3%	5.0%	2.5%	3.3%
Silica, SiO_2 as C_2S or C_3S	2.0%	1.0%	1.5%	3.0%	2.0%	3.0%	1.5%	2.0%
Chromia, Cr_2O_4								
Titania-Alumina $TiO{\cdot}Al_2O_3$								
Magnesia, MgO								
Spinel, $MgAl_2O_4$								
Dead Burnt Magnesia, MgO	33.3%	66.7%	50.0%		33.3%		50.0%	33.3%
Alumina, Al_2O_4								
Cerium Oxide, CeO								
FINISHED COUPONS								
Coupon 1								
Sinter Temperature, °C	1200	1200	1200	1200	1200	1200	1200	1200
Density, gm/cc	4.03	4.13	0.00	4.35	4.36	3.42	3.62	3.67
Coupon 2								
Sinter Temperature, °C	1200	1200	1200	1200	1200	1200	1200	1200
Density, gm/cc	3.90	4.14	4.33	4.08	4.14	3.27	3.64	3.76
Coupon 3								
Sinter Temperature, °C	1200	1200	1200	1200	1200	1200	1200	1200
Density, gm/cc	3.69	4.27	4.26	4.20	4.30	3.59	3.50	3.63
Open Porosity (min)	10.3%	7.6%	6.8%	6.4%	6.3%	9.5%	9.6%	8.8%
DENSITY SUMMARY								
Std Dev	0.17	0.08	0.05	0.14	0.11	0.16	0.08	0.06
Average	3.87	4.18	4.29	4.21	4.27	3.43	3.58	3.69

Table 4.2. Density and Open Porosity Results (continued).

BATCH NUMBER	B3-24-1	B3-25-1	B3-26-1	B3-29-1	B3-30-1	B3-31-1	B4-1-1	B4-2-1
DESCRIPTION	CA	CA	CA	CA	CA	CA	CA	CA
Cement %, of Batch	20	15	20	20	20	20	10	40
Reinforcement, % Batch	40	40	60	60	60	60	60	60
Additive % of Batch	40	45	20	20	20	20	30	
MATRIX COMPOSITION								
Alumina, Al O as CA or	20.7%	15.5%	31.0%	31.0%	31.0%	31.0%	15.5%	62.0%
Calcia, CaO as CA or CA_2	10.0%	7.5%	15.0%	15.0%	15.0%	15.0%	7.5%	30.0%
Iron Oxide, Fe_3O_4 as C_4AF	1.7%	1.3%	2.5%	2.5%	2.5%	2.5%	1.3%	5.0%
Silica, SiO_2 as C_2S or C_3S	1.0%	0.8%	1.5%	1.5%	1.5%	1.5%	0.8%	3.0%
Chromia, Cr_2O_4			16.8%	25.0%	33.2%	9.8%	16.8%	
Titania-Alumina $TiO{\cdot}Al_2O_3$								
Magnesia, MgO			33.2%	25.0%	16.8%	40.2%	8.2%	
Spinel, $MgAl_2O_4$								
Dead Burnt Magnesia, MgO	66.7%	75.0%						
Alumina, Al_2O_4								
Cerium Oxide, CeO								
FINISHED COUPONS								
Coupon 1								
Sinter Temperature, °C	1200	1200	1200	1200	1200	1200	1200	1200
Density, gm/cc	3.65	3.62	3.83	3.81	3.91	3.89	3.73	2.91
Coupon 2								
Sinter Temperature, °C	1200	1200	1200	1200	1200	1200	1200	1200
Density, gm/cc	3.82	3.84	4.01	3.92	3.81	3.91	3.55	3.06
Coupon 3								
Sinter Temperature, °C	1200	1200	1200	1200	1200	1200	1200	1200
Density, gm/cc	3.78	3.74	4.14	4.00	3.70	3.92	3.97	2.96
Open Porosity (min)	9.7%	9.4%	7.6%	7.7%	7.0%	8.0%	6.3%	8.7%
DENSITY SUMMARY								
Std Dev	0.09	0.11	0.15	0.09	0.10	0.01	0.21	0.08
Average	3.75	3.73	3.99	3.91	3.81	3.91	3.75	2.97

Table 4.2. Density and Open Porosity Results (continued).

BATCH NUMBER	B4-5-1	B4-6-1	B4-14-1	B4-15-1	B4-16-1	B4-19-1	B4-20-1	B4-21-1
DESCRIPTION	CA	CA	CA	CA	CA	CA	CA	CA
Cement %, of Batch	40	20	40	13	10	60	30	20
Reinforcement, % Batch	60	60	60	60	60	40	40	40
Additive % of Batch		20		27	30		30	40
MATRIX COMPOSITION								
Alumina, Al O as CA or	62.0%	31.0%	62.0%	20.9%	15.5%	62.0%	31.0%	20.7%
Calcia, CaO as CA or CA_2	30.0%	15.0%	30.0%	10.1%	7.5%	30.0%	15.0%	10.0%
Iron Oxide, Fe_3O_4 as C_4AF	5.0%	2.5%	5.0%	1.7%	1.3%	5.0%	2.5%	1.7%
Silica, SiO_2 as C_2S or C_3S	3.0%	1.5%	3.0%	1.0%	0.8%	3.0%	1.5%	1.0%
Magnesia, MgO								
Spinel, $MgAl_2O_4$								
Dead Burnt Magnesia, MgO		50.0%	0.0%	66.3%	75.0%	0.0%	50.0%	66.7%
FINISHED COUPONS								
Coupon 1								
Sinter Temperature, °C	1200							
Density, gm/cc	3.11							
Coupon 2								
Sinter Temperature, °C	1200							
Density, gm/cc	2.91							
Coupon 3								
Sinter Temperature, °C	1200	1200	1200	1200	1200	1200	1200	1200
Density, gm/cc	3.04	3.07	3.24	3.23	3.22	3.01	3.20	3.23
Open Porosity (min)	8.2%	7.7%	8.0%	6.9%	6.4%	11.1%	9.8%	8.4%
Coupon 4								
Sinter Temperature, °C		1200	1200		1200	1200		1200
Density, gm/cc		3.17	3.14		3.09	3.31		3.23
Open Porosity (min)		7.3%	10.6%		7.7%	6.1%		8.5%
DENSITY SUMMARY								
Std Dev	0.10	0.08	0.07		0.09	0.21		0.00
Average	3.02	3.12	3.19	3.23	3.16	3.16	3.20	3.23

Table 4.2. Density and Open Porosity Results (continued).

BATCH NUMBER	B4-27-1	B4-28-1	B4-29-1	B4-30-1	B5-10-1	B5-12-1	SP7-6-1	SP7-7-1
DESCRIPTION	CA	CA	CA	CA	CA	CA	CA	CA
Cement %, of Batch	60	30	40	20	15	25	20	20
Reinforcement, % Batch	40	40	40	40	40	75	60	60
Additive % of Batch		30	20	40	45		20	20
MATRIX COMPOSITION								
Alumina, Al O as CA or	62.0%	31.0%	41.3%	20.7%	15.5%	62.0%	31.0%	31.0%
Calcia, CaO as CA or CA_2	30.0%	15.0%	20.0%	10.0%	7.5%	30.0%	15.0%	15.0%
Iron Oxide, Fe_3O_4 as C_4AF	5.0%	2.5%	3.3%	1.7%	1.3%	5.0%	2.5%	2.5%
Silica, SiO_2 as C_2S or C_3S	3.0%	1.5%	2.0%	1.0%	0.8%	3.0%	1.5%	1.5%
Dead Burnt Magnesia, MgO	0.0%	50.0%	33.3%	66.7%	75.0%	0.0%	50.0%	50.0%
FINISHED COUPONS								
Coupon 1								
Sinter Temperature, °C							1200	1200
Density, gm/cc							3.21	3.16
Open Porosity (min)							8.2%	7.7%
Coupon 2								
Sinter Temperature, °C							1200	1200
Density, gm/cc							3.24	3.26
Open Porosity (min)							7.3%	7.0%
Coupon 3								
Sinter Temperature, °C	1200	1200	1200	1200	1200	1200	1200	1200
Density, gm/cc	2.89	2.99	3.17	3.20	3.17	3.05	3.24	4.15
Open Porosity (min)	10.3%	8.9%	9.7%	8.3%	8.1%	5.9%	7.3%	7.0%
Coupon 4								
Sinter Temperature, °C	1200							
Density, gm/cc	3.07							
Open Porosity (min)	10.8%							
DENSITY SUMMARY								
Std Dev	0.12						0.02	0.54
Average	2.98	2.99	3.17	3.20	3.17	3.05	2.23	3.52

Table 4.2. Density and Open Porosity Results (continued).

BATCH NUMBER	SP7-8-1	SP7-9-1	SP7-11-1	SP7-12-1	SP7-13-1	SP7-14-1	SP7-15-1	SP7-16-1
DESCRIPTION	CA	CA	CA	CA	CA	CA	CA	CA
Cement %, of Batch	27	27	27	27	20	20	20	20
Reinforcement, % Batch	60	60	60	60	60	60	60	60
Additive % of Batch	13	13	13	13	20	20	20	20
MATRIX COMPOSITION								
Alumina, Al O as CA or	41.3%	41.3%	41.3%	41.3%	31.0%	31.0%	31.0%	31.0%
Calcia, CaO as CA or CA_2	20.0%	20.0%	20.0%	20.0%	15.0%	15.0%	15.0%	15.0%
Iron Oxide, Fe_3O_4 as C_4AF	3.3%	3.3%	3.3%	3.3%	2.5%	2.5%	2.5%	2.5%
Silica, SiO_2 as C_2S or C_3S	2.0%	2.0%	2.0%	2.0%	1.5%	1.5%	1.5%	1.5%
Chromia, Cr_2O_4								
Titania-Alumina $TiO{\cdot}Al_2O_3$								
Magnesia, MgO								
Spinel, $MgAl_2O_4$								
Dead Burnt Magnesia, MgO	33.3%	33.3%	33.3%	33.3%	50.0%	50.0%	50.0%	50.0%
FINISHED COUPONS								
Coupon 1								
Sinter Temperature, °C	1200	1200	1200	1200	1200	1200	1200	1200
Density, gm/cc	3.19	3.05	3.25	3.07	3.09	3.16	3.12	3.04
Open Porosity (min)	8.3%	7.7%	8.7%	8.3%	8.4%	8.4%	8.3%	7.6%
Coupon 2								
Sinter Temperature, °C	1200	1200	1200	1200	1200	1200	1200	1200
Density, gm/cc	3.06	3.12	3.22	3.21	3.06	3.26	3.17	3.12
Open Porosity (min)	7.5%	6.9%	8.2%	8.2%	8.2%	7.1%	8.6%	7.4%
Coupon 3								
Sinter Temperature, °C	1200	1200	1200	1200	1200	1200	1200	1200
Density, gm/cc	3.15	3.21	0.96	2.91	3.16	3.21	3.14	3.17
Open Porosity (min)	7.1%	6.9%	7.7%	8.0%	8.2%	8.3%	9.1%	8.5%
DENSITY SUMMARY								
Std Dev	0.06	0.08	1.31	0.15	0.05	0.05	0.03	0.06
Average	3.13	3.13	2.48	3.06	3.10	3.21	3.14	3.11

Table 4.2. Density and Open Porosity Results (continued).

BATCH NUMBER	SP7-17-1	SP7-18-1	SP7-19-1	SP7-20-1	SP7-21-1	SP7-22-1	SP7-23-1	SP7-26-1
DESCRIPTION	CA	CA	CA	CA	CA	CA	CA	CA
Cement %, of Batch	27	27	27	13	20	24	10	10
Reinforcement, % Batch	60	60	60	60	60	60	60	60
Additive % of Batch	13	13	13	27	20	16	30	30
MATRIX COMPOSITION								
Alumina, Al O as CA or	41.3%	41.3%	41.3%	20.7%	31.0%	37.2%	15.5%	15.5%
Calcia, CaO as CA or CA_2	20.0%	20.0%	20.0%	10.0%	15.0%	18.0%	7.5%	7.5%
Iron Oxide, Fe_3O_4 as C_4AF	3.3%	3.3%	3.3%	1.7%	2.5%	3.0%	1.3%	1.3%
Silica, SiO_2 as C_2S or C_3S	2.0%	2.0%	2.0%	1.0%	1.5%	1.8%	0.8%	0.8%
Chromia, Cr_2O_4								
Titania-Alumina $TiO{\cdot}Al_2O_3$				33.3%	25.0%	20.0%	25.0%	50.0%
Magnesia, MgO								
Spinel, $MgAl_2O_4$								
Dead Burnt Magnesia, MgO	33.3%	33.3%	33.3%	33.3%	25.0%	20.0%	50.0%	25.0%
FINISHED COUPONS								
Coupon 1								
Sinter Temperature, °C	1200	1200	1200	1200	1200	1200	1200	1200
Density, gm/cc	2.94	2.18	3.45	3.29	3.32	3.03	3.17	3.12
Open Porosity (min)	8.8%	8.2%	8.8%	9.4%	8.8%	9.8%	8.1%	7.7%
Coupon 2								
Sinter Temperature, °C	1200	1200	1200	1200	1200	1200	1200	1200
Density, gm/cc	3.14	3.20	3.18	3.28	3.24	3.24	3.17	3.21
Open Porosity (min)	8.7%	8.0%	8.8%	8.0%	8.4%	8.6%	7.5%	8.0%
Coupon 3								
Sinter Temperature, °C	1200	1200	1200	1200	1200	1200	1200	1200
Density, gm/cc	3.14	3.29	3.24	3.27	3.18	3.15	3.18	3.01
Open Porosity (min)	8.5%	7.0%	8.8%	8.0%	8.2%	8.1%	7.1%	8.3%
DENSITY SUMMARY								
Std Dev	0.12	0.62	0.14	0.01	0.07	0.11	0.00	0.10
Average	3.07	2.89	3.29	3.28	3.25	3.14	3.17	3.11

Table 4.2. Density and Open Porosity Results (continued).

BATCH NUMBER	SP7-27-1	SP7-28-1	SP7-29-1	SP7-30-1	SP7-31-1	SP8-2-1	SP8-3-1
DESCRIPTION	CA	CA	CA	CA	CA	CA	CA
Cement %, of Batch	8	20	13	13	20	24	10
Reinforcement, % Batch	60	60	60	60	60	60	60
Additive % of Batch	32	20	27	27	20	16	30
MATRIX COMPOSITION							
Alumina, Al O as CA or	12.4%	31.0%	20.7%	20.7%	31.0%	37.2%	15.5%
Calcia, CaO as CA or CA_2	6.0%	15.0%	10.0%	10.0%	15.0%	18.0%	7.5%
Iron Oxide, Fe_3O_4 as C_4AF	1.0%	2.5%	1.7%	1.7%	2.5%	3.0%	1.3%
Silica, SiO_2 as C_2S or C_3S	0.6%	1.5%	1.0%	1.0%	1.5%	1.8%	0.8%
Titania-Alumina $TiO{\cdot}Al_2O_3$	60.0%	50.0%	66.7%				
Magnesia, MgO							
Dead Burnt Magnesia, MgO	20.0%			33.3%	25.0%	20.0%	50.0%
Alumina, Al_2O_4							
Cerium Oxide, CeO				33.3%	25.0%	20.0%	25.0%
FINISHED COUPONS							
Coupon 1							
Sinter Temperature, °C	1200	1200	1200	1200	1200	1200	1200
Density, gm/cc	3.24	3.27	3.33	3.41	3.45	3.23	3.46
Open Porosity (min)	8.1%	9.4%	7.4%	7.2%	6.8%	7.9%	6.8%
Coupon 2							
Sinter Temperature, °C	1200	1200	1200	1200	1200	1200	1200
Density, gm/cc	3.28	3.40	3.31	3.47	3.39	3.37	3.28
Open Porosity (min)	7.7%	9.4%	7.5%	6.6%	10.7%	7.1%	6.5%
Coupon 3							
Sinter Temperature, °C	1200	1200	1200	1200	1200	1200	1200
Density, gm/cc	2.98	3.27	3.38	3.37	3.41	3.30	3.34
Open Porosity (min)	8.0%	9.0%	7.5%	6.5%	6.9%	7.0%	6.9%
DENSITY SUMMARY							
Std Dev	0.16	0.08	0.04	0.05	0.03	0.07	0.09
Average	3.16	3.31	3.34	3.42	3.42	3.30	3.36

Table 4.2. Density and Open Porosity Results (continued).

BATCH NUMBER	SP8-4-1	SP8-6-1	SP8-9-1	SP8-10-1	SP8-11-1	SP8-12-1
DESCRIPTION	CA	CA	CA	CA	CA	CA
Cement %, of Batch	10	13	20	24	10	10
Reinforcement, % Batch	60	60	60	60	60	60
Additive % of Batch	30	27	20	16	30	30
MATRIX COMPOSITION						
Alumina, Al O as CA or	15.5%	20.7%	31.0%	37.2%	15.5%	15.5%
Calcia, CaO as CA or CA	7.5%	10.0%	15.0%	18.0%	7.5%	7.5%
Iron Oxide, Fe O as C AF	1.3%	1.7%	2.5%	3.0%	1.3%	1.3%
Silica, SiO as C S or C S	0.8%	1.0%	1.5%	1.8%	0.8%	0.8%
Magnesia, MgO						
Spinel, MgAl O						
Dead Burnt Magnesia, MgO	25.0%	33.3%	25.0%	20.0%	50.0%	25.0%
Alumina, Al O		33.3%	25.0%	20.0%	25.0%	50.0%
Cerium Oxide, CeO	50.0%					
FINISHED COUPONS						
Coupon 1						
Sinter Temperature, °C	1200	1200	1200	1200	1200	1200
Density, gm/cc	3.48	3.17	3.08	3.13	3.06	3.25
Open Porosity (min)	6.2%	8.4%	9.6%	9.6%	8.8%	9.1%
Coupon 2						
Sinter Temperature, °C	1200	1200	1200	1200	1200	1200
Density, gm/cc	3.60	3.23	3.17	3.07	3.37	3.40
Open Porosity (min)	6.5%	8.8%	9.1%	8.7%	8.5%	8.6%
Coupon 3						
Sinter Temperature, °C	1200	1200	1200	1200	1200	1200
Density, gm/cc	3.64	3.21	3.06	3.02	3.14	3.04
Open Porosity (min)	6.5%	7.6%	9.0%	8.5%	7.8%	8.6%
DENSITY SUMMARY						
Std Dev	0.08	0.03	0.06	0.06	0.16	0.18
Average	3.57	3.21	3.10	3.07	3.19	3.23

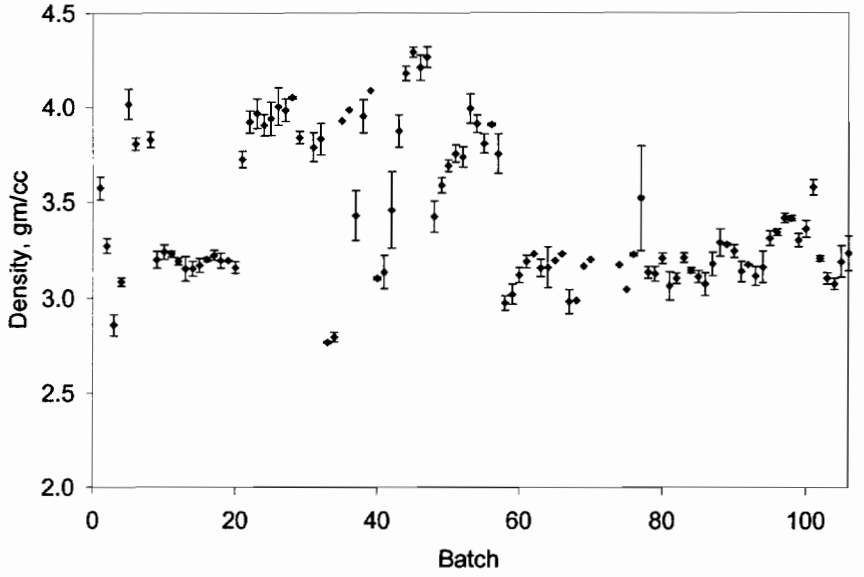

Figure 4.32. The batch mean density and standard deviation illustrates the variation of the density with similar test parameters. All coupons are Fondu and calcium dialuminate sintered at 1200°C.

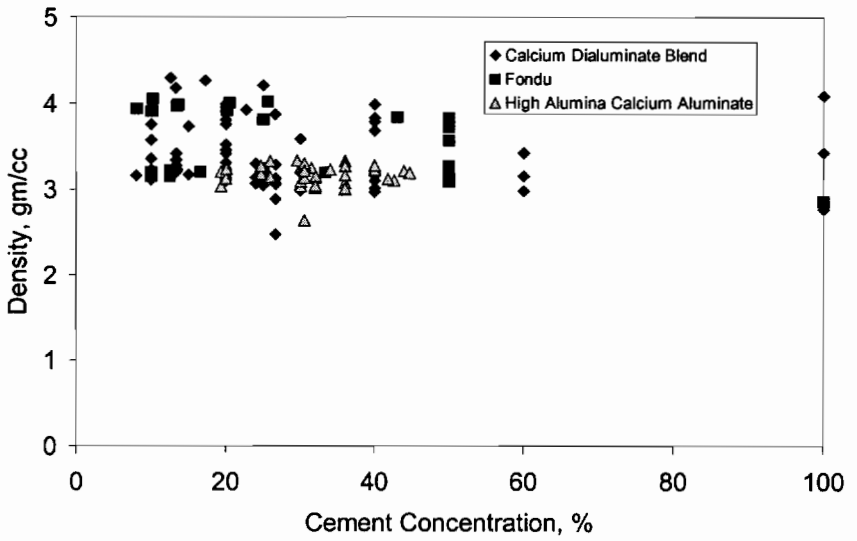

Figure 4.33. Mean sintered density change with the cement concentration. Density data is separated for each of the calcium aluminate cements.

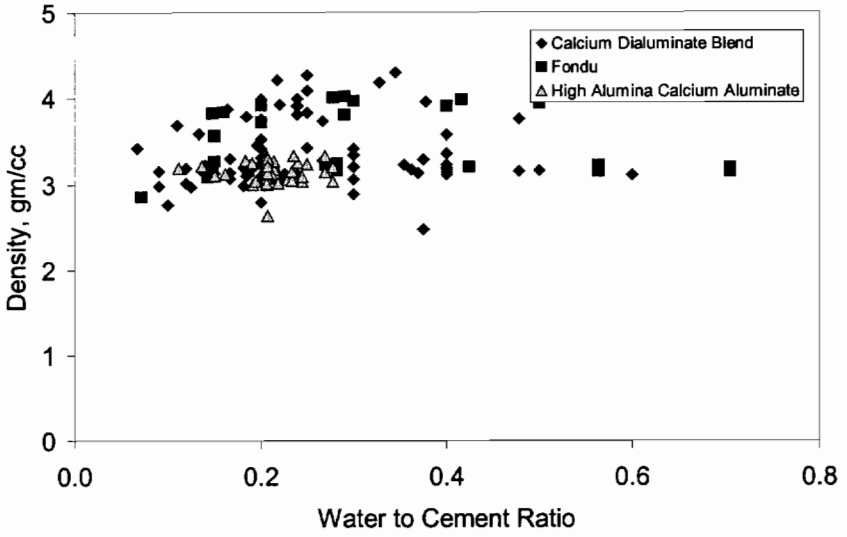

Figure 4.34. Final sintered density relationship to the water to cement (W/C) ratio separated by the type of matrix cement.

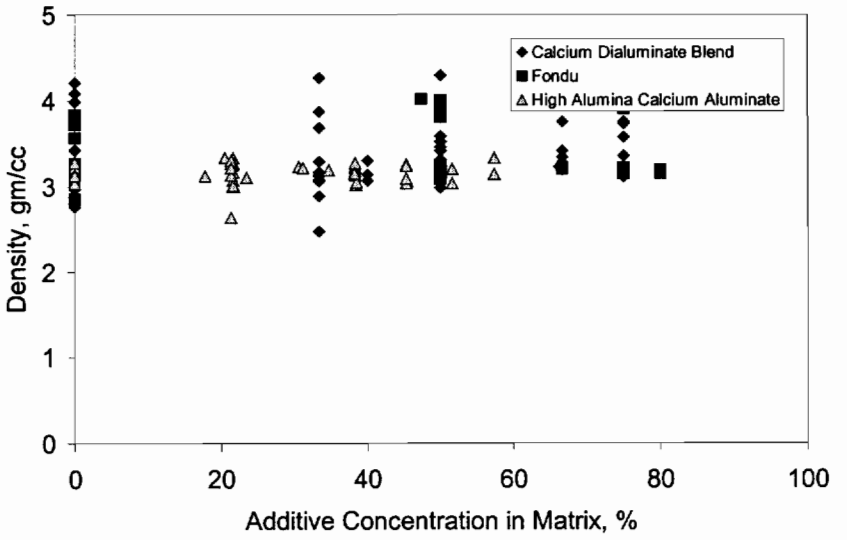

Figure 4.35. Final sintered density compared with total additive concentration separated by the type of matrix cement.

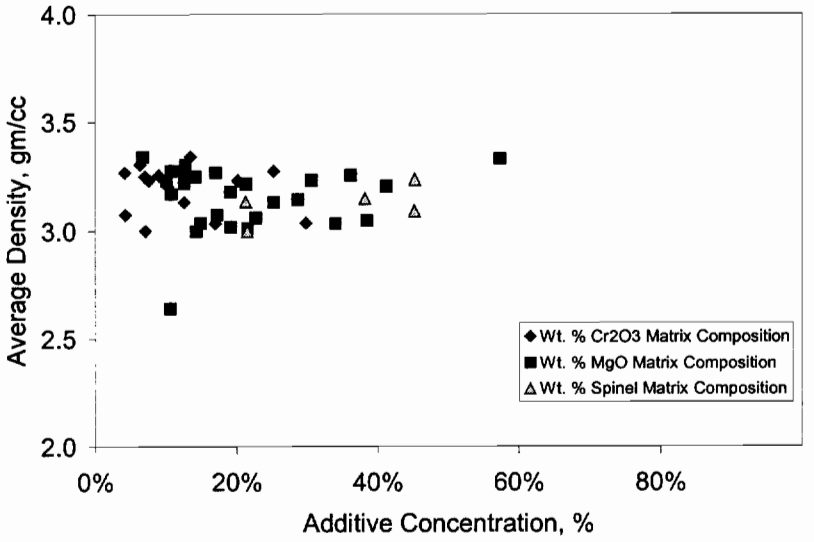

Figure 4.36. Final sintered density compared to the additive concentration of the three additives to the high alumina calcium aluminate premix cement.

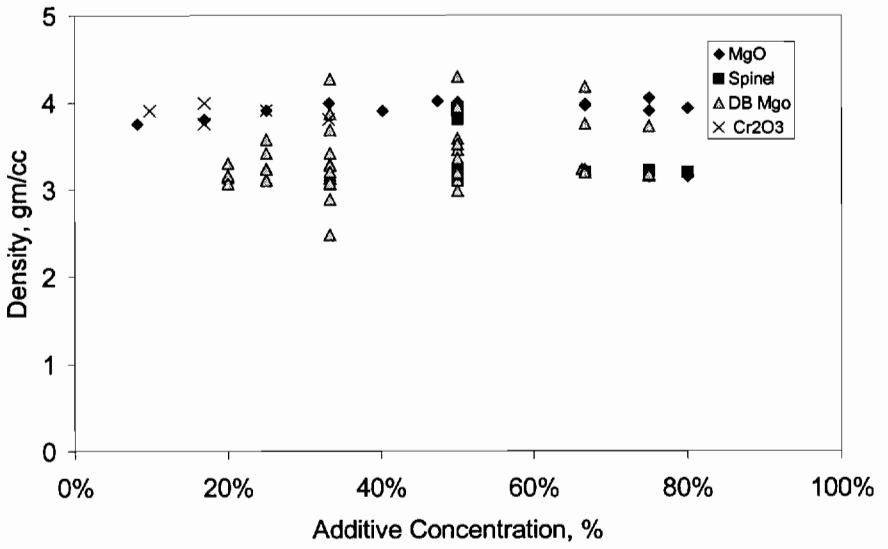

Figure 4.37. Influence of the additive concentrations: Cr_2O_3, MgO, DB-MgO and spinel on the coupon density for the fondu cement and the calcium dialuminate blend cement.

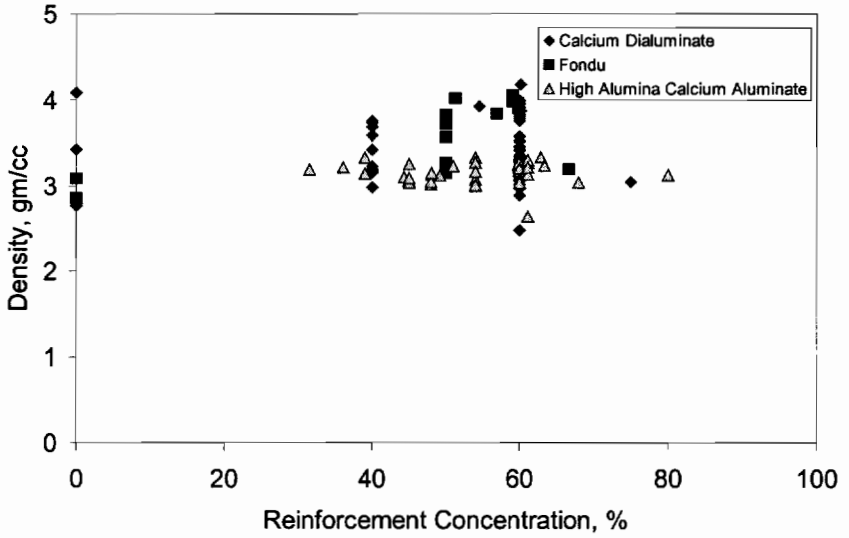

Figure 4.38. The final sintered density compared with reinforcement concentration. Density data is separated for each of the calcium aluminate cement types.

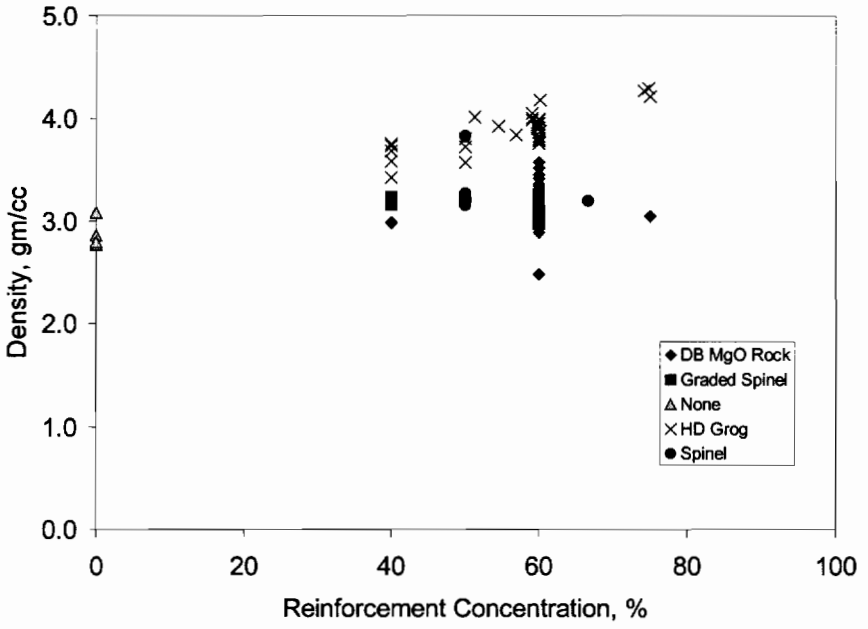

Figure 4.39. Coupon density relationship with the reinforcement concentration separated into the different reinforcement types for the Fondu cement and the calcium dialuminate blend.

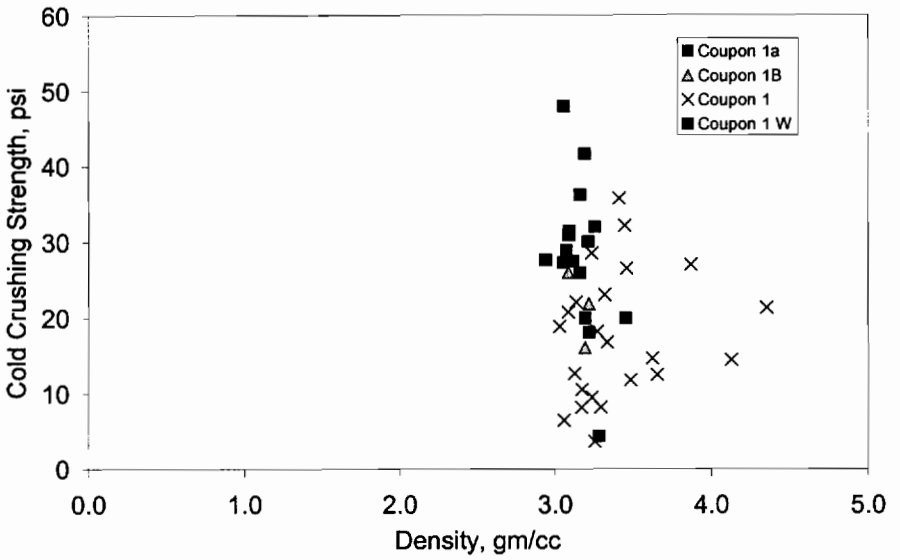

Figure 4.40. Coupon density relationship to compression strength for three test conditions: half-size, full size and water saturated coupons.

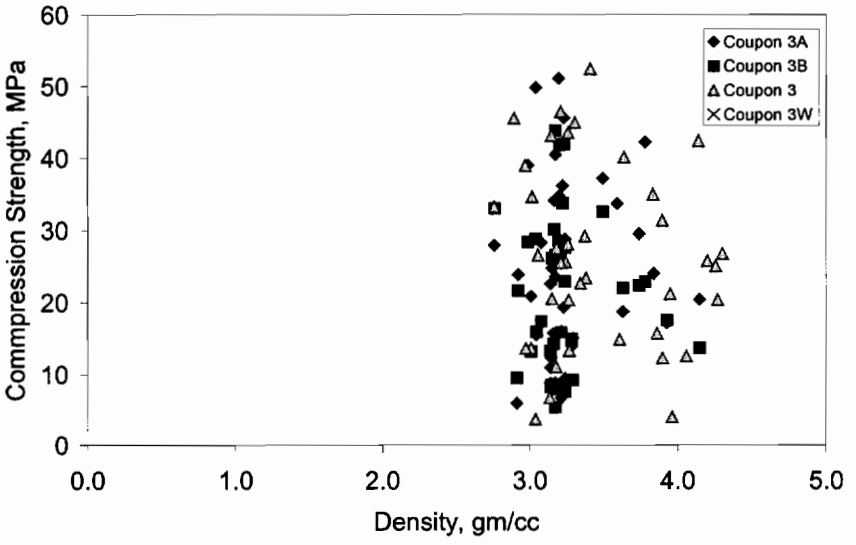

Figure 4.41. Coupon density relationship to compression strength for three test conditions: half-size, full size and water saturated coupons.

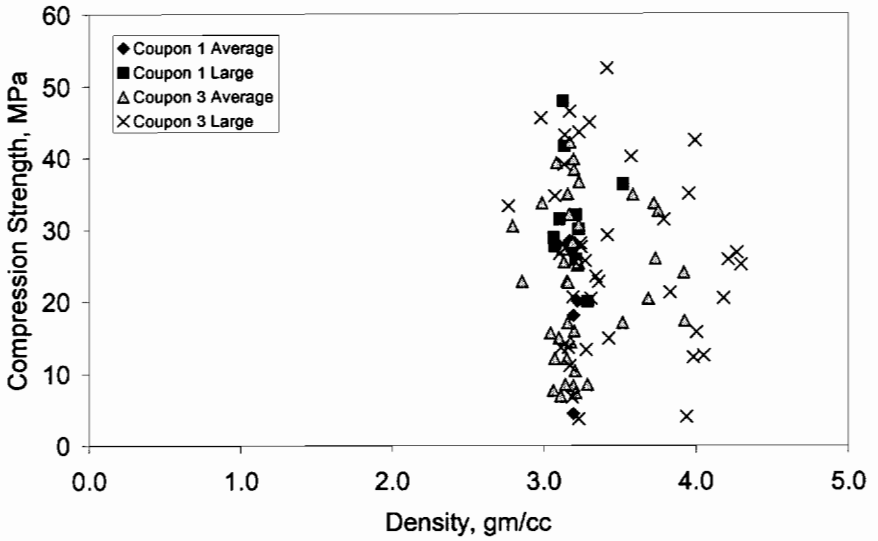

Figure 4.42. Coupon density and cold compression strength relationship for all cement types. Data presentation compares compression strength of half size coupons to the full size coupons, both coupons #1 and #3 are presented. The average is that of the two half size coupons sectioned from the same fired coupon.

4.5 Thermal Conductivity

The experimental approach used a known material to calibrate a furnace for a specific geometry and heat flow over a range of temperatures. The thermal conductivity of unknown experimental formulations can be calculated using the calibrated heat flow at same furnace temperature and load. The validity of the experimental approach is based on one direction heat flow in a zone of material and the ability to accuracy measure the temperature. Verification of heat flow in one dimension uses a specially instrumented refractory reference monolithic test block with 17 type K thermocouples positioned in an array around the relative center of the furnace opening. The test block was made from a commercial calcium silicate pressed insulation board with a reported thermal conductivity of 1.38 W/m-K (0.8 Btu/ft-h-F) at 800 °F. The test block was made to fit similar dimensions as the experimental cast CAC test blocks. The furnace chamber was

equilibrated for 24 hours prior to temperature measurements to assure standardization. Temperatures were measured at hot face temperatures of 300, 540, 700 and 800 °C. Sets of three measurements were taken at each temperature and the average used to profile the heat flow through the test block. Figure 4.43 illustrates the thermal profile generated at a hot face temperature of 800°C. An approximate 4 by 4 cm region in the center of the test block indicates one directional heat flow.

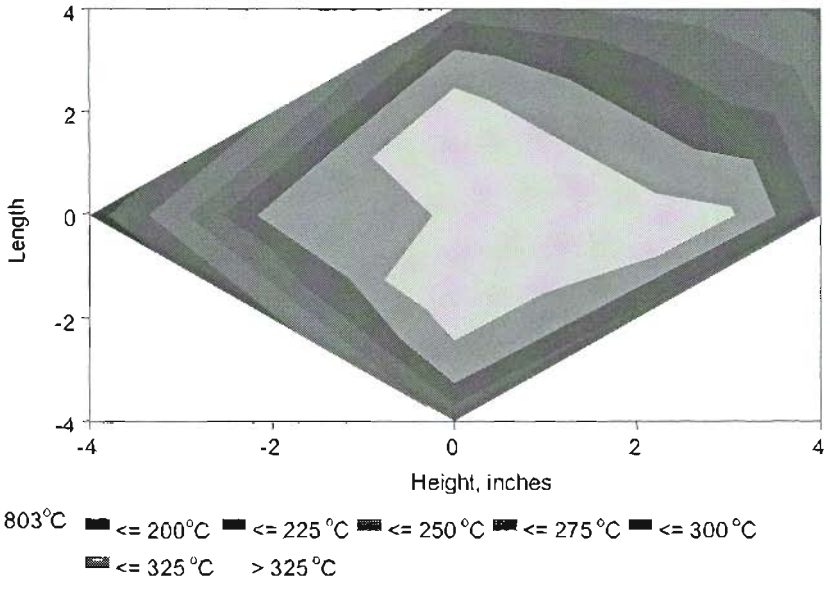

Figure 4.43. Thermal profile indicating central zone of one direction heat flow. Test results from reference profile block.

Calibration of the furnace used a standard square refractory kiln block measuring 23 x 23 x 11.5 cm. A commercial high temperature pressed brick, Green Free HP Brick®, produced by AP Green Refractories was used as the reference standard to determine the heat flow from the furnace at each temperature. The manufacturer supplied data sheet thermal conductivity values are published and listed in Table 4.3. Three thermal conductivity values were curve fit to produce a continuous set of thermal conductivity values using a power law relationship, $y = 22.5x^{-0.304}$ that $R^2 = 0.988$.

Table 4.3 Reference Block Thermal Conductivity.

Mean Temperature, °C	Thermal Conductivity, W/m-K
300	4.0
700	3.0
1000	2.8

The reference brick was fitted with four type K thermocouples positioned within the area of one dimensional heat flow, as determined by earlier testing. The furnace and brick equilibrated for 24 hours at each temperature setting. Temperature measurements were taken at hot face temperatures 120°, 300°, 400°, 700°, 800°, 1000° and 1100°C. Repeat measurements were taken twice at 700°C and once at 300° and 1000°C to check experimental technique. Three measurements were taken at each interval and the average used in the calculations. The heat flow was calculated for each mean temperature between each set of thermocouples. A total of 66 calculated heat flow values were determined for the thermocouple separation, Δx listed in Table 4.4.

Table 4.4. Distance between Thermocouples in Reference Brick.

Thermocouple Set	Δx Distance, m
TC1-TC2	0.0406
TC1-TC3	0.0182
TC1-TC4	0.0665
TC3-TC2	0.0224
TC3-TC4	0.0483
TC2-TC4	0.0258

The combined heat flow for the mean temperatures is illustrated in Figure 4.44. The poor curve fit indicated one or more of the thermocouples was not positioned at the distance used in the calculations. The data was reevaluated separating each thermocouple

set to determine the best fit. Figure 4.45 illustrates the separated data. Thermocouples 1, 2 and 3 provide the best fit for furnace heat flow. Based on the results, a mean slope for the heat flow used in the thermal conductivity determinations is y = 0.738x.

The thermal conductivity was experimentally determined on six test blocks from 100°C through 1200°C. The thermal conductivity measurements on the experimental test blocks are presented in the set of Figures 4.15 through 4.20. Tables 4.3 through 4.8 present the thermocouple positions for the test blocks. The same furnace elements, controller and equilibration were used for all experiments. Data deemed in error are not shown.

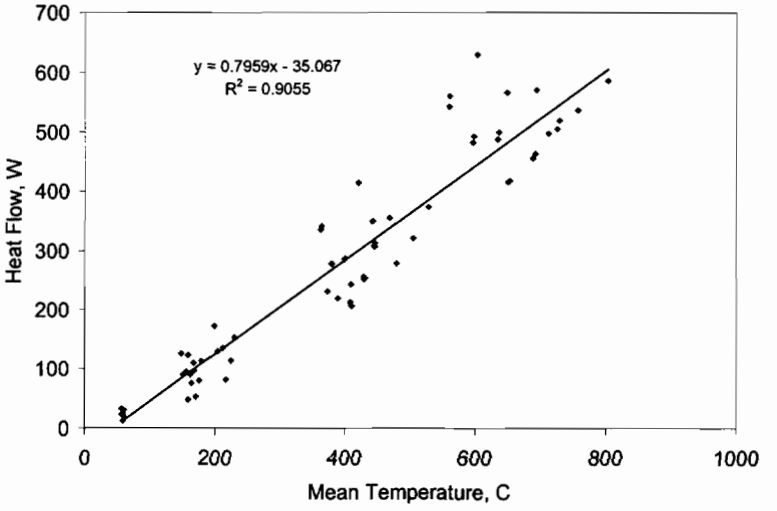

Figure 4.44. Furnace heat flow using reference brick, all data illustrated.

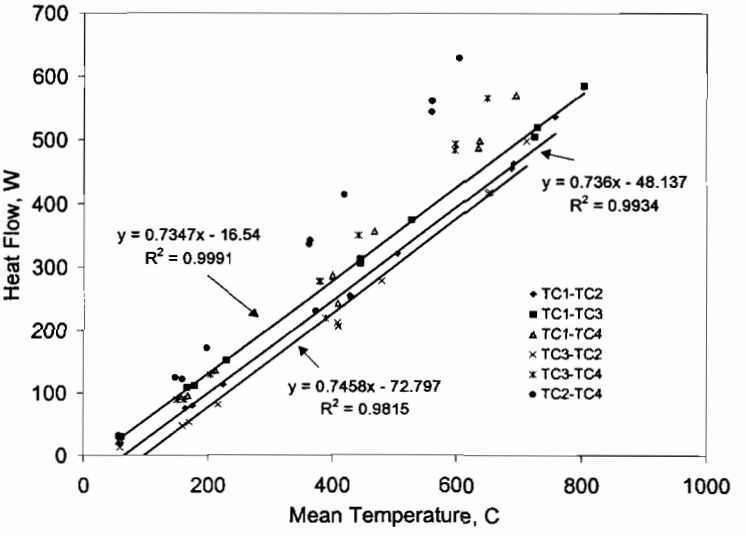

Figure 4.45. Furnace heat flow determined using reference brick separated by the sets of thermocouples.

Table 4.5. Thermocouple Positions in the High Alumina Calcium Aluminate Premix Cement with Zircon Reinforcement

Thermocouple Number	**Distance from Hot Face, m**		**ΔZ, m**
TC 1	0.0128	TC2-TC4	0.0005
TC 2	0.0032	TC2-TC1	0.0097
TC 3	0.0363	TC2-TC3	0.0331
TC 4	0.0037	TC4-TC1	0.0091
TC 5	0.0540	TC4-TC3	0.0326
		TC1-TC3	0.0235

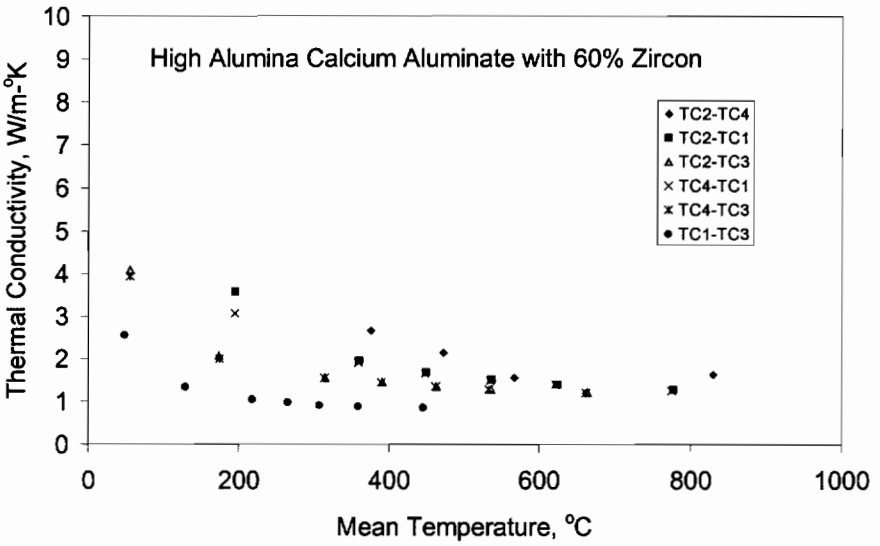

Figure 4.46. Calculated thermal conductivity results for premix cement 60% zircon reinforcement

Table 4.6. Thermocouple Positions in Cement Fondu Cement without Reinforcement

Thermocouple Number	Distance from Hot Face, m		ΔZ, m
TC 1	0.0590	TC2-TC1	0.0401
TC 2	0.0189	TC2-TC3	0.0233
TC 3	0.0422	TC2-TC4	0.0325
TC 4	0.0514	TC3-TC1	0.0168
TC 5	0.1016	TC3-TC4	0.0092
		TC4-TC1	0.0076

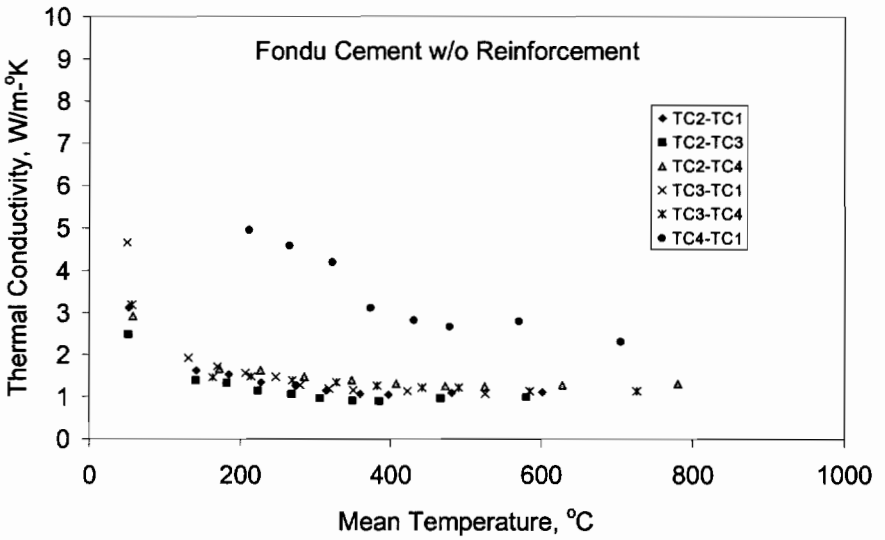

Figure 4.47. Calculated thermal conductivity results for cement fondu with no reinforcement.

Table 4.7. Thermocouple Positions in Calcium Dialuminate Cement Blend w/o Reinforcement.

Thermocouple Number	Distance from Hot Face, m		ΔZ, m
TC 1	0.0151	TC1-TC2	0.0370
TC 2	0.0522	TC1-TC3	0.0523
TC 3	0.0674	TC1-TC4	0.0737
TC 4	0.0888	TC2-TC3	0.0153
TC 5	0.1189	TC2-TC4	0.0367
		TC3-TC4	0.0214

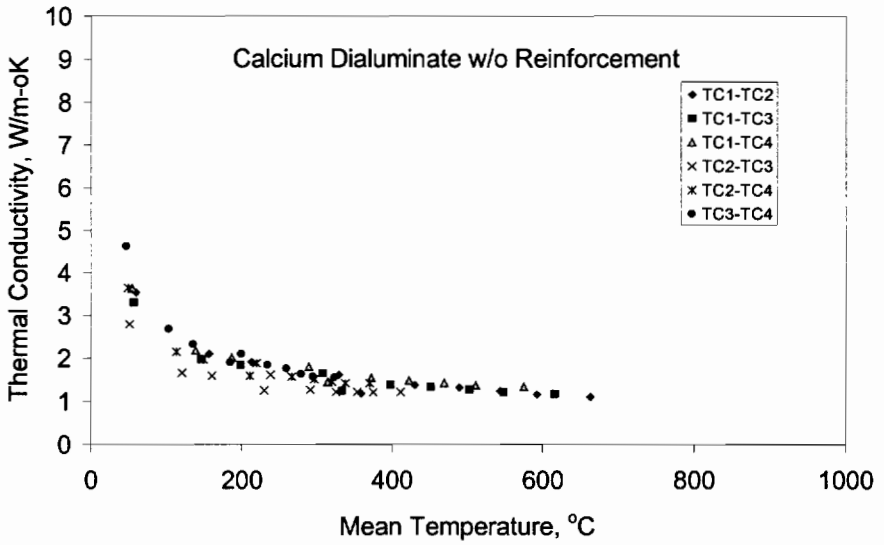

Figure 4.48. Calculated thermal conductivity results for calcium dialuminate cement blend with no reinforcement.

Table 4.8. Thermocouple Positions in Cement Fondu Cement with 60% High Density Zirconia Grog Reinforcement.

Thermocouple Number	Distance from Hot Face, m		ΔZ, m
TC 1	0.0381	TC3-TC4	0.0176
TC 2	0.0476	TC3-TC1	0.0369
TC 3	0.0012	TC3-TC2	0.0464
TC 4	0.0187	TC4-TC1	0.0194
TC 5	0.0873	TC4-TC2	0.0289
		TC1-TC2	0.0095

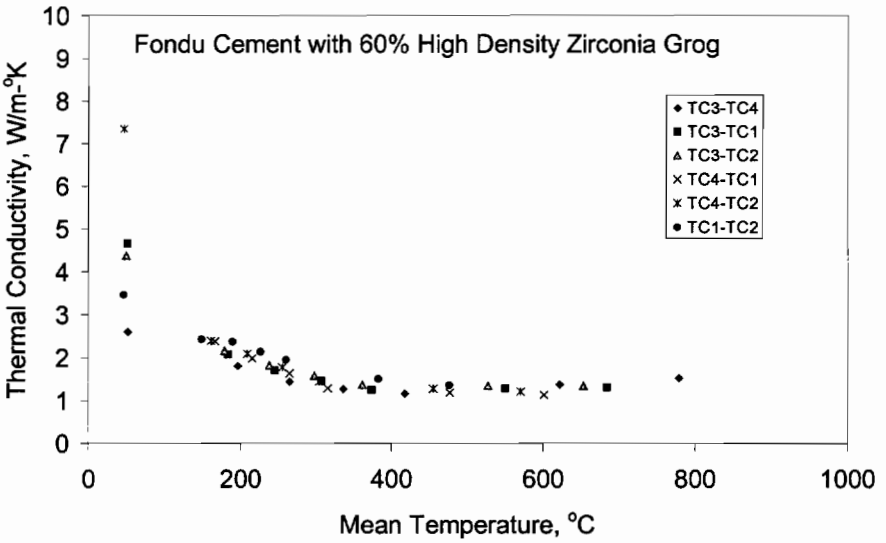

Figure 4.49. Calculated thermal conductivity results for cement fondu cement with 60% high density zirconia grog reinforcement.

Table 4.9. Thermocouple Positions in Cement Dialuminate Cement Blend with 60% High Density Zirconia Grog

Thermocouple Number	Distance from Hot Face, m		ΔZ, m
TC 1	0.0320	TC2-TC1	0.0270
TC 2	0.0050	TC2-TC3	0.0203
TC 3	0.0253	TC2-TC4	0.0581
TC 4	0.0631	TC3-TC1	0.0067
TC 5	0.0909	TC3-TC4	0.0378
		TC1-TC4	0.0311

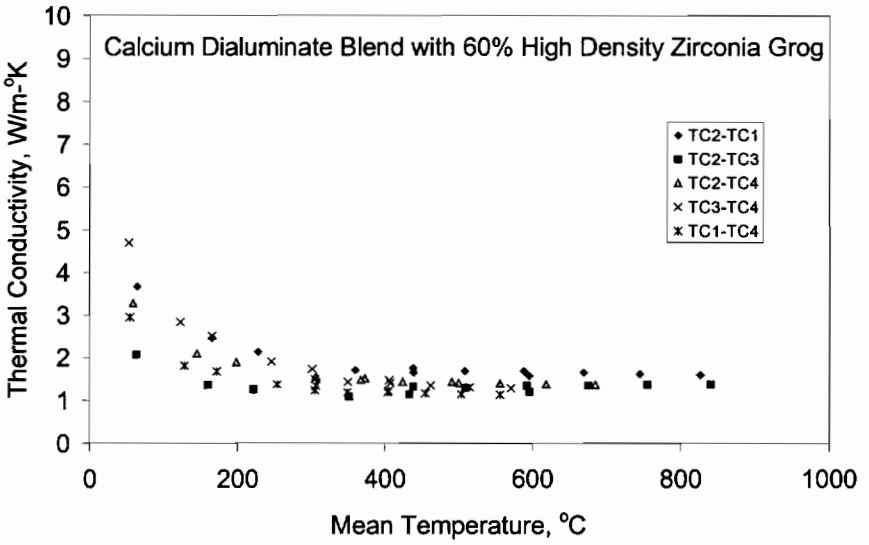

Figure 4.50. Calculated thermal conductivity results for cement dialuminate cement blend with 60% high density zirconia grog.

Table 4.10. Thermocouple Positions in Calcium Dialuminate Cement with 75% High Density Zirconia Grog Reinforcement.

Thermocouple Number	**Distance from Hot Face, m**		**ΔZ, m**
TC 1	0.0015	TC1-TC2	0.0146
TC 2	0.0161	TC1-TC3	0.0406
TC 3	0.0421	TC1-TC4	0.0126
TC 4	0.0141	TC4-TC2	0.0020
TC 5	0.1041	TC4-TC3	0.0280
		TC2-TC3	0.0260

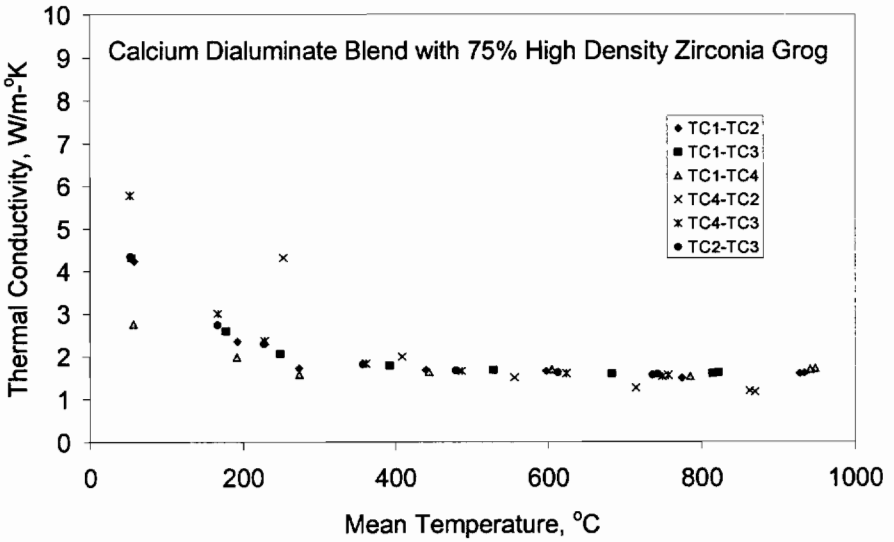

Figure 4.51. Calculated thermal conductivity results for calcium dialuminate cement with 75% high density zirconia grog reinforcement.

4.6 Abrasive Wear Test Results

4.6.1 Synopsis of Wear Test Results

The dry sand rubber wheel test data is used to produce comparisons of the different formulations. The test method is destructive and uses a relatively simple sample geometry that minimizes handling and other experimental sources of error. The wear test results are shown in Table 4.11 for 139 batches. Coupons were tested in the fired condition, 96 hours at 1000°C or 1200°C depending on the coupon number. The table presents a comprehensive reporting of the wear rate and the relevant formulation data for each batch. The wear test results include the wear scar analysis information. The dry sand rubber wheel test results are semi-quantitative and therefore reference standards, control samples and statistical procedures are needed to remove errors and validate the data used to develop trends. Appendix III presents a discussion of the reference coupons and wear scar analysis. The appendix also presents a discussion of correction factors used to determine the corrected wear rates and allow for comparisons between the coupons.

Table 4.11. Abrasive Wear Test Results.

BATCH NUMBER	B1-28-1	B2-2-1	B2-4-1	B2-7-1	B2-12-1	B2-16-1	B2-18-1	B2-23-1
DESCRIPTION	1:1 Blend	Control	Control	MgO	1:4 Blend	1:1 Blend	1:1 Blend	1:2 Blend
Premix Cement, % of Batch	26.0	40.0	40.0	26.0	30.0	30.0	32.0	32.0
Reinforcement, % Batch	39.0	60.0	60.0	39.0	45.1	45.0	48.0	48.1
Additive % of Batch	35.0			35.0	24.9	25.0	20.0	19.9
Chromia, Cr_2O_3	28.7%				9.1%	22.7%	19.2%	12.6%
Magnesia, MgO	28.7%			57.4%	36.3%	22.7%	19.2%	25.3%
Coupon 2 Wear Test Results								
Side 1, R Squared	0.99617	0.98784	0.98327	0.99120	0.93743	0.96195	0.99276	0.99854
Wear Area, mm^2	430.49	465.72	382.72			441.25	408.61	395.5
Reinforcement Area, mm^2	97.69	232.47	210.5			103.57	106.29	65.04
Wear Scar Area Change	42.1%	53.8%	26.4%			45.7%	34.9%	30.6%
Corrected Wear Rate, mg/m	**1.58**	**0.65**	**0.79**	**3.87**	**0.63**	**0.86**	**1.09**	**0.84**
Side 2, R Squared	0.99839	0.99902	0.99517		0.98929	0.99741	0.99789	0.99382
Wear Area, mm^2	543.71	475.09	437.65			486.93	480.13	496.24
Reinforcement Area, mm^2	97.86	221.76	232.33			119.82	146.84	167.32
Wear Scar Area Change	79.5%	56.9%	44.5%			60.8%	58.5%	63.9%
Corrected Wear Rate, mg/m	**0.95**	**0.35**	**0.31**		**0.36**	**0.41**	**0.38**	**0.43**
Coupon 4 Wear Test Results								
Side 1, R Squared	0.99014	0.99725	0.99492		0.99631	0.99244	0.99471	0.98708
Wear Area, mm^2	472.78		411.75		485.52	421.4	434.94	441.54
Reinforcement Area, mm^2	123.89		100.1		231.62	130.07	70.13	67.72
Wear Scar Area Change	56.1%		36.0%		60.3%	39.1%	43.6%	45.8%
Corrected Wear Rate, mg/m	**1.92**	**0.99**	**0.73**		**1.17**	**1.05**	**1.35**	**2.17**
Side 2, R Squared	0.98740	0.99626	0.99675		0.97959	0.99630	0.99035	0.99175
Wear Area, mm^2	435.67		418.96		490.68	392.29	423.5	418.99
Reinforcement Area, mm^2	96.41		156.89		171.46	101.11	122.3	147.53
Wear Scar Area Change	43.9%		38.3%		62.0%	29.5%	39.8%	38.3%
Corrected Wear Rate, mg/m	**0.67**	**0.44**	**0.32**		**0.58**	**0.63**	**0.38**	**0.60**

Table 4.11. Abrasive Wear Test Results (continued).

BATCH NUMBER	B2-25-1	B3-2-1	B3-4-1	B3-6-1	B3-10-1	B3-12-1	B3-16-1	B3-18-1
DESCRIPTION	1:2 Blend	2:1 Blend	2:1 Blend	2:1 Blend	1:2 Blend	1:2 Blend	1:4 Blend	1:1 Blend
Premix Cement, % of Batch	36.0	30.0	34.0	29.6	31.5	24.7	24.7	24.7
Reinforcement, % Batch	54.0	45.1	51.0	62.8	59.8	59.9	59.9	59.9
Additive % of Batch	10.0	24.9	15.0	7.6	8.6	15.4	15.4	15.4
Chromia, Cr_2O_3	7.2%	29.9%	20.2%	13.5%	7.1%	12.6%	7.7%	19.2%
Magnesia, MgO	14.3%	15.0%	10.1%	6.8%	14.2%	25.3%	30.7%	19.2%
Coupon 2 Wear Test Results								
Side 1, R Squared	0.99231	0.99784	0.99299	0.99722	0.99136	0.99692	0.99133	0.99530
Wear Area, mm^2	339.9	380.57	357.71	415.87	414.62	436.65	453.23	432.27
Reinforcement Area, mm^2	115.19	73.22	86.77	161.88	192.46	252.94	280.88	216.41
Wear Scar Area Change	12.2%	25.7%	18.1%	37.3%	36.9%	44.2%	49.7%	42.7%
Corrected Wear Rate, mg/m	**0.63**	**0.75**	**0.67**	**0.35**	**0.33**	**0.46**	**0.32**	**0.31**
Side 2, R Squared	0.99597	0.99575	0.99815	0.99088	0.99262	0.99519	0.98827	0.99544
Wear Area, mm^2	433.06	445.46	436.39	435.57	438.99	453.31	457.27	430.01
Reinforcement Area, mm^2	181.39	117.38	109.91	190.32	151.52	207.69	247.41	194.74
Wear Scar Area Change	43.0%	47.1%	44.1%	43.8%	44.9%	49.7%	51.0%	42.0%
Corrected Wear Rate, mg/m	**0.41**	**0.42**	**0.40**	**0.40**	**0.35**	**0.37**	**0.44**	**0.28**
Coupon 4 Wear Test Results								
Side 1, R Squared	0.99090	0.98830	0.99007	0.98152	0.99426	0.99218	0.98627	0.99066
Wear Area, mm^2	421.1	420.29	420.19	421.62	396.32	389.42	418.4	391.97
Reinforcement Area, mm^2	113.28	80.84	79.24	102.91	84.53	119.96	159.41	150.5
Wear Scar Area Change	39.0%	38.8%	38.7%	39.2%	30.9%	28.6%	38.1%	29.4%
Corrected Wear Rate, mg/m	**1.20**	**1.99**	**0.96**	**1.51**	**1.15**	**1.04**	**0.96**	**0.89**
Side 2, R Squared	0.99995	0.99619	0.98549	0.99995	0.98985	0.99743	0.99972	0.99954
Wear Area, mm^2	382.1	420.93	359.89	389.49	374.7	409.97	399.57	416.83
Reinforcement Area, mm^2	107.27	110.35	120.11	124.51	103.32	147.85	174.9	130.87
Wear Scar Area Change	26.2%	39.0%	18.8%	28.6%	23.7%	35.4%	31.9%	37.6%
Corrected Wear Rate, mg/m	**0.37**	**0.69**	**0.53**	**0.47**	**0.59**	**1.32**	**1.30**	**1.53**

Table 4.11. Abrasive Wear Test Results (continued).

BATCH NUMBER	**B3-30-1**	**B4-1-1**	**B4-3-1**	**B4-6-1**	**B4-8-1**	**B4-13-1**	**B4-16-1**	**B4-20-1**
DESCRIPTION	2:1 Blend	1:4 Blend	1:2 Blend	EC	EC	EC	Cr_2O_3	1:1 Blend
Premix Cement, % of Batch	24.7	19.4	19.4	42.6	44.0	44.8	36.0	36.0
Reinforcement, % Batch	59.9	60.0	60.0	44.4	36.1	31.5	54.1	54.1
Additive % of Batch	15.4	20.6	20.6	13.0	19.9	23.8	9.9	9.9
Chromia, Cr_2O_3	25.3%	10.3%	17.0%				21.6%	10.8%
Magnesia, MgO	12.6%	41.3%	34.1%					10.8%
Coupon 2 Wear Test Results								
Side 1, R Squared	0.99523	0.99673	0.99653	0.99432	0.98172	0.99414	0.99028	0.99363
Wear Area, mm^2	420.49	515.43	447.22	457.01	469.85	487.68	402.51	426.96
Reinforcement Area, mm^2	201.37	123.62	276.32	243.84	213.64	178.56	175.88	189.27
Wear Scar Area Change	38.8%	70.2%	47.7%	50.9%	55.1%	61.0%	32.9%	41.0%
Corrected Wear Rate, mg/m	**0.27**	**1.44**	**0.31**	**0.37**	**0.34**	**0.48**	**0.28**	**0.72**
Side 2, R Squared	0.99468	0.99081	0.99207	0.99573	0.99550	0.99539	0.99651	0.99935
Wear Area, mm^2	441.59	485.64	466.77	432.33	556.24	480.06	414.87	442.01
Reinforcement Area, mm^2	181.76	214.4	148.38	216.55	242.69	172.01	138.47	196.22
Wear Scar Area Change	45.8%	60.4%	54.1%	42.7%	83.7%	58.5%	37.0%	45.9%
Corrected Wear Rate, mg/m	**0.29**	**0.36**	**0.51**	**0.44**	**0.87**	**0.48**	**0.33**	**0.33**
Coupon 4 Wear Test Results								
Side 1, R Squared	0.99802	0.99541	0.99629	0.99887	0.99581	0.99516	0.99314	0.99832
Wear Area, mm^2	394.48	429.96	402.04	419.14	477.96	424.19	405.53	389.87
Reinforcement Area, mm^2	85.57	110.46	81.05	86	158	123.12	89.98	92.95
Wear Scar Area Change	30.3%	42.0%	32.7%	38.4%	57.8%	40.1%	33.9%	28.7%
Corrected Wear Rate, mg/m	**0.94**	**1.27**	**1.00**	**1.24**	**1.47**	**1.92**	**1.57**	**1.47**
Side 2, R Squared	0.99093	0.98954	0.99855	0.99466	0.99142	0.99497	0.99166	0.99857
Wear Area, mm^2	385.26	426.62	412.7	393.15	466.58	420.46	445.44	430.17
Reinforcement Area, mm^2	124.71	172.03	157	111.56	172.03	159.48	83.12	57.43
Wear Scar Area Change	27.2%	40.9%	36.3%	29.8%	54.1%	38.8%	47.1%	42.0%
Corrected Wear Rate, mg/m	**1.01**	**1.21**	**0.91**	**1.55**	**1.96**	**1.93**	**1.95**	**2.05**

Table 4.11. Abrasive Wear Test Results (continued).

BATCH NUMBER	**B4-22-1**	**B4-24-1**	**B4-27-1**	**B4-29-1**	**B5-1-1**	**B5-4-1**	**B5-6-1**	**B5-8-1**
DESCRIPTION	1:4 Blend	1:1 Blend	EC	Spinel	Spinel	MgO	MgO	Spinel
Premix Cement, % of Batch	36.0	36.0	41.8	36.0	30.0	36.0	32.0	32.1
Reinforcement, % Batch	54.1	54.1	49.2	54.1	45.1	54.1	48.0	48.1
Additive % of Batch	9.9	9.9	9.0	9.9	24.9	9.9	20.0	19.9
Chromia, Cr_2O_3	4.3%	10.8%						
Magnesia, MgO	17.3%	10.8%				21.6%	38.5%	
Spinel, $MgAl_2O_4$				21.6%	45.3%			38.3%
Coupon 2 Wear Test Results								
Side 1, R Squared	0.99219	0.99081	0.98938	0.99398	0.98240	0.99027	0.98677	0.98244
Wear Area, mm^2	424.83	413.05	417.66	411.88	424.81	395.68	483.49	427.75
Reinforcement Area, mm^2	114.39	202.02	101.79	141.35	191.81	118.25	210.47	126.06
Wear Scar Area Change	40.3%	36.4%	37.9%	36.0%	40.3%	30.6%	59.6%	41.2%
Corrected Wear Rate, mg/m	**0.65**	**0.34**	**0.37**	**0.41**	**0.29**	**0.26**	**0.61**	**0.36**
Side 2, R Squared	0.99724	0.99605	0.99773	0.99943	0.99355	0.99696	0.99486	0.99514
Wear Area, mm^2	456.13	448.72	423.62	421.29	441.19	426.33	498.8	450.71
Reinforcement Area, mm^2	202/16	208.17	208.91	237.76	190.98	183.84	218.5	132.31
Wear Scar Area Change	50.6%	48.2%	39.9%	39.1%	45.7%	40.8%	64.7%	48.8%
Corrected Wear Rate, mg/m	**0.25**	**0.35**	**0.21**	**0.29**	**0.27**	**0.25**	**0.39**	**0.43**
Coupon 4 Wear Test Results								
Side 1, R Squared	0.99923	0.99898	0.99615	0.99475	0.99356	0.99645	0.99108	0.99545
Wear Area, mm^2	386.08	396.13	378.06	413.05	474.92	404.44	380.93	413.42
Reinforcement Area, mm^2	119.84	49.5	73.32	103.29	138.93	129.96	107.18	105.41
Wear Scar Area Change	27.5%	30.8%	24.8%	36.4%	56.8%	33.5%	25.8%	36.5%
Corrected Wear Rate, mg/m	**1.23**	**1.57**	**1.46**	**1.62**	**2.49**	**1.96**	**4.38**	**1.59**
Side 2, R Squared	0.99917	0.97744	0.99995	0.99504	0.99817	0.99833	0.99767	0.99900
Wear Area, mm^2	424.13	378.7	379.39	416.06	382.31	386.48	394.23	363.39
Reinforcement Area, mm^2	140.7	87.13	118.36	132.62	166.99	124.23	125.05	139.52
Wear Scar Area Change	40.0%	25.0%	25.3%	37.4%	26.2%	27.6%	30.2%	20.0%
Corrected Wear Rate, mg/m	**1.94**	**2.21**	**1.27**	**0.62**	**0.64**	**1.12**	**0.92**	**0.85**

Table 4.11. Abrasive Wear Test Results (continued).

BATCH NUMBER	B5-13-1	B5-15-1	B5-18-1	B5-20-1	B5-22-1	B5-26-1	B5-28-1
DESCRIPTION	EA	Spinel-EA	Spinel-EA	1:4 Bld-EA	1:1 Bld-EA	1:2 Bld-EA	MgO-EA
Premix Cement, % of Batch	20.0	20.0	30.6	30.6	30.6	30.6	30.6
Reinforcement, % Batch	80.0	63.3	61.1	61.1	61.1	61.1	61.1
Additive % of Batch	0.0	16.6	8.3	8.3	8.3	8.3	8.3
Chromia, Cr_2O_3				4.3%	10.7%	7.5%	
Magnesia, MgO				17.1%	10.7%	13.5%	21.3%
Spinel, $MgAl_2O_4$		45.4%	21.3%				
Coupon 2 Wear Test Results							
Side 1, R Squared	0.98945	0.98364	0.98786	0.98929			
Wear Area, mm^2	418.86	376.85	410.4	423.19			
Reinforcement Area, mm^2	159.25	187.71	212.05	235.06			
Wear Scar Area Change	38.3%	24.4%	35.5%	39.7%			
Corrected Wear Rate, mg/m	**0.27**	**0.45**	**0.27**	**0.25**			
Side 2, R Squared	0.99266	0.99608	0.99805	0.99744			
Wear Area, mm^2	429.18	435.67	419.65	448.48			
Reinforcement Area, mm^2	118.76	222.91	241.73	227.73			
Wear Scar Area Change	41.7%	43.9%	38.6%	48.1%			
Corrected Wear Rate, mg/m	**0.28**	**0.23**	**0.24**	**0.30**			
Coupon 4 Wear Test Results							
Side 1, R Squared	0.99403	0.99307	0.99730	0.98760	0.99762	0.99739	0.99722
Wear Area, mm^2	465.6	494.39	400.35	397.38	398.94	378.83	448.62
Reinforcement Area, mm^2	169.17	177.84	144.56	110.57	123.86	183.79	258.45
Wear Scar Area Change	53.7%	63.2%	32.2%	31.2%	31.7%	25.1%	48.1%
Corrected Wear Rate, mg/m	**1.30**	**1.17**	**1.51**	**1.34**	**1.16**	**1.41**	**2.43**
Side 2, R Squared	0.99788	0.99833	0.98882	0.98934	0.99416	0.99512	0.99912
Wear Area, mm^2	415.13	402.02	375.35	479.02	430.28	380.37	416.9
Reinforcement Area, mm^2	156.32	187.48	185	187.48	120.27	153.53	270.13
Wear Scar Area Change	37.1%	32.7%	23.9%	58.2%	42.1%	25.6%	37.7%
Corrected Wear Rate, mg/m	**0.85**	**0.56**	**0.50**	**0.38**	**0.57**	**0.47**	**0.55**

Table 4.11. Abrasive Wear Test Results (continued).

BATCH NUMBER	B8-24-1	B8-28-1	B9-1-1	B9-3-1	B9-8-1	B9-10-1	B9-26-1	B9-28-1
Description								
Reinforcement	LD	Zircon	None	None	HD	HD	Spinel	Spinel
Cement and Additive	CA	CA	CA	CA-MgO	CA-MgO	CA-Sp	CA	CA
Cement %, of Batch	50	50	100	50	26	25	50	50
Reinforcement, % Batch	50	50			51	50	50	50
Additive % of Batch				50	23	25		
Matrix Composition								
Alumina, Al_2O_3 as CA or CA_3	40.0%	40.0%	40.0%	20.0%	21.1%	20.0%	40.0%	40.0%
Calcia, CaO as CA or CA_2	45.0%	45.0%	45.0%	22.5%	23.7%	22.5%	45.0%	45.0%
Iron Oxide, Fe_3O_4 as C_4AF	13.0%	13.0%	13.0%	6.5%	6.8%	6.5%	13.0%	13.0%
Silica, SiO_2 as C_2S or C_3S	2.0%	2.0%	2.0%	1.0%	1.1%	1.0%	2.0%	2.0%
Chromia, Cr_2O_4								
Titania-Alumina $TiO{\cdot}Al_2O_3$								
Magnesia, MgO				50.0%	47.4%			
Spinel, $MgAl_2O_4$						50.0%		
Dead Burnt Magnesia, MgO								
Alumina, Al_2O_4								
Cerium Oxide, CeO								
Coupon 2 Wear Test Results								
Side 1, R Squared	0.98909	0.99695	0.99022	0.99706	0.99659	0.99705	0.99934	0.99906
Wear Area, mm^2		442.68	509.12	577.57	470.61	387.69	373.3	393.21
Reinforcement Area, mm^2		79.94	0	53.65	23.44	15.53	7.88	81.47
Wear Scar Area Change		46.2%	68.1%	90.7%	55.4%	28.0%	23.3%	29.8%
Corrected Wear Rate, mg/m	**1.38**	**0.65**	**4.92**	**8.21**	**1.85**	**0.78**	**1.04**	**1.00**
Side 2, R Squared		0.99540	0.99549	0.99919	0.99046	0.99606	0.99847	0.99790
Wear Area, mm^2		431.2	477.03	468.91	414.52	354.33	356.47	375.58
Reinforcement Area, mm^2		91.81	0	34.41	67.17	19.4	30.61	69
Wear Scar Area Change		42.4%	57.5%	54.8%	36.9%	17.0%	17.7%	24.0%
Corrected Wear Rate, mg/m		**0.63**	**0.72**	**1.89**	**1.02**	**0.80**	**1.45**	**1.60**

Table 4.11. Abrasive Wear Test Results (continued).

BATCH NUMBER	B10-2-1	B10-5-1	B10-7-1	B10-12-1	B10-14-1	B10-16-1	B10-19-1	B10-21-1
Description								
Reinforcement	Spinel	Spinel	Spinel	Spinel	Spinel	Spinel	Spinel	Spinel
Cement and Additive	CA-Sp	CA-MgO	CA-MgO	CA-MgO	Ca-Sp	Ca-Sp	CA-Sp	CA-Sp
Cement %, of Batch	25	50	13	10	25	17	13	10
Reinforcement, % Batch	50	50	50	50	50	50	50	50
Additive % of Batch	25		38	40	25	33	38	40
Matrix Composition								
Alumina, Al_2O_3 as CA or CA_3	20.0%	40.0%	10.0%	8.0%	20.0%	13.3%	10.0%	8.0%
Calcia, CaO as CA or CA_2	22.5%	45.0%	11.3%	9.0%	22.5%	15.0%	11.3%	9.0%
Iron Oxide, Fe_3O_4 as C_4AF	6.5%	13.0%	3.3%	2.6%	6.5%	4.3%	3.3%	2.6%
Silica, SiO_2 as C_2S or C_3S	1.0%	2.0%	0.5%	0.4%	1.0%	0.7%	0.5%	0.4%
Chromia, Cr_2O_4								
Titania-Alumina $TiO{\cdot}Al_2O_3$								
Magnesia, MgO			75.0%	80.0%				
Spinel, $MgAl_2O_4$	50.0%				50.0%	66.7%	75.0%	80.0%
Dead Burnt Magnesia, MgO								
Alumina, Al_2O_4								
Cerium Oxide, CeO								
Coupon 2 Wear Test Results								
Side 1, R Squared	0.97900	0.99676	0.99855	0.99016	0.99937	0.99999	0.99780	0.99852
Wear Area, mm^2	378.66	627.53	515.95	460.68	380.26	322.36	482.08	522.39
Reinforcement Area, mm^2	47.5	110.37	88.72	105.95	65.68	72.87	130.46	118.26
Wear Scar Area Change	25.0%	107.2%	70.4%	52.1%	25.6%	6.4%	59.2%	72.5%
Corrected Wear Rate, mg/m	**1.83**	**4.90**	**7.76**	**7.45**	**0.74**	**1.51**	**2.80**	**4.92**
Side 2, R Squared	0.99879	0.99930	0.99534	0.97993	0.99627	0.98573	0.98866	0.98220
Wear Area, mm^2	352.41	591.59	517.14	415.91	347.54	390.17	498.89	523.06
Reinforcement Area, mm^2	30.27	166.64	200.89	205.54	36.01	140.69	74.79	152.26
Wear Scar Area Change	16.4%	95.3%	70.8%	37.3%	14.8%	28.8%	64.7%	72.7%
Corrected Wear Rate, mg/m	**1.32**	**6.54**	**4.92**	**5.70**	**1.74**	**2.43**	**4.43**	**5.14**

Table 4.11. Abrasive Wear Test Results (continued).

BATCH NUMBER	B11-23-1	B11-30-1	B12-1-1	B12-2-1	B12-3-1	B12-7-1	B12-8-1	B12-18-2
Description								
Reinforcement	HD Grog	HD Grog	HD Grog	HD Grog	HD Grog	HD Grog	HD Grog	HD Grog
Cement and Additive	CA	CA-MgO	CA-Mgo	CA-Mgo	CA-Mgo	CA-Mgo	CA-Mgo	CA
Cement %, of Batch	50	20	13	10	8	20	14	43
Reinforcement, % Batch	50	60	60	60	60	59	59	57
Additive % of Batch		20	27	30	32	20	27	
Matrix Composition								
Alumina, Al_2O_3 as CA or CA_3	40.0%	20.0%	13.3%	10.0%	8.0%	20.0%	13.3%	40.0%
Calcia, CaO as CA or CA_2	45.0%	22.5%	15.0%	11.2%	9.0%	22.5%	15.0%	45.0%
Iron Oxide, Fe_3O_4 as C_4AF	13.0%	6.5%	4.3%	3.2%	2.6%	6.5%	4.3%	13.0%
Silica, SiO_2 as C_2S or C_3S	2.0%	1.0%	0.7%	0.5%	0.4%	1.0%	0.7%	2.0%
Chromia, Cr_2O_4								
Titania-Alumina $TiO{\cdot}Al_2O_3$								
Magnesia, MgO		50.0%	66.7%	75.0%	80.0%	50.0%	66.7%	
Spinel, $MgAl_2O_4$								
Dead Burnt Magnesia, MgO								
Alumina, Al_2O_4								
Cerium Oxide, CeO								
Coupon 2 Wear Test Results								
Side 1, R Squared	0.97444	0.99874	0.98568	0.96522	0.95829	0.98446	0.99025	0.99666
Wear Area, mm^2	516.13	449.91	461.81	605.3	638.12	545.79	465.53	452.92
Reinforcement Area, mm^2	38.39	32.95	26.73	21.71	139.58	98.51	53.72	15.16
Wear Scar Area Change	70.4%	48.6%	52.5%	99.9%	110.7%	80.2%	53.7%	49.5%
Corrected Wear Rate, mg/m	**7.23**	**2.00**	**7.28**	**21.86**	**13.08**	**1.44**	**0.92**	**0.78**
Side 2, R Squared	0.99498	0.99999				0.98458	0.98157	0.99331
Wear Area, mm^2	481.43	519.9				506.22	484.38	397.14
Reinforcement Area, mm^2	20.76	35.33				138.79	70.29	27.11
Wear Scar Area Change	59.0%	71.7%				67.1%	59.9%	31.1%
Corrected Wear Rate, mg/m	**1.76**	**1.55**				**1.91**	**2.64**	**1.12**

Table 4.11. Abrasive Wear Test Results (continued).

BATCH NUMBER	B1-12-1	B1-15-1	B1-19-1	B1-20-1	B1-28-1	B1-29-2	B2-10-1
Description							
Reinforcement	HD Grog	HD Grog	None	None	HD Grog	None	HD Grog
Cement and Additive	CA_2	CA_2	CA_2	CA_2	CA_2	CA_2	CA_2-MgO
Cement %, of Batch	40	40	100	100	40	100	20
Reinforcement, % Batch	60	60			60		60
Additive % of Batch							20
Matrix Composition							
Alumina, Al_2O_3 as CA or CA_3	62.0%	62.0%	62.0%	62.0%	62.0%	62.0%	31.0%
Calcia, CaO as CA or CA_2	30.0%	30.0%	30.0%	30.0%	30.0%	30.0%	15.0%
Iron Oxide, Fe_3O_4 as C_4AF	5.0%	5.0%	5.0%	5.0%	5.0%	5.0%	2.5%
Silica, SiO_2 as C_2S or C_3S	3.0%	3.0%	3.0%	3.0%	3.0%	3.0%	1.5%
Chromia, Cr_2O_4							
Titania-Alumina $TiO{\cdot}Al_2O_3$							
Magnesia, MgO							
Spinel, $MgAl_2O_4$							
Dead Burnt Magnesia, MgO							50.0%
Alumina, Al_2O_4							
Cerium Oxide, CeO							
Coupon 2 Wear Test Results							
Side 1, R Squared	0.98762	0.98930	0.98442	0.99960	0.99561	0.99025	0.98993
Wear Area, mm^2	408.07	451.37	575.57	492.11	473.83	602.4	498.79
Reinforcement Area, mm^2	55.13	35.47	0	0	NA	0	35.03
Wear Scar Area Change	34.7%	49.0%	90.0%	62.5%	56.5%	98.9%	64.7%
Corrected Wear Rate, mg/m	**1.57**	**2.02**	**7.05**	**3.13**	**1.46**	**1.83**	**2.36**
Side 2, R Squared	0.99693	0.99739	0.99557	0.99893	0.99104	0.99583	0.99335
Wear Area, mm^2	389.75	386.49	398.99	411.18	419.11	470.23	410.9
Reinforcement Area, mm^2	32.09	15.47	0	0	NA	0	74.86
Wear Scar Area Change	28.7%	27.6%	31.7%	35.8%	38.4%	55.3%	35.7%
Corrected Wear Rate, mg/m	**1.26**	**1.14**	**1.88**	**1.86**	**1.14**	**2.66**	**1.28**

Table 4.11. Abrasive Wear Test Results (continued).

BATCH NUMBER	B2-14-2	B2-22-1	B2-24-1	B2-25-1	B3-9-1	B3-10-1	B3-11-1	B3-12-1
Description								
Reinforcement	None	DB Rock	DB Rock	DB Rock	HD Grog	HD Grog	HD Grog	HD Grog
Cement and Additive	CA	CA2	CA_2-MgO	CA_2-MgO	CA_2-MgO	CA_2-MgO	CA_2-MgO	CA_2
Cement %, of Batch	100	40	20	20	27	13	13	25
Reinforcement, % Batch		60	60	60	60	60	75	75
Additive % of Batch			20	20	13	27	13	
Matrix Composition								
Alumina, Al_2O_3 as CA or CA_3	40.0%	62.0%	31.0%	31.0%	41.3%	20.7%	31.0%	62.0%
Calcia, CaO as CA or CA_2	45.0%	30.0%	15.0%	15.0%	20.0%	10.0%	15.0%	30.0%
Iron Oxide, Fe_3O_4 as C_4AF	13.0%	5.0%	2.5%	2.5%	3.3%	1.7%	2.5%	5.0%
Silica, SiO_2 as C_2S or C_3S	2.0%	3.0%	1.5%	1.5%	2.0%	1.0%	1.5%	3.0%
Chromia, Cr_2O_4								
Titania-Alumina $TiO{\cdot}Al_2O_3$								
Magnesia, MgO								
Spinel, $MgAl_2O_4$								
Dead Burnt Magnesia, MgO			50.0%	50.0%	33.3%	66.7%	50.0%	
Alumina, Al_2O_4								
Cerium Oxide, CeO								
Coupon 2 Wear Test Results								
Side 1, R Squared	0.98192	0.99927	0.99890	0.99717	0.99845	0.99584	0.96897	0.97335
Wear Area, mm^2	483.02	428.93	506.64	447.12	411.33	426.25	407.76	457.82
Reinforcement Area, mm^2	273.78	160.3	266.12	191.98	98.72	78.89	58.65	50.44
Wear Scar Area Change	59.5%	41.6%	67.3%	47.6%	35.8%	40.7%	34.6%	51.2%
Corrected Wear Rate, mg/m	**1.41**	**1.25**	**2.67**	**2.17**	**1.35**	**1.27**	**0.29**	**0.47**
Side 2, R Squared	0.99287	0.99164	0.99923	0.99716	0.99812	0.99710	0.98832	0.99176
Wear Area, mm^2	518.97	459.37	439.51	465.15	405.21	408.63	378.45	400.41
Reinforcement Area, mm^2	233.26	225.9	238.42	199.9	112.25	99.22	97.25	26.23
Wear Scar Area Change	71.4%	51.7%	45.1%	53.6%	33.8%	34.9%	25.0%	32.2%
Corrected Wear Rate, mg/m	**0.90**	**1.80**	**1.75**	**2.38**	**0.96**	**1.01**	**0.64**	**0.53**

Table 4.11. Abrasive Wear Test Results (continued).

BATCH NUMBER	B3-14-1	B3-16-1	B3-23-1	B3-24-1	B3-25-1	B3-26-1	B3-29-1	B3-31-1
Description								
Reinforcement	HD Grog	HD Grog	HD Grog	HD Grog	HD Grog	HD Grog	HD Grog	HD Grog
Cement and Additive	CA_2	CA_2-MgO	CA_2-MgO	CA_2-MgO	CA_2-MgO	CA_2-K-M	CA_2-K-M	CA_2-K-M
Cement %, of Batch	60	30	40	20	15	20	20	20
Reinforcement, % Batch	40	40	40	40	40	60	60	60
Additive % of Batch		30	20	40	45	20	20	20
Matrix Composition								
Alumina, Al_2O_3 as CA or CA_3	62.0%	31.0%	41.3%	20.7%	15.5%	31.0%	31.0%	31.0%
Calcia, CaO as CA or CA_2	30.0%	15.0%	20.0%	10.0%	7.5%	15.0%	15.0%	15.0%
Iron Oxide, Fe_3O_4 as C_4AF	5.0%	2.5%	3.3%	1.7%	1.3%	2.5%	2.5%	2.5%
Silica, SiO_2 as C_2S or C_3S	3.0%	1.5%	2.0%	1.0%	0.8%	1.5%	1.5%	1.5%
Chromia, Cr_2O_4						16.8%	25.0%	9.8%
Titania-Alumina $TiO{\cdot}Al_2O_3$								
Magnesia, MgO						33.2%	25.0%	40.2%
Spinel, $MgAl_2O_4$								
Dead Burnt Magnesia, MgO		50.0%	33.3%	66.7%	75.0%			
Alumina, Al_2O_4								
Cerium Oxide, CeO								
Coupon 2 Wear Test Results								
Side 1, R Squared	0.99132	0.99119	0.99765	0.99740	0.99650	0.98943	0.99917	0.99796
Wear Area, mm^2	430.11	492.51	421.26	424.02	436.94	476.87	459.01	467.32
Reinforcement Area, mm^2	40.19	0	0	0	0	26.2	12.2	8.63
Wear Scar Area Change	42.0%	62.6%	39.1%	40.0%	44.3%	57.5%	51.6%	54.3%
Corrected Wear Rate, mg/m	**1.02**	**2.31**	**1.99**	**2.82**	**1.61**	**1.67**	**2.14**	**2.37**
Side 2, R Squared	0.99701	0.98921	0.99639	0.99409	0.99541	0.99451	0.99609	0.99984
Wear Area, mm^2	427.02	483.44	441.48	468.06	462.32	419.04	410.91	467.08
Reinforcement Area, mm^2	41.77	0	0	0	0	49.29	54.93	76.75
Wear Scar Area Change	41.0%	59.6%	45.8%	54.5%	52.7%	38.4%	35.7%	54.2%
Corrected Wear Rate, mg/m	**1.09**	**2.55**	**2.20**	**1.30**	**2.28**	**0.96**	**1.22**	**1.36**

Table 4.11. Abrasive Wear Test Results (continued).

BATCH NUMBER	B4-1-1	B4-2-1	B4-5-1	B4-6-1	B4-14-1	B4-15-1	B4-16-1	B4-20-1
Description								
Reinforcement	HD Grog	Graded Sp	Graded Sp	Graded Sp	Graded Sp	Graded Sp	Graded Sp	Graded Sp
Cement and Additive	CA_2-K-M	CA_2	CA_2	CA_2-M	CA_2-M	CA_2-M	CA_2-M	CA_2-M
Cement %, of Batch	10	40	40	20	40	13	10	30
Reinforcement, % Batch	60	60	60	60	60	60	60	40
Additive % of Batch	30			20		27	30	30
Matrix Composition								
Alumina, Al_2O_3 as CA or CA_3	15.5%	62.0%	62.0%	31.0%	62.0%	20.9%	15.5%	31.0%
Calcia, CaO as CA or CA_2	7.5%	30.0%	30.0%	15.0%	30.0%	10.1%	7.5%	15.0%
Iron Oxide, Fe_3O_4 as C_4AF	1.3%	5.0%	5.0%	2.5%	5.0%	1.7%	1.3%	2.5%
Silica, SiO_2 as C_2S or C_3S	0.8%	3.0%	3.0%	1.5%	3.0%	1.0%	0.8%	1.5%
Chromia, Cr_2O_4	16.8%							
Titania-Alumina $TiO{\cdot}Al_2O_3$								
Magnesia, MgO	8.2%							
Spinel, $MgAl_2O_4$								
Dead Burnt Magnesia, MgO				50.0%		66.3%	75.0%	50.0%
Alumina, Al_2O_4								
Cerium Oxide, CeO								
Coupon 2 Wear Test Results								
Side 1, R Squared	0.99957	0.99754	0.99697	0.99983	0.99855	0.99978	0.99910	0.99901
Wear Area, mm^2	424.82	392.47	430.34			404.7	409.65	395.81
Reinforcement Area, mm^2	4.23	83.92	77.47			95.46	108.01	32.57
Wear Scar Area Change	40.3%	29.6%	42.1%			33.6%	35.3%	30.7%
Corrected Wear Rate, mg/m	**1.72**	**0.84**	**1.13**	**3.06**	**1.55**	**2.00**	**1.54**	**1.34**
Side 2, R Squared	0.99985	0.99912	0.99945	0.99893	0.98420	0.99892	0.99718	0.99936
Wear Area, mm^2	426.37	400.55	407.53			429.49	402.03	392.42
Reinforcement Area, mm^2	11.54	96.38	101.21			164.41	75.29	12.82
Wear Scar Area Change	40.8%	32.3%	34.6%			41.8%	32.7%	29.6%
Corrected Wear Rate, mg/m	**1.44**	**1.25**	**1.45**	**2.14**	**1.18**	**2.32**	**1.71**	**1.33**

Table 4.11. Abrasive Wear Test Results (continued).

BATCH NUMBER	B4-21-1	B4-27-1	B4-28-1	B4-29-1	B4-30-1	B5-3-1	B5-4-1	B5-10-1
Description								
Reinforcement	Graded Sp	DB-Rock	DB-Rock	DB-Rock	DB-Rock	Cement	Cement	DB-Rock
Cement and Additive	CA_2-M	CA_2	CA_2-MgO	CA_2-MgO	CA_2-MgO	Control	Control	CA_2-MgO
Cement %, of Batch	20	60	30	40	20	40	40	15
Reinforcement, % Batch	40	40	40	40	40	60	60	40
Additive % of Batch	40		30	20	40			45
Matrix Composition								
Alumina, Al_2O_3 as CA or CA_3	20.7%	62.0%	31.0%	41.3%	20.7%	62.0%	62.0%	15.5%
Calcia, CaO as CA or CA_2	10.0%	30.0%	15.0%	20.0%	10.0%	30.0%	30.0%	7.5%
Iron Oxide, Fe_3O_4 as C_4AF	1.7%	5.0%	2.5%	3.3%	1.7%	5.0%	5.0%	1.3%
Silica, SiO_2 as C_2S or C_3S	1.0%	3.0%	1.5%	2.0%	1.0%	3.0%	3.0%	0.8%
Chromia, Cr_2O_4								
Titania-Alumina $TiO{\cdot}Al_2O_3$								
Magnesia, MgO								
Spinel, $MgAl_2O_4$								
Dead Burnt Magnesia, MgO	66.7%		50.0%	33.3%	66.7%			75.0%
Alumina, Al_2O_4								
Cerium Oxide, CeO								
Coupon 2 Wear Test Results								
Side 1, R Squared	0.99769	0.99899	0.99891	0.99998	0.99974	0.99920	0.99853	0.99978
Wear Area, mm^2			418.5	392.49	435.81		386.72	467.4
Reinforcement Area, mm^2			90.92	57.76	61.65		121.91	109.54
Wear Scar Area Change			38.2%	29.6%	43.9%		27.7%	54.3%
Corrected Wear Rate, mg/m	**4.84**	**1.52**	**1.53**	**1.20**	**2.04**	**1.59**	**1.68**	**3.12**
Side 2, R Squared	0.98968	0.99720	0.99931	0.99981	0.99913	0.98706		0.99965
Wear Area, mm^2			406.93	409.26	429.53			473.67
Reinforcement Area, mm^2			64.96	109.44	108.47			206.52
Wear Scar Area Change			34.4%	35.1%	41.8%			56.4%
Corrected Wear Rate, mg/m	**5.28**	**1.74**	**1.40**	**1.56**	**1.72**	**2.04**		**2.43**

Table 4.11. Abrasive Wear Test Results (continued).

BATCH NUMBER	B5-12-1	SP7-6-1	SP7-7-1	SP7-8-1	SP7-9-1	SP7-12-1	SP7-13-1	SP7-14-1
Description								
Reinforcement	DB-Rock	DB-Rock	DB-Rock	DB-Rock	DB-Rock	DB-Rock	DB-Rock	DB-Rock
Cement and Additive	CA_2-MgO	CA_2-MgO	CA_2-MgO	CA_2-MgO	CA_2-MgO	CA_2-MgO	CA_2-MgO	CA_2-MgO
Cement %, of Batch	25	20	20	27	27	27	20	20
Reinforcement, % Batch	75	60	60	60	60	60	60	60
Additive % of Batch								
Matrix Composition	0.00	0.20	0.20	0.13	0.13	0.13	0.20	0.20
Alumina, Al_2O_3 as CA or CA_3	62.0%	31.0%	31.0%	41.3%	41.3%	41.3%	31.0%	31.0%
Calcia, CaO as CA or CA_2	30.0%	15.0%	15.0%	20.0%	20.0%	20.0%	15.0%	15.0%
Iron Oxide, Fe_3O_4 as C_4AF	5.0%	2.5%	2.5%	3.3%	3.3%	3.3%	2.5%	2.5%
Silica, SiO_2 as C_2S or C_3S	3.0%	1.5%	1.5%	2.0%	2.0%	2.0%	1.5%	1.5%
Chromia, Cr_2O_4								
Titania-Alumina $TiO{\cdot}Al_2O_3$								
Magnesia, MgO								
Spinel, $MgAl_2O_4$								
Dead Burnt Magnesia, MgO	0.0%	50.0%	50.0%	33.3%	33.3%	33.3%	50.0%	50.0%
Alumina, Al_2O_4								
Cerium Oxide, CeO								
Coupon 2 Wear Test Results								
Side 1, R Squared	0.99946	0.99905	0.99940	0.99913	0.99427	0.99684	0.99794	0.99536
Wear Area, mm^2	451.11							
Reinforcement Area, mm^2	229.36							
Wear Scar Area Change	49.0%							
Corrected Wear Rate, mg/m	**1.31**	**2.43**	**2.20**	**1.88**	**2.55**	**1.89**	**2.82**	**3.18**
Side 2, R Squared	0.99133	0.99919	0.99945	0.99834	0.99848	0.99874	0.99958	0.99769
Wear Area, mm^2	397.33							
Reinforcement Area, mm^2	259.49							
Wear Scar Area Change	31.2%							
Corrected Wear Rate, mg/m	**1.44**	**1.54**	**1.50**	**1.44**	**1.62**	**1.33**	**1.45**	**1.53**

Table 4.11. Abrasive Wear Test Results (continued).

BATCH NUMBER	SP7-15-1	SP7-16-1	SP7-17-1	SP7-18-1	SP7-19-1	SP7-21-1	SP7-22-1	SP7-23-1
Description								
Reinforcement	DB-Rock	DB-Rock	DB-Rock	DB-Rock	DB-Rock	DB-Rock	DB-Rock	DB-Rock
Cement and Additive	CA_2-M	CA_2-M	CA_2-M	CA_2-M	CA_2-M	CA_2-M-AT	CA_2-M-AT	CA_2-M-AT
Cement %, of Batch	20	20	27	27	27	20	24	10
Reinforcement, % Batch	60	60	60	60	60	60	60	60
Additive % of Batch	20	20	13	13	13	20	16	30
Matrix Composition								
Alumina, Al_2O_3 as CA or CA_3	31.0%	31.0%	41.3%	41.3%	41.3%	31.0%	37.2%	15.5%
Calcia, CaO as CA or CA_2	15.0%	15.0%	20.0%	20.0%	20.0%	15.0%	18.0%	7.5%
Iron Oxide, Fe_3O_4 as C_4AF	2.5%	2.5%	3.3%	3.3%	3.3%	2.5%	3.0%	1.3%
Silica, SiO_2 as C_2S or C_3S	1.5%	1.5%	2.0%	2.0%	2.0%	1.5%	1.8%	0.8%
Chromia, Cr_2O_4								
Titania-Alumina $TiO{\cdot}Al_2O_3$						25.0%	20.0%	25.0%
Magnesia, MgO								
Spinel, $MgAl_2O_4$								
Dead Burnt Magnesia, MgO	50.0%	50.0%	33.3%	33.3%	33.3%	25.0%	20.0%	50.0%
Alumina, Al_2O_4								
Cerium Oxide, CeO								
Coupon 2 Wear Test Results								
Side 1, R Squared	0.99518	0.99695	0.99693	0.99762	0.99535	0.99827	0.99804	0.99917
Wear Area, mm^2						426.66	404.10	571.14
Reinforcement Area, mm^2						157.98	173.03	216.08
Wear Scar Area Change						40.9%	33.4%	88.6%
Corrected Wear Rate, mg/m	**4.61**	**3.03**	**3.72**	**2.65**	**2.85**	**2.42**	**2.34**	**5.47**
Side 2, R Squared	0.99988	0.99913	0.99789	0.99626	0.99736	0.99891	0.99503	0.94336
Wear Area, mm^2						443.24	396.71	552.08
Reinforcement Area, mm^2						194.37	175.67	236.43
Wear Scar Area Change						46.4%	31.0%	82.3%
Corrected Wear Rate, mg/m	**1.59**	**1.23**	**1.45**	**1.39**	**1.28**	**3.38**	**2.28**	**12.17**

Table 4.11. Abrasive Wear Test Results (continued).

BATCH NUMBER	SP7-26-1	SP7-27-1	SP7-28-1	SP7-29-1	SP7-30-1	SP8-2-1	SP8-3-1	SP8-4-1
Description								
Reinforcement	DB-Rock	DB-Rock	DB-Rock	DB-Rock	DB-Rock	DB-Rock	DB-Rock	DB-Rock
Cement and Additive	CA_2-M-AT	CA_2-M-AT	CA_2-M-AT	CA_2-M-AT	CA_2-M-Ce	CA_2-M-Ce	CA_2-M-Ce	CA_2-M-Ce
Cement %, of Batch	10	08	20	13	13	24	10	10
Reinforcement, % Batch	60	60	60	60	60	60	60	60
Additive % of Batch	30	32	20	27	27	16	30	30
Matrix Composition								
Alumina, Al_2O_3 as CA or CA_3	15.5%	12.4%	31.0%	20.7%	20.7%	37.2%	15.5%	15.5%
Calcia, CaO as CA or CA_2	7.5%	6.0%	15.0%	10.0%	10.0%	18.0%	7.5%	7.5%
Iron Oxide, Fe_3O_4 as C_4AF	1.3%	1.0%	2.5%	1.7%	1.7%	3.0%	1.3%	1.3%
Silica, SiO_2 as C_2S or C_3S	0.8%	0.6%	1.5%	1.0%	1.0%	1.8%	0.8%	0.8%
Chromia, Cr_2O_4								
Titania-Alumina $TiO{\cdot}Al_2O_3$	50.0%	60.0%	50.0%	66.7%				
Magnesia, MgO								
Spinel, $MgAl_2O_4$								
Dead Burnt Magnesia, MgO	25.0%	20.0%			33.3%	20.0%	50.0%	25.0%
Alumina, Al_2O_4								
Cerium Oxide, CeO					33.3%	20.0%	25.0%	50.0%
Coupon 2 Wear Test Results								
Side 1, R Squared	0.99795	0.99905	0.99845	0.99746	0.99791	0.99771	0.99791	0.99103
Wear Area, mm^2	539.17	519.31	532.96	565.06	452.66	415.67	474.69	456.58
Reinforcement Area, mm^2	248.86	245.69	210.84	198.33	173.35	177.11	285.98	257.77
Wear Scar Area Change	78.0%	71.5%	76.0%	86.6%	49.5%	37.2%	56.7%	50.8%
Corrected Wear Rate, mg/m	**4.59**	**6.87**	**2.52**	**3.63**	**2.28**	**1.87**	**2.86**	**3.09**
Side 2, R Squared	0.99951	0.99397	0.91063	0.99828	0.99237	0.99784	0.99539	0.99915
Wear Area, mm^2	548.84	472.33	531.03	571.95	443.11	471.71	458.65	448.96
Reinforcement Area, mm^2	271.18	278.64	259.08	146.92	162.35	198.58	292.66	228.73
Wear Scar Area Change	81.2%	56.0%	75.3%	88.8%	46.3%	55.8%	51.4%	48.2%
Corrected Wear Rate, mg/m	**4.32**	**7.23**	**16.17**	**4.97**	**3.19**	**2.17**	**2.60**	**2.90**

Table 4.11. Abrasive Wear Test Results (continued).

BATCH NUMBER	SP8-6-1	SP8-9-1	SP8-10-1	SP8-11-1	SP8-12-1
Description					
Reinforcement	DB-Rock	DB-Rock	DB-Rock	DB-Rock	DB-Rock
Cement and Additive	CA_2-M-A	CA_2-M-A	CA_2-M-A	CA_2-M-A	CA_2-M-A
Cement %, of Batch	13	20	24	10	10
Reinforcement, % Batch	60	60	60	60	60
Additive % of Batch	27	20	16	30	30
Matrix Composition					
Alumina, Al_2O_3 as CA or CA_3	20.7%	31.0%	37.2%	15.5%	15.5%
Calcia, CaO as CA or CA_2	10.0%	15.0%	18.0%	7.5%	7.5%
Iron Oxide, Fe_3O_4 as C_4AF	1.7%	2.5%	3.0%	1.3%	1.3%
Silica, SiO_2 as C_2S or C_3S	1.0%	1.5%	1.8%	0.8%	0.8%
Chromia, Cr_2O_4					
Titania-Alumina $TiO{\cdot}Al_2O_3$					
Magnesia, MgO					
Spinel, $MgAl_2O_4$					
Dead Burnt Magnesia, MgO	33.3%	25.0%	20.0%	50.0%	25.0%
Alumina, Al_2O_4	33.3%	25.0%	20.0%	25.0%	50.0%
Cerium Oxide, CeO					
Coupon 2 Wear Test Results					
Side 1, R Squared	0.99721	0.99839	0.99653	0.99992	0.99639
Wear Area, mm^2	509.87	505.34	478.90	518.94	662.49
Reinforcement Area, mm^2	227.00	217.75	237.44	308.11	315.45
Wear Scar Area Change	68.4%	66.9%	58.1%	71.3%	118.7%
Corrected Wear Rate, mg/m	**2.95**	**2.29**	**2.51**	**3.56**	**8.81**
Side 2, R Squared	0.99820	0.99626	0.99761	0.99645	0.97672
Wear Area, mm^2	503.34	502.14	473.86	502.96	509.12
Reinforcement Area, mm^2	248.21	215.09	242.14	296.82	308.90
Wear Scar Area Change	66.2%	65.8%	56.5%	66.1%	68.1%
Corrected Wear Rate, mg/m	**5.00**	**2.40**	**2.90**	**4.06**	**17.16**

Examples of the wear scar caused by the dry sand rubber wheel test are presented in the set of Figures 4.52 through 4.59. The Figures illustrate the wear scar on coupons formulated with each of the three matrix cements and the four reinforcement materials. The reinforcement material is clearly shown contrasted against the matrix. Figures 4.52 and 4.53 illustrate the wear scar on low wear rate coupons and Figures 4.54 and 4.55 are from high wear rate coupons formulated with high alumina calcium aluminate matrix cement. The reinforcement was found to be standing above the matrix in the first two coupons. The reinforcement particles are shown to wear at an equal rate with the matrix in the last two photographs. Figures 4.56 and 4.57 show examples of wear scars on coupons formulated with Fondu cement using spinel and zirconia grog reinforcement as labeled in the Figures. Several of the shown coupons are truncated or cut, because sections were removed for microscopic examination before the photographs were taken. Figures 4.58 and 4.59 show examples of the wear scar on coupons formulated with the calcium aluminate blend cement using dead burnt magnesia rock reinforcement. These examples are presented to illustrate a relatively even wear scar shape and coverage on the surface of the coupon. In all cases the wear scars were in the center of the coupon flat, free from edge effects. The wear scars also illustrate the difference in the size of the reinforcement particles and how the size compared to the wear scar.

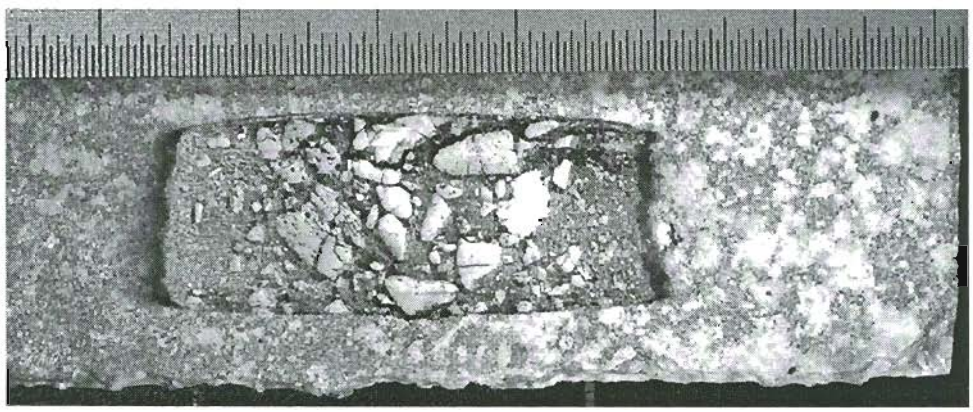

Figure 4.52. DSRW wear scar on coupon B2-16-C2 side 2, high alumina calcium aluminate matrix cement and the zircon reinforcement, low wear rate coupon.

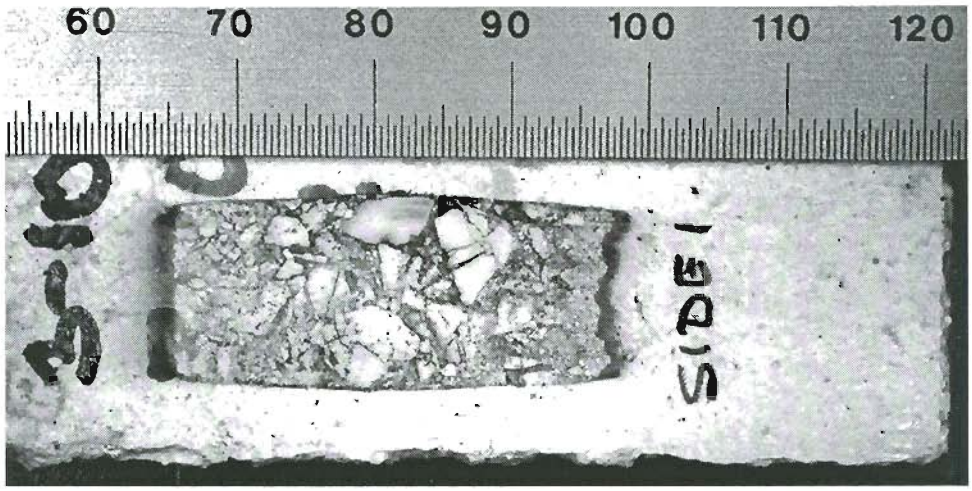

Figure 4.53. DSRW wear scar on coupon B3-10-C2 side 1, high alumina calcium aluminate matrix cement and the zircon reinforcement, low wear rate coupon.

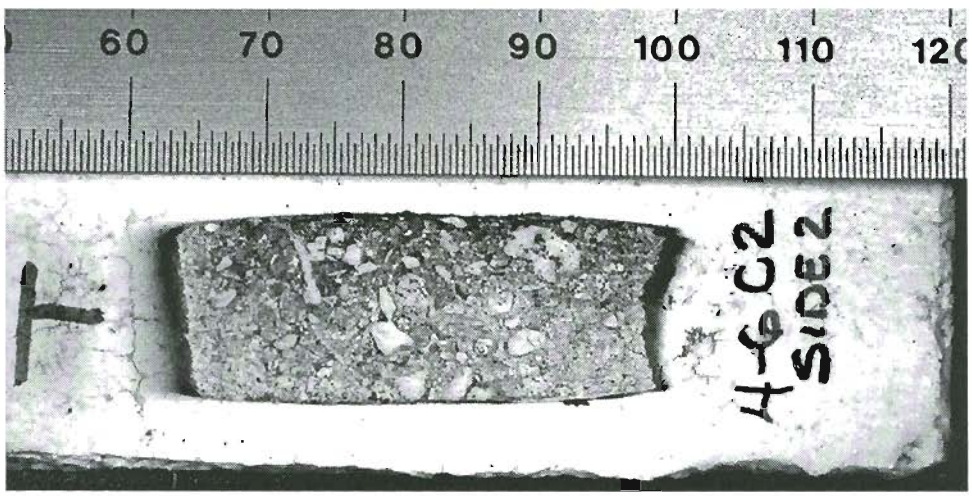

Figure 4.54. DSRW wear scar on coupon B4-6-C2 side 2, high alumina calcium aluminate matrix cement and the zircon reinforcement, high wear rate coupon.

Figure 4.55. DSRW wear scar on coupon B4-8-C2 side 2, high alumina calcium aluminate matrix cement and the zircon reinforcement, high wear rate coupon.

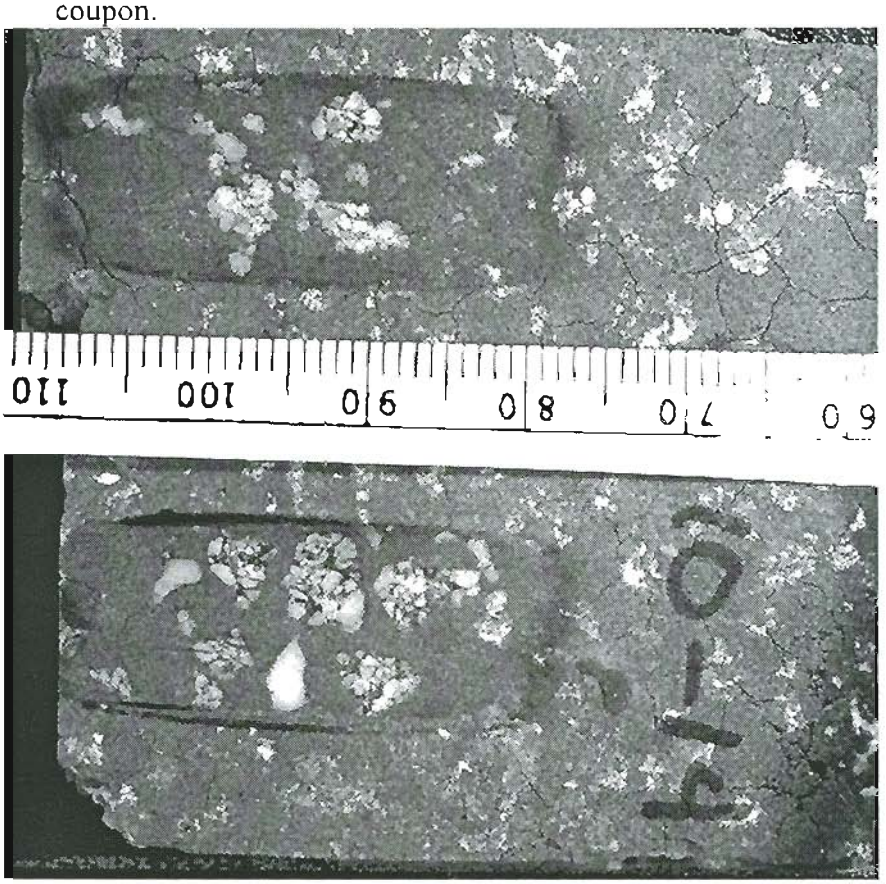

Figure 4.56. DSRW wear scar on coupons B10-21-C2 (Top) and B10-19 C2 (Bottom) Side 1 illustrating the Fondu cement matrix and crushed spinel brick reinforcement.

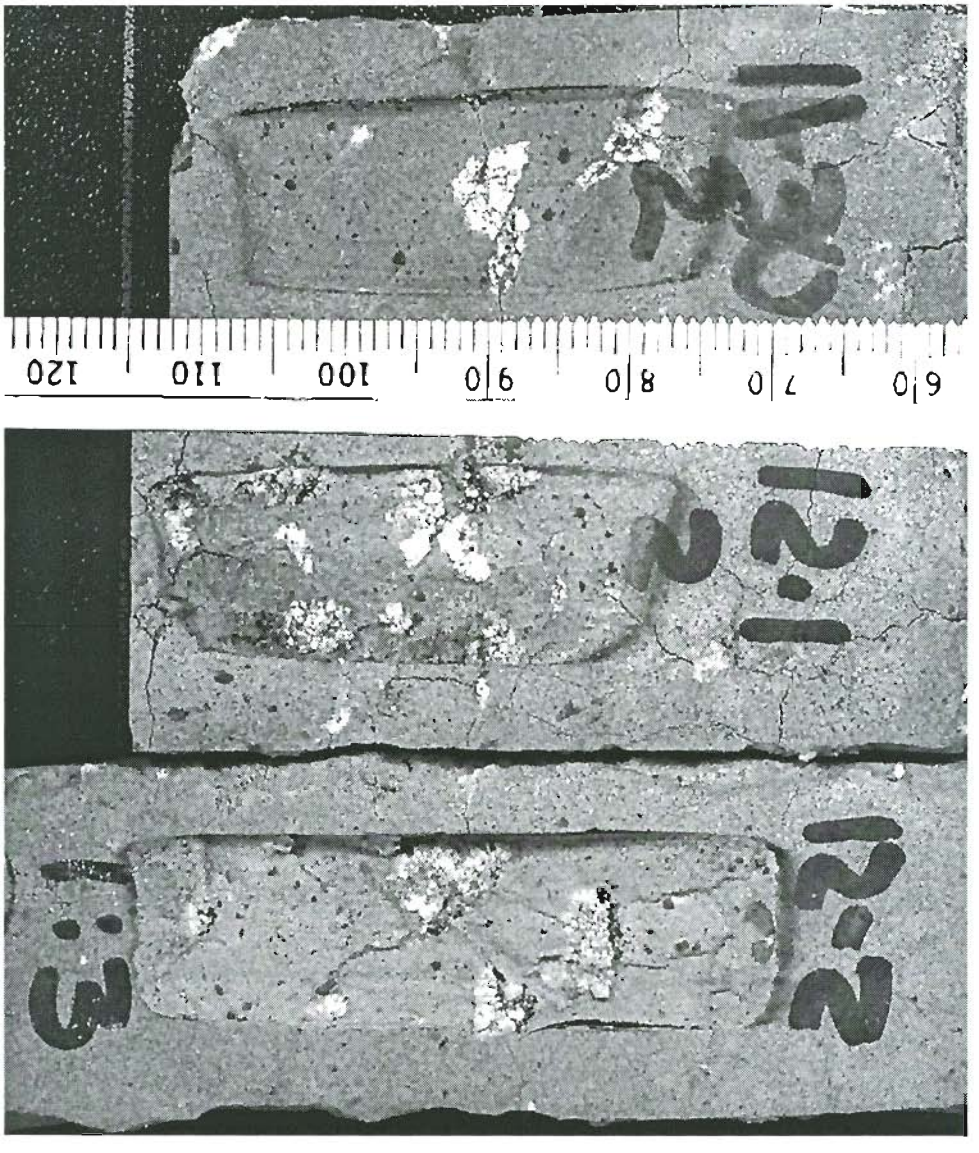

Figure 4.57. DSRW wear scar on coupons B11-30-C2, B12-1-C2 and B12-2-C2 side 1 illustrating the Fondu cement matrix and high density zirconia grog reinforcement.

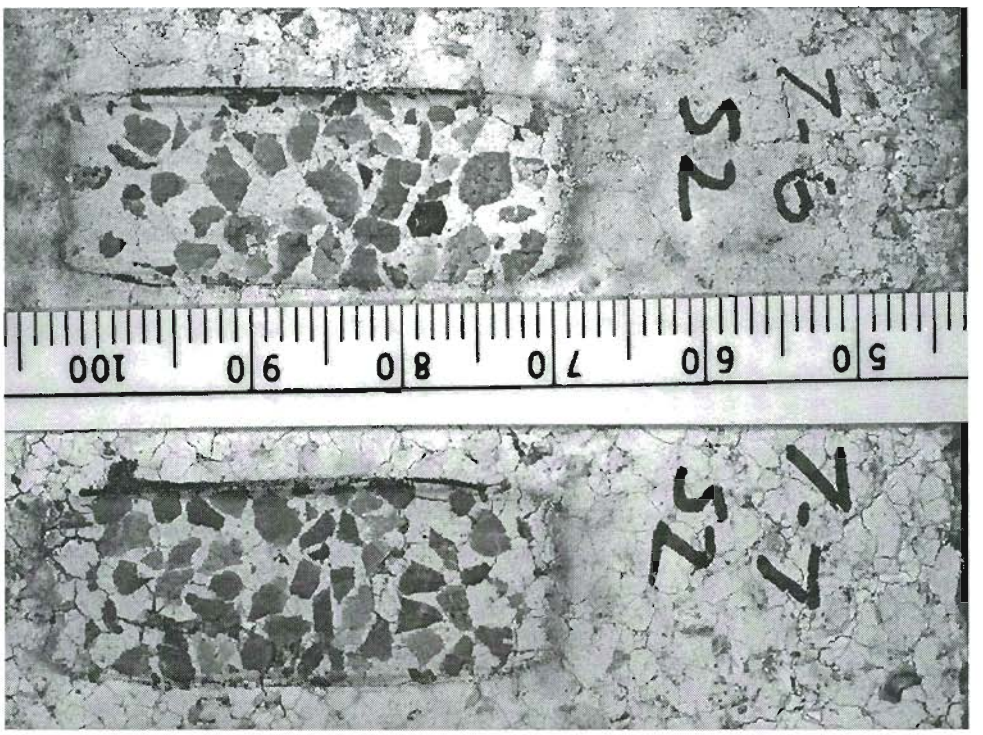

Figure 4.58. DSRW wear scar on coupons B7-6-C2 and B7-7-C2 side 2 illustrating the calcium aluminate cement matrix and the dead burnt magnesia rock reinforcement.

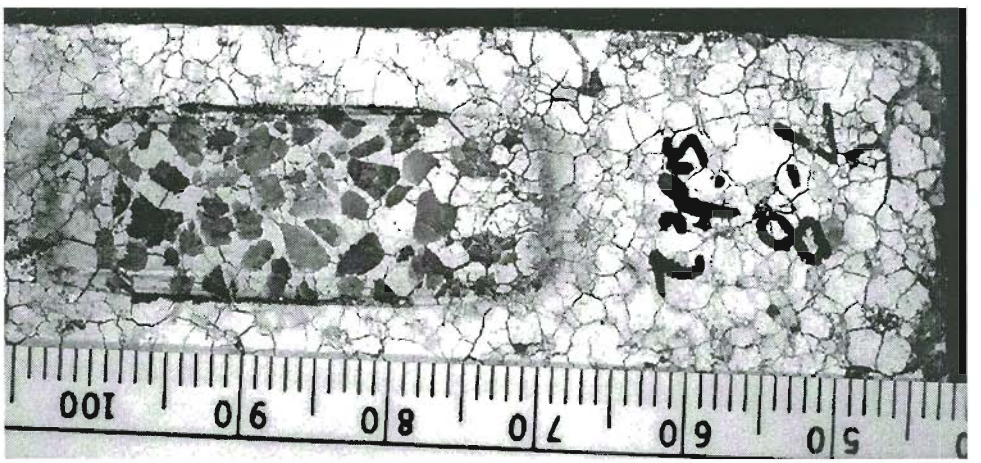

Figure 4.59. DSRW wear scar on coupons B7-8-C2 side 2 illustrating the calcium aluminate cement matrix and the dead burnt magnesia rock reinforcement.

The dry sand rubber wheel test method was used to determine the influence of different additives and reinforcements on the calcium aluminate cements. The results are summarized graphically in Appendix IV according to the type of cement, additive

and reinforcement. The sections 2 and 3 of Appendix IV present the results with the emphasis on the overall matrix cements, the change in the coupon wear characteristics caused by the various sample preparation, sintering and testing conditions. These two sections separate the premix cement and the combined Fondu and calcium dialuminate cements. Section 4 of Appendix IV presents the wear results emphasizing the changing concentrations of the different additives and reinforcement materials.

4.6.2 Synopsis of High Alumina Calcium Aluminate Cement

Coupon orientation was maintained during curing, sintering and testing. The entire set of wear data was analyzed to determine the bias related to the coupon preparation or testing. The orientation of the coupon face was found to produce different results because the pressing operation produced a packing factor gradient. The data are parsed according to the side of the coupon being tested. The high alumina calcium aluminate cement formulations were sintered at two temperatures. The Coupon #2's were sintered at 1200°C for 96 hours whereas Coupon #4's were sintered at 1000°C for 96 hours. All coupons were wear tested on both sides.

The high alumina calcium aluminate (premix cement) data are presented in order of the general experimental objectives. Complete plots of the wear rate data are shown in Section 2 of Appendix IV. Table 4.12 is used as a guide to find the corresponding appendix figure to the wear rate data relationship of interest.

The influence of coupon density to the wear rate is shown in Figure AIV.1. The water to cement ratio influence is evaluated in terms of wear rate in Figure AIV.3. The coupon wear rate and strength are used to determine the influence of additives on the matrix cement properties. The magnesia, chromia and spinel matrix concentrations are compared against the wear rate in Figures AIV.6, AIV.7 and AIV.8. The batch formulations used a blend of magnesia and chromia to understand the relative activity in the premix cement. The magnesia to chromia ratio is used to compare the influence on the wear rate shown in Figure AIV.10.

The reinforcement phase influence on the wear rate is studied from two perspectives, the volume fraction added to the batch and the area fraction determined from the wear scar analysis. Assuming ideal conditions, the volume fraction and the area fraction should be the same, however, the wear scar represents a volume instead of a plane. Wear scar analysis results shown in Figure AIV.13 illustrate the influence of exposed reinforcement area in the wear scar area. Figure AIV.14 illustrates the influence of the reinforcement volume fraction on the wear rate. Figure AIV.15 compares the reinforcement volume fraction to the exposed reinforcement area. The analysis of the data pointed to a bias between the two sides of the coupon. The data are separated according to the coupon numbers and side in Figures AIV.16, AIV.17, AIV.18 and AIV.19.

Table 4.12. Wear Test Results Appendix Figure Guide for the High Alumina Calcium Aluminate Cement Batch Formulations.

Figure	Format of Data Relationship
AIV.1	The influence of coupon density to the wear rate
AIV.3	The water to cement ratio is evaluated against wear rate.
AIV.6 AIV.7 AIV.8	The magnesia, chromia and spinel matrix concentrations are compared against the wear rate
AIV.10	The magnesia to chromia ratio compared to the wear rate
AIV.13	Wear scar analysis results show influence of exposed reinforcement particle area
AIV.14	Reinforcement volume fraction compared to the wear rate
AIV.15	Reinforcement volume fraction compared to the exposed reinforcement area in the wear scar
AIV.16 AIV.17 AIV.18 AIV.19	The data sets separated the wear rate data according to the coupon numbers and side tested. (bias illustrated graphically)

4.6.3 Fondu and Calcium Dialuminate Blend

The dry sand rubber wheel wear test results are summarized for both the Fondu cement and the calcium dialuminate blend cement together. Data are analyzed to determine general trends and recognize bias cause by sample preparation. The wear rate data are sorted according to the orientation of the coupon in the mold to understand the trends. Figures of the data are found in Appendix IV, Section 3. A summary guide to the plots is listed in Table 4.13.

Figure AIV.20 is a plot of the coupon density to the wear rate separated for the coupon side being tested. The water to cement ratio influence on the wear rate is shown in Figure AIV.21. Magnesia, chromia, spinel dead burnt magnesia, alumina, alumina-titania blend and cerium oxide were used to modify the matrix. Figures AIV.27, AIV.28, AIV.29, AIV.30 and AIV.31 show the wear rate change with the increasing concentrations of the various additives. The data in these Figures are separated according to the side and of the coupon tested. The maximum magnesia that can be added before the wear properties start to falloff is ~ 50% by weight fraction of the matrix. The Chromia and cerium oxide additives did not influence the wear properties with increasing concentration. The alumina titania additive resulted in poor wear resistance at all concentrations. The dead burnt magnesia population of data suggests a relatively neutral influence with the exception of several data points outside the range. The reinforcement phase influence on the wear rate is based on the batch volume fraction and the wear scar area fraction. The total area of the wear scar and the exposed reinforcement are compared to the wear rate in Figures AIV.32 and AIV.33. The trend indicates an increasing wear rate with wear scar size. These Figures are condensed into the relative ratio of the exposed reinforcement phase in the total wear scar shown in Figure AIV.34. The batch volume fraction of the reinforcement phase compared to the wear rate is shown in Figure AIV.35 for sides 1and 2. The influence of the wear scar size change and exposed reinforcement area were found independent on the side of the coupon being tested.

Table 4.13. Wear Test Results Appendix Figure Guide for the Fondu and Calcium Dialuminate Blend Batch Formulations.

Figure	Format of Data Relationship
AIV.20	Coupon density to the wear rate is separated into side 1 and side 2 (demonstrating that mixing side 1 and 2 wear rate data make separation of trends more difficult)
AIV.21	The water to cement ratio influence on the wear rate
AIV.27 AIV.28 AIV.29 AIV.30 AIV.31	Wear rate change with the changing concentration of additive separated into side 1 and side 2
AIV.32 AIV.33	The total area of the wear scar and exposed reinforcement compared to the wear rate
AIV.34	Relative ratio of the exposed reinforcement phase in the total wear scar to the wear rate
AIV.35	The batch volume fraction of the reinforcement phase compared to the wear rate is shown in for sides 1and 2

4.6.4 Influence of Additives and Reinforcements Materials

The experimental test matrix was designed to develop relationships between the wear resistance and the additive used to improve the thermal stability. The test matrix was used to formulate more than 227 batches for testing. Analysis of the results separates the different matrix, additive and reinforcement materials to develop relative trends. Plots of the relationships are found in Appendix IV Section 4. Table 4.14 lists the dry sand rubber wheel test results that compare changing concentrations of the various additives and reinforcements.

Table 4.14. Wear Test Results Appendix Figure Guide for the Influence of Additives and Reinforcements of all Cement Batch Formulations.

Figure	Format of Data Relationship
AIV.38	Dry sand rubber wheel test results show magnesia concentration influence on the wear rate
AIV.40	Dry sand rubber wheel test results show spinel concentration influence on wear rate, Coupon #2 side 2
AIV.41	Wear scar results show the exposed reinforcement influence on the wear rate. The batch reinforcement volume fractions are 10%, 20% and 25%
AIV.43	Dry sand rubber wheel test results show MgO & Cr_2O_3 1:1 Blend influence on the wear rate, Coupon #2 side 2
AIV.44	Wear scar results show MgO & Cr_2O_3 1:1 Blend influence on the wear rate, Coupons #2 and #4 sides 1 and 2
AIV.47	Dry sand rubber wheel test results show MgO & Cr_2O_3 1:2 additive influence on the wear rate, Coupon #2 side 2
AIV.48	Wear scar results show MgO & Cr_2O_3 1:2 Blend additive influence on the wear rate, Coupon #2 sides 1 and 2
AIV.50	Dry sand rubber wheel test results show MgO & Cr_2O_3 1:4 additive influence on the wear rate, Coupon #2 side 2
AIV.51	Wear scar results show the MgO & Cr_2O_3 1:4 Blend additive influence on the wear rate, Coupon #2 and #4 sides 1 and 2
AIV.53	Dry sand rubber wheel test results show changing reinforcement concentration wear rate influence by the reinforcement, range is 41 to 80%, Coupon #2 and #4 sides 1 and 2
AIV.54	Wear scar results show the control coupon wear rate conditions and influence of changing reinforcement, reinforcement range is 41 to 80%, Coupon #2 and #4 sides 1 and 2
AIV.55	Wear scar results show a comparison between exposed reinforcement and changing volume fraction of reinforcement, range is 41 to 80%, Coupon #2 and #4 sides 1 and 2

Table 4.14. Wear Test Results Appendix Figure Guide for the Influence of Additives and Reinforcements of all Cement Batch Formulations (continued).

Figure	Format of Data Relationship
AIV.58	Dry sand rubber wheel test results show influence of MgO additive, Coupon #2 sides 1 and 2
AIV.60	Dry sand rubber wheel test results show influence of MgO additive, Coupon #2 sides 1 and 2
AIV.62	Dry sand rubber wheel test results show influence of spinel additive, Coupon #2 sides 1 and 2
AIV.63	Dry sand rubber wheel test results show influence of water to cement ratio, Coupon #2 sides 1 and 2
AIV.65	Wear scar results show difference between high density grog and spinel reinforcement, MgO additive concentration constant at 50%, Coupon #2 sides 1 and 2
AIV.66	Wear scar results show difference between high density grog and spinel reinforcement. Spinel additive concentration constant at 50%, Coupon #2 sides 1 and 2
AIV.67	Dry sand rubber wheel test results show influence batch water on the wear rate, Coupon #2 sides 1 and 2
AIV.69	DSRW test results show the influence of changing reinforcement on the wear rate, reinforcement at 40, 60 and 75%.
AIV.70	Dry sand rubber wheel wear scar results show the influence of changing exposed reinforcement on the wear rate, reinforcement at 40 and 75%
AIV.72	Dry sand rubber wheel test results show influence of changing reinforcement on the wear rate, reinforcement at 40 and 60%.
AIV.73	Dry sand rubber wheel test results show influence of changing reinforcement on the wear rate, reinforcement at 40, 60 and 75%.
AIV.75	Dry sand rubber wheel test results show dead burnt magnesia influence on the wear rate, Coupon #2 sides 1 and 2, reinforcement at 40%.

Table 4.14. Wear Test Results Appendix Figure Guide for the Influence of Additives and Reinforcements of all Cement Batch Formulations (continued).

Figure	Format of Data Relationship
AIV.76	Wear scar results show the exposed reinforcement influence on the wear rate, Coupon #2 sides 1 and 2, reinforcement at 40%
AIV.79	Dry sand rubber wheel test results show dead burnt magnesia influence on the wear rate, Coupon #2 sides 1 and 2, reinforcement at 40 and 60%.
AIV.80	Dry sand rubber wheel test results show influence of reinforcement on wear rate, reinforcement at 40 and 60%, additive at 50, 66 and 75%
AIV.81	Wear scar results show exposed reinforcement influence on wear rate, Coupon #2 sides 1 and 2 reinforcement at 40 and 60% by batch weight
AIV.84	Dry sand rubber wheel test results show dead burnt magnesia influence on the wear rate, Coupon #2 side 2, reinforced at 40, 60 and 75%
AIV.85	Dry sand rubber wheel test results show the reinforcement influence on the wear rate, Coupon #2 side 2 reinforced at 40, 60 and 75%, dead burnt magnesia at 33, 50, 66, 75 wt. %
AIV.86	Wear scar results show influence of exposed reinforcement on the wear rate, Coupon #2 sides 1 and 2, reinforced at 40, 60 and 75%, dead burnt magnesia at 33, 50, 66, 75 wt. %
AIV.89	Dry sand rubber wheel wear rate results show the magnesia chromia blend additive influence on the wear rate, Coupon #2 side 2, four blends of fuse cast chromia to magnesia additive are used 1:1 Blend, 1:2 Blend, 1:4 Blend and 2:1 Blend, reinforced at 60 wt. %
AIV.90	Dry sand rubber wheel wear rate results show dead burnt magnesia and alumina blend additive influence on the wear rate, Coupon #2 sides 1 and 2, reinforced at 60 wt. %
AIV.92	Dry sand rubber wheel wear rate results show influence of alumina-titania blend additive on wear rate, Coupon #2 sides 1 and 2, reinforced at 60 wt. %

Table 4.14. Wear Test Results Appendix Figure Guide for the Influence of Additives and Reinforcements of all Cement Batch Formulations (continued).

Figure	Format of Data Relationship
AIV.93	Dry sand rubber wheel wear rate results show influence of dry dead burnt magnesia additive on the wear rate, Coupon #2 sides 1 and 2, reinforced at 60 wt. %
AIV.95	Dry sand rubber wheel wear rate results influence of cerium additive on the wear rate, Coupon #2 sides 1 and 2, reinforced at 60 wt. %
AIV.96	Wear scar results illustrates influence of magnesia-cerium oxide-cement blend exposed reinforcement, Coupon #2 sides 1 and 2, reinforced at 60 wt. %
AIV.98	Dry sand rubber wheel test results show influence of changing water on the wear rate, batch water adjusted at 2.8, 4, 6, 8 and 10 %, dead burnt magnesia additive at 50%, reinforced at 60%
AIV.100	Dry sand rubber wheel test results show influence of water on the wear rate batch water adjusted at 4, 6, 8, 10 and 12 %, dead burnt magnesia additive at 50%, reinforced at 60%

4.6.4.1 Premix Cement and MgO Additive and Zircon Reinforcement

The influence of magnesia on cement binder in the HACA premix cement is illustrated in four batches B2-7-1, B5-4-1, B5-6-1 and B5-28-1. Magnesia concentrations were formulated to 10%, 15%, 20% and 35% by weight of the total batch. The premix zircon reinforcement range was determined to range between 39 to 61%. The wear data from both sides of Coupon #2 and #4 are shown in Figure AIV.38 to illustrate the data spread between the 1000°C and 1200°C sinter and the top versus the bottom of the coupon. The wear rate increases with the increasing magnesia concentration.

4.6.4.2 Premix Cement and Spinel Additive and Zircon Reinforcement

The influence of spinel additive on cement binder in the HACA premix cement is illustrated in five batches B4-29-1, B5-1-1, B5-8-1, B5-15-1 and B5-18-1. Spinel concentrations were formulated to 10%, 20% and 25% by weight of the total batch. The premix zircon reinforcement range was formulated to range between 45 to 63 %. The wear data from both sides of Coupon #2 side 2 are shown in Figure AIV.40. The wear rate is not sensitive to the spinel concentration over the range of 20 to 50%. Figure AIV.41 illustrates the wear rate variation with the exposed wear scar reinforcement for Coupons #2 and #4 with both sides presented. The Coupon #2 side 2 wear rate data are not influenced by the change of exposed reinforcement area.

4.6.4.3 Premix Cement and MgO & Cr_2O_3 1:1 Blend Additive and Zircon Reinforcement

The influence of MgO & Cr_2O_3 1:1 blend additive on cement binder in the high alumina calcium aluminate cement is illustrated in seven batches B1-28-1, B2-16-1, B2-18-1, B3-18-1, B4-20-1, B4-24-1 and B5-22-1. The blend formulations were made at 10, 20, 25 and 35% by weight of the batch. Duplicate batches were made at 10 and 20% concentrations. The premix zircon reinforcement range was determined to range between 39% to 61%. The wear data from Coupon #2 side 2 are shown in Figure AIV.43. The wear rate was found sensitive to the blend concentration. Figure AIV.44 presents the wear scar analysis results from Coupon #2 and #4 sides 1 and 2. The data show decreasing wear rate with increasing exposed reinforcement in the wear scar.

4.6.4.4 Premix Cement and MgO & Cr_2O_3 1:2 Blend Additive and Zircon Reinforcement

The influence of MgO & Cr_2O_3 1:2 blend additive on cement binder in the high alumina calcium aluminate cement is illustrated in six batches B2-23-1, B2-25-1, B3-10-1, B3-12-1, B4-3-1 and B5-26-1. The blend formulations were made at 10, 20 and 30% by weight of the batch. Duplicate batches were made at 10 and 20% concentrations. The premix zircon reinforcement range was determined to range between 48 to 61%. The

wear data from Coupon #2 side 2 are shown in Figure AIV.47. The wear rate change with additive concentration is relatively constant or increases slightly from 20 to 50%. Figure AIV.48 presents wear scar analysis results from Coupon #2 sides 1 and 2. The wear rate is shown to decrease with the increasing reinforcement exposed.

4.6.4.5 Premix Cement and MgO & Cr_2O_3 1:4 Blend Additive and Zircon Reinforcement

The influence of MgO & Cr_2O_3 1:4 blend additive on cement binder in the high alumina calcium aluminate cement is illustrated in five B2-12-1, B3-16-1, B4-1-1, B4-22-1 and B5-20-1. The blend formulations were made at 10, 20, 30 and 35% by weight of the batch. Duplicate batches were made at 10 % additive concentration. The premix zircon reinforcement range was between 45 to 61%. The wear data from Coupon #2 side 2 are shown in Figure AIV.50. The wear rate change with additive concentration is unchanged. Figure AIV.51 presents wear scar analysis results from Coupon #2 and #4 sides 1 and 2. The wear rate is shown to decrease with the increasing reinforcement exposed.

4.6.4.6 Premix Cement and no Additives and Zircon Reinforcement

The influence of changing reinforcement concentration with out additives in the HACA premix cement is illustrated in B2-2-1, B2-4-1, B5-11-1, B5-13-1, B4-27-1, B4-6-1, B4-8-1 and B4-13-1. The premix zircon reinforcement ranged from 41 to 80% by batch weight. The compositions were adjusted by adding screened cement and reinforcement. The wear data from Coupon #2 and #4 sides 1 and 2 are shown in Figure AIV.53. The wear rate change with increasing volume fraction of the reinforcement is more dramatic for the coupons fired at 1000°C than those fired at 1200°C. A decreasing wear rate is found in each case. Figure AIV.54 presents wear scar analysis results from Coupon #2 and #4 sides 1 and 2. The wear rate trends are different for the #4 and #2 coupons. The low fired coupon exhibit an increase in the wear rate as more reinforcement is exposed in the wear scar. The high fired coupons exhibit a relative un

changing wear rate with increasing exposed reinforcement. Figure AIV.55 is a comparative illustration of the exposed reinforcement to the volume fraction. The trend is that less reinforcement is exposed than the volume fraction in the batch. The experimental method is likely to have a bias because of the three dimensional nature of the wear scar, but the significance is the grouping for the high fired and low fired coupons. The two sets of data points are batch formulations that used sifted reinforcement that produces a different reinforcement distribution.

4.6.4.7 Fondu Cement and MgO Additive and Zirconia Grog Reinforcement

The influence of changing magnesia on Fondu cement microstructure and mechanical properties is determined using ten batch formulations: B11-23-1, B12-18-2, B9-8-1, B11-30-1, B12-7-1, B12-1-1, B12-8-1, B12-2-1, B12-9-1 and B12-3-1. The data set includes additive concentrations of 0, 50, 66, 75 and 80% by weight of the batch. Three duplicate batches were made. The high-density zirconia grog reinforcement range is 50 to 60%. The wear data from Coupon #2 sides 1 and 2 are shown in Figure AIV.58. The wear rate change with additive concentration increases sharply above 50% of the matrix composition. The data as presented also indicates a difference between side one and side two. This is likely the influence of the reinforcement material and the method the coupons are cast into the mold.

4.6.4.8 Fondu Cement and MgO Additive and Spinel Reinforcement

The influence of changing magnesia on Fondu cement microstructure and mechanical properties is determined using seven batch formulations: B9-28-1, B10-26-1, B9-30-1, B10-23-1, B10-5-1, B10-7-1 and B10-12-1. The data set includes additive concentrations of 0, 50, 66, 75 and 80% by weight of the batch. One duplicate batch was made. The crushed spinel brick reinforcement range is 50 to 60%. The wear data from Coupon #2 sides 1 and 2 are shown in Figure AIV.60. The wear rate increases with added magnesia, the data exhibits more scatter than the similar set using the zirconia grog.

4.6.4.9 Fondu Cement and Spinel Additive and Spinel Reinforcement

The influence of changing spinel on the Fondu cement mechanical properties is determined using seven batch formulations: B9-28-1, B10-26-1 B10-2-1, B10-16-1, B10-14-1, B10-19-1 and B10-21-1. The data set includes additive concentrations of 0, 50, 66, 75 and 80% by weight of the batch. One duplicate batch was made. The crushed spinel brick reinforcement was held constant at 50% by batch weight. The wear rate data is from Coupon #2 sides 1 and 2 shown in Figures AIV.62 and AIV.63. The wear rate increases with added magnesia and the results from both sides of the coupon are relatively consistent.

4.6.4.10 Fondu Cement and MgO Additive and Zirconia Grog and Spinel Reinforcement

The influence of changing reinforcement material on Fondu cement at a given additive concentration is studied using six batch formulations: B9-8-1, B11-30-1, B12-7-1, B9-3-1, B9-30-1 and B10-23-1. Reagent grade magnesia was used in the batch formulations and held constant at 50% by batch weight. The reinforcement was formulated at 50 and 60% by batch weight. High-density zirconia grog and crushed spinel brick reinforcement materials were used. The wear scar analysis data from Coupon #2 sides 1 and 2 are shown in Figure AIV.65. The wear rate change with the reinforcements is relatively the same for both reinforcements with the exception of one coupon. The spinel reinforcement wear rate data has greater scatter than the zirconia grog reinforcement.

4.6.4.11 Fondu Cement and Spinel Additive and Zirconia Grog and Spinel Reinforcement

The influence of changing reinforcement material on Fondu cement at a given additive concentration is studied using six batch formulations: B9-10-1, B10-2-1, B11-23-1, B12-18-2, B9-28-1 and B10-26-1. Reagent grade spinel was used in the batch formulations and held constant at 50% by batch weight. The reinforcement was

formulated at 50 and 66% by batch weight. High-density zirconia grog and crushed spinel brick reinforcement materials were used. The wear scar analysis data from Coupon #2 sides 1 and 2 are shown in Figure AIV.66. The wear rate change with the exposed reinforcement is relatively constant for both reinforcement types.

4.6.4.12 CA_2 Cement and no Additive and no Reinforcement

The wear resistance of the calcium dialuminate blend independent of additives and reinforcement materials was determined in three batches B1-19-1, B1-20-1 and B1-29-2. The batches were formulated using three water to cement ratios to provide a boundary to assess other parameters. The wear rates for the three identical batches are shown in Figure AIV.67.

4.6.4.13 CA_2 Cement and no Additive and Dead Burnt MgO Rock Reinforcement

The wear resistance of the calcium dialuminate cement independent of additives using dead burnt magnesia rock reinforcement were determined using three batches B4-27-1, B2-22-1 and B5-12-1. The batches were formulated at concentrations of 40, 60 and 75% by batch weight. The wear rate and the wear scar analysis results are shown in Figures AIV.69 and AIV.70. The wear rate is not sensitive to the reinforcement concentration over the range formulated. The wear rate spread between the two sides is small.

4.6.4.14 CA_2 Cement and no Additives and Graded Spinel Reinforcement

The wear resistance of the calcium dialuminate blend independent of additives with graded crushed spinel brick reinforcement were determined using three batches B4-19-1, B4-2-1 and B4-5-1. The batches were formulated at concentrations of 40 and 60 %

by batch weight. The wear rate results for Coupon #2 sides 1 and 2 are shown in Figure AIV.72. The wear rate decreases with increasing reinforcement concentration. The wear rate spread between the two sides is small.

4.6.4.15 CA_2 Cement and no Additives and Zirconia Grog Reinforcement

The wear resistance of the calcium dialuminate blend independent of additives with high-density zirconia grog reinforcement was determined using five batches B3-14-1, B1-12-1, B3-12-1, B1-15-1 and B1-28-1. The batches were formulated at reinforcement concentrations of 40, 60 and 75% by batch weight. The wear rate results are shown in Figures AIV.73. The wear rate decreases with the increasing reinforcement.

4.6.4.16 CA_2 Cement and Dead Burnt MgO Additive and Dead Burnt MgO Reinforcement

The influence of dead burnt magnesia additive on the calcium dialuminate blend cement binder is illustrated in four batches B4-28-1, B4-30-1, B5-10-1 and B4-29-1. The additive was formulated at concentrations of 33, 50, 66, 75 wt. % by weight of the batch. Dead burnt magnesia rock was used for reinforcement at a concentration of 40%. The wear data from Coupon #2 side 2 are shown in Figure AIV.75. The wear rate increases with additive concentration. Figure AIV.76 presents wear scar analysis results from Coupon #2 sides 1 and 2. The wear rate is shown to decrease with the increasing reinforcement exposed.

4.6.4.17 CA_2 Cement and Dead Burnt MgO Additive and Spinel Reinforcement

The influence of dead burnt magnesia additive on the calcium dialuminate blend cement binder is illustrated in nine batches B4-20-1, B4-21-1, B4-19-1, B4-6-1, B4-15-1, B4-16-1, B4-14-1, B4-2-1 and B4-5-1. The additive was formulated at concentrations of 50, 66, 75 wt. % by weight of the batch. Influence of crushed and graded (1:4 size ratio)

spinel brick reinforcement is also included. The data includes two reinforcement concentrations 40 and 60 wt. %. The wear data from Coupon #2 sides 1 and 2 are shown in Figures AIV.79 and AIV.80. The wear rate increases with additive concentration. Figure AIV.81 presents wear scar analysis results from Coupon #2 sides 1 and 2. The wear rate is shown to decrease with the increasing reinforcement exposed.

4.6.4.18 CA_2 Cement and Dead Burnt MgO Additive and Zirconia Grog Reinforcement

The influence of dry milled dead burnt magnesia additive on the calcium dialuminate blend cement binder is illustrated in fourteen batches, B3-16-1, B3-24-1, B3-25-1, B3-23-1, B3-10-1, B2-10-1, B3-9-1, B3-11-1, B3-13-1, B3-14-1, B1-12-1, B1-15-1, B1-28-1 and B3-12-1. The magnesia was added at concentrations of 33, 50, 66, 75 wt. % by batch weight. The batches were reinforced with high-density zirconia grog at three concentrations 40, 60 and 75% by batch weight. The wear data from Coupon #2 side 2 are shown in Figure AIV.84. The wear rate is shown to increase with added magnesia concentration for all three reinforcement concentrations. Figure AIV.85 presents the Coupon #2 side 2 wear rate change as the volume fraction of reinforcement changes. The wear rate is shown to decrease with increasing reinforcement added to the matrix. The analysis of the wear scar is shown in Figure AIV.86, indicating little influence in the wear rate with increasing exposed reinforcement.

4.6.4.19 CA_2 Cement and MgO &Cr_2O_3 Additive and Zirconia Grog Reinforcement

The influence of magnesia chromia blend on the calcium dialuminate cement binder is illustrated in five batches B3-29-1, B3-26-1, B3-31-1, B3-30-1 and B4-1-1. Four blends of fused cast dense chromia to magnesia additive are used, namely, 1:1 Blend, 1:2 Blend, 1:4 Blend and 2:1 Blend. All batches were reinforced with high-density zirconia grog at 60 wt. % by batch weight. The influence of changing chromia concentration is illustrated in the wear data from Coupon #2 side 2 and shown in Figure AIV.89. The wear rate trend decreases with added chromia concentration.

4.6.4.20 CA_2 Cement and Dead Burnt MgO-Al_2O_3 Additive and Dead Burnt MgO Reinforcement

The influence of dry milled dead burnt magnesia and alumina blend on the calcium dialuminate cement was determined in five batch formulations: SP8-6-1, SP8-12-1, SP8-11-1, SP8-9-1 and SP8-10-1. Five ternary compositions of calcium aluminate blend, magnesia and alumina system were formulated. Dry milled dead burnt magnesia and milled fuse cast alumina were blended with the calcium dialuminate. All batch formulations were reinforced with 60% by weight dead burnt magnesia rock. The influence of changing magnesia and alumina concentration were determined using wear rate data. Figure AIV.90 illustrates the wear rate data from Coupon #2 sides 1 and 2. The wear rate is lower in batches formulated with greater cement. The wear rate is highest for those coupons formulated with greater alumina.

4.6.4.21 CA_2 Cement and Dead Burnt MgO and Al_2O_3-TiO_2 Additive and Dead Burnt MgO Reinforcement

The influence of dry milled dead burnt magnesia and alumina-titania blend on the calcium dialuminate cement was determined in eight batch formulations SP7-28-1, SP7-29-1, SP7-20-1, SP7-26-1, SP7-27-1, SP7-23-1, SP7-21-1 and SP7-22-1. Eight ternary compositions of calcium aluminate blend, magnesia and alumina-titania blend system were formulated. All batch formulations were reinforced with 60% by weight dead burnt magnesia rock. Influence of changing magnesia and alumina-titania concentrations were determined using wear rate. Figures AIV.92 and AIV.93 illustrate the wear rate data from Coupon #2 sides 1 and 2. The wear rate is increases with additions to the cement.

4.6.4.22 CA_2 Cement and Dead Burnt MgO-CeO_2 Additive and Dead Burnt MgO Reinforcement

The influence of dry milled dead burnt magnesia and cerium oxide on the calcium dialuminate cement was determined in five batch formulations SP7-30-1, SP8-4-1, SP8-3-1, SP7-31-1 and SP8-2-1. Five ternary compositions of the CA_2-M-Ce system were formulated to the following ratios: 1:1:1, 1:1:2, 1:2:1, 2:1:1 and 3:1:1. All batch formulations were reinforced with 60% by weight dead burnt magnesia rock. Influence of changing magnesia and cerium oxide concentrations were determined using wear rate data. Figures AIV.95 and AIV.96 illustrate the wear rate data from Coupon #2 sides 1 and 2. The wear rate increases with the addition of the blend to the cement. The wear scar analysis indicates that increasing the reinforcement increases the wear rate.

4.6.4.23 CA_2 Cement and Dead Burnt MgO Additive and Dead Burnt MgO Reinforcement

The water to cement ratio influence on the properties was determined by formulating a number of batches holding the additive and reinforcement concentrations constant and changing the quantity of batch water. At high water concentrations, the water was squeezed during pressing. To increase the water, additional batches were prepared using a vibration table that did not involve pressing and allowed the samples to cure unrestrained. The batches were formulated with constant additive and reinforcement concentrations. The batch water was adjusted at 2.8, 4, 6, 8 and 10% batch weight for the first set of pressed samples and 4, 6, 8, 10 and 12 % by batch weight for the second set of vibrated samples. Greater batch water formulations were not possible because the mix was far too runny to remain in the mold. Unrestrained batches used the same mold and the vibration energies were held to the same level on each batch. The cure time was the same for all batches. All batches were formulated with dry milled dead burnt magnesia at 50% concentration and dead burnt magnesia rock reinforcement at 60% concentration. The wear rate data are presented for the two sets. The first set included six batches SP7-6-1, SP7-7-1, SP7-8-1, SP7-9-1, SP7-12-1 and SP7-11-1. The second set included seven batches compacted on a vibration table SP7-13-1, SP7-14-1, SP7-15-1, SP7-16-1, SP7-17-1, SP7-18-1 and SP7-19-1. The wear properties for the first set are shown in Figure AIV.98. The wear rate data from Coupon #2 sides 1 and 2 indicate little change with

changing water over the range tested. The batch water concentration influence on the wear rate is shown in Figure AIV.100.

4.7 Compression Strength Test Results

4.7.1 Synopsis of Compression Strength Test Results

The cold compressive strength test methods are used to produce comparisons and relative rankings of the different refractory formulations. The compression test is destructive using a simple sample geometry. Multiple samples, reference brick samples and duplicate samples were used. A discussion of the reference coupons is included in Appendix III. The cold compression strength test results are presented in Table 4.15.

The cold compression strength test applies a load to the coupon at a constant rate until a maximum load is reached. Internal cracking lead to the shedding of material from the sides of the sample forming an hourglass like appearance before the sample ended up pulverized into a dust. The compressive load could be stopped after reaching maximum load before crumbling and complete destruction to maintain intact coupons. Several of these coupons were carefully preserved for fracture surface examination. Magnified observations were made using stereo microscope between 7 and 50 times magnification. The fracture crack direction in most cases was parallel to the applied compressive load. The multiple cracking events were observed as well as the crack path through or around the reinforcement.

Test coupons from all cement matrix materials appeared to initiate fracture internally. Debris from the coupons was sifted and reinforcement pieces were pulled out for examination. The reinforcement particle surfaces were mostly clean from coupons formulated with the Fondu cement, especially the zirconia grog. Relatively little cement residue was attached even in the deep reinforcement surface pores. The observation was less evident in the chromia formulated coupons but especially prominent in the high magnesia and spinel additive formulations. The cement was not bonding with the reinforcement.

Table 4.15. Compression Strength Test Results.

BATCH NUMBER DESCRIPTION	**B1-28-1**	**B2-4-1**	**B2-12-1**	**B2-16-1**	**B2-18-1**	**B2-23-1**	**B2-25-1**	**B3-2-1**
Additive Cement	1:1 M-K Premix	Control Premix	1:4 M-K Premix	1:1 M-K Premix	1:1 M-K Premix	1:2 M-K Premix	1:2 M-K Premix	2:1 M-K Premix
Cement, % of Batch	26.0	40.0	30.0	30.0	32.0	32.0	36.0	30.0
Reinforcement, % Batch	39.0	60.0	45.1	45.0	48.0	48.1	54.0	45.1
Additive % of Batch	35.0		24.9	25.0	20.0	19.9	10.0	24.9
Wt.% H_2O, Total	7.0	7.3	7.2	6.9	7.0	6.9	6.9	7.4
W/C ratio	0.27	0.18	0.24	0.23	0.22	0.21	0.19	0.24
MATRIX COMPOSITION								
Additive % of Matrix	57.4	0.0	45.3	45.5	38.5	38.3	21.7	45.3
Cement % of Matrix	42.6	100.0	54.7	54.5	61.5	61.7	78.3	54.7
Chromia, Cr_2O_3	28.7%		9.1%	22.7%	19.2%	12.6%	7.2%	29.9%
Magnesia, MgO	28.7%		36.3%	22.7%	19.2%	25.3%	14.3%	15.0%
Spinel, $MgAl_2O_4$								
Alumina, Al_2O_3	34.1%	80.0%	43.7%	43.6%	49.2%	49.3%	62.6%	43.8%
Calcia, CaO	4.3%	10.0%	5.5%	5.5%	6.2%	6.2%	7.8%	5.5%
Silica, SiO_2	4.3%	10.0%	5.5%	5.5%	6.2%	6.2%	7.8%	5.5%
COMPRESSION TEST								
Cold Crushing Strength								
Coupon 1								
Sample A, psi	**3286**		**1503**		**4512**		**5009**	
Sample B, psi	**3700**		**686**		**3747**		**5080**	
Coupon 3								
Full Size Sample, psi	**6001**	**4763**	**1688**	**7823**	**4121**	**6110**	**10837**	**6194**

Table 4.15. Compression Strength Test Results (continued).

BATCH NUMBER DESCRIPTION	**B3-4-1**	**B3-6-1**	**B3-10-1**	**B3-12-1**	**B3-16-1**	**B3-18-1**	**B3-30-1**	**B4-1-1**
Additive Cement	2:1 M-K Premix	2:1 M-K Premix	1:2 M-K Premix	1:2 M-K Premix	1:4 M-K Premix	1:1 M-K Premix	2:1 M-K Premix	1:4 M-K Premix
Cement, % of Batch	34.0	29.6	31.5	24.7	24.7	24.7	24.7	19.4
Reinforcement, % Batch	51.0	62.8	59.8	59.9	59.9	59.9	59.9	60.0
Additive % of Batch	15.0	7.6	8.6	15.4	15.4	15.4	15.4	20.6
Wt.% H_2O, Total	7.0	8.5	6.9	6.9	6.9	6.9	6.9	7.8
W/C ratio	0.21	0.24	0.19	0.21	0.21	0.21	0.21	0.28
MATRIX COMPOSITION								
Additive % of Matrix	30.6	20.5	21.5	38.3	38.3	38.3	38.3	51.6
Cement % of Matrix	69.4	79.5	78.5	61.7	61.7	61.7	61.7	48.4
Chromia, Cr_2O_3	20.2%	13.5%	7.1%	12.6%	7.7%	19.2%	25.3%	10.3%
Magnesia, MgO	10.1%	6.8%	14.2%	25.3%	30.7%	19.2%	12.6%	41.3%
Spinel, $MgAl_2O_4$								
Alumina, Al_2O_3	55.5%	63.6%	62.8%	49.3%	49.3%	49.3%	49.3%	38.7%
Calcia, CaO	6.9%	8.0%	7.9%	6.2%	6.2%	6.2%	6.2%	4.8%
Silica, SiO_2	6.9%	8.0%	7.9%	6.2%	6.2%	6.2%	6.2%	4.8%
COMPRESSION TEST								
Cold Crushing Strength								
Coupon 1								
Sample A, psi	**6312**							
Sample B, psi	**6312**							
Coupon 3								
Full Size Sample, psi	**9686**	**8708**	**9735**	**7613**	**4332**	**7858**	**11254**	**3836**

Table 4.15. Compression Strength Test Results (continued).

BATCH NUMBER DESCRIPTION	**B4-3-1**	**B4-6-1**	**B4-8-1**	**B4-13-1**	**B4-16-1**	**B4-20-1**	**B4-22-1**	**B4-24-1**
Additive	1:2 M-K	EC	EC	EC	Cr_2O_3	1:1 M-K	1:4 M-K	1:1 M-K
Cement	Premix	Premix	Premix	Premix	Premix	Premix	Premix	Premix
Cement, % of Batch	19.4	42.6	44.0	44.8	36.0	36.0	36.0	36.0
Reinforcement, % Batch	60.0	44.4	36.1	31.5	54.1	54.1	54.1	54.1
Additive % of Batch	20.6	13.0	19.9	23.8	9.9	9.9	9.9	9.9
Wt.% H_2O, Total	7.8	7.4	7.5	6.6	7.4	7.4	7.4	7.4
W/C ratio	0.28	0.15	0.14	0.11	0.21	0.21	0.21	0.21
MATRIX COMPOSTION								
Additive % of Matrix	51.6	23.4	31.2	34.7	21.6	21.6	21.6	21.6
Cement % of Matrix	48.4	53.1	37.6	30.7	78.4	78.4	78.4	78.4
Chromia, Cr_2O_3	17.0%				21.6%	10.8%	4.3%	10.8%
Magnesia, MgO	34.1%					10.8%	17.3%	10.8%
Spinel, $MgAl_2O_4$								
Alumina, Al_2O_3	38.7%	80.0%	80.0%	80.0%	62.7%	62.7%	62.7%	62.7%
Calcia, CaO	4.8%	10.0%	10.0%	10.0%	7.8%	7.8%	7.8%	7.8%
Silica, SiO_2	4.8%	10.0%	10.0%	10.0%	7.8%	7.8%	7.8%	7.8%
COMPRESSION TEST								
Cold Crushing Strength, psi								
Coupon 1								
Sample A					**5874**	**4934**		
Sample B					**7422**	**4137**		
Coupon 3								
Full Size Sample	**4659**	**4198**	**2587**	**3836**	**4544**	**4075**	**7148**	**4813**

Table 4.15. Compression Strength Test Results (continued).

BATCH NUMBER DESCRIPTION	**B4-27-1**	**B4-29-1**	**B5-1-1**	**B5-4-1**	**B5-6-1**	**B5-8-1**	**B5-13-1**	**B5-15-1**
Additive	EC	Spinel	Spinel	MgO	MgO	Spinel	EA	Spinel-EA
Cement	Premix	Premix	Premix	Premix	Premix	Premix	Premix	Premix
Cement, % of Batch	41.8	36.0	30.0	36.0	32.0	32.1	20.0	20.0
Reinforcement, % Batch	49.2	54.1	45.1	54.1	48.0	48.1	80.0	63.3
Additive % of Batch	9.0	9.9	24.9	9.9	20.0	19.9	0.0	16.6
Wt.% H_2O, Total	7.4	7.4	7.4	7.4	7.5	7.5	8.4	7.5
W/C ratio	0.16	0.21	0.24	0.21	0.23	0.23	0.21	0.25
MATRIX COMPOSITION								
Additive % of Matrix	17.7	21.6	45.3	21.6	38.5	38.3	0.0	45.4
Cement % of Matrix	64.5	78.4	54.7	78.4	61.5	61.7	100.0	54.6
Chromia, Cr_2O_3								
Magnesia, MgO				21.6%	38.5%			
Spinel, $MgAl_2O_4$		21.6%	45.3%			38.3%		45.4%
Alumina, Al_2O_3	80.0%	62.7%	43.8%	62.7%	49.2%	49.4%	80.0%	43.7%
Calcia, CaO	10.0%	7.8%	5.5%	7.8%	6.1%	6.2%	10.0%	5.5%
Silica, SiO_2	10.0%	7.8%	5.5%	7.8%	6.1%	6.2%	10.0%	5.5%
COMPRESSION TEST								
Cold Crushing Strength								
Coupon 1								
Sample A, psi		**6084**	**4942**	**5861**		**4405**		
Sample B, psi		**6427**	**8355**	**7262**		**2538**		
Coupon 3								
Full Size Sample, psi	**5625**	**6550**	**4019**	**4606**	**4001**	**4069**	**4956**	**5133**

Table 4.15. Compression Strength Test Results (continued).

BATCH NUMBER DESCRIPTION	**B5-18-1**	**B5-20-1**	**B5-22-1**	**B5-26-1**	**B5-28-1**
Additive	Spinel-EA	1:4 Blend-EA	1:1 Blend-EA	1:2 Blend-EA	MgO-EA
Cement	Premix	Premix	Premix	Premix	Premix
Cement, % of Batch	30.6	30.6	30.6	30.6	30.6
Reinforcement, % Batch	61.1	61.1	61.1	61.1	61.1
Additive % of Batch	8.3	8.3	8.3	8.3	8.3
Wt.% H_2O, Total	7.5	7.5	7.5	7.5	7.5
W/C ratio	0.21	0.21	0.21	0.21	0.21
MTRIX COMPOSITION					
Additive % of Matrix	21.3	21.3	21.3	21.3	21.3
Cement % of Matrix	78.7	78.7	78.7	78.7	78.7
Chromia, Cr_2O_3		4.3%	10.7%	7.5%	
Magnesia, MgO		17.1%	10.7%	13.5%	21.3%
Spinel, $MgAl_2O_4$	21.3%				
Alumina, Al_2O_3	62.9%	62.9%	62.9%	62.9%	62.9%
Calcia, CaO	7.9%	7.9%	7.9%	7.9%	7.9%
Silica, SiO_2	7.9%	7.9%	7.9%	7.9%	7.9%
COMPRESSION TEST					
Cold Crushing Strength Coupon 3					
Full Size Sample, psi	**7204**	**4183**	**7498**	**6753**	**6886**

Table 4.15. Compression Strength Test Results (continued).

BATCH NUMBER DESCRIPTION	B8-28-1	B9-1-1	B9-3-1	B10-2-1	B10-5-1	B10-7-1	B10-12-1
Reinforcement	Zircon	None	None	Spinel	Spinel	Spinel	Spinel
Cement and Additive	CA	CA	CA-MgO	CA-Sp	CA	CA-MgO	CA-MgO
Cement, % of Batch	50	100	50	25	50	12	10
Reinforcement, % Batch	50			50	50	50	50
Additive % of Batch			50	25		38	40
Wt.% H_2O, Total	7.5%	7.1%	7.1%	6.7%	7.0%	7.0%	7.0%
W/C ratio	0.15	0.07	0.14	0.27	0.14	0.56	0.70
MATRIX COMPOSITION							
Additive % of Matrix	None	None	50	50	None	75	80
Cement % of Matrix	100	100	50	50	100	25	20
Alumina, Al_2O_3 as CA or CA_3	40.0%	40.0%	20.0%	20.0%	40.0%	10.0%	8.0%
Calcia, CaO as CA or CA_2	45.0%	45.0%	22.5%	22.5%	45.0%	11.3%	9.0%
Iron Oxide, Fe_3O_4 as C_4AF	13.0%	13.0%	6.5%	6.5%	13.0%	3.3%	2.6%
Silica, SiO_2 as C_2S or C_3S	2.0%	2.0%	1.0%	1.0%	2.0%	0.5%	0.4%
Chromia, Cr_2O_4							
Titania-Alumina $TiO{\cdot}Al_2O_3$							
Magnesia, MgO			50.0%			75.0%	80.0%
Spinel, $MgAl_2O_4$				50.0%			
Dead Burnt Magnesia, MgO							
COMPRESSION TEST							
Cold Crushing Strength							
Coupon 3							
Sample A, psi	**3707**	**3457**	**7213**	**6311**	**2979**	**2173**	**4094**
Sample B, psi		**3136**	**4169**			**1334**	**2515**

Table 4.15. Compression Strength Test Results (continued).

BATCH NUMBER DESCRIPTION	B10-14-1	B10-16-1	B10-19-1	B10-21-1	B10-26-1	B11-23-1	B11-30-1	B12-3-1
Reinforcement	Spinel	Spinel	Spinel	Spinel	Spinel	Zr-Grog	Zr-Grog	Zr-Grog
Cement and Additive	Ca-Sp	Ca-Sp	CA-Sp	CA-Sp	CA	CA	CA-MgO	CA-MgO
Cement, % of Batch	25	17	13	10	50	50	20	08
Reinforcement, % Batch	50	50	50	50	50	50	60	60
Additive % of Batch	25	33	38	40			20	32
Wt.% H_2O, Total	7.0%	7.1%	7.0%	7.0%	9.3%	10.0%	4.0%	4.0%
W/C ratio	0.28	0.42	0.56	0.70	0.19	0.20	0.20	0.50
MATRIX COMPOSITION								
Additive % of Matrix	50	67	75	80	None	None	50	80
Cement % of Matrix	50	33	25	20	100	100	50	20
Alumina, Al_2O_3 as CA or CA_3	20.0%	13.3%	10.0%	8.0%	40.0%	40.0%	20.0%	8.0%
Calcia, CaO as CA or CA_2	22.5%	15.0%	11.3%	9.0%	45.0%	45.0%	22.5%	9.0%
Iron Oxide, Fe_3O_4 as C_4AF	6.5%	4.3%	3.3%	2.6%	13.0%	13.0%	6.5%	2.6%
Silica, SiO_2 as C_2S or C_3S	1.0%	0.7%	0.5%	0.4%	2.0%	2.0%	1.0%	0.4%
Magnesia, MgO							50.0%	80.0%
Spinel, $MgAl_2O_4$	50.0%	66.7%	75.0%	80.0%				
COMPRESSION TEST								
Cold Crushing Strength								
Coupon 1								
Sample A, psi	**4472**		**2619**	**635**				
Sample B, psi	**3760**		**3166**					
Coupon 3								
Sample A, psi	**6730**	**2310**	**3407**	**1269**	**3273**	**4873**	**3482**	**581**
Sample B, psi		**2295**	**3842**	**1144**				

Table 4.15. Compression Strength Test Results (continued).

BATCH NUMBER DESCRIPTION	B12-7-1	B12-8-1	B1-12-1	B1-15-1	B1-19-1	B1-20-1	B1-29-2	B2-10-1
Reinforcement	Zr-Grog	Zr-Grog	Zr-Grog	Zr-Grog	None	None	None	Zr-Grog
Cement and Additive	CA-MgO	CA-MgO	CA_2	CA_2	CA_2	CA_2	CA_2	CA_2-MgO
Cement, % of Batch	20	14	40	40	100	100	100	20
Reinforcement, % Batch	59	59	60	60				60
Additive % of Batch	20	27						20
Wt.% H_2O, Total	5.7%	5.7%	7.4%	10.0%	10.0%	20.0%	25.0%	7.6%
W/C ratio	0.28	0.42	0.18	0.25	0.10	0.20	0.25	0.38
MATRIX COMPOSITION								
Additive % of Matrix	50	67	None	None	None	None	None	50
Cement % of Matrix	50	33	100	100	100	100	100	50
Alumina, Al_2O_3 as CA or CA_3	20.0%	13.3%	62.0%	62.0%	62.0%	62.0%	62.0%	31.0%
Calcia, CaO as CA or CA_2	22.5%	15.0%	30.0%	30.0%	30.0%	30.0%	30.0%	15.0%
Iron Oxide, Fe_3O_4 as C_4AF	6.5%	4.3%	5.0%	5.0%	5.0%	5.0%	5.0%	2.5%
Silica, SiO_2 as C_2S or C_3S	1.0%	0.7%	3.0%	3.0%	3.0%	3.0%	3.0%	1.5%
Magnesia, MgO	50.0%	66.7%						
Spinel, $MgAl_2O_4$								
Dead Burnt Magnesia, MgO								50.0%
COMPRESSION TEST								
Cold Crushing Strength								
Coupon 1								
Full Size Sample, psi						**3906**		**3912**
Coupon 3								
Sample A, psi	**2278**	**1774**	**4542**	**3076**	**4819**	**4041**	**2153**	**5068**
Sample B, psi						**4782**		

Table 4.15. Compression Strength Test Results (continued).

BATCH NUMBER DESCRIPTION	B2-14-2	B3-10-1	B3-11-1	B3-12-1	B3-16-1	B3-23-1	B3-24-1	B3-25-1
Reinforcement	None	Zr-Grog	Zr-Grog	Zr-Grog	Zr-Grog	Zr-Grog	Zr-Grog	Zr-Grog
Cement and Additive	CA_2	CA_2-MgO	CA_2-MgO	CA_2	CA_2-MgO	CA_2-MgO	CA_2-MgO	CA_2-MgO
Cement, % of Batch	100	13	13	25	30	40	20	15
Reinforcement, % Batch		60	75	75	40	40	40	40
Additive % of Batch		27	13		30	20	40	45
Wt.% H_2O, Total	25.0%	4.4%	4.3%	5.4%	4.0%	4.4%	4.0%	4.0%
W/C ratio	0.25	0.33	0.34	0.22	0.13	0.11	0.20	0.27
MATRIX COMPOSITION								
Additive % of Matrix	None	67	50	None	50	33	67	75
Cement % of Matrix	100	33	50	100	50	67	33	25
Alumina, Al_2O_3 as CA or CA_3	40.0%	20.7%	31.0%	62.0%	31.0%	41.3%	20.7%	15.5%
Calcia, CaO as CA or CA_2	45.0%	10.0%	15.0%	30.0%	15.0%	20.0%	10.0%	7.5%
Iron Oxide, Fe_3O_4 as C_4AF	13.0%	1.7%	2.5%	5.0%	2.5%	3.3%	1.7%	1.3%
Silica, SiO_2 as C_2S or C_3S	2.0%	1.0%	1.5%	3.0%	1.5%	2.0%	1.0%	0.8%
Spinel, $MgAl_2O_4$								
Dead Burnt Magnesia, MgO		66.7%	50.0%		50.0%	33.3%	66.7%	75.0%
COMPRESSION TEST								
Cold Crushing Strength								
Coupon 1								
Full Size Sample, psi	**1575**	**2097**	**2139**	**3084**			**1806**	**2123**
Coupon 3								
Sample A, psi		**2956**	**3634**	**3735**	**5390**	**2711**	**6116**	**4272**
Sample B, psi					**4713**	**3189**	**3321**	**3240**

Table 4.15. Compression Strength Test Results (continued).

BATCH NUMBER DESCRIPTION	B3-26-1	B4-6-1	B4-14-1	B4-15-1	B4-16-1
Reinforcement	Zr-Grog	Graded Sp	Graded Sp	Graded Sp	Graded Sp
Cement and Additive	CA_2-K-M	CA_2-M	CA_2	CA_2-M	CA_2-M
Cement, % of Batch	20	20	40	13	10
Reinforcement, % Batch	60	60	60	60	60
Additive % of Batch	20	20		27	30
Wt.% H_2O, Total	4.8%	4.8%	4.8%	4.8%	4.8%
W/C ratio	0.24	0.24	0.12	0.35	0.48
MATRIX COMPOSITION					
Additive % of Matrix	50	50	None	66	75
Cement % of Matrix	50	50	100	34	25
Alumina, Al_2O_3 as CA or CA_3	31.0%	31.0%	62.0%	20.9%	15.5%
Calcia, CaO as CA or CA_2	15.0%	15.0%	30.0%	10.1%	7.5%
Iron Oxide, Fe_3O_4 as C_4AF	2.5%	2.5%	5.0%	1.7%	1.3%
Silica, SiO_2 as C_2S or C_3S	1.5%	1.5%	3.0%	1.0%	0.8%
Chromia, Cr_2O_4	16.8%				
Magnesia, MgO	33.2%				
Dead Burnt Magnesia, MgO		50.0%		66.3%	75.0%
COMPRESSION TEST					
Cold Crushing Strength					
Coupon 1					
Full Size Sample, psi		**3636**			
Coupon 3					
Sample A, psi	**6147**		**4164**	**2794**	**5238**
Sample B, psi			**3996**	**6075**	**4892**

Table 4.15. Compression Strength Test Results (continued).

BATCH NUMBER DESCRIPTION	B4-20-1	B4-21-1	B4-27-1	B4-28-1	B4-29-1	B4-30-1
Reinforcement	Graded Sp	Graded Sp	DB-Rock	DB-Rock	DB-Rock	DB-Rock
Cement and Additive	CA_2-M	CA_2-M	CA_2	CA_2-M	CA_2-M	CA_2-M
Cement, % of Batch	30	20	60	30	40	20
Reinforcement, % Batch	40	40	40	40	40	40
Additive % of Batch	30	40		30	20	40
Wt.% H_2O, Total	5.4%	5.4%	5.4%	5.4%	5.4%	5.4%
W/C ratio	0.18	0.27	0.09	0.18	0.14	0.27
MATRIX COMPOSITION						
Additive % of Matrix	50	67	None	50	33	67
Cement % of Matrix	50	33	100	50	67	33
Alumina, Al_2O_3 as CA or CA_3	31.0%	20.7%	62.0%	31.0%	41.3%	20.7%
Calcia, CaO as CA or CA_2	15.0%	10.0%	30.0%	15.0%	20.0%	10.0%
Iron Oxide, Fe_3O_4 as C_4AF	2.5%	1.7%	5.0%	2.5%	3.3%	1.7%
Silica, SiO_2 as C_2S or C_3S	1.5%	1.0%	3.0%	1.5%	2.0%	1.0%
Spinel, $MgAl_2O_4$						
Dead Burnt Magnesia, MgO	50.0%	66.7%	0.0%	50.0%	33.3%	66.7%
COMPRESSION TEST						
Cold Crushing Strength						
Coupon 1						
Full Size Sample, psi					**3304**	**4132**
Coupon 3						
Sample A, psi	**7401**	**6601**	**6598**	**5652**	**4939**	**5036**
Sample B, psi	**4130**	**4016**		**4110**	**4359**	**6056**

Table 4.15. Compression Strength Test Results (continued).

BATCH NUMBER DESCRIPTION	B5-3-1	B5-4-1	B5-10-1	B5-12-1	SP7-6-1	SP7-7-1	SP7-8-1	SP7-9-1
Reinforcement			DB-Rock	DB-Rock	DB-Rock	DB-Rock	DB-Rock	DB-Rock
Cement and Additive	Cement	Cement	CA_2-MgO	CA_2	CA_2	CA_2	CA_2	CA_2
Cement, % of Batch	40	40	15	25	20	20	27	27
Reinforcement, % Batch	60	60	40	75	60	60	60	60
Additive % of Batch			45		20	20	13	13
Wt.% H_2O, Total	6.0%	5.6%	5.4%	5.4%	2.8%	4.0%	4.0%	6.0%
W/C ratio	0.15	0.14	0.36	0.22	0.14	0.20	0.15	0.23
MATRIX COMPOSITION								
Additive % of Matrix	None	None	75	None	50	50	33	33
Cement % of Matrix	100	100	25	100	50	50	67	67
Alumina, Al_2O_3 as CA or CA_3	62.0%	62.0%	15.5%	62.0%	31.0%	31.0%	41.3%	41.3%
Calcia, CaO as CA or CA_2	30.0%	30.0%	7.5%	30.0%	15.0%	15.0%	20.0%	20.0%
Iron Oxide, Fe_3O_4 as C_4AF	5.0%	5.0%	1.3%	5.0%	2.5%	2.5%	3.3%	3.3%
Silica, SiO_2 as C_2S or C_3S	3.0%	3.0%	0.8%	3.0%	1.5%	1.5%	2.0%	2.0%
Dead Burnt Magnesia, MgO			75.0%		50.0%	50.0%	33.3%	33.3%
COMPRESSION TEST								
Cold Crushing Strength								
Coupon 1								
Full Size Sample, psi	**2321**	**5305**			**4350**	**5255**	**6030**	**6947**
Coupon 3								
Sample A, psi			**5862**	**2235**	**4012**	**2957**	**3585**	**3856**
Sample B, psi			**6348**	**2299**	**3318**	**1983**	**3780**	**4051**
Coupon 5								
Full Size Sample, Green, psi	**2157**	**3727**			**6108**	**11848**	**11635**	**8521**

Table 4.15. Compression Strength Test Results (continued).

BATCH NUMBER DESCRIPTION	SP7-12-1	SP7-13-1	SP7-14-1	SP7-15-1	SP7-16-1	SP7-17-1	SP7-18-1	SP7-19-1
Reinforcement	DB-Rock	DB-Rock	DB-Rock	DB-Rock	DB-Rock	DB-Rock	DB-Rock	DB-Rock
Cement and Additive	CA_2	CA_2	CA_2	CA_2	CA_2	CA_2	CA_2	CA_2
Cement, % of Batch	27	20	20	20	20	27	27	27
Reinforcement, % Batch	60	60	60	60	60	60	60	60
Additive % of Batch	13	20	20	20	20	13	13	13
Wt.% H_2O, Total	8.0%	4.0%	6.0%	8.0%	12.0%	6.0%	8.0%	10.0%
W/C ratio	0.30	0.20	0.30	0.40	0.60	0.23	0.30	0.38
MATRIX COMPOSITION								
Additive % of Matrix	33	50	50	50	50	33	33	33
Cement % of Matrix	67	50	50	50	50	67	67	67
Alumina, Al_2O_3 as CA or CA_3	41.3%	31.0%	31.0%	31.0%	31.0%	41.3%	41.3%	41.3%
Calcia, CaO as CA or CA_2	20.0%	15.0%	15.0%	15.0%	15.0%	20.0%	20.0%	20.0%
Iron Oxide, Fe_3O_4 as C_4AF	3.3%	2.5%	2.5%	2.5%	2.5%	3.3%	3.3%	3.3%
Silica, SiO_2 as C_2S or C_3S	2.0%	1.5%	1.5%	1.5%	1.5%	2.0%	2.0%	2.0%
Dead Burnt Magnesia, MgO	33.3%	50.0%	50.0%	50.0%	50.0%	33.3%	33.3%	33.3%
COMPRESSION TEST								
Cold Crushing Strength								
Coupon 1								
Full Size Sample, psi	**4182**	**4556**	**3750**	**3972**		**4002**	**3948**	**2895**
Coupon 3								
Sample A, psi	**852**	**2272**	**961**	**1262**	**1220**	**1580**	**2014**	**1362**
Sample B, psi	**1371**	**2059**	**1159**	**1182**	**774**	**1917**	**2156**	**1097**
Coupon 5								
Full Size Sample, Green, psi	**9525**	**2287**	**3692**	**3881**	**3268**	**3765**	**4273**	**4292**

Table 4.15. Compression Strength Test Results (continued).

BATCH NUMBER DESCRIPTION	SP7-21-1	SP7-22-1	SP7-23-1	SP7-26-1	SP7-27-1	SP7-28-1	SP7-29-1	SP7-30-1
Reinforcement	DB-Rock	DB-Rock	DB-Rock	DB-Rock	DB-Rock	DB-Rock	DB-Rock	DB-Rock
Cement and Additive	CA_2-M-AT	CA_2-M-AT	CA_2-M-AT	CA_2-M-AT	CA_2-M-AT	CA_2-M-AT	CA_2-M-AT	CA_2-M-Ce
Cement, % of Batch	20	24	10	10	08	20	13	13
Reinforcement, % Batch	60	60	60	60	60	60	60	60
Additive % of Batch	20	16	30	30	32	20	27	27
Wt.% H_2O, Total	4.0%	4.0%	4.0%	4.0%	4.0%	4.0%	4.0%	4.0%
W/C ratio	0.20	0.17	0.40	0.40	0.50	0.20	0.30	0.30
MATRIX COMPOSITION								
Additive % of Matrix	50	40	75	75	80	50	67	67
Cement % of Matrix	50	60	25	25	20	50	33	33
Alumina, Al_2O_3 as CA or CA_3	31.0%	37.2%	15.5%	15.5%	12.4%	31.0%	20.7%	20.7%
Calcia, CaO as CA or CA_2	15.0%	18.0%	7.5%	7.5%	6.0%	15.0%	10.0%	10.0%
Iron Oxide, Fe_3O_4 as C_4AF	2.5%	3.0%	1.3%	1.3%	1.0%	2.5%	1.7%	1.7%
Silica, SiO_2 as C_2S or C_3S	1.5%	1.8%	0.8%	0.8%	0.6%	1.5%	1.0%	1.0%
Titania-Alumina $TiO{\cdot}Al_2O_3$	25.0%	20.0%	25.0%	50.0%	60.0%	50.0%	66.7%	
Dead Burnt Magnesia, MgO	25.0%	20.0%	50.0%	25.0%	20.0%			33.3%
Cerium Oxide, CeO								33.3%
COMPRESSION TEST								
Cold Crushing Strength								
Coupon 1								
Full Size Sample, psi	**3334**	**2730**	**1178**	**1831**	**1375**	**2637**	**2434**	**5186**
Coupon 3								
Full Size Sample, psi	**3989**	**6253**	**1607**	**1969**	**1969**	**2951**	**3391**	**4233**

Table 4.15. Compression Strength Test Results (continued).

BATCH NUMBER DESCRIPTION	SP8-2-1	SP8-3-1	SP8-4-1	SP8-6-1	SP8-9-1	SP8-10-1	SP8-11-1	SP8-12-1
Reinforcement	DB-Rock	DB-Rock	DB-Rock	DB-Rock	DB-Rock	DB-Rock	DB-Rock	DB-Rock
Cement and Additive	CA_2-M-Ce	CA_2-M-Ce	CA_2-M-Ce	CA_2-M-A	CA_2-M-A	CA_2-M-A	CA_2-M-A	CA_2-M-A
Cement, % of Batch	24	10	10	13	20	24	10	10
Reinforcement, % Batch	60	60	60	60	60	60	60	60
Additive % of Batch	16	30	30	27	20	16	30	30
Wt.% H_2O, Total	4.0%	4.0%	4.0%	4.0%	4.0%	4.0%	4.0%	4.0%
W/C ratio	0.17	0.40	0.40	0.30	0.20	0.17	0.40	0.40
MATRIX COMPOSITION								
Additive % of Matrix	40	75	75	67	50	40	075	75
Cement % of Matrix	60	25	25	33	50	60	25	25
Alumina, Al_2O_3 as CA or CA_3	37.2%	15.5%	15.5%	20.7%	31.0%	37.2%	15.5%	15.5%
Calcia, CaO as CA or CA_2	18.0%	7.5%	7.5%	10.0%	15.0%	18.0%	7.5%	7.5%
Iron Oxide, Fe_3O_4 as C_4AF	3.0%	1.3%	1.3%	1.7%	2.5%	3.0%	1.3%	1.3%
Silica, SiO_2 as C_2S or C_3S	1.8%	0.8%	0.8%	1.0%	1.5%	1.8%	0.8%	0.8%
Dead Burnt Magnesia, MgO	20.0%	50.0%	25.0%	33.3%	25.0%	20.0%	50.0%	25.0%
Alumina, Al_2O_4				33.3%	25.0%	20.0%	25.0%	50.0%
Cerium Oxide, CeO	20.0%	25.0%	50.0%					
COMPRESSION TEST								
Cold Crushing Strength								
Coupon 1								
Full Size Sample, psi	**4128**	**3837**	**1704**	**1524**	**2998**	**3189**	**934**	**527**
Coupon 3								
Full Size Sample, psi	**6511**	**3283**	**5811**	**3697**	**3848**	**5016**	**965**	**537**

Low additive formulations were observed to retain more of the cement on the surface but much less than the coupons formulated using the spinel reinforcement. Cement debris was found on all of the zircon reinforcement pieces formulated using the high alumina calcium aluminate premix cement. Calcium dialuminate cement debris was found on coupons formulated using zirconia reinforcement, spinel and dead burnt magnesia rock. However, that the debris on the dead burnt magnesia rock reinforcement was not as adherent as the zirconia and spinel reinforcements.

Examples of the CCS test coupons are shown in the set of Figures 4.60 through 4.65. The coupons were prepared by pressure casting a standard clear mounting epoxy to preserve the condition and enable polishing to highlight the cracks and other features. In each Figure the load was applied from the top and bottom surfaces, parallel with the image plane. Figure 4.60 shows the cross section of test coupon B4-20-3. The coupon was formulated using calcium dialuminate cement matrix and dead burnt magnesia additive at 1:1 ratio. Reinforcement is graded crushed spinel at 40% concentration. Cracking followed a matrix path. Figure 4.61 shows the cross section test coupon B4-21-3 formulated using calcium dialuminate cement matrix and dead burnt magnesia additive at 1:2 ratio. Reinforcement is graded crushed spinel at 40% concentration. Figure 4.62 shows the cross section of test coupon B3-24-3 formulated with calcium dialuminate cement matrix and dead burnt magnesia additive at 1:2 ratio. Reinforcement is high density zirconia grog at 40% concentration. Cracking is observed to follow the path adjacent to the reinforcement and two examples of cracks through the reinforcement are shown.

Figures 4.63, 4.64 and 4.65 show cross sections of coupons B4-27-3, B4-29-3 and B4-30-3. These illustrate a set of compression test specimens formulated with calcium dialuminate cement matrix and reinforced with dead burnt magnesia rock at 40% concentration. The concentration of the dead burnt magnesia additive changes from 0% to 33% to 66% of the matrix, respectively. The observed cracking follows the inter reinforcement path in each of the prepared coupon surfaces.

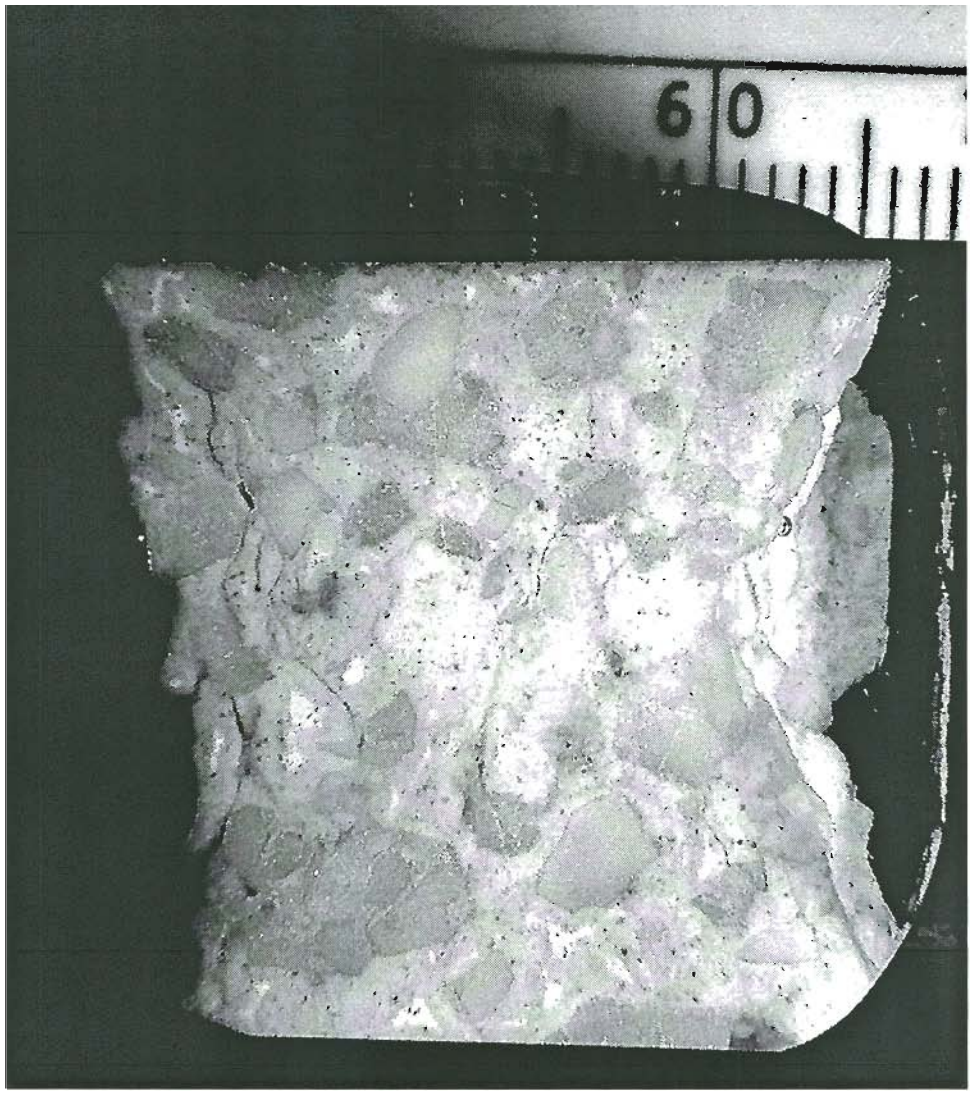

Figure 4.60. Cross section of cold compression test coupon B4-20-3. Calcium dialuminate cement matrix and dead burnt magnesia additive at 1:1 ratio. Reinforcement is graded crushed spinel at 40% concentration.

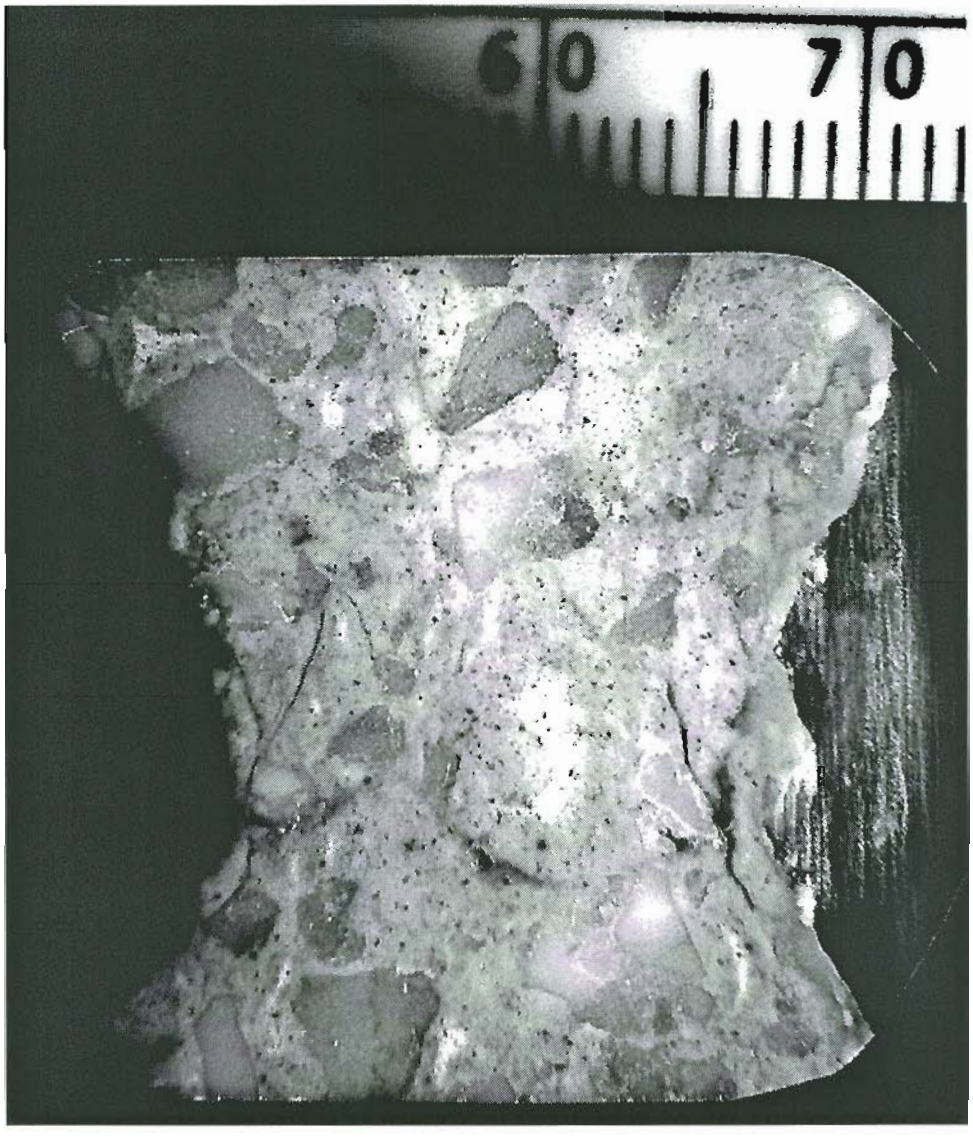

Figure 4.61. Cross section of cold compression test coupon B4-21-3. Calcium dialuminate cement matrix and dead burnt magnesia additive at 1:2 ratio. Reinforcement is graded crushed spinel at 40% concentration.

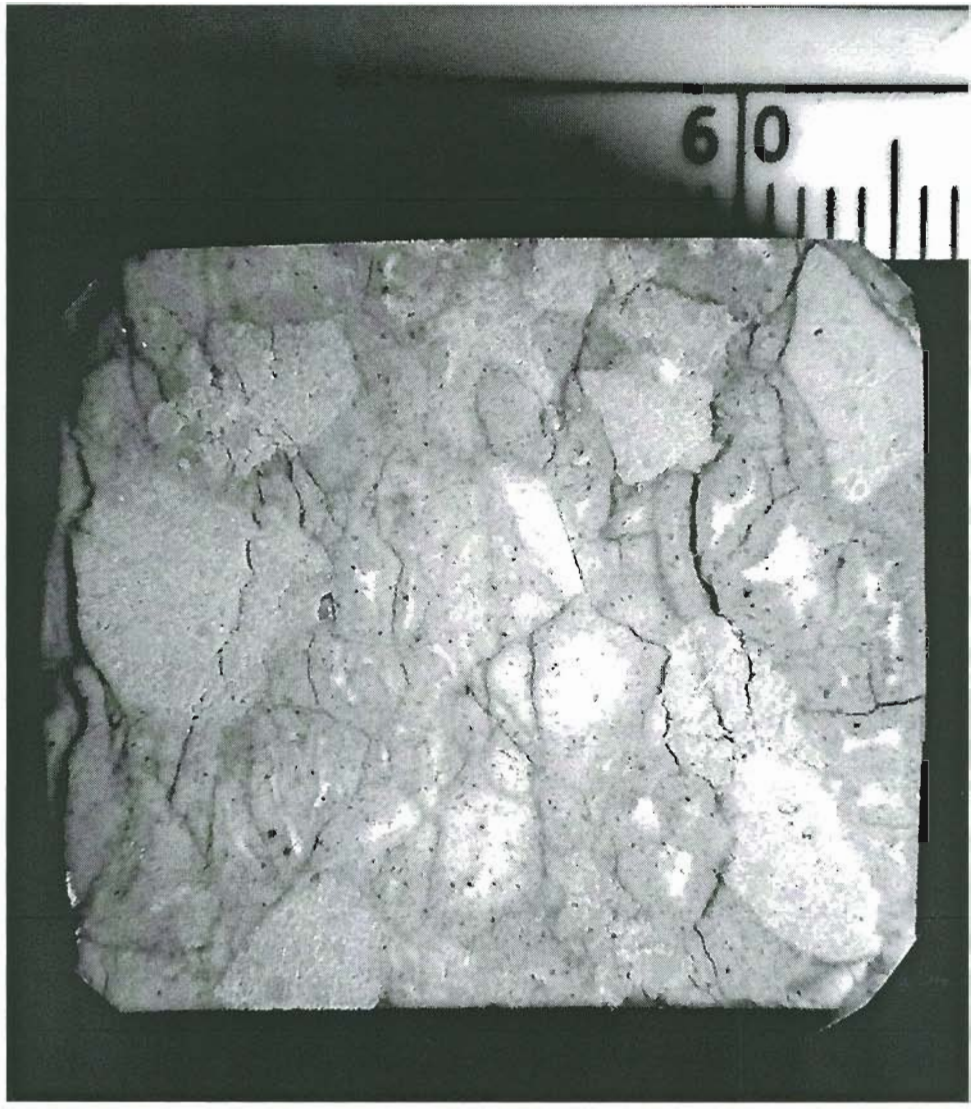

Figure 4.62. Cross section of cold compression test coupon B3-24-3. Calcium dialuminate cement matrix and dead burnt magnesia additive at 1:2 ratio. Reinforcement is high density zirconia grog at 40% concentration.

Figure 4.63. Cross section of cold compression test coupon B4-27-3. Calcium dialuminate cement matrix. Reinforcement is dead burnt magnesia rock at 40% concentration.

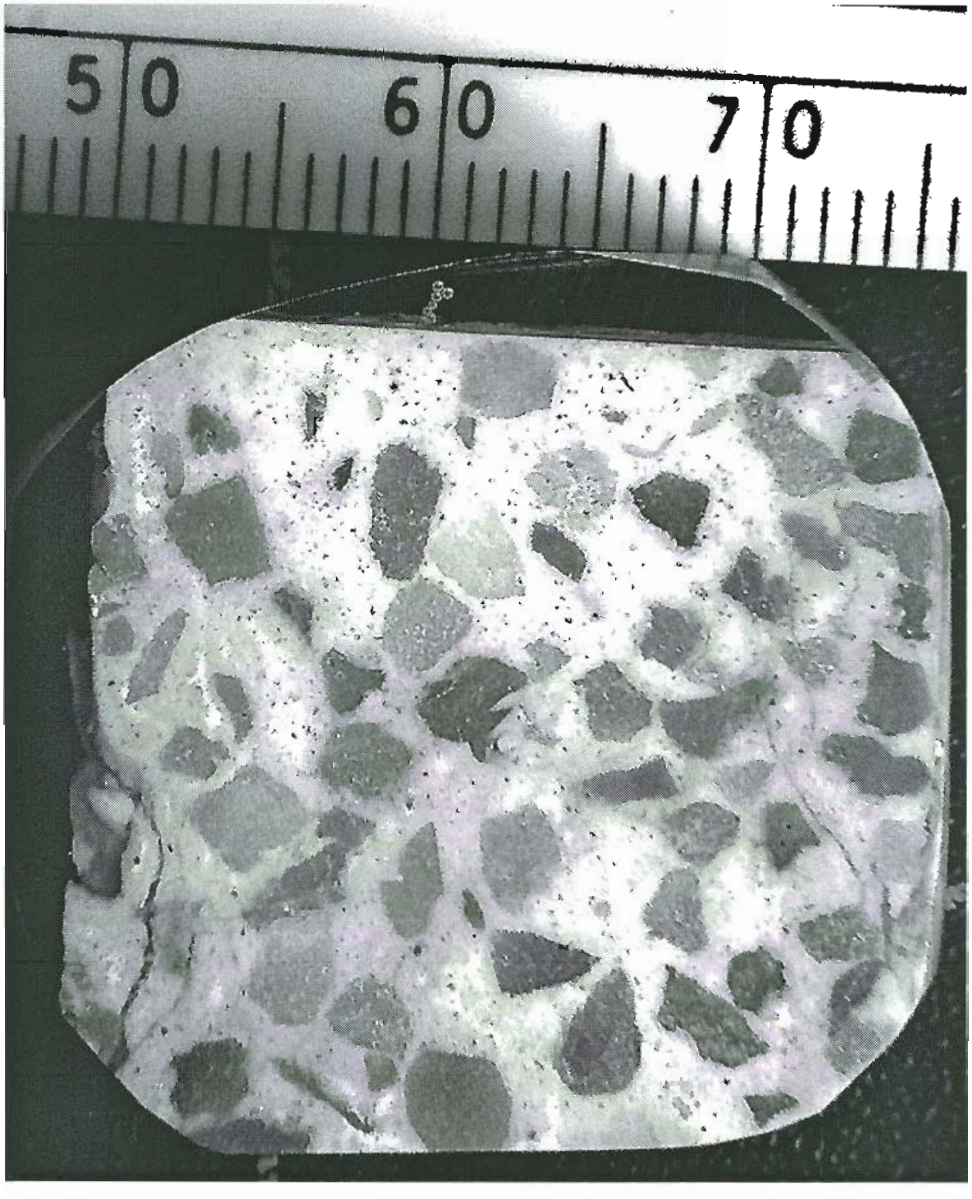

Figure 4.64. Cross section of cold compression test coupon B4-29-3. Calcium dialuminate cement matrix and dead burnt magnesia additive at 2:1 ratio. Reinforcement is dead burnt magnesia rock at 40% concentration.

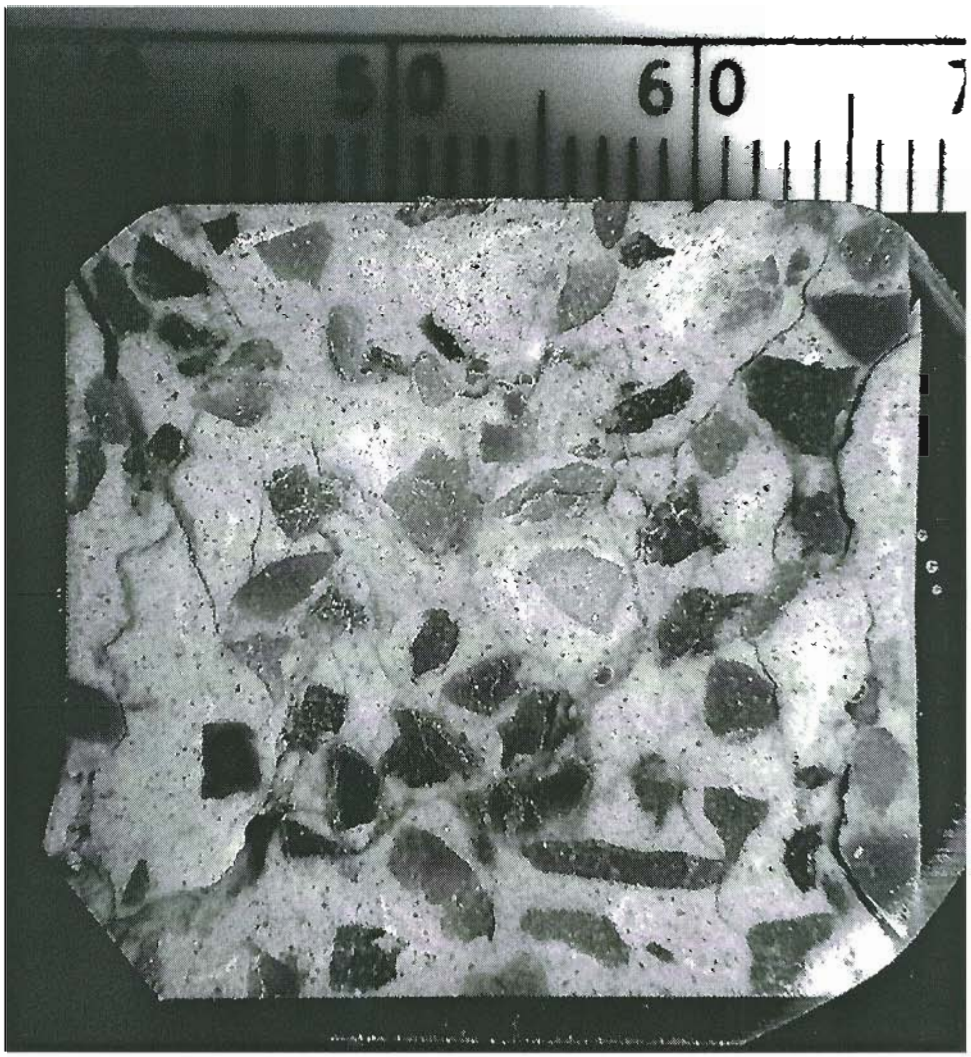

Figure 4.65. Cross section of cold compression test coupon B4-30-3. Calcium dialuminate cement matrix and dead burnt magnesia additive at 1:2 ratio. Reinforcement is dead burnt magnesia rock at 40% concentration.

The compression strength test methods are used to measure the material properties to determine the influence of different additives and reinforcements on the matrix calcium aluminate cements. The results are summarized graphically in Appendix IV in three sections similar to the wear test results. The Sections 2 and 3 present the results with the emphasis on the overall properties of the matrix cements and the influence caused by the various sample preparation, sintering and testing conditions on the matrix cement. The Section 4 emphasizes the test results with respect to the different

additives and reinforcement phases. The analysis and presentation of the compression strength follows the experimental objectives presented in Appendix II. The results from the compression strength measurements are presented for coupons #3, #2 and #5. The sample size is listed in the table. All coupons designated for compression testing were sintered at 1200°C with the exception of the reference samples and the "green" or un-sintered full size coupons.

4.7.2 Synopsis of High Alumina Calcium Aluminate Cement

The high alumina calcium aluminate (premix cement) compression strength data are summarized in data plots in order of the experimental objectives. Plots are found in Appendix IV Section 2. Table 4.16 is used as a guide to find the corresponding Figure to the relationship of interest.

Table 4.16. Compressive Strength Test Results Appendix Figure Guide for the High Alumina Calcium Aluminate Cement Batch Formulations.

Figure	Format of Data Relationship
AIV.2	Influence of open porosity on the cold crushing strength, full size, Coupon #3.
AIV.4	The water to cement ratio influence on the compression strength.
AIV.5	The influence of changing volume of cement independent of the reinforcement concentration.
AIV.9	All additives and volume concentration of matrix cement are compared to the compression strength
AIV.11	The magnesia to chromia ratio influence on the compression strength
AIV.12	The changing of reinforcement and matrix cement volume concentrations are compared to compression strength

Figure AIV.2 illustrates the influence of open porosity on the cold crushing strength for full size Coupon #3. The water to cement ratio influence is evaluated in terms of strength in Figure AIV.4. The influences on compression strength of all

additives are compared in Figure AIV.9. The cold compression strength is an important test of the interface strength and the influence of the reinforcement phase on the matrix. The batch formulations used a blend of magnesia and chromia to determine the influence of chromia on the reinforcement interface in the premix cement. The compression strength change is shown in Figure AIV.11. The changing volume fraction of reinforcement and the matrix cement concentration are compared to the compression strength in Figure AIV.12.

4.7.3 Synopsis of Fondu and Calcium Dialuminate Blend

The results from cold crushing strength measurements are presented for both the Fondu cement and the calcium dialuminate blend cement. Coupon #3's and #1's were used for cold compression strength testing. Summary plots of the data relationships are found in Appendix IV Section 3. Table 4.17 is used as a guide to find the corresponding Figure to the relationship of interest.

Table 4.17. Compression Strength Test Results Appendix Figure Guide for the Fondu and Calcium Dialuminate Blend Batch Formulations.

Figure	Format of Data Relationship
AIV.22	The water to cement ratio influence on cold compression strength
AIV.23	Open porosity influence on the compression strength
AIV.24	Concentrations of all additives in the matrix cement are compared against the compressive strength in wear rate?
AIV.25 AIV.26	The compression strength change with additive concentration, concentrations are separated for type
AIV.36	The changing volume fraction of reinforcement and the matrix cement concentration are compared to the compression strength
AIV.37	Shows green strength and sintered strength using the mean density to contrast the two sets.

The water to cement ratio influence on the cold compression strength is shown in Figure AIV.22. Compression test results are used to show the influence of the open porosity in Figure AIV.23. Magnesia, chromia, spinel dead burnt magnesia, alumina, alumina-titania blend and cerium oxide were used to modify the matrix. Concentrations of all additives in the matrix cement are compared against the compressive strength in Figure AIV.24. The compression strength change with concentration is separated for each of the different type of additive in Figures AIV.25 and AIV.26. The cold compression strength is an important test of the interface of the reinforcement phase to the matrix. The changing volume fraction of reinforcement and the matrix cement concentration are compared to the compression strength in Figure AIV.36. The sintered compression strength is compared to the green strength in Figure AIV.37.

4.7.4 Synopsis of the Influence of Additives and Reinforcements Materials

The experimental test matrix was designed to develop relationships between the strength and the changing composition of the additives and reinforcements used to improve the thermal stability. The results are presented to separates the different matrix, additive and reinforcement materials and develop relative trends. Table 4.18 below lists the relationships found in Appendix IV Section 4.

Table 4.18. Compression Strength Test Results Appendix Figure Guide for the Influence of Additives and Reinforcements of all Cement Batch Formulations.

Figure	Format of Data Relationship
AIV.39	Cold compression strength test results show magnesia concentration influence on compression strength, Coupon #3
AIV.42	Cold compression strength test results show spinel concentration influence on compression strength, full size coupons only
AIV.845	Cold compression strength test results show the influence of the MgO & Cr_2O_3 1:1 Blend on the compression strength, full size coupons
AIV.49	Cold compression strength test results show MgO & Cr_2O_3 1:2 Blend additive influence on the wear rate, full size coupons

Table 4.18. Compression Strength Test Results Appendix Figure Guide for the Influence of Additives and Reinforcements of all Cement Batch Formulations (continued).

Figure	Format of Data Relationship
AIV.52	Cold compression strength test results MgO & Cr_2O_3 1:4 Blend additive influence on the compression strength, full size coupons
AIV.56	Cold compression strength test results show the matrix wear rate with no additives and changing reinforcement concentration
AIV.57	Cold compression strength test results show the relationship between the compression strength and the open porosity
AIV.59	Cold compression strength test results show the influence of MgO additive
AIV.61	Cold compression strength test results show the influence of MgO additive
AIV.64	Cold compression strength test results show the influence of spinel additive
AIV.68	Cold compression strength test results show influence batch water on the compression strength
AIV.71	Cold compression strength test results show the influence of changing reinforcement on the compression strength, reinforcement at 40 and 75%
AIV.74	Cold compression strength test results show influence of changing reinforcement on the wear rate, reinforcement at 60 and 75%
AIV.77	Cold compression strength test results show the influence of dead burnt magnesia on compression strength, Coupon #3, reinforcement at 40%
AIV.78	Cold compression strength test results are compared to the open porosity, Coupon #3 reinforcement at 40%
AIV.82	Cold compression strength test results show influence of dead burnt magnesia on compression strength, Coupon #3 reinforcement at 40 and 60%

Table 4.18. Compression Strength Test Results Appendix Figure Guide for the Influence of Additives and Reinforcements of all Cement Batch Formulations (continued).

Figure	Format of Data Relationship
AIV.83	Cold compression strength test results are compared to reinforcement at 40 and 60%, Coupon #3, dead burnt magnesia additive at 50, 66 and 75%
AIV.87	Cold compression strength test results show influence of dead burnt magnesia additive on compression strength, Coupon #3, reinforced at three 40, 60 and 75%
AIV.88	Cold compression strength test results show influence of reinforcement on the compression strength, Coupon #3, reinforced at 40, 60 and 75% , dead burnt magnesia at of 33, 50, 66, 75 wt. %
AIV.91	Cold compression strength test results show influence of dead burnt magnesia and alumina blend additive on the compression strength, reinforced at 60 wt. %
AIV.94	Cold compression strength test results show influence dead burnt magnesia and alumina-titania blend additives on the compression strength, reinforced at 60 wt. %
AIV.97	Cold compression strength test results show influence of magnesia-cerium oxide blend additive on the compression strength, reinforced at 60 wt. %
AIV.99	Cold compression strength test results show influence of water on the compression strength, batch water adjusted at 2.8, 4, 6, 8 and 10 %, dead burnt magnesia additive at 50% and reinforced at 60%
AIV.101	Cold compression strength test results show influence of water on the compression strength, batch water adjusted at 4, 6, 8, 10 and 12 %, dead burnt magnesia additive at 50%, reinforced at 60%

4.7.4.1 Premix Cement and MgO Additive and Zircon Reinforcement

The influence of magnesia on cement binder in the HACA premix cement is illustrated in four batches: B2-7-1, B5-4-1, B5-6-1 and B5-28-1. Magnesia concentrations were formulated to 10%, 15%, 20% and 35% by weight of the total batch. The premix zircon reinforcement range was formulated to range between 39 to 61%. The compression strength data used full size coupons, and Figure AIV.39 shows a decreasing strength with the addition of more magnesia.

4.7.4.2 Premix Cement and Spinel Additive and Zircon Reinforcement

The influence of spinel additive on cement binder in the HACA premix cement is illustrated in five batches: B4-29-1, B5-1-1, B5-8-1, B5-15-1 and B5-18-1. Spinel concentrations were formulated to 10%, 20% and 25% by weight of the total batch. The premix zircon reinforcement range was formulated to range between 45 to 63 %. The compression strength data presented is from full size coupons. Figure AIV.42 shows the compression strength decreasing with the addition of spinel to the matrix phase.

4.7.4.3 Premix Cement and MgO & $Cr_2O_3$1:1 Blend Additive and Zircon Reinforcement

The influence of MgO & $Cr_2O_3$1:1 blend additive on cement binder in the high alumina calcium aluminate cement is illustrated in seven batches: B1-28-1, B2-16-1, B2-18-1, B3-18-1, B4-20-1, B4-24-1 and B5-22-1. The blend formulations were made at 10, 20, 25 and 35% by weight of the batch. Duplicate batches were made at 10 and 20% concentrations. The premix zircon reinforcement range was determined to range between 39% to 61%. Cold compression strength test results are shown in Figure AIV.45. A compression strength and blend concentration tend is not indicated. The coupons from this data set were further examined for physical property trends with an increasing chromia concentration. Specifically, the relationship between the strength and density and the effect of added chromia to the density. Figure AIV.46 shows a relatively insensitive density change with increasing chromia.

4.7.4.4 Premix Cement and MgO & Cr_2O_3 1:2 Blend Additive and Zircon Reinforcement

The influence of MgO & Cr_2O_3 1:2 blend additive on cement binder in the high alumina calcium aluminate cement is illustrated in six batches: B2-23-1, B2-25-1, B3-10-1, B3-12-1, B4-3-1 and B5-26-1. The blend formulations were made at 10, 20 and 30% by weight of the batch. Duplicate batches were made at 10 and 20% concentrations. The premix zircon reinforcement range was determined to range between 48 to 61%. Cold compression strength test results are shown in Figure AIV.49, a decreasing compression strength trend with blend concentration is indicated.

4.7.4.5 Premix Cement and MgO & Cr_2O_3 1:4 Blend Additive and Zircon Reinforcement

The influence of MgO & Cr_2O_3 1:4 blend additive on cement binder in the high alumina calcium aluminate cement is illustrated in five batches: B2-12-1, B3-16-1, B4-1-1, B4-22-1 and B5-20-1. The blend formulations were made at 10, 20, 30 and 35% by weight of the batch. Duplicate batches were made at 10 % additive concentration. The premix zircon reinforcement range was between 45 to 61%. Cold compression strength test results are shown in Figure AIV.52. The data indicates a decreasing compression strength with increasing blend concentration.

4.7.4.6 Premix Cement and no Additives and Zircon Reinforcement

The influence of changing reinforcement concentration with out additives is illustrated in eight batches: B2-2-1, B2-4-1, B5-11-1, B5-13-1, B4-27-1, B4-6-1, B4-8-1 and B4-13-1. The premix zircon reinforcement ranged from 41 to 80% by batch weight. The compositions were adjusted by adding screened cement and reinforcement. Cold compression strength test results from full size #3 coupons are shown in Figure AIV.56. Increasing compression strength with increasing reinforcement volume fraction is shown. Included in the presentation of the compression strength results is Figure AIV.57 that illustrates a clear trend with the changing open porosity. Combining Figures AIV.56 and AIV.57, the open porosity decreases with increasing reinforcement.

4.7.4.7 Fondu Cement and MgO Additive and Zirconia Grog Reinforcement

The influence of changing magnesia on Fondu cement microstructure and mechanical properties is determined using ten batch formulations: B11-23-1, B12-18-2, B9-8-1, B11-30-1, B12-7-1, B12-1-1, B12-8-1, B12-2-1, B12-9-1 and B12-3-1. The data set includes additive concentrations of 0, 50, 66, 75 and 80% by weight of the batch. Three duplicate batches were made. The high-density zirconia grog reinforcement range is 50 to 60%. Cold compression strength test results are shown in Figure AIV.59. A decreasing compression strength trend is illustrated with increasing magnesia concentration.

4.7.4.8 Fondu Cement and MgO Additive and Spinel Reinforcement

The influence of changing magnesia on Fondu cement microstructure and mechanical properties is determined using seven batch formulations: B9-28-1, B10-26-1, B9-30-1, B10-23-1, B10-5-1, B10-7-1 and B10-12-1. The data set includes additive concentrations of 0, 50, 66, 75 and 80% by weight of the batch. One duplicate batch was made. The crushed spinel brick reinforcement range is 50 to 60%. Cold compression strength test results are shown in Figure AIV.61. A decreasing compression strength trend is illustrated with increasing magnesia concentration.

4.7.4.9 Fondu Cement and Spinel Additive and Spinel Reinforcement

The influence of changing spinel on the Fondu cement mechanical properties is determined using seven batch formulations: B9-28-1, B10-26-1 B10-2-1, B10-16-1, B10-14-1, B10-19-1 and B10-21-1. The data set includes additive concentrations of 0, 50, 66, 75 and 80% by weight of the batch. One duplicate batch was made. The crushed spinel brick reinforcement was held constant at 50% by batch weight. Cold compression strength test results are shown in Figure AIV.64. A decreasing compression strength trend is illustrated with increasing magnesia concentration.

4.7.4.10 CA_2 Cement and no Additive and no Reinforcement

The compression strength of the calcium dialuminate cement independent of additives and reinforcement materials was determined in three batches: B1-19-1, B1-20-1 and B1-29-2. The batches were formulated using three water to cement ratios to provide a boundary to assess other parameters. The compression strength for the three batches are shown in Figure AIV.68.

4.7.4.11 CA_2 Cement and no Additive and Dead Burnt MgO Rock Reinforcement

The compression strength of the calcium dialuminate blend independent of additives with dead burnt magnesia rock reinforcement were determined using three batches: B4-27-1, B2-22-1 and B5-12-1. The batches were formulated at concentrations of 40, 60 and 75% by batch weight. The compression strength for two of the batches is shown in Figure AIV.71. Compression strength from B4-27-1 was discounted because sample damage led to anomalous values.

4.7.4.12 CA_2 Cement and no Additives and Zirconia Grog Reinforcement

The compression strength of the calcium dialuminate blend independent of additives with zirconia grog reinforcement were determined using five batches: B3-14-1, B1-12-1, B3-12-1, B1-15-1 and B1-28-1. The batches were formulated at reinforcement concentrations of 40, 60 and 75% by batch weight. The compression strength results are shown in Figure AIV.74.

4.7.4.13 CA_2 Cement and Dead Burnt MgO Additive and Dead Burnt MgO Reinforcement

The influence of dead burnt magnesia additive on the calcium dialuminate blend cement binder is illustrated in four batches: B4-28-1, B4-30-1, B5-10-1 and B4-29-1.

The additive was formulated at concentrations of 33, 50, 66, 75 wt. % by weight of the batch. Dead burnt magnesia rock was used for reinforcement at a concentration of 40%. Compression strength test results are shown in Figure AIV.77. A clear trend for increasing strength with increasing magnesia concentration is presented. The increase is relatively small and could be a result of increased coupon density. The cold compression strength results are compared to the open porosity measured on each coupon shown in Figure AIV.78. Magnesia additive exhibits little influence to the strength over the 30 to 75 wt % concentration range. The strength decreases with the increasing open porosity.

4.7.4.14 CA_2 Cement and Dead Burnt MgO Additive and Spinel Reinforcement

The influence of dead burnt magnesia additive on the calcium dialuminate blend cement binder is illustrated in nine batches: B4-20-1, B4-21-1, B4-19-1, B4-6-1, B4-15-1, B4-16-1, B4-14-1, B4-2-1 and B4-5-1. The additive was formulated at concentrations of 50, 66, 75 wt. % by weight of the batch. Influence of crushed and graded (1:4 size ratio) spinel brick reinforcement is also included. The data includes two reinforcement concentrations 40 and 60 wt. %. Cold compression strength test results are shown in Figure AIV.82. A clear trend for increasing strength with increasing magnesia concentration is presented. Figure AIV.83 shows the cold compression strength test results as a function of the volume fraction of the reinforcement.

4.7.4.15 CA_2 Cement and Dead Burnt MgO Additive and Zirconia Grog Reinforcement

The influence of dry milled dead burnt magnesia additive on the calcium dialuminate blend cement binder is illustrated in fourteen batches: B3-16-1, B3-24-1, B3-25-1, B3-23-1, B3-10-1, B2-10-1, B3-9-1, B3-11-1, B3-13-1, B3-14-1, B1-12-1, B1-15-1, B1-28-1 and B3-12-1. The magnesia was added at concentrations of 33, 50, 66, 75 wt. % by batch weight. The batches were reinforced with high-density zirconia grog at three

concentrations 40, 60 and 75% by batch weight. Cold compression strength test results influenced by the additive magnesia and reinforcement are shown in Figures AIV.87 and AIV.88. No compressive strength trend for changing magnesia or zirconia reinforcement is indicated.

4.7.4.16 CA_2 Cement and Dead Burnt MgO-Al_2O_3 Additive and Dead Burnt MgO Reinforcement

The influence of dry milled dead burnt magnesia and alumina blend on the calcium dialuminate cement was determined in five batch formulations: SP8-6-1, SP8-12-1, SP8-11-1, SP8-9-1 and SP8-10-1. Five ternary compositions of calcium aluminate blend, magnesia and alumina system were formulated. Dry milled dead burnt magnesia and milled fused cast alumina were blended with the calcium dialuminate. All batch formulations were reinforced with 60% by weight dead burnt magnesia rock. Influence of changing magnesia and alumina concentrations were determined using compression strength data. The compression strength data is shown in Figure AIV.91. The compression data indicates a lower strength for batches made with higher additive concentrations.

4.7.4.17 CA_2 Cement and Dead Burnt MgO and Al_2O_3-TiO_2 Additive and Dead Burnt MgO Reinforcement

The influence of dry milled dead burnt magnesia and alumina-titania blend on the calcium dialuminate cement was determined in eight batch formulations: SP7-28-1, SP7-29-1, SP7-20-1, SP7-26-1, SP7-27-1, SP7-23-1, SP7-21-1 and SP7-22-1. Eight ternary compositions of calcium aluminate blend, magnesia and alumina-titania blend system were formulated. All batch formulations were reinforced with 60% by weight dead burnt magnesia rock. The compression strength data is shown in Figure AIV.94. The compression data indicates a lower strength for batches made with higher additive concentrations.

4.7.4.18 CA_2 Cement and Dead Burnt MgO-CeO_2 Additive and Dead Burnt MgO Reinforcement

The influence of dry milled dead burnt magnesia and cerium oxide on the calcium dialuminate cement was determined in five batch formulations; SP7-30-1, SP8-4-1, SP8-3-1, SP7-31-1 and SP8-2-1. Five ternary compositions of the CA_2-M-Ce system were formulated to the following ratios: 1:1:1, 1:1:2, 1:2:1, 2:1:1 and 3:1:1. All batch formulations were reinforced with 60% by weight dead burnt magnesia rock. The compression strength data is shown in Figure AIV.97. The compression data indicates a lower strength for batches made with higher additive concentrations.

4.7.4.19 CA_2 Cement and Dead Burnt MgO Additive and Dead Burnt MgO Reinforcement

The water to cement ratio influence on the properties was determined by formulating a number of batches holding the additive and reinforcement concentrations constant and changing the quantity of batch water. At high water concentrations the water was squeezed during pressing. To increase the water several batches were prepared using a vibration table and no pressing. The samples cured unrestrained. The batch water was adjusted at 2.8, 4, 6, 8 and 10% batch weight for the first set of pressed samples and 4, 6, 8, 10 and 12 % by batch weight for the second set of vibrated samples. Greater batch water formulations were not possible because the mix was far too runny to stay in the mold. Unrestrained batches used the same mold and the vibration energies were held to the same level on each batch. The cure time was the same for all batches. All batches were formulated with dry milled dead burnt magnesia at 50% concentration and dead burnt magnesia rock reinforcement at 60% concentration.

The compression strength data are presented for the two sets. The first set included six batches: SP7-6-1, SP7-7-1, SP7-8-1, SP7-9-1, SP7-12-1 and SP7-11-1. The second set included seven batches compacted on a vibration table: SP7-13-1, SP7-14-1, SP7-15-1, SP7-16-1, SP7-17-1, SP7-18-1 and SP7-19-1. The strength properties for the first is shown in Figure AIV.99. The compression strength decreases with increasing water. The batch water concentration influence on the strength is shown in Figure AIV.101.

5.0 DISCUSSION

5.1 Introduction

The research objective was to design and develop a wear resistant, high strength, low thermal conductivity material for high temperature applications. The design and development of specialized ceramic composite formulations for elevated temperature applications has been demonstrated. The technology is applicable to several industries and industrial processes such as power plant burner nozzles, petrochemical cracking columns, high duty calciners and furnaces. A formulation of dead burnt magnesia additive to CA_2 cement using either zirconia grog or dead burnt magnesia reinforcement could be tailored for use in high temperature (>1800°C) liquid and glass processing. Lower temperature applications could use a formulation with a matrix of spinel and Fondu cement and zirconia grog reinforcement. A novel application could use the CA_2 matrix with dead burnt magnesia reinforcement to hold a catalytic oxide like titania or cerium oxide to control NOx emissions. For a given flow and abrasive, the wear rate can be adjusted with increasing reinforcement to make a catalytic liner that exposes fresh catalyst surface area continually with wear. The corrosion resistance of the zirconia grog reinforcement could find application in molten salt processing. There are a wide range of potential products that could be based on the castable refractory cement.

5.2 Concrete Design

The properties of monolithic ceramic materials are derived from the microstructure. High strength is a function of small grain size, uniform microstructure, density and flaw free structures. Duplex microstructures, controlled porosity and uniform distribution are used to arrest cracking and impart high toughness. Duplex and multi-phase microstructures with high aspect ratio reinforcement phases provide superior shear strength and high toughness. Large grain size and absence of amorphous and glassy phases along the grain boundaries have proven to bring about high creep resistance. High chemical resistance is obtained from materials with nearly theoretical densities (no open porosity), while highly porous microstructures with a fine pore size distribution exhibit the greatest resistance to heat flow.

The concrete microstructure is divided into three constituents: matrix, reinforcement and interface. The concrete material uses castable calcium aluminate cement plus a high temperature oxide to create a matrix to bind together high temperature aggregates for strength, thermal resistance and durability. The final ceramic composite structure becomes a graded microstructure of cement hydrates, mechanically interlocked particles and grains held together by ceramic bonds. Figure 5.1 illustrates the castable refractory wall cross section over the range of temperatures from ambient to melting. The refractory hot face wall is bound together by ceramic bonds formed using *in situ* firing techniques. As shown in the Figure, a large portion of the cross section retains the concrete microstructure and only a relatively thin layer has a dense ceramic microstructure caused by thermally activated rearrangement processes.

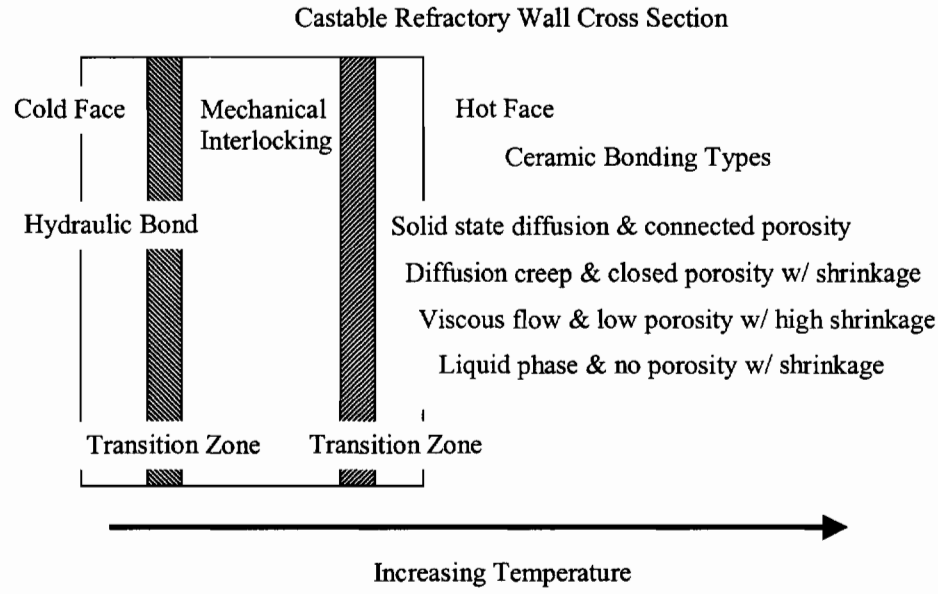

Figure 5.1. Illustration of the cohesive bonding across a section of *in situ* fired refractory cement.

Inter particle ceramic bonds are formed at elevated temperatures, through the sintering process. The thermal energy drives the molecular rearrangement towards more stable and equilibrium phases, although equilibrium structures are not likely to be reached. The temperature required for mass transport is specific to the ceramic molecules. Other thermodynamic and physical considerations apply to the mass movement at elevated temperatures, for example surface tension and compound formation. The ceramic bonds develop properties based on the material and cross section area of the bond. The growth of bond material depends on the temperature and thermal history relative to the intrinsic thermal activity of the molecules. Thermal activity is not significant at temperatures less than $0.8T_m$ over short intervals, however, over longer periods changes will take place at lower temperatures which is the reason the thermal history becomes important. Over the temperature range of $0.8T_m$ to T_m the surface energy is also important to the molecular activity and formation of ceramic bonds. Fine powders with higher surface area form ceramic bonds more rapidly due to the low energy required for surface diffusion. Other low energy processes become significant to ceramic diffusion bond development as the temperature increases, for example cation self-diffusion, impurity diffusion and oxygen diffusion.

The refractory concrete is designed for casting into the final shape and *in situ* firing from one side. A typical refractory concrete installation is 20 to 30 cm thick. One of the design functions of a refractory material is to perform as a thermal barrier to limit thermal conductivity and aid overall thermal management. A steep thermal gradient limits the thickness of the zone of material that reaches temperatures capable of driving ceramic bond development to only 10 to 20% of the thickness. The cement microstructure is critical for strength development in the bulk of the refractory installation. The sacrifice of strength to improve thermal stability is offset using reinforcement phases. Experimental results indicated that increasing the additives greater than 50% of the matrix volume starts to degrade the wear resistance and mechanical properties decrease rapidly. Increasing the reinforcement volume fraction greater than 60%, depending on the reinforcement material coefficient of thermal expansion (CTE), can similarly have diminishing improvement.

The calcium aluminate cement has the lowest melting point of the three ingredients in the composite, 1605°C. Impurities like silica and iron oxides reduce the melting point further. In sufficient concentrations, the impurities promote the formation of intermediate phases with lower melting points. The experimental results found evidence of a highly viscous phase in the high alumina calcium aluminate premix and Fondu cement samples fired at 1200°C. No liquid formation or solidification microstructures were observed but intermediate compounds with softening points less than CA were formed. Figures 4.70 and 4.71 are examples of the intermediate "chromium-rich" phases surrounding a chromia particle. Additives (phases) with solubility can "soak up" the impurities and promote elevated temperature stability. Reducing the concentrations of the cement in the matrix by increasing the amount of inert additives increases the bulk melting point and overall thermal stability. Reducing the matrix cement volume in favor of high temperature inert particles can also have unfavorable consequences. Too much inert material lowered the total volume of material capable of forming ceramic bonds at lower temperatures. Two adjacent high temperature ceramic additive grains do not bond at the lower temperatures. The ceramic bond is formed from the more active cement impurities.

Structural stability is required throughout the installed thickness. The installed composite refractory cement is exposed to abrasive wear on the hot face by hot gas and entrained abrasive particles. Mechanical loads resulting from thermal stresses can also be significant. Thermal expansion mismatch and thermal shock stresses are the principal loads. Dead weight loads can be high, from 20 to 50 MPa. The reinforcement strengthens the matrix and provides wear resistance. The reinforcement improves properties in the ceramic and mechanical interlocking bond zones. Reinforcement using high temperature materials was shown to improve cold compressive strength and dry sand rubber wheel abrasion test results. Dense homogenous reinforcement materials with low fracture toughness offer high strength to the composite. Porous ceramic reinforcement material and closely matched CTE provides for good thermal shock resistance and reduced cracking. Slightly reactive reinforcements produced improved and more coherent interfaces. Large reinforcement sizes were found to improve the strength but increase the net thermal expansion stress, exaggerating the interface mismatch. Small size reinforcement is not as effective with strength improvement but the matrix more easily accommodates the expansion mismatch stresses. Reinforcement with high solubility for the matrix cations more readily forms a coherent interface.

Compressive strength and abrasive wear resistance of the composite are defined by the interface strength. Mechanical processes in brittle materials find the weakest component, which in this case is located at the interface. Cracks and discontinuities caused by thermal expansion mismatch stress are the primary weakness of the ceramic composite. Photomicrographs of the interface indicated both coherent and incoherent structures. The zircon reinforcement has the lowest melting point and was found to diffuse into the matrix cement. The zirconia grog reinforcement was found to set up a diffusion or reaction layer at the interface. The spinel and dead burnt magnesia was not found to react with the matrix. The dead burnt magnesia reinforcement did form a tight interface.

Mechanical properties are improved with compatible matrix reinforcement, but too much reinforcement reduces the strength by excessive thermal expansion mismatch or reinforcement binding.

Figure 4.61 illustrates a high degree of cracking in a formulation with 75% zirconia reinforcement. The volume of matrix surrounding the reinforcement was not sufficient to dissipate the thermal expansion stress.

One experimental goal was to determine the cross over point between property improvement and property degradation. This was accomplished by developing a test matrix to understand the relationships between properties and the additives and reinforcements.

Important microstructural features of a castable concrete refractory are based on the functionality and intended life. The properties of the composite cement are dependent on the thermal history and temperature, which are reflected in the bonding microstructure. Bonding is found as one of three general types: chemical hydrate, mechanical bonding and ceramic bonding. Ceramic bonding is further sub-divided into four microstructural zones; solid state diffusion with connected porosity, diffusion creep bonding with closed porosity and shrinkage, viscous flow bonding with moderate to low porosity and high shrinkage, liquid or solidification microstructures in the bonding phase with no porosity and high shrinkage.

The target phase fields are the periclase and spinel regions where the thermodynamic and stoichiometric ranges are large. These crystal structures accommodate large concentrations of lattice impurities found in the calcium aluminate base cement. The temperature effect on the equilibrium-based kinetics is great. The cement hydrate structure, through most of the temperature range, is that of fine elongated branches or plates. The hydrate branches thicken with increasing temperature through the absorption of oxygen and impurities that fill open sites formed during the decomposition of the chemically absorbed water. The transition to diffusion bonding is gradual starting with evaporation and condensation of atoms along the free surface of the pore. The atoms condense at the high angle boundaries between grains. As the thermal energy increases, bulk solid state diffusion of surface absorbed atoms across former particle boundaries dominate mass transfer.

The low melting point impurities and intermediate phases form viscous liquids which are pulled into the triple points by surface tension forces and close off porosity causing adjacent particles to bond. Bonding takes place where the surface energy of the semi liquid is greater than the particle surface tension.

The optimum structure for strength is found at the point where the strength between the mechanically bonded thick hydrate structures is similar to the shear strength of the viscous material that forms the bond or the shear strength of the solid state diffusion bond. The ceramic bond strength drops sharply with the onset of grain boundary flow or diffusion creep. This description is greatly simplified, in actuality the cement is a heterogeneous structure with a random collection of materials for the energy related bonding processes: solid state diffusion, viscous flow, creep and pore removal and all competing simultaneously to reduce the free energy of the structure.

The kinetic ranges of the various mechanistic bonding processes in a steep temperature gradient are important to the development of the various microstructures formed. The higher temperature mechanistic processes produce bond layer structures that are thinner and contribute less to the overall properties of the refractory. The wider kinetic range processes represent a thicker layer of material and contribute more to the bulk properties. At atmospheric conditions the oxygen anion diffusion is one of the lowest energy processes in the periclase and spinel lattices. The oxygen saturates the anion lattice sites at elevated temperature and provides for easy pathways for cation diffusion into the equilibrium octahedral and tetrahedral sites of the parent lattice. Diffusion of silicon, iron, aluminum and calcium into the lattice readily assist the formation of continuous bonding material between magnesia and matrix cement particles. Because the steep thermal gradient the precursor materials to the formation of the intermediate bond phases are oxygen or anion saturated. Solid state diffusion bonding has the widest kinetic range and therefore is the process that produces the microstructure representative of the properties in the bulk of the front wall of the castable refractory.

5.3 Materials Selection

The properties, economics and impurity concentrations are considerations used in the selection of additive raw materials. Thermal stability, strength, chemical stability and thermal expansion compatibility are materials selection considerations. Magnesia, chromia and spinel are compatible with the calcium aluminate cements. Pure materials increase the thermal stability and with their high solubility for impurities promote good diffusion bonding at the higher temperatures > 1800°C. The high melting point additives detract from the direct ceramic bonding between particles and intermediate phases tend to form. Intermediate lower temperature phases form first with the calcium aluminate impurities: enstatite (MS 1557 °C), forsterite (M_2S 1890 °C), monticellite (CMS 1495 °C), dicalcium ferrite (C_2F 1435°C) and magnesia ferrite (MF 1750 °C). As a general rule, the higher purity materials are thermally more inert but ceramic bonding at lower temperatures is more difficult. High purity magnesia and spinel can take advantage of commercial purity cements with impurities to form more ceramic bonds at intermediate temperatures as their high solubility accommodates impurities at higher temperatures. Conversely, high purity calcium aluminate cements can utilize commercial purity additives with higher levels of impurities to form ceramic bonds at intermediate to high temperatures.

The concrete is a heterogeneous structure with the resultant properties and processing depend on the relative amounts, shapes, distributions and preparations of the constituents. Two forms of magnesia additives were selected for experimental formulations. A fused cast, highly dense, inert, high purity reagent grade material was used as a single additive and blended with chromia. This form of magnesia is not reactive and did not form intermediate bonds with either of the cements. The particle size was relatively large and exhibited a relatively narrow log normal distribution with respect to the other additives. The other form of magnesia was a dry milled ground and sized dead burnt (DB) magnesia. The crushed powder is finer than the fused cast magnesia and has a broad distribution towards the finer sizes. The dead burnt magnesia is less pure; periclase grains are bonded by an enstatite (MS) phase. The dead burnt magnesia powder is more reactive than the fused magnesia but not so reactive that it slaked with

atmospheric moisture. One of the detrimental aspects of magnesia refractory products is the swelling and formation of magnesia hydroxides when exposed to moisture. This can be catastrophic to structures due to the volume expansion of the hydrated magnesia. The dead burnt magnesia is stabilized against hydration but is far more economical than the fused cast high purity magnesia. Refractory cements produced using dead burnt magnesia additives have considerable economic advantage over the fused magnesia. Reagent grade chromia powder was also used in experimental blends with fused magnesia. Chromia and chromite refractories are in disfavor internationally because of the environmental cost but the historical superior performance warrants study for comparison. Chromium oxides readily form good bonding phases in all three of the calcium aluminate cements. The experimental formulations also were made using a fused cast spinel as the additive. The powder used was a high purity reagent grade with a small size distribution. Spinel additives offered a compatible structure with a wide stoichiometric range.

Other additives like alumina, alumina-titania blend and cerium oxide were formulated with the calcium dialuminate cement. The alumina used was a dense form, reagent grade and relatively large particle size with a narrow distribution of sizes. The alumina-titania was a dense form, reagent grade and extra fine particle sizes with a narrow distribution of sizes. The cerium oxide was an extra fine, reagent grade and dense additive. Alumina additions provided insight to the matrix property change with large particle size whereas the alumina-titania and ceria oxide were used to illustrate the changes at the other end of the size scale. The compatibility of these oxides with the calcium dialuminate cement was studied. Titania and cerium oxides are important high temperature catalysts used in the chemical and refining industries. The calcium dialuminate cement composites may be used to replace conventional refractory bricks in reactor structures and chemical processing plants. Compatibility with catalyst beds and the stability of the catalyst carrier structures is important for high temperature conversions.

The reinforcement materials are optimized for size, distribution, strength, and material thermal and chemical properties. The structural stability of the composite is defined by the reinforcement to matrix interface properties. The distribution of the shear

stress and the transfer of load to the reinforcement are important. Four reinforcement materials are tested: zircon, zirconia, spinel and magnesia. Zircon reinforcement offers a better thermal expansion match and the highest particle shape aspect ratio of all reinforcements, between 5:1 and 7:1. Zircon is dense and more reactive and diffuses with the matrix at the lowest temperature. Zirconia grog is porous and chemically inert at high temperatures. Zirconia forms a coherent diffusion bond with the matrix calcium aluminate at elevated temperatures. Zirconia has a moderate aspect ratio between 3:1 to 5:1, and large particle size for improved strengthening but the thermal expansion mismatch is high which leads to poor thermal shock resistance. The spinel reinforcement is porous and chemically compatible with the additives. The aspect ratio is near unity and thermal expansion mismatch improves with increasing additive concentrations. Dead burnt magnesia rock reinforcement is dense, chemically inert but compatible with the additives and calcium aluminate. The periclase phase readily dissolves silica, iron and calcia and is thermally stable over the entire temperature range. The size is small and the aspect ratio near unity. The thermal expansion mismatch is more easily accommodated due to the smaller size particles.

5.4 Experimental

Experimentation in a heterogeneous, non-equilibrium system is a time consuming, tedious and resource intensive process. The complexity of multi-component and impure oxide systems limits the ability to be quantitative. However, for applicability it is important to test actual commercial grade cement materials. Empirical relationships and relative comparisons of material properties as the formulation changes can be used to screen and select optimum formulations suitable for field testing and further development. Reducing the complex system to the important parameters is essential. Knowledge of the intended application and service provides for experimental simplification. Castable refractory cement and concrete materials are used to line furnace walls, gas nozzles, ladles and calciners where the exposed surface is subjected to abrasive wear conditions. The experimental parameters are based on the most limiting material degradation mechanism, abrasive wear, to reduce the experimentation scope.

Standardization of procedures, materials and test conditions also simplifies experimentation. Empirical results are meaningful when the boundaries of the relationships are known and comparative testing is performed. High confidence can be obtained if the experimental variables are minimized.

5.5 Density

Density and porosity are important parameters in conventional ceramic materials. In conventional ceramics the pores are considered flaws, the greater porosity results in lower strength. The one-sided firing of the installed concrete produces a graded microstructure. The density and porosity are dynamic functions of temperature and thermal history. Porosity in the castable concrete is beneficial for thermal insulation properties and shock resistance. The porosity limits the conduction of heat through the refractory structure. Experimentally, the fired coupon density is important because it provides insight to the type of bonding in the prepared coupons and the validity of the material property comparisons.

The results present eleven charts that compare the density to the various parameters important to cement properties. These results illustrate similar trends and indicate possible similar sintering bonding mechanisms in all the coupons fired. The first chart, Figure 4.1, presents a "big picture" look at the range of average density and clearly illustrated coupons that were bad and not to be tested. The chart shows a density range of approximately of one and a half gm/cc for the 106 batches made from Fondu and calcium dialuminate cements. The control density of Fondu and calcium dialuminate cements with no additives or reinforcement is 3.2 and 3.0 gm/cc, respectively. The measured density of the coupons falls within 15 to 20% of the theoretical density of sintered pure cement. This compares well with the 7 to 12% open porosity.

The standard deviations of densities from same batch coupons are small, indicating relatively precise measurements and adequate experimental technique. The microstructure and density measurements indicate ceramic bonding in the coupons fired at 1200°C for 96 hours.

The microstructure and open porosity indicate solid state surface diffusion bonding. The data in Figure 4.1 also illustrates several groupings that correspond to the type of cement and the reinforcement used in the formulation.

The high alumina calcium aluminate cement density was not as sensitive to the total cement concentration, total additive concentration or the water to cement ratio as the Fondu. This would be expected from higher purity cement with higher softening temperatures. More time would be needed to reach the same degree of ceramic bonding. However, analysis of the microstructures did not indicate a great difference in the bonding or open porosity. The water to cement ratio does not have an influence on the final the sintered density. The water to cement ratio would be expected to influence the hydration microstructure and had firing not been sufficient to wipe out the mechanical interlocking hydrate microstructure something more than a random presentation of the data would have been expected. Figure 4.4 shows the density and total additive concentration relationship. The zero additive coupon densities are included on the left axis to give the perspective. No clear trend to the data is shown in this format, suggesting the data should be sorted according to the specific type of additives. Figures 4.5 and 4.6 separate the additives and the cement type. Again, no difference with the type of additive on the high alumina calcium aluminate cement was found indicating the densities of the additives and the cement are too close to differentiate with the techniques used. However, the technique used do pick up the difference between the spinel, magnesia and chromia in the Fondu and calcium dialuminate, Figure 4.6. The density trend does not change with increasing concentration of the additive. The result may indicate an effect not related to thermal densification but a physical process, for example particle size influencing the packing factor.

A density change with the reinforcement is expected to be more pronounced in combinations of the lowest cement concentration and the highest reinforcement density. The magnesia stabilized zirconia grog density is 4.6 g/cc, dead burnt magnesia 3.6 gm/cc and the spinel is around 3.5 gm/cc. The density variation with the reinforcement is presented in Figures 4.7 and 4.8. These Figures separate the data by the different cements and reinforcements. The high alumina calcium aluminate cement coupons were premixed with the zircon reinforcement (theoretical density of 4.2 gm/cc). A density

change with increasing reinforcement is not observed over an approximate 50 wt.% span of the reinforcement concentration. Fondu and calcium dialuminate cements exhibit a trend of increasing density with increasing reinforcement. The trend is more pronounced for the zirconia grog reinforcement than the spinel or the dead burnt magnesia rock. The density trend follows the rule of mixtures.

The porosity is understood to have a large impact on the strength of conventional sintered ceramic materials. Fracture in the brittle ceramic material is a statistical process based on the size and quantity of flaws at or near the critical flaw size. Porosity is a flaw or crack initiation source in conventional ceramic materials. An effective toughening approach to ceramic strength improvement is the use of crack arrest phases, duplex structures and reinforcements. Porosity can also perform as a crack arrest. The cold compression strength has been selected as a property to be used to compare the relative differences between additives and reinforcement materials. The compression strength is a valid measure of the reinforcement interface property if it can be demonstrated to be independent to the porosity. Figures 4.9, 4.10 and 4.11 illustrate the compression test results showing strength independent of density. The compression strength and density relationship indicates the porosity has saturated the microstructure uniformly and possibly the largest pore size is less than the critical flaw size for the matrix material. Photomicrographs of compression test samples indicate crack paths that follow the reinforcement interface and proceed through the reinforcement phase. The porosity in the matrix is an effective crack arrest feature in the composite ceramic cement.

5.6 Thermal Conductivity

Thermal conductivity is a direct measure of the insulating properties of the castable concrete. Based on the photomicrographs and the lowest softening temperature constituent, the ceramic bonding begins at temperatures greater than the 900 to 1000°C. The predominant bonding modes at temperatures lower than this are mechanical interlocking and hydrate bonding. Figure 5.1 illustrates a typical steady state thermal profile in a 12 cm thick cast installation. The thermal gradient is steep, 200°C/cm of thickness perpendicular to the plane of the heat flow. The zone of material that develops

ceramic bonding at the maximum hot face temperatures of 1200°C is only 10 to 15% of the total thickness. Simple mechanical interlocking makes up roughly 80% of the cross section thickness. The mechanical interlocking microstructure is characterized by open porosity that is highly connected. The microstructural arrangement is an optimum configuration for low thermal conduction.

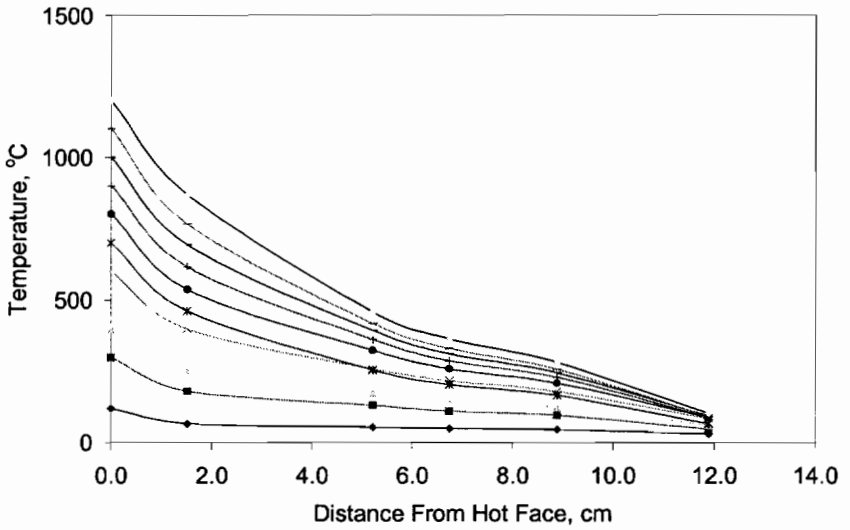

Figure 5.1. Thermal profile as a function of hot face temperature in calcium dialuminate cement cast block, no reinforcement.

The thermal conductivity was determined experimentally for six conditions and presented in Figures 4.15 through 4.20. The conditions included all three calcium aluminate cements and reinforcement concentrations of 0, 60 and 75% by weight. The thermal conductivity at the highest mean temperatures ranged between 0.9 and 1.4 W/m-°K, in all experimental formulations. Any difference between the formulations was not great. All castable cement formulations performed better than the premium reference brick used as the standard. A few stress cracks developed during the heating and testing but these were not severe. The condition and durability of the cast blocks after testing were similar to each other.

5.7 Differential Thermal Expansion

Heating or cooling of a ceramic material will often result in the propagation of micro cracks. The micro cracks are detrimental and result in bulk strength loss. Thermal shock failures occur when the thermal gradient produces thermal stresses that exceed the minimum load necessary to initiate and propagate an intrinsic microcrack. Cooling contracts the free surface while the bulk of the body remains at higher temperatures. The theories that surround the resistance of brittle materials to thermal fracture have developed from the observations of the effects of heating and cooling and linear-elastic-fracture-mechanics.

Simple observations made on the refractory cement coupons indicate a characteristically different type of cracks on heating and cooling. First it is important to note that all the cracks initiate from a free surface. Cracks formed on cooling grew perpendicular and inward from the surface. Cracks caused by heating are oriented at an angle from the surface into the coupon close to 45° from the surface flat or flat side of a reinforcement particle. Heating cracks were observed in the furnace from the open door. Cooling cracks have a time delay between the temperature change and the development of the crack whereas the heating cracks often develop during the ramp up to temperature. The time delay is believed to have been the result of the slow cooling of the material in the center of the coupon.

Thermal stresses are complicated in composite materials like concrete by the thermal gradient and the differential thermal dilation of the two or more phases. The thermal differential dimension changes between the reinforcement phase and the matrix phase with its various heterogeneous sub-phases result in stress build up. The strain energy of the system increases until the strain energy causes the cracks to absorb the excess strain energy. Since the process is the conversion of excess strain energy into surface energy the crack extension is proportional to the difference in thermal dilation between the two phases and temperature. The crack extends until the strain energy is compensated.

Characteristically the batches formulated using the zirconia grog exhibited a greater degree of cracking on cooling than the other reinforcement formulations. It is believed that the cracking results from a combination of high aspect ratio, high CTE mismatch and large size of the reinforcement aggregate. Formulations using the zircon exhibited the least amount of cracking on cooling because of the closer matched CTE. Formulations made with the crushed spinel and the dead burnt magnesia rock exhibited similar levels of cracking. The behavior is related to the smaller size and aspect ratio of the reinforcement particles.

5.8 Abrasive Wear Properties

The refractory concrete is designed for application as the first wall thermal barrier in combustion chambers, cement rotary kilns, calcining vessels and glass melters. The environments are varied but include exposure to hot gases, abrasive particles, viscous fluids and high thermal gradients. The cement is applied in thick layers and must be capable of supporting dead weight, compressive and thermal loads.

The DSRW test is a three-body abrasive wear test that applies the load or contact pressure through thousands of small point contacts. The sand grain diameter and morphology are controlled to assure even contact pressure. The sand contact area is the same scale as a grain of the cement or additive, ~ 5-20 microns. The small size of the contact is well suited to test the ceramic bond strength between grains, loading a single grain at a time. The reinforcement particle size is much larger than the abrasive particles. The load transferred to the reinforcement is through many hundreds of sand particles resulting in the energy being dissipated through the formation of wear debris, crushing the sand particle or distributed into the bulk of the matrix, away from the wear surface.

The dry sand rubber wheel abrasive test produces conditions where the abrasive particle and the contact pressure remain reasonably constant. In single phase microstructure materials the counter face hardness is uniform over the wear scar. Abrasive testing of duplex materials is complicated by the different hardness or abrasion resistance of the two phases (matrix and reinforcement). A simplified analysis of the two materials is presented in the literature review of this thesis. The concrete microstructure

not only has the matrix and reinforcement phases but also is complicated by the porosity and the additive materials. The mechanism of wear may be different not just for the reinforcement but also for the different constituents of the matrix. Table 5.1 illustrates the wide range of hardness for the materials. Cement formulations using the harder materials should exhibit greater wear resistance if the wear mechanism is controlled by the hardness. This was not found to be the case. Coupons formulated with the spinel did not outperform coupons formulated using chromia. Hardness does not appear to have as great an impact as the ceramic bonding reflected in the coupons fired at 1000°C versus those at 1200°C. Examination of the wear debris found particles that ranged from submicrometer size up to a few microns. The qualitative identification of single grains of spinel and chromia were possible using the SEM. The wear mechanism is believed to be a combinations of scraping, crushing and breaking the interparticle ceramic bond. The relative size of the wear debris to the sand particles ($d_{debris} < d_{sand}$) was similar in nearly all of the wear coupons tested. The relative size difference indicates the same wear three body wear mechanism and allows for a comparisons to be made between formulations. As complex as the mechanism is, the DSRW test is used as a relative measure of the integrity of the formulated product if all other processing and testing parameters could be controlled and made constant.

Table 5.1. Relative Hardness Ratio of the Constituents.

Component	**Hardness (Knoop)**	**Hardness Ratio H_x/H_{SiO2}**
SiO_2	1100	1.00
MgO	450	0.41
Al_2O_3	2000	1.82
$MgAl_2O_4$	1200	1.09
TiO_2	985	0.84
Cr_2O_3	400	0.36
CA	700	0.63
CA_2	850	0.77
CeO_2	450	0.41
ZrO_2	1520	1.38
$ZrSiO_4$	1150	1.045

5.9 Compression Strength Properties

The CCS test distributes the load throughout the volume along a single axis, top and bottom surfaces. Linear elastic behavior is expected in the porous ceramic cement material. The highest load obtained is the critical stress required for unstable crack formation. The ceramic composite cement contains many flaws that range in size. Theoretically critical stress is flaw size dependent and therefore only the largest flaws become the flaws of interest in the composite cement coupons. Microstructural observations demonstrate the largest flaws are found along the interface between the matrix and the reinforcement. The cause of these flaws is presumed to be the interfacial strain due to the thermal expansion mismatch between matrix and reinforcement.

The results illustrate consistent strength results between size samples made from the same formulation of cement, additive and reinforcement. The high alumina calcium aluminate cement set of data also includes examples from both half and full size samples. The disagreement of the test results is random across the various batch formulations and the agreement between the half size and full size samples is remarkably close. The agreement is less than the 20% deviation observed for the reference coupons. The data set from half size and full size coupons made with the calcium dialuminate cement illustrate two trends related to formulation. The strengths for the batches prepared without reinforcement phase were similar. The batches prepared using the zirconia grog reinforcement exhibited a greater strength than batches reinforced with dead burnt magnesia rock. The compression strength change with the type and concentration of reinforcement are better understood in later sections where other influences are drawn from the data.

Comparisons of the fired and green coupons show a loss of strength brought about by sintering. The batches SP13 through 19 are differentiated by their compaction method, vibration vs. pressing. Vibration compacted batches were found to have a gravity segregated reinforcement and a lower compression strength. The water saturation comparison was made using the dead burnt magnesia powder additive to the calcium dialuminate cement. A 25 to 50% loss of strength is found in coupons saturated with water.

The cross-section photomicrographs shown in the results illustrate compressive shear failure crack path characteristics. The crack path orientations are parallel to the applied compression load, a clear indication of a shear failure mode. The photomicrographs illustrate the crack path and the relationship to the different reinforcements. The crack path in the batches formulated with the spinel reinforcement follows the interface boundaries in most cases. The path in samples formulated with zirconia grog also follows the interface but clearly reinforcement fracturing is observed. The dead burnt magnesia rock samples show a matrix fracture path and also crack arrest at the reinforcement is illustrated. The dead burnt magnesia is the better reinforcement for crack arrest.

5.10 High Alumina Calcium Aluminate Cement and Concrete

The formulations made using high alumina calcium aluminate premix cement were mixed with additives to improve thermal, abrasion resistance and strength properties. Improvements with the various additives and reinforcement concentration were more obvious in the melting tests and abrasive wear resistance. The overall improvements for these formulations are summarized below.

Although the melt test results are not quantitative, the thermal stability of the concrete was found to improve with increasing additions of chromia, magnesia and spinel. The microstructures indicated the magnesia and spinel remain relatively inert up to the melting point as indicated in the photo micrographs that show defined grains with relatively uniform size at elevated temperatures. The chromia grains were found to form reaction layers around their perimeter.

Coupon density was not found to influence the wear rates. Given that the density and measured porosity are related and the pore is a flaw, the critical flaw size was greater than the largest pore size found in the 1200°C sintered microstructure. The coupons fired a 1000°C would be expected to exhibit greater scatter because of the less developed microstructure.

The temperature and thermal history have been stressed as important to the microstructural development of the ceramic bond. The normalizing of the temperature and history influence is critical for multiple sintering batch experiments. Even though the composite is a heterogeneous structure a relatively uniform development of the ceramic bonding across the test sample is important for batch to batch ranking of the influences by additives and reinforcements. Coupons from identical mold positions were fired at two temperatures, 1000 and 1200°C. Property differences are evident between the coupons fired at the two temperatures. The lower temperature fired coupons did not fully develop the ceramic bond as demonstrated in the wear rate as shown in several presentations of the data. Coupons fired at 1200°C have lower wear rates and exhibit lower data scatter than compared to the coupons fired at 1000°C. These presentations also indicate a bias due to the relative face of the coupon to the mold. The wear results are more precise for side #2 on both the high temperature and low temperature fired coupons. Explanation of the bias is not obvious, analysis of the reinforcement exposed in the wear scar indicates the bias is not a function of the reinforcement. Microstructural analysis on several prepared cross sections are not conclusive, however, qualitative interpretations indicates a possible porosity change, decrease, in the zone of material adjacent to side #2. This remains an area for further investigation. However, these results indicate that the influences of the specific additive and reinforcement materials should be sorted such that side #2 wear data is compared to other side #2 data.

The cold compression strength in the high alumina calcium aluminate premix concrete formulations was shown to drop as the open porosity is increased. The strength and porosity relationship relates well with other ceramic materials and follows the accepted understanding that flaws and porosity are one in the same.

The water to cement ratio does not influence the wear rate or the compression strength. The influence of the total additives and total cement concentration on the compressive strength and wear rate are not evident when the data is viewed as a whole. When the additive influence is sorted by the specific additives trends of increasing wear rate with additive concentration are indicated. The ratio of magnesia to chromia influences the compression strength but not the wear rate. As the chromia concentration is increased the strength is increased. A volume fraction of reinforcement effect in the

high alumina calcium aluminate matrix materials is not indicated in the compression strength test results however a trend is indicated in the wear test results, coupon 2 side #2. The influence of increasing reinforcement on lowering the wear rate is more evident using the wear scar analysis results. The wear scar analysis examined the influence of the exposed reinforcement in the wear scar on the wear rate and found a wear rate improvement with increased reinforcement. The reinforcement area in the wear scar and volume fraction of reinforcement in the batch was compared with the understanding that the relationship should be linear, $V_r/V = A_r/A$. Figure IV.A.15 illustrates a large segment of the data falling on one side of the line. Although the bias is small, this leads to the conclusion that the exposed reinforcement in the wear scar is less than the actual volume fraction of the formulation. This may be an effect of pull out, although none was observed, or that the reinforcement on the surface was not representative of the volume fraction. The latter is likely because of the sample preparation and sample size. Being that all the samples were mixed and prepared using the same standard process the relative differences between the formulations should be the same.

5.11 Fondu and Calcium Dialuminate Cement and Concrete

The Fondu and calcium dialuminate cement testing followed the HACA coupon testing and benefited with the understanding of the need to fire at a single temperature, 1200°C, to gain higher data precision. All of these coupons were fired at the higher temperature. The same side #2 to side #1 effect was observed with these batches, clearly indicating a coupon processing effect.

The test results were organized to determine a relationship between the mixing water to cement ratio and the strength and wear rate. Only the coupons formulated with spinel additives showed a relationship of increasing wear with increasing water, (Figure IV.C.26). This series of formulations changed the water to cement ratio varies from 15 to 75%. The results exhibit a five-fold increase in wear rate with the water to cement ratio from 0.4 to 0.7. At water ratios of less than 0.4 a wear rate change is not observed. A calcium dialuminate set of batches (Figure IV.C. 61) confirms little change to the wear rate at ratios less than 0.4. The compression strength values are found to decrease with

the increasing water in both cements and in most additives (Figure IV.C.23) the highest compression strengths are found in batches made with low water. The changing water influences the hydration reactions, reaction products and the shrinkage. Increasing water increases the shrinkage cracking, shrinkage cracks are intrinsic flaws and therefore result in lower compression strengths and higher wear rates.

The porosity over the 5 to 12% range does not influence the wear rate. The compression strength results do not indicate a possible relationship with increasing porosity in, Figure VI.C.24. However in a set of calcium dialuminate coupons with low reinforcement concentrations found a clear trend of decreasing compressive strength with increasing porosity is shown, Figure IV.C.41. The influence of porosity is just not as obvious in these cements as observed in the HACA cement coupons. As a general rule, as the concentration of the inert additives (fused magnesia, fused spinel, alumina) increased the compressive strength was found to decrease whereas with the more active dead burnt magnesia, the compression strength stayed the same as the additive levels were increased. The wear rates increased with additive concentrations greater than 40 to 50% in most cases.

The influence of reinforcement on the wear properties was not obvious until concentrations exceeded 60%. This was evident for each of the reinforcement phases. The reinforcement particles distribute the contact pressure deeper into the sample. The contact pressure loads are spread to a greater volume of material, as a greater area fraction of the wear scar becomes reinforcement. At the highest reinforcement loading, reinforcement to reinforcement contact was observed which correlated to diminished matrix phase surrounding the reinforcement. The thermal cycle and CTE mismatch lead to cracking and poor strength as evidenced in the CCS results and the microstructure analysis. The compression strength results indicated higher strengths were possible in samples with higher reinforcement up to 75%, but clearly the results were scattered and required sorting into the specific types of reinforcement and additives to observe trends.

The wear scar analysis of the exposed reinforcement exhibited a high level of precision on both side one and side two results. A decreasing wear rate trend with increasing exposed reinforcement was not clearly observed indicating other factors, for example CTE and porosity. Also the wear scar analysis did not exhibit a decreasing

wear rate with increasing wear scar area, in fact just the opposite. An increase in the wear rate did not increase the wear scar area. The conventional understanding of tribological loading of metallic materials states the wear rate should exhibit contact pressure dependence. For the three body wear test, DSRW, a given dead weight load produces a contact pressure that is constant based on the surface area of the wear scar. As the wear scar increases size the load is spread over a greater area and the contact pressure is reduced therefore a lower wear rate is expected. The cement coupon wear scar analysis exhibit an increasing wear rate with increasing wear scar size. In several examples the wear scar size increases more than 50%, drastically reducing the contact pressure but the wear rate does not decrease. The wear rate increases with increasing wear scar area. The abrasive wear rate does not follow conventional thinking over the range of conditions in the test. The brittle nature or linear elastic behavior of the ceramic bonds and the area of the inter particle bond is likely more responsible for the wear behavior exhibited in the ceramic composite cement material. The likely mechanism is that of a sand grain loading the composite surface and fracturing a ceramic bond. The load far exceeds the strength of the ceramic bond.

The influence of the reinforcement on the cement produced mixed wear rate results. Only two batches were formulated using zircon reinforcement and these batches outperformed the other reinforcement materials. The reasons may be related to the thermal expansion match or that the high aspect ratio produced better matrix to reinforcement interface. However, melt testing and microstructure analysis indicates poor thermal stability of the zircon and degradation even at the sintering temperatures. The zirconia grog outperformed the other reinforcements in the wear testing but performed poorly in compression strength testing. The high thermal coefficient of expansion mismatch produced high interface cracking and microstructural studies indicate reinforcement to reinforcement binding at volume fractions greater than 50%. The dead burnt magnesia rock could be added to high concentrations and reduce the wear rate. The dead burnt magnesia improved the compression strength and exhibited high thermal stability in the microstructural studies. The dead burnt magnesia and the calcium dialuminate are well suited for high temperature stability and improved thermal shock resistance. The crushed spinel reinforcement is well suited for thermal cycling and

chemical inertness. The spinel did not exhibit an improvement over the other reinforcements. Only one batch was prepared using the zircon reinforcement and Fondu cement. The zircon was compatible with the cement and exhibited improved wear resistance over the high alumina calcium aluminate cement. Additional studies using the zircon reinforcement and the Fondu cement would produce insight for improved formulations.

5.12 Other Testing

The experimental formulations can be refined and further material property testing performed. Larger coupon sizes should also be tested. The wear related degradation can also be simulated using an erosion test technique. This technique can be modified to include hot gases, entrained particles and heated coupon holders to obtain relative rankings near their expected operating temperatures. One of the obvious areas of research to be considered is high temperature softening or pyrometric cone equivalent (PCE) measurements. The PCE is common to most refractory specifications and will be a requirement for future commercialization. Testing of the castable cement application method should be investigated. The use of "shot-crete" application methods requires specific flow characteristics of the dry powder. Use of polymers and moisture stabilizers will be needed to reach the requirements. Concentrations are optimized using experimental formulations mixed in larger batches and applied on simulated hangers.

6.0 Conclusions

Advanced refractory materials with superior thermal stability wear resistance and strength can be designed using calcium aluminate cements, high temperature additives and reinforcements. Materials Science provides the basis for selection of materials to design composite microstructures with improved properties. The high temperature properties of calcium aluminate cement can be improved by blending higher temperature oxides and compensating for the loss of strength using a reinforcement aggregate. More than 200 formulations have been produced during the course of this research and many possess wear resistance and strength properties equal to or exceeding the cements with out additives. The following material relationships are concluded by experimentation.

1. The cement thermal stability was found to rank from high to low: calcium dialuminate, premix (high alumina calcium aluminate) and Fondu cement. Cement formulations with dead burnt magnesia, reagent grade magnesia, chromia-magnesia blends and spinel additives were found to increase the temperature of the first liquid to form. Higher concentrations increased the temperature.
2. Additions of inert magnesia up to 20% does not influence the wear resistance which is par with the reference firebrick and batches prepared without additives. Inert magnesia concentrations from 20% up to 40% produces a moderate decrease in wear resistance. Increasing inert magnesia concentrations greater than 50% has marked loss of wear resistance. All concentrations of inert magnesia added to the cements are detrimental to the compression strength.

3. Dead burnt magnesia can be added to CA_2 cements up to 50% and not influence the wear rate. Adding and increasing dead burnt magnesia concentrations does not greatly change the compression strength up to 60%. Higher concentrations degrade the properties. The wear and strength properties of CA_2 cement and dead burnt magnesia additives are nearly the same as or slightly improved with respect to the reference firebrick. It is concluded that dead burnt magnesia is an effective additive to castable cement.
4. The influence of spinel additive to premix and Fondu cements was not found to change the wear and strength up to 20%. Spinel concentrations greater that 50% produce a large drop to the wear and strength properties. The spinel is not an effective additive.
5. The blends of chromia and reagent grade magnesia used as an additive were found to improve the wear resistance and compression strength greater than magnesia additive alone. The blends maintain an improved wear rate and compressive strength in additions up to 35% concentration. The blends with the higher chromia exhibited the greatest property improvement of the magnesia to chromia blends. The increase in compressive strength is more pronounced in blends with higher chromia concentrations. The properties are improved above the reference materials and the cements with no additives. The improvement to the CA_2 cement wear rate is not as effective as the dead burnt magnesia additive. Chromia and magnesia are effective additives.
6. Alumina added to the CA_2 cement is detrimental to the wear resistance. The influence on the compression strength is not conclusive. The wear and strength properties of the properties of the reference material and additive free cements perform better than batches made with alumina. Batches made using alumina-titania additives exhibit poor wear resistance over all concentrations and a pronounced drop in strength at concentrations greater than 40%, similar to the effects of alumina.

7. Cerium oxide added to the CA_2 cement does not change the wear resistance in CA_2 cement. The wear rate is constant over the range additive concentrations. The compression strength at 40% concentration was improved slightly over the reference material and CA_2 cement without additives.
8. Zircon reinforcement volume fraction slightly increases the wear resistance with increasing concentration in the premix cement. The reinforcement increases the compression strength.
9. High-density zirconia grog reinforcement phase reduces the wear rate in Fondu and CA_2 cements. Higher concentrations increased the wear resistance. The reinforcement does not improve the compression strength in either of the cements. The wear resistance improved slightly over the reference firebrick. Formulations with concentrations greater than 60% lost structural integrity following sintering due to coefficient of thermal expansion miss match. The properties of the Fondu and CA_2 cements are improved with zirconia reinforcement at concentrations less than 50%.
10. Spinel reinforcement has a negative effect on the wear and strength properties of the Fondu and CA_2 cements. A graded distribution of the spinel reinforcement improved the wear resistance. High concentrations of the spinel reinforcement caused the coupons to lose structural integrity. The compressive strength using spinel is lower than cements with out reinforcement.
11. The dead burnt magnesia reinforcement phase improves the wear resistance with increasing concentration. The compressive strengths are improved with dead burnt magnesia reinforcement up to 50%. Coupons maintained structural integrity following sintering. Dead burnt magnesia is an effective reinforcement.

In summary, there is a wide range of castable compositions that can now be tailored for elevated temperature performance, high wear resistance and improved strength. The compositions for elevated temperature use include formulations of high purity calcium aluminate cement and dead burnt magnesia added up to 50%. Castable ceramics intended for high wear resistance can be formulated with Fondu and Calcium aluminate cements and blended with lower additive concentrations but increased reinforcement like dead

burnt magnesia rock or zirconia grog up to 60 %. Castable ceramic refractory materials intended for high strength would be formulated with a zircon reinforcement and matrix of Fondu cement blended with chromia. Additives that are catalytic to combustion gases are compatible with calcium aluminate castable cement and further study is warranted for a new class of castable ceramics designed for their chemical properties.

References

1) R. Roy, "Rational Molecular Engineering of Ceramic Materials," Journal of American Ceramic Society, Vol. 60, (7-8), 1977, pp. 350-363.

2) United States Department of Commerce, "Current Industrial Reports," Economics and Statistical Administration, Bureau of the Census, Refractories – MA32C, September 1997.

3) The Refractory Institute, Refractories, 650 Smithfield St. Pittsburgh, Pennsylvania 15222, Copyright 1966.

4) Engineered Materials Handbook, Vol. 4, "Ceramics and Glasses," ASM International, Metals Park Ohio 1991.

5) L. H. Van Vlack, "Physical Ceramics for Engineers," Addison-Wesley Publishing 1964.

6) W. D. Kingery, "Introduction to Ceramics," Wiley & Sons, 1960.

7) M. Barsoum, "Fundamentals of Ceramics," McGraw-Hill, 1997.

8) V. Smith, B. Deckman and D. Brueck, "Where Do We Go From Here?," American Ceramic Society Bulletin, Vol 73, (12), 1994.

9) H. J. Heine, "Refractories Revisited," Metal Producing, Vol. 33, June 1996, pp. 25-32.

10) "Global Ceramics Industry," American Ceramic Society Bulletin, Vol. 72, (7), 1993, pp.107-109.

11) W. G. Holroyd and W. H. McCracken, "Refractory Industrial Minerals from the People's Republic of China: Development and Future," Mining Engineering, Vol. 55, (1), 1993, pp. 49-53.

12) "Short Term Future of Refractories Looks Strong," Ceramic Industry, Vol. 146, (9), 1996, pp. 56, 58-59.

13) "Giants in Refractories," Ceramic Industry, Vol. 145, 1995, pp. 47-49.

14) C. E. Semler, "The Refractories Industry Never Sleeps," Ceramic Industry, Vol. 147, (8), 1997, p. 32.

15) M. Madono, R. P. Racher and M. K. Kunka, "Minerals Review," American Ceramic Society Bulletin, Vol. 76, (6), 1998, pp. 81-132.

16) J. Liska, "Using Refractory Concrete for Lining Injection Lances," Metallurgical Journal, Vol. 46 (1-2), 1991, pp. 55-64.

17) T. P. Nosova et al., "Refractory Concrete for Steel Teeming Ladles," Proceedings, Plenum Publishing Corporation, UCD 666.974.2, 1989, pp. 66-68, (Translated from Ogneuporty, No. 2, pp.5-6, February 1989).

18) A. J. Brewster, "Free Flow Refractory Castables take the Shape," Steel Times, Vol. 223, (1), 1995, pp. 15-17.

19) D. A. Brosnan, M. S. Crowley and R. C. Johnson, "CPI Drive Refractory Advances, Chemical Engineering," Vol. 105, (11), 1995, [8 pp.].

20) R. J. Volk, "Ultralow Cement Castables," Iron and Steel Engineer, Vol. 26, (9), 1989, pp. 44-46.

21) D.P. Sciaretta and R. B. Vedetto, "New Age Monolithic Refractory Castables," Metal Producing, Vol. 33, June 1989 pp. 30-34.

22) S. Smith, "Precision Manufactured Castables for Cast House Application," Light Metals, 1995, Proceedings of the 124th TMS Annual Meeting, Las Vegas, 1995. Minerals, Metals and Metallurgical Society, 1995, pp. 1121-1126.

23) S. Banerjee, "Monolithic Refractories," America Ceramic Society, World Scientific Publishing Co., 1998.

24) R. T. Oxnard, "Refractory Recycling," Am. Ceram. Soc. Bulletin, Vol. 73, (10), 1994, pp. 46-49.

25) L. D. Alexander, "Waste Disposal Options for Refractory Tearout," American Ceramic Society Bulletin, 74, (1), 1995, pp.68-70.

26) Annual Book of ASTM Standards, Vol. 15.01, American Society for Testing Materials.

27) American Ceramic Society, "A Synthetic Mullite Refractory," American Ceramic Society Bulletin, Vol. 72, (7), 1993, pp. 40-42.

28) D. J. Bray, "Toxicity of Chromium Compounds Formed in Refractories," American Ceramic Society Bulletin, Vol. 64 (7), 1985, pp. 1012-16.

29) N. J. Cooney, "Status of MSDS of Brick," American Ceramic Society Bulletin, Vol. 74 (2), 1995, pp. 67-68.

30) G. Geiger, "Refractory Installations and Tearout," American Ceramic Society Bulletin, Vol. 73 (10), 1994, pp. 51-52.

31) H. Fukuyama, J. R. Donald, and J. M. Toguri, "Wetting behavior between Fayalite-Type Slags and Solid Magnesia," Journal of American Ceramic Society, Vol. 80 (9), 1997, pp. 2229-36.

32) K. Goto and W. E. Lee,"The Direct Bond in Magnesia Chromite and Magnesia Spinel Refractories," Journal of American Ceramic Society, Vol. 78 (7), 1995, pp. 1753-60.

33) J. G. M. van Mier, "Fracture Processes of Concrete," CRC Press, 1997.

34) H. F. W. Taylor, "Cement Chemistry," Second Edition, American Society of Civil Engineers, Tomas Telford Services Ltd., 1997.

35) M. Bohner, J. Lemaître, T.A. Ring, "Effects of Sulfate, Pyrophosphate and Citrate Ions on the Physico-Chemical Properties of Cements made of Betatricalcium Phosphate - Phosphoric Acid - Water Mixtures," Journal of American Ceramic Society, Vol. 79, 1996, pp. 1427-34.

36) M. Bohner, P. Van Landuyt, H.P. Merkle, J. Lemaître, "Composition effects on the pH of a hydraulic calcium phosphate cement," Journal of Material Science Materials in Medicine, Vol. 8, (11), 1997, pp. 675-681.

37) P. W. Brown and M. Fulmer, "Kinetics of Hydroxyapatite Formation at Low Temperature," Journal of American Ceramic Society, Vol. 74, (5), 1991, pp. 934-40.

38) T. Sugama, and E. Wetzel, "Microsphere-filled Lightweight Calcium Phosphate Cements," BNL 48543, Journal of Material Science, Vol. 29, 1994, pp. 5165.

39) Concrete Manual, Eighth Edition, U. S. Department of the Interior, U. S. Government Printing Office, 1975.

40) J. J. Waddell, "Concrete Inspection Manual," International Conference of Building Officials, 1976.

41) Dale P. Bentz, "Three-dimensional Computer Simulation of Portland Cement Hydration and Microstructure Development," Journal of American Ceramic Society, Vol. 80, (1), 1997, pp. 3-21.

42) M. Collepardi, G. Baldini, M. Pauri, "Retardation of Tricalcium Aluminate Hydration by Calcium Sulfate," Journal of American Ceramic Society, Vol. 62, (1-2), 1979, pp. 33-35.

43) D. E. Macphee, D. C. Sinclair, and S. L. Cormack, "Development of an Equivalent Circuit Model for Cement Pastes from Microstructural Considerations," Journal of American Ceramic Society, Vol. 80, (11), 1997, pp. 2976-84.

44) W-G. Lei and L. J Struble, "Microstructure and Flow Behavior of Fresh Cement Paste," Journal of American Ceramic Society, Vol. 80, (8), 1997, pp. 2021-2028.

45) N. Bell, S. Venigalla, P. Gill and J. Adair, "Morphological Forms of Tobermorite in Hydrothermally Treated Calcium Silicate Hydrate Gels," Journal of American Ceramic Society, Vol. 79, (8), 1996, pp. 2175-78.

46) K. Sujata and H. M. Jennings, "Formation of a Protective Layer During the Hydration of Cement," Journal of American Ceramic Society, Vol. 75, (6), 1992, pp. 1669-73.

47) M. Daimon, S. Abo-el-Enein, G. Hosaka, S. Goto and R. Kondo, "Pore Structure of Calcium Silicate Hydrate in Hydrated Tricalcim Silicate," Journal of American Ceramic Society, Vol. 60, (3-4), 1977, pp. 110-114.

48) N. K. Katyal, S. C. Ahluwalia and R. Parkash, "Solid Solution and Hydration Behaviour of Magnesium-Bearing Tricalcium Silicate Phase," Cement and Concrete Research, Vol. 28, No.6, 1998, pp. 867-875.

49) B. Marchese, "Microstructure of Mature Alite Pastes," Journal of American Ceramic Society, Vol. 61, (7-8), 1978, pp.349-355.

50) B. Marchese, Comment on "Composition and Morphology of Hydrated Tricalcium Silicate," Journal of American Ceramic Society, Vol. 60, (9-10), 1977, pp. 459-51.

51) R. B. Williamson, Solidification of Portland Cement, Materials Science, Pergamon Press, New York, Vol. 15, (3), 1972.

52) J. F. Yong, H. S. Tong and R. L. Berger, "Compositions of Solutions in Contact with Hydrating Tricalcium Silicate Pastes," Journal of American Ceramic Society, Vol. 60, (5-6), 1977, pp. 193-97.

53) H. S. Tong and J. F. Young, "Composition of Solutions in Contact with Hydrating Beta-Dicalcium Silicate," Journal of American Ceramic Society, Vol. 60, (7-8), 1977, pp. 321-323.

54) N. L. Thomas, "Corrosion Problems in Reinforced Concrete: why accelerators of cement hydration usually promote corrosion of steel". Journal of Materials Science, Vol. 22, 1987, pp. 3328-3334.

55) D. Lankard and L. Hackman, "Use of Admixtures in Refractory Concretes," American Ceramic Society Bulletin, Vol. 62, (9), 1983, pp. 1019-1023.

56) T. Sugama and N. Carciello, "Strength Development in Phosphate Bonded Calcium Aluminate Cements," Journal of American Ceramic Society, Vol. 74, (5), 1991, pp. 1023-30.

57) T. Sugama and L.E. Kukacka, "Characteristics of Magnesium Polyphosphate Cements Derived From Ammonium Polyphosphate Solutions," Cement and Concrete Research, Vol. 13, 1983, pp. 499-506.

58) T. Sugama and L.E. Kukacka, "Magnesium Monophosphate Cements Derived from Diammonium Phosphate Solutions," Cement and Concrete Research, Vol. 13, (3), 1983, pp. 407-416.

59) X. Fu and D.D.L. Chung, "Sensitivity of the Bond Strength to the Structure of the Interface Between Reinforcement and Cement, and the Variability of this Structure," Cement and Concrete Research, Vol. 28, (6), 1998, pp. 787-793.

60) H. M Jennings, "Design of High Strength Cement Based Materials: Part 3 State of the Art," Materials Science and Technology, Vol. 4, 1988, pp. 291-300.

61) A Bentur and M. D. Cohen, "Effect of Condensed Silica Fume on the Microstructure of the Interfacial Zone in Portland Cement Mortars," Journal of American Ceramic Society, Vol. 70, (10), 1987, pp. 738-43.

62) B. D. Barnes, S. Diamond, and W. L. Dolch, "Micromorphology of the Interfacial Zone Around Aggregates in Portland Cement Mortar," Journal of American Ceramic Society, Vol. 62, (1-2), 1979, pp. 21-24.

63) R. L. Coble, "Effects of Particle-size Distribution in Initial-Stage Sintering," Journal of American Ceramic Society, Vol. 56, (9), 1973, pp. 461-466.

64) S. K. Das, K.K. Singh and P. K. Das Poddar, "Role of Reactive Additives on the Strength Development of Calcium Di-aluminate Based Refractory Cement," IRMA Journal, Vol. 29, (1), 1996, pp. 20-23.

65) O. E. Omotoso, D.G. Ivey and R. Mikula, "Hexavalent Chromium in Tricalcium Silicate, Part I Quantitative X-ray Diffraction Analysis of Crystalline Hydration Products," Journal of Materials Science, Vol. 33, 1998, pp. 507-513.

66) O. E. Omotoso, D.G. Ivey and R. Mikula, "Hexavalent Chromium in Tricalcium Silicate, Part II Effects of Cr^{VI} on the Hydration of Tricalcium Silicate," Journal of Materials Science, Vol. 33, 1998, pp. 515-522.

67) H. Teramoto and S. Koie, "Early Hydration of a Superhigh-Early-Strength Portland Cement Containing Chromium," Journal of American Ceramic Society, Vol. 59, (11-12), 1976, pp. 522-25.

68) J. Skalny and M. E. Tadros, "Retardation of Tricalcium Aluminate Hydration by Surfaces," Journal of American Ceramic Society, Vol. 60, (3-4), 1977, pp. 174-75.

69) B. Matkovic, S. Popovic, V. Rogic and T. Zuic, "Reaction Products in Magnesium Oxychloride Cement Pastes System Mgo-$MgCl_2$-H_2O," Journal of American Ceramic Society, Vol. 60, (11-12), 1977, pp. 504-507.

70) C. Sorreell and C. Armstrong, "Reactions and Equilibria in Magnesium Oxychloride Cements," Journal of American Ceramic Society, Vol. 59, (1-2), 1976, pp. 51-54.

71) F. F. Lange, "Sinterability of Agglomerated Powders," Journal of American Ceramic Society, Vol. 67, (2), 1984, pp. 83-89.

72) R. W. Dunys and J. W. Halloran, "Influence of Aggregates on Sintering," Journal of American Ceramic Society, Vol. 67, (9), 1984, pp.596-601.

73) D. L. Johnson, "A General Model for the Intermediate Stage of Sintering," Journal of American Ceramic Society, Vol. 53, (10), 1970, pp. 574-577.

74) Y. S. Kwon, G. Son, J. Suh and K. T. Kim, "Densification and Grain Growth of Porous Alumina Compacts," Journal of American Ceramic Society, Vol. 77, (12), 1994, pp. 3137-41.

75) F. J. T. Lin and L. C. DeJonghe, "Initial Coarsening and Microstructural Evolution of Fast Fired and MgO Doped Al_2O_3," Journal of American Ceramic Society, Vol. 80, (11), 1997, pp. 2891-96.

76) F. J. T. Lin and L. C. DeJonghe, "Microstructure Refinement of Sintered Alumina by a Two Step Sintering Technique," Journal of American Ceramic Society, Vol. 80, (9), 1997, pp. 2269-77.

77) C. M. Kramer and R. M. German, "Low Temperature Sintering of Iron Oxides," Journal of American Ceramic Society, Vol. 61, (7-8), 1997, pp. 340-342.

78) H. Al-Kjaiat and M. N. Haque, "Effect of Initial Curing on Early Strength and Physical Properties of Lightweight Concrete," Cement and Concrete Research, Vol. 28, (6), 1998, pp. 859-66.

79) A.B. Auskern and W. H. Horn, "Effect of Curing Conditions on the Capillary Porosity of Hardened Portland Cement Pastes," Journal of American Ceramic Society, Vol. 59, (1-2), 1978, pp. 29-33.

80) T. C. Powers, L. E. Copeland, J. C. Hayes and H. M. Mann, "Permeability of Portland Cement Paste," Journal of American Concrete Institute, Vol. 26, (3), 1954, pp. 285-298.

81) W. H. Gitzen and L. D. Hart, "Explosive Spalling of Refractory Castables Bonded with Calcium Aluminate Cement," Ceramic Bulletin, Vol. 40, (8), 1961, pp. 503-510.

82) Z. Gong and A. Mujumdar, "A Two Dimensional Finite Element Model for Kiln Drying of Refractory Concrete," Drying Technology, Vol. 13, (3), 1995, pp. 585-605.

83) Z. Gong, B. Song and A. Mujumdar, "Numerical Simulation of Drying of Refractory Concrete," Drying Technology, Vol. 9, (2), 1991, pp. 479-500.

84) Z. Bazant and W. Thonguthal, "Pore Pressure and Drying of Concrete at High Temperature," Journal of the Engineering Mechanics Division, American Society of Civil Engineers, Vol. EM5, 1978, pp. 1059-1079.

85) P. Kofstad, Nonstoichiometry, Diffusion and Electrical Conductivity in Binary Metal Oxides, Wiley-Interscience Publishers, 1972.

86) V. Tikare and J. Cawley, "Application of the Potts Model to Simulation of Ostwald Ripening," Journal of American Ceramic Society, Vol. 81 (3), 1998, pp. 485-491.

87) I. Nettleship and W. Slaughter, "Dimensionless Parameters for Microstructural Pathways in Sintering," Journal of American Ceramic Society, Vol. 81 (3), 1998, pp. 700-704.

88) H. Zhou and J. Derby, "Three Dimensional Finite Element Analysis of Viscous Sintering," Journal of American Ceramic Society, Vol. 81 (3), 1998, pp. 533-540.

89) K. Kato, "Tribology of Ceramics," Wear, 136, 1990, pp. 117-133.

90) M. A. Moore and F. S. King, "Abrasive Wear of Brittle Solids," Wear, Vol. 60, (1), 1980, pp. 123-140.

91) T. Yamamoto, M. Olsson and S. Hogmark, "Three-body Abrasive Wear of Ceramic Materials," Wear, Vol. 174, 1994, pp. 21-31.

92) A Mumaroglu, F. Yilmaz and C. S. Okumus, "Reliability of Wear Volume Measurement Approaches in Relation to the Effect of Surface Finish on Friction and Wear of Al_2O_3," Tribology Transactions, Vol. 40, (2), 1997, pp. 381-385.

93) M. Terheci, "Grain Boundary and Testing Procedure: A New Approach to the Tribology of Alumna Materials," Wear, Vol. 211, 1997, pp. 289-301.

94) K. Cherif, B. Geroult, M. Rigaud, "Al_2O_3-ZrO_2 Debris Life Cycle During Wear: Effects of the Third Body on Wear and Friction," Wear, Vol. 208, 1997, pp. 161-168.

95) A. Misra and I. Finnie, "A Classification of Three-body Abrasive Wear and Design of a New Tester," Wear, Vol. 60, 1980, pp. 111-121.

96) Friction and Wear Testing Source Book, American Society for Testing Materials, Philadelphia Pennsylvania, USA, 1997.

97) D. H. Buckley and K. Miyoshi, "Friction and Wear of Ceramics," Wear, Vol. 100, 1984, pp. 333-353.

98) N. Axen and S. Jacobson, "A Model for the Abrasive Wear Resistance of Multiphase Materials," Wear, Vol. 174, 1994, pp. 187-199.

99) N. Axen and B Lundberg, "Abrasive Wear in Intermediate Mode of Multiphase Materials," Tribology International, Vol. 28, (8), 1995, pp. 523-529.

100) N. Axen and I. M. Hutchings, "Analysis of Abrasive Wear and Friction Behavior of Composites," Materials Science and Technology, Vol. 12, 1996, pp. 757-765.

101) N. Axen, I. M. Hutchings and S. Jacobson, "A Model for the Friction of Multiphase Materials in Abrasion," Tribology International Vol. 29, (6), 1996, pp. 467-475.

102) W. M. Garrison, "Khruschov's Rule and the Abrasive Wear Resistance of Multiphase Solids," Wear, Vol. 82, 1982, pp. 213-220.

APPENDIX I

RAW MATERIALS AND PHASE EQUILIBRIA DIAGRAMS

AI. Introduction

The castable refractory cement is a heterogeneous composite system. The cement has three primary components and two secondary components. Changing the relative amounts of each component makes the experimental formulations. Formulations also include admixtures. The interface zone between particles is filled with hydrates and concentrates the admixtures that do not volatilize. The interface zone components are the first sinter. Upon sintering the interface material will likely form a number of transient liquid phases depending on the various binary, ternary and quaternary nearest neighbors. The large number of possible combinations is possible. The appendix is a collection of the important phase equilibrium diagrams for the primary components, secondary components, admixtures and additives.

AI.2 Background

Research results on phase equilibrium diagrams for the refractory oxide systems are reported in a number of international journals. Examples or these publications are The Journal of the American Ceramic Society, Journal of the Electrochemical Society, Transactions of the British Ceramic Society and Journal of American Science to name a few. These journals have a long history of editorial excellence and tend to attract the latest work. The American Ceramic Society (ACS) was responsible for initiating a compendium of diagrams pertaining to oxide and other ceramic materials. The data are pulled form the published literature and reproduced in the compendia provided the quality of the work passes strict peer review. Since the first publication in 1964 the ACS has been joined by the National Institute of Standards and Technology (NIST) and the US Department of Commerce to produce at total of ten updates to the first volume. Update number eleven was scheduled for 1997-98 completion but is not yet not available.

Volume I was published in 1964 and supplements were published as follows: Volume II (1969), Volume III (1975), Volume IV (1981), Volume V (1983), Volume VI (1987), Volume VII (1989), Volume VIII (1990) Volume IX (1992), Volume X (1994), Volume XI (1995) and Volume XII (not finished). Over the last 40 years the ceramic phase equilibria diagrams have multiplied to more than 11000 entries.

A survey of these volumes indicates a several trends. The contributions are international. The laboratories have different capabilities and methods used to generate phase equilibria data vary. The modern laboratory is very much different from the laboratory used by Sir William Chandler Roberts-Austen who is credited with the first equilibrium diagram in 1897. Early studies used relatively crude furnaces and temperature recording devices whereas new equipment are highly accurate and automated. The age of painstakingly synthesizing ultra pure chemicals, melting, crushing, remelting, quantitative microscopy and x ray phase analysis have evolved and include readily available reagent grade materials, differential scanning calorimetric, electron diffraction and photoelectron spectroscopy. Electrochemical methods and calculation models are also used develop composition temperature diagrams based on thermodynamic properties. The new methods have increased the precision that has allowed a better understand of the impurity influence. Four and five component systems are studied with a surprising accuracy.

Shorthand notations are used in the literature. The end member components and the common compounds are abbreviated. Examples are as follows: A = Al_2O_3, C = CaO, M = MgO, S = SiO_2, F = Fe_3O_4 or $FeO{\cdot}FeO_2$, CA = $CaAl_2O_4$ or $CaO{\cdot}Al_2O_3$, CA_2 = $CaAl_4O_7$ or $CaO{\cdot}2Al_2O_3$, MA = $MgAl_2O_4$ or $MgO{\cdot}Al_2O_3$, P = P_2O_5, Z = ZrO_2 and C_2AS = $Ca_2Al_2SiO_7$ or $2CaO{\cdot}Al_2O_3{\cdot}SiO_2$.

AI.3 Raw Materials

Alumina and calcia are the principal end members in the conventional castable refractory cements. The alumina and calcia are calcined to form a clinker. Three clinkers are common calcium mono aluminate (CA), calcium dialuminate (CA_2) and the third is $C_{12}A_7$. Experimental formulations for improved castable cements include magnesia as a third major component to this system. Magnesia is added either as periclase (MgO) or as spinel ($MgA1_2O_3$).

Typically the calcium aluminate contains several impurity components depending on the grade of the product. The iron oxide and silica are two of the most common impurities found in commercial clinkers. The iron oxides may be added to the clinker to reduce the calcining temperature. The calcium aluminoferrite clinker exhibits fair hydration properties and helps produce a less costly product. The silica is tramp addition but also tends to lower the calcining temperature.

Experimental formulations will be made using admixtures to promote specific hydration reactions. The admixtures are compounds like CaCl, H_2SO_4, $MgCl_2$, HPO_2, $NH_4H_2PO_4$ and citric acid. The low melting point and organic admixture components will tend to volatilize upon sintering. The remaining material will form compounds with other impurities at lower temperatures. The solubility of the periclase and spinel are relatively high and at higher temperatures the admixture components will tend to diffuse

into the matrix. It is likely equilibrium will not be reached throughout the cement and impurity rich compounds will form at the interface and edges of pores.

An important component of the castable refractory cement is the aggregate. A zirconia-based aggregate has been selected for this research because of the high temperature stability. The aggregate and interface interactions at the sintering temperatures are to be expected. Like periclase the zirconia phase also has relatively high solubility for impurities if the thermal energies are sufficient to support diffusion. Because of the non-equilibrium sintering conditions aggregate impurity compounds need to be considered in a phase diagram study of this refractory system.

AI.3.1 Calcia

Calcia	CaO	T_{mp} = 2613°C	
	CaO	FCC Fm3m	NaCl Structure
	CaO_2	BCT I4/mmm	$CaCl_2$ Structure

Calcia refers to the calcined form of calcium oxide (CaO). Other terms for calcia are lime, burnt lime, calyx, fluxing lime, quicklime or unslaked lime. Traditionally calcia is a product of a limestone roasting (elevated temperature leaching) process followed by thermal decomposition of the calcium carbonate $CaCO_3$ + heat = CaO + CO_2. Limestone deposits are abundant and lime kilns are found in nearly every industrialized region. Coastal lime plants can also use crushed oyster shells to produce calcium carbonate. Lime is an important constituent in ceramic materials like mortars, glazes, plaster, and cement.

AI.3.2 Alumina

Alumina	Al_2O_3	T_{mp} = 2054°C	
	a-Al_2O_3	HCP R3m	a-Al_2O_3 Structure

Alumina is a specific term for aluminum oxide, Al_2O_3. Alumina is abundant on the earth's crust found mostly as hydroxides with a wide variety of impurities. The hydroxide mineral form of alumina is called bauxite. The alumina hydroxides have three polymorphs: gibbsite, boehmite and diaspore. Bauxite is a naturally occurring heterogeneous material. The composition includes aluminum hydroxides, silica, iron oxides, titania and other impurities. Bauxite is mined conventionally in open pits. Bauxite ore is processed to alumina through a wet chemical caustic leach method called the Bayer process. The Bayer process involves the hydrothermal digestion of the ore to get aluminate ions into solution using NaOH under pressure at 150 to 160 °C. The SiO_2, Fe_2O_3 and TiO_2 are not totally dissolved in this process and need to be removed by filtration. After filtration the solution is cooled and gibbsite precipitated using CO_2. The principal impurity is NaO_2 and depending on the filtration technology and the quality of mined bauxite a 99.5% alumina can be produced.

Bauxite deposits are abundant and depending on the purity bauxite it can be used directly. Majority of high purity, refractory grade bauxite is imported from China and Guyana, (Minerals Review). The bauxite is dried or calcined prior to shipment to reduce water and therefore the shipping costs per ton. Domestic production of bauxite is a mixture of bauxite and bauxitic clay, silicate impurities. The domestic bauxite has lower Al_2O_3 concentration and is seldom used as Bayer process feed stock. Domestic bauxite is ideal for production of calcium aluminate and intermediate duty refractories. The imported premium grade calcined refractory bauxite contains at a minimum 85% alumina where the domestic bauxite refractory grade has typically 40 to 70% alumina.

AI.3.3 Magnesia

Magnesi	MgO	T_{mp} =	°C	
	MgO	FCC		NaCl structure (Lattice parameter of 4.20 Å)

Magnesia (MgO) is an important component in refractory products. The mineral form, periclase, is naturally occurring but not abundant in clean deposits sufficient to supply commercial industry. Magnesite, $MgCO_3$, is a more common form of magnesium that is easily mined. Magnesite is the raw material to produce magnesia by thermal decomposition. Magnesite deposits are found in Australia, China, Brazil, North America and much of central Europe. Silica, iron, aluminum, manganese and calcium are the common impurities found in the ores. Because of the high solubility of periclase the impurity atoms are found both dissolved and in their mineral forms; dolomite, quartz, talc, serpentine, mica, magnetite, chlorite and pyrite. Magnesite mining can be costly because the impurity minerals are not uniformly distributed. The ores require beneficiation before chemical conversion to magnesite. Beneficiation processes vary with the ore but may include crushing, screening, washing, magnetic separation, sorting, and froth flotation and heavy media liquid separation.

Magnesia can also be produced from seawater and magnesium rich salt brines. The largest source of magnesium is the oceans where it appears in chloride form, $MgCl_4$. Seawater is approximately 0.13 % magnesium and represents an almost in exhaustible supply. Thirteen countries produce magnesia from seawater for export: China, France, India, Ireland, Israel, Italy, Japan, Mexico, Norway, South Korea, United Kingdom, The Netherlands and The Untied States. Seawater brines are made by evaporation in tidal flats. The brine is re dissolved and calcium hydroxide is added. A simple exchange reaction with the magnesium forming calcium chloride and an insoluble precipitate, magnesium hydroxide. The magnesium hydroxide precipitate is removed by gravity separation. The magnesium hydroxide filtered, calcined and sized. Calcium or other stabilizers are added during calcining to avoid atmospheric hydration. The alkali used to precipitate the hydroxide becomes one of the principal contaminants in the calcined magnesia.

The impurities and thermal decomposition parameters govern the physical and chemical properties of the magnesia. The magnesia grains grow in size with longer times and increased calcining temperatures. The reactivity and porosity of the grains decrease with increasing size. Magnesia is produced in three forms caustic-calcined, dead-burned and fused. Limiting the reaction temperatures too less than 900°C produces caustic-

calcined magnesia. The product is a high surface area, highly reactive form of magnesia. It is used as mineral supplements, fertilizers, cements, ceramics, petroleum additives and industrial buffering agents to list a few. The dead-burned magnesia is produced at temperatures greater than 1200°C and less than 1400°C. The product is characterized as having low reactivity and chemically resistant to basic slags. The dead-burned product is almost exclusively used in the nonferrous metal and refractory industries. Refractory industry uses crushed dead burned magnesia for sintered brick production and castable cement products. Fused magnesia is produced at temperatures greater than 2750°C in an electric arc furnace. The product is crushed and used in production of premium refractory products like the magnesia carbon products. The fused magnesia has superior abrasion resistance, strength and chemical reactivity over the dead-burned magnesia.

AI.3.4 Silica

Silica	SiO_2	$T_{mp} = 1723°C$			
	SiO_2	$T_{Poly} = 547°C$	HCP	Low Quartz	$P3_121$ or $P3_221$
	SiO_2	$T_{Poly} = 870°C$	HCP	High Quartz	$P6_266$ or $P6_422$
	SiO_2	$T_{Poly} = 1470°C$	HCP	Tridymite	$P6_3/mmc$
	SiO_2		FCC	High Cristobalite	Fd3m

Silica may exist in a number of polymorphic or crystal modifications. Silicon is reported to have 15 different modifications when considering geologic pressures and both the crystalline and amorphous forms. Silica exists in three main polymorph forms at atmospheric pressure: quartz, tridymite and cristobalite.

Crystalline quartz has widely different contaminant levels and the contaminants play an important role in the self-diffusion. Silica is usually an unwanted but essential component in many refractory ores. For most refractory products the refractoriness is decreased with the silica concentration. However, relatively pure silica exhibits good refractory properties and quartz glassware is the standard for high temperature and chemical inertness. Less than one percent of all produced silica is used for refractory production. Sources include siliceous rocks such like quartzite or gannister, which are silica and clay. Quartzite has small amounts of impurities such as calcia, alumina, titania and flint colloidal silica.

Designing a refractory system around the three polymorphic transformations has proven to be difficult. Thermal cycling through the polymorphic transformations will cause cracking in the ceramic bonding phase and eventual brick disintegration. For several decades before the premium refractories blast furnaces were lined with super dense silica bricks because of the resistance to slag. The furnace lining of silica brick was pre conditioned above 870°C for 10 weeks and as long as the temperature does not go below the polymorphic transformation temperature the furnaces have been known to last 25 years. Transitions within a form such as the high and low quartz are called displacive so that no atomic bonds are broken. The transformations take place by bond stretching and are instantaneous. Transitions between the quartz to tridymite are reconstructive, Si-O bonds are broken and rearrangement occurs.

AI.3.5 Iron Oxides

Iron Oxides Fe_2O_3 $T_{mp} = 1566°C$

The iron oxygen phase diagrams shows three oxides wustite (FeO), magnetite (Fe_3O_4), and hematite (Fe_2O_3). Wustite and magnetite are both face centered cubic oxygen lattices where wustite has the NaCl structure and magnetite has the spinel structure. Hematite has the corundum structure. Wustite is only stable above 570°C and has a wide stoichiometry range and the field widens with increasing temperature. The oxide is metal cation deficient. Magnetite is stoichiometric at the wustite to magnetite phase boundary.

Magnetite is a metal deficient oxide with respect to stoichiometric composition: $Fe_{3-y}O_4$. The value of y is a function of the partial pressure in the 1200°C to 1450°C temperature ranges. Magnetite has the spinel structure. The unit cell contains 32 cation octahedral sites and 64 tetrahedral sites. One half of the octahedral sites and one eighth of the tetrahedral sites are occupied by cations. At room temperature magnetite is an inverse spinel one eighth of the tetrahedral sites and one fourth of the octahedral sites are occupied by trivalent Fe ions. One fourth of the octahedral sites are occupied by the bivalent Fe ions. Hematite is an oxygen deficient oxide Fe_2O_{3-x}. The value of x ranges from .0015 at 1000°C to .011 at 1500°C. Diffusion studies indicate that the Fe ions and O ions diffuse at near the same rate at elevated temperatures.

AI.3.6 Spinel

Spinel $MgAl_2O_3$ $T_{mp} = 2135°C$

The spinel structure is based on the FCC closed packed oxygen sub-lattice in which a fraction of the octahedral and tetrahedral sited are filled. In the FCC oxygen lattice there are cubic sub-cells on half of the octahedral sites and one eight of the tetrahedral sites are occupied. The magnesia and alumina form in the spinel structure, $MgO{\cdot}Al_2O_3$ this is termed a normal or mineral spinel. The Al^{3+} cations occupy half of the octahedral sites and the Mg^{2+} cations are one eighth of the tetrahedral sites.

AI.3.7 Zirconia

Zirconia	ZrO_2	$T_{mp} = 2710°C$	
	ZrO_2	$T_{Poly} = 1170°C$	Monoclinic
	ZrO_2	$T_{Poly} = 2370°C$	Tetragonal
	ZrO_2		Cubic

Zirconia may be present in three different polymorphs, cubic, tetragonal and monoclinic. The high temperature transformation from cubic phase to the two phase cubic + tetragonal region occurs between 2260°C and 2370°C depending on the source of the raw materials. The difference points out the influence by impurities on this transformation temperature, for example Hafnium. The monoclinic to tetragonal

transformation occurs wit a corresponding volume change. The material has poor thermal shock resistance when the zirconia goes through the transformation. The volume of the unit cell becomes smaller as the oxide is made oxygen deficient, which suggests the major defect structure is oxygen vacancies. Kofstad considered that oxygen is by far the most mobile atomic species in each of the various modifications of ZrO_2

AI.4 Phase Equilibria

The refractory castable cement and the experimental formulations are best understood from the quaternary or ternary presentation of the equilibrium liquidus surface and phase boundaries. Only a few quaternary diagrams are reported. A larger number of ternary combinations have been reported and nearly all of the binary combinations of the refractory castable cement components have been reported. Table AI.1 lists a summary of a survey of the phase diagrams available in the literature with the year when the diagram first appeared.

AI.4.1Quaternary System A-M-C-S

The A-M-C-S is one of the few four component oxide systems ever studied in detail. The alumina, magnesia and calcia are principal end members in the refractory castable cement system. Silica is important because of the role silica plays in the formation of hydrates and the liquid phase sintering. The important phase tetrahedra for cement like materials are M-MA-CA-C_2AS and MA-C_2AS-CA-CA_2.

AI.4.2 Ternary Systems A-M-C

Compound	Melting Temp. °C	Name	Al_2O_3	MgO	CaO
A	2020	Corundum	100		
M	2800	Periclase		100	
MA	2135	Spinel	71.5	28.5	
C_5A_3	1455		52.2		47.8
CA	1600		64.6		35.4
C_3A_5	1720		75.2		24.8
C_3A	1535		37.8		62.2

The system has eight compounds and six ternary and eight binary invariant points. The lowest melting point occurs at two points on the diagram. The two eutectic temperatures have the same temperature 1345°C. The three phases in equilibrium are M, C_3A and C_5A_3 and M, C_5A_3 and CA. Six phase diagrams within the boundaries of these systems are reported in the ceramic literature.

AI.4.3 Ternary System A-M-S

Compound	Melting Temp. °C	Name	Al_2O_3	MgO	SiO_2
A	2020	Corundum	100		
M	2800	Periclase		100	
MA	2135	Spinel	71.5	28.5	
A_3S	1850	Mullite	72		28
$M_4A_5S_2$	Decomposes	Sapphrine	65	20	15

The alumina-magnesia-silica system is shown as Figure 712 in the compendium handbook of ceramic phase diagrams. The present diagram was revised and redrawn in 1960 by Osborn and Muan. The system contains eleven compounds, eleven ternary invariant points and 12 binary invariant points. The region of interest for the modified refractory cement, at low concentrations of SiO_2, has three predominant compound periclase, spinel and corundum. Sapphrine and mullite compounds connect two composition triangles.

AI.4.4 Ternary System A-M-F

No references found.

AI.4.5 Ternary System A-M-Z

No references found.

AI.4.6 Ternary System A-C-S

Compound	Melting Temp. °C	Name	Al_2O_3	SiO_2	CaO
A	2020	Corundum	100		
C	2570	Lime		100	
MA	2135	Spinel	71.5	28.5	
C_5A_3	1455		52.2		47.8
CA	1600		64.6		35.4
C_3A_5	1720		75.2		24.8
C3A	1535		37.8		62.2

The alumina-calcia-silica system is one of the more important systems when considering the refractory cements. The system is well studied because it makes up the compositions for the Portland cement clinker.

AI.4.7 Ternary System A-C-Z

No references found.

AI.4.8 Ternary System M-C-S

One reference to the ternary system is referenced in the literature. Osborn studied the system in 1906.

AI.4.9 Ternary System A-S-K

No references found.

AI.4.10Ternary System C-S-F

Two references to the ternary and a compound binary are cited in the literature. The diagram was part of the larger body of work in the cement materials published by Osborn in 1960. Twenty six years later Canha published an experimentally derived binary diagram if the CS-F system.

AI.4.11 Binary System Alumina-Magnesia

Compound $MgAl_2O_4$ 74% Al_2O_3 26% MgO

Rankin and Merwin first reported this binary system in their study of the CaO-Al_2O_3-MgO ternary system in 1916. The binary system contains two eutectics and one intermediate compound $MgAl_2O_4$. Roy et al. in 1953 published a partial diagram, Figure 260. The binary join from $MgAl_2O_4$-Al_2O_3 showed considerable solubility of alumina in the previously thought to be a stiochiometric compound. The maximum solubility of Al_2O_3 is estimated to be 82%. The eutectic temperature is not reported but estimated near 2000°C. Coble in 1961 discovered MgO as a sintering aid to Al_2O_3. Roy and Coble reported solubility in the range of a few ppm. Alper et al. in 1963 published the other half of the diagram that also exhibited a large solubility of MgO in the spinel, Figure 259. Their diagram showed a eutectic temperature of 1995°C and indicated a MgO or periclase solubility in the spinel. Also the diagram indicated a solid solubility of spinel in periclase, up to 18% alumina.

Grabmaier and Watson studied the solubility of the Mg-Al spinel in in 1968. Following problems with flame fusion techniques the Czochralski method of single crystal growth was used to produce of spinel single crystals at different MgO to Al_2O_3 ratios. A ratio 1:1.8 (16% MgO) molar maximum was obtained before alumina precipitates were observed. The solubility limit is in good agreement with Roy's early work.

AI.4.12 Binary System Alumina-Calcia

Compounds	$Ca_3Al_2O_6$	1535 T°C
	$Ca_{12}Al_{14}O_{33}$	1415 T°C
	$CaAl_2O_4$	1600 T°C
	$CaAl_4O_7$	1765 T°C
	$CaAl_{12}O_{19}$	1875 T°C

Between the two end members Al_2O and CaO the system contains five intermediate compounds. Rankin also studied the alumina calcia system in 1915. Chatterjee and Zhmoidin report the latest reported work in 1972. The diagram shows two eutectics one at 1390°C and the other at 1400°C. The two eutectics are separated by a compound phase that melts congruently at 1415°C.

AI.4.13 Binary System Magnesia-Calcia

The magnesia calcia binary system has few citations. Doman et. al published their work in 1963. The system is a simple eutectic with no intermediate compounds. The eutectic temperature is 2370°C. Both end members exhibit a seldom seen solid solubility in the refractory oxide.

AI.4.14 Binary System Calcia-Silica

Compounds	3CaO SiO_2	Ca_3SiO_5	2070	C_3S
	2CaO SiO_2	Ca_2SiO_4	2130	C_2S
	3CaO $2SiO_2$	$Ca_3Si_2O_7$	1464	C_3S_2
	CaO SiO_2	$CaSiO_4$	1544	CS

Calcia-Silica system is important to the cement or hydration processes as a precursor to sintering. The hydration reaction products are silicate based molecules. The closest neighbors react first when thermal processes control the atomic movement. The calcium silica system contains four low temperature binary compounds, CS, C_3S_2, C_2S, C_3S and a number of different polymorphs. There are four eutectics: 2050, 1460, 1436 and 1705°C. The calcium rich composition has two principal phases, a low temperature Ca_2SiO_4 + CaO and high temperature Ca_3SiO_5 + CaO. The solid state transformation temperature is 1250°C. The low temperature phase Ca_2SiO_4 + CaO undergoes the polymorphic change to Ca_2SiO_4 + CaO at 725°C. The relative melting point of calcia changes little with the addition of 5 to 10% silica. The eutectic composition of interest is at 30% silica. The calcia and liquid incongruently solidify twenty degrees above the eutectic temperature.

AI.4.15 Binary System Alumina-Silica

The Al_2O_3-SiO_2 system is the base of many refractory compositions. The alumino-silicate refractories include silica, semisilica, fireclay, low alumina, mullite, high alumina and corundum. Davis and Pask performed the most recent published work on

the binary phase diagram in 1972. The system has two eutectics at 1595°C and 1840°C. The intermediate compound called mullite (70% Al_2O_3) separates the eutectics. Davis and Pask reported the formation of an amorphous phase at sub solidus temperatures in the reaction zone between mullite and fused silica. The amorphous phase formed prior to nucleation of an equilibrium mullite phase from the liquid. The liquid was found to react immediately to nucleate mullite and form a liquid richer in silica.

AI.4.16 Binary System Magnesia-Silica

Bowen and Andersen have revised the MgO-SiO_2 system only once since the 1914 diagram. The latest 1927 version of the diagram is shown as Figure 266. The binary system has three eutectics at 1850, 1543 and 1695°C. Two intermediate compounds can be formed Forsterite and Clinoenstatite, Mg_2SiO_4 and $MgSiO_3$. A very large Periclase and Forsterite phase field with no polymorphic transformations characterizes the system. rlw

AI.4.17 Binary System Alumina-Zirconia

The ZrO_2-Al_2O_3 system is a relatively simple eutectic system that exhibits solid solubility in both end members. The eutectic temperature of 1880°C occurs at an approximate composition of 40 wt%. Zirconia is soluble in the alumina up to a few percent. The precipitation of zirconia as a dispersed oxide can limit grain growth and improve densification by pinning grain boundaries. Also the zirconia can act as a grain boundary glassy phase scavenger.

AI.4.18 Binary System Magnesia-Zirconia

Duwiz, Odell and Brown first proposed the MgO-ZrO_2 system in 1952. Much of the high temperature and zirconia side of the diagram remained un published until 1967 where Grain revised the diagram. Du and Duran have performed the most recent work.

AI.4.19 Binary System Zirconia-Calcia

Four diagrams have been published on this system. The publications range from 1929 through 1992.

Table AI.1. Summary List of Phase Diagrams Published in the American Ceramic Society compendium.

Quaternary System A-M-C-S			
Q.1 Quaternary Diagram A-M-C-S	Rait	1949	Fig. 880
Q.2 Quaternary Diagram A-M-C-S	Rao	1968	Fig. 1 Ref. 4
Q.3 Ternary Set C_2AS-MA-CA_2 and C_2AS-MA-CA	Rao	1968	Fig. 4/5 Ref. 4
Q.4 Ternary CA_2-CA-MA and Sub Quaternary CA_2-CA-C_2AS-MA	Rao	1968	Fig. 6/7 Ref. 4
Q.5 Ternary C-A-S at 10% MgO	Prince	1954	Fig. 882
Q.6 Binary Set CAS_2-M and CA_2S_2-M	DeVries	1957	Fig. 903/904
Q.7 Ternary M-MA-C_2S	Prince	1951	Fig. 886
Q.8 Binary Set MA-CAS_2 and M_2S-CAS_2	Welch/Osborn	1956/1952	Fig. 905/906
Ternary System A-M-C			
T1.1 Ternary A-M-C	Rankin and Merwin	1916	Fig. 596
T1.2 Ternary A-MA-C_2AS	DeVries	1957	Fig. 913
T1.3 Ternary A-M-CAS_2	DeVries	1957	Fig. 895
T1.4 Ternary M-M-CA	Mel'nik	1989	Fig. 10041
T1.5 Binary MA-C_2S	Prince	1951	Fig. 887
T1.6 Binary Set CA-MA and CA_2-MA	Rao	1968	Fig. 2/3 Ref. 4
Ternary System A-M-S			
T2.1 Ternary A-M-S	Osborn	1960	Fig. 712
Ternary System A-C-S			
T3.1 Ternary A-C-S	Osborn	1960	Fig. 630
T3.2 Binary Set CS-CAS_2 and CS-CAS_2	Osborn/Baisanov	1942/1986	Fig. 635/9950
T3.3 Binary CS-C_2S	Teoreanu	1985	Fig. 10047
T3.4 Binary Set C_2S-C_2AS, C_2AS-CAS_2 and CS-CA	Rankin	1915/1915/1941	Fig. 639/636/637

Table AI.1. Summary List of Phase Diagrams Published in the American Ceramic Society compendium (continued).

Ternary System M-C-S			
T4.1 Ternary M-C-S	Osborn	1960	Fig. 589
Ternary System C-S-F			
T5.1 Ternary C-S-F	Osborn	1960	Fig. 656
T5.2 Binary CS-F	Canha	1986	Fig. 9747
Binary System A-M			
B1.1 Binary Set A-M and MA-A	Alper/Roy	1962/1953	Fig. 259/260
B1.2 Binary MA-A	Viechnicki	1974	Fig. 1 Ref. 2
Binary System A-C			
B2.1 Binary A-C	Rankin	1915	Fig. F-3 Ref. 3
B2.2 Binary A-C	Lea	1956	Fig. 231
B2.3 Binary Set A-C and A-C	Wisnyi/Auriol	1955/1962	Fig. 233/232
B2.4 Binary A-C	Chatterjee	1973	Fig. 5141
B2.5 Binary A-C	Zaitsev	1991	Fig. 9893
Binary System A-S			
B3.1 Binary Set A-S and A-S	Welch/Aramaki	1961/1962	Fig. 313/314
B3.2 Binary A-S	Davis	1973	Fig. 5190
B3.3 Binary A-S	Klug	1990	Fig. 9269

Table AI.1. Summary List of Phase Diagrams Published in the American Ceramic Society compendium (continued).

Binary System M-C			
B4.1 Binary Set M-C and M-C	Doman/Kamenetskaya	1963/1985	Fig. 229/9217
Binary System M-S			
B5.1 Binary Set M-S and M-S	Bowen/Bowen	1914/1927	Fig. F-12 Ref. 3/266
B5.2 Binary M-S	Kambayashi	1984	Fig. 9243
Binary System C-S			
B6.1 Binary C-S	Phillips	1959	Fig. 237
B6.2 Binary C-S	Taylor	1990	Fig. 9224
B6.3 Ternary C-H-S	Wyllie	1965	Fig. 4086/4087
Binary System C-Z			
B7.1 Binary Set C-Z and C-Z	Ruff/Duwez	1929 1952	Fig. 242/243
B7.2 Binary Set C-Z	Duran	1987	Fig. 9898
B7.3 Binary C-Z	Stubican	1988	Fig. 9227
B7.4 Binary C-Z	Duran	1992	Fig. 9899
Binary System M-Z			
B8.1 Binary M-Z	Du	1991	Fig. 9251
B8.2 Binary M-Z	Du	1990	Fig. 9250
B8.3 Binary M-Z	Lopato	1990	Fig. 9917
B8.4 Binary M-Z	Duran	1991	Fig. 9252

Table AI.1. Summary List of Phase Diagrams Published in the American Ceramic Society compendium (continued).

Portland Cement Supplemental Diagrams			
S1.1 Ternary C-CA-C_2F	Newkirk	1958	Fig. 627
S1.2 Ternary A-S-F	Muan	1957	Fig. 133
S1.3 Binary CA-CF	Hansen	1928	Fig. 629
S1.4 Binary C_4AF-CS	Lea	1934	Fig. 951
S1.5 Binary C_4AF-C_3S	Lea	1934	Fig. 952
S1.6 Binary S-F	Bowen	1932	Fig. 80
Phosphate Cement Supplemental Diagrams			
S2.1 Four Component Binary C_3P-MS	Toshiyuki	1958	Fig. 936
S2.2 Ternary A-C-P	Stone	1956	Fig. 640
S2.3 Ternary C-S-P	Margot-Mrette	1966	Fig. 5394
S2.4 Binary Set AP-C_2P and AP-C_3P	Stone	1956	Fig. 643/644
S2.5 Binary Set A-CP and AP_3-CP	St. Pierre/Stone	1954/1956	Fig. 641/642
S2.6 Binary AP_3-AP	Stone	1956	Fig. 328
S2.7 Binary F-C_3P	Oelsen	1941	Fig. 595
S2.8 Binary M_3P-C_3P	Ando	1959	Fig. 613
S2.9 Binary M-P	Berak	1958	Fig. 272

APPENDIX II

MATERIALS AND BATCH FORMULATION MATRIX

AII.1 Introduction

Experimental materials are separated into three groups: matrix cement, high temperature additives and reinforcement aggregates. The raw materials are characterized by the mineral chemistry, impurities and particle size. Manufacture provided information and experimental characterization of the raw materials are presented.

AII.2 Matrix Materials

Three high temperature calcium aluminate cement (CAC) clinkers are selected as the base matrix material for composite formulations. The three cements are a Fondu Calcium Aluminate, Calcium Dialuminate Blend and a High Alumina Calcium Aluminate premix. Calcium aluminate is a synthetic material produced by calcination.

AII.2.1 Fondu Calcium Aluminate

Fondu cement, CA + $C_{12}A_7$, is dark brown in color and represents the lowest cost calcium aluminate cement. The clinker is prepared using a reverberatory furnace in which the raw materials are melted to form the two-phase base material. The fused dense clinker is moisture stable and shipped to pulverization and sizing facilities closer to the markets in bulk without concern for degradation. The clinkers are finely ground into cement powder to 4000 cm^2/g Blaine surface area. Once ground the material shelf life is approximately 9 to 12 months. Fondu cement has an alumina (Al_2O_3) content of approximately 40% and at least 50% is calcium aluminate ($CaAl_2O_4$). Iron is typically found, up to 16%, from the alumina containing clays used as raw material. Iron also serves as a natural sintering aid at temperatures above 1100°C. The generic composition and properties provided by the manufacturer, LaFarge Calcium Aluminates, are shown in Table 3.2.1 and Table 3.2.2. The commercially supplied product does not contain reactive additives or deflocculents to control flow or set characteristics.

AII.2.1 Calcium Dialuminate Blend

Calcium dialuminate blend is a combination of CA + CA_2 and is principally used as a raw material for ramming mixtures and castable products. The commercial product is prepared in rotary kilns by solid state reactions under close mineralogical control. The white calcium aluminate clinker is highly reactive in the fresh ground state. The recommended shelf life is 9 months. Additives for set control and sintering are not added. Calcium aluminate cement blend has an alumina content of approximately 70%, composed almost entirely (+99%) of calcium aluminate phases. The mineralogy is nearly a molar balance of calcium aluminate ($CaAl_2O_4$), and calcium dialuminate ($CaAl_4O_7$). The two aluminates are blended to optimize hydration to produce a hydrated structure for high mechanical strength. Roughly 70% of the strength is obtained in the first 24 hours. The sintered clinker is finely ground to 3850 cm^2/g Blaine surface area. The compound has less than 0.6% other oxides and a PCE rating of cone 20 (1563° C). The relative small particle size and high purity are suitable for low water applications. The blend is suitable for applications requiring rapid set, resistance to abrasion, mechanical shock and high temperature exposure. The generic composition and properties provided by the manufacturer, Lafarge Calcium Aluminates, are shown in Table 3.2.1 and Table 3.2.2.

AII.2.1 High Alumina Calcium Aluminate Blend

The higher alumina containing cements are not commercially available in the pure form because of the high reactivity. The high alumina castable cements readily hydrate with atmospheric water and tend to be unstable. Blending, hermetic packaging and polymers are added to stabilize adsorption. Commercial products using calcium dialuminate and alumina are available only with proprietary additives. A product called DuraCast manufactured by DuraWear is a pre-formulated product selected for the matrix cement. The total alumina content is approximately 80%. The calcium dialuminate clinker was co-ground with alumina to create the premix. Silica is added to improve sintering and a proprietary multi component admixture is added to control the set. Estimated composition and properties are listed in Table 3.2.1 and Table 3.2.2. The product is a light gray cement powder with white $ZrSiO_3$ aggregate added. The DuraCast aggregate to cement ratio is approximately 60/40 by weight.

Table AII.1. Calcium Aluminate Cement, Composition and Property Summary.

Constituent	Matrix Type		
	Fondu *	**Calcium Dialuminate ***	**Commercial Castable****
Al_2O_3	> 37.0	> 68.5	> 78.1
CaO	< 39.8	< 31.0	< 12.0
SiO_2	< 6.0	< 0.8	< 10.0
Fe_2O_3	< 18.5	< 0.3	-
TiO_2	< 4.0	< 0.25	-
MgO	< 1.5	< 0.5	-
SO_3	< .4	< 0.3	-
$K_2O + Na_2O$	< .4	< 0.5	-
Properties			
Principal Phases	CA, C_4AF and C_2S	CA and CA_2	CA, CA_2 and A
Bulk Density, gm/cc	1.16 – 1.37	1.04 – 1.23	.089 – 1.07
Specific Gravity, gm/cc	3.2	3.0	3.0
PCE, °C	1270	1563	1780
Initial Set Time	> 120 min	> 165 min	> 45 min
Green Strength, @ 24 hrs	> 33.8 MPa 4900 psi	> 31.7 MPa 4600 psi	> 16.5 MPa 2400 psi
* Supplier Specified ** Determined			

AII.3 Additive Materials

Magnesia, spinel, chromia, alumina, alumina-titania and cerium oxides are used to blend with the calcium aluminate cements. The additives are considered hydraulically inert and are not expected to contribute significantly to the hydraulic properties. The additives include reagent grade powders, commercial ceramic powders and products that were ground and sized manually in our laboratory.

AII.3.1 Magnesia Powder

Magnesia, MgO, or periclase is an important refractory component. Periclase has high solubility for the cement clinker base components: silica, iron and chromia. Periclase easily forms two-phase mineral compounds. Fused cast and dead burnt forms of magnesia are used in the formulations. The fused cast and ground magnesia powder is manufactured by CERAC. Fused magnesia is produced at temperatures greater than 2750°C in an electric arc furnace to remove porosity. The magnesia powder is graded and sized, less than Tyler Standard No. 325 mesh or 45 micron sieve opening. The powder was further classified using a Lecotrac LT100 Particle Size Analyzer. The particle size distribution is summarized by 95% of the particles are less than 50.95 microns with a surface area of 0.259 m^2/cm^3. The bulk density is 1.46 gm/cm^3. The theoretical density of MgO is 3.60 gm/cc. The equivalent Blaine surface area for comparison is 460.34 cm^2/gm.

Possehl Inc, suppliers of ceramic raw materials produces the dead-burned magnesia. The dead-burned magnesia is supplied in rock form produced by rotary calcining at temperatures greater than 1300°C. The material was shipped as -7 and + 10 Tyler Standard mesh. The equivalent sieve size range is 2.80 mm to 2.00 mm. The dead burnt rock was ball milled dry in our laboratory mill using steel balls. The fresh powders are classified prior to blending with the cement powders. The final powder used measured less than 325 Tyler Standard mesh or 45 micron sieve opening. Mean bulk density was 1.29 gm/cm^3. The theoretical density of MgO is 3.60 gm/cc. The equivalent Blaine surface area for comparison is 239 cm^2/gm.

AII.3.2 Spinel

Spinel or magnesia aluminate, Al_2MgO_4, is an important refractory compound. Spinel has a wide stoichiometric range and high solubility for cement clinker components. Reagent grade spinel is non-reactive in the fused cast form; the shelf life is unlimited. The crushed and sized powder is manufactured by CERAC. The spinel powder is graded and sized, less than Tyler Standard No. 50 mesh or 300 microns and greater than 325 mesh or 45 micron sieve opening. The powder sample is further classified using a Lecotrac LT100 Particle Size Analyzer to determine the distribution. The particle size distribution is log normal and summarized by 95% of the particles are less than 93.91 microns with a surface area of 0.107 m^2/cm^3. The mean bulk density is 1.85 gm/cm^3. The theoretical density of spinel is 3.58 gm/cc. The equivalent Blaine surface area for comparison is 269 cm^2/gm.

AII.3.3 Alumina

Alumina or aluminum oxide, Al_2O_3, is found with a wide variety of impurities: silica, iron oxide, titania and other impurities. The impurities depend on the source of bauxite, but it is common to produce 98.5% pure alumina. The precipitation process can be controlled to produce near theoretical density particles and particle size distribution optimized for fineness. Dynateck manufactures 99.5% commercial grade alumina. The powder is supplied to Tyler Standard –325 mesh or 45 microns. Mean bulk density is 1.64 gm/cm^3. The theoretical density of alumina is 3.98 gm/cc. The equivalent Blaine surface area for comparison is 274 cm^2/gm.

AII.3.4 Chromite Additive

Chromite ore, Cr_2O_3, is dark brown to jet black, a spinel structure with impurities at interstitial positions. The chromium sesquioxide, Cr_2O_3, is a dark power chemically precipitated and thermally converted to oxide, fused and ground to size. Commercial grades are available for thermal spray applications at 99 % purity by AMDRY and Plasmalloy.

The powder material size is greater than Tyler Standard 500 mesh or 22 microns and less than 325 mesh or 45 microns. The particle size distribution is bimodal with peaks at 20 and 60 microns. The total surface area is determined to be 0.156 m^2/cm^3 and bulk density was 2.67 gm/cm^3. The Blaine surface area in units compared to the binder is 289 cm^2/gm.

AII.3.5 Alumina-Titania

Alumina and titania, $Al_2O_3.TiO_2$, is a 50:50 blend by weight or a slight titania rich blend. The blend is a white powder commercial available from Sultzer Metco, Powder #110. The commercial grade was intended for thermal spray applications at 99 % purity. The powder material size is greater than Tyler Standard 270 mesh or 53 microns. The mean theoretical density is 4.12 gm/cc. The bulk density is 2.0 gm/cm^3. The Blaine surface area is 275 cm^2/gm.

AII.3.6 Cerium Oxide

Cerium Oxide, CeO_2, is a rare earth metal oxide precipitated and thermally converted to an oxide. The process produces a 99% pure product for commercial applications as thermal barrier coatings and catalysts. AESAR/ALFA Chemicals produce the yellow powder. The powder material size is less than Tyler Standard 400 mesh or 38 micron diameter particle. Using a mean theoretical density of 7.20 gm/cc and bulk density is determined to be 3.0 gm/cm^3. The Blaine surface area in units compared to the binder is 328 cm^2/gm.

AII.4 Reinforcement Materials

The four reinforcement phases selected are zirconium silicate, zirconia grog, refractory spinel and dead burnt magnesia rock. The commercial grade zirconium silicate (Zircon) contains high alumina and it is actually a two phase material of zircon and mullite. The zircon mullite is a multi phase material, dense, matched matrix thermal expansion, high aspect ratio, high angle edges, low surface roughness but poor materials selection and thermal stability. The zirconia grog, is a polycrystal, single-phase partially sintered, highly porous, moderate aspect ratio and high surface roughness engineered product with uniform size. The spinel is a multi particle, multi phase, and partially sintered, highly porous engineered product with low angle edges using both single and bimodal distributions optimized for packing factor. Dead burnt magnesia rock is a single phase, low porosity product with uniform size.

Four reinforcement materials are selected to highlight the differences between the thermal expansion and the mismatch stress. Zircon mullite has nearly identical thermal expansion coefficients as the matrix CAC. The spinel and dead burnt magnesia rock are nearly spherical and have higher thermal expansion but one is porous and the other is smaller size. The zirconia grog has high thermal expansion difference but is compensated by internal porosity. The interface area also plays an important role in structural durability of the composite. The coherent interface transfers the load between the reinforcement and the matrix. The interface contact area can be increased with high

surface roughness. Textured reinforcement phases in the composite can produce a directional strengthening caused by increasing the interface area that distributes the shear load. The composite design can be directionally strengthened using high aspect ratio reinforcement.

AII.4.1 Fused Zircon Mullite

Zircon mullite or zirconium alumina silicate, $ZrSiO_4{\cdot}Si_2Al_6O_{13}$ is an important compound designed for refractory and abrasive properties. The mullite improves the elevated temperature stability of the compound. The fuses cast process produces a dense, hard and wear resistant form. The chemical inertness and physical characteristics make it a desirable component in glass and steel industries.

Commercial sources are available as specialty products from a number of refractory suppliers. The zirconium mullite reinforcement phase was premixed with the cement matrix. The product is called DuraCast™ manufactured by DuraWear. The premix reinforcement to cement ratio is 60/40 by weight. Reinforcement particles were physically separated from the bulk and sized. The reinforcement material used was sized greater than Tyler Standard mesh No. 20 or 0.85 millimeter and less than 8 millimeters. The aspect ratio ranged from 3:1 to 7:1. The fused and crushed product has low surface roughness.

Table AII.2. Typical Properties Commercial Refractory Grade, $ZrSiO_4$, Zircon.

Mineral Component	**Chemical Analysis**
Al_2O_3	45.8%
SiO_2	17.1%
Fe_2O_3	0.1%
TiO_2	0.1%
CaO	0.1%
MgO	0.05%
Na_2O/K_2O	.2%
ZrO_2/HfO_2	36.5%
Free Iron Grains	0.02% maximum
Grain apparent porosity	1.5%
Grain bulk density	3.67 g/cc
Refractoriness	1743°C, (PCE 33/34)

AII.4.2 Zirconia Grog

Zirconium oxide, ZrO_2, or zirconia reinforcement phases are engineered (stabilized) ceramics that resist thermal shock, wear and high impact loads in severe environments. Zirconia is resistant to the corrosive attack by molten metal, organic solvents, caustics, and acids. Stabilized zirconia has a high melting point and is inert at temperatures up to 1300°C. Zirconia has high wear resistance because of the high strength and toughness. The high temperatures processing makes zirconia more difficult

to produce and therefore more costly. Spray forming zirconia at high temperatures reduces costs. The spray formed product is call grog, which is an agglomerate of dense particles that form a highly porous microstructure. The grog chemistry is uniform and the density easily controlled by the spray parameters, time and temperature. The high coefficient of thermal expansion is compensated with the high porosity in the grog.

The grog can be produced in a variety of compositions and stabilized with either calcia or magnesia. Low density (1.50 gm/cc) and high density (1.97 gm/cc) grog were screened for use as the reinforcement. The low density grog was friable and spalled easily but had a high surface area for matrix bonding and high porosity for improved thermal performance. The higher density grog was selected for reinforcement because of the strength. The table below lists some typical properties of zirconia grog. The zirconia grog was produced by Zircoa, supplied in the size range of 5.6 mm (-3.5 mesh) to 3.35 mm (+6 mesh).

Table AII.3. Comparison of Zirconia Properties.

	High Fired Zirconia	**Commercial Fired Zirconia**	**Magnesia Stabilized Zirconia**	**Calcia Stabilized Zirconia**
ZrO_2, %	97	97	95	95
Density g/cc	5.7	5.5	4.6	4.3
Apparent Porosity %	0	0	18	23
MOR at RT.	621 M Pa 90000 psi	414 M Pa 60000 psi	3000 psi	3000 psi
Tensile Strength at RT.	414 M Pa 60000 psi	248 M Pa 36000 psi		
Compressive Strength	285000 psi	285000 psi		
Young's Modulus	248 Gpa $36x10^6$ psi	221 Gpa $32x10^6$ psi		
Thermal Expansion	$\Delta L/L\ ^oC10^{-6}$			
600 °C	9.8	2.4	7.0	8.0
1000 °C	10.3	3.4	6.0	9.5
1300 °C	10.8	6.4	2.5	8.0
Thermal Conductivity W/m°K @ 800°C	2	2	1.6	1.4

AII.4.3 Crushed Spinel Refractory

Magnesium aluminum oxide, $MgAl_2O_4$, spinel is an important high temperature refractory compound. Fused spinel is a premium refractory material resistant to basic slags; nonferrous metals and oxidizing kiln environments. The spinel reinforcement material was made from high performance spinel magnesia bricks. The bricks were obtained from AP Green Refractories under the trade name of Greenfree 92. The bricks were crushed using a carbon steel motorized jaw crusher set to ¼ inch or 6.3 mm opening. The crushed material was sized using Tyler Standard mesh numbers 5, 20 and 25 and a Roto-Tap machine. The process produced two reinforcement particle diameter

ranges; the largest is -4.0 to +0.85 mm and the smaller size –0.85 to +0.71 mm. The reinforcement particle aspect ratio was nearly 1:1 in both size ranges. The particles had high surface roughness and porosity. Mixing equal weight made a graded blend of the two size ranges. The graded reinforcement particle diameters were sized to produce the maximum packing factor for a two diameter system ($D_{smaller} = 0.2\ D_{larger}$).

Table AII.4. Spinel Magnesia Brick Properties.

	Typical Chemical Analysis
MgO	90.5 %
Fe_2O_3	0.5 %
Al_2O_3	6.0 %
SiO_2	1.1 %
CaO	1.9 %
Bulk Density (g/cc)	2.86
Modulus of Rupture Mpa (Psi)	3.8 (550)
Apparent Porosity	18.3 %
Cold Crushing Strength Mpa (Psi)	8.3 (4100)
Linear Thermal Expansion, RT to 1400°C	1.9 %

AII.4.4 Dead Burnt Magnesia Rock

Dead burned magnesite or magnesia is manufactured in briquette or rock form and is usually white, brown or gray. The color generally indicates the level and type of impurity. White magnesia is relatively pure periclase with a low concentration of spinel phase material. The brown and red colors are from iron and silica impurities and gray color is from calcia. The impurities are tramp minerals found in the natural magnesite deposit. The dead-burned magnesia was supplied in rock form produced by rotary calcining at temperatures greater than 1300°C. The dead-burned magnesia was obtained from Possehl Inc. The material was shipped as -7 and + 10 Tyler Standard mesh. The equivalent sieve size range is 2.80 mm to 2.00 mm.

Table AII.5. Typical Composition of Dead Burnt Magnesia.

	Manufactures Guarantee, wt %	**Typical Values, wt%**
MgO	90.0 min	92.43
SiO_2	4.5 max	3.17
CaO	2.0 max	1.73
Al_2O_3	1.5 max	1.27
Fe_2O_3	1.5 max	1.21
LOI	0.3 max	0.19

AII.5 Density Determination

The powders and reinforcement material are first soaked in an autoclave to drive atmospheric water and standardize the starting point before blending and mixing. The samples are soaked for 24 hrs at ~75°C. The powder is cooled to RT and a volume measured in a 50-ml graduated cylinder. The weight was recorded using a Metler 240 analytical balance. Weights are determined to .1 microgram. The sample compaction is avoided by careful handling. The average of at least 5 runs is used to determine the bulk density in gm/cm^3.

The accuracy of the volume determination limits the bulk density measurement precision. The volume by visual determination on a 50 ml graduated cylinder is accurate to ± 1.0 ml for powders and ± 2.0 ml for the reinforcements. Measurement volumes ranged between 25 and 45 ml. For example, a 40-cc sample 1 ml change in volume is equivalent to a 5% spread in bulk density or a ± 2.5%.

The sensitivity to sample condition was evaluated by changing the starting condition and compaction influences. The atmospheric moisture influence, with and without autoclave soak, varies the bulk density a maximum of 5%. Compaction influence on a series of dry powder samples vibrated at 50 Hz for 15 seconds increased the density less than 1%.

AII.6 Formulation Matrix

Formulations for mechanical property testing (strength and wear resistance) are made from all three CAC cement types. Efforts are taken to standardized preparations to enable cement to cement and batch to batch comparisons. Duplicate and control batch formulations were made to develop secondary relationships between formulations. A summary of the formulations is presented in Table 3. .

The premix high alumina calcium aluminate blend formulation matrix is limited to compositions along the two main binary joins in the cement-magnesia-spinel ternary subsystem. A series of formulations using a blend of magnesia and chromia are designed to bring the compositions into the cement-magnesia-chromia ternary subsystem. The compositions provide for the comparisons of the bonding phase with the concentration of magnesia, spinel and chromia.

The Fondu cement formulation matrix is limited to compositions along the two main binary joins in the cement-magnesia-spinel ternary subsystem. The batches are formulated to include both high density zirconia grog and crushed spinel brick as the reinforcement phases. A reinforcement materials survey set of formulations included a preparation using sifted zircon reinforcement to benchmark to the premix cement formulations.

Calcium aluminate blend formulation matrix branches to include a number of compositional binary and ternary joins. Crushed and milled commercial dead burnt magnesia is the primary additive in these tests. Other formulations include fuse cast magnesia and chromia blends, alumina, alumina and titania blends, and cerium oxide. Three standard concentrations of the additives enable batch to batch comparisons.

The formulations also adjusted the cement to water ratio and compared two compaction methods. The formulations also expanded the types of reinforcements and concentrations better understanding the influences of the different materials, range of concentrations and size distribution.

Table AII.6. Formulation Matrix for Initial Microstructure Studies.

Type of CAC	Additive	Formulation Objective
Premix	Cr_2O_3	Influence of increasing chromia from 0 to 35%
Premix	Control	Influence of cement to water ratio, 10, 20 and 30%
Premix	Cr_2O_3	Influence of increasing chromia in the range 0 to 15%
Premix	MgO	Influence of increasing magnesia, range 0 to 20%
Premix	MgO & Cr_2O_3 Blend	Influence on composition range of 0 to 55% for 2:1 Blend, 1:1 Blend and 1:2 Blend.
Premix	MgO & Cr_2O_3 Blend	Blend 2:1 Influence on range from 20 to 35%
Premix	MgO & Cr_2O_3 Blend.	Blend 1:1 Influence on range from 20 to 30%.
Premix	MgO.	Magnesia composition range: Control, 15%, 25% and 30%. Influence of magnesia on the cement binder.
Premix	Spinel	Influence of spinel on the cement binder. Composition range: Control, 20%, 25%, and 30%.
Premix	MgO & Cr_2O_3	Two composition blends of magnesia to chromia: 1:2 Blend and 1:4 Blend, range 20, 25, 30, and 35%. Influence of chromia and magnesia on the cement binder.

Table AII.7. Formulation Matrix for Wear and Compression Strength Testing.

Type of CAC	Additive	Formulation Objective
Premix	Control	Establish reference microstructure and properties.
Premix	MgO	Concentrations: 10%, 15%, 20% and 35%. Influence of magnesia on cement binder. Reinforcement range from 39 to 61%.
Premix	Spinel	Concentrations: 10%, 20% and 25%. Influence of spinel on cement binder. Reinforcement from ranges from 45 to 63 %.
Premix	Cr_2O_3.	Concentration: 10% Reinforcement 54%.
Premix	MgO & Cr_2O_3 Blend	Blend 1:1 Concentrations: 10, 20, 25 and 35%. Duplicates at 10 and 20%. Reinforcement range from 39% to 61%.
Premix	MgO & Cr_2O_3 Blend	Blend 1:2 Concentrations: 10, 20 and 30%. Duplicate samples at 10 and 20%. Reinforcement range from 48 to 61%.
Premix	MgO & Cr_2O_3 Blend	Blend 1:4 Concentrations: 10, 20, 30 and 35%. Duplicate sample at 10%. Reinforcement ranges from 45 to 61%.
Premix	MgO & Cr_2O_3 Blend	Blend 2:1 Concentrations: 10, 15, 20, and 25%. Reinforcement ranges from 45 to 63%.

Table AII.7. Formulation Matrix for Wear and Compression Strength Testing (continued).

Type of CAC	Additive	Formulation Objective
Premix	No Additives.	Influence of reinforcement on properties and microstructure Reinforcement range is 41 to 80%.
Fondu	MgO	Concentrations: 0, 50, 66, 75 and 80% Three duplicate batches. Influence of increasing magnesia on cement properties. High-density zirconia grog reinforcement range from 50 to 60%.
Fondu	MgO	Concentrations: 0, 50, 66, 75 and 80% One duplicate batch. Influence of increasing magnesia on cement properties. Crushed spinel brick reinforcement range from 50 to 66%
Fondu	Spinel	Concentrations: 0, 50, 66, 75 and 80% One duplicate batch. Influence of increasing spinel on cement properties. Crushed spinel brick reinforcement constant at 50%.
Fondu	None	Influence on reinforcement phase on the density. Batches reinforced with high-density grog, low-density grog, crushed spinel brick and zircon. Reinforcement constant at 50%.
Fondu	MgO	Concentration: 50 wt %. Influence of additive and reinforcement type. High-density grog and the crushed spinel brick. Reinforcement range from 50 to 66%.
Fondu	Spinel	Concentration: 50 wt %. Influence of additive and reinforcement type. Influence on density with changing reinforcement type. High-density grog and the crushed spinel brick. Reinforcement range from 50 to 66%.
$CA+CA_2$ Blend	No Additive	Establish a reference microstructure. Three duplicates.
$CA+CA_2$ Blend	No Additive	Influence of reinforcement concentration and establish the reference interface microstructure. Dead burnt magnesia rock. Reinforcement at 40, 60 and 75%.
$CA+CA_2$ Blend	No Additive	Influence of reinforcement concentration and establish the reference interface microstructure. Graded crushed spinel brick. Reinforcement at 40 and 60%.
$CA+CA_2$ Blend	No Additive	Influence of reinforcement concentration and establish the reference interface microstructure. High-density zirconia grog. Reinforcement at 40, 60 and 75%.
$CA+CA_2$ Blend	DB MgO	Concentration: 33, 50, 66, 75 wt. %. Influence of magnesia on cement microstructure. Dead burnt magnesia rock at 40%.
$CA+CA_2$ Blend	DB MgO	Concentration: 33, 50, 66, 75 wt. %. Influence of crushed and graded (1:4 size ratio) spinel brick reinforcement. Concentrations: series one 40 wt. % and series two at 60 wt. %.

Table AII.7. Formulation Matrix for Wear and Compression Strength Testing (continued).

Type of CAC	Additive	Formulation Objective
$CA+CA_2$ Blend	DB MgO	Concentration: 33, 50, 66, 75 wt. %. Influence of high-density zirconia grog reinforcement. Concentrations: 40, 60 and 75%.
$CA+CA_2$ Blend	MgO & Cr_2O_3 Blend	Four blends of fuse cast dense chromia to magnesia additive: 1:1 Blend, 1:2 Blend, 1:4 Blend and 2:1 Blend. Influence of changing chromia and magnesia. High-density zirconia grog reinforcement 60 wt. %.
$CA+CA_2$ Blend	DB MgO and Al_2O_3	Nine ternary compositions of calcium dialuminate with magnesia and alumina CA-M-A. One duplicate composition. Dry milled dead burnt magnesia and fuse cast alumina added in following ratios, 1:0:1, 1:0:2, 1:1:1, 1:1:2, 1:1:3, 1:2:1, 2:1:1 and 3:1:1. Concentration of dead burnt magnesia rock reinforcement constant at 60 wt. %.
$CA+CA_2$ Blend	DB MgO & Alumina-Titania Blend	Eight ternary compositions of calcium aluminate blend dry milled dead burnt magnesia and fuse cast alumina titania blends. CA-M-AT in following ratios: 1:0:1, 1:0:2, 1:1:1, 1:1:2, 1:1:3, 1:2:1, 2:1:1 and 3:1:1. Influence of changing magnesia and alumina. Dead burnt magnesia rock reinforcement at 60 wt. %.
$CA+CA_2$ Blend	DB MgO & CeO_2	Five ternary compositions of calcium aluminate blend dry milled dead burnt magnesia and precipitation formed cerium oxide. CA-M-Ce in following ratios: 1:1:1, 1:1:2, 1:2:1, 2:1:1 and 3:1:1. Influence of changing magnesia and cerium. Dead burnt magnesia rock reinforcement at 60 wt. %.
$CA+CA_2$ Blend	DB MgO	Concentration 50 wt. %. Influence of water: 7, 10, 15, 20 and 25 %. Dead burnt magnesia rock reinforcement at 60 wt. %.
$CA+CA_2$ Blend	DB MgO	Concentration 50 wt. % Influence of water: 7, 10, 15, 20 and 25 %. Batches compacted by vibration. Dead burnt magnesia rock reinforcement at 60 wt. %.

AII.7 Experimental Batches

Six experimental batch formulations were made for thermal conductivity testing. The final mixing parameters and the compositions are shown in Tables II.8 and II.9. The composition batches are arranged according to the type of cement used. Type I cement is the high alumina calcium aluminate, Type II cement is the Fondu cement and Type III cement is the calcium dialuminate blend.

Table AII.8. Summary of Batch Mixing Parameters, Thermal Conductivity Samples.

Batch Number	Composite, wt. %			W/C Ratio	H_2O wt. %
	Cement	Reinforcement	Type		
B12-10-1	100.0		I	0.08	8.0
B12-18-1	43.1	56.9	II	0.16	6.9
B1-14-1	40.0	60.0	III	0.19	7.5
B1-29-1	100.0		III	0.25	25.0
B2-14-1	100.0		II	0.25	25.0
B2-25-2	25.0	75.0	III	0.20	5.0
Reference Brick					

Table AII.9. Composition Summary, Thermal Conductivity Samples.

Batch Number	Composition, wt. %				
	MgO	Al_2O_3	CaO	Fe_3O_4	SiO_2
B12-10-1		80.0	10.0	0.0	10.0
B12-18-1		40.0	45.0	13.0	2.0
B1-14-1		62.0	30.0	5.0	3.0
B1-29-1		62.0	30.0	5.0	3.0
B2-14-1		40.0	45.0	13.0	2.0
B2-25-2		62.0	30.0	5.0	3.0
Reference Brick	90.5	6.0	1.9	0.5	1.1

Batches were formulated for material property testing, CCS, DSRW, density and microstructural analysis. A summary of the batch formulations and the compositions are presented in Tables II.10 through II.15.

Table AII.10. Summary of Batch Mixing Parameters, High Alumina Calcium Aluminate Cement Material Property Evaluation Samples.

Batch Number	Composite, wt. %			W/C Ratio	H_2O wt.%
	Cement	Reinforcement	Additive		
B1-28-1	26.0	39.0	35.0	0.27	7.0
B2-2-1	40.0	60.0		0.19	7.5
B2-4-1	40.0	60.0		0.18	7.3
B2-7-1	26.0	39.0	35.0	0.27	7.0
B2-12-1	30.0	45.1	24.9	0.24	7.2
B2-16-1	30.0	45.0	25.0	0.23	6.9
B2-18-1	32.0	48.0	20.0	0.22	7.0
B2-23-1	32.0	48.1	19.9	0.21	6.9
B2-25-1	36.0	54.0	10.0	0.19	6.9
B3-2-1	30.0	45.1	24.9	0.24	7.4
B3-4-1	34.0	51.0	15.0	0.21	7.0
B3-6-1	29.6	62.8	7.6	0.24	8.5
B3-10-1	31.5	59.8	8.6	0.19	6.9
B3-12-1	24.7	59.9	15.4	0.21	6.9
B3-16-1	24.7	59.9	15.4	0.21	6.9
B3-18-1	24.7	59.9	15.4	0.21	6.9
B3-20-1	24.7	59.9	15.4	0.21	6.9
B3-30-1	24.7	59.9	15.4	0.21	6.9
B4-1-1	19.4	60.0	20.6	0.28	7.8
B4-3-1	19.4	60.0	20.6	0.28	7.8
B4-6-1	42.6	44.4	13.0	0.15	7.4
B4-8-1	44.0	36.1	19.9	0.14	7.5
B4-13-1	44.8	31.5	23.8	0.11	6.6
B4-16-1	36.0	54.1	9.9	0.21	7.4
B4-20-1	36.0	54.1	9.9	0.21	7.4
B4-22-1	36.0	54.1	9.9	0.21	7.4
B4-24-1	36.0	54.1	9.9	0.21	7.4
B4-27-1	41.8	49.2	9.0	0.16	7.4
B4-29-1	36.0	54.1	9.9	0.21	7.4
B5-1-1	30.0	45.1	24.9	0.24	7.4
B5-4-1	36.0	54.1	9.9	0.21	7.4
B5-6-1	32.0	48.0	20.0	0.23	7.5
B5-8-1	32.1	48.1	19.9	0.23	7.5
B5-11-1	32.0	68.0		0.19	7.8
B5-13-1	20.0	80.0		0.21	8.4
B5-15-1	20.0	63.3	16.6	0.25	7.5
B5-18-1	30.6	61.1	8.3	0.21	7.5
B5-20-1	30.6	61.1	8.3	0.21	7.5
B5-22-1	30.6	61.1	8.3	0.21	7.5
B5-26-1	30.6	61.1	8.3	0.21	7.5
B5-28-1	30.6	61.1	8.3	0.21	7.5

Table AII.11. Composition Summary, High Alumina Calcium Aluminate Cement Material Property Evaluation Samples.

Batch Number	Matrix Additives, wt. %			Cement, wt. %		
	Cr_2O_3	MgO	$MgAl_2O_4$	Al_2O_3	CaO	SiO_2
B1-28-1	28.7	28.7		34.1	4.3	4.3
B2-2-1				80.0	10.0	10.0
B2-4-1				80.0	10.0	10.0
B2-7-1		57.4		34.1	4.3	4.3
B2-12-1	9.1	36.3		43.7	5.5	5.5
B2-16-1	22.7	22.7		43.6	5.5	5.5
B2-18-1	19.2	19.2		49.2	6.2	6.2
B2-23-1	12.6	25.3		49.3	6.2	6.2
B2-25-1	7.2	14.3		62.6	7.8	7.8
B3-2-1	29.9	15.0		43.8	5.5	5.5
B3-4-1	20.2	10.1		55.5	6.9	6.9
B3-6-1	13.5	6.8		63.6	8.0	8.0
B3-10-1	7.1	14.2		62.8	7.9	7.9
B3-12-1	12.6	12.6		49.3	6.2	6.2
B3-16-1	7.7	30.7		49.3	6.2	6.2
B3-18-1	19.2	19.2		49.3	6.2	6.2
B3-20-1	19.2	19.2		49.3	6.2	6.2
B3-30-1	25.3	12.6		49.3	6.2	6.2
B4-1-1	10.3	41.3		38.7	4.8	4.8
B4-3-1	17.0	34.1		38.7	4.8	4.8
B4-6-1				80.0	10.0	10.0
B4-8-1				80.0	10.0	10.0
B4-13-1				80.0	10.0	10.0
B4-16-1	21.6			62.7	7.8	7.8
B4-20-1	10.8	10.8		62.7	7.8	7.8
B4-22-1	4.3	17.3		62.7	7.8	7.8
B4-24-1	10.8	10.8		62.7	7.8	7.8
B4-27-1				80.0	10.0	10.0
B4-29-1			21.6	62.7	7.8	7.8
B5-1-1			45.3	43.8	5.5	5.5
B5-4-1		21.6		62.7	7.8	7.8
B5-6-1		38.5		49.2	6.1	6.1
B5-8-1			38.3	49.4	6.2	6.2
B5-11-1				80.0	10.0	10.0
B5-13-1				80.0	10.0	10.0
B5-15-1			45.4	43.7	5.5	5.5
B5-18-1			21.3	62.9	7.9	7.9
B5-20-1	4.3	17.1		62.9	7.9	7.9
B5-22-1	10.7	10.7		62.9	7.9	7.9
B5-26-1	6.4	12.8		62.9	7.9	7.9
B5-28-1	0.0	21.3		62.9	7.9	7.9

Table AII.12. Summary of Batch Mixing Parameters, Fondu Cement Samples.

Batch Number	Composite, wt. %				W/C Ratio	H_2O wt.%
	Cement	Reinforcement		Additive		
B8-24-1	50.0	50.0	LD Grog		0.15	7.5
B8-28-1	50.0	50.0	Zircon		0.15	7.5
B9-1-1	100.0				0.07	7.1
B9-3-1	50.0			50.0	0.14	7.1
B9-8-1	25.6	51.3	Zirconia	23.1	0.29	7.4
B9-10-1	25.0	50.0	Zirconia	25.0	0.29	7.3
B9-28-1	50.0	50.0	Spinel	0.0	0.15	7.4
B9-30-1	25.0	50.0	Spinel	25.0	0.28	7.0
B10-2-1	25.0	50.0	Spinel	25.0	0.27	6.7
B10-5-1	50.0	50.0	Spinel		0.14	7.0
B10-7-1	12.5	50.0	Spinel	37.5	0.56	7.0
B10-12-1	10.0	50.0	Spinel	40.0	0.70	7.0
B10-14-1	25.0	50.0	Spinel	25.0	0.28	7.0
B10-16-1	16.6	50.1	Spinel	33.3	0.42	7.1
B10-19-1	12.5	50.0	Spinel	37.5	0.56	7.0
B10-21-1	10.0	50.0	Spinel	40.0	0.70	7.0
B10-23-1	33.3	66.7	Spinel		0.28	9.4
B10-26-1	50.0	50.0	Spinel		0.19	9.3
B11-23-1	50.0	50.0	Zirconia		0.20	10.0
B11-30-1	20.1	59.8	Zirconia	20.1	0.20	4.0
B12-1-1	13.4	59.8	Zirconia	26.8	0.30	4.0
B12-2-1	10.0	59.8	Zirconia	30.2	0.40	4.0
B12-3-1	8.0	59.8	Zirconia	32.2	0.50	4.0
B12-7-1	20.5	59.1	Zirconia	20.5	0.28	5.7
B12-8-1	13.6	59.1	Zirconia	27.3	0.42	5.7
B12-9-1	10.2	59.1	Zirconia	30.7	0.56	5.7
B12-18-2	43.1	56.9	Zirconia		0.16	6.9

Table AII.13. Composition Summary, Fondu Cement Samples.

Batch Number	Matrix Additives, wt. %			Cement, wt. %			
	MgO	DB MgO	$MgAl_2O_4$	Al_2O_3	CaO	Fe_3O_4	SiO_2
B8-24-1				40.0	45.0	13.0	2.0
B8-28-1				40.0	45.0	13.0	2.0
B9-1-1				40.0	45.0	13.0	2.0
B9-3-1	50.0			20.0	22.5	6.5	1.0
B9-8-1	47.4			21.1	23.7	6.8	1.1
B9-10-1			50.0	20.0	22.5	6.5	1.0
B9-28-1				40.0	45.0	13.0	2.0
B9-30-1			50.0	20.0	22.5	6.5	1.0
B10-2-1			50.0	20.0	22.5	6.5	1.0
B10-5-1				40.0	45.0	13.0	2.0
B10-7-1	75.0			10.0	11.3	3.3	0.5
B10-12-1	80.0			8.0	9.0	2.6	0.4
B10-14-1			50.0	20.0	22.5	6.5	1.0
B10-16-1			66.7	13.3	15.0	4.3	0.7
B10-19-1			75.0	10.0	11.3	3.3	0.5
B10-21-1			80.0	8.0	9.0	2.6	0.4
B10-23-1				40.0	45.0	13.0	2.0
B10-26-1				40.0	45.0	13.0	2.0
B11-23-1				40.0	45.0	13.0	2.0
B11-30-1	50.0			20.0	22.5	6.5	1.0
B12-1-1	66.7			13.3	15.0	4.3	0.7
B12-2-1	75.0			10.0	11.2	3.2	0.5
B12-3-1	80.0			8.0	9.0	2.6	0.4
B12-7-1	50.0			20.0	22.5	6.5	1.0
B12-8-1	66.7			13.3	15.0	4.3	0.7
B12-9-1	75.0			10.0	11.3	3.3	0.5
B12-18-2				40.0	45.0	13.0	2.0

Table AII.14. Summary of Batch Mixing Parameters, Calcium Dialuminate Cement.

Batch Number	Composite, wt. %				W/C Ratio	H_2O wt.%
	Cement	Reinforcement		Additive		
B1-12-1	40.0	60.0	Zirconia		0.18	7.4
B1-15-1	40.0	60.0	Zirconia		0.25	10.0
B1-19-1	100.0				0.10	10.0
B1-20-1	100.0				0.20	20.0
B1-22-1	22.7	54.5	Zirconia	22.7	0.22	5.0
B1-25-1	45.5	54.5	Zirconia		0.13	5.7
B1-28-1	40.0	60.0	Zirconia		0.20	8.0
B1-29-2	100.0				0.25	25.0
B2-10-1	20.0	60.0	Zirconia	20.0	0.38	0.0
B2-14-2	100.0				0.25	25.0
B2-22-1	40.0	60.0	DB MgO		0.18	7.4
B2-24-1	20.0	60.0	DB MgO	20.0	0.37	7.4
B2-25-1	20.0	60.0	DB MgO	20.0	0.20	3.9
B3-9-1	26.6	60.1	Zirconia	13.3	0.16	4.4
B3-10-1	13.3	60.1	Zirconia	26.6	0.33	4.4
B3-11-1	12.6	74.8	Zirconia	12.6	0.34	4.3
B3-12-1	25.0	75.0	Zirconia		0.22	5.4
B3-13-1	17.2	74.2	Zirconia	8.6	0.25	4.3
B3-14-1	60.0	40.0	Zirconia		0.07	4.0
B3-16-1	30.0	40.0	Zirconia	30.0	0.13	4.0
B3-23-1	40.0	40.0	Zirconia	20.0	0.11	4.4
B3-24-1	20.0	40.0	Zirconia	40.0	0.20	4.0
B3-25-1	15.0	40.0	Zirconia	45.0	0.27	4.0
B3-26-1	20.0	60.0	Zirconia	20.0	0.24	4.8
B3-29-1	20.0	60.0	Zirconia	20.0	0.24	4.8
B3-30-1	20.0	60.0	Zirconia	20.0	0.24	4.8
B3-31-1	20.0	60.0	Zirconia	20.0	0.24	4.8
B4-1-1	10.0	60.0	Zirconia	30.0	0.48	4.8
B4-2-1	40.0	60.0	Gr. Spinel		0.13	5.0
B4-5-1	40.0	60.0	Gr. Spinel		0.12	4.8
B4-6-1	20.0	60.0	Gr. Spinel	20.0	0.24	4.8
B4-14-1	40.0	60.0	Gr. Spinel		0.12	4.8
B4-15-1	13.5	60.0	Gr. Spinel	26.5	0.35	4.8
B4-16-1	10.0	60.0	Gr. Spinel	30.0	0.48	4.8
B4-19-1	60.0	40.0	Gr. Spinel		0.09	5.4
B4-20-1	30.0	40.0	Gr. Spinel	30.0	0.18	5.4
B4-21-1	20.0	40.0	Gr. Spinel	40.0	0.27	5.4
B4-27-1	60.0	40.0	DB MgO		0.09	5.4
B4-28-1	30.0	40.0	DB MgO	30.0	0.18	5.4

Table AII.14. Summary of Batch Mixing Parameters, Calcium Dialuminate Cement (continued).

Batch Number	Composite, wt. %				W/C Ratio	H_2O wt.%
	Cement	Reinforcement		Additive		
B4-29-1	40.0	40.0	DB MgO	20.0	0.14	5.4
B4-30-1	20.0	40.0	DB MgO	40.0	0.27	5.4
B4-31-1	40.0	60.0	Rock		0.19	7.7
B5-1-1	40.0	60.0	Rock		0.15	6.0
B5-3-1	40.0	60.0	Rock		0.15	6.0
B5-4-1	40.0	60.0	Rock		0.14	5.6
B5-10-1	15.0	40.0	DB MgO	45.0	0.36	5.4
B5-12-1	25.0	75.0	DB MgO		0.22	5.4
SP7-6-1	20.0	60.0	DB MgO	20.0	0.14	2.8
SP7-7-1	20.0	60.0	DB MgO	20.0	0.20	4.0
SP7-8-1	26.7	60.0	DB MgO	13.3	0.15	4.0
SP7-9-1	26.7	60.0	DB MgO	13.3	0.23	6.0
SP7-11-1	26.7	60.0	DB MgO	13.3	0.38	10.0
SP7-12-1	26.7	60.0	DB MgO	13.3	0.30	8.0
SP7-13-1	20.0	60.0	DB MgO	20.0	0.20	4.0
SP7-14-1	20.0	60.0	DB MgO	20.0	0.30	6.0
SP7-15-1	20.0	60.0	DB MgO	20.0	0.40	8.0
SP7-16-1	20.0	60.0	DB MgO	20.0	0.60	12.0
SP7-17-1	26.7	60.0	DB MgO	13.3	0.23	6.0
SP7-18-1	26.7	60.0	DB MgO	13.3	0.30	8.0
SP7-19-1	26.7	60.0	DB MgO	13.3	0.38	10.0
SP7-20-1	13.3	60.0	DB MgO	26.7	0.27	3.6
SP7-21-1	20.0	60.0	DB MgO	20.0	0.20	4.0
SP7-22-1	24.0	60.0	DB MgO	16.0	0.17	4.0
SP7-23-1	10.0	60.0	DB MgO	30.0	0.40	0.0
SP7-26-1	10.0	60.0	DB MgO	30.0	0.40	4.0
SP7-27-1	8.0	60.0	DB MgO	32.0	0.50	4.0
SP7-28-1	20.0	60.0	DB MgO	20.0	0.20	4.0
SP7-29-1	13.3	60.0	DB MgO	26.7	0.30	4.0
SP7-30-1	13.3	60.0	DB MgO	26.7	0.30	4.0
SP7-31-1	20.0	60.0	DB MgO	20.0	0.20	4.0
SP8-2-1	24.0	60.0	DB MgO	16.0	0.17	4.0
SP8-3-1	10.0	60.0	DB MgO	30.0	0.40	4.0
SP8-4-1	10.0	60.0	DB MgO	30.0	0.40	4.0
SP8-6-1	13.3	60.0	DB MgO	26.7	0.30	4.0
SP8-9-1	20.0	60.0	DB MgO	20.0	0.20	4.0
SP8-10-1	24.0	60.0	DB MgO	16.0	0.17	4.0
SP8-11-1	10.0	60.0	DB MgO	30.0	0.40	4.0
SP8-12-1	10.0	60.0	DB MgO	30.0	0.40	4.0

Table AII.15. Composition Summary, Calcium Dialuminate Cement Samples.

Batch Number	Matrix Additives, wt. %							Cement, wt. %			
	Cr_2O_3	MgO	DB MgO	$MgAl_2O_4$	Al_2O_3	$TiO{\cdot}Al_2O_3$	CeO_2	Al_2O_3	CaO	Fe_3O_4	SiO_2
B1-12-1								62.0	30.0	5.0	3.0
B1-15-1								62.0	30.0	5.0	3.0
B1-19-1								62.0	30.0	5.0	3.0
B1-20-1								62.0	30.0	5.0	3.0
B1-22-1				50.0				31.0	15.0	2.5	1.5
B1-25-1								62.0	30.0	5.0	3.0
B1-28-1								62.0	30.0	5.0	3.0
B1-29-2								62.0	30.0	5.0	3.0
B2-10-1			50.0					31.0	15.0	2.5	1.5
B2-14-2								62.0	30.0	5.0	3.0
B2-22-1								62.0	30.0	5.0	3.0
B2-24-1			50.0					31.0	15.0	2.5	1.5
B2-25-1			50.0					31.0	15.0	2.5	1.5
B3-9-1			33.3					41.3	20.0	3.3	2.0
B3-10-1			66.7					20.7	10.0	1.7	1.0
B3-11-1			50.0					31.0	15.0	2.5	1.5
B3-12-1								62.0	30.0	5.0	3.0
B3-13-1			33.3					41.3	20.0	3.3	2.0
B3-14-1								62.0	30.0	5.0	3.0
B3-16-1			50.0					31.0	15.0	2.5	1.5
B3-23-1			33.3					41.3	20.0	3.3	2.0
B3-24-1			66.7					20.7	10.0	1.7	1.0

Table AII.15. Composition Summary, Calcium Dialuminate Cement Samples (continued).

Batch Number	Matrix Additives, wt. %							Cement, wt. %			
	Cr_2O_3	MgO	DB MgO	$MgAl_2O_4$	Al_2O_3	$TiO{\cdot}Al_2O_3$	CeO_2	Al_2O_3	CaO	Fe_3O_4	SiO_2
B3-25-1			75.0					15.5	7.5	1.3	0.8
B3-26-1	16.8	33.2						31.0	15.0	2.5	1.5
B3-29-1	25.0	25.0						31.0	15.0	2.5	1.5
B3-30-1	33.2	16.8						31.0	15.0	2.5	1.5
B3-31-1	9.8	40.2						31.0	15.0	2.5	1.5
B4-1-1	16.8	8.2						15.5	7.5	1.3	0.8
B4-2-1								62.0	30.0	5.0	3.0
B4-5-1								62.0	30.0	5.0	3.0
B4-6-1			50.0					31.0	15.0	2.5	1.5
B4-14-1								62.0	30.0	5.0	3.0
B4-15-1			66.3					20.9	10.1	1.7	1.0
B4-16-1			75.0					15.5	7.5	1.3	0.8
B4-19-1								62.0	30.0	5.0	3.0
B4-20-1			50.0					31.0	15.0	2.5	1.5
B4-21-1			66.7					20.7	10.0	1.7	1.0
B4-27-1								62.0	30.0	5.0	3.0
B4-28-1			50.0					31.0	15.0	2.5	1.5
B4-29-1			33.3					41.3	20.0	3.3	2.0
B4-30-1			66.7					20.7	10.0	1.7	1.0
B4-31-1								62.0	30.0	5.0	3.0
B5-1-1								62.0	30.0	5.0	3.0
B5-3-1								62.0	30.0	5.0	3.0
B5-4-1								62.0	30.0	5.0	3.0
B5-10-1			75.0					15.5	7.5	1.3	0.8
B5-12-1								62.0	30.0	5.0	3.0

Table AII.15. Composition Summary, Calcium Dialuminate Cement Samples (continued).

Batch Number	Matrix Additives, wt. %							Cement, wt. %			
	Cr_2O_3	MgO	DB MgO	$MgAl_2O_4$	Al_2O_3	$TiO{\cdot}Al_2O_3$	CeO_2	Al_2O_3	CaO	Fe_3O_4	SiO_2
SP7-6-1			50.0					31.0	15.0	2.5	1.5
SP7-7-1			50.0					31.0	15.0	2.5	1.5
SP7-8-1			33.3					41.3	20.0	3.3	2.0
SP7-9-1			33.3					41.3	20.0	3.3	2.0
SP7-11-1			33.3					41.3	20.0	3.3	2.0
SP7-12-1			33.3					41.3	20.0	3.3	2.0
SP7-13-1			50.0					31.0	15.0	2.5	1.5
SP7-14-1			50.0					31.0	15.0	2.5	1.5
SP7-15-1			50.0					31.0	15.0	2.5	1.5
SP7-16-1			50.0					31.0	15.0	2.5	1.5
SP7-17-1			33.3					41.3	20.0	3.3	2.0
SP7-18-1			33.3					41.3	20.0	3.3	2.0
SP7-19-1			33.3					41.3	20.0	3.3	2.0
SP7-20-1			33.3			33.3		20.7	10.0	1.7	1.0
SP7-21-1			25.0			25.0		31.0	15.0	2.5	1.5
SP7-22-1			20.0			20.0		37.2	18.0	3.0	1.8
SP7-23-1			50.0			25.0		15.5	7.5	1.3	0.8
SP7-26-1			25.0			50.0		15.5	7.5	1.3	0.8
SP7-27-1			20.0			60.0		12.4	6.0	1.0	0.6
SP7-28-1						50.0		31.0	15.0	2.5	1.5
SP7-29-1						66.7		20.7	10.0	1.7	1.0
SP7-30-1			33.3				33.3	20.7	10.0	1.7	1.0

Table AII.15. Composition Summary, Calcium Dialuminate Cement Samples (continued).

Batch Number	Matrix Additives, wt. %							Cement, wt. %			
	Cr_2O_3	MgO	DB MgO	$MgAl_2O_4$	Al_2O_3	$TiO{\cdot}Al_2O_3$	CeO_2	Al_2O_3	CaO	Fe_3O_4	SiO_2
SP7-31-1			25.0				25.0	31.0	15.0	2.5	1.5
SP8-2-1			20.0				20.0	37.2	18.0	3.0	1.8
SP8-3-1			50.0				25.0	15.5	7.5	1.3	0.8
SP8-4-1			25.0				50.0	15.5	7.5	1.3	0.8
SP8-6-1			33.3		33.3			20.7	10.0	1.7	1.0
SP8-9-1			25.0		25.0			31.0	15.0	2.5	1.5
SP8-10-1			20.0		20.0			37.2	18.0	3.0	1.8
SP8-11-1			50.0		25.0			15.5	7.5	1.3	0.8

APPENDIX III

WEAR TEST COUPON CORRECTION FACTOR AND COMPRESSION STRENGTH REFERENCE COUPONS

AIII.1 Abrasive Wear Testing

The DSRW testing was conducted over a period of two years. The testing comprised of 27 test campaigns that totaled more than 360 individual coupon wear tests. The wear rate on each surface was determined over a total sliding distance range of 150 to 200 meters using 8 to 12 measurement intervals. Weight loss measurements were used to determine the wear rate. A simple linear regression analysis was performed and the best fit selected. In most cases the weight loss from the first three intervals or "burn in" period was eliminated from the wear rate determinations. Abrasive wear testing was performed on each side of the coupon. Table AIII.1 lists the test schedule used for DSRW testing. Reference firebrick coupons were tested with the coupons on all but the first three campaigns. The first three campaigns used a combination of a D-2 ASTM reference standard and fire brick coupons over a short test interval, approximately 30 hour period. A number of independent tests were made using reference material to determine the wear rate sensitivity to experimental parameters. The humidity or absorbed atmospheric moisture and the friction caused surface temperature rise influenced the results. The humidity influence was normalized by the autoclaving prior to testing and testing in small enough groups that the total test time was less than 3 hours. Maintaining a relative short sliding distance during a wear interval kept the surface temperatures down. The test procedure used red and tan firebrick as reference coupons during each test campaign. Campaign to campaign variation was normalized by developing a correction factor. Figure AIII.1 shows a comparison of the wear rates determined on each of the reference coupons for each of the test campaigns. The results indicate a consistent trend between reference coupons tested. A set of reference coupons was prepared and tested independent of all tests over a single test campaign. These results are presented in Figure AIII.4. Representative surfaces of the wear scar area from the reference fire brick coupons are shown in Figures AIII.2 and AIII.3.

Table AIII.1 Summary of Abrasive Wear Testing.

DSRW TEST SCHEDULE AND CORRECTION FACTOR								
TEST SET		**CF**	**COUPONS**					
DC Set 1	Side 1	0.69	B1-28-C2	B2-2-C2	B2-4-C2	B2-9-C2	B2-12-C2	B2-16-C2
			B2-18-C2	B2-23-C2	B2-24-C2	B3-2-C2	B3-4-C2	
DC Set 1	Side 2	0.69	B1-28-C2	B2-2-C2	B2-4-C2	B2-9-C2	B2-12-C2	B2-16-C2
			B2-18-C2	B2-23-C2	B2-24-C2	B3-2-C2	B3-4-C2	
DC Set 2	Side 1	0.69	B3-6-C2	B3-10-C2	B3-12-C2	B3-16-C2	B3-18-C2	B3-30-C2
			B4-1-C2	B4-3-C2	B4-6-C2	B4-8-C2	B4-13-C2	B4-16-C2
DC Set 2	Side 2	0.41	B3-6-C2	B3-10-C2	B3-12-C2	B3-16-C2	B3-18-C2	B3-30-C2
			B4-1-C2	B4-3-C2	B4-6-C2	B4-8-C2	B4-13-C2	B4-16-C2
DC Set 3	Side 1	0.48	B4-20-C2	B4-22-C2	B4-24-C2	B4-27-C2	B4-29-C2	B5-1-C2
			B5-4-C2	B5-6-C2				
			B5-8-C2	B5-11-C2	B5-13-C2	B5-15-C2	B5-18-C2	B5-20-C2
DC Set 3	Side 2	0.66	B4-20-C2	B4-22-C2	B4-24-C2	B4-27-C2	B4-29-C2	B5-1-C2
			B5-4-C2	B5-6-C2	B5-8-C2	B5-11-C2	B5-13-C2	B5-15-C2
			B5-18-C2	B5-20-C2				
DC Set 4	Side 1	1.34	B1-28-C4	B2-2-C4	B2-4-C4	B2-9-C4	B2-12-C4	B2-16-C4
			B2-18-C4	B2-23-C4	B2-24-C4			
CA Set 1	Side 1	1.35	B3-2-C4	B3-4-C4	B8-24-C2	B8-28-C2	B9-1-C2	B9-3-C2
			B9-6-C2	B9-10-C2				
CA Set 1	Side 1	1.35	B8-28-C2	B9-1-C2	B9-3-C2	B9-6-C2	B9-10-C2	
DC Set 5	Side 1	1.49	B3-6-C4	B3-10-C4	B3-12-C4	B3-16-C4	B3-18-C4	B3-30-C4
			B4-1-C4	B4-3-C4	B4-6-C4	B4-8-C4		
			B4-20-C4	B4-22-C4	B4-24-C4	B4-27-C4		
DC Set 6	Side 1	1.95	B4-13-C4	B4-16-C4	B4-29-C4	B5-1-C4	B5-4-C4	B5-6-C4
			B5-8-C4	B5-11-C4	B5-13-C4	B5-15-C4		
			B5-18-C4	B5-20-C4	B5-22-C4	B5-26-C4	B5-28-C4	
CA Set 2	Side 1	0.90	B9-26-C2	B9-28-C2	B10-2-C2	B10-5-C2	B10-7-C2	B10-12-C2
			B10-14-C2	B10-16-C2	B10-19-C2	B10-21-C2		

Table AIII.1 Summary of Abrasive Wear Testing (continued).

DSRW TEST SCHEDULE AND CORRECTION FACTOR								
TEST SET		**CF**	**COUPONS**					
			B10-23-C2	B9-30-C2				
CA Set 2	Side 2	1.24	B9-26-C2	B9-28-C2	B10-2-C2	B10-5-C2	B10-7-C2	B10-12-C2
			B10-14-C2	B10-16-C2	B10-19-C2	B10-21-C2	B10-23-C2	B9-30-C2
DC Set 4	Side 2	0.87	B1-28-C4	B2-2-C4	B2-4-C4	B2-9-C4	B2-12-C4	B2-16-C4
			B2-18-C4	B2-23-C4	B2-24-C4	B3-2-C4	B3-4-C4	B3-6-C4
			B3-10-C4					
DC Set 5	Side 2a	1.16	B3-12-C4	B3-16-C4	B3-18-C4	B3-30-C4	B4-1-C4	B4-3-C4
			B4-6-C4	B4-8-C4	B4-13-C4			
DC Set 5	Side 2b	1.44	B4-16-C4	B4-20-C4	B4-22-C4	B4-24-C4	B4-27-C4	B11-23-C2
CA Set 3	Side 1	1.81	B11-30-C2	B12-1-C2	B12-2-C2	B12-3-C2		
CA Set 3	Side 2	1.70	B11-23-C2	B11-30-C2	B12-1-C2	B12-2-C2	B12-3-C2	
DC Set 6	Side 2	1.29	B4-29-C4	B5-1-C4	B5-4-C4	B5-6-C4	B5-8-C4	B5-11-C4
			B5-13-C4	B5-15-C4	B5-18-C4	B5-20-C4	B5-22-C4	B5-26-C4
			B5-28-C4					
CA Set 4	Side 1	0.99	B12-7-C2	B12-8-C2	B12-9-C2	B12-18-C2	B1-12-C2	B1-15-C2
			B1-19-C2	B1-20-C2	B1-22-C2	B1-28-C2	B1-29-C2	B2-10-C2
			B2-12-C2	B2-22-C2	B2-24-C2	B2-26-C2	B3-9-C2	B3-10-C2
			B3-11-C2	B3-12-C2	B3-13-C2	B3-14-C2		
CA Set 4	Side 2	1.70	B12-7-C2	B12-8-C2	B12-9-C2	B12-18-C2	B1-12-C2	B1-15-C2
			B1-19-C2	B1-20-C2	B1-22-C2	B1-28-C2	B1-29-C2	B2-10-C2
			B2-12-C2	B2-22-C2	B2-24-C2	B2-26-C2	B3-9-C2	B3-10-C2
			B3-11-C2	B3-12-C2	B3-13-C2	B3-14-C2		
CA Set 5	Side 1	0.94	B3-15-C2	B3-23-C2	B3-24-C2	B3-25-C2	B3-26-C2	B3-29-C2
			B3-30-C2	B3-31-C2	B4-1-C2	B4-2-C2	B4-5-C2	PGE
CA Set 5	Side 2	1.28	B3-15-C2	B3-23-C2	B3-24-C2	B3-25-C2	B3-26-C2	B3-29-C2
			B3-30-C2	B3-31-C2	B4-1-C2	B4-2-C2	B4-5-C2	PGE
CA Set 6	Side 1	1.03	B4-15-C2	B4-20-C2	B4-28-C2	B4-29-C2	B4-30-C2	B5-10-C2

Table AIII.1 Summary of Abrasive Wear Testing (continued).

DSRW TEST SCHEDULE AND CORRECTION FACTOR								
TEST SET		**CF**	**COUPONS**					
CA Set 6	Side 2	0.94	B5-12-C2 B4-15-C2	B4-20-C2	B4-28-C2	B4-29-C2	B4-30-C2	B5-10-C2
CA MU	Side 1	1.35	B5-12-C2 B4-6-C4 B5-1-C4	B4-14-C4 B5-3-C4	B4-16-C4 B5-4-C4	B4-19-C4	B4-21-C4	B4-27-C4
CA MU	Side 2	1.49	B4-6-C4 B51-C4	B4-14-C4 B5-3-C4	B4-16-C4 B5-4-C4	B4-19-C4	B4-21-C4	B4-27-C4
SP Set 1	Side 1	1.39	SP7-6-C2 SP7-13-C2 SP7-19-C2	SP7-7-C2 SP7-14-C2	SP7-8-C2 SP7-15-C2	SP7-9-C2 SP7-16-C2	SP7-11-C2 SP7-17-C2	SP7-12-C2 SP7-18-C2
SP Set 1	Side 2	0.87	SP7-6-C2 SP7-13-C2 SP7-19-C2	SP7-7-C2 SP7-14-C2	SP7-8-C2 SP7-15-C2	SP7-9-C2 SP7-16-C2	SP7-11-C2 SP7-17-C2	SP7-12-C2 SP7-18-C2
SP Set 2	Side 1	1.03	SP7-20-C2 SP7-28-C2 SP8-04-C2	SP7-21-C2 SP7-29-C2 SP8-06-C2	SP7-22-C2 SP7-30-C2 SP8-09-C2	SP7-23-C2 SP7-31-C2 SP8-10-C2	SP7-26-C2 SP8-02-C2 SP8-11-C2	SP7-27-C2 SP8-03-C2 SP8-12-C2
SP Set 2	Side 2	1.24	SP7-20-C2 SP7-28-C2 SP8-04-C2	SP7-21-C2 SP7-29-C2 SP8-06-C2	SP7-22-C2 SP7-30-C2 SP8-09-C2	SP7-23-C2 SP7-31-C2 SP8-10-C2	SP7-26-C2 SP8-02-C2 SP8-11-C2	SP7-27-C2 SP8-03-C2 SP8-12-C2

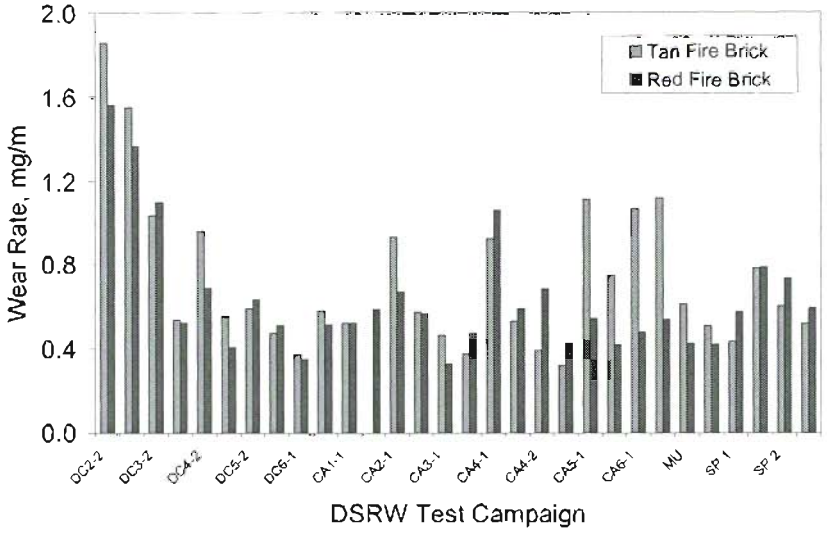

Figure AIII.1 DSRW test results showing the reference standard fire brick wear rate over all test campaigns.

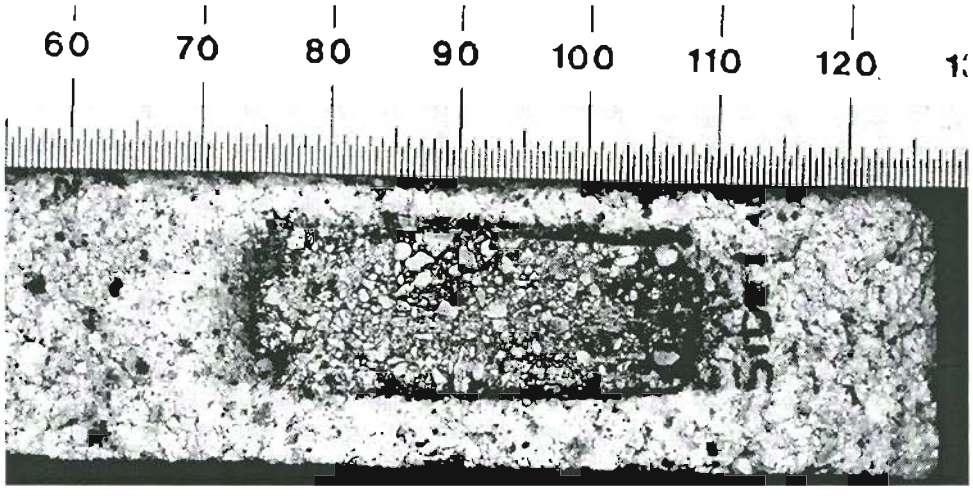

Figure AIII.2 DSRW wear scar image showing a Tan fire brick reference material.

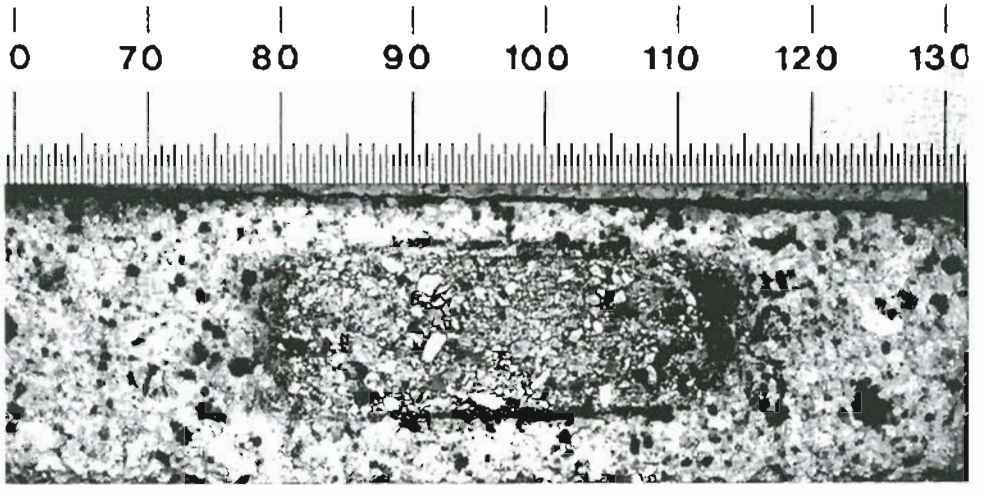

Figure AIII.3. DSRW wear scar image showing a Red fire brick reference material.

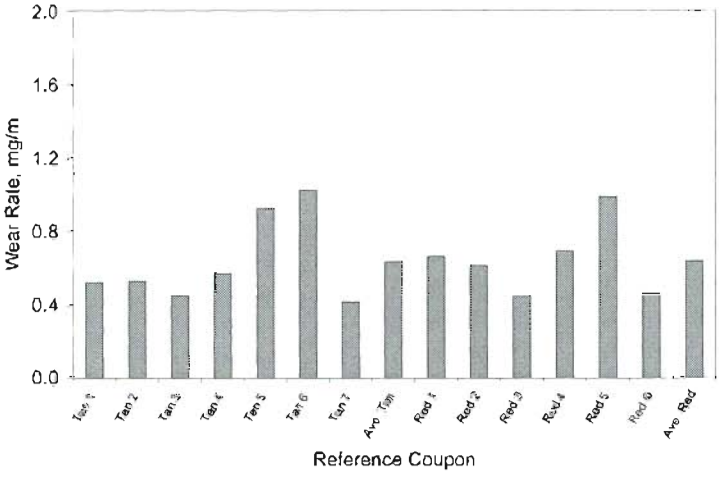

Figure AIII.4 DSRW test results showing reference brick wear rate. Independent testing of reference material wear rate illustrating the range in wear rate determined on identical coupons.

AIII.1.1 Wear Test Coupon Correction Factor

The errors encountered during DSRW wear testing are both random and systematic. Large random errors are addressed by a through review of the data and discounting the data as defective when found. Examples of random errors are number transposing or non wear related weight loss due to miss handling coupons or edge crumbling. Random errors are minimized using careful laboratory practice and performing tests in sets allowing time to avoid rushing the process. Test to test systematic errors can be estimated and corrected using careful controls on experimental procedure and the use of control reference materials or standards. Sources of systematic errors can be sand flow variability, wheel vibration, retained moisture, surface temperature changes, rubber wheel grooving and balance drift.

The coupons are tested in groups of 12 to 16 coupons over a period of two years. Along with the test coupons each group also tested two control or reference coupons. Control coupons are made from two different types of pressed and fired alumina silicate refractory brick: high duty and standard duty fire brick. The experimental notes refer to the bricks as red for high duty and tan for standard duty. The reference fire brick has similar density, relatively uniform porosity and uniform particle size. Based on testing, wear debris observations, microstructural analysis the three body abrasive wear mechanism at the same test conditions is similar to the refractory cement with the absence of the reinforcement to matrix interface. Wear test samples of the fire brick are cut from refractory using a carbide tip blade band saw. A water-based lubricant was used to reduce heat and allow a faster cutting rate. Both types of reference standards are tested along side the formulated batch coupons.

A correction factor was used to normalize the systematic errors between test group to test group and allow comparisons of the wear rate data. The tan and red control coupon wear rates are used to develop the correction factor. The correction factor is determined independently for each test group by averaging a wear rate multiplier for both tan and red reference coupons for each test. The tan or red coupon multiplier is the ratio of the wear rate for a specific test group to the average of all test groups.

The accuracy of the weight measurement dominates the sources of error.

$$CF_{testgroup} = \frac{M_t + M_r}{2}$$

As compared to testing of metallic DSRW test specimens, ceramic materials with half the

$$M_t = \frac{(W_t)n}{\sum W_t} \qquad\qquad M_r = \frac{(W_r)n}{\sum W_r}$$

density need twice the wear scar volume for the same weight change. The combined influence of the lower density and low contact pressure worked against high total weight change for increased accuracy. Relative humidity and temperature influences are greater for low weight measurements.

AIII.1.2 Wear Scar Documentation

The tribological boundary conditions are defined by the wear mechanism. By wear debris microstructural observations, examination of the wear scar and microstructural analysis of wear scar cross sections the wear mechanism on the castable refractory cement is a chipping, flaking and brittle fracture of cement grains from the matrix. The comparative relationships drawn from abrasive wear testing are not valid for coupons worn are different wear mechanism, for example plowing and reinforcement spalling or pull out.

The contact pressure, abrasive material, test temperature, relative humidity and test material define the three-body abrasive wear process. The abrasive material is constant throughout the test. The temperature rise during testing is relatively small and standardized using a constant sliding distance between weight measurements for all coupons tested. All coupons are autoclaved prior to testing to remove absorbed water and eliminate hydroxide formation. Coupons are tested in groups small enough that the

entire testing interval is between 2 to 4 hours, insufficient to be affected by atmospheric humidity. The two remaining parameters are contact pressure and the coupon formulation variables.

The contact pressure changes with the size of the wear scar from the beginning of the test to the end of the test because the constant dead weight load on the lever arm is spread over a greater surface area. The initial wear scar area is the same but as the material is lost the scar area increases. The area size change is a function of the wear rate. The contact area is a function load, radius of the wheel, rubber hardness and the rubber wheel contact surface profile. The profiles are maintained flat and radius measured throughout the test campaign. The wheels are surfaced and dressed as needed.

The wear scar size is measured using a digital camera mounted on a light table with high intensity lights. The digital images of the wear scar are taken using a 55mm lens set at a f22 aperture opening and maintaining 1/100-second exposure. The image files are manipulated using a MAC Quadra personal computer station and NIH Image version 2.0 image analysis software developed by the National Institute of Health. The captured wear scar images are taken as 256 gray scale image. Thresholding the gray levels enable manual separation of matrix and reinforcement. Images were digitally captured and the analysis preformed at approximately 5 to 7 times magnification. A laboratory scale is placed along side the wear scar and used to calibrate the scale in each image. The scale is made to fill as much as possible the 1028 pixel image. Calibration distances are made to fill the image to minimize edge effects on large wear scars. The evaluation process was standardized to allow comparisons of the different coupons. Examples of the wear scar and the three steps used to document the wear scar area and the reinforcement area are shown in Figure AIII.5.

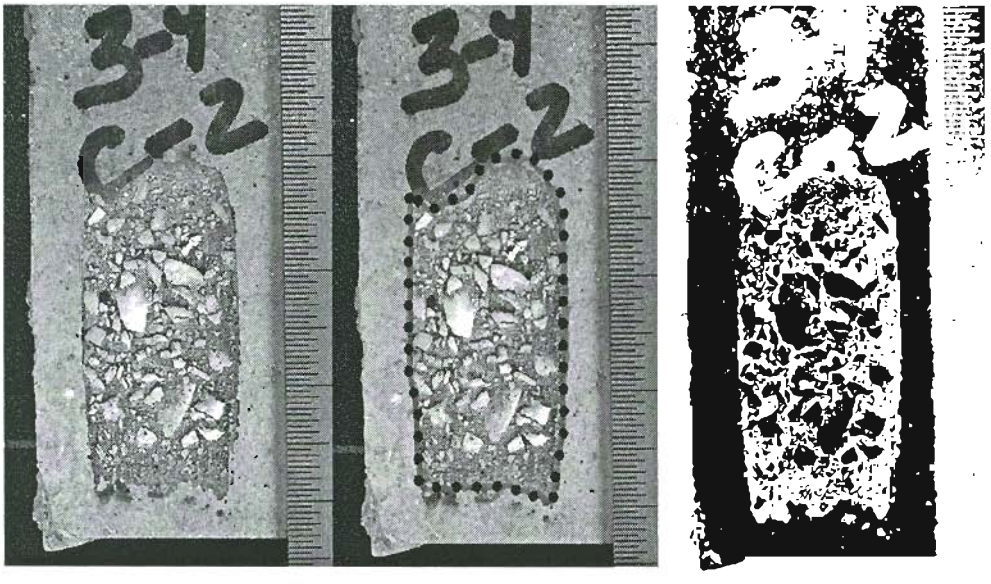

Figure AIII.5 Wear scar analysis technique illustrated. The first frame is the initial wear scar surface, the second frame shows the hand drawn outline of the wear scar and the third is the inverse image for pixel counting. The image is scaled using the laboratory rule calibrated to 0.5 mm.

The wear scars are qualitatively divided into set according to the surface profile. The surface profile can be one of two types; flat profiles or profiles with the reinforcement particles standing above the matrix. The flat profile indicates a constant wear rate for the matrix and reinforcement phase. The uneven surface indicates that the wear rate is not the same for the matrix as the reinforcement. Pull out of the reinforcement indicates a weak interface. The wear scar surface profiles are observed with a stereo microscope and oblique lighting at 10 to 70 times magnification.

AIII.2 CCS Reference Coupons

Standard reference firebrick tan and red coupons were tested with coupons made from the experimental formulations. The standard reference coupons were cut from the same standard reference fire brick used for DSRW wear testing. The reference coupons were dehumidified prior to testing. Coupons were held at >100°C for a minimum of 24 hours prior to testing. A total of nine red and eight tan reference coupons were tested. The average and standard deviation of the tested coupons are listed in Table AIII.2. The results of each test are plotted in Figure AIII.6.

Table AIII.2 Reference Brick Cold Crushing Strength

Coupons Type	Average CCS, Mpa
Red Fire Brick	20.1
Std. Deviation	4.1
Tan Fire Brick	10.8
Std. Deviation	1.6

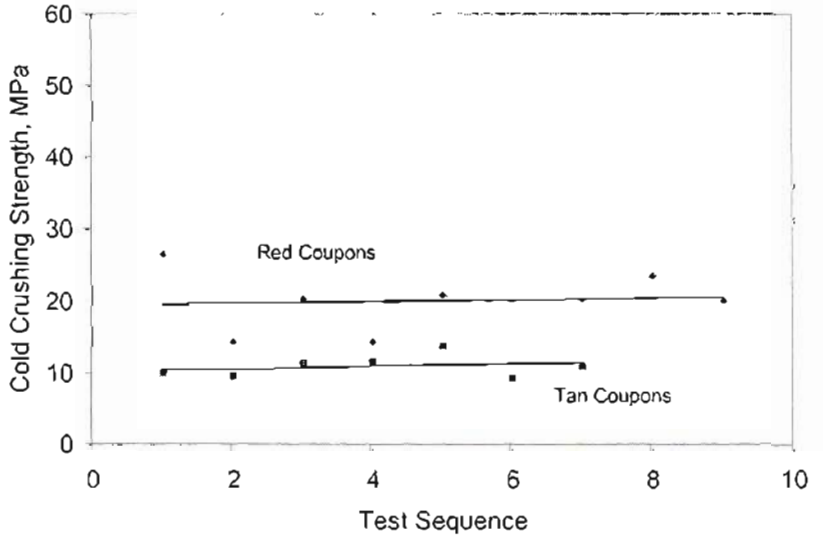

Figure AIII.6 CCS test results illustrate the range of the compression strength for the reference fire brick coupons tested.

AIII.2.1 Coupon Size Influence

Coupons from position number 1, 3 and 5 were used for compression testing. To increase the number of data points some of the coupons were cut into two samples. Coupons from position #1 were cut and compared to the full size position #3 coupons. Figures AIII.7 and AIII.8 illustrates the variation of compression strength with the coupon size for the premix cement and the calcium dialuminate batches.

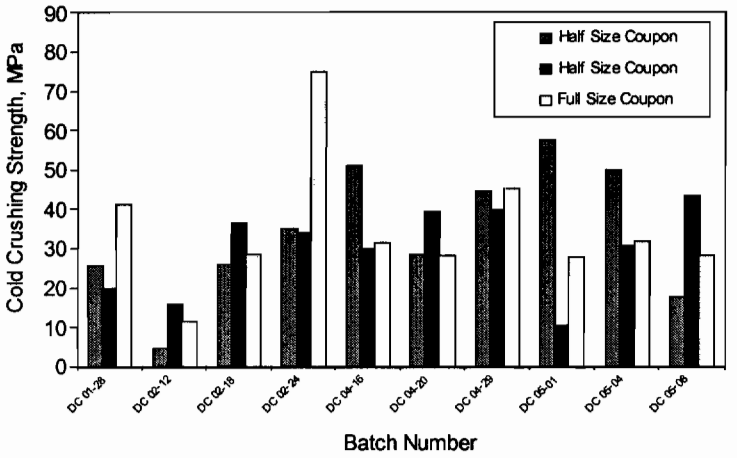

Figure AIII.7. CCS test results illustrate the influence of test sample size on the compression strength for batches made from the high alumina calcium aluminate.

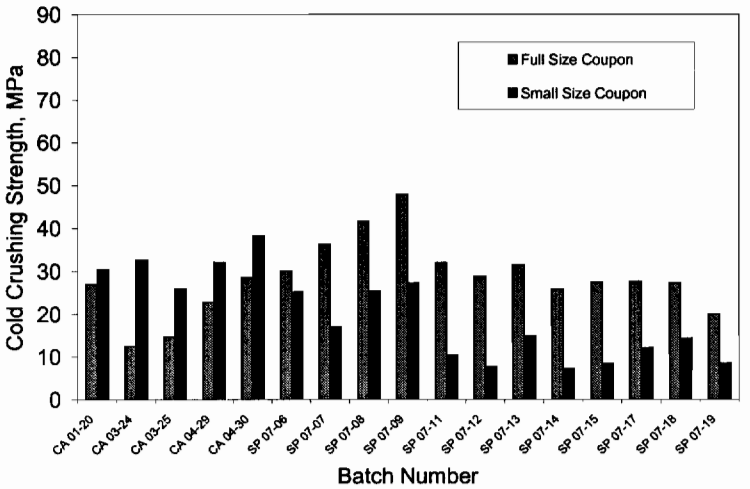

Figure AIII.8. CCS test results illustrate the influence of sample size on the compression strength for bacthes made from the calcium dialuminate cement.

AIII.2.2 Influence of Sintering

The cold crushing strength of sintered versus non sintered or green composite formulations were studied. The test included coupons from both the premix commercial castable and the calcium dialuminate batch formulations. Figure AIII.9 presents the results form the calcium dialuminate batch formulations. The coupon position number five was selected to provide green CCS results. The sintered data presented are from coupon position number 3 and 1. These were sintered for 96 hours at 1200°C. Coupon positions number three were sectioned to increase the number of samples. The number five coupons were cured and dried similar to the coupons to be sintered. The unsintered coupons were soaked at > 100°C before testing. In nearly all coupons of this set the green strength was found greater than the sintered strength.

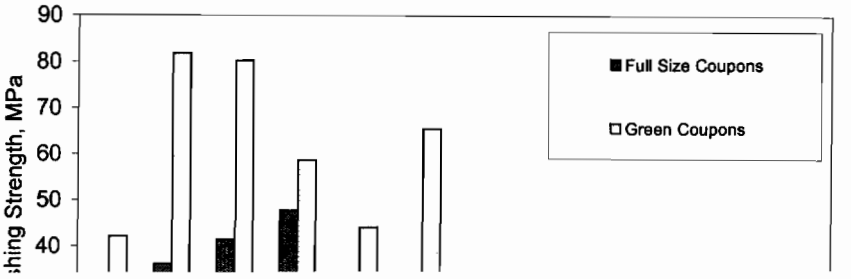

The wear scars are qualitatively divided into set according to the surface profile. The surface profile can be one of two types; flat profiles or profiles with the reinforcement particles standing above the matrix. The flat profile indicates a constant wear rate for the matrix and reinforcement phase. The uneven surface indicates that the wear rate is not the same for the matrix as the reinforcement. Pull out of the reinforcement indicates a weak interface. The wear scar surface profiles are observed with a stereo microscope and oblique lighting at 10 to 70 times magnification.

AIII.2 CCS Reference Coupons

Standard reference firebrick tan and red coupons were tested with coupons made from the experimental formulations. The standard reference coupons were cut from the same standard reference fire brick used for DSRW wear testing. The reference coupons were dehumidified prior to testing. Coupons were held at >100°C for a minimum of 24 hours prior to testing. A total of nine red and eight tan reference coupons were tested. The average and standard deviation of the tested coupons are listed in Table AIII.2. The results of each test are plotted in Figure AIII.6.

Table AIII.2 Reference Brick Cold Crushing Strength

Coupons Type	Average CCS, Mpa
Red Fire Brick	20.1
Std. Deviation	4.1
Tan Fire Brick	10.8
Std. Deviation	1.6

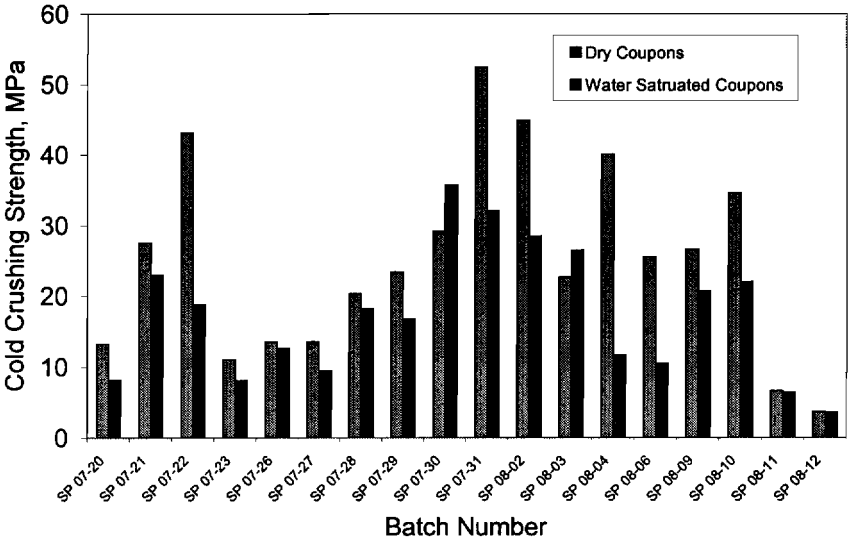

Figure AIII.10. CCS test results illustrating the influence of water saturation on the compression strength.

APPENDIX IV

DSRW AND CCS TEST RESULTS

AIV.1 Introduction

The Dry Sand Rubber Wheel (DSRW) wear test and the Cold Crushing Strength (CCS) tests were used to rank the formulations and help develop empirical relationships with the changing additive and reinforcement materials. The abrasive wear and the mechanical property test data were tabulated in log books, reduced and placed into spread sheets for analysis. The highest compressive load was directly read from the test instrument. The data was not statistically manipulated. The weight loss data was taken over long sliding distances with frequent intermittent weight loss measurements. The steady state wear rate was determined using an regression curve fit over a number of data points, the first several data measurements were truncated because of burn-in concerns. The number of data points included in the set are optimized to maintain a high "r^2" or as close to unity as possible. Often, the square of the residuals was found between .99 and .999. Wear rate data with an "r^2" values less than .95 resulted in further review of the data. Depending on the observations of the wear scar, errors in log book entries and consistency with the other side of the coupon the data was rejected or included. Less than 5% of all the data was discarded as laboratory errors, for example transposing numbers, laboratory balance drift and dropped coupons. The test procedure is explained in the experimental section of this thesis.

The wear and compression data are presented in detail in this appendix. The data are separated into three groups. The first two presentations are sorted to show the differences between the three matrix cements. The wear test results and the compression strength are used to illustrate property change with the variable cement parameters, for example total additive or total reinforcement. The third presentation is organized to present the influence of specific additives and reinforcements on all three of the different types of cement. The test matrix is presented in Section 3.3. The test matrix is a complex set of three, 2^n matrixes that vary additive composition and volume fraction of reinforcement. The analysis presented follows the experimental objectives. The analysis is presented in the order of determining the influence on the cement properties, influence of cement with additive properties and finally the influence of the reinforcement.

A.IV.2 High Alumina Calcium Aluminate Cement

The results from the DSRW wear test and the CCS measurements are presented for the high alumina calcium aluminate cement premix system. The cement and additives were blended dry make a standard size coupons for testing. The coupons are interchangeable for the wear test and strength test. However, experimental practice was to maintain orientation and coupon numbers throughout testing.

The set of data was reviewed to determine experimental related trends or bias introduced by the coupon preparation, handling or testing. The data are parsed into several groups sorting for global trends related to coupon position number, sinter temperature (1000°C or 1200°C), coupon side (1 or 2), influence of water and density. The greatest test influence found was the sintering temperature and the next greatest bias was found with the orientation of the coupon with respect to the mold and pressing direction. Coupon #2's were sintered at 1200°C for 96 hours whereas Coupon #4's were sintered at 1000°C for 96 hours, all the lower temperature data exhibited greater scatter and poorer performance than the high temperature fired coupon. The coupon orientation also proved to be a source of bias. The surface adjacent to the bottom of the mold exhibited a reduced wear rate over the top surface. This influence is believed to be a result of green packing factor is higher on the bottom and less on the top. CCS test results were found to be sensitive to the coupon position in the mold. For a given batch, the Coupon #3 positions exhibited greater CCS with all other parameters held constant. Even though the mold design tried to minimize the pressure differential between the edges and center the difference is attributed to the pressure distribution during pressing and cure. The pressure gradient is the greatest in the end coupons because of wall resistance.

The high alumina calcium aluminate cement data is presented to assess the influence of the cement concentration, additive concentration and reinforcement volume fraction on the properties. The data are graphically presented in the order of determining the influence on the cement with out additives, cement with additives and cement with changes to the reinforcement.

Table AVI.1 High Alumina Calcium Aluminate Cement.

Figure	Format of Data Relationship
AIV.1	The influence of coupon density to the wear rate
AIV.2	Influence of open porosity on the cold crushing strength, full size, Coupon #3.
AIV.3 AIV.4	The water to cement ratio is evaluated in both wear and strength testing.
AIV.5	The influence of changing volume of cement independent of the reinforcement concentration.
AIV.6 AIV.7 AIV.8	The magnesia, chromia and spinel matrix concentrations are compared against the wear rate
AIV.9	All additives and volume concentration of matrix cement are compared to the compression strength
AIV.10 AIV.11	The magnesia to chromia ratio compared to the wear rate and compression strength
AIV.12	The changing of reinforcement and matrix cement volume concentrations are compared to compression strength
AIV.13	Wear scar analysis results show influence of exposed reinforcement particle area
AIV.14	Reinforcement volume fraction compared to the wear rate
AIV.15	Reinforcement volume fraction compared to the exposed reinforcement area in the wear scar
AIV.16 AIV.17 AIV.18 AIV.19	The data sets separated the wear rate data according to the coupon numbers and side tested. (bias illustrated graphically)

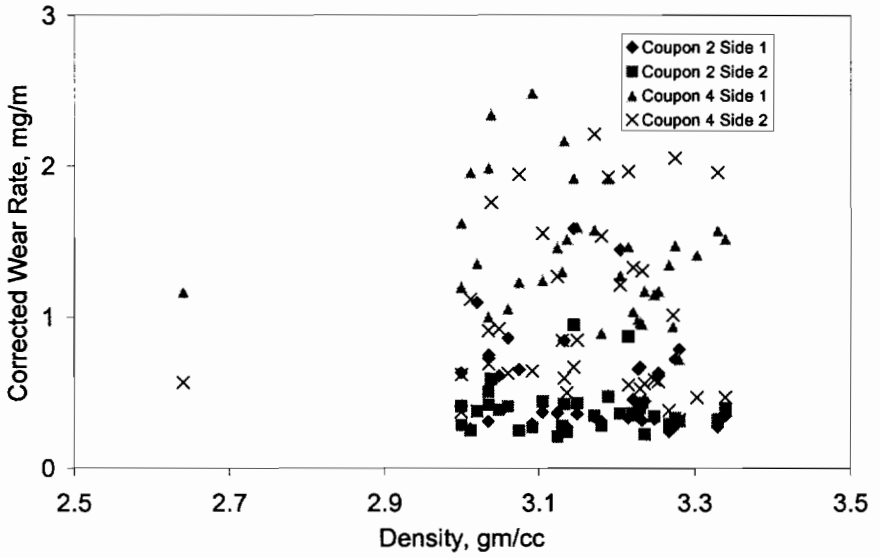

Figure AIV.1. DSRW test results illustrate the changing coupon density on the wear rate.

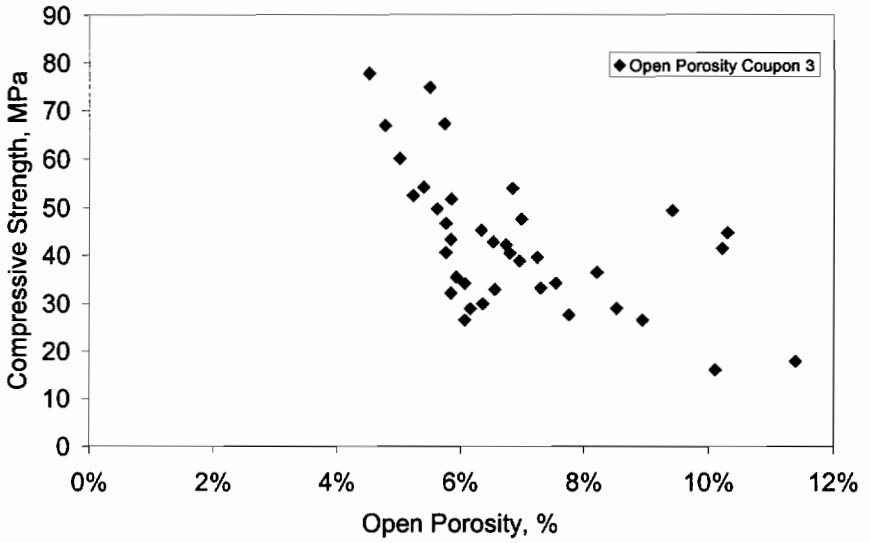

Figure AIV.2. CCS test results show the influence of the open porosity on the cold crushing strength for full size Coupon #3.

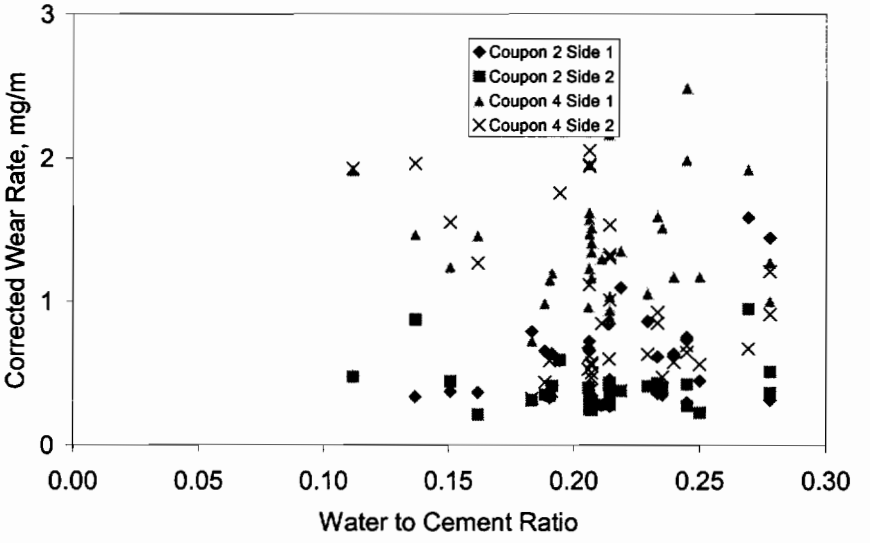

Figure AIV.3. DSRW test results illustrate the influence of W/C ratio on the wear rate; the data is separated by the coupon surface tested.

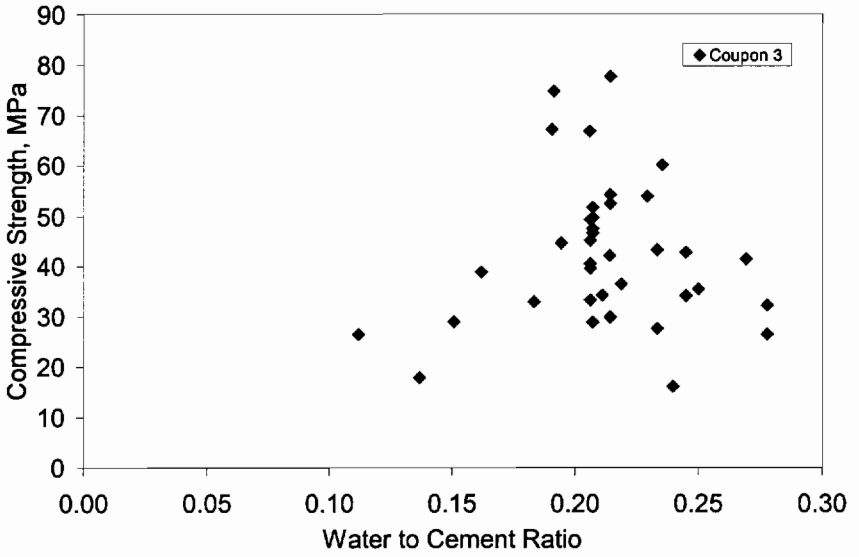

Figure AIV.4. CCS test results show the influence of W/C ratio on the compression strength.

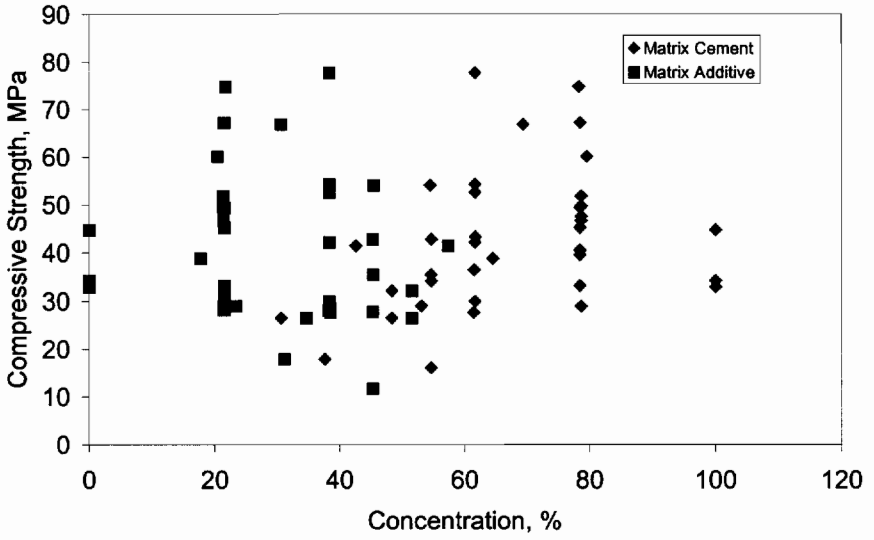

Figure AIV.5. CCS test results shows the influence of increasing cement and additive concentration on the cold crushing strength.

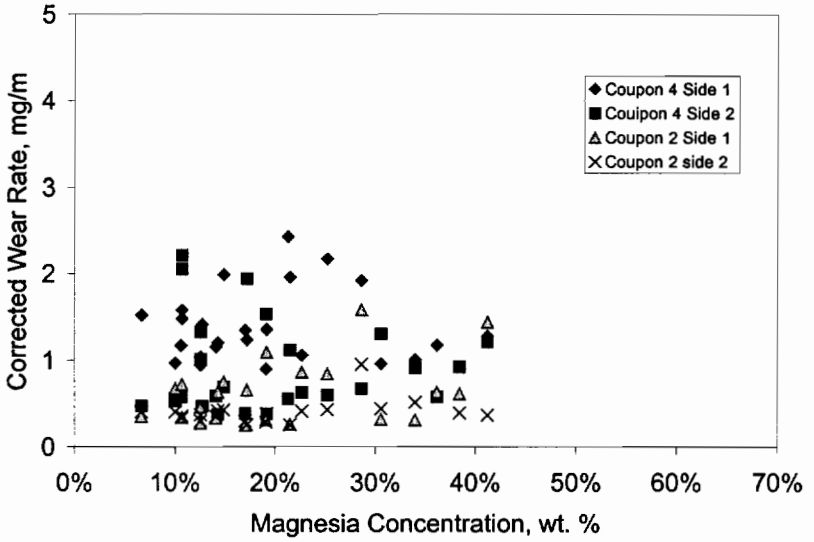

Figure AIV.6. DSRW test results illustrate Magnesia influence on the wear rate.

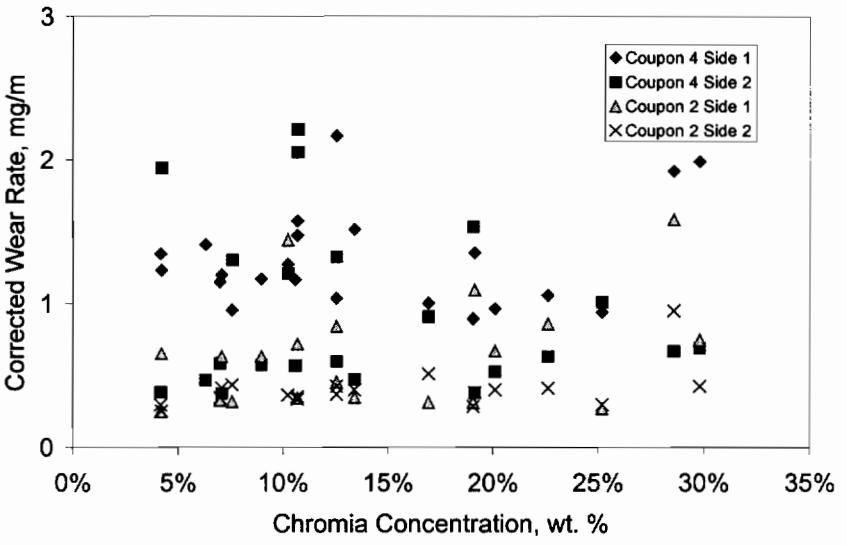

Figure AIV.7. DSRW test results illustrate Chromia influence on the wear rate.

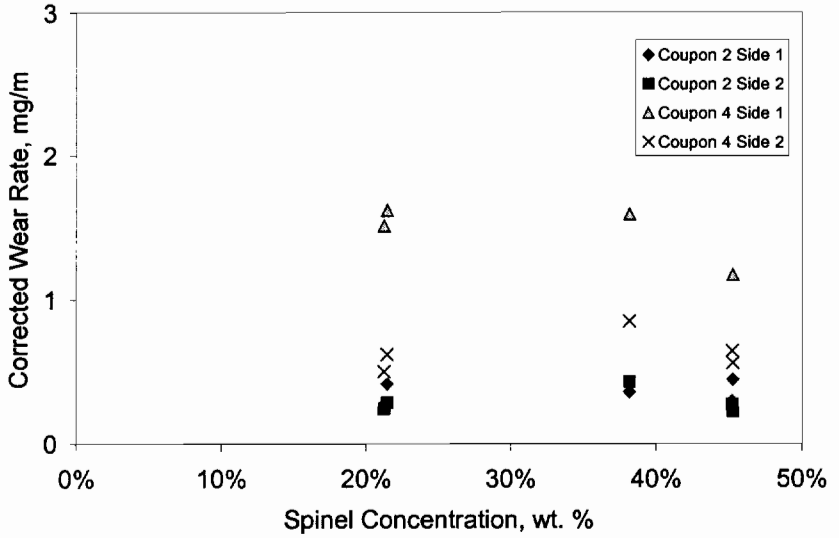

Figure AIV.8. DSRW test results illustrate Spinel influence on the wear rate.

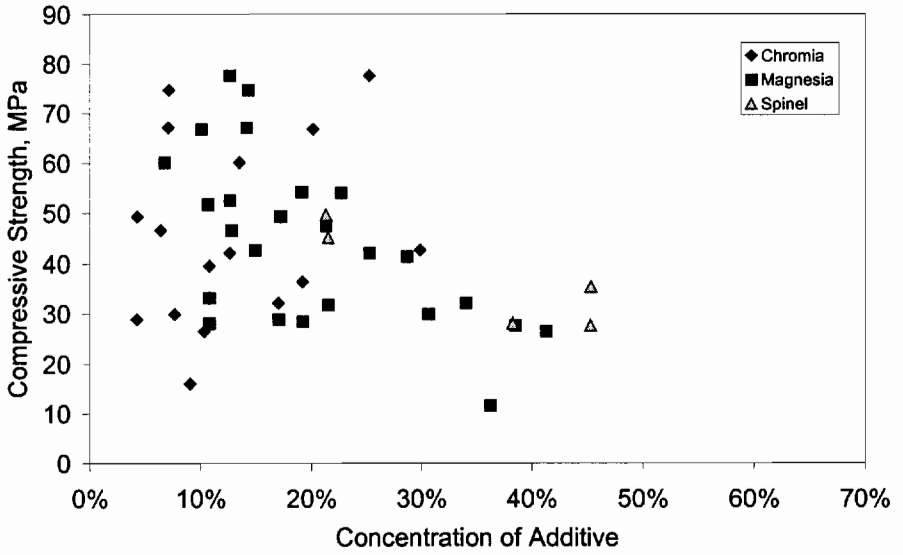

Figure AIV.9. CCS test results show the influence of Chromia, Magnesia and Spinel additive concentrations on the cold crushing strength.

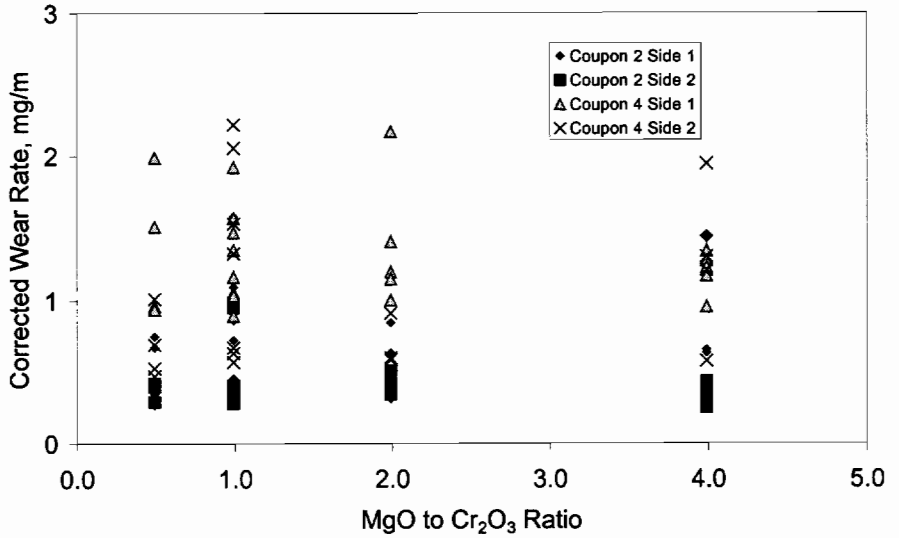

Figure AIV.10. DSRW test results illustrate Magnesia to Chromia ratio influence on the wear rate.

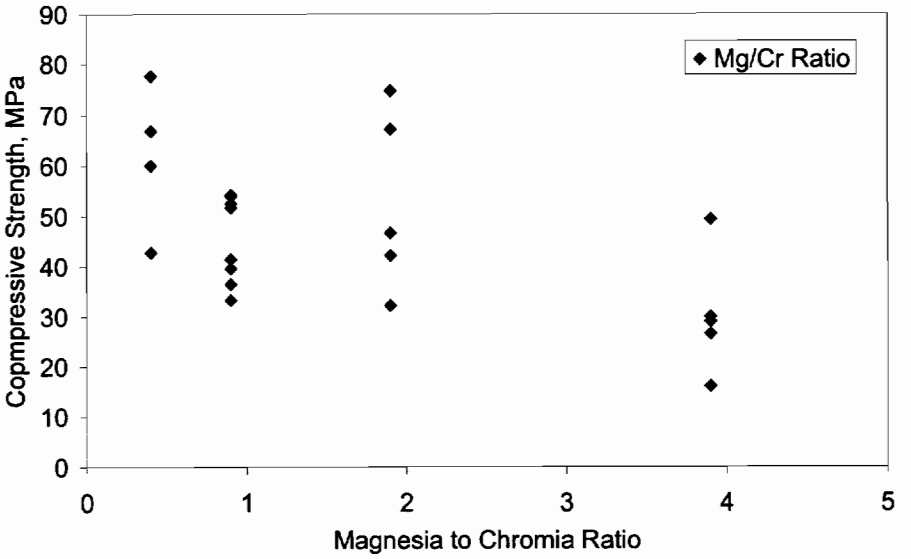

Figure AIV.11. CCS test results show the influence of the magnesia to chromia ratio on the cold crushing strength.

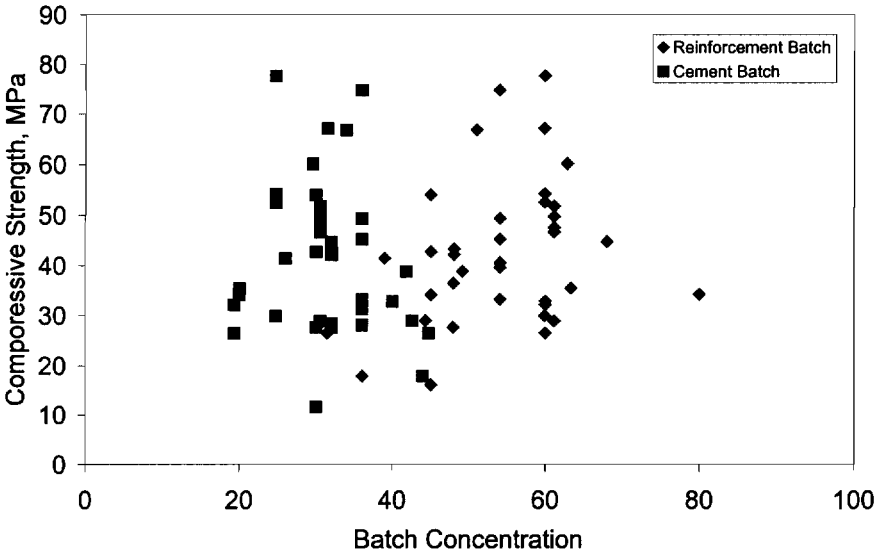

Figure AIV.12. CCS test results illustrate the changing volume fraction of reinforcement and cement batch concentration on the cold crushing strength.

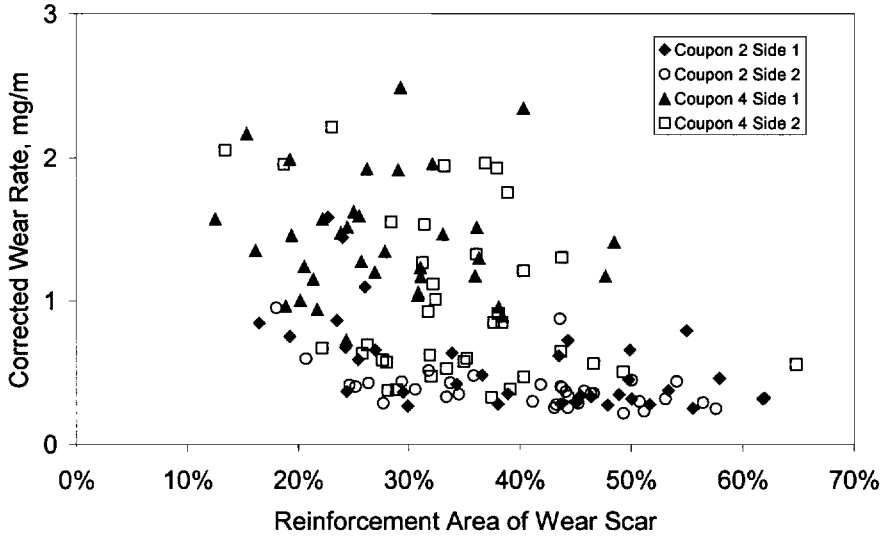

Figure AIV.13. DSRW test results illustrate the influence of exposed reinforcement area of the wear scar area.

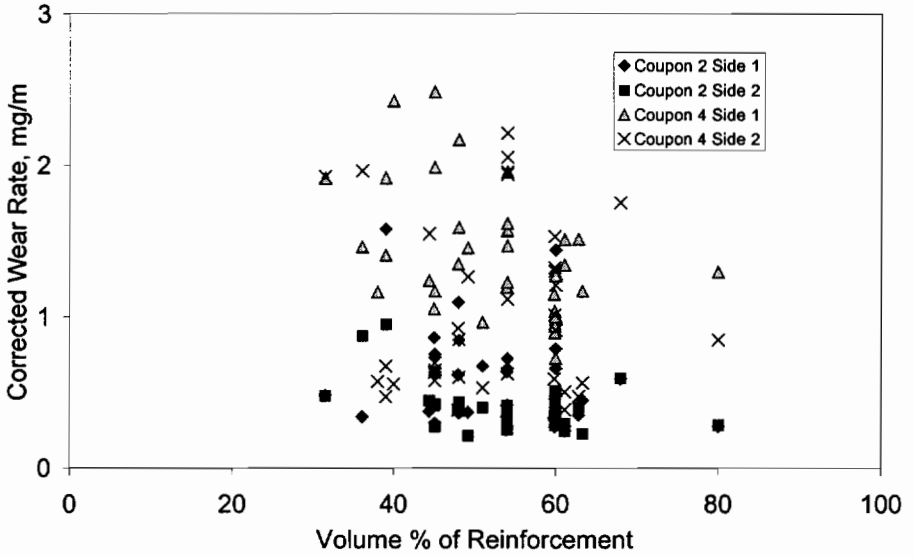

Figure AIV.14. DSRW test results illustrate the influence of the volume fraction of the reinforcement phase.

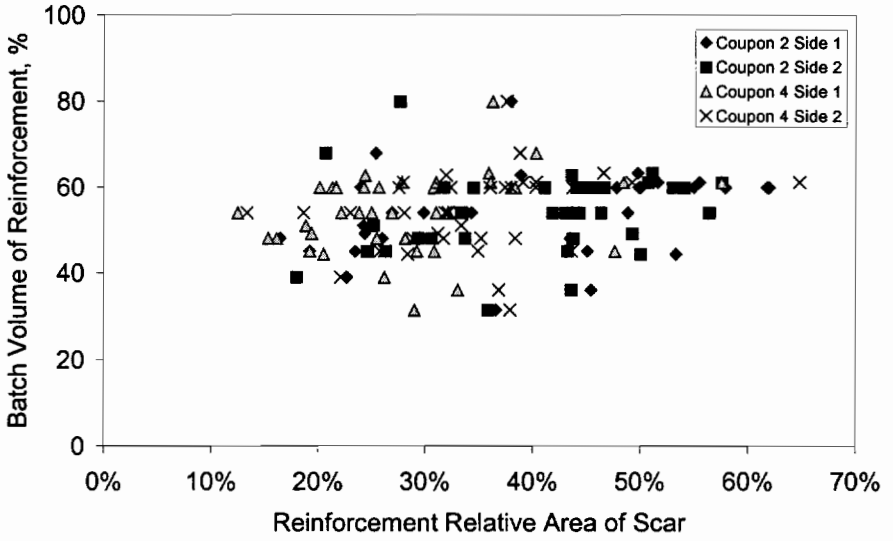

Figure AIV.15. DSRW test results illustrate a comparison of the reinforcement volume fraction to the reinforcement area in the wear scar.

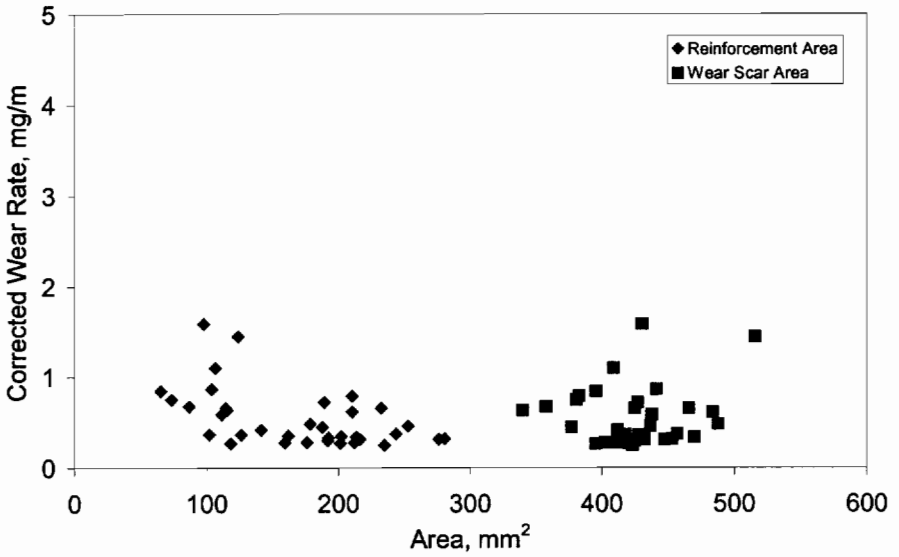

Figure AIV.16. DSRW test results show the influence of exposed reinforcement area and the influence of wear scar area on the wear rate for Coupon #2 Side 1.

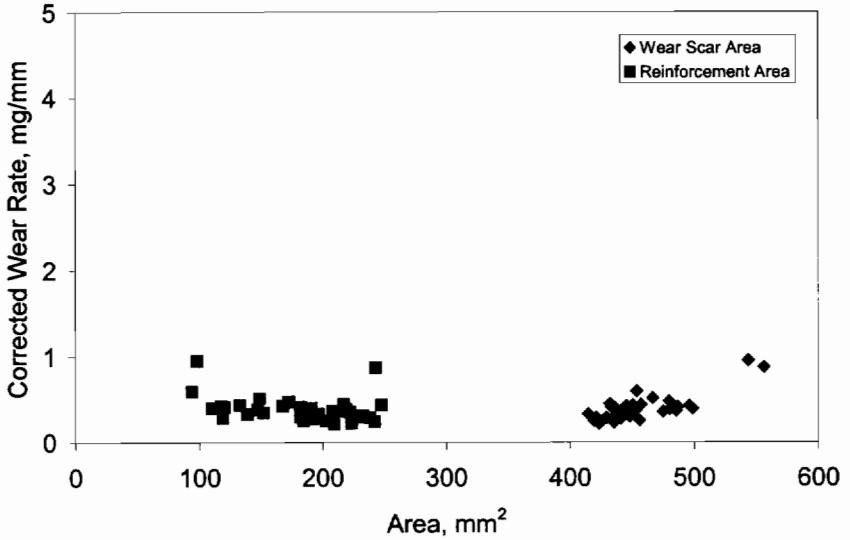

Figure AIV.17. DSRW test results show the influence of exposed reinforcement area and the influence of wear scar area on the wear rate for Coupon #2 Side 2.

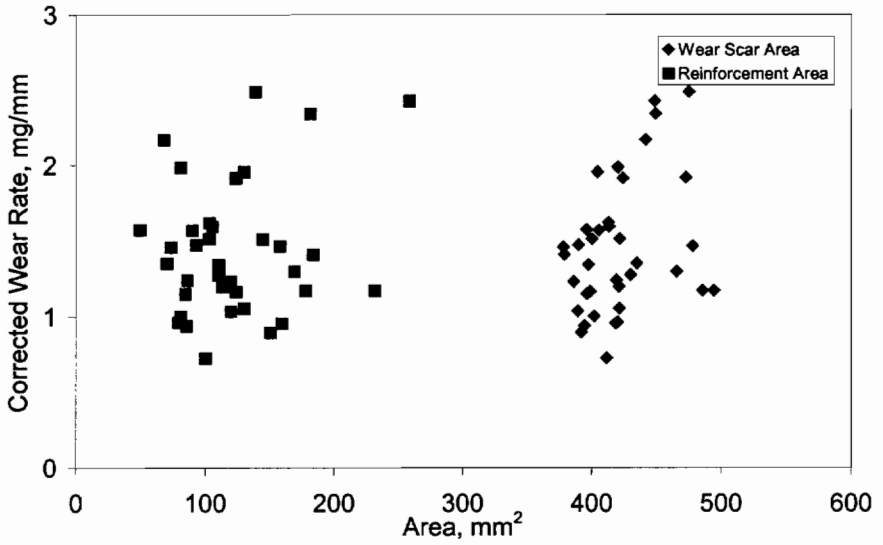

Figure AIV.18. DSRW test results show the influence of exposed reinforcement area and the influence of wear scar area on the wear rate for Coupon #4 Side 1.

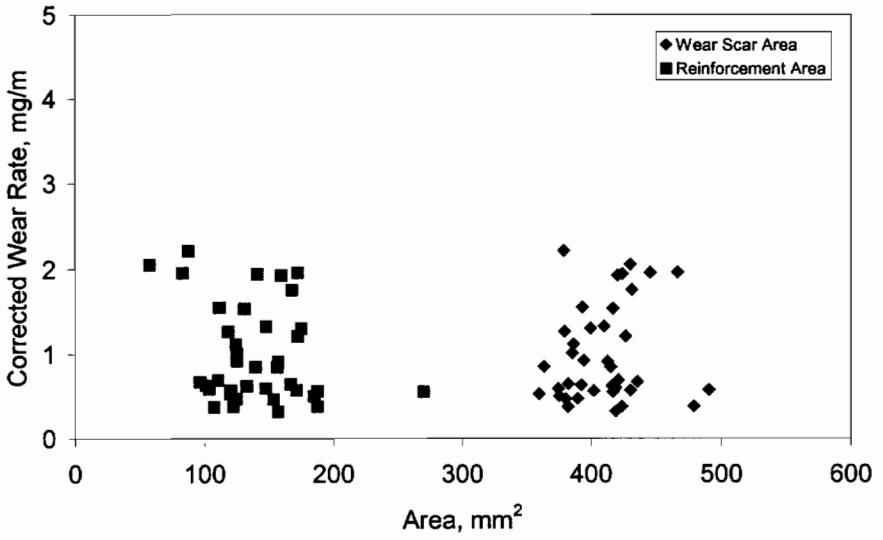

Figures AIV.19. DSRW test results show the influence of exposed reinforcement area and the influence of wear scar area on the wear rate for Coupon #4 Side 2.

AIV.3 Fondu and Calcium Dialuminate Blend

The results from the Dry Sand Rubber Wheel (DSRW) wear test and the Cold Crushing Strength (CCS) measurements are presented for both the Fondu cement and the calcium dialuminate blend cement. The cement was blended dry with additive powders and reinforcement phases to produce standard test coupons. Efforts were taken to maintain the wear surface orientation and mold position. Data from both cement types are treated together because of the similar to determine general trends and recognize the bias cause by sample preparation. The data are designated as side #1 and side #2 to better understand the trends with additives and reinforcements. Coupon #3's and #1's were used for CCS testing.

The analysis is presented to follow the order of experimental objectives. The analysis is presented in the order of determining the influence on the cement properties, influence of cement with additive properties and finally the influence of the reinforcement.

Table AIV.2. Fondu and Calcium Dialuminate Blend.

Figure	Format of Data Relationship
AIV.20	Coupon density to the wear rate is separated into side 1 and side 2 (mixing data may be questionable)
AIV.21 AIV.22	The water to cement ratio influence on the wear rate and cold compression strength
AIV.23	Open porosity influence on the compression strength
AIV.24	Concentrations of all additives in the matrix cement are compared against the compressive strength in wear rate?
AIV.25 AIV.26	The compression strength change with additive concentration, concentrations are separated for type
AIV.27 AIV.28 AIV.29 AIV.30 AIV.31	Wear rate change with the changing concentration of additive separated into side 1 and side 2
AIV.32 AIV.33	The total area of the wear scar and exposed reinforcement compared to the wear rate
AIV.34	Relative ratio of the exposed reinforcement phase in the total wear scar to the wear rate
AIV.35	The batch volume fraction of the reinforcement phase compared to the wear rate is shown in for sides 1and 2
AIV.36	The changing volume fraction of reinforcement and the matrix cement concentration are compared to the compression strength
AIV.37	Shows green strength and sintered strength using the mean density to contrast the two sets.

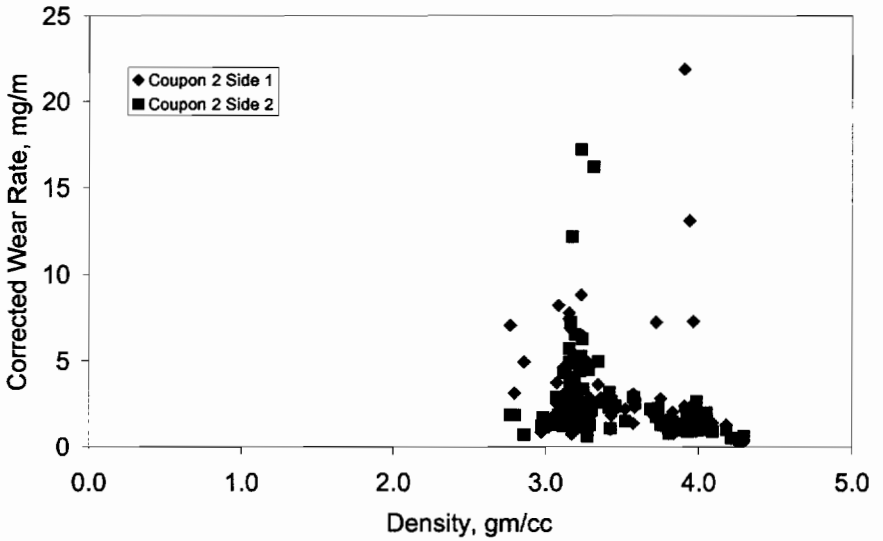

Figure AIV.20. DSRW test results show the influence of the density separated for Coupon #2 Side 1&2.

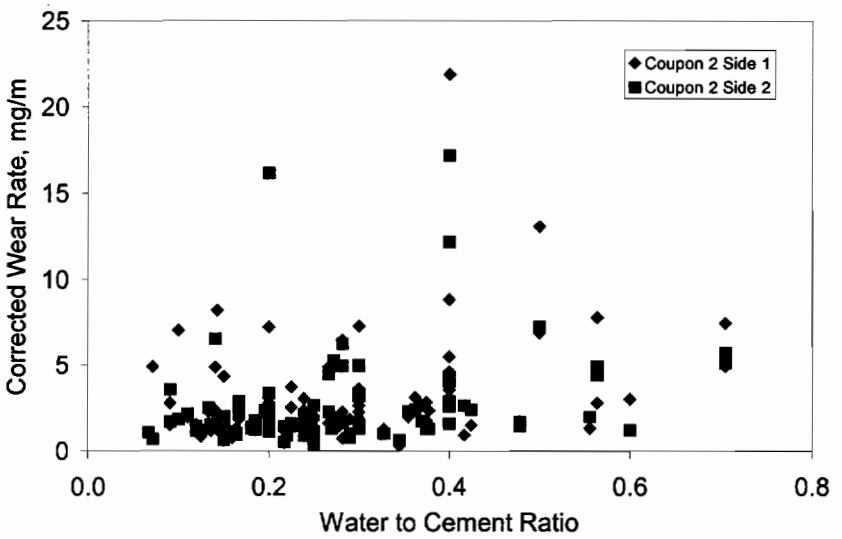

Figure AIV.21. DSRW test results show the influence of wear rate of Coupon #2 Side 1&2 to the batch water to cement ratio fraction of reinforcement.

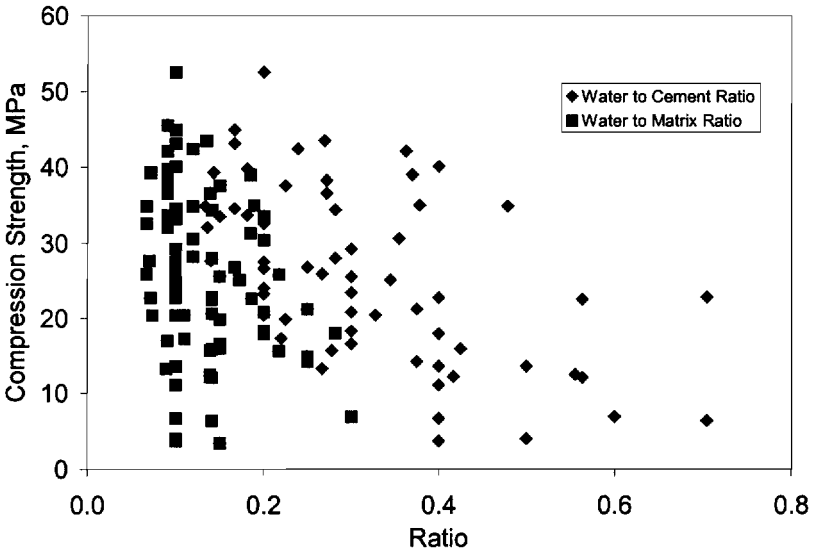

Figure AIV.22. CCS test results show influence of the water to cement ratio on the cold compression strength.

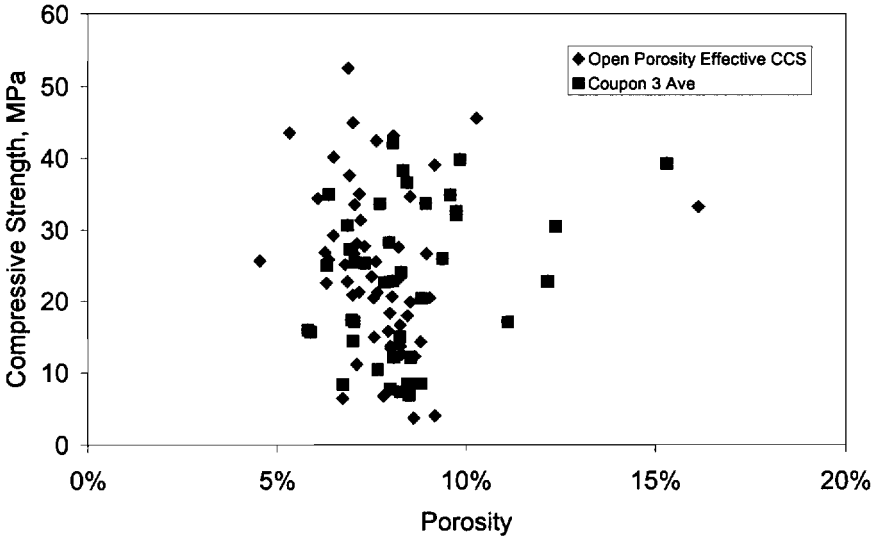

Figure AIV.23. CCS test results show the influence of the open porosity on the cold crushing strength.

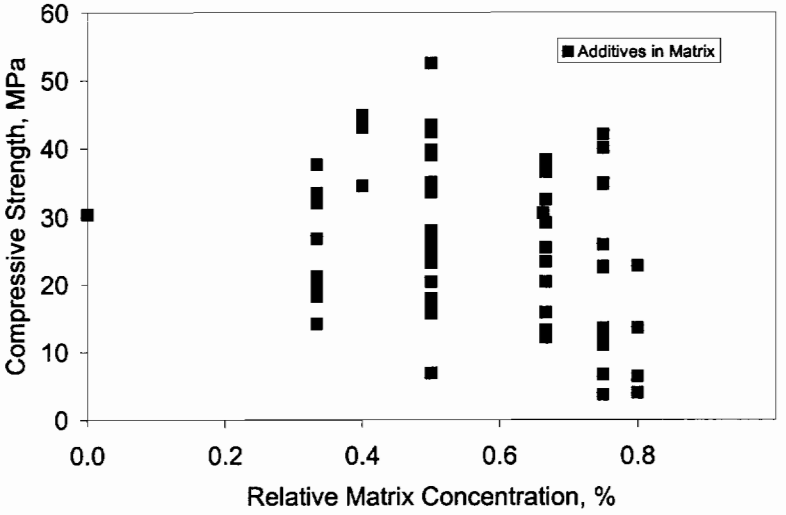

Figure AIV.24. CCS test results show the influence of additives on the change in the maximum cold crushing strength.

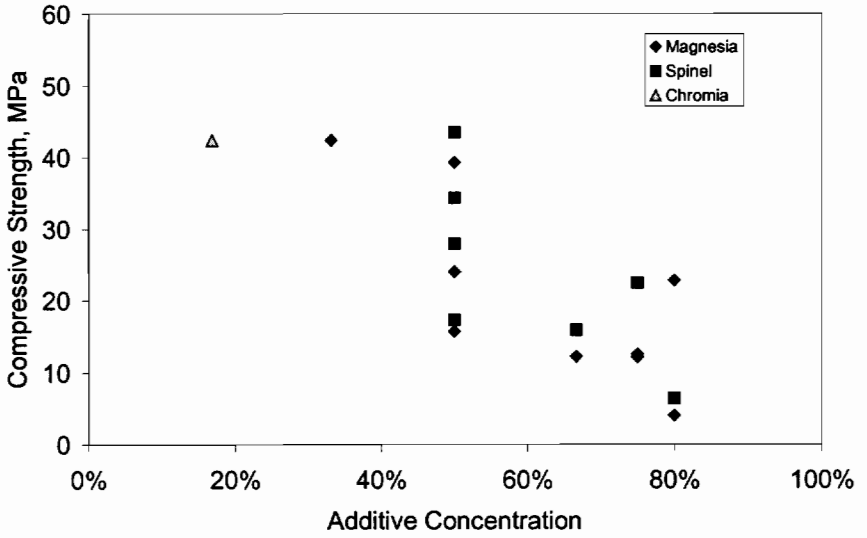

Figure AIV.25. CCS test results show the influence of Magnesia, Spinel and Chromia additives on the cold crushing strength.

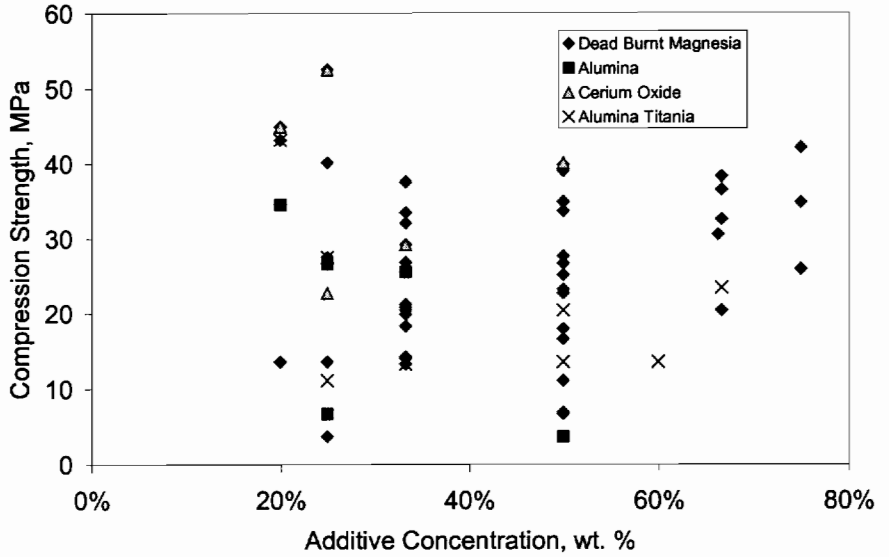

Figure AIV.26. CCS test results show the influence of Dead Burnt Magnesia, Alumina, Alumina Titania Blend and Cerium oxide additives on the cold crushing strength.

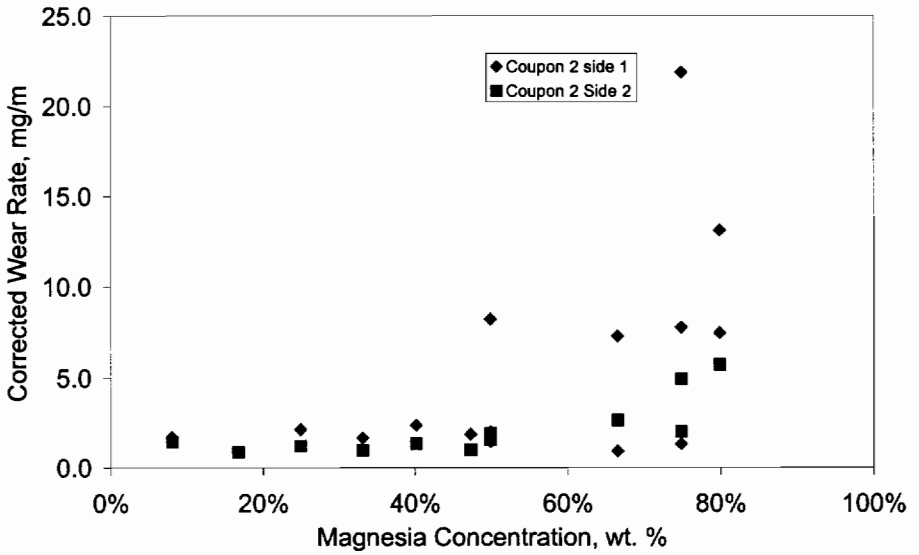

Figure AIV.27. DSRW test results show the influence of Magnesia additive on the wear rate of Coupon #2, Sides 1&2 data are presented.

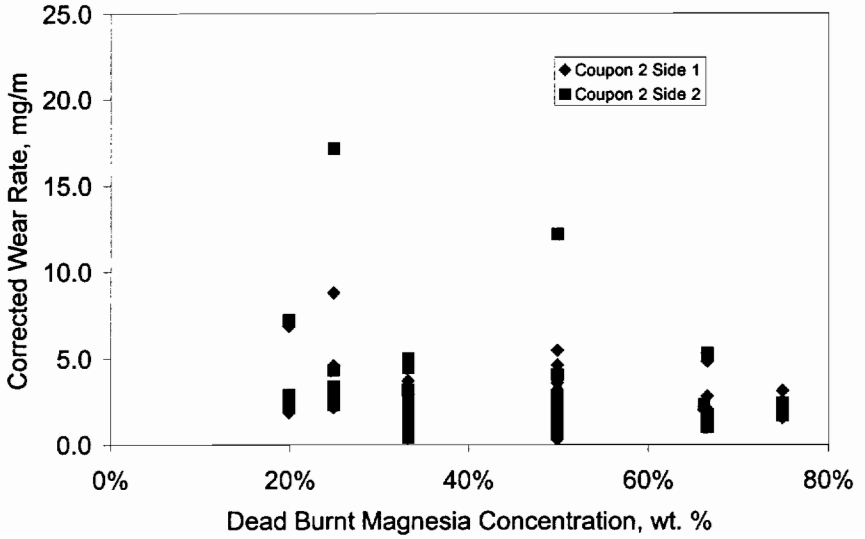

Figure AIV.28. DSRW test results show the influence of Dead Burnt Magnesia additive on the wear rate of Coupon #2, Sides 1&2 data are presented.

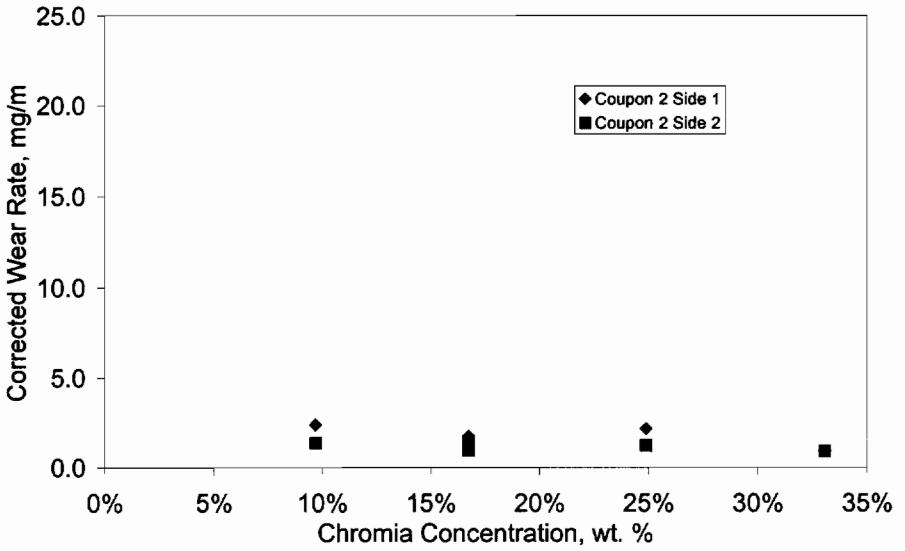

Figure AIV.29. DSRW test results show the influence of Chromia additive on the wear rate of Coupon #2, Sides 1&2 data are presented.

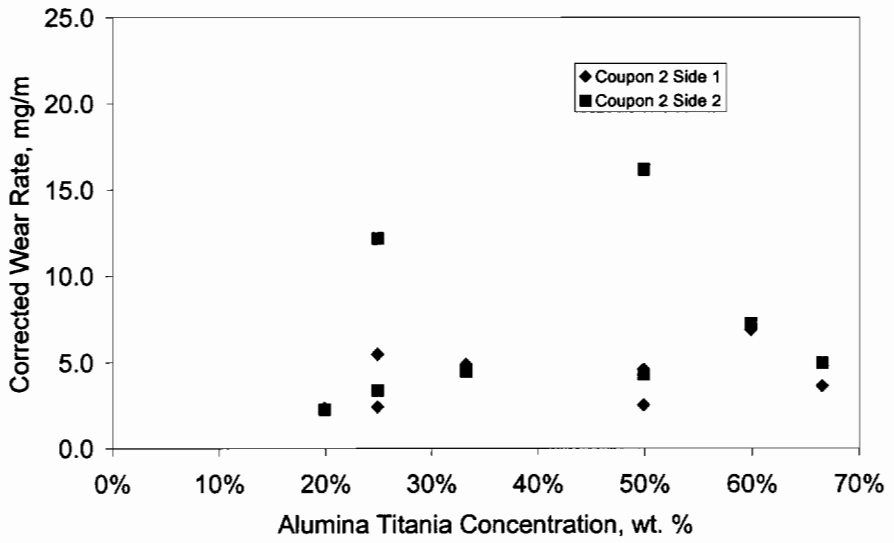

Figure AIV.30. DSRW test results show the influence of Alumina Titania additive on the wear rate of Coupon #2, Sides 1&2 data are presented.

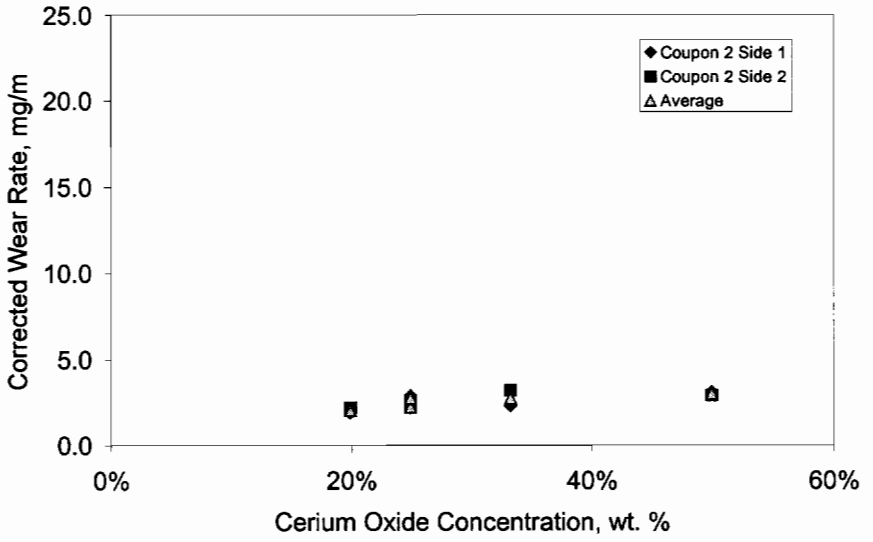

Figure AIV.31. DSRW test results show the influence of Cerium Oxide additive on the wear rate of Coupon #2, Sides 1&2 data are presented.

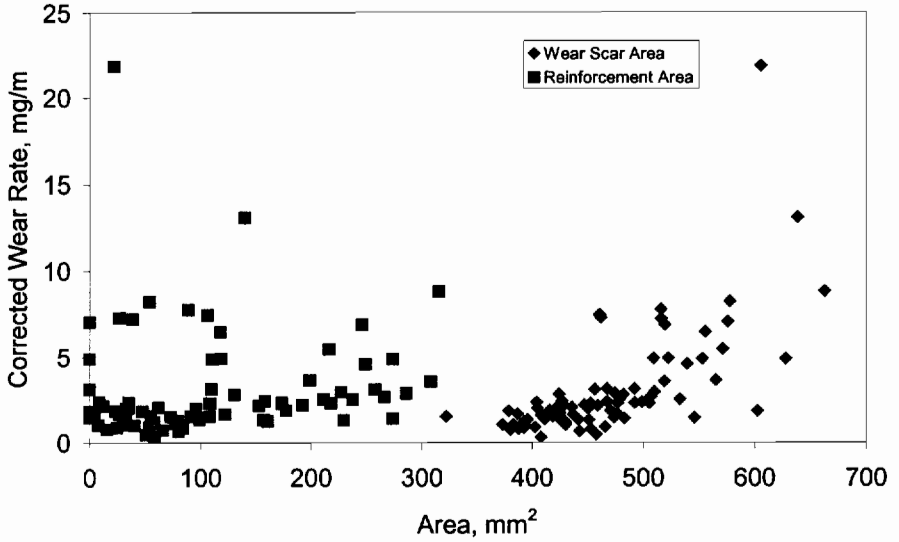

Figure AIV.32. DSRW test results show the influence of reinforcement area and wear scar size on the wear rate of Coupon #2 Side 1.

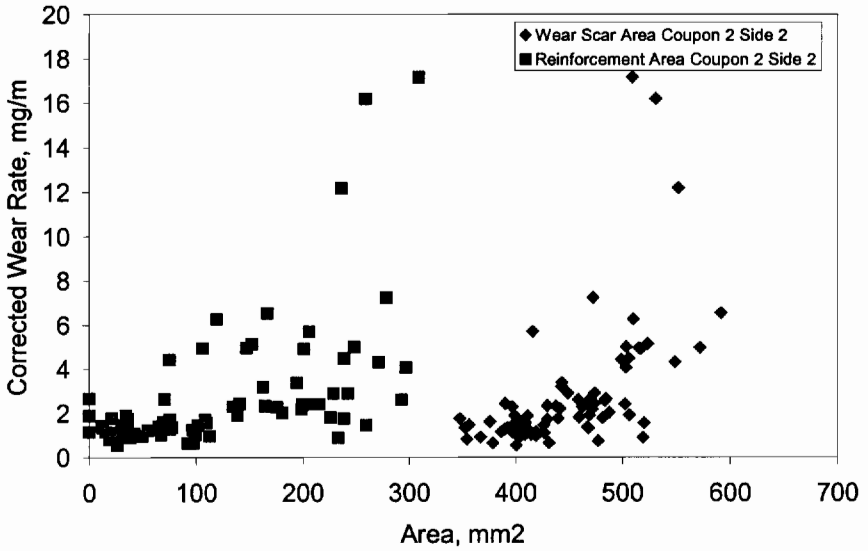

Figure AIV.33. DSRW test results show the influence of reinforcement area and wear scar size on the wear rate of Coupon #2 Side 2.

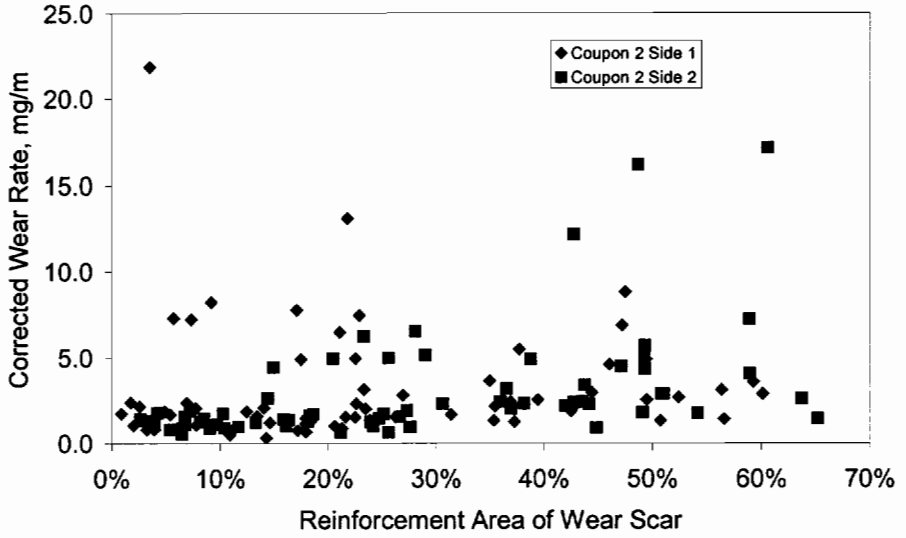

Figure AIV.34. DSRW test results show the influence of exposed reinforcement area to the total wear scar area is compared to the wear rate of Coupon #2, Sides 1&2.

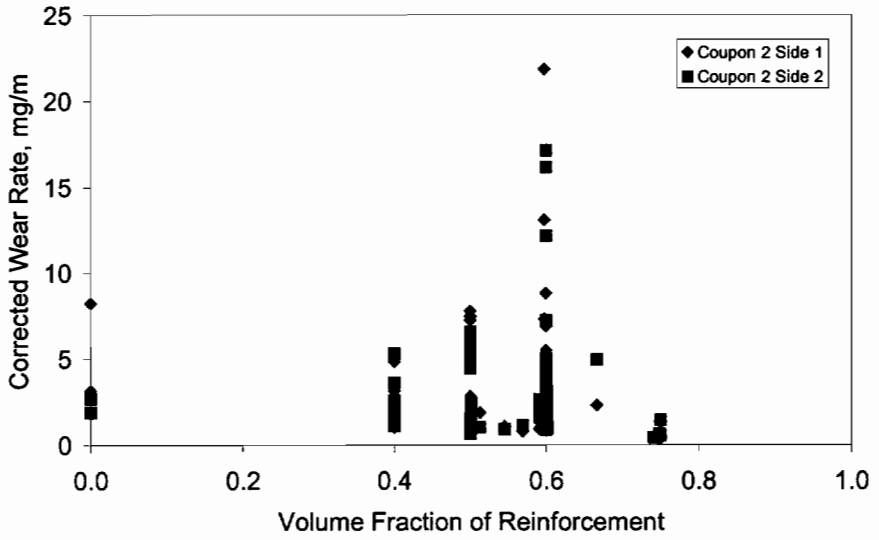

Figure AIV.35. DSRW test results show the influence of volume fraction reinforcement on the wear rate of Coupon #2, Sides 1&2 data are presented.

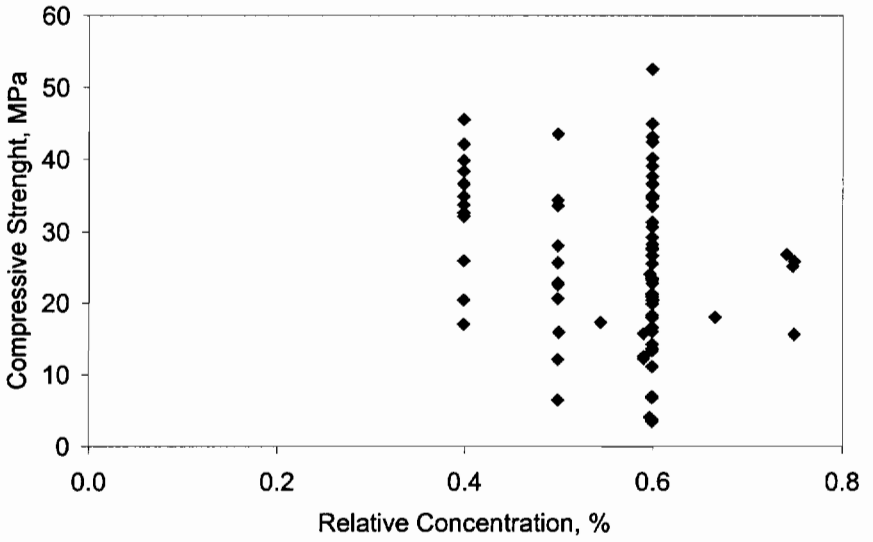

Figure AIV.36. CCS test results show the influence reinforcement on the cold crushing strength.

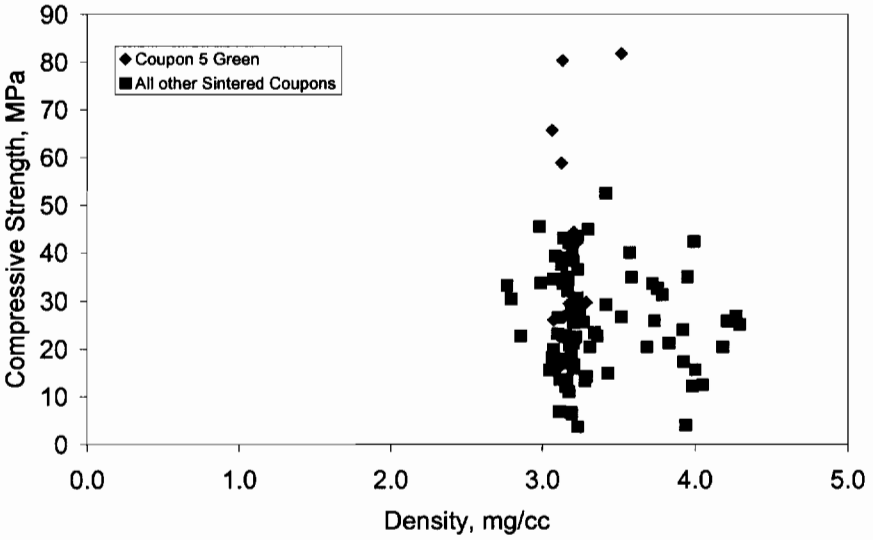

Figure AIV.37. CCS test results use mean density to contrast the difference between green strength and sintered strength using the cold crushing strength.

AIV.4 Influence of Additives and Reinforcement

The test matrix presented a number of relationships that needed understanding to reach the experimental goal to develop improved ceramic composite refractory cement. The test matrix was used to formulate more than 146 batches for DSRW and CCS testing. The results of the testing are separated according to the matrix and presented to develop relative trends. The presentation of the data follows the experimental objectives. The data are presented in graphical format and organized to understand the influence of the base cement followed by the additives and then the reinforcement. A table describing the data relationship precedes each set of graphs.

Table AIV.3. Premix Cement/ MgO/Zircon.

Premix Cement and MgO additive and Zircon reinforcement	
Figure	**Format of Data Relationship**
AIV.38	DSRW test results show magnesia concentration influence on the wear rate
AIV.39	CCS test results show magnesia concentration influence on compression strength, Coupon #3

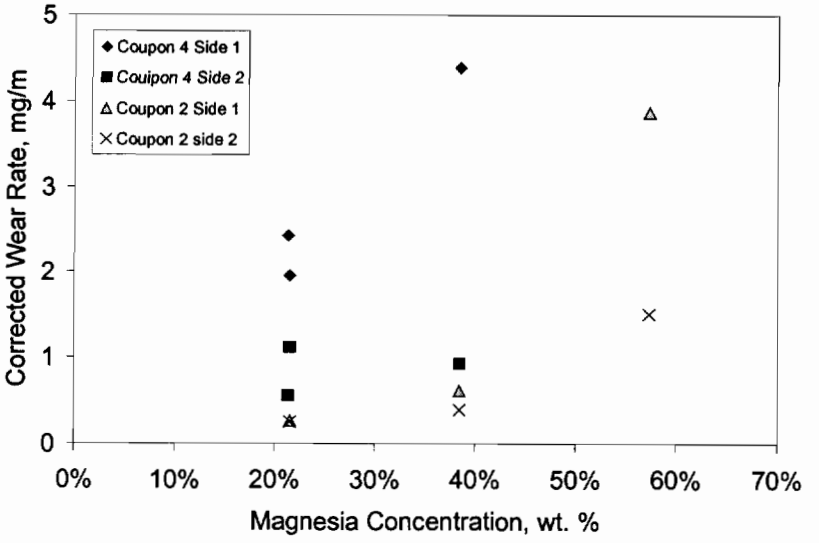

Figure AIV.38. DSRW test results show magnesia concentration influence on the wear rate. Data from three batches are presented B2-7-1, B5-4-1 and B5-6-1.

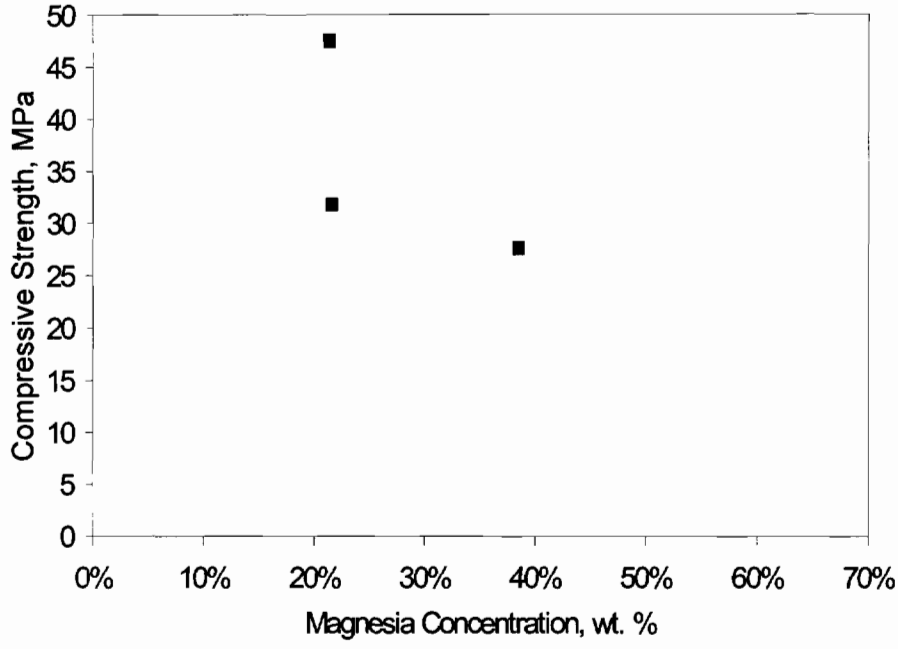

Figure AIV.39. CCS test results show magnesia concentration influence on compression strength, Coupon #3 batches B5-4-1, B5-6-1 and B5-28-1.

Table AIV.4. Premix Cement/ Spinel/ Zircon.

Premix Cement and Spinel Additive and Zircon Reinforcement	
Figure	**Format of Data Relationship**
AIV.40	DSRW test results show spinel concentration influence on wear rate, Coupon #2 side 2
AIV.41	Wear scar results show the exposed reinforcement influence on the wear rate. The batch reinforcement volume fractions are 10%, 20% and 25%
AIV.42	CCS test results show spinel concentration influence on compression strength, full size coupons

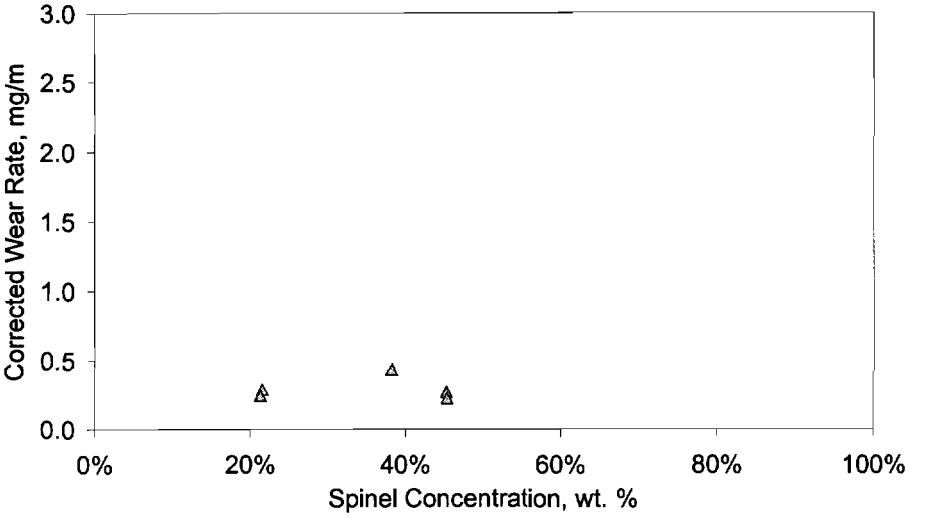

Figure AIV.40. DSRW test results show spinel concentration influence on wear rate for five batches formulations B4-29-1, B5-1-1, B5-8-1, B5-15-1 and B5-18-1. Results from Coupon #2 side 2 are shown.

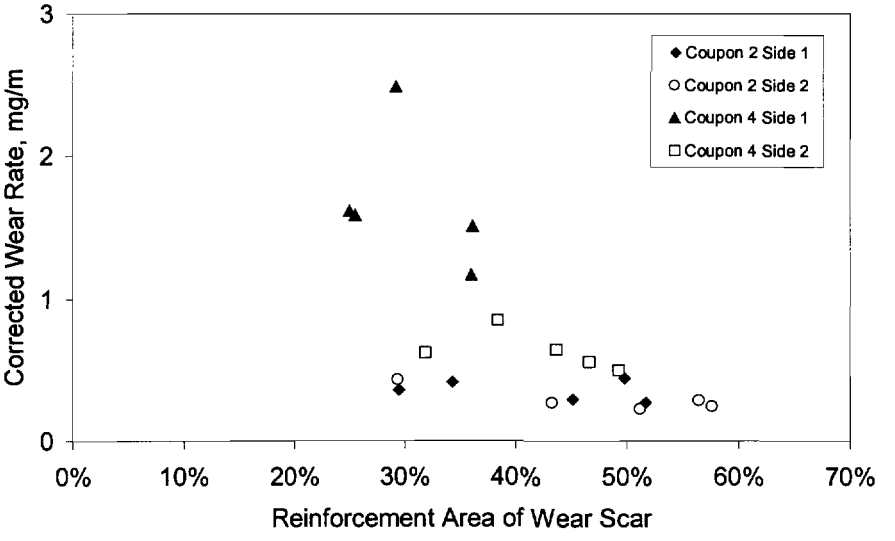

Figure AIV.41. DSRW wear scar analysis results show the influence of the exposed reinforcement on the wear rate. Both coupons and sides are shown for the five batches B4-29-1, B5-1-1, B5-8-1, B5-15-1 and B5-18-1. The batch reinforcement volume fractions are 10, 20, and 25%.

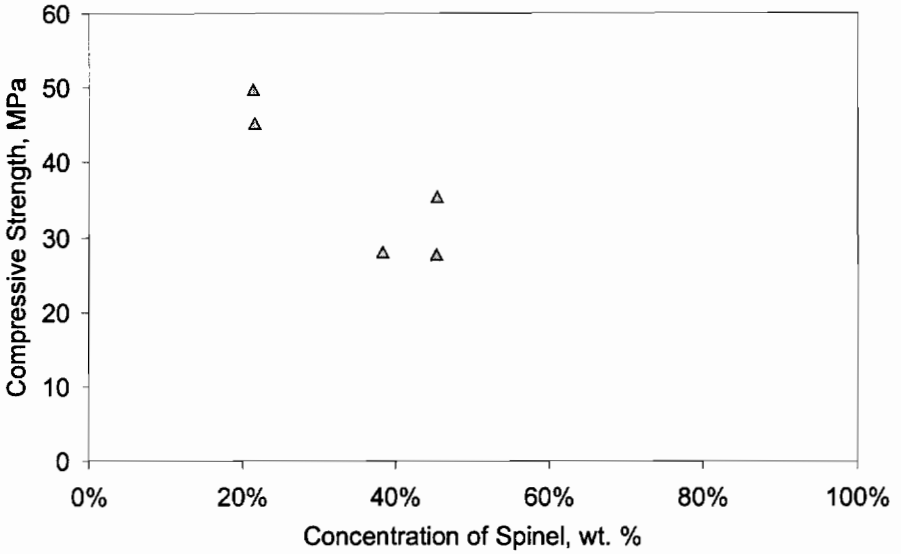

Figure AIV.42. CCS test results show spinel concentration influence on compression strength. Data from five full size coupons batches B4-29-1, B5-1-1, B5-8-1, B5-15-1 and B5-18-1 are shown.

Table AIV.5. Premix Cement/ MgO & $Cr_2O_3$1:1/ Zircon.

Premix Cement and MgO & Cr_2O_3 1:1 Blend Additive and Zircon Reinforcement	
Figure	**Format of Data Relationship**
AIV.43	DSRW test results show MgO & Cr_2O_3 1:1 Blend influence on the wear rate, Coupon #2 side 2
AIV.44	Wear scar results show MgO & Cr_2O_3 1:1 Blend influence on the wear rate, Coupons #2 and #4 sides 1 and 2
AIV.45	CCS test results show the influence of the MgO & Cr_2O_3 1:1 Blend on the compression strength, full size coupons
AIV.46	Chromia concentration and the Coupon #3 density relationship are shown, 1:1 MgO & Cr_2O_3 Blend at 10, 20, 25 and 35%

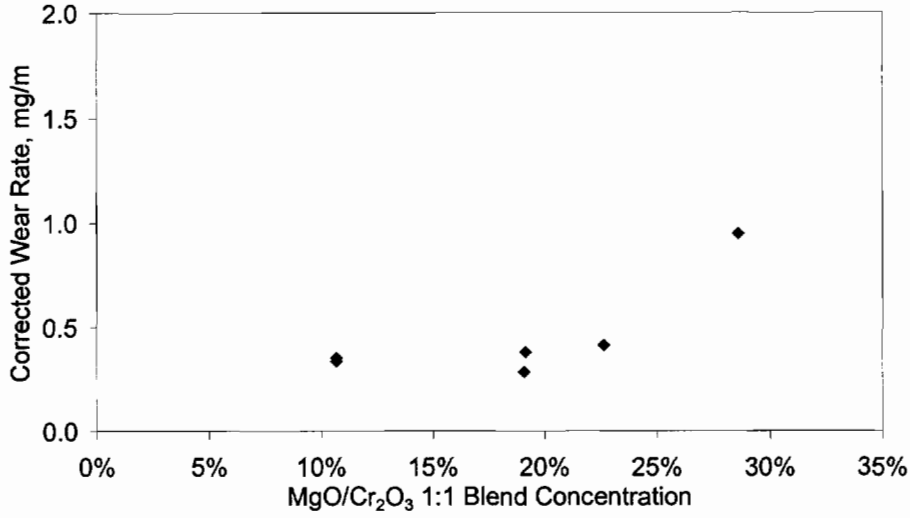

Figure AIV.43. DSRW test results show MgO & Cr_2O_3 1:1 Blend influence on the wear rate. Coupon #2 side 2 data from seven batches are used B1-28-1, B2-16-1, B2-18-1, B3-18-1, B4-20-1, B4-24-1 and B5-22-1.

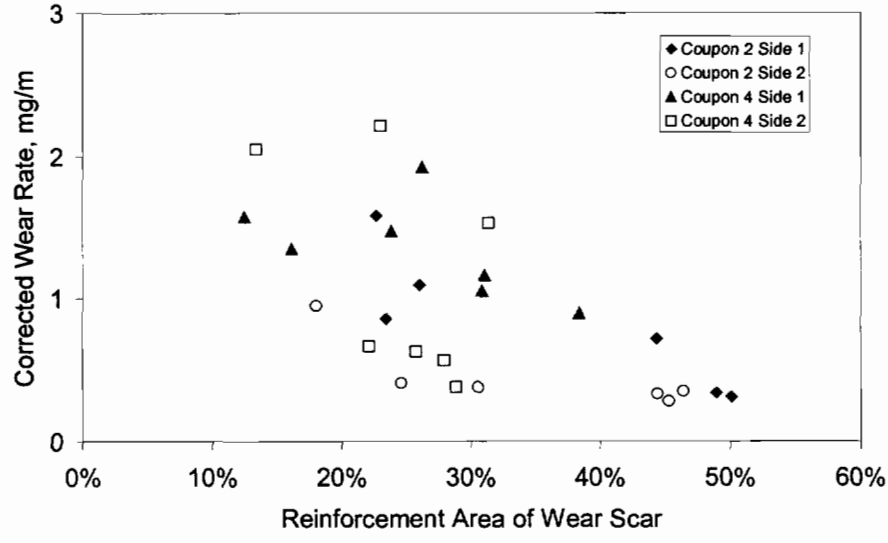

Figure AIV.44. DSRW wear scar analysis results show MgO & Cr_2O_3 1:1 Blend influence on the wear rate. Data from Coupon #2 and #4 sides 1 and 2 are shown from seven batches B1-28-1, B2-16-1, B2-18-1, B3-18-1, B4-20-1, B4-24-1 and B5-22-1.

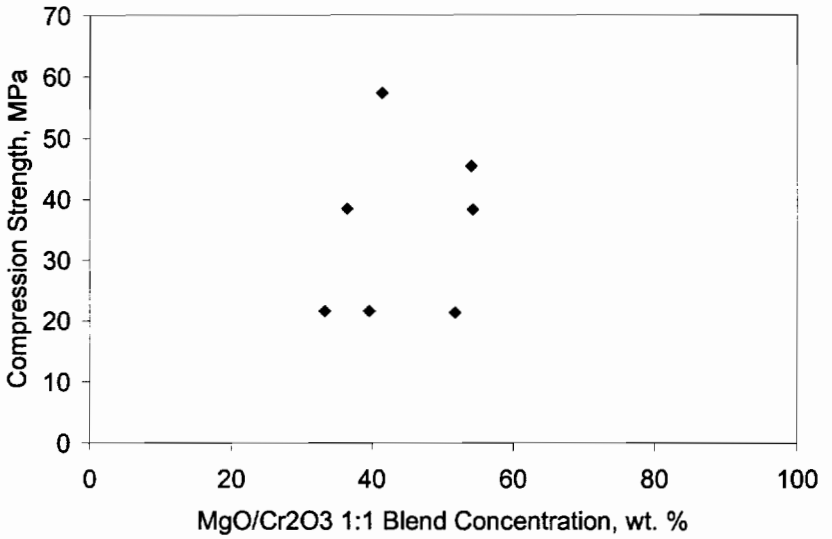

Figure AIV.45. CCS test results show the influence of the MgO & Cr_2O_3 1:1 Blend on the compression strength. Coupons from seven batches were tested B1-28-1, B2-16-1, B2-18-1, B3-18-1, B4-20-1, B4-24-1 and B5-22-1.

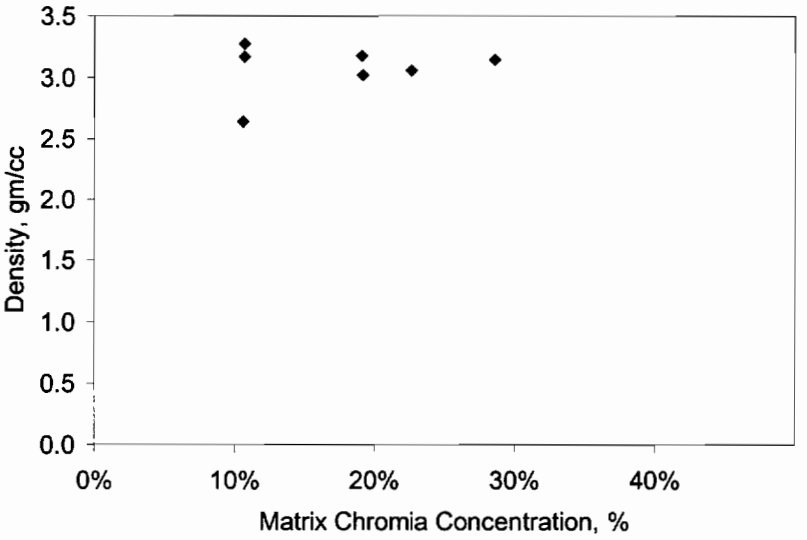

Figure AIV.46. Chromia concentration and the Coupon #3 density are shown for the seven batch formulations that used the 1:1 MgO & Cr_2O_3 Blend. Seven batches are B1-28-1, B2-16-1, B2-18-1, B3-18-1, B4-20-1, B4-24-1 and B5-22-1. Blend ratio used at concentrations: 10, 20, 25 and 35% with duplicate batches at 10 and 20% concentrations.

Table AIV.6. Premix Cement / MgO & $Cr_2O_3$1:2 / Zircon.

Premix Cement and MgO & Cr_2O_3 1:2 blend Additive and Zircon Reinforcement	
Figure	**Format of Data Relationship**
AIV.47	DSRW test results show MgO & Cr_2O_3 1:2 additive influence on the wear rate, Coupon #2 side 2
AIV.48	Wear scar results show MgO & Cr_2O_3 1:2 Blend additive influence on the wear rate, Coupon #2 sides 1 and 2
AIV.49	CCS test results show MgO & Cr_2O_3 1:2 Blend additive influence on the wear rate, full size coupons

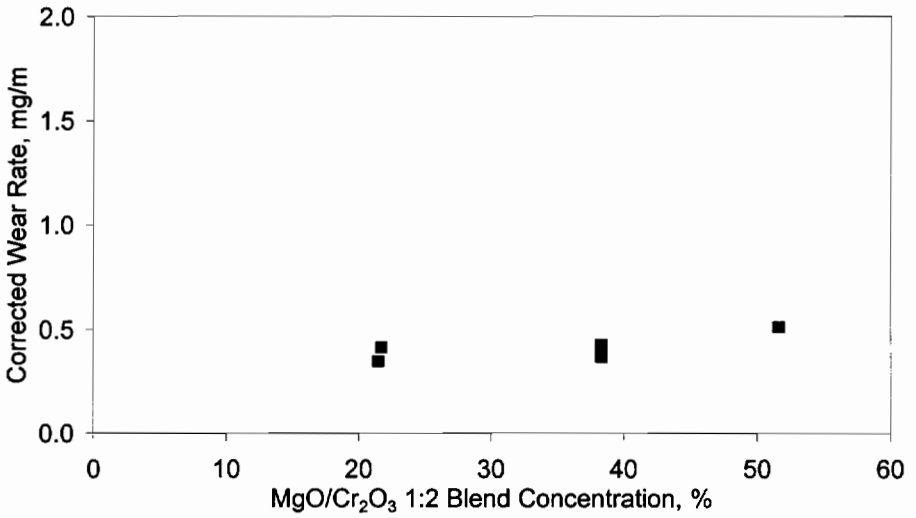

Figure AIV.47. DSRW test results show MgO & Cr_2O_3 1:2 additive influence on the wear rate. Coupon #2 side 2 data from five batches are shown, B2-23-1, B2-25-1, B3-10-1, B3-12-1 and B4-3-1.

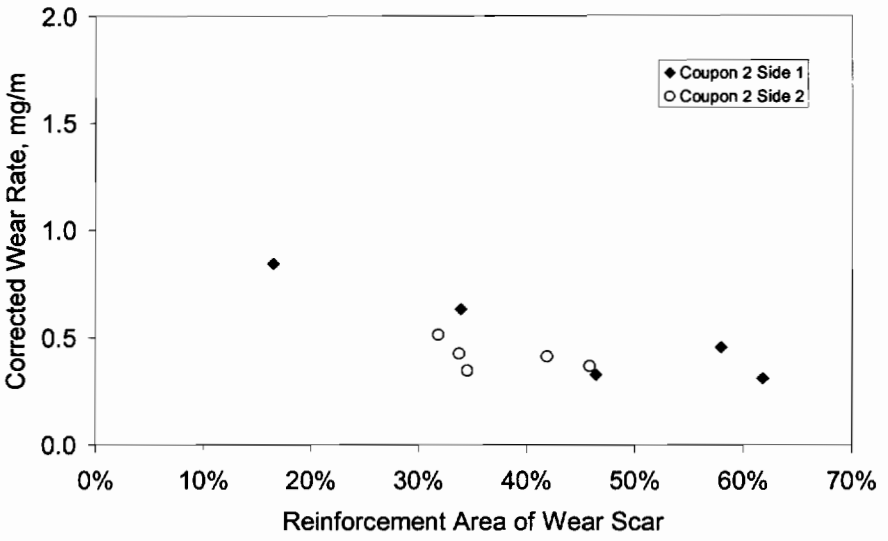

Figure AIV.48. DSRW wear scar analysis results show the MgO & Cr_2O_3 1:2 Blend additive influence on the wear rate. Data from Coupon #2 sides 1 and 2 are shown from five batches B2-23-1, B2-25-1, B3-10-1, B3-12-1 and B4-3-1.

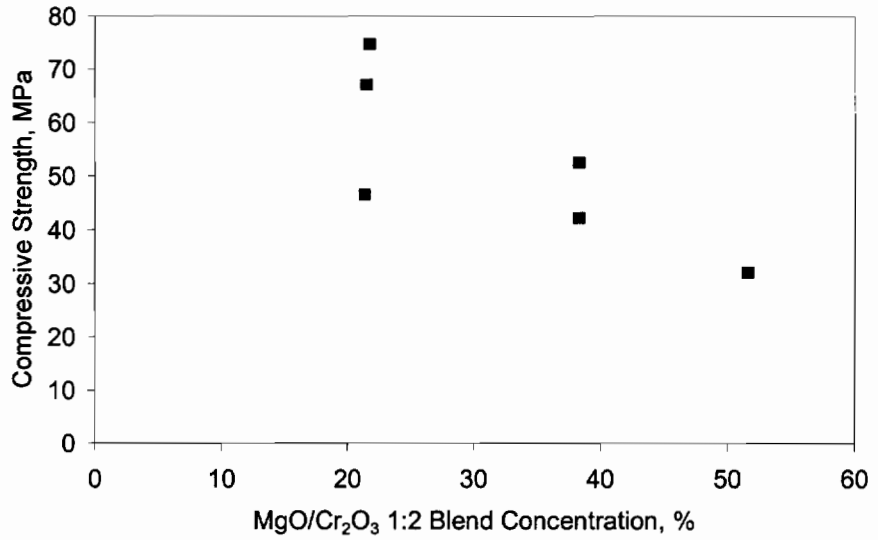

Figure AIV.49. CCS test results MgO & Cr_2O_3 1:2 Blend additive influence on the wear rate. Data are shown from six batches B2-23-1, B2-25-1, B3-10-1, B3-12-1, B4-3-1 and B5-26-1.

Table AIV.7. Premix Cement/ MgO & $Cr_2O_3$1:4 Blend / Zircon.

Premix Cement and MgO & Cr_2O_3 1:4 Blend Additive and Zircon Reinforcement	
Figure	**Format of Data Relationship**
AIV.50	DSRW test results show MgO & Cr_2O_3 1:4 additive influence on the wear rate, Coupon #2 side 2
AIV.51	Wear scar results show the MgO & Cr_2O_3 1:4 Blend additive influence on the wear rate, Coupon #2 and #4 sides 1 and 2
AIV.52	CCS test results MgO & Cr_2O_3 1:4 Blend additive influence on the compression strength, full size coupons

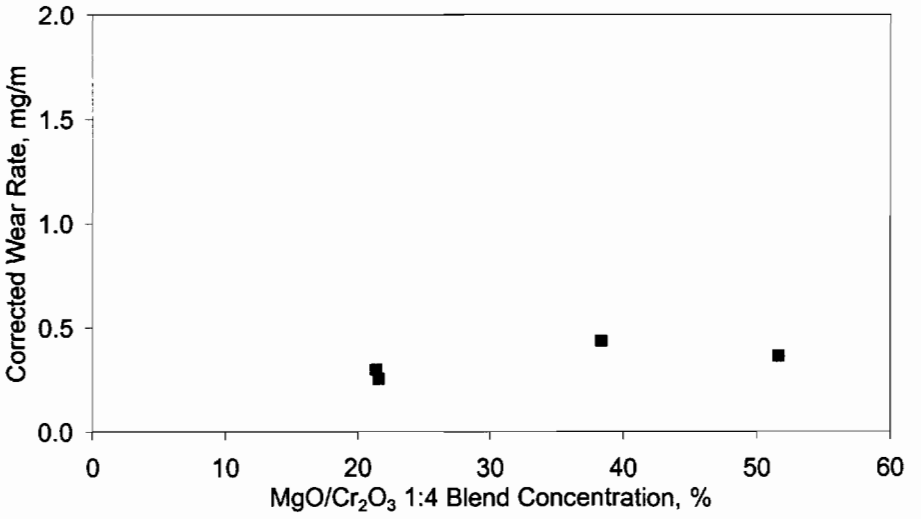

Figure AIV.50. DSRW test results show MgO & Cr_2O_3 1:4 additive influence on the wear rate. Coupon #2 side 2 data from five batches are shown, five B2-12-1, B3-16-1, B4-1-1, B4-22-1 and B5-20-1.

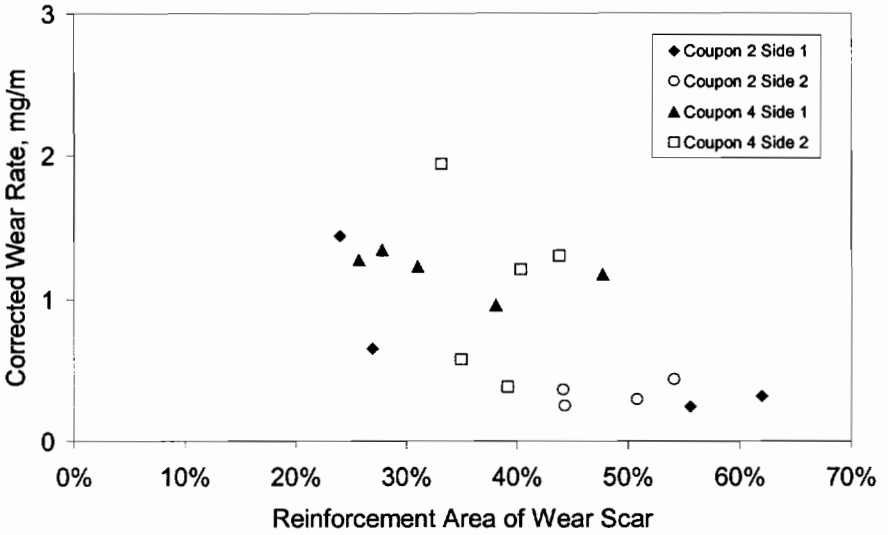

Figure AIV.51. DSRW wear scar analysis results show the MgO & Cr_2O_3 1:4 Blend additive influence on the wear rate. Data from Coupon #2 and #4 sides 1 and 2 are shown from five batches, B2-12-1, B3-16-1, B4-1-1, B4-22-1 and B5-20-1.

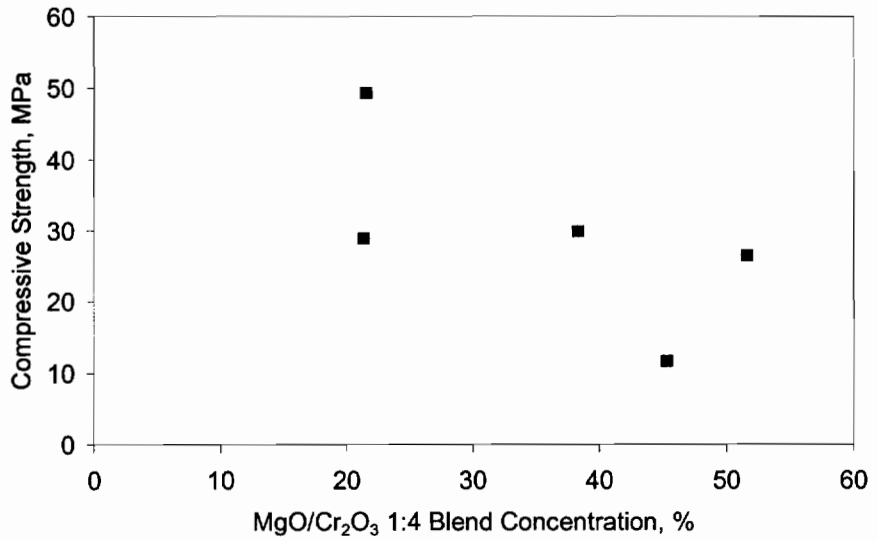

Figure AIV.52. CCS test results MgO & Cr_2O_3 1:4 Blend additive influence on the wear rate. Data are shown from five batches, B2-12-1, B3-16-1, B4-1-1, B4-22-1 and B5-20-1.

Table AIV.8. Premix Cement/ No Additives/ Zircon.

Premix Cement and No Additives and Zircon Reinforcement	
Figure	**Format of Data Relationship**
AIV.53	DSRW test results show changing reinforcement concentration wear rate influence by the reinforcement, range is 41 to 80%, Coupon #2 and #4 sides 1 and 2
AIV.54	Wear scar results show the control coupon wear rate conditions and influence of changing reinforcement, reinforcement range is 41 to 80%, Coupon #2 and #4 sides 1 and 2
AIV.55	Wear scar results show a comparison between exposed reinforcement and changing volume fraction of reinforcement, range is 41 to 80%, Coupon #2 and #4 sides 1 and 2
AIV.56	CCS test results show the matrix wear rate with no additives and changing reinforcement concentration
AIV.57	CCS test results show the relationship between the compression strength and the open porosity

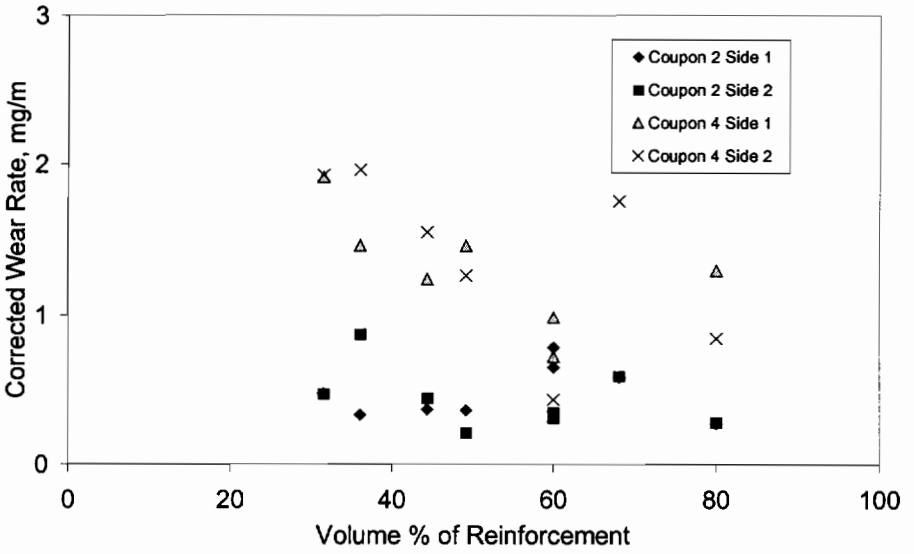

Figure AIV.53. DSRW test results show base line wear rate conditions with no additives and the influence of changing reinforcement concentration. Eight batches were prepared B2-2-1, B2-4-1, B5-11-1, B5-13-1, B4-27-1, B4-6-1, B4-8-1 and B4-13-1. The reinforcement range 41 to 80%. Wear rate data is from Coupon #2 and #4 sides 1 and 2.

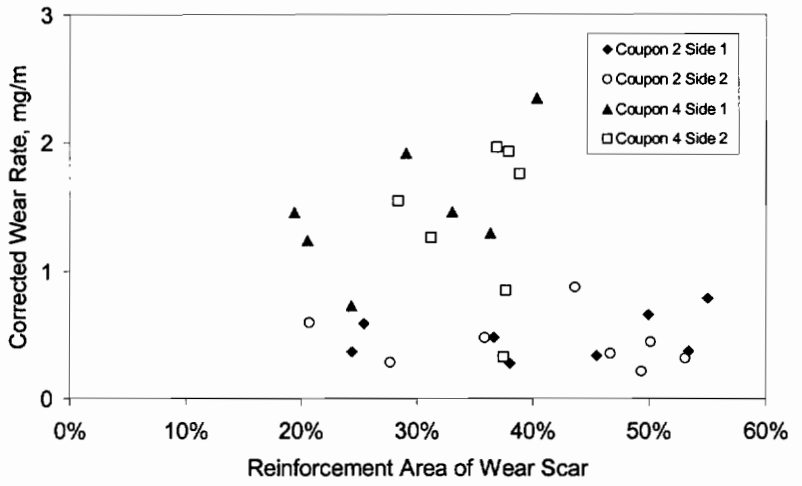

Figure AIV.54. DSRW wear scar analysis results show the base line wear rate conditions and the influence of changing reinforcement concentration. Eight batches were prepared B2-2-1, B2-4-1, B5-11-1, B5-13-1, B4-27-1, B4-6-1, B4-8-1 and B4-13-1. The reinforcement range is 41 to 80%. Wear scar analysis is shown for Coupon #2 and #4 sides 1 and 2.

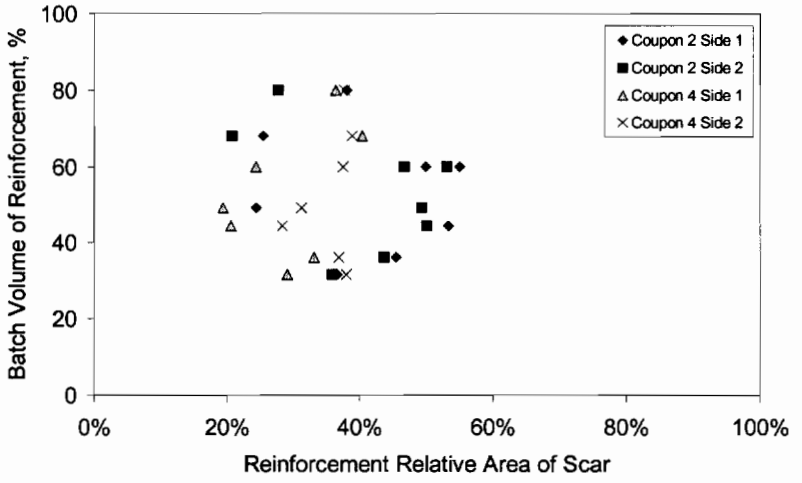

Figure AIV.55. DSRW wear scar analysis results show a comparison between the exposed reinforcement material and the changing volume fraction of reinforcement concentration. Eight batches were prepared B2-2-1, B2-4-1, B5-11-1, B5-13-1, B4-27-1, B4-6-1, B4-8-1 and B4-13-1. The reinforcement range is 41 to 80%. Wear scar analysis is shown for Coupon #2 and #4 sides 1 and 2.

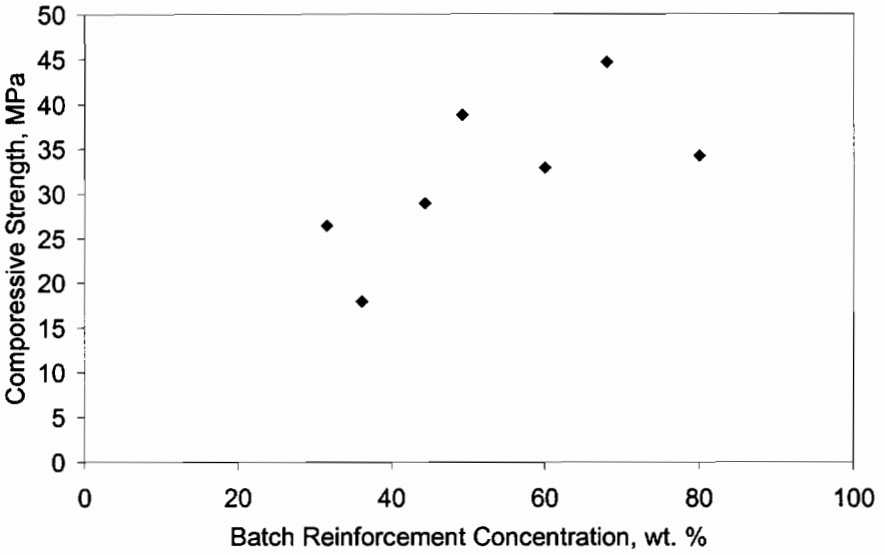

Figure AIV.56. CCS test results show the matrix wear rate with no additives and changing reinforcement concentration. Seven batches were tested B2-4-1, B5-11-1, B5-13-1, B4-27-1, B4-6-1, B4-8-1 and B4-13-1.

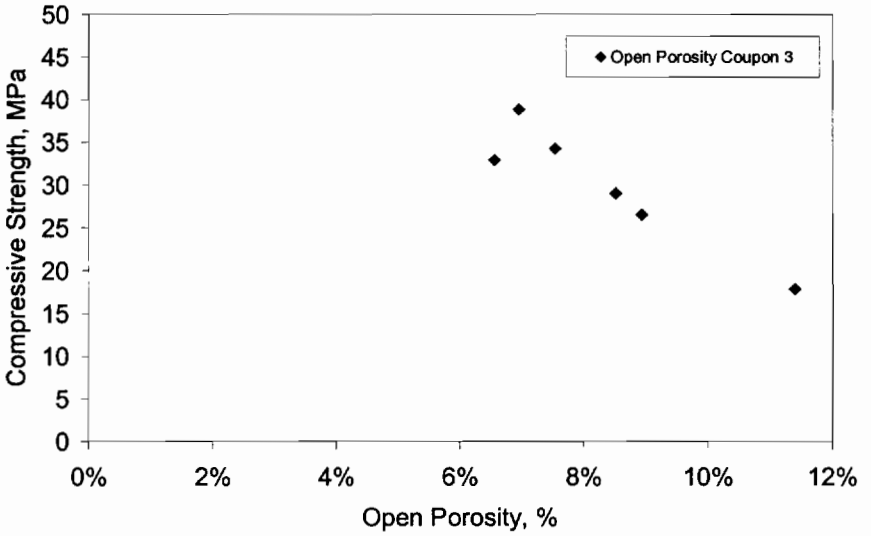

Figure AIV.57. CCS test results show the relationship between the compression strength and the open porosity. Seven batches were tested B2-4-1, B5-11-1, B5-13-1, B4-27-1, B4-6-1, B4-8-1 and B4-13-1.

Table AIV.9 Fondu Cement /MgO / Zirconia.

Fondu Cement and MgO Additive and Zirconia Grog Reinforcement	
Figure	**Format of Data Relationship**
AIV.58	DSRW test results show influence of MgO additive, Coupon #2 sides 1 and 2
AIV.59	CCS test results show the influence of MgO additive

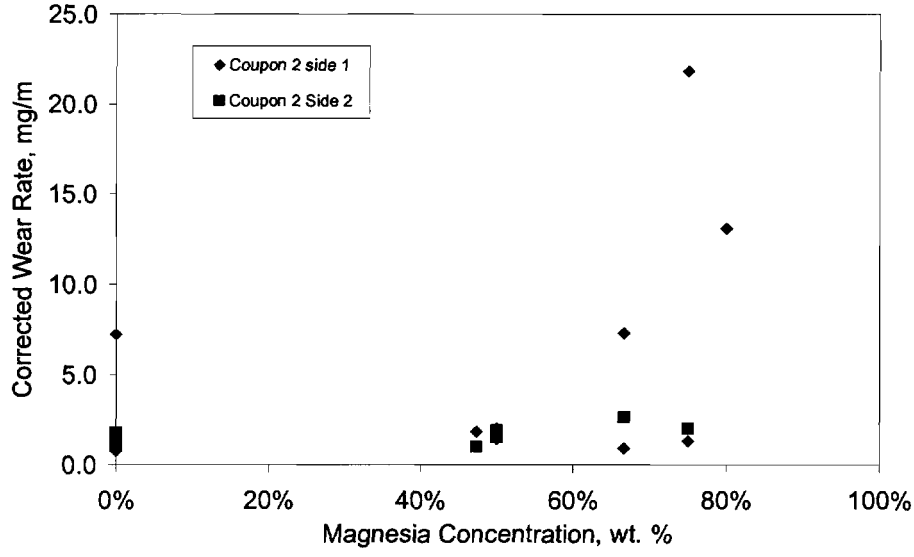

Figure AIV.58. DSRW test results show influence of MgO additive on Fondu cement. Coupon #2 sides 1 and 2 data from ten batches are shown: B11-23-1, B12-18-2, B9-8-1, B11-30-1, B12-7-1, B12-1-1, B12-8-1, B12-2-1, B12-9-1 and B12-3-1. High-density zirconia grog reinforcement was used.

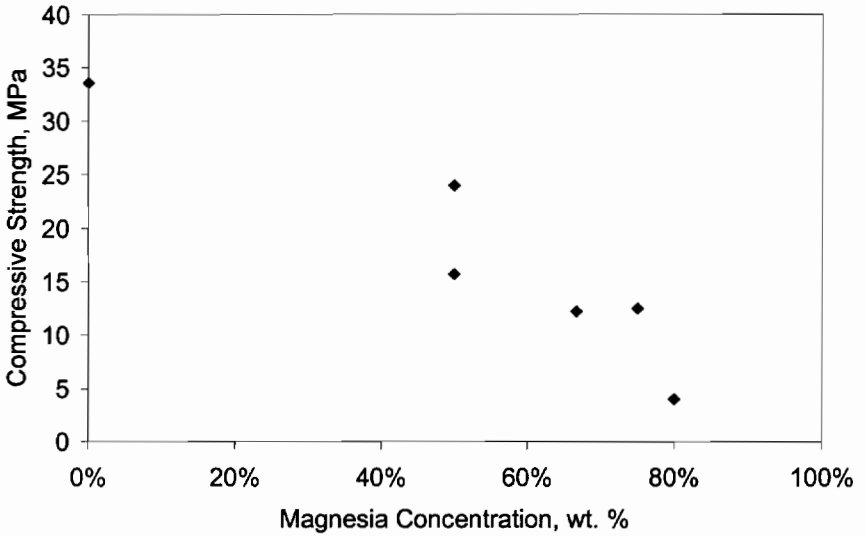

Figure AIV.59. CCS test results show the influence of MgO additive on Fondu cement. Ten batches with two controls: B11-23-1, B12-18-2, B9-8-1, B11-30-1, B12-7-1, B12-1-1, B12-8-1, B12-2-1, B12-9-1 and B12-3-1. High-density zirconia grog reinforcement was used.

Table AIV.10 Fondu Cement/ MgO / Spinel.

Fondu Cement and MgO Additive and Spinel Reinforcement	
Figure	**Format of Data Relationship**
AIV.60	DSRW test results show influence of MgO additive, Coupon #2 sides 1 and 2
AIV.61	CCS test results show the influence of MgO additive

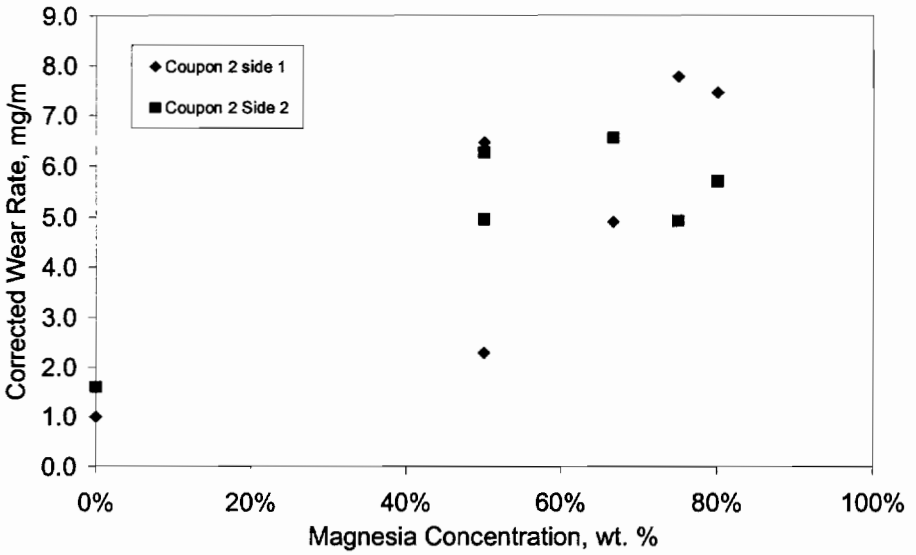

Figure AIV.60. DSRW test results show influence of MgO additive on Fondu cement. Coupon #2 sides 1 and 2 data from seven batches are shown: B9-28-1, B10-26-1, B9-30-1, B10-23-1, B10-5-1, B10-7-1 and B10-12-1.. Crushed spinel brick reinforcement was used.

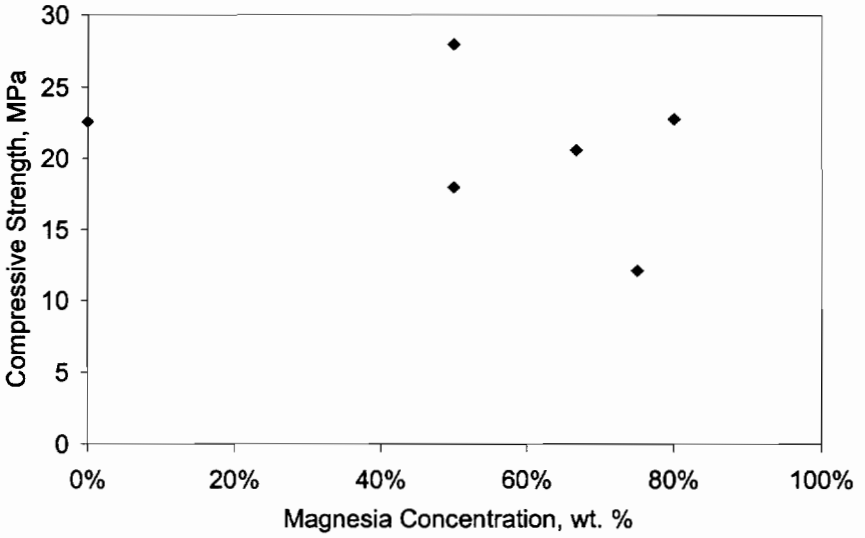

Figure AIV.61. CCS test results show the influence of MgO additive on Fondu cement. The data from seven batches are shown: B9-28-1, B10-26-1, B9-30-1, B10-23-1, B10-5-1, B10-7-1 and B10-12-1. Crushed spinel brick reinforcement was used.

Table AIV.11 Fondu Cement and Spinel Additive and Spinel Reinforcement.

Fondu Cement and Spinel Additive and Spinel Reinforcement	
Figure	**Format of Data Relationship**
AIV.62	DSRW test results show influence of spinel additive, Coupon #2 sides 1 and 2
AIV.63	DSRW test results show influence of water to cement ratio, Coupon #2 sides 1 and 2
AIV.64	CCS test results show the influence of spinel additive

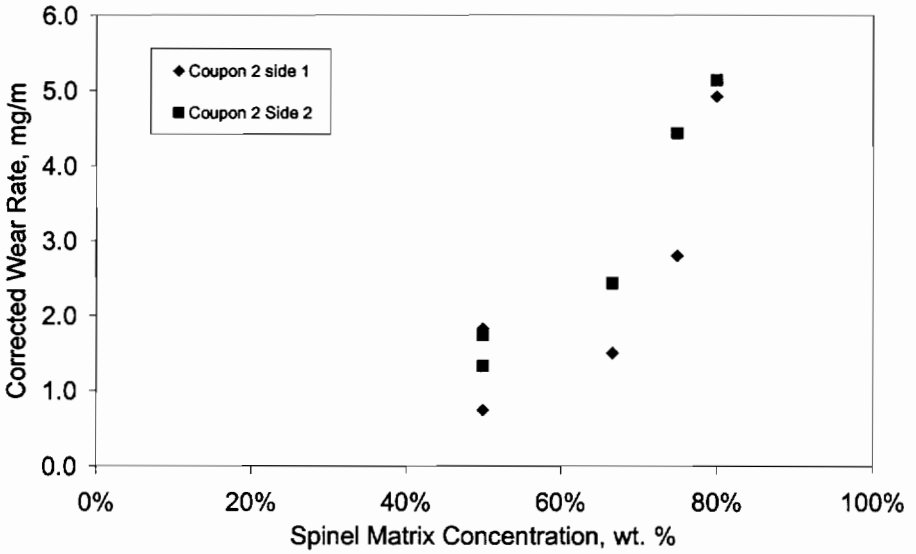

Figure AIV.62. DSRW test results show influence of spinel additive on Fondu cement. Coupon #2 sides 1 and 2 data from six batches are shown: B9-28-1, B10-26-1 B10-2-1, B10-16-1, B10-14-1, and B10-19-1. Crushed spinel brick reinforcement was used.

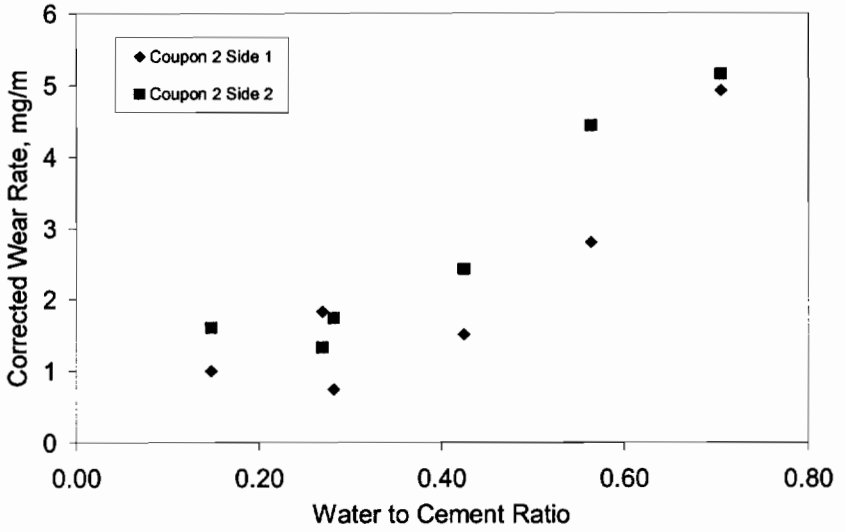

Figure AIV.63. DSRW test results show influence of the water to cement ratio of the data set that studies the influence of spinel additive on Fondu cement. Coupon #2 sides 1 and 2 data from six batches are shown B9-28-1, B10-26-1 B10-2-1, B10-16-1, B10-14-1 and B10-19-1. Crushed spinel brick reinforcement was used.

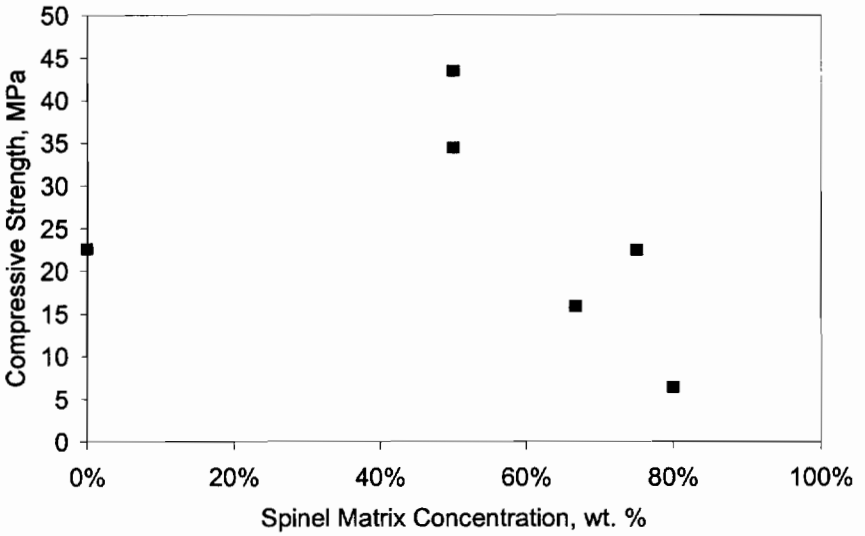

Figure AIV.64. CCS test results show the influence of spinel additive on Fondu cement. The data from six batches are shown B10-26-1 B10-2-1, B10-16-1, B10-14-1, B10-19-1 and B10-21-1. Crushed spinel brick reinforcement was used.

Table AIV.12 Fondu Cement/ MgO / Zirconia and Spinel.

Fondu Cement and MgO Additive and Zirconia Grog and Spinel Reinforcement	
AIV.65	Wear scar results show difference between high density grog and spinel reinforcement, MgO additive concentration constant at 50%, Coupon #2 sides 1 and 2

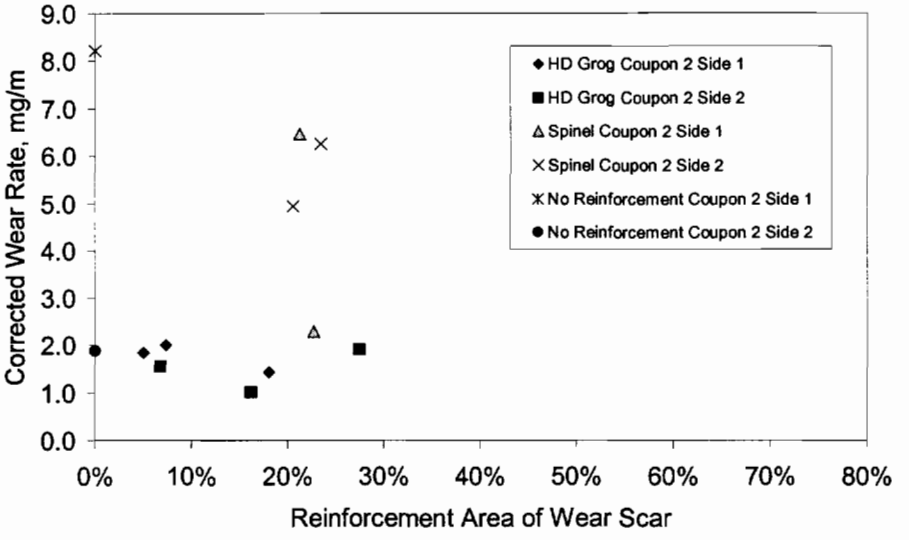

Figure AIV.65. DSRW wear scar analysis results show the relative difference between the high density grog and the spinel reinforcement formulated with the Fondu cement. MgO additive was used and concentration held constant at 50% by batch weight. Coupon #2 sides 1 and 2 data from six batches are shown: B9-8-1, B11-30-1, B12-7-1, B9-3-1, B9-30-1 and B10-23-1.

Table AIV.13 Fondu Cement/Spinel/Zirconia and Spinel.

Fondu Cement and Spinel Additive and Zirconia Grog and Spinel Reinforcement	
Figure	**Format of Data Relationship**
AIV.66	Wear scar results show difference between high density grog and spinel reinforcement. Spinel additive concentration constant at 50%, Coupon #2 sides 1 and 2

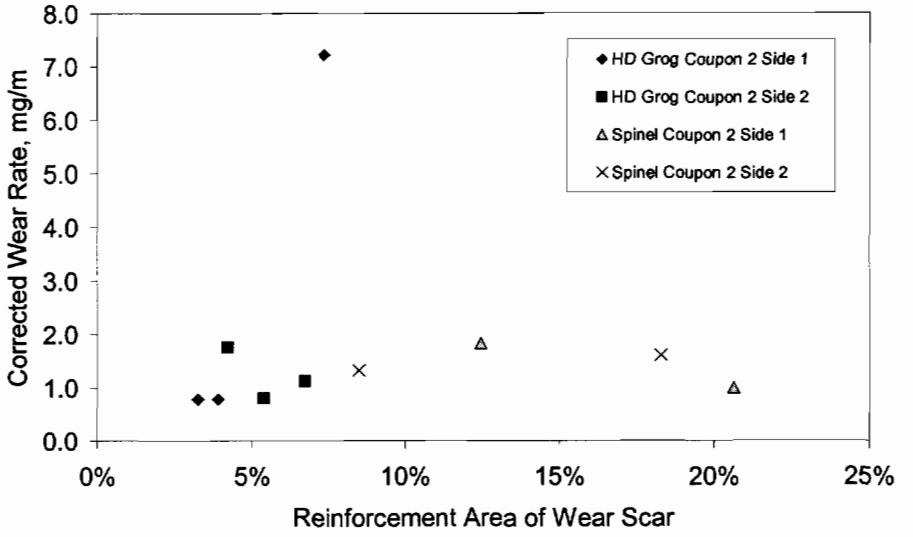

Figure AIV.66. DSRW wear scar analysis results show the relative difference between the high density grog and the spinel reinforcement formulated with the Fondu cement. Spinel additive was used and concentration held constant at 50% by batch weight. Coupon #2 sides 1 and 2 data from six batches are shown: B9-10-1, B10-2-1, B11-23-1, B12-18-2, B9-28-1 and B10-26-1.

Table AIV.14 CA_2 Cement/ No Additive/ No Reinforcement.

CA_2 Cement and No Additive and No Reinforcement	
Figure	**Format of Data Relationship**
AIV.67	DSRW test results show influence batch water on the wear rate, Coupon #2 sides 1 and 2
AIV.68	CCS test results show influence batch water on the compression strength

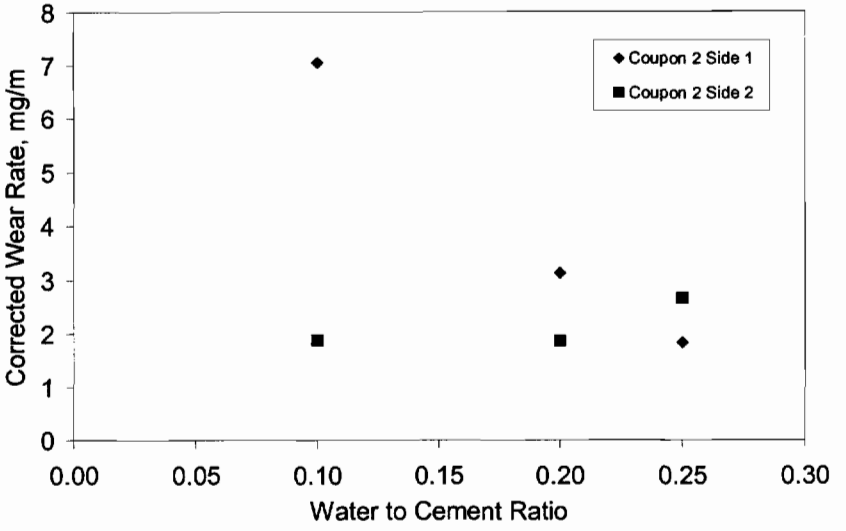

Figure AIV.67. DSRW test results show influence batch water on the wear rate of coupons made using the calcium dialuminate blend cement. Coupon #2 sides 1 and 2 data from three batches are shown: B1-19-1, B1-20-1 and B1-29-2.. No reinforcement was used.

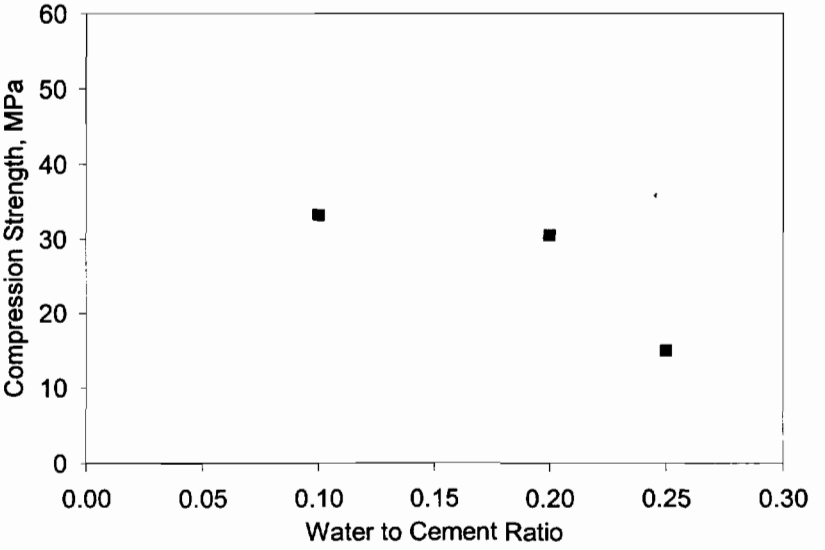

Figure AIV.68. CCS test results show influence batch water on the compression strength of coupons made using the calcium dialuminate blend cement. Coupon #2 sides 1 and 2 data from three batches are shown B1-19-1, B1-20-1 and B1-29-2. No reinforcement was used.

Table AIV.15 CA_2 Cement/ No Additive/ DB MgO.

CA_2 Cement and No Additive and DB MgO Rock Reinforcement	
Figure	**Format of Data Relationship**
AIV.69	DSRW test results show the influence of changing reinforcement on the wear rate, reinforcement at 40, 60 and 75%.
AIV.70	DSRW wear scar results show the influence of changing exposed reinforcement on the wear rate, reinforcement at 40 and 75%
AIV.71	CCS test results show the influence of changing reinforcement on the compression strength, reinforcement at 40 and 75%

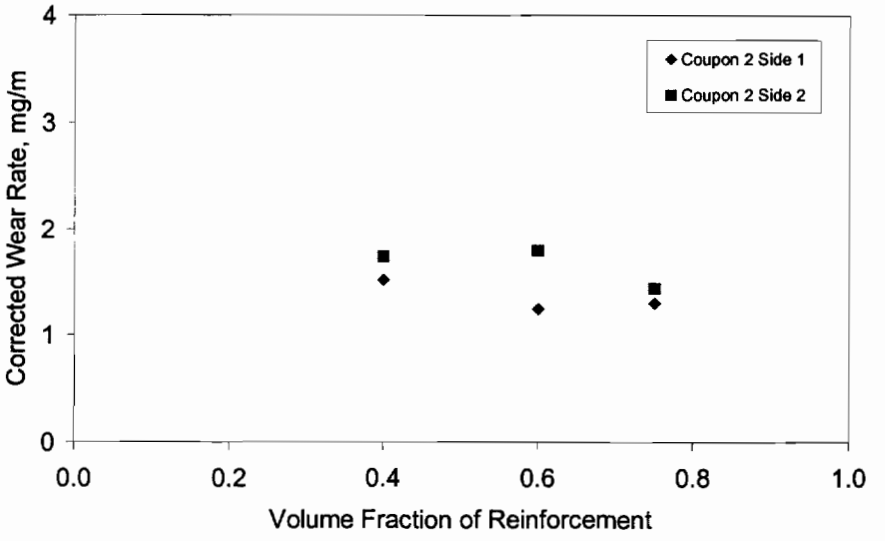

Figure AIV.69. DSRW test results show the influence of changing reinforcement volume fraction on the wear rate. Three batches: B4-27-1, B2-22-1 and B5-12-1 at three reinforcement concentrations. Dead burnt magnesia rock reinforcement at 40, 60 and 75%.

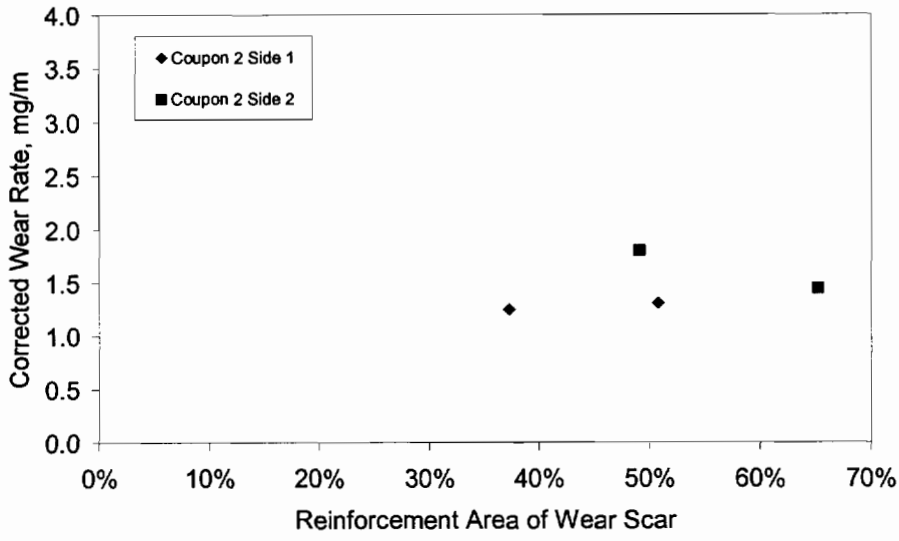

Figure AIV.70. DSRW wear scar analysis results show the influence of changing the exposed reinforcement area on the wear rate. Results from two batches, B2-22-1 and B5-12-1, are shown. Dead burnt magnesia rock at 40 and 75% was used for reinforcement.

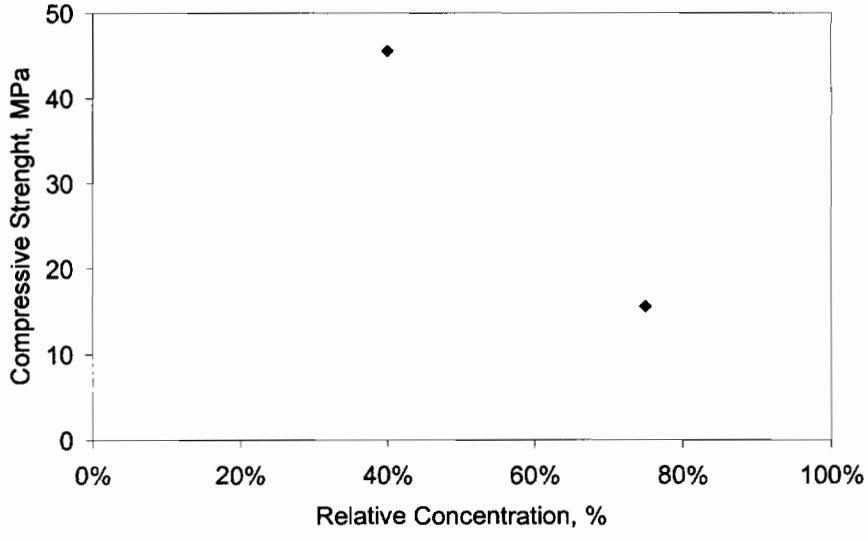

Figure AIV.71. CCS test results show the influence of changing reinforcement concentration on the compression strength. Results from batches B2-22-1 and B5-12-1 at reinforcement concentrations of 40 and 75% by weight are shown. Dead burnt magnesia rock reinforcement was the reinforcement material.

Table AIV.16 CA_2 Cement/ No Additives/ Graded Spinel.

CA_2 Cement and No Additives and Graded Spinel Reinforcement	
Figure	**Format of Data Relationship**
AIV.72	DSRW test results show influence of changing reinforcement on the wear rate, reinforcement at 40 and 60%.

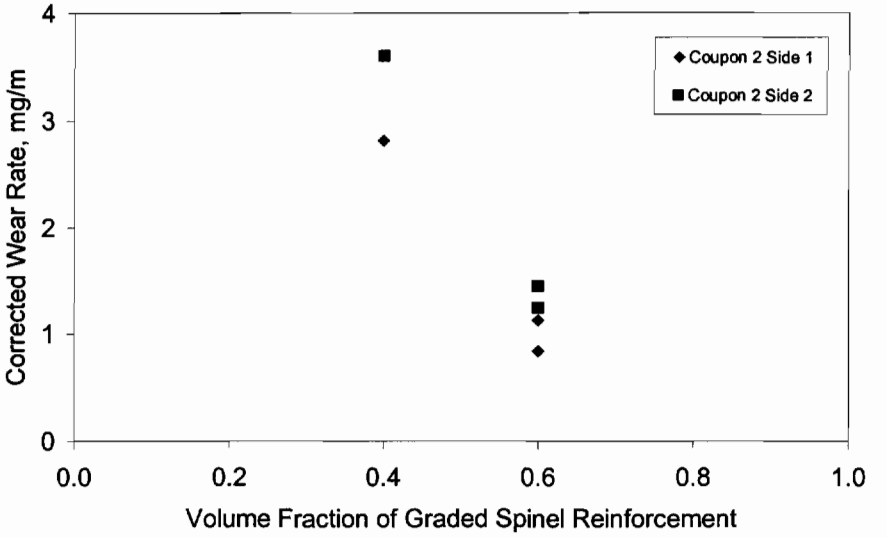

Figure AIV.72. DSRW test results show the influence of changing reinforcement volume fraction on the wear rate. Three batches were formulated B4-19-1, B4-2-1 and B4-5-1 using graded blend of crushed spinel refractory brick reinforcement at 40 and 60%.

Table AIV.17. CA_2 Cement/No Additives/Zirconia.

CA_2 Cement and No Additives and Zirconia Grog Reinforcement	
Figure	**Format of Data Relationship**
AIV.73	DSRW test results show influence of changing reinforcement on the wear rate, reinforcement at 40, 60 and 75%.
AIV.74	CCS test results show influence of changing reinforcement on the wear rate, reinforcement at 60 and 75%

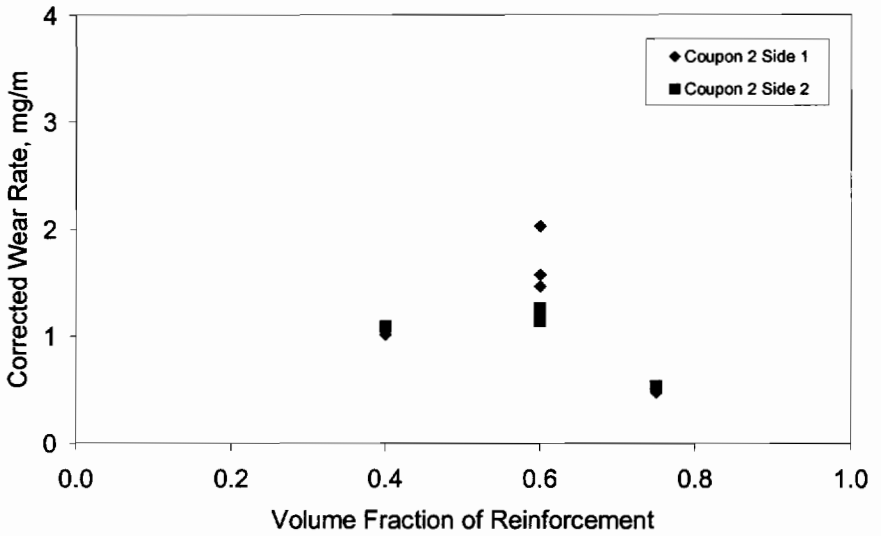

Figure AIV.73. DSRW test results show influence of changing high density zirconia grog reinforcement concentration on the wear rate. Five batches: B3-14-1, B1-12-1, B3-12-1, B1-15-1 and B1-28-1 at three reinforcement concentrations 40, 60 and 75%.

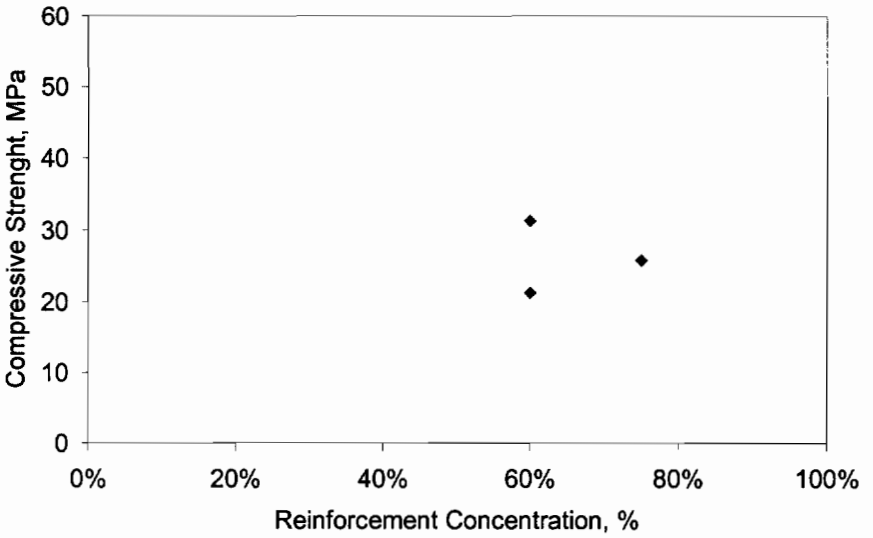

Figure AIV.74. CCS test results show influence of changing high density zirconia grog reinforcement concentration on the wear rate. Three batches: B1-12-1, B3-12-1and B1-15-1 and at three reinforcement concentrations 60 and 75%.

Table AIV.18 CA_2 Cement/ DB MgO/DB MgO.

CA_2 Cement and DB MgO Additive and DB MgO Reinforcement	
Figure	**Format of Data Relationship**
AIV.75	DSRW test results show dead burnt magnesia influence on the wear rate, Coupon #2 sides 1 and 2, reinforcement at 40%.
AIV.76	Wear scar results show the exposed reinforcement influence on the wear rate, Coupon #2 sides 1 and 2, reinforcement at 40%
AIV.77	CCS test results show the influence of dead burnt magnesia on the compression strength, Coupon #3, reinforcement at 40%
AIV.78	CCS test results are compared to the open porosity, Coupon #3 reinforcement at 40%

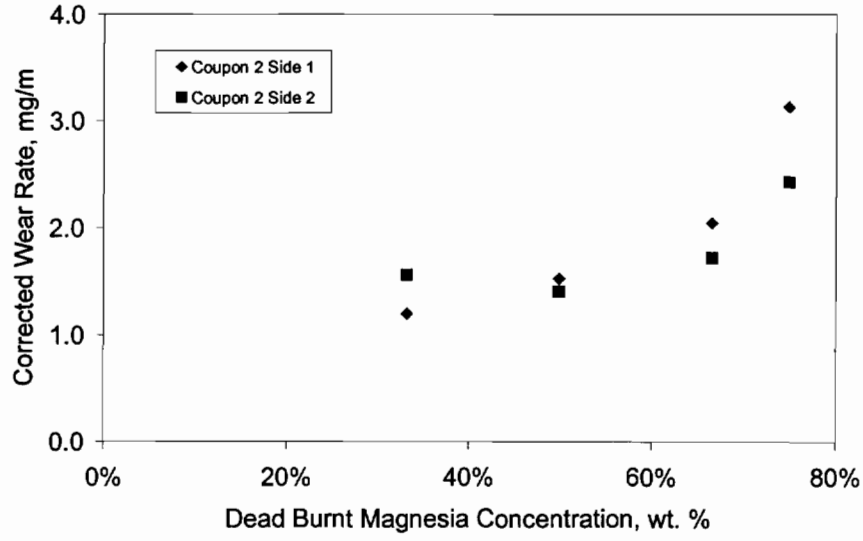

Figure AIV.75. DSRW test results show dry milled dead burnt magnesia influence on the wear rate. The data from Coupon #2 sides 1 and 2 batches B4-28-1, B4-30-1, B5-10-1 and B4-29-1 are presented. The dead burnt magnesia rock reinforcement concentration was held constant at 40%.

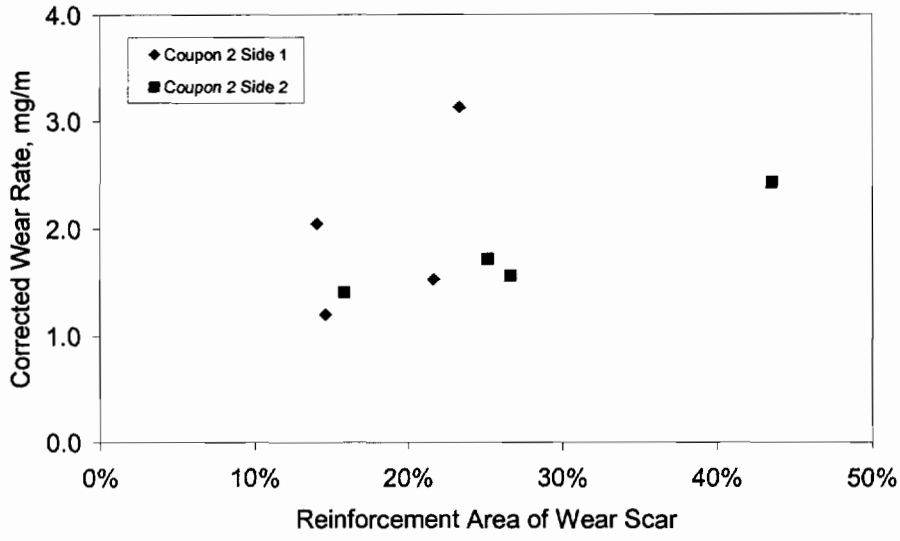

Figure AIV.76. DSRW wear scar analysis results show the exposed reinforcement and wear rate relationship. The data from Coupon #2 sides 1 and 2 batches B4-28-1, B4-30-1, B5-10-1 and B4-29-1 are presented. The dead burnt magnesia rock reinforcement concentration was held constant at 40%.

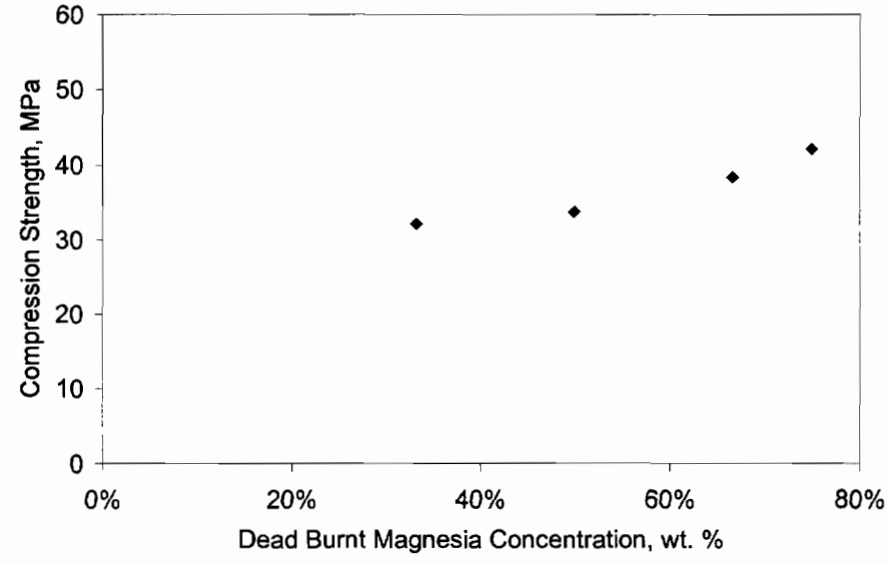

Figure AIV.77. CCS test results show the influence of increasing dry milled dead burnt magnesia on the compression strength. The data are from Coupon #3 batches B4-28-1, B4-30-1, B5-10-1 and B4-29-1. The dead burnt magnesia rock reinforcement concentration was held constant at 40%.

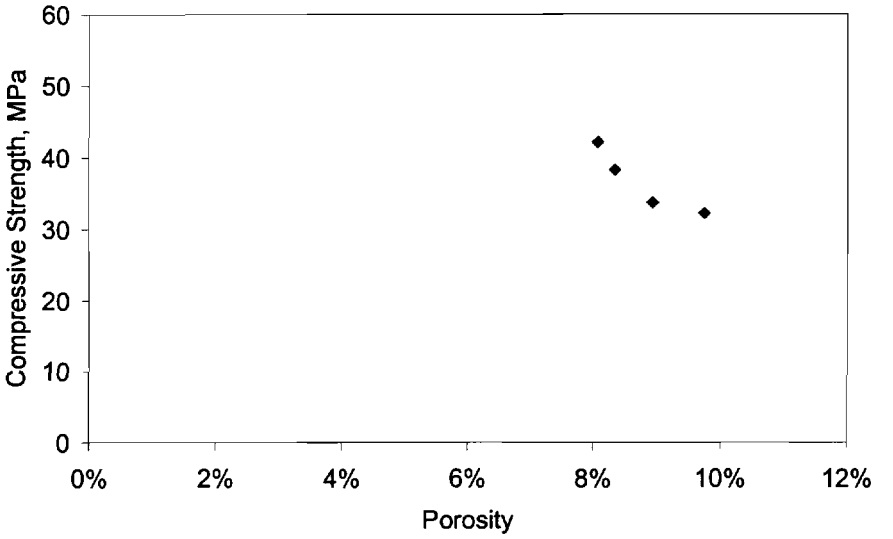

Figure AIV.78. CCS test results are compared to the open porosity determined for each coupon. The data are from Coupon #3 batches B4-28-1, B4-30-1, B5-10-1 and B4-29-1. The dead burnt magnesia rock reinforcement concentration was held constant at 40%.

Table AIV.19. CA_2 Cement/ DB MgO/ Spinel.

CA_2 Cement and DB MgO Additive and Graded Spinel Reinforcement	
Figure	**Format of Data Relationship**
AIV.79	DSRW test results show dead burnt magnesia influence on the wear rate, Coupon #2 sides 1 and 2, reinforcement at 40 and 60%.
AIV.80	DSRW test results show influence of reinforcement on wear rate, reinforcement at 40 and 60%, additive at 50, 66 and 75%
AIV.81	Wear scar results show exposed reinforcement influence on wear rate, Coupon #2 sides 1 and 2 reinforcement at 40 and 60% by batch weight
AIV.82	CCS test results show influence of dead burnt magnesia on compression strength, Coupon #3 reinforcement at 40 and 60%
AIV.83	CCS test results are compared to reinforcement at 40 and 60%, Coupon #3, dead burnt magnesia additive at 50, 66 and 75%

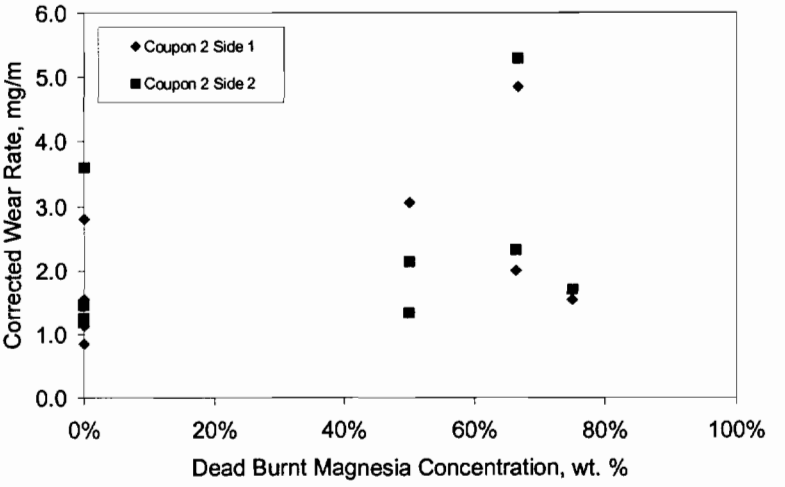

Figure AIV.79. DSRW test results show dry milled dead burnt magnesia influence on the wear rate. The data from Coupon #2 sides 1 and 2 of nine batches B4-20-1, B4-21-1, B4-19-1, B4-6-1, B4-15-1, B4-16-1, B4-14-1, B4-2-1 and B4-5-1 are presented. The batches used crushed and graded (1:4 size ratio) spinel brick reinforcement at 40 and 60% by batch weight.

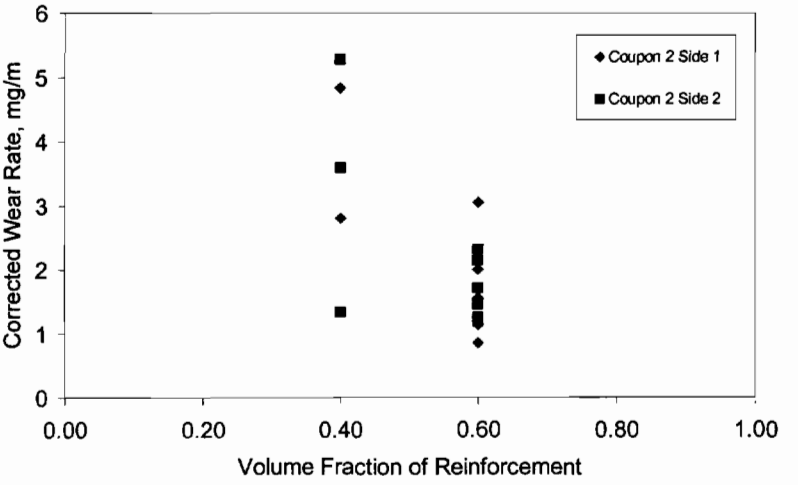

Figure AIV.80. DSRW test results show the wear rate influence of crushed and graded (1:4 size ratio) spinel brick reinforcement at 40 and 60% by batch weight. The data from Coupon #2 sides 1 and 2 of nine batches B4-20-1, B4-21-1, B4-19-1, B4-6-1, B4-15-1, B4-16-1, B4-14-1, B4-2-1 and B4-5-1 are presented. The batches used three concentrations of dry milled dead burnt magnesia, 50, 66 and 75% by batch weight.

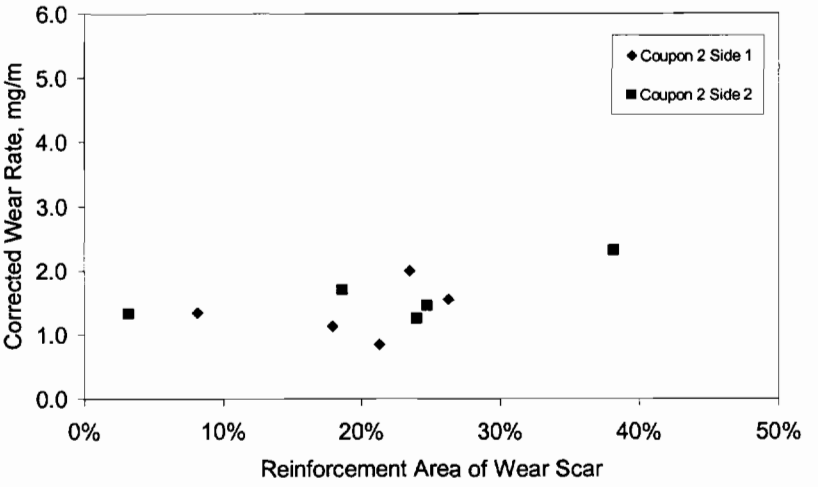

Figure AIV.81. DSRW wear scar analysis results show the exposed reinforcement and wear rate relationship. The data from Coupon #2 sides 1 and 2 of nine batches B4-20-1, B4-21-1, B4-19-1, B4-6-1, B4-15-1, B4-16-1, B4-14-1, B4-2-1 and B4-5-1are presented. The batches used crushed and graded (1:4 size ratio) spinel brick reinforcement at 40 and 60% by batch weight.

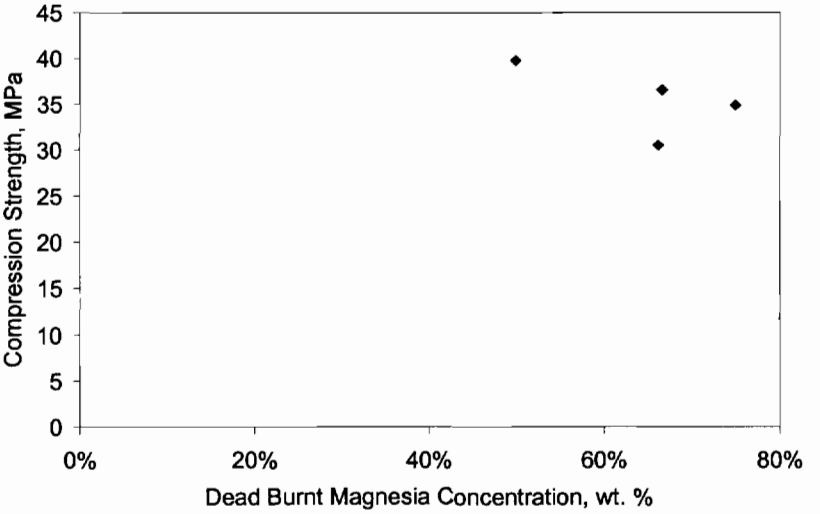

Figure AIV.82. CCS test results show the influence of increasing dry milled dead burnt magnesia on the compression strength. The data are from Coupon #3 batches nine batches B4-20-1, B4-21-1, B4-19-1, B4-6-1, B4-15-1, B4-16-1, B4-14-1, B4-2-1 and B4-5-1. The batches used crushed and graded (1:4 size ratio) spinel brick reinforcement at 40 and 60% by batch weight.

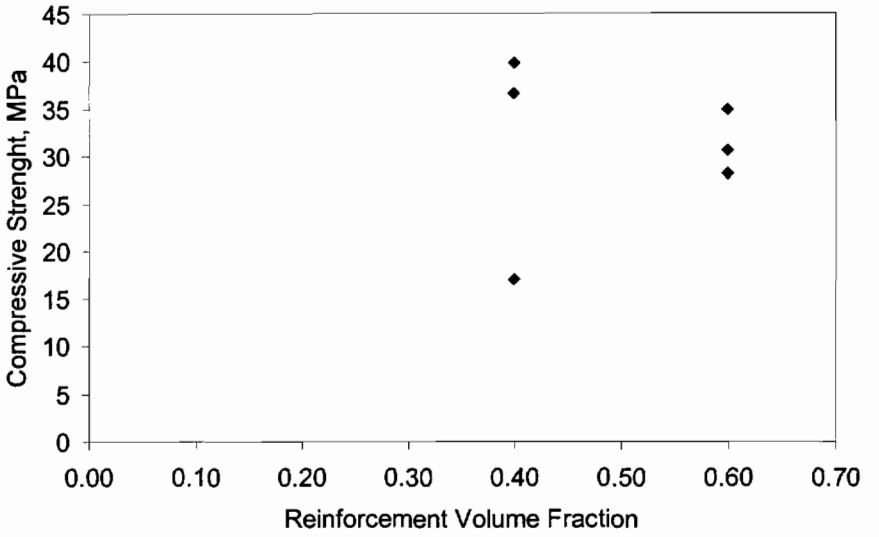

Figure AIV.83. CCS test results are compared to the crushed and graded (1:4 size ratio) spinel brick reinforcement at 40 and 60% by batch weight. The data are from Coupon #3 batches nine batches B4-20-1, B4-21-1, B4-19-1, B4-6-1, B4-15-1, B4-16-1, B4-14-1, B4-2-1 and B4-5-1. The batches were formulated using dry milled dead burnt magnesia powder additive at 50, 66 and 75% by batch weight.

Table AIV.20. CA_2 Cement/DB MgO/Zirconia.

CA_2 Cement and DB MgO Additive and Zirconia Grog Reinforcement	
Figure	**Format of Data Relationship**
AIV.84	DSRW test results show dead burnt magnesia influence on the wear rate, Coupon #2 side 2, reinforced at 40, 60 and 75%
AIV.85	DSRW test results show the reinforcement influence on the wear rate, Coupon #2 side 2 reinforced at 40, 60 and 75%, dead burnt magnesia at 33, 50, 66, 75 wt. %
AIV.86	Wear scar results show influence of exposed reinforcement on the wear rate, Coupon #2 sides 1 and 2, reinforced at 40, 60 and 75%, dead burnt magnesia at 33, 50, 66, 75 wt. %
AIV.87	CCS test results show influence of dead burnt magnesia additive on compression strength, Coupon #3, reinforcement at 40, 60 and 75%
AIV.88	CCS test results show influence of reinforcement, Coupon #3, reinforced at 40, 60 and 75% , DB magnesia at 33, 50, 66, 75 wt. %

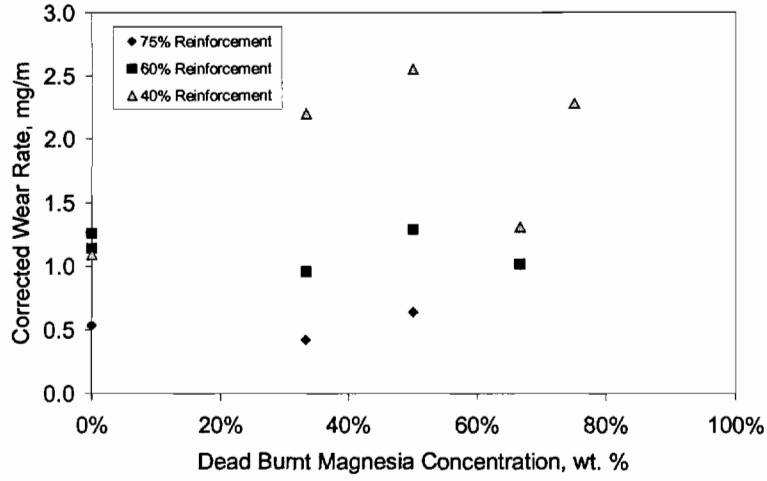

Figure AIV.84. DSRW test results show dry milled dead burnt magnesia influence on the wear rate. The data from Coupon #2 side 2 are shown for batches B3-16-1, B3-24-1, B3-25-1, B3-23-1, B3-10-1, B2-10-1, B3-9-1, B3-11-1, B3-13-1, B3-14-1, B1-12-1, B1-15-1, B1-28-1 and B3-12-1. The batches were reinforced with high-density zirconia grog at three concentrations 40, 60 and 75% by batch weight.

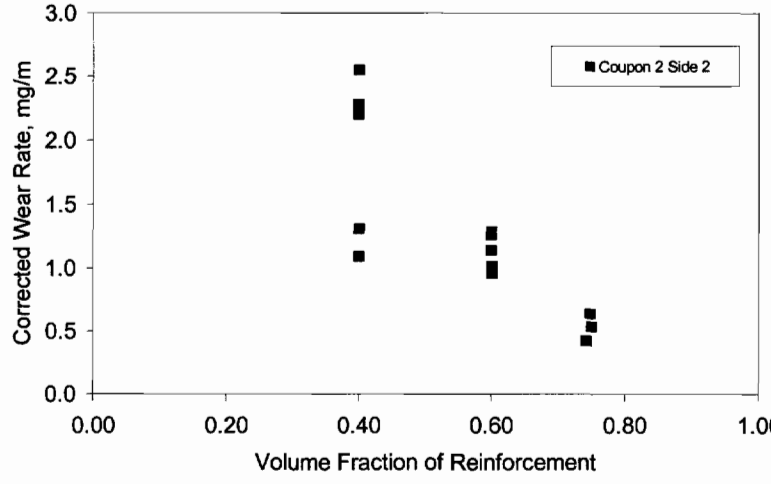

Figure AIV.85. DSRW test results show the high density zirconia grog influence on the wear rate. The data from Coupon #2 side 2 are shown for batches B3-16-1, B3-24-1, B3-25-1, B3-23-1, B3-10-1, B2-10-1, B3-9-1, B3-11-1, B3-13-1, B3-14-1, B1-12-1, B1-15-1, B1-28-1 and B3-12-1. The batches were reinforced at concentrations of 40, 60 and 75% by batch weight. Dry milled dead burnt magnesia is added at concentrations of 33, 50, 66, and 75 wt. % by batch weight.

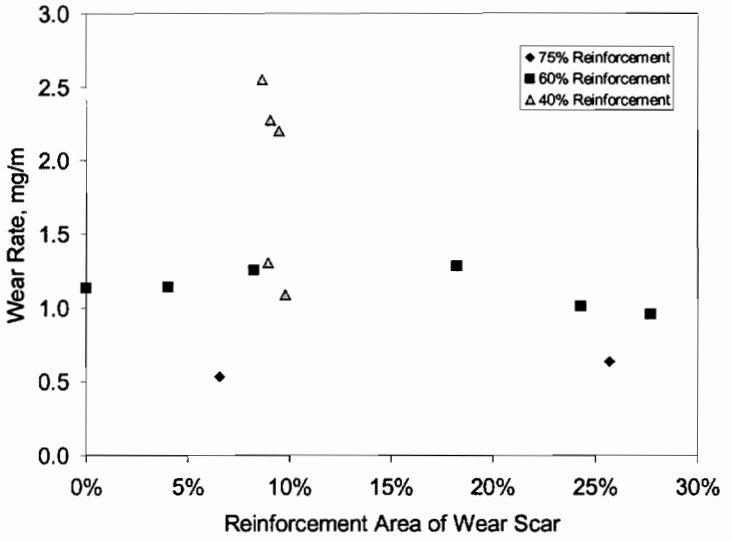

Figure AIV.86. DSRW wear scar analysis results show the exposed reinforcement and wear rate relationship. The data from Coupon #2 sides 1 and 2 for batches B3-16-1, B3-24-1, B3-25-1, B3-23-1, B3-10-1, B2-10-1, B3-9-1, B3-11-1, B3-13-1, B3-14-1, B1-12-1, B1-15-1, B1-28-1 and B3-12-1. The batches were reinforced at concentrations of 40, 60 and 75% by batch weight of high density zirconia grog. Dry milled dead burnt magnesia is added at concentrations of 33, 50, 66, 75 wt. % by batch weight.

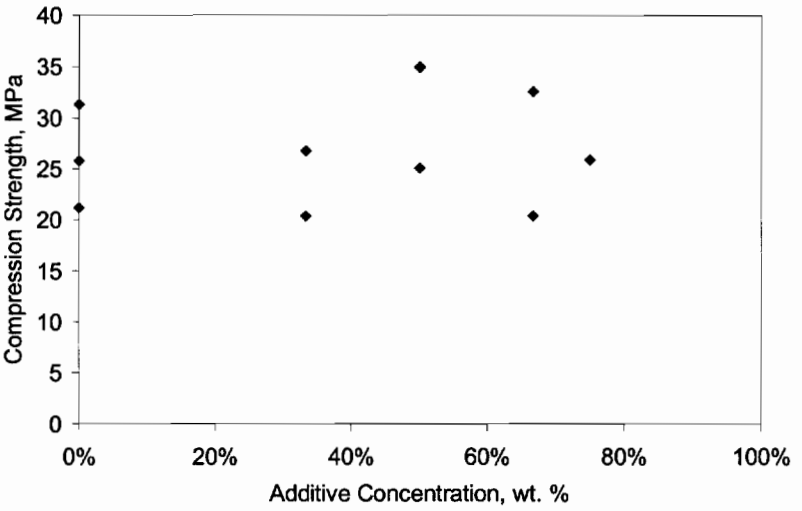

Figure AIV.87. CCS test results show the influence of dry milled dead burnt magnesia additive on the compression strength. Data are shown for batches B3-16-1, B3-24-1, B3-25-1, B3-23-1, B3-10-1, B2-10-1, B3-9-1, B3-11-1, B3-13-1, B3-14-1, B1-12-1, B1-15-1, B1-28-1 and B3-12-1. The batches were reinforced with high-density zirconia grog at three concentrations 40, 60 and 75% by batch weight.

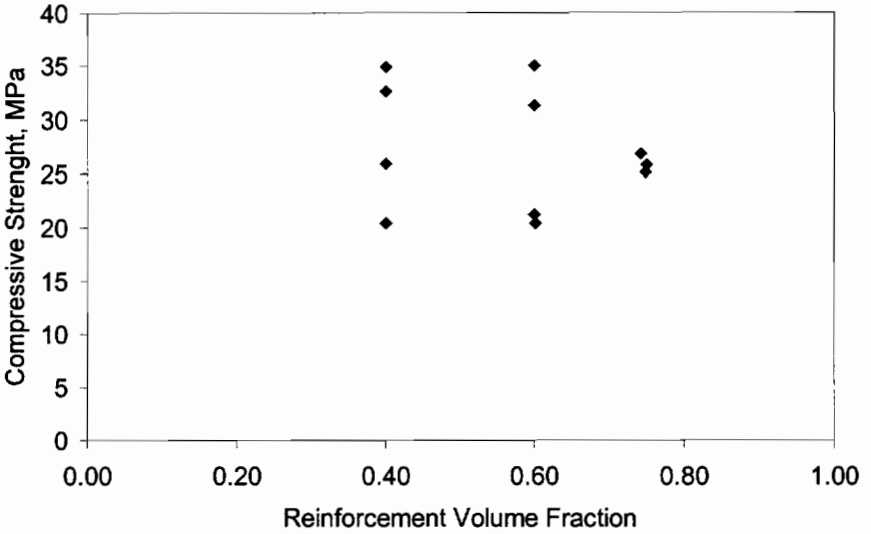

Figure AIV.88. CCS test results show the high-density zirconia grog reinforcement influence on the compression strength. The data are shown for batches B3-16-1, B3-24-1, B3-25-1, B3-23-1, B3-10-1, B2-10-1, B3-9-1, B3-11-1, B3-13-1, B3-14-1, B1-12-1, B1-15-1, B1-28-1 and B3-12-1. The batches were reinforced at concentrations of 40, 60 and 75% by batch weight. Dry milled dead burnt magnesia is added at concentrations of 33, 50, 66, and 75 wt. % by batch weight.

Table AIV.21 CA_2 Cement/MgO &Cr_2O_3 Blend/ Zirconia.

CA_2 Cement and MgO &Cr_2O_3 Additive and Zirconia Grog Reinforcement	
Figure	**Format of Data Relationship**
AIV.89	DSRW wear rate results show the magnesia chromia blend additive influence on the wear rate, Coupon #2 side 2, four blends of fuse cast chromia to magnesia additive are used 1:1 Blend, 1:2 Blend, 1:4 Blend and 2:1 Blend, reinforced at 60 wt. %

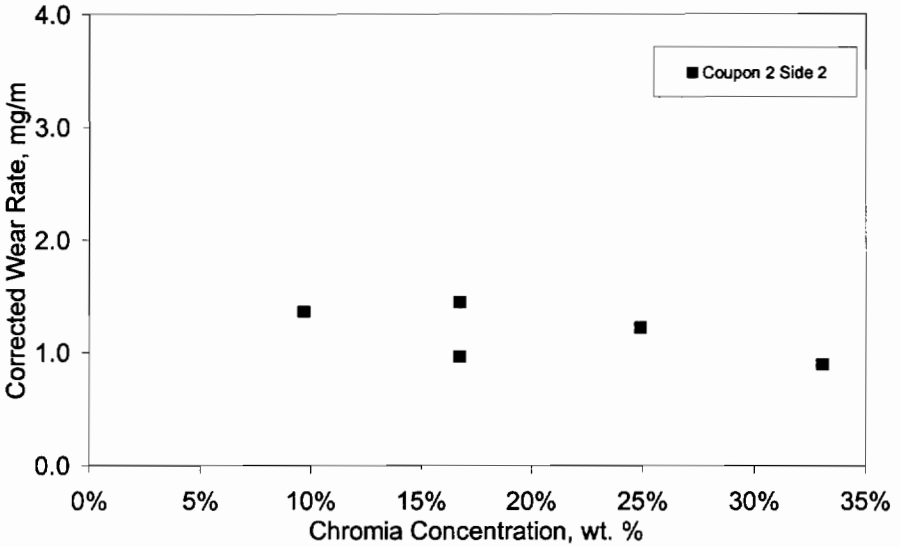

Figure AIV.89. DSRW wear rate results show the influence of magnesia chromia blend on the calcium dialuminate cement binder. Data from Coupon #2 side 2 are shown for five batches B3-29-1, B3-26-1, B3-31-1, B3-30-1 and B4-1-1. Four blends of fuse cast dense chromia to magnesia additive are used 1:1 Blend, 1:2 Blend, 1:4 Blend and 2:1 Blend. All batches were reinforced with high-density zirconia grog at 60 wt. % by batch weight.

Table AIV.22 CA_2 Cement/DB MgO-Al_2O_3 Blend/DB MgO.

CA_2 Cement and DB MgO-Al_2O_3 Additive and DB MgO Reinforcement	
AIV.90	DSRW wear rate results show dead burnt magnesia and alumina blend additive influence on the wear rate, Coupon #2 sides 1 and 2, reinforced at 60 wt. %
AIV.91	CCS test results show influence of dead burnt magnesia and alumina blend additive on the compression strength, reinforced at 60 wt. %

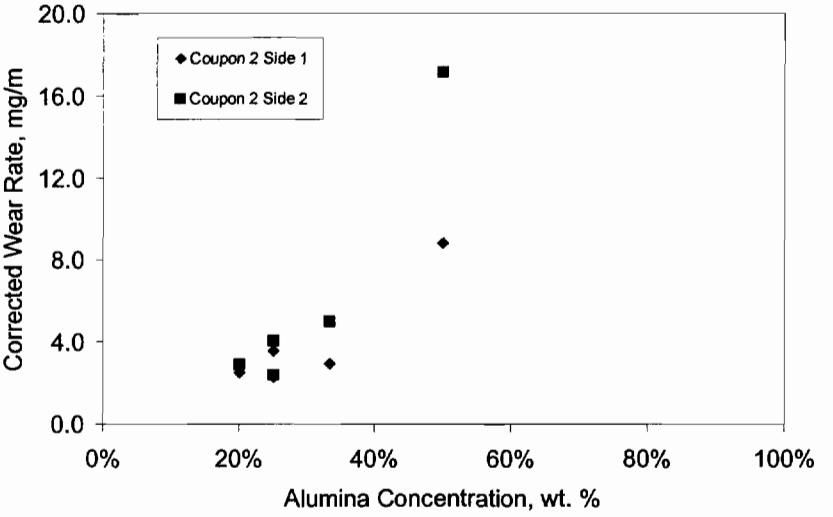

Figure AIV.90. DSRW wear rate results show the wear rate influence of dry milled dead burnt magnesia and alumina blend on the calcium dialuminate cement. Data from Coupon #2 sides 1 and 2 are shown for five batches SP8-6-1, SP8-12-1, SP8-11-1, SP8-9-1 and SP8-10-1. All batches are reinforced with dead burnt magnesia rock at 60 wt. % by batch weight.

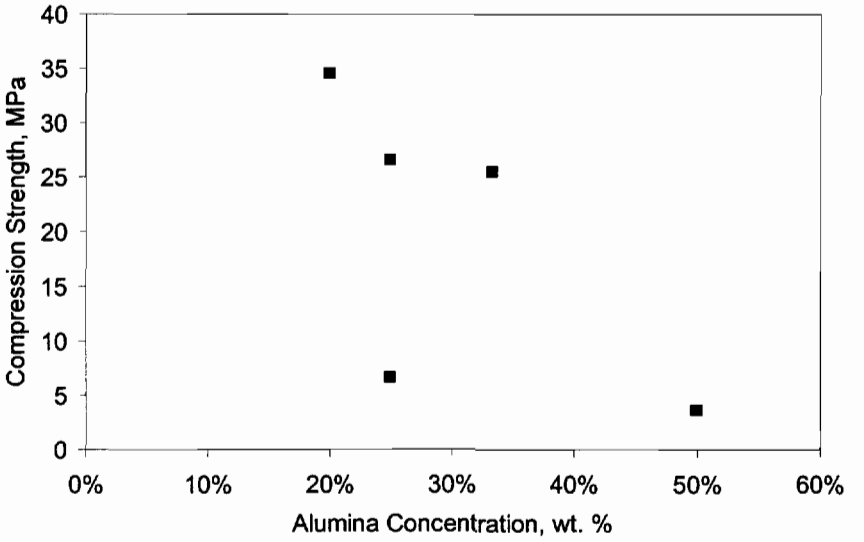

Figure AIV.91. CCS test results show the compression strength influence of dry milled dead burnt magnesia and alumina blend on the calcium dialuminate cement. Data are shown for five batches SP8-6-1, SP8-12-1, SP8-11-1, SP8-9-1 and SP8-10-1. All batches are reinforced with dead burnt magnesia rock at 60 wt. % by batch weight.

Table AIV.23. CA_2 Cement/ DB MgO and Al_2O_3-TiO_2 /DB MgO.

CA_2 Cement and DB MgO and Al_2O_3-TiO_2 Additive and DB MgO Reinforcement	
Figure	**Format of Data Relationship**
AIV.92	DSRW wear rate results show influence of alumina-titania blend additive on wear rate, Coupon #2 sides 1 and 2, reinforced at 60 wt. %
AIV.93	DSRW wear rate results show influence of dry dead burnt magnesia additive on wear rate, Coupon #2 sides 1 and 2, reinforced at 60 wt. %
AIV.94	CCS test results show influence dead burnt magnesia and alumina-titania blend additives on compression strength, reinforced at 60 wt. %

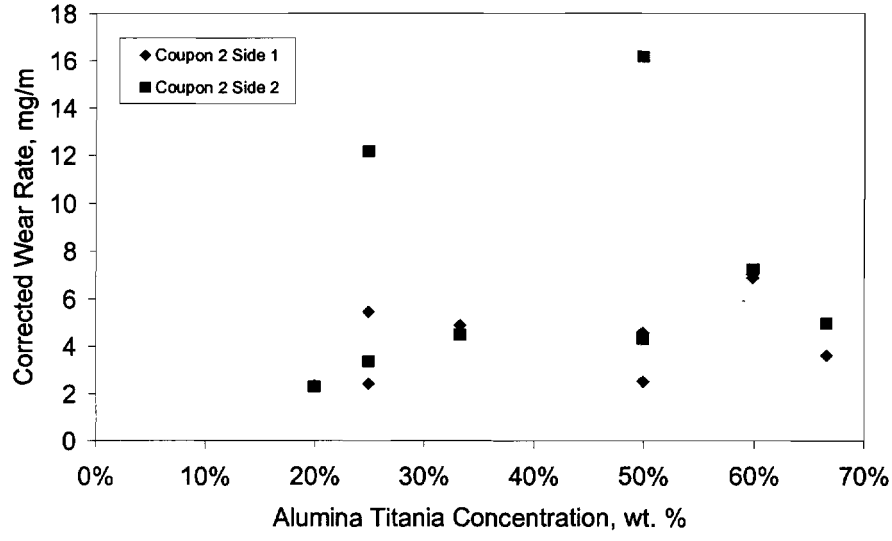

Figure AIV.92. DSRW wear rate results show the wear rate influence as a function of increasing alumina-titania blend concentration. Data from Coupon #2 sides 1 and 2 are shown for eight batches SP7-28-1, SP7-29-1, SP7-20-1, SP7-26-1, SP7-27-1, SP7-23-1, SP7-21-1 and SP7-22-1. All batches are reinforced with dead burnt magnesia rock at 60 wt. % by batch weight.

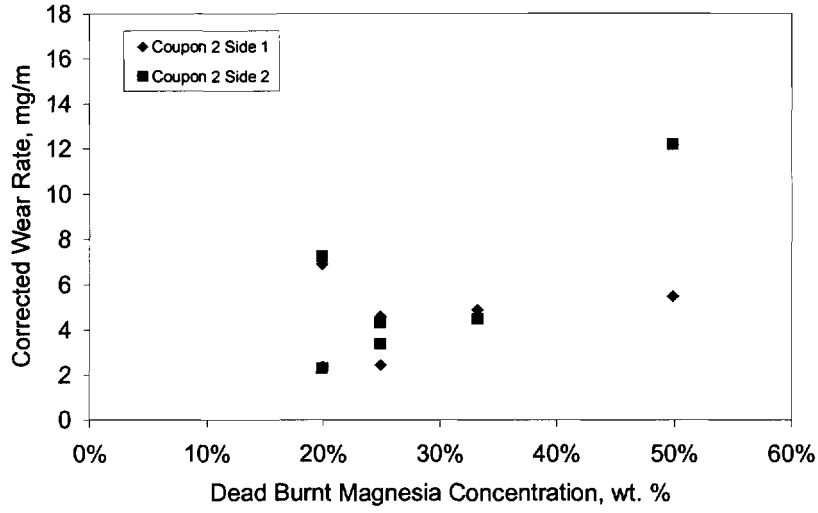

Figure AIV.93. DSRW wear rate results show the wear rate influence as a function of dry milled dead burnt magnesia concentration. Data from Coupon #2 sides 1 and 2 are shown for eight batches SP7-28-1, SP7-29-1, SP7-20-1, SP7-26-1, SP7-27-1, SP7-23-1, SP7-21-1 and SP7-22-1. All batches are reinforced with dead burnt magnesia rock at 60 wt. % by batch weight

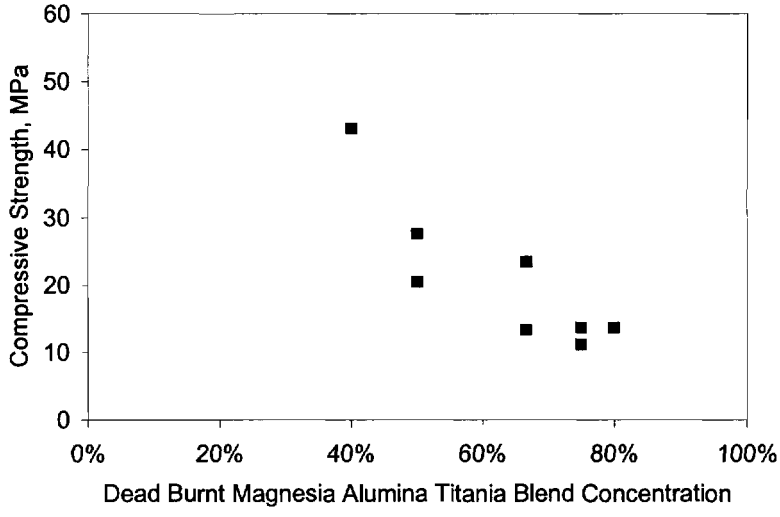

Figure AIV.94. CCS test results show the compression strength influence of dry milled dead burnt magnesia and alumina-titania blend on the calcium dialuminate cement. Data from eight batches are presented SP7-28-1, SP7-29-1, SP7-20-1, SP7-26-1, SP7-27-1, SP7-23-1, SP7-21-1 and SP7-22-1. All batches are reinforced with dead burnt magnesia rock at 60 wt. % by batch weight.

Table AIV.24. CA_2 Cement/ DB MgO-CeO_2 Blend/DB MgO.

CA_2 Cement and DB MgO-CeO_2 Additive and DB MgO Reinforcement	
Figure	**Format of Data Relationship**
AIV.95	DSRW wear rate results influence of cerium additive on the wear rate, Coupon #2 sides 1 and 2, reinforced at 60 wt. %
AIV.96	Wear scar results illustrates influence of magnesia-cerium oxide-cement blend exposed reinforcement, Coupon #2 sides 1 and 2, reinforced at 60 wt. %
AIV.97	CCS test results show influence of magnesia-cerium oxide blend additive on the compression strength, reinforced at 60 wt. %

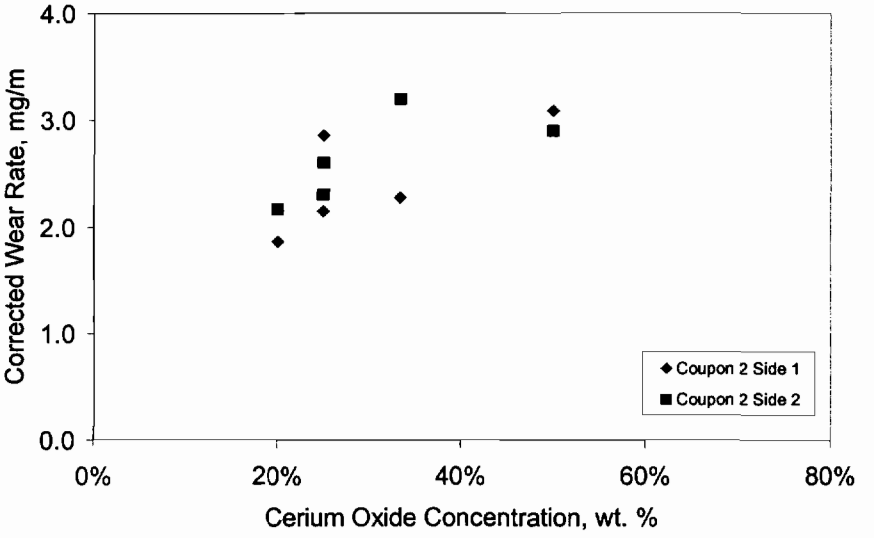

Figure AIV.95. DSRW wear rate results show the wear rate influence as a function of increasing cerium blend concentration. Data from Coupon #2 sides 1 and 2 are shown for five batch formulations SP7-30-1, SP8-4-1, SP8-3-1, SP7-31-1 and SP8-2-1. All batches are reinforced with dead burnt magnesia rock at 60 wt. % by batch weight.

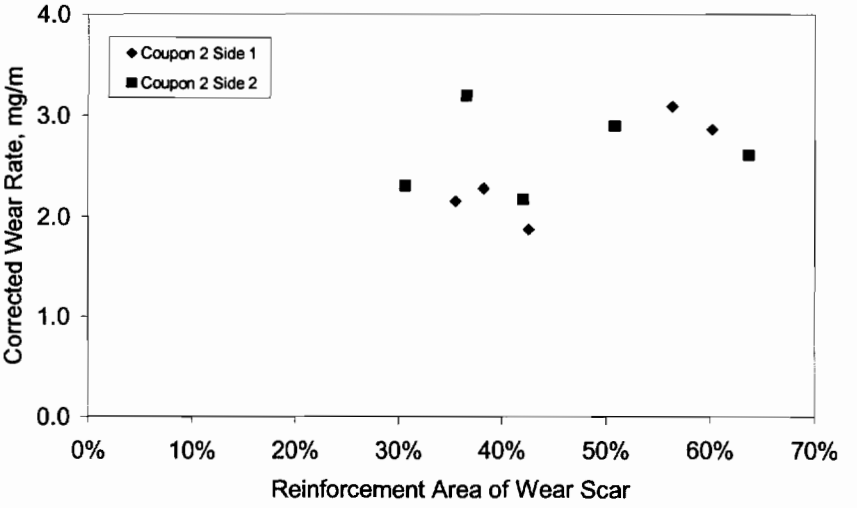

Figure AIV.96. DSRW wear scar analysis illustrates the wear rate change as a function of exposed reinforcement in the magnesia-cerium oxide-cement blend batches. Data from Coupon #2 sides 1 and 2 are shown for five batch formulations SP7-30-1, SP8-4-1, SP8-3-1, SP7-31-1 and SP8-2-1. All batches are reinforced with dead burnt magnesia rock at 60 wt. % by batch weight

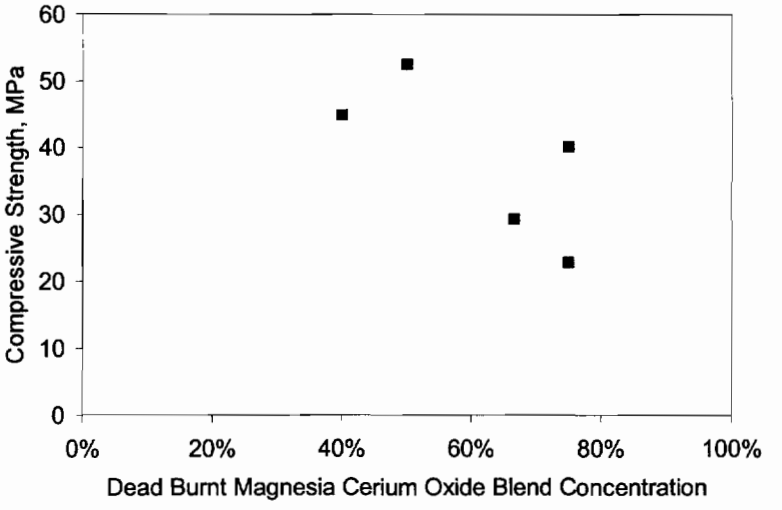

Figure AIV.97. CCS test results show the compression strength change as a function of the total magnesia-cerium oxide blend concentration. Data are presented from five batch formulations SP7-30-1, SP8-4-1, SP8-3-1, SP7-31-1 and SP8-2-1. All batches are reinforced with dead burnt magnesia rock at 60 wt. % by batch weight

Table AIV.25. CA_2 Cement/ DB MgO/ DB MgO.

CA_2 Cement and DB MgO Additive and DB MgO Reinforcement	
Figure	**Format of Data Relationship**
AIV.98	DSRW test results show influence of changing water on the wear rate, batch water adjusted at 2.8, 4, 6, 8 and 10 %, dead burnt magnesia additive at 50%, reinforced at 60%
AIV.99	CCS test results show influence of water on the compression strength, batch water adjusted at 2.8, 4, 6, 8 and 10 %, dead burnt magnesia additive at 50% and reinforced at 60%
AIV.100	DSRW test results show influence of water on the wear rate batch water adjusted at 4, 6, 8, 10 and 12 %, dead burnt magnesia additive at 50%, reinforced at 60%
AIV.101	CCS test results show influence of water on the compression strength, batch water adjusted at 4, 6, 8, 10 and 12 %, dead burnt magnesia additive at 50%, reinforced at 60%

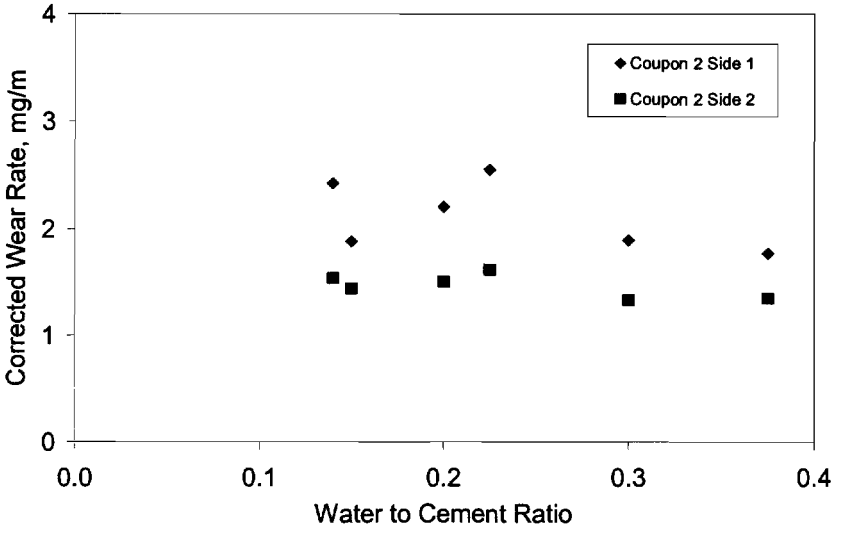

Figure AIV.98. DSRW test results show influence changing water concentration on the wear rate. Batch water was adjusted at 2.8, 4, 6, 8 and 10 % by batch weight. Wear rate data from batches SP7-6-1, SP7-7-1, SP7-8-1, SP7-9-1, SP7-12-1 and SP7-11-1 are shown. The batches were formulated using dry milled dead burnt magnesia additive at 50% and dead burnt magnesia rock at 60% by batch weight.

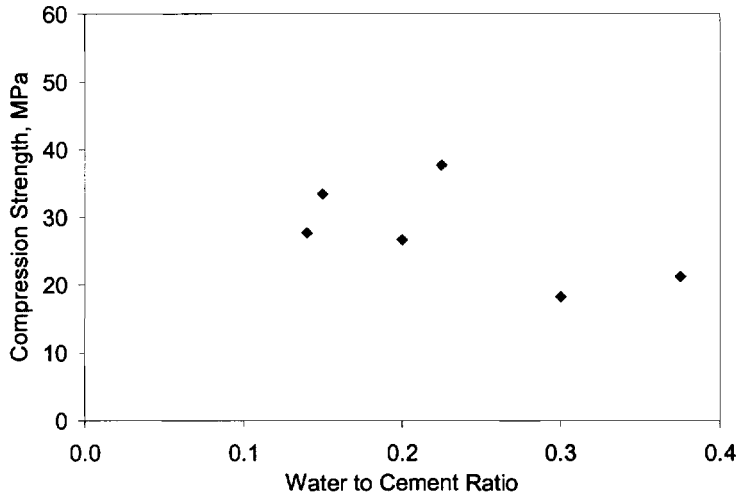

Figure AIV.99. CCS test results show influence changing water concentration on the compression strength. Batch water was adjusted at 2.8, 4, 6, 8 and 10 % by batch weight. Wear rate data from batches SP7-6-1, SP7-7-1, SP7-8-1, SP7-9-1, SP7-12-1 and SP7-11-1 are shown. The batches were formulated using dry milled dead burnt magnesia additive at 50% and dead burnt magnesia rock at 60% by batch weight.

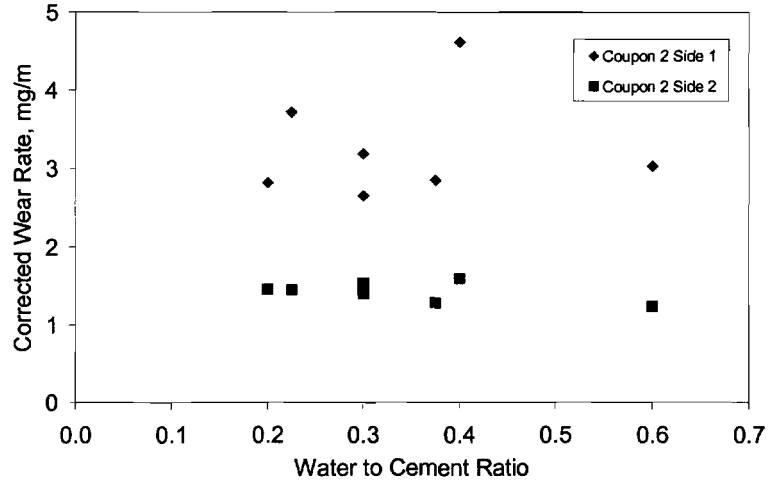

Figure AIV.100. DSRW test results show influence changing water concentration on the wear rate. Batch water was adjusted at 4, 6, 8, 10 and 12 % by batch weight. Wear rate data from batches SP7-13-1, SP7-14-1, SP7-15-1, SP7-16-1, SP7-17-1, SP7-18-1 and SP7-19-1are shown. The batches were formulated using dry milled dead burnt magnesia additive at 50% and dead burnt magnesia rock at 60% by batch weight.

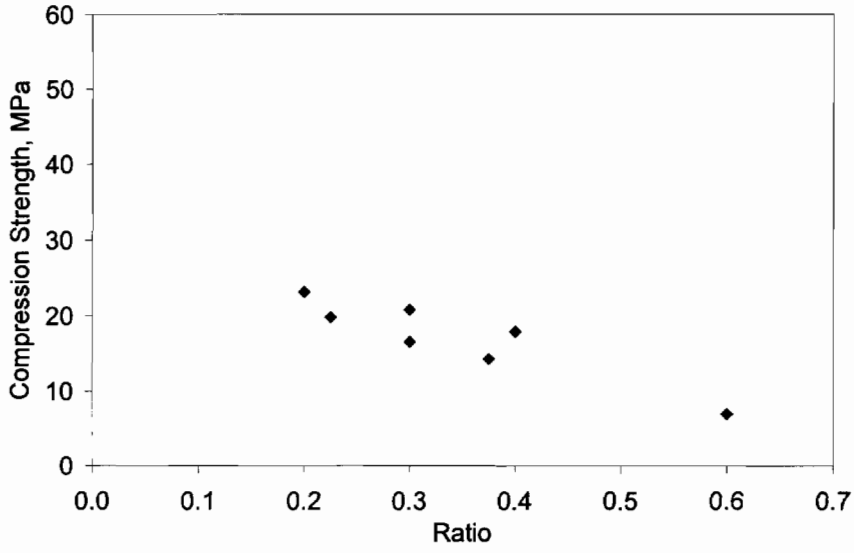

Figure AIV.101. CCS test results show influence changing water concentration on the compression strength. Batch water was adjusted at 4, 6, 8, 10 and 12 % by batch weight. Wear rate data from SP7-13-1, SP7-14-1, SP7-15-1, SP7-16-1, SP7-17-1, SP7-18-1 and SP7-19-1 are shown. The batches were formulated using dry milled dead burnt magnesia additive at 50% and dead burnt magnesia rock at 60% by batch weight.

BIOGRAPHICAL SKETCH

Robert Bruce Davis

I call the great Pacific Northwest home, as I was born in 1952 in the Seattle area and lived there until age seven when a move was made to Spokane and later, to Longview, Washington, where the family settled. I have three younger brothers, Larry, Rick, Lance and an older sister Debra. The Boy Scouts of America played a very important part in my youth; joining as a Cub Scout, becoming a Boy Scout and finally an Explorer Scout. My father and mother were very involved in our family life directing all their children toward the right path. I attended Mark Morris High School, I participated in sports, honor society, and attended Boy's State for Youth Government. Shortly before graduating in 1971, I received my draft lottery notification for the Viet Nam war and so was quite unsure of my future. That summer the war ended and I entered Washington State University with an undeclared major. Through random selection, I was assigned Dr. Bruce Mason as my student advisor. Dr. Mason proved to be very important in my life, encouraging, teaching, and becoming my friend.

I discovered a real passion for one of the oldest engineering sciences, Physical Metallurgy. I graduated from Washington State in 1976 with a Bachelors of Science degree and began my career at the Energy Research and Development Agency's National Laboratory at the Hanford Site near Richland Washington. While pursuing my engineering career working on advanced breeder reactor fuel development and spent fuel disposal strategies, I continued to attend classes in materials science and nuclear engineering at the Joint Center for Graduate Study. Later, I was asked to join the Idaho National Laboratory to work toward the reprocessing of spent nuclear fuels as an employee of Exxon Nuclear. I joined the Washington Public Power Supply System in 1981 to assist with construction and operation of commercial nuclear power stations in Washington.

In 1996 I was awarded a grant from the State of Washington to begin graduate studies in materials science. I applied for admission, and was accepted into the Masters program at the Oregon Graduate Institute. In the spring of 1998, I completed the requirements for, and received my Masters Degree in Materials Science and Engineering, which led me to pursue doctoral research in the Design and Development of Advanced Castable Refractory Materials.

Awards

1995 "EPRI Innovators in Technology" award for work with Microbiologically Influenced Corrosion, from the Electric Power Research Institute.

1986 "Engineer of the Year" award by the Inland Empire Section of the National Association of Corrosion Engineers for my work in the formation of the Southeast Washington Underground Corrosion Coordinating Council.

1979 "Distinguished Research Engineer" award by Westinghouse Advanced Energy Systems Division for Project Management work on the nation's first demonstrated disposal of spent commercial nuclear fuel at the Nevada Test Site.

Publications

1. R. Davis and A. Johnson, "Research Productivity of Academic Materials Scientists," Journal of Metals, June 1975.

2. R. Davis and J. Krogness, "Engineering Test Plan for the Materials Interaction Test," TC-1226, Hanford Engineering and Development Laboratory, Richland, WA, September 1978.

3. D. Cantley, R. Davis, and J. Krogness, "Survey Test of Canister, Geology and Fuel Cladding Material Interactions," American Nuclear Society Transactions, June 9-12, PP 426,1980.

4. R. Davis et. al, "Remote Characterization of Spent LWR Fuel For Geological Disposal Demonstrations," American Nuclear Society Transactions, June 9-23, PP 838, 1980.

5. R. Davis, "Microstructural Relationship to Flow Accelerated Corrosion," American Society of Mechanical Engineers, PVP Vol. 285, ASME 1994.

6. R. Davis, "Overview of BWR Erosion/Corrosion: The First Ten Years," Fourth International FAC Symposium, Electric Power Research Institute, 1994.

7. R. Davis, "Preparation of Samples for Mechanical Property Testing Using the FIB Workstation," Conference Proceedings, International Metallographic Society, July 1997.

8. R. Davis and M. Scholl, "Materials Selection Methodology of Refractories for Furnace Walls," Proceedings of the Pacific Northwest Materials and Manufacturing Conference, Portland Oregon, 1999.

9. D. G. Atteridge, R. Davis, M. Scholl, G. Tewksbury and M. Becker, "High Energy Plasma Spray Coating Using Micrometer and Nanometer Scale Tungsten Carbide Powder," Proceedings of the Thermal Spray Processing of Nanoscale Materials II, Quebec Canada, 1999.